frontiers | Research Topics

The urban fluvial and hydro-environment system

Edited by
Jaan H. Pu, Jiaye Li, Alfrendo Satyanaga, Snehasis Kundu,
Manish Pandey, Prashanth Reddy Hanmaiahgari
and Songdong Shao

Published in
Frontiers in Environmental Science

ISSN 1664-8714
ISBN 978-2-83250-989-0
DOI 10.3389/978-2-83250-989-0

About Frontiers

Frontiers is more than just an open access publisher of scholarly articles: it is a pioneering approach to the world of academia, radically improving the way scholarly research is managed. The grand vision of Frontiers is a world where all people have an equal opportunity to seek, share and generate knowledge. Frontiers provides immediate and permanent online open access to all its publications, but this alone is not enough to realize our grand goals.

Frontiers journal series

The Frontiers journal series is a multi-tier and interdisciplinary set of open-access, online journals, promising a paradigm shift from the current review, selection and dissemination processes in academic publishing. All Frontiers journals are driven by researchers for researchers; therefore, they constitute a service to the scholarly community. At the same time, the *Frontiers journal series* operates on a revolutionary invention, the tiered publishing system, initially addressing specific communities of scholars, and gradually climbing up to broader public understanding, thus serving the interests of the lay society, too.

Dedication to quality

Each Frontiers article is a landmark of the highest quality, thanks to genuinely collaborative interactions between authors and review editors, who include some of the world's best academicians. Research must be certified by peers before entering a stream of knowledge that may eventually reach the public - and shape society; therefore, Frontiers only applies the most rigorous and unbiased reviews. Frontiers revolutionizes research publishing by freely delivering the most outstanding research, evaluated with no bias from both the academic and social point of view. By applying the most advanced information technologies, Frontiers is catapulting scholarly publishing into a new generation.

What are Frontiers Research Topics?

Frontiers Research Topics are very popular trademarks of the *Frontiers journals series*: they are collections of at least ten articles, all centered on a particular subject. With their unique mix of varied contributions from Original Research to Review Articles, Frontiers Research Topics unify the most influential researchers, the latest key findings and historical advances in a hot research area.

Find out more on how to host your own Frontiers Research Topic or contribute to one as an author by contacting the Frontiers editorial office: frontiersin.org/about/contact

The urban fluvial and hydro-environment system

Topic editors
Jaan H. Pu — University of Bradford, United Kingdom
Jiaye Li — Dongguan University of Technology, China
Alfrendo Satyanaga — Nazarbayev University, Kazakhstan
Snehasis Kundu — National Institute of Technology, Jamshedpur, India
Manish Pandey — National Institute of Technology Warangal, India
Prashanth Reddy Hanmaiahgari — Indian Institute of Technology Kharagpur, India
Songdong Shao — Dongguan University of Technology, China

Citation
Pu, J. H., Li, J., Satyanaga, A., Kundu, S., Pandey, M., Hanmaiahgari, P. R., Shao, S., eds. (2022). *The urban fluvial and hydro-environment system*.
Lausanne: Frontiers Media SA. doi: 10.3389/978-2-83250-989-0

Table of contents

Frontiers in Environmental Science

TYPE Editorial
PUBLISHED 21 November 2022
DOI 10.3389/fenvs.2022.1075282

EDITED AND REVIEWED BY
Angela Helen Arthington,
Griffith University, Australia

*CORRESPONDENCE
Jaan H. Pu,
j.h.pu1@bradford.ac.uk

SPECIALTY SECTION
This article was submitted
to Freshwater Science,
a section of the journal
Frontiers in Environmental Science

RECEIVED 20 October 2022
ACCEPTED 14 November 2022
PUBLISHED 21 November 2022

CITATION
Pu JH, Pandey M, Li J, Satyanaga A, Kundu S and Hanmaiahgari PR (2022), Editorial: The urban fluvial and hydro-environment system.
Front. Environ. Sci. 10:1075282.
doi: 10.3389/fenvs.2022.1075282

Editorial: The urban fluvial and hydro-environment system

Jaan H. Pu[1]*, Manish Pandey[2], Jiaye Li[3], Alfrendo Satyanaga[4], Snehasis Kundu[5] and Prashanth Reddy Hanmaiahgari[6]

[1]Faculty of Engineering and Informatics, University of Bradford, Bradford, United Kingdom, [2]National Institute of Technology, Warangal, India, [3]Dongguan University of Technology, Dongguan, China, [4]Nazarbayev University, Nur-Sultan, Kazakhstan, [5]National Institute of Technology, Jamshedpur, India, [6]Indian Institute of Technology, Kharagpur, India

KEYWORDS

urbanization, river network, hydrodynamics, hydro-environment, sustainability, fluvial management, urban flood management

Editorial on the Research Topic
The urban fluvial and hydro-environment system

Introduction

With the rapid urbanization of cities around the world, water security, flood control, and urban hydro-environmental management have become important tasks to tackle. The majority of large to megacities are located in delta regions surrounded by river networks, due to their historical development. They are not only threatened by floods from upstream river basins, but also endangered by the challenges of urban hydro-environmental governance. Fast urbanization causes interference and fragmentation of the river system and impedes its hydrodynamic potential, which is a primary driver of flooding, pollution, and sediment deposition. Consequently, water security and environmental problems are major issues for sustainable urban development.

The purpose of this Research Topic (RT) is to examine the latest advances and developments in addressing the challenges in urban fluvial and freshwater systems as well as to discuss the opportunities they create for improvement in modelling, management practices and governance. This RT consists of twenty research articles from 99 authors under three different research themes, which feature contributions on urban space management, water pollution mitigation and urban watercourse behavioural sciences to strengthen resilience. The RT includes the following themes:

- State-of-the-art numerical models,
- Urban environmental and hydrological advances, and
- Sustainable cities implementation.

State-of-the-art numerical models

Urban river networks are usually subjected to physical and environmental changes over time. Numerical studies present an effective way to investigate such networks and their alteration in structure and function. The work by Wang et al. employed numerical non-stochastic quasi-uniform iterative binary tree networks (QU-IBTNs) to simulate two natural river networks. The Yellow River in China and the Amazon River in South America have been used for the validation of the proposed model. Liu et al. further investigated the Smoothed Particle Hydrodynamics (SPH) model using two types of Particles Shifting Techniques (PSTs). Their proposed model with optimized PST was suggested for the practical applications. Tian et al. proposed a SPH-SWE (Smoothed Particle Hydrodynamics-Shallow Water Equations) diffusion model to study the diffusion process of soluble and insoluble pollutants transport in the Nanmenxia River. Their study demonstrates that the SPH-SWE method has great potential for simulating the dispersal process of pollutants. In terms of flood modelling, Ding et al. studied the Gengdi village flash flood incident with an efficient and accurate coupled water-sediment model. The proposed model was established with a Godunov-type finite volume depth-averaged flow approach. Moreover, a sediment module and OPENMP parallel computing module were added to enhance the model's capability. They found a direct relationship between the sedimentation intensity and the magnitude of Alpine flash floods, thus proving to be a powerful tool for the detection of the effects of flash floods on sedimentation processes.

In small-scale hydrodynamic modelling, Cho et al. characterized open channel flows for rough bed and rigid lid (rigid cover to flow) using Computational Fluid Dynamics (CFD). It was observed that turbulent structures produced from the rough bed flow interact with the free water surface. However, for rigid lid flow, its Reynolds stresses associated with the vertical velocity fluctuation were artificially reduced to zero near the lid due to the boundary condition assignation. That led to no vertical fluctuations, and thus reduced the turbulence structure estimation accuracy near the lid. The investigation by Wang et al. studied the generation and transport of turbulence associated with flow separation around submerged structures. Results of the study showed that the developed Incompressible Smoothed Particle Hydrodynamics (ISPH) method with the k-ε turbulence closure model is capable of reproducing the velocity fields and the turbulence characteristics accurately, and thus can be used to represent comprehensive hydrodynamics of flow-structure interactions in urban hydro-environmental systems. Liu et al. described model integration methods for the hydro-model platform under cloud computing environments, and proposed two methods of model integration, namely EXE integration and interactive integration methods. It suggested a solution to the plug-and-play problem when running more than one software model under concurrent simulations. The different scenarios were passed among the software to encapsulate different conditions. It was found that the interactive integration method can be used as a tool to solve the problem of real-time data transfer. Also, these integrated models can be accessed by end-users anywhere and can be driven by the described platform to perform real simulations.

Urban environmental and hydrological advances

Fluvial environments around the world have been increasingly stressed and altered by the urbanization process. One such stresses is the sediment transport and debris-induced flow that can cause pollutant related issues. The study by Shu et al. found that the overflow rate was dominant in controlling the debris flow formation in partial and en masse dam failure modes. While the vertical grading parameter appears to have a secondary impact, the dam height showed a negligible influence on dam failure. Peng et al. evaluated five flow resistance formulae for sand bed channels. A total of 1,636 sets of field data were recorded from the hydrological stations of two large Chinese river systems, the Yellow and Yangtze Rivers. They found that the fitting of the Yellow and Yangtze Rivers' data to those formulae are described by relatively high root-mean-square error, hence, all formulae still need improvement in their predictive ability. Wang et al. studied the relative fractions of the overall bed load yields produced during the rising and falling limbs of all symmetrical hydrographs (i.e. the bed load yield ratio), which are shown to be predominantly reliant on bed load transport hysteresis. Their finding demonstrated that the relationship between the bed load yield ratio and the ratio of reference stresses for the fractional sediment motion of each size class on both limbs follows a power law.

Rainfall intensity has increased in many regions through global climate change. Various studies have investigated rainfall characteristics in urban contexts. The study of Nazrien Ng et al. investigated the Sg Langat behaviour under the influence of extreme rainfall. The study focused on determining slope angles' effects on slope stability and assessing the development of pore water pressure. They also studied how extreme rainfall can influence the safety factor of the slope. The landslide research by Choi et al. developed two criteria for its efficient management, namely Surface displacement-based evacuation management and Surface angle-based evacuation management. In the Surface displacement-based criteria, they further developed short-term-based management criteria using experimental studies and long-term-based management criteria using collapse data. Bai et al. investigated the critical response characteristics of micro-droplets under the action of low-frequency acoustic waves, i.e. by studying the response of microdroplets. They found that the width of Droplet Size with Significant Response (DSSR) was affected by both microdroplet sizes and concentration. Also, the critical Sound Pressure Level (SPL) and its equilibrium response time were presented based on average droplet size increment and variation of droplet size respectively.

Offshore structures and artificial reefs can be subjected to wave and wind loads. Their effects are complicated, but need to be understood for successful implementation of structures in urban hydro-environments. Wang et al. developed a theoretical potential flow method to calculate the motion of offshore wind turbines. The study successfully simulated the motion characteristics and aeroelastic responses of the DTU-10MW semi-floating offshore wind turbine under the coupling effect of wind and wave. Liu et al. further studied the hydrodynamic characteristics around the circular pile in the Guoyuan Project in Chongqing Port with the help of fixed pressure sensing system as well as a dynamic signal test. They found the hydrodynamic pressure signal in the Yangtze River water flows to be a low-frequency signal. Shu et al. described the influences of typical artificial reefs on flow hydrodynamics and carbon sequestration potential using offshore Juehua Island in the Bohai Sea as a targeted site. They aimed to study the effects of square and M-shaped artificial reefs on localized flow fields, biomass production, and offshore carbon sink capacity. It has been found that although the offshore ground attached to M-shaped artificial reefs was only three times larger than those with square artificial reefs, the total carbon sink potential was up to seven times greater than that of regions covered by square artificial reefs.

Sustainable cities implementation

In the search for the best sustainable practice in urban spaces and fluvial managements, many factors need to be considered. Climate, flood risk and sediment-laden fluvial systems are among those factors under constant investigation in research programs. Chen et al. studied the combined effects of climate warming and grazing in the Qinghai-Tibet Plateau. The grazing effects were separated with a climate-driven probability model and scenario comparison, using the Normalized Difference Vegetation Index (NDVI). The study revealed that grazing has positive effects on NDVI at the beginning and end of the growing season, and negative effects in the middle. Liu et al. developed a time-dependent model for the corrosion of steel components under sediment-laden flow. They presented an evaluation method for the resistance degradation of steel piles and proposed a time-dependent model for the corrosion of steel components under sediment-laden flow. The article by Tallar and Geldoffer used the Flood Potential Index (FPI) to carry out a micro-scale study of flood risk assessment in urban fluvial areas in DKI Jakarta. Flood Potential Hazard Maps (2021–2024) for each sub-district of DKI Jakarta were developed by the analysis of rainfall data. The NDVI was obtained from Landsat eight interpretation and population density. The result predicted 10 sub-districts with high flooding potential, 219 with medium potential, and 32 with low flood potential in 2024. Kim et al. researched the hydrological behaviours of a green roof system using a SEEP/W model. The actual observed data from a test bed of the green roof system was validated with the simulated results of rainfall-runoff relationships within the green roof system to verify the applicability of the SEEP/W model. The authors found that the model shows good agreement with observed data.

Overall, this RT highlights the challenges and opportunities in urban and fluvial systems through a wide-range of research papers, models and techniques currently being used and/or developed to improve the resilience of urban water infrastructure, simulate effects of increased rainfall intensity, enhance flood prediction, evaluate sedimentation processes, and propose pollution mitigation and related efforts. All of the selected contributions help to discover innovative theories, advanced technologies, and application examples in these targeted fields of study. Finally, we would like to thank all the editors, reviewers and authors for their crucial contributions to this RT.

Author contributions

All authors listed have made a substantial, direct, and intellectual contribution to the work and approved it for publication.

Conflict of interest

The authors declare that the research was conducted in the absence of any commercial or financial relationships that could be construed as a potential conflict of interest.

Publisher's note

frontiers
in Environmental Science

ORIGINAL RESEARCH
published: 02 December 2021
doi: 10.3389/fenvs.2021.797971

Combined Effects of Warming and Grazing on Rangeland Vegetation on the Qinghai-Tibet Plateau

Chen Chen[1,2], Tiejian Li[1,3,4]*, Bellie Sivakumar[1,5], Ashish Sharma[6], John D. Albertson[7], Li Zhang[1] and Guangqian Wang[1,3,4]

[1]State Key Laboratory of Hydroscience and Engineering, Tsinghua University, Beijing, China, [2]School of Environment and Civil Engineering, Dongguan University of Technology, Dongguan, China, [3]State Key Laboratory of Plateau Ecology and Agriculture, Qinghai University, Xining, China, [4]Sanjiangyuan Collaborative Innovation Center, Qinghai University, Xining, China, [5]Department of Civil Engineering, Indian Institute of Technology Bombay, Mumbai, India, [6]UNSW Water Research Centre, School of Civil and Environmental Engineering, The University of New South Wales, Kensington, NSW, Australia, [7]School of Civil and Environmental Engineering, Cornell University, Ithaca, NY, United States

Climate warming has increased grassland productivity on the Qinghai-Tibet Plateau, while intensified grazing has brought increasing direct negative effects. To understand the effects of climate change and make sustainable management decisions, it is crucial to identify the combined effects. Here, we separate the grazing effects with a climate-driven probability model and elaborate scenario comparison, using the Normalized Difference Vegetation Index (NDVI) of the grassland on the Qinghai-Tibet Plateau. We show that grazing has positive effects on NDVI in the beginning and end of the growing season, and negative effects in the middle. Because of the positive effects, studies tend to underestimate and even ignore the grazing pressure under a warming climate. Moreover, the seasonality of grazing effects changes the NDVI-biomass relationship, influencing the assessment of climate change impacts. Therefore, the seasonality of grazing effects should be an important determinant in the response of grassland to warming in sustainability analysis.

Keywords: climate change, grazing, vegetation, sustainability, qinghai-tibet plateau

Edited by:
Jaan H. Pu,
University of Bradford,
United Kingdom

Reviewed by:
Lubo Liu,
California State University, Fresno,
United States
Zhihua Xie,
Cardiff University, United Kingdom
Yujun Yi,
Beijing Normal University, China
Asaad Shamseldin,
The University of Auckland,
New Zealand

Correspondence:
Tiejian Li
litiejian@tsinghua.edu.cn

Specialty section:
This article was submitted to
Freshwater Science,
a section of the journal
Frontiers in Environmental Science

Received: *19 October 2021*
Accepted: *08 November 2021*
Published: *02 December 2021*

Citation:
Chen C, Li T, Sivakumar B, Sharma A, Albertson JD, Zhang L and Wang G (2021) Combined Effects of Warming and Grazing on Rangeland Vegetation on the Qinghai-Tibet Plateau. Front. Environ. Sci. 9:797971. doi: 10.3389/fenvs.2021.797971

INTRODUCTION

Grasslands provide food and habitats for humankind and animals (de Jong et al., 2013), but are facing increasing pressure under climate change, in addition to intensifying human activities and increasing food demands (Chen et al., 2013; Seddon et al., 2016; Zhu et al., 2016). A key concern, at the current time, is whether grassland systems are sustainable under these double threats. While grasslands are among the most important indicators of the impacts of climate change (Li et al., 2018a), only very little research has been done on the role of human activities on the grasslands in climate change models (Väisänen et al., 2014).

The Three-River Headwaters Region (TRHR) on the Qinghai-Tibet Plateau is a crucial rangeland ecosystem with great importance to water resources and ecological security of China (**Figure 1A**) (Zhang et al., 2016; Han et al., 2018). Dubbed as China's Water Tower, the TRHR is the source of the Yellow River, the Yangtze River, and the Lancang River (the upper part of the Mekong River). The Plateau grassland, covering 91% of the land surface with a mean altitude of 4,500 m above mean sea level (Zheng et al., 2018), is mainly used as rangeland of nomadic Tibetans, providing grass for Tibetan yak and sheep, as well as wild animals, to graze (**Figures 1B,C**).

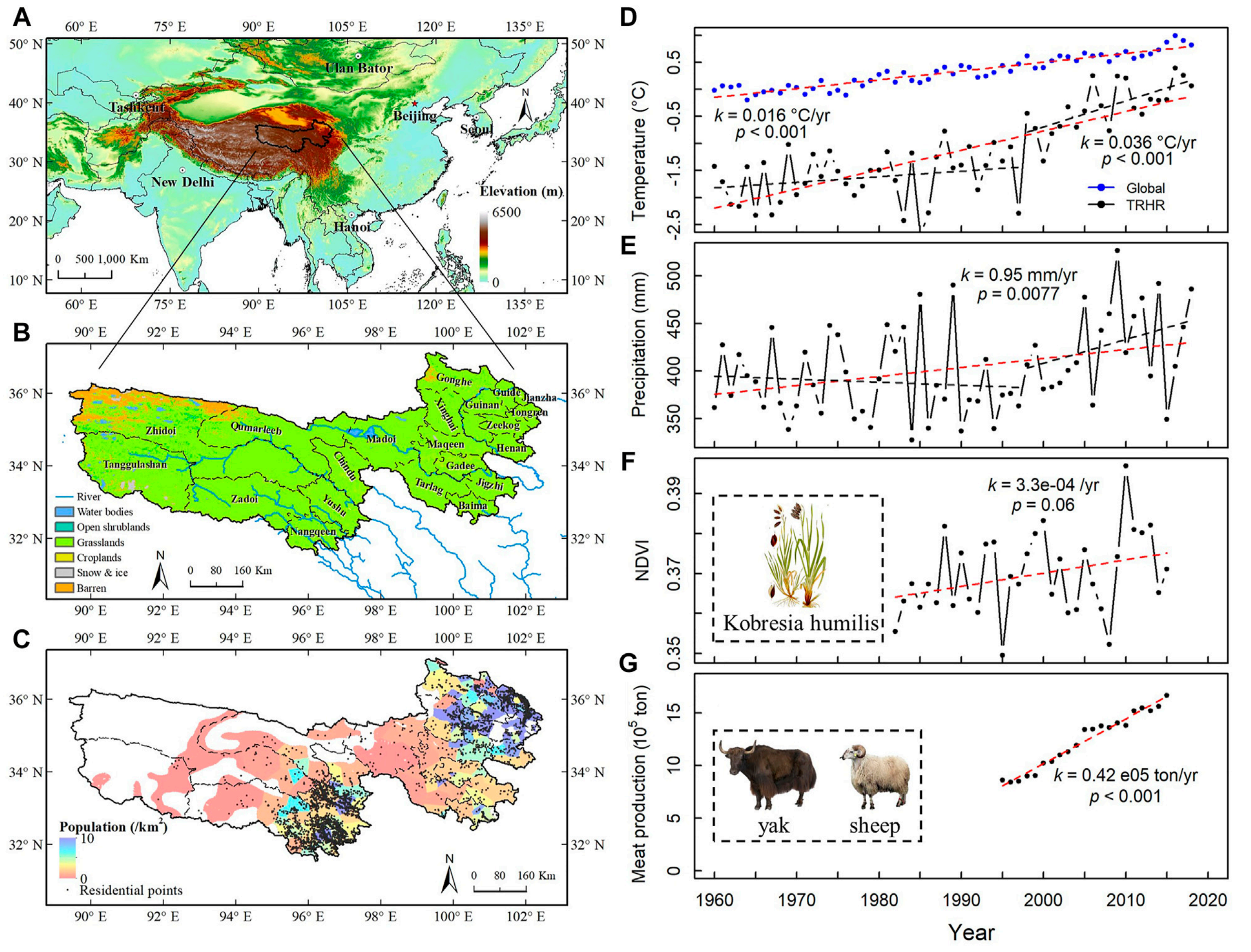

FIGURE 1 | The background and climate change of the Three-River Headwaters Region (TRHR). **(A)** Location of the TRHR; **(B)** Land cover of the TRHR; **(C)** Population density in 2015; **(D)** Station-based annual mean air temperature from 1961 to 2018; **(E)** Station-based annual mean precipitation from 1961 to 2018; **(F)** Growing season (May to September) NDVI from 1981 to 2015; **(G)** Grazing meat production from 1995 to 2015.

Weather station data revealed that air temperature and precipitation had increased significantly from 1960 to 2018 in the TRHR, and the increasing trend had particularly accelerated since the 1990s (**Figures 1D,E**). The warming trend in the TRHR (at a rate of 0.036°C/yr) had been much stronger than that at the global level (0.016°C/yr), with more than double the rate (**Figure 1D**). Climate change, including warming and CO_2 fertilizing, currently contributes to the greening of vegetation (**Figure 1F**) in the water-temperature-constrained TRHR (Nemani et al., 2003). On the other hand, the grazing intensity (represented by meat production throughout this paper) almost doubled from 1995 to 2015 (**Figure 1G**), exerting great pressure on the grassland ecosystem. The sustainability of the rangeland as well as the heritage of this unique Tibetan nomadic culture are facing huge challenges. However, the effects of grazing and climate change combine together to impact vegetation [e.g., yielding an overall rising Normalized Difference Vegetation Index (NDVI)], thus making it difficult to analyze and assess the influences and impacts, not to mention the complex nature of the individual factors involved as well as their interactions.

The combined effects of climate change and grazing on vegetation productivity, phenology and ecosystem properties have been explored by some studies (Klein et al., 2007; Zhang et al., 2015; Li et al., 2018c; Kohli et al., 2021). On the one hand, grazing alters the response of vegetation to climate change by modulating the dependency of vegetation growth on temperature (Wei et al., 2020). On the other hand, warming offsets the grazing effects on vegetation through altering the vegetation living state, i.e. increasing the plant height and the aboveground biomass (Zhang et al., 2015; Tang et al., 2019). The complexity associated with climate change and grazing and, hence, their combined effects on vegetation has generated contrasting results (Li et al., 2011; Wang et al., 2012; Xu et al., 2014; Ge et al., 2021). For example, grazing could exert both positive and negative influences on biomass due to the complex relationships between livestock grazing and biomass (Li et al., 2019a). How climate change and grazing interactively affect the biomass, biodiversity and ecosystem sustainability needs further investigation (Li et al., 2018c).

We analyzed the combined effects of climate change and grazing with elaborate scenario comparison (O'Neill and Nakicenovic, 2008; Huntzinger et al., 2013; McKenna et al., 2021), using a climate-driven probability model for time series, i.e., the Non-Homogeneous Hidden Markov Model (NHMM) (Holsclaw et al., 2017). First, we used the NHMM to simulate the vegetation dynamics month by month at county scale (a total of 414 months and 22 counties, **Figure 1B**, **Supplementary Table S1**), with the standardized climate inputs and NDVI. Then, we devised two scenarios to separate the grazing effects. We find that, besides the negative effects on NDVI in the middle of the growing season (May to September), grazing shows surprising but obvious positive effects in the beginning and end of the growing season. This seasonal pattern has important implications for better understanding of the grazing pressure on grasslands and for modifying the existing NDVI-biomass relationships, towards a more reliable indication of climate change.

MATERIALS AND METHODS

Data

Climate data. In general, climatic factors impose complex and varying limitations on vegetation growth (Nemani et al., 2003). Therefore, monthly precipitation and temperature data were obtained from the Climate Hazards Group Infrared Precipitation with Stations (CHIRPS) (Funk et al., 2015) and ERA-Interim (Dee et al., 2011), respectively, to feed the NHMM. The data from CHIRPS have a spatial resolution of 0.05° for the period from 1981 to the time being, and the monthly-mean surface temperature at 2-m from ERA-interim has a resolution of 0.125° for the period from 1979 to the present. To evaluate the amplitude of climate change on the Qinghai-Tibet Plateau study area, the monthly gauging station data from 1960 to 2018 provided by the China Meteorological Administration were used. Moreover, global temperature anomaly data were obtained from the National Oceanic and Atmospheric Administration (NOAA) to make comparison between regional and global warming, and to demonstrate the relatively extraordinary effects of warming on rangeland vegetation on the Qinghai-Tibet Plateau. Since the non-stationary climate system might also be related to vegetation growth, the climate oscillation indexes from NOAA were used as candidate predictors in our model.

Vegetation data. NDVI, a proxy of vegetation greenness and production, was acquired from the Global Inventory Monitoring and Modelling Studies (GIMMS) NDVI3g (Tucker et al., 2005). The biweekly datasets span from July 1981 to December 2015 with a spatial resolution of 0.083°. Monthly NDVI was composited from the biweekly data using the Maximum Value Composite method (Holben, 1986). The moderate-resolution imaging spectroradiometer (MODIS) land cover data (MCD12Q1) (Friedl et al., 2010), with 500 m resolution, were utilized to composite a binary pasture mask. The grassland pixels were classified as the pasture area. Apart from the non-grassland pixel, the surrounding eight pixels were masked out to make the classifying result more robust.

Anthropogenic data. Yak and sheep meat production data, for the period 1995–2015, were obtained from the records of the Qinghai Statistical Almanacs, considering the lack of information and reliability on the livestock population data. Here it is noted that during our study analysis, we have found a clear correlation between the meat production and the livestock population data, thus meat production could be used as a convincing surrogate for the grazing effect. The livestock density (LD) for each county was defined as meat production divided by pasture area. Annual time series were converted to monthly series based on linear interpolation. The Gridded Population of the World, Version 4 (Center for International Earth Science Information Network - CIESIN - Columbia University, 2018) was used to demonstrate population density of the study area.

The linear regression method was applied for the trend analysis, with Student's two-tailed *t*-test for significance test, and the Pettitt change point test was used for change point detection (Pettitt, 1979). Since livestock data were at the county scale, the gridded climate data and NDVI were aggregated to county scale after eliminating the non-pasture area. The assumption for the attribution of grazing effects was that the climate zone was homogeneous across the TRHR and, therefore, it was reasonable to calibrate the NHMM for one county and apply it to another. To meet this assumption, the climate data and NDVI were further processed with standardized normalization. The standardized NDVI was denoted as NDVI*. The period from July 1981 to December 2015 (a total of 414 months) was selected for the model construction, as GIMMS NDVI3g was available only for this time period.

Model

Viovy and Saint (1994) adopted the Hidden Markov Model (HMM) for modelling the vegetation dynamics, but it has the issues of poor representation in the temporal variability and spatial variability (Holsclaw et al., 2016). In our study, the NHMM (Hughes and Guttorp, 1994; Hughes et al., 1999) was applied for modelling the monthly vegetation time series, i.e. NDVI*. We chose the NHMM for its simplicity; further, it could not only simulate the complicated temporal variability in the response using hidden state variables, but also consider climate variables as the external factors. The model involved an underlying hidden, or not observed, stochastic process, during which the hidden state evolved according to a first-order Markov chain (**Supplementary Figure S1**). In vegetation modelling, the hidden state was usually interpreted as a weather state. The observed process, e.g. vegetation index, was conditional on the hidden states through the state-dependent emission distribution. The conditional likelihood for the model can be written as:

$$\boldsymbol{P}\left(\boldsymbol{Vg}\middle|\boldsymbol{W},\boldsymbol{X},\boldsymbol{z},\ \boldsymbol{\zeta},\ \boldsymbol{\theta}\right)=\prod\nolimits_{t=1}^{T}\boldsymbol{P}\left(\boldsymbol{z}_t|\boldsymbol{z}_{t-1},\boldsymbol{X}_t,\ \boldsymbol{\zeta}\right)\boldsymbol{f}\left(\boldsymbol{Vg}_t|\boldsymbol{W}_t,\boldsymbol{z}_t,\ \boldsymbol{\theta}\right) \tag{1}$$

where $P(z_t|z_{t-1},X_t,\ \zeta)$ is the Markov transition probability modelled by a multinomial logistic link function at time t, $f(Vg_t|W_t,z_t,\ \theta)$ is the emission distribution modelled *via* a mixture of Normal distribution, z is the hidden state, X_t are exogenous variables that regulate the transition of hidden Markov state, W_t are exogenous variables that control the possibility of emission distribution, and ζ and θ are for the transition parameters and emission distribution parameters, respectively.

In the NHMM, we introduced two types of exogenous variables (Holsclaw et al., 2016; Holsclaw et al., 2017). Time series X were the first exogenous covariate series, reflecting large-scale spatial phenomena and long-range temporal effects. In this study, the candidate variables for X included four harmonic terms ($\sin(\frac{\pi}{6}t)$, $\sin(\frac{\pi}{3}t)$, $\cos(\frac{\pi}{6}t)$, and $\cos(\frac{\pi}{3}t)$), representing seasonal variability, and five climate oscillation indexes (Pacific Decadal Oscillation, Arctic Oscillation, North Atlantic Oscillation, Southern Oscillation Index, and Pacific North American Oscillation) related to the study area, representing inter-annual variability. The other exogenous covariate time series, W, were introduced to allow the underlying distributional characteristics of vegetation to change for each hidden state. Here, monthly precipitation and temperature, 2–4 months accumulated precipitation and temperature, and 2–3 months lagged precipitation and temperature were chosen as the candidate variables for W. In total, we proposed nine candidate exogenous variables for X and 12 for W. The least absolute shrinkage and selection operator (LASSO) was performed to reduce the dimension of the candidate variables and to avoid overfitting. To ensure that the NHMM functioned well and was parsimonious (**Supplementary Figure S2**), five exogenous variables were retained, i.e. $\sin(\frac{\pi}{6}t)$, $\sin(\frac{\pi}{3}t)$, monthly precipitation, 2-months accumulated precipitation, and 2-months accumulated temperature.

The Markov chain Monte Carlo (MCMC) algorithm (Holsclaw et al., 2017) was applied to estimate the posterior full conditional distributions for z, ζ, and θ. Two metrics for quantifying the performance of the NHMM, i.e. Bayesian Information Criteria (BIC) for model calibration performance and Predictive Log Score (PLS) for model validation performance (Holsclaw et al., 2017), were utilized to determine the number of hidden states (K) and the number of mixed Normal distributions (nmix) in emission distribution. The model with the minimum BIC and maximum PLS was the preferable one. The BIC was estimated from the model calibrated with the first 31 years of data (372 monthly data), and the PLS was calculated from the model validated with the remaining 42-months data. That is to say, the first 372-months data were used for the model calibration, and the remaining 42-months data were used for the model validation. For parsimony and interpretability, we chose the model with seven states and two mixed Normal distributions, as BIC score and PLS score were found to be the best for this model (**Supplementary Figure S3**).

Scenario Setting

For the purpose of attribution of grazing effects, we devised two scenarios in opposite directions. Scenario 1 (S1) was to calibrate and verify the model in five counties that had the least grazing density, to get five sets of model parameters (i.e., five similar calibrated models), and then apply them to the remaining 17 counties (**Supplementary Table S1**; **Supplementary Figure S4**). For each of the 17 application sites, we got five sets of simulation results. Scenario 2 (S2) was the opposite of S1, i.e. to calibrate the models in five counties that had the highest grazing density. For either of these scenarios, the grazing effects were estimated by comparison between the five-county and 17-county groups, and the results were cross-verified by the opposite directions for confirmation. The NHMMs always explicitly used local climate forcing as inputs for each county, and then yielded NDVI results for each county. This way, the results for the application counties would reflect the grazing impacts, as at the counties where the model was calibrated, implicitly through parameters. Therefore, we hypothesized that the difference in the results and model performance of the NHMMs would reflect the livestock density that differs between model calibration and application counties. In S1, the simulated standardized NDVI values ($\mathrm{NDVI}^*_{\mathrm{ref}}$) in model application counties have the least impacts of grazing (because S1 models were calibrated for the counties that had the least grazing density), and should have been greater (if grazing decreased NDVI) than the observed standardized values ($\mathrm{NDVI}^*_{\mathrm{obs}}$) for each county, and vice versa in S2.

If we denote $\mathrm{NDVI}^*_{\mathrm{diff}}$ as the difference between $\mathrm{NDVI}^*_{\mathrm{ref}}$ and $\mathrm{NDVI}^*_{\mathrm{obs}}$, then the relationship between $\mathrm{NDVI}^*_{\mathrm{ref}}$ and $\mathrm{NDVI}^*_{\mathrm{obs}}$ for S1 can be written as:

$$\mathbf{NDVI}^*_{\mathbf{obs}} = \mathbf{NDVI}^*_{\mathbf{ref}} + \varepsilon_{\mathbf{LD}} + \varepsilon_{\boldsymbol{r}} \tag{2}$$

where $\varepsilon_{\mathrm{LD}}$ is the error induced by livestock impacts, ε_r is the model random error, and $\mathrm{NDVI}^*_{\mathrm{diff}} = \varepsilon_{\mathrm{LD}} + \varepsilon_r$.

For S2, the relationship between $\mathrm{NDVI}^*_{\mathrm{ref}}$ and $\mathrm{NDVI}^*_{\mathrm{obs}}$ was $\mathrm{NDVI}^*_{\mathrm{obs}} = \mathrm{NDVI}^*_{\mathrm{ref}} - \varepsilon_{\mathrm{LD}} + \varepsilon_r$. Here, $\mathrm{NDVI}^*_{\mathrm{diff}} = \varepsilon_{\mathrm{LD}} - \varepsilon_r$.

For both scenarios, we assumed that $|\varepsilon_r| \ll |\varepsilon_{\mathrm{LD}}|$, thus $\mathrm{NDVI}^*_{\mathrm{diff}}$ correlated with the difference in livestock density ($\mathrm{LD} - \mathrm{LD}_0$) between the model application counties and the model calibration ones.

Sensitivity Analysis

Consistent with the definition of ecological resilience (Holling, 1973), vegetation sensitivity to grazing was defined as the ratio of change in vegetation to change in livestock density:

$$S_n = \frac{\mathbf{NDVI}^*_{\mathbf{obs}} - \mathbf{NDVI}^*_{\mathbf{ref}}}{\mathbf{LD} - \mathbf{LD}_0} \tag{3}$$

where S_n is sensitivity, $\mathrm{NDVI}^*_{\mathrm{obs}}$ corresponds to the livestock density at model application county, LD, while $\mathrm{NDVI}^*_{\mathrm{ref}}$ corresponds to the model calibration county, LD_0.

It was assumed that vegetation sensitivity to grazing was a function of climate forcing. Therefore, vegetation sensitivity to grazing was evaluated at different temperature-precipitation ranges.

RESULTS AND DISCUSSION

Attribution of Grazing Effects

Consistent with our hypothesis, the performance metric of the model used in this study, i.e. root-mean-square deviation (RMSE), correlated with livestock density. For S1, the performance of the five model applications became worse

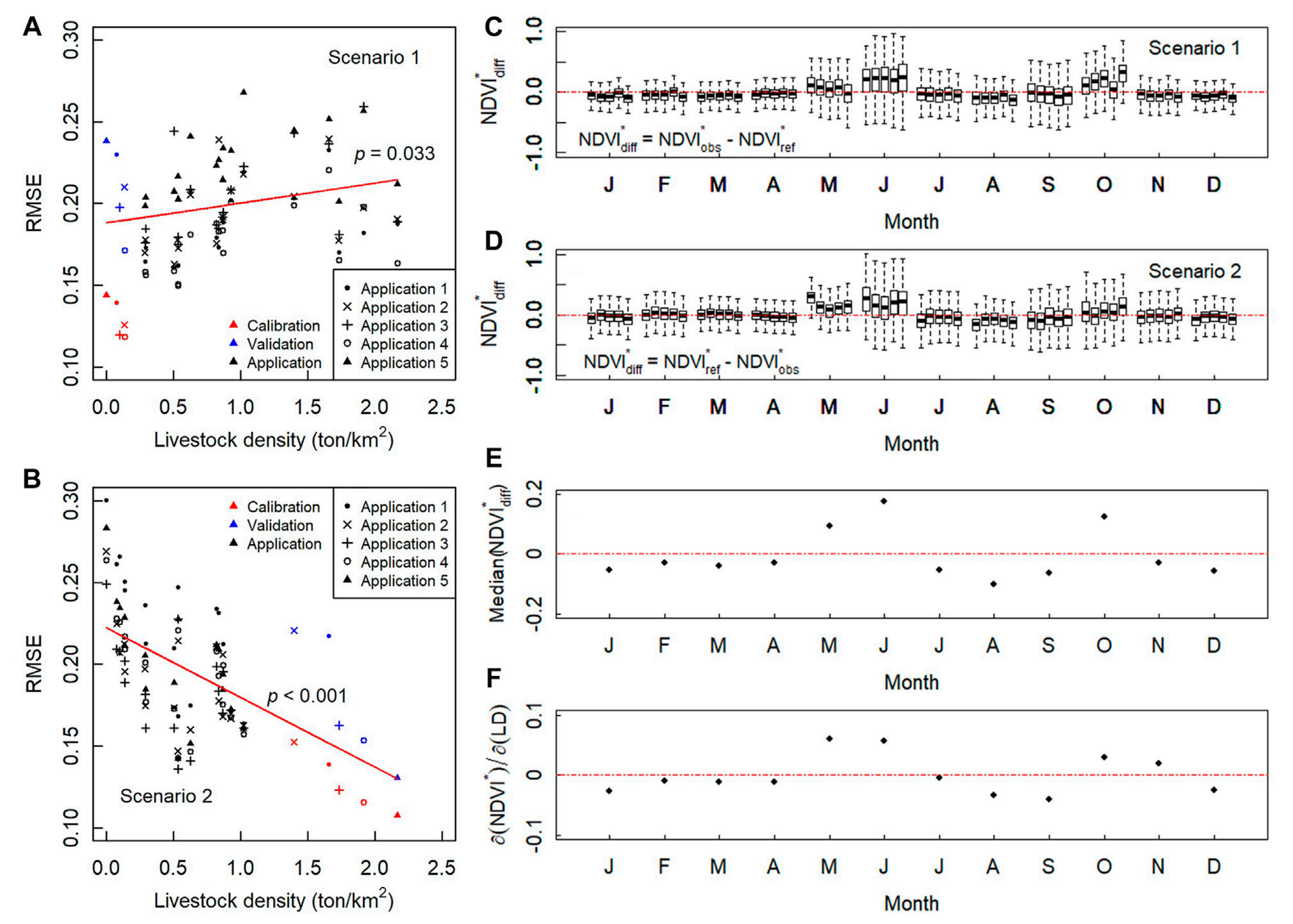

FIGURE 2 | Attribution of grazing effects. **(A)** RMSE for S1; **(B)** RMSE for S2; **(C)** $NDVI^*_{diff}$ for S1; **(D)** $NDVI^*_{diff}$ for S2; **(E)** Median $NDVI^*_{diff}$; **(F)** Slope for the linear relationship between $NDVI^*_{diff}$ and $(LD - LD_0)$ (Related scatter points are presented in **Supplementary Figure S7**).

when they were migrated to counties with increasing livestock density (**Figure 2A**). Meanwhile, for the models calibrated in counties that had the highest grazing density (S2), model performance became worse in counties that had less grazing density (**Figure 2B**). The results suggested that the livestock density was a strong controlling factor of NDVI. As the results from the two scenarios yielded reliable cross-verification, we have general confidence that the model could detect the signal of the impacts of grazing.

We attributed the difference in standardized NDVI ($NDVI^*_{diff}$) between the results from the simulations and observations to grazing effects; a negative value means a grazing-induced decrease in NDVI. As shown in **Figures 2C,D**, $NDVI^*_{diff}$ was plotted as the box-plots, and each box-plot stood for one model application in 1 month representing 17 counties and 34 years. To our surprise, the direction of $NDVI^*_{diff}$ changed with season for the five sets of applications as well as for the two scenarios. This, however, was not due to a systematic model error or phenology difference at different elevations (**Supplementary Figures S5 and S6**). For July, August, and September (the middle of the growing season), the grazing effects were generally negative across the counties from 1982 to 2015. However, grazing mostly showed positive effects on NDVI for May, June, and October, i.e., at the beginning and end of the growing season. In the non-growing season, grazing did not exhibit any apparent positive or negative effects, partly because of the small and unreliable NDVI values (Tucker et al., 2005). The median value of $NDVI^*_{diff}$, which was integrated from the two scenarios, clearly exhibited the seasonal pattern (**Figure 2E**). Therefore, we can construe that grazing activities can have seasonal, including both negative and positive, influence on rangelands on the Qinghai-Tibet Plateau.

Since $NDVI^*_{diff}$ was induced by the difference in livestock density between the model application counties and the model calibration counties, we assumed that the magnitude of $NDVI^*_{diff}$ correlated with the livestock density difference. Therefore, we examined the linear relationship between $NDVI^*_{diff}$ and $(LD - LD_0)$ for each month using data points from all scenarios, years, and counties. The results (**Figure 2F, Supplementary Figure S7**) showed that the slope (i.e., sensitivity) had a similar seasonal pattern as that of $NDVI^*_{diff}$, and the relationships were statistically significant for every month. Therefore, it may be inferred that, even though the direction of the effects of grazing differed seasonally, the magnitude of NDVI was sensitive to livestock density for each month.

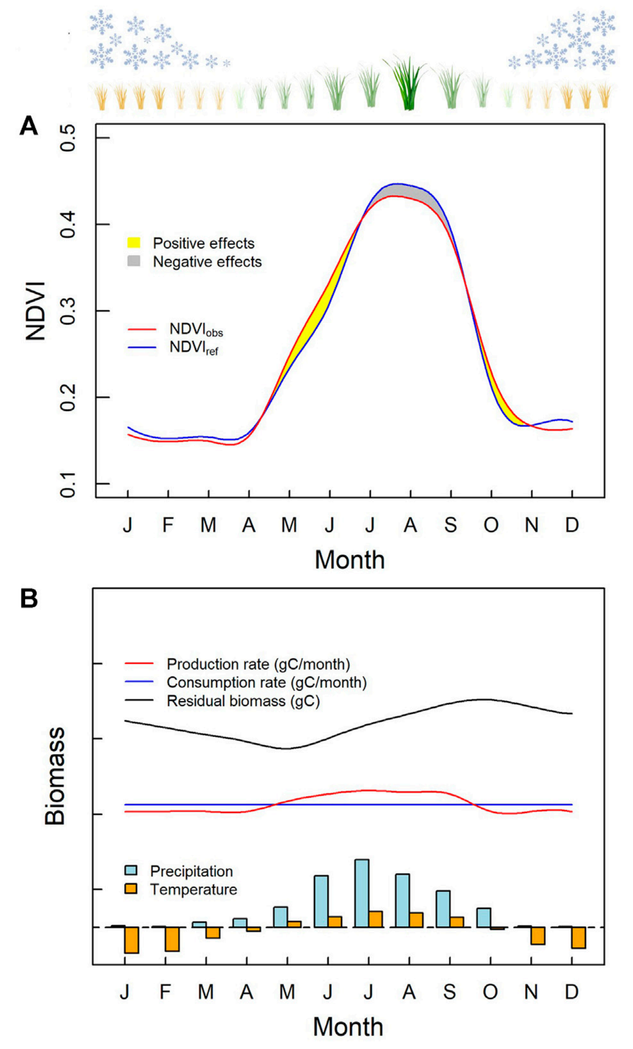

FIGURE 3 | Seasonal grazing effects on vegetation. **(A)** Seasonality of grazing effects on NDVI; **(B)** Seasonality of grazing effects on biomass. The reference NDVI ($NDVI_{ref}$) was estimated by deducting grazing effects using the $NDVI^{*}_{diff}$ ~ ($LS - LS_0$) relationship from the observed NDVI ($NDVI_{obs}$).

Seasonal Grazing Effects on Vegetation

With these results, we quantified the seasonal grazing effects on rangeland NDVI for the TRHR, and only focused on the growing season. After recovering $NDVI^{*}_{ref}$ to the same scale with the observation value, we found that, due to negative grazing effects, the peak value of NDVI decreased by 0.015 from an estimated 0.445 to the observed 0.430 in August (**Figure 3A**). The NDVI decrease in July and September was less, with an amplitude of 0.005–0.010, respectively. In the early (May and June) and late (October) growing season, on the contrary, grazing seemed to benefit the grassland, as NDVI increased by 0.015 from an estimated 0.234 to the observed 0.249 in May. This observation is in agreement, to some extent, with the positive grazing effects reported by some past studies using controlled experiment (Klein et al., 2007), and also for other regions, such as the Inner Mongolian grassland (Ren et al., 2016) and the Norwegian tundra (Mysterud et al., 2011). For the early growing season, grazing could contribute to the removal of snow (Mårell et al., 2006) and dried grass, and stimulate young and protein-rich regrowth (Mysterud et al., 2011; Ren et al., 2016). For the late growing season, grazing could also melt snow, remove aged leaves, and delay the deterioration of plant biomass by keeping it in young phenological stages (Albon and Langvatn, 1992; Hebblewhite et al., 2008; Mysterud et al., 2011; Li et al., 2018b). Therefore, the effects of grazing, at least on NDVI, can be overall positive.

It is appropriate to note, at this point, that NDVI is an index of the earth surface's status of greenness (Nemani et al., 2003; Tucker et al., 2005). Grazing effects on increasing NDVI values in the early and late growing season are partly benefited from the exposure of chlorophyll-rich grass parts. This, however, does not guarantee the improvement of grassland productivity and ecology. An effective quantification of grassland productivity is biomass production. Here, we proposed a conceptual diagram to illustrate the seasonal processes of biomass production rate, grazing consumption rate, and residual biomass (**Figure 3B**). During the growing season, the mean temperature was above zero and the amount of precipitation constituted most of a year. The biomass production rate was estimated from NDVI using the empirical relationship (Zhao and Running, 2010), and the grazing consumption rate was assumed to be constant, for the simplicity. The residual biomass was calculated from the accumulated difference between the biomass production rate and the grazing consumption rate. Within an annual cycle, the production rate of biomass only exceeded the grazing consumption rate during the middle of the growing season. Therefore, the residual biomass reached its maximum after maximum NDVI appeared in July or August without any coverage.

Implications of Seasonal Grazing Effects

From biomass point of view, the sustainability of rangeland is determined by considering whether the maximum residual biomass, reached in the late growing season, is sufficient for grazing until biomass production surplus occurs in the next growing season. Both climate and grazing factors influence the accumulation for the maximum residual biomass. The climate is related to the biomass production, and the grazing is linked with the biomass consumption. To represent the maximum residual biomass by NDVI, as well as the grazing effects on biomass, the best indicator is the NDVI in August. This is because August is the closest month before the maximum biomass appears in September and has the maximum in both NDVI value and grazing effects on NDVI.

In view of this, we plotted the monthly mean NDVI anomaly ($NDVI_{mon}$) of TRHR for the period 1982–2015 in **Figure 4A**, where August ($NDVI_{aug}$) and growing season ($NDVI_{gs}$) were marked. We also used the monthly values to calculate and compare their trends. For $NDVI_{gs}$ and $NDVI_{mon}$, the growing trends were statistically significant; on the other hand, the trend of $NDVI_{aug}$ was milder and insignificant. We also calculated the inter-annual trends by using the annual means of $NDVI_{gs}$ and $NDVI_{mon}$, and found similar results

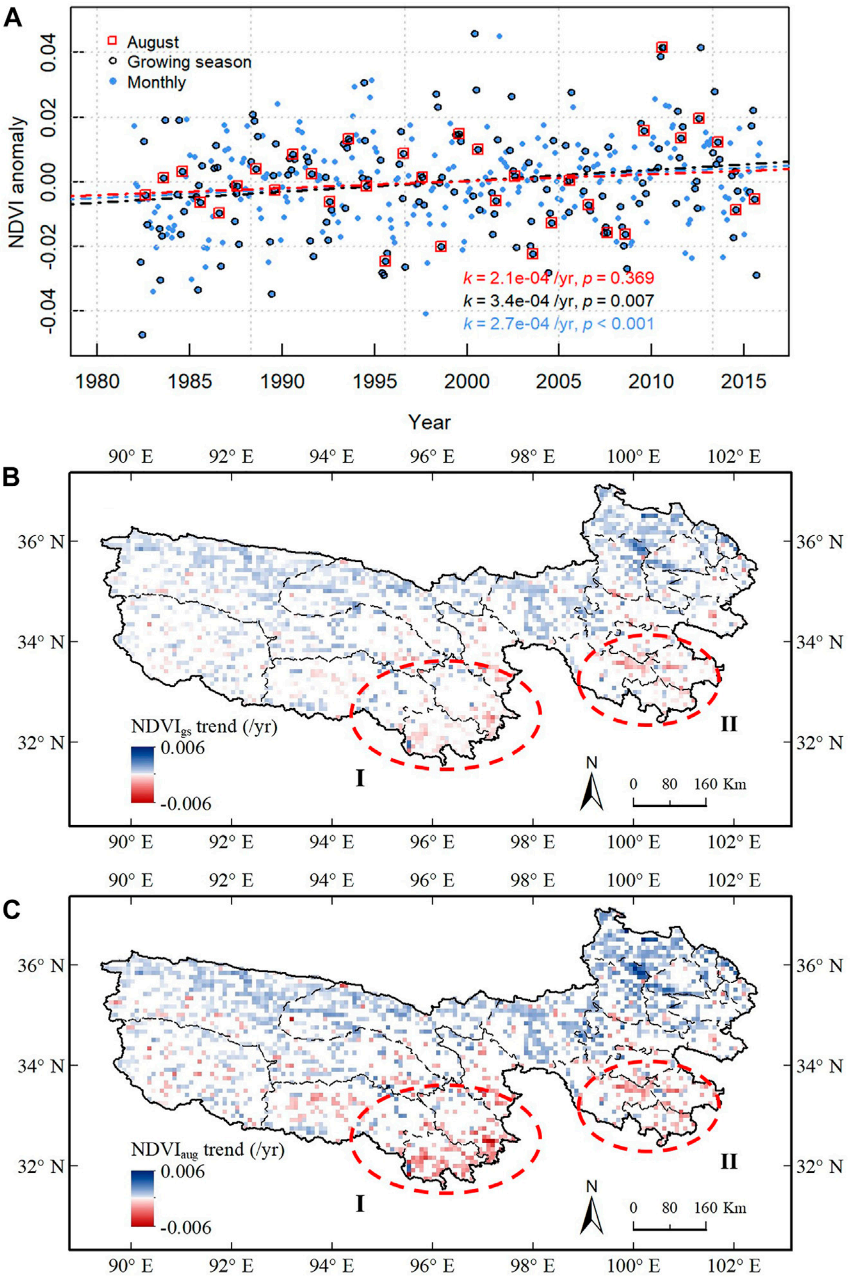

FIGURE 4 | Assessment of grazing pressure on vegetation. **(A)** Inter-annual trends of $\mathrm{NDVI}_{\mathrm{aug}}$ $\mathrm{NDVI}_{\mathrm{gs}}$, and $\mathrm{NDVI}_{\mathrm{mon}}$ for the TRHR during the period 1982–2015; **(B)** Spatial distribution of inter-annual trend for $\mathrm{NDVI}_{\mathrm{gs}}$ during the period 1982–2015; **(C)** Spatial distribution of inter-annual trend for $\mathrm{NDVI}_{\mathrm{aug}}$ during the period 1982–2015.

(**Supplementary Figure S8**). The NDVI trend results not only provided further evidence for the negative grazing effects in August, but also cautioned about possible underestimation of the grazing effects if using whole-year or growing-season NDVI for analysis.

Underestimation of the grazing effects by using $\mathrm{NDVI}_{\mathrm{gs}}$ trend, instead of $\mathrm{NDVI}_{\mathrm{aug}}$ trend, could also be observed in terms of spatial distribution. As shown in **Figures 4B,C**, the blue and red pixels indicate the greening and browning trends with significance ($p < 0.05$), respectively, and the white ones represent the trend without significance. For $\mathrm{NDVI}_{\mathrm{gs}}$, the percentage of pixels with significant greening and browning trends were 37.44% and 5.84%, and while for $\mathrm{NDVI}_{\mathrm{aug}}$, the numbers were 23.83% and 9.49%, respectively. The greening trend estimated from $\mathrm{NDVI}_{\mathrm{aug}}$ was not as prevailing as that from $\mathrm{NDVI}_{\mathrm{gs}}$. Besides, a large number of pixels with browning trend were found in the southern parts of the TRHR (Circle I and Circle II in **Figures 4B,C**) by using $\mathrm{NDVI}_{\mathrm{aug}}$, and the locations of these pixels matched well with the regions with high population density (**Figure 1C**). The results also cautioned about the

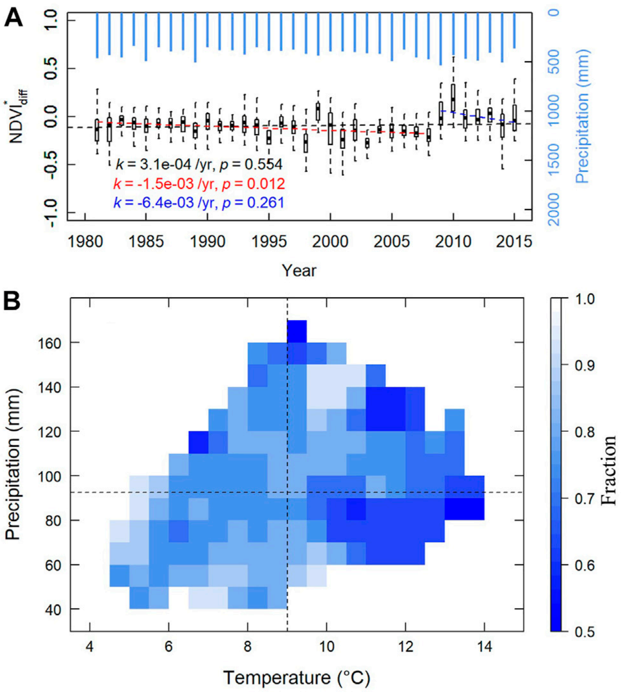

FIGURE 5 | Trend and sensitivity of grazing impacts on August NDVI. **(A)** Inter-annual trend of August $NDVI^*_{diff}$; **(B)** Percentage of negative S_n distributed in August climate space (with 0.5°C temperature interval and 10 mm precipitation interval).

locations where pressures exerted by livestock grazing and other human activities were higher.

The positive grazing effects in the beginning and end of the growing season would offset the negative grazing effects on NDVI. However, they had little to do with biomass production and accumulation. Therefore, when the overall whole-year or growing-season trend was used to investigate the rangeland sustainability, it might have given an illusion that the climate change benefit overwhelmed the grazing impacts. This might not be true, however; the grassland condition index that represented the yearly biomass surplus best, i.e., August NDVI, did not have a significant increasing trend.

The difficulty in assessing the effects of grazing also emphasizes the need to better understand the climate change effects on vegetation. Grazing activities regulate the responses of the grassland to climate change, even if biomass is used instead of NDVI. Because remotely-sensed biomass is also derived from NDVI, the underlying relationship between NDVI (for greenness) and biomass (for production) is widely evaluated for different vegetation types and seasons (Hansen and Schjoerring, 2003; Wessels et al., 2006); however, grazing and other human activities can change the NDVI-biomass relationship by reducing biomass and shifting the phenological process (Li et al., 2019b), with inconsistent change in greenness. Unfortunately, this has seldom been considered in studies evaluating the large-scale effects of climate change on vegetation, which requires some modifications to consider the grazing effects. Particularly, since the seasonality in grazing effects changes the NDVI-biomass relationships, modifications to the existing relationships should be different for different seasons, and even for different months.

Finally, we examined the historical trend of grazing effects and also whether the rangeland ecosystem would be sustainable in the future. For **Figure 5A**, each boxplot represents August $NDVI^*_{diff}$ of two scenarios and five sets of applications for all counties in August. The trend of August $NDVI^*_{diff}$ was calculated by linear fitting of the median values in the boxplots. The whole trend for August $NDVI^*_{diff}$ was insignificant from 1981 to 2015, but a change point was found in 2009. The sudden rise in NDVI in 2009 and 2010 (**Figure 1F**), contributing to the change point to positive August $NDVI^*_{diff}$, was mainly caused by abundant precipitation (Chen et al., 2020). However, for the divided sub-periods (i.e. before and after 2009), though the vegetation growth was under different climatic conditions (**Supplementary Figure S9**), the grazing impacts increased and drew August $NDVI^*_{diff}$ back to negative. The results revealed that even though the degree of grazing pressure exerted on grassland was influenced by climate, the increasing trend of grazing impacts still existed. We also evaluated the response of grazing pressure on climate variables, using the percentage of negative S_n in different temperature-precipitation ranges. **Figure 5B** was calculated from two scenarios and five sets of applications for all the counties and all the years, plotted by a 0.5 °C temperature interval and 10 mm precipitation interval. We observed a remarkable pattern; the percentage of negative effects was the highest when both temperature and precipitation were lower than their historical means (dashed lines in **Figure 5B**). With increase in temperature and precipitation, the percentage of negative effects reduced. However, the overall percentage of negative effects still exceeded 50%, which revealed that grazing still exerted pressure on grassland under climatic conditions within this range.

CONCLUSION

This research revealed the seasonal grazing effects on rangeland NDVI, biomass, and its sustainability in the TRHR on the Qinghai-Tibet Plateau. It also revealed the possible underestimation of grazing effects when the growing-season or whole-year NDVI values were used in evaluation, as what has normally been done in most studies. The seasonality in grazing effects on NDVI also brought uncertainties in the application of the existing NDVI-biomass relationships to derive biomass data products, which have commonly been used for climate change impact assessment. Although climate change has been found to provide more favorable conditions for grassland on the Qinghai-Tibet Plateau, the grazing effects have been generally negative and their magnitude still growing. Therefore, the sustainability of the rangeland ecosystem might degrade, provided grazing intensity continues to rise and warming temperature causes droughts in some regions by increasing the evapotranspiration demands. While there is a broad consensus among researchers that climate in the future will continue to change, evidence shows that the relationship between temperature and vegetation activity is weakening for the boreal region (Piao et al., 2014). Therefore, more attention should be paid to the combined effects of climate change and human activities on those fragile vegetation ecosystems. Further experimental and field observations will help to improve our statistical model and disclose the fundamental physics of the problem. This would constitute our future work.

DATA AVAILABILITY STATEMENT

The original contributions presented in the study are included in the article/**Supplementary Material**, further inquiries can be directed to the corresponding authors.

AUTHOR CONTRIBUTIONS

CC, TL, and GW conceived the initial idea, CC and TL performed the analysis, CC, BS, AS, JA, LZ, and GW contributed to the manuscript, TL and GW provided the funding.

FUNDING

This study was funded by the Major Project of Qinghai Provincial Department of Science and Technology (2021-SF-A6), the State Key Laboratory of Hydroscience and Engineering of Tsinghua University (2017-KY-04), and the National Key Research and Development Program of China (2016YFE0201900, 2017YFC0403600).

SUPPLEMENTARY MATERIAL

The Supplementary Material for this article can be found online at: https://www.frontiersin.org/articles/10.3389/fenvs.2021.797971/full#supplementary-material

REFERENCES

Albon, S. D., and Langvatn, R. (1992). Plant Phenology and the Benefits of Migration in a Temperate Ungulate. *Oikos* 65, 502–513. doi:10.2307/3545568

Center for International Earth Science Information Network - CIESIN - Columbia University (2018). *Gridded Population of the World, Version 4 (GPWv4): Population Density, Revision 11*. Palisades, NY: NASA Socioeconomic Data and Applications Center. doi:10.7927/H49C6VHW

Chen, C., Li, T., Sivakumar, B., Li, J., and Wang, G. (2020). Attribution of Growing Season Vegetation Activity to Climate Change and Human Activities in the Three-River Headwaters Region, China. *J. Hydroinform.* 22, 186–204. doi:10.2166/hydro.2019.003

Chen, H., Zhu, Q., Peng, C., Wu, N., Wang, Y., Fang, X., et al. (2013). The Impacts of Climate Change and Human Activities on Biogeochemical Cycles on the Qinghai-Tibetan Plateau. *Glob. Change Biol.* 19, 2940–2955. doi:10.1111/gcb.12277

de Jong, R., Schaepman, M. E., Furrer, R., De Bruin, S., and Verburg, P. H. (2013). Spatial Relationship between Climatologies and Changes in Global Vegetation Activity. *Glob. Change Biol.* 19, 1953–1964. doi:10.1111/gcb.12193

Dee, D. P., Uppala, S. M., Simmons, A. J., Berrisford, P., Poli, P., Kobayashi, S., et al. (2011). The ERA-Interim Reanalysis: Configuration and Performance of the Data Assimilation System. *Q.J.R. Meteorol. Soc.* 137, 553–597. doi:10.1002/qj.828

Friedl, M. A., Sulla-Menashe, B., Schneider, A., Ramankutty, N., Sibley, A., and Huang, X. (2010). Sulla-MenasheMODIS Collection 5 Global Land Cover: Algorithm Refinements and Characterization of New Datasets. *Remote Sensing Environ.* 114, 168–182. doi:10.1016/j.rse.2009.08.016

Funk, C., Peterson, P., Landsfeld, M., Pedreros, D., Verdin, J., Shukla, S., et al. (2015). The Climate Hazards Infrared Precipitation with Stations-A New Environmental Record for Monitoring Extremes. *Sci. Data* 2, 150066. doi:10.1038/sdata.2015.66

Ge, W., Deng, L., Wang, F., and Han, J. (2021). Quantifying the Contributions of Human Activities and Climate Change to Vegetation Net Primary Productivity Dynamics in China from 2001 to 2016. *Sci. Total Environ.* 773, 145648. doi:10.1016/j.scitotenv.2021.145648

Han, Z., Song, W., Deng, X., and Xu, X. (2018). Grassland Ecosystem Responses to Climate Change and Human Activities within the Three-River Headwaters Region of China. *Sci. Rep.* 8, 9079. doi:10.1038/s41598-018-27150-5

Hansen, P. M., and Schjoerring, J. K. (2003). Reflectance Measurement of Canopy Biomass and Nitrogen Status in Wheat Crops Using Normalized Difference Vegetation Indices and Partial Least Squares Regression. *Remote Sensing Environ.* 86, 542–553. doi:10.1016/s0034-4257(03)00131-7

Hebblewhite, M., Merrill, E., and McDermid, G. (2008). A Multi-Scale Test of the Forage Maturation Hypothesis in a Partially Migratory Ungulate Population. *Ecol. Monogr.* 78, 141–166. doi:10.1890/06-1708.1

Holben, B. N. (1986). Characteristics of Maximum-Value Composite Images from Temporal AVHRR Data. *Int. J. Remote Sensing* 7, 1417–1434. doi:10.1080/01431168608948945

Holling, C. S. (1973). Resilience and Stability of Ecological Systems. *Annu. Rev. Ecol. Syst.* 4, 1–23. doi:10.1146/annurev.es.04.110173.000245

Holsclaw, T., Greene, A. M., Robertson, A. W., and Smyth, P. (2016). A Bayesian Hidden Markov Model of Daily Precipitation over South and East Asia. *J. Hydrometeorol.* 17, 3–25. doi:10.1175/Jhm-D-14-0142.1

Holsclaw, T., Greene, A. M., Robertson, A. W., and Smyth, P. (2017). Bayesian Nonhomogeneous Markov Models via Pólya-Gamma Data Augmentation with Applications to Rainfall Modeling. *Ann. Appl. Stat.* 11, 393–426. doi:10.1214/16-aoas1009

Hughes, J. P., and Guttorp, P. (1994). A Class of Stochastic Models for Relating Synoptic Atmospheric Patterns to Regional Hydrologic Phenomena. *Water Resour. Res.* 30, 1535–1546. doi:10.1029/93wr02983

Hughes, J. P., Guttorp, P., and Charles, S. P. (1999). A Non-homogeneous Hidden Markov Model for Precipitation Occurrence. *J. R. Stat. Soc. Ser. C (Applied Statistics)* 48, 15–30. doi:10.1111/1467-9876.00136

Huntzinger, D. N., Schwalm, C., Michalak, A. M., Schaefer, K., King, A. W., Wei, Y., et al. (2013). The North American Carbon Program Multi-Scale Synthesis and Terrestrial Model Intercomparison Project - Part 1: Overview and Experimental Design. *Geosci. Model. Dev.* 6, 2121–2133. doi:10.5194/gmd-6-2121-2013

Klein, J. A., Harte, J., and Zhao, X.-Q. (2007). Experimental Warming, Not Grazing, Decreases Rangeland Quality on the Tibetan Plateau. *Ecol. Appl.* 17, 541–557. doi:10.1890/05-0685

Kohli, M., Mijiddorj, T. N., Suryawanshi, K. R., Mishra, C., Boldgiv, B., and Sankaran, M. (2021). Grazing and Climate Change Have Site-dependent Interactive Effects on Vegetation in Asian Montane Rangelands. *J. Appl. Ecol.* 58, 539–549. doi:10.1111/1365-2664.13781

Li, C., de Jong, R., Schmid, B., Wulf, H., and Schaepman, M. E. (2019a). Spatial Variation of Human Influences on Grassland Biomass on the Qinghai-Tibetan Plateau. *Sci. Total Environ.* 665, 678–689. doi:10.1016/j.scitotenv.2019.01.321

Li, G., Jiang, C., Cheng, T., and Bai, J. (2019b). Grazing Alters the Phenology of alpine Steppe by Changing the Surface Physical Environment on the Northeast

Qinghai-Tibet Plateau, China. *J. Environ. Manage.* 248, 109257. doi:10.1016/j.jenvman.2019.07.028

Li, L., Zhang, Y., Liu, L., Wu, J., Li, S., Zhang, H., et al. (2018a). Current Challenges in Distinguishing Climatic and Anthropogenic Contributions to alpine Grassland Variation on the Tibetan Plateau. *Ecol. Evol.* 8, 5949–5963. doi:10.1002/ece3.4099

Li, P., Peng, C., Wang, M., Luo, Y., Li, M., Zhang, K., et al. (2018b). Dynamics of Vegetation Autumn Phenology and its Response to Multiple Environmental Factors from 1982 to 2012 on Qinghai-Tibetan Plateau in China. *Sci. Total Environ.* 637-638, 855–864. doi:10.1016/j.scitotenv.2018.05.031

Li, W., Li, X., Zhao, Y., Zheng, S., and Bai, Y. (2018c). Ecosystem Structure, Functioning and Stability under Climate Change and Grazing in Grasslands: Current Status and Future Prospects. *Curr. Opin. Environ. Sustainability* 33, 124–135. doi:10.1016/j.cosust.2018.05.008

Mårell, A., Hofgaard, A., and Danell, K. (2006). Nutrient Dynamics of Reindeer Forage Species along Snowmelt Gradients at Different Ecological Scales. *Basic Appl. Ecol.* 7, 13–30. doi:10.1016/j.baae.2005.04.005

McKenna, C. M., Maycock, A. C., Forster, P. M., Smith, C. J., and Tokarska, K. B. (2021). Stringent Mitigation Substantially Reduces Risk of Unprecedented Near-Term Warming Rates. *Nat. Clim. Change* 11, 126–131. doi:10.1038/s41558-020-00957-9

Mysterud, A., Hessen, D. O., Mobæk, R., Martinsen, V., Mulder, J., and Austrheim, G. (2011). Plant Quality, Seasonality and Sheep Grazing in an alpine Ecosystem. *Basic Appl. Ecol.* 12, 195–206. doi:10.1016/j.baae.2011.03.002

Na, L., Genxu, W., Yan, Y., Yongheng, G., and Guangsheng, L. (2011). Plant Production, and Carbon and Nitrogen Source Pools, Are Strongly Intensified by Experimental Warming in alpine Ecosystems in the Qinghai-Tibet Plateau. *Soil Biol. Biochem.* 43, 942–953. doi:10.1016/j.soilbio.2011.01.009

Nemani, R. R., Keeling, C. D., Hashimoto, H., Jolly, W. M., Piper, S. C., Tucker, C. J., et al. (2003). Climate-driven Increases in Global Terrestrial Net Primary Production from 1982 to 1999. *Science* 300, 1560–1563. doi:10.1126/science.1082750

O'Neill, B. C., and Nakicenovic, N. (2008). Learning from Global Emissions Scenarios. *Environ. Res. Lett.* 3, 045014. doi:10.1088/1748-9326/3/4/045014

Pettitt, A. N. (1979). A Non-parametric Approach to the Change-point Problem. *Appl. Stat.* 28, 126–135. doi:10.2307/2346729

Piao, S., Nan, H., Huntingford, C., Ciais, P., Friedlingstein, P., Sitch, S., et al. (2014). Evidence for a Weakening Relationship between Interannual Temperature Variability and Northern Vegetation Activity. *Nat. Commun.* 5, 5018. doi:10.1038/ncomms6018

Ren, H., Han, G., Lan, Z., Wan, H., Schönbach, P., Gierus, M., et al. (2016). Grazing Effects on Herbage Nutritive Values Depend on Precipitation and Growing Season in Inner Mongolian Grassland. *Jpecol* 9, 712–723. doi:10.1093/jpe/rtw011

Seddon, A. W. R., Macias-Fauria, M., Long, P. R., Benz, D., and Willis, K. J. (2016). Sensitivity of Global Terrestrial Ecosystems to Climate Variability. *J. Plant Ecol.* 531, 229–232. doi:10.1038/nature16986

Tang, L., Zhong, L., Xue, K., Wang, S., Xu, Z., Lin, Q., et al. (2019). Warming Counteracts Grazing Effects on the Functional Structure of the Soil Microbial Community in a Tibetan Grassland. *Soil Biol. Biochem.* 134, 113–121. doi:10.1016/j.soilbio.2019.02.018

Tucker, C. J., Pinzon, J. E., Brown, M. E., Slayback, D. A., Pak, E. W., Mahoney, R., et al. (2005). An Extended AVHRR 8-km NDVI Dataset Compatible with MODIS and SPOT Vegetation NDVI Data. *Int. J. Remote Sensing* 26, 4485–4498. doi:10.1080/01431160500168686

Väisänen, M., Ylänne, H., Kaarlejärvi, E., Sjögersten, S., Olofsson, J., Crout, N., et al. (2014). Consequences of Warming on Tundra Carbon Balance Determined by Reindeer Grazing History. *Nat. Clim. Change* 4, 384–388. doi:10.1038/nclimate2147

Viovy, N., and Saint, G. (1994). Hidden Markov Models Applied to Vegetation Dynamics Analysis Using Satellite Remote Sensing. *IEEE Trans. Geosci. Remote Sensing* 32, 906–917. doi:10.1109/36.298019

Wang, S., Duan, J., Xu, G., Wang, Y., Zhang, Z., Rui, Y., et al. (2012). Effects of Warming and Grazing on Soil N Availability, Species Composition, and ANPP in an alpine Meadow. *Ecology* 93, 2365–2376. doi:10.1890/11-1408.1

Wei, D., Zhao, H., Zhang, J., Qi, Y., and Wang, X. (2020). Human Activities Alter Response of alpine Grasslands on Tibetan Plateau to Climate Change. *J. Environ. Manage.* 262, 110335. doi:10.1016/j.jenvman.2020.110335

Wessels, K. J., Prince, S. D., Zambatis, N., Macfadyen, S., Frost, P. E., and Van Zyl, D. (2006). Relationship between Herbaceous Biomass and 1-km2 Advanced Very High Resolution Radiometer (AVHRR) NDVI in Kruger National Park, South Africa. *Int. J. Remote Sensing* 27, 951–973. doi:10.1080/01431160500169098

Xu, X., Luo, Y., Shi, Z., Zhou, X., and Li, D. (2014). Consistent Proportional Increments in Responses of Belowground Net Primary Productivity to Long-Term Warming and Clipping at Various Soil Depths in a Tallgrass Prairie. *Oecologia* 174, 1045–1054. doi:10.1007/s00442-013-2828-z

Zhang, Y., Gao, Q., Dong, S., Liu, S., Wang, X., Su, X., et al. (2015). Effects of Grazing and Climate Warming on Plant Diversity, Productivity and Living State in the alpine Rangelands and Cultivated Grasslands of the Qinghai-Tibetan Plateau. *Rangel. J.* 37, 57–65. doi:10.1071/rj14080

Zhang, Y., Zhang, C., Wang, Z., Chen, Y., Gang, C., An, R., et al. (2016). Vegetation Dynamics and its Driving Forces from Climate Change and Human Activities in the Three-River Source Region, China from 1982 to 2012. *Sci. Total Environ.* 563-564, 210–220. doi:10.1016/j.scitotenv.2016.03.223

Zhao, M., and Running, S. W. (2010). Drought-Induced Reduction in Global Terrestrial Net Primary Production from 2000 through 2009. *Science* 329, 940–943. doi:10.1126/science.1192666

Zheng, Y., Han, J., Huang, Y., Fassnacht, S. R., Xie, S., Lv, E., et al. (2018). Vegetation Response to Climate Conditions Based on NDVI Simulations Using Stepwise Cluster Analysis for the Three-River Headwaters Region of China. *Ecol. Indicators* 92, 18–29. doi:10.1016/j.ecolind.2017.06.040

Zhu, Z., Piao, S., Myneni, R. B., Huang, M., Zeng, Z., Canadell, J. G., et al. (2016). Greening of the Earth and its Drivers. *Nat. Clim. Change* 6, 791–795. doi:10.1038/nclimate3004

Conflict of Interest: The authors declare that the research was conducted in the absence of any commercial or financial relationships that could be construed as a potential conflict of interest.

frontiers in Environmental Science

ORIGINAL RESEARCH
published: 24 December 2021
doi: 10.3389/fenvs.2021.800832

Hysteretic Implications for Graded Bed Load Sediment Transport in Symmetrical Hydrograph Flows

Le Wang[1], Dayu Wang[2], Alan Cuthbertson[3]*, Deyu Zhong[4,5]* and Gareth Pender[6]

[1]School of Water Resources and Hydropower Engineering, North China Electric Power University, Beijing, China, [2]Department of Sediment Research, China Institute of Water Resources and Hydropower Research, Beijing, China, [3]School of Science and Engineering (Civil Engineering), University of Dundee, Dundee, United Kingdom, [4]State Key Laboratory of Hydroscience and Engineering, Tsinghua University, Beijing, China, [5]State Key Laboratory of Plateau Ecology and Agriculture, Qinghai University, Xining, China, [6]Deputy Principal Research and Innovation, Heriot-Watt University, Edinburgh, United Kingdom

Differential parametric values associated with bed load sediment transport, that result at the same discharge levels on the rising and falling limbs of a flood hydrograph, are usually defined as bed load hysteresis. This hysteresis in bed load sediment transport rates is of considerable interest in the field of fluvial hydraulics. Within this study, a series of well-defined, symmetrical hydrograph flows are generated over a graded, mobile sediment bed to fully examine the hysteresis of the resulting bed load sediment transport in terms of the threshold of motion, and differential bed load transport rates and bed load yields during the hydrographs. The experiments are conducted in a titling flume without sediment supply specified at the upstream inlet, thereby representing typical river reach conditions immediately downstream of a dam that are exclusively subject to net in-channel bed degradation from sediment transport initiated during flood events. Our results show that the fractional bed load transport of defined fine, medium and coarse size classes within the graded sediment bed generally display clockwise, no/mixed and counter-clockwise hysteresis patterns, respectively, with clockwise hysteresis most commonly found for the coarse size class mobilised by hydrographs with long durations. By contrast, counter-clockwise hysteresis is usually observed for fine size class transported by hydrographs with short durations. Accordingly, the corresponding reference stresses for each size class vary between different hydrographs and are primarily controlled by the hydrograph flashiness (i.e. unsteadiness) and magnitude (i.e. total water work). Moreover, it is shown that the hysteresis effect, particularly for those size classes and hydrograph combinations that result in clockwise and counter-clockwise behaviour, should be fully accounted for when reproducing bed load transport rates using separate-limb based method. Finally, we investigate the relative fractions of the overall bed load yields generated during the rising and falling limbs of all symmetrical hydrographs (i.e. the bed load yield ratio), which are found to be primarily dependent on bed load transport hysteresis. Finally, the relationship between the bed load yield ratio and the ratio of reference stresses for the fractional sediment motion of each size class on both limbs is found to follow a power law.

Keywords: hysteresis, bed load sediment, incipient motion, bed-load yield, symmetrical hydrograph

Edited by:
Jaan H. Pu,
University of Bradford,
United Kingdom

Reviewed by:
Songdong Shao,
Dongguan University of Technology,
China
Peng Hu,
Zhejiang University, China

***Correspondence:**
Alan Cuthbertson
a.j.s.cuthbertson@dundee.ac.uk
Deyu Zhong
zhongdy@tsinghua.edu.cn

Specialty section:
This article was submitted to
Freshwater Science,
a section of the journal
Frontiers in Environmental Science

Received: *24 October 2021*
Accepted: *12 November 2021*
Published: *24 December 2021*

Citation:
Wang L, Wang D, Cuthbertson A,
Zhong D and Pender G (2021)
Hysteretic Implications for Graded Bed
Load Sediment Transport in
Symmetrical Hydrograph Flows.
Front. Environ. Sci. 9:800832.
doi: 10.3389/fenvs.2021.800832

INTRODUCTION

Hysteresis is a non-linear loop-like behaviour associated with sediment transport during flood events (e.g., Mao et al., 2014; Zuecco et al., 2016) that is generally shown as a time lag between the peak values of flow and sediment transport rates (American Society of Civil Engineers, 2008). This is described quantitatively by two different values of sediment transport (i.e., dependent variable) being associated with a single value of discharge (i.e., independent variable) on the ascending and descending limbs of a flood hydrograph (Phillips, 2003). For this reason, it was widely acknowledged that sediment transport during flood flows is extremely difficult to predict accurately using one-to-one (i.e., flow-to-sediment rate) relationships typically developed under steady flow conditions, as a result of hysteresis effects (e.g., Gaeuman et al., 2009; Ahanger et al., 2018; Guusolus and Binns, 2018; Redolfi et al., 2018). This hysteresis effect therefore constitutes a distinct physical basis that distinguishes sediment transport in unsteady flood hydrographs from equivalent transport behaviour under steady uniform flow conditions, and therefore consititutes an important topic when studying and predicting sediment transport during flood flows.

According to previous studies, observed hysteresis could typically be classified as either 1) clockwise (i.e., higher sediment transport rates on the rising limb than the falling limb of a flood hydrograph), 2) counter-clockwise (i.e., higher sediment transport rates on the falling limb than the rising limb), 3) single-valued (i.e., the same sediment transport rates on both limbs), 4) single-valued plus a loop (i.e., a combination of 1) and either 2) or 3)), and 5) figure-8 (i.e., combining clockwise and anticlockwise hysteresis) (e.g., Gunsolus and Binns, 2018; Ahanger et al., 2008; Williams, 1989; Aich et al., 2014). However, these defined classifications were originally developed for suspended sediment transport (Williams, 1989). By contrast, no systematical exploration of hysteresis has been performed for bed-load transport (e.g., Gaeuman, 2010; Mao et al., 2014; Plumb et al., 2020), as direct measurements of bed-load transport rates during flood events in mountainous streams are relatively difficult, expensive, and often dangerous to undertake (Vericat and Batalla, 2006).

Recently, increased effort has been undertaken to investigate the hysteresis behaviour associated with bed-load sediment transport, mobilised under unsteady flows, as well as their underlying mechanisms (e.g., Gunsolus and Binns, 2018) in both field and laboratory studies (Plumb et al., 2020). Basic factors that have been suggested to influence the category of observed hysteresis with respect to bed load sediment transport in unsteady flows include: 1) boundary conditions such as the tempo-spatial availability of sediment in the river channel (e.g., Hassan et al., 2006; Humphries et al., 2012; Guney et al., 2013; Curran et al., 2015) and their distance to the sediment transport measurement station (e.g., Reid et al., 1985; Moog and Whiting, 1998; Mano et al., 2009; Mao et al., 2014); 2) fluvial bed conditions in terms of surface texture or structure (e.g., surface armouring, e.g., Kuhnle, 1992; Mao, 2018), bed sediment composition (e.g., quasi-uniform or heterogeneous sediment, e.g., Wang, 2016; Gunsolus and Binns, 2018), fractional hiding and exposure effects (e.g., Gaeuman, 2010), and bed morphological features or channel irregularities (e.g., William, 1989; Lee et al., 2004; Martin and Jerolmack, 2013; Reesink et al., 2013); and 3) unsteady flood flow conditions represented by flood hydrograph shape (Bombar et al., 2011), flood duration or unsteadiness (Graf and Qu, 2004; Lee et al., 2004; Hassan et al., 2006; Plumb et al., 2020), flood magnitude (e.g., Lee et al., 2004; Wang et al., 2015), antecedent flow conditions (e.g., Reid et al., 1985; Piedra et al., 2012; Guney et al., 2013; Mao et al., 2014), as well as the origin of runoff dynamics from snowmelt/glacier melting (e.g., Mao et al., 2014).

On the basis of a fuller understanding of above physical connections between various hysteresis and their origins, hysteresis in bed load sediment transport could potentially be used in the literature to infer the degree of sediment availability (Mao et al., 2014), bed-surface composition (e.g., Kuhnle, 1992), bed morphological adjustments (Gunsolus and Binns, 2018), flood history (e.g., Camporese et al., 2014; Mao et al., 2014), runoff generation at various scales (Spence, 2010) or sediment transport dynamics (Mao et al., 2014). Also, it is important to note that accounting for the hysteresis effects could lead to an overall improvement in the estimation of the bed load-flow regression, consequently defined as the bimodal rating curve or separate-limb method (Moog and Whiting, 1998; Waters and Curran, 2015). However, strictly speaking, within these studies, the bed load sediment transport rates generated during the rising and falling limbs of the hydrograph are only treated separately on a limb-dependent basis, implying the difference in sediment transport rates on both limbs has been recognised regardless of different hysteresis behaviour. This approach is appropriate in studies where a particular kind of hysteresis is encountered exclusively over a range of unsteady flow conditions [e.g. bed load transport followed counter-clockwise hysteresis exclusively in Lee et al. (2004)]. In fact, the correspondence between bed load transport rates at a given discharge on both hydrograph limbs will clearly be completely different when sediment transport exhibits clockwise and counterclockwise hysteresis. As such, the implications of different hysteretic loops on the estimation of sediment transport during unsteady hydrograph flows are still not fully understood or examined to date, especially for complex, graded bed load transport that features strong intergranular interactions (e.g., Ahanger et al., 2008; Wang, 2016; Mrokowska et al., 2018; Redolfi et al., 2018). Moreover, it can be anticipated that the critical flow conditions for the initial and final sediment motion on the rising and falling limbs of a hydrograph, respectively, are probably different (e.g., Gaeuman, 2010), rather than a constant discharge as usually assumed in previous research (e.g., Phillips et al., 2018). This also leads to an open question as how these hysteresis cycles are linked to variability in the incidence of sediment transport on the ascending and descending limbs throughout a hydrograph flow process. In order to better understand the importance of different hysteretic behaviour associated with graded bed load sediment transport induced within a wide range of unsteady flows, the current study investigates a series of single-peaked, symmetrical hydrographs that are generated in a tilting sediment bed flume system to facilitate quantitative determination of the bed load sediment transport hysteresis. Within these experiments, no additional sediment is supplied from upstream (or recirculated during the experiments) to ensure consistent boundary conditions are achieved at upstream inlet for the different unsteady hydrograph flows tested.

SCALING CONSIDERATIONS

Hydrograph Magnitude, Unsteadiness and Shape

A series of unsteady hydrograph flows were generated with the primary aim of producing different hysteresis loops associated with bed load sediment transport. Previous studies have been shown that the magnitude, duration and shape of unsteady flow hydrographs have significant impact on the hysteresis modes observed in resulting bed load sediment transport (e.g., Poff et al., 1997; Guusolus and Binns, 2018; Mao, 2018). Therefore, the typical smoothed triangular hydrographs employed in the present study were quantified by using three basic parameters, namely: total water work W_k, unsteadiness Γ_{HG}, and shape η (Graf and Suszka, 1985; Suszka, 1987; Yen and Lee, 1995; Lee et al., 2004; Bombar et al., 2011; Waters and Curran, 2015; Wang et al., 2015; 2019) that are expressed in the following forms,

$$W_k = \frac{u_b^{*2} V_{ol}}{g H_b^3 B} \tag{1}$$

$$\Gamma_{HG} = \frac{1}{u_b^*}\frac{\Delta H}{\Delta T} \tag{2}$$

$$\eta = \frac{\Delta T_R}{\Delta T_F} \tag{3}$$

where $u_b{}^*$ is the bed shear velocity for the base flow conditions (prior to the hydrograph), V_{ol} is the total water volume under the unsteady flow hydrograph (i.e., excluding the base flow condition), H_b is the initial base flow depth, B is the channel width, g is the gravitational acceleration, ΔH is the difference of water surface elevation for peak and base flows (i.e., $\Delta H = H_p – H_b$), ΔT is the total hydrograph duration (i.e., $\Delta T = \Delta T_R + \Delta T_F$), and ΔT_R and ΔT_F represent the duration of the rising and falling limbs, respectively. According to Wang et al. (2015), $\eta = 1$ (i.e., $\Delta T_R = \Delta T_F$) typically represent symmetrical hydrograph, while ratios $\eta > 1$ and $\eta < 1$ clearly represent asymmetrical hydrographs with relatively long rising ($\Delta T_R > \Delta T_F$) and falling ($\Delta T_F > \Delta T_R$) limb durations, respectively. It is noted here that the current study considers only symmetrical hydrographs, i.e., $\eta = 1.0$, with flow rates Q and flow gradients (dQ/dt) on the two limbs facilitating the quantitative determination of sediment transport hysteresis throughout the unsteady hydrograph flows.

Initial Bed Load Motion and General Sediment Transport

In our study, the initiation of bed load motion and the general bed load sediment transport rates throughout the unsteady hydrograph flows could be determined by using the widely employed dimensionless reference shear stress approach, developed by Parker et al. (1982), which is written for fractional sediment transport in the following form:

$$W_i^* = m\left(1 - 0.8531\frac{\tau_{ri}^*}{\tau_r^*}\right)^n \tag{4}$$

Here, m and n are modified transport coefficients derived using nonlinear regression (Waters and Curran, 2015), $\tau_{ri}{}^*$ corresponds to a dimensionless reference transport rate for different size class (denoted by subscript i) that corresponds to $W_i^* = q_{bi}^*/\tau_i^{*3/2} = 0.002$, in which $q_{bi}{}^*$ is the normalized Einstein bed-load parameter (Einstein, 1942), expressed as

$$q_{bi}^* = \frac{q_{bi}}{\rho_s\sqrt{\left(\frac{\rho_s}{\rho} - 1\right) g d_i^3}} \tag{5}$$

where q_{bi} are fractional bed-load transport rates (kg·m^{-1}·s^{-1}), ρ_s and ρ are the sediment and fluid densities, respectively, and d_i denotes the average grain size within a particular size class in non-uniform sediment mixture.

Similarly, fractional sediment mass flux transported over the duration of the unsteady hydrograph can be represented by normalized total and fractional bed load yield parameters $W_t{}^*$ and $W_{ti}{}^*$, respectively (e.g. Bombar et al., 2011), such that

$$W_{ti}^* = \frac{W_{ti}}{\rho_s b d_i^2} \tag{6}$$

where W_{ti} is fractional bed load mass transport (kg) collected in a sediment trap over the hydrograph duration, and b is the sediment trap width (<channel width B).

Hysteresis for Bed Load Sediment Transport

Hysteretic relations are commonly observed for well-known variables in natural system. Generally, quantitative indices are valuable tools to develop a classification of hysteretic patterns in the past decade (Zuecco et al., 2016). For example, Mao (2018) used the hysteresis index of Langlois et al. (2005) to analyze the temporal dynamics of liquid discharge and bed load sediment transport, this index is defined as the ratio of the area below the regression lines fitted with the rising and falling limb hydrograph data, which is particularly suited for sediment transport in symmetrical the hydrographs and could be formulated as

$$H = \frac{\int_{Q_{min}}^{Q_{max}} q_{bi,r}}{\int_{Q_{min}}^{Q_{max}} q_{bi,f}} \tag{7}$$

in which, Q_{min}, Q_{max} represent the minimum and maximum discharges that correspond to measurable sediment transport rates in each limb within a hydrograph, $q_{bi,r}$, $q_{bi,f}$ are the bed load transport rates for a particular size class measured on rising and falling limb, respectively. Since the hysteresis index H is calculated as a ratio, a value of $H \approx 1.0$ means a lack of hysteresis, $H > 1.0$ indicates clockwise hysteresis, and $H < 1.0$

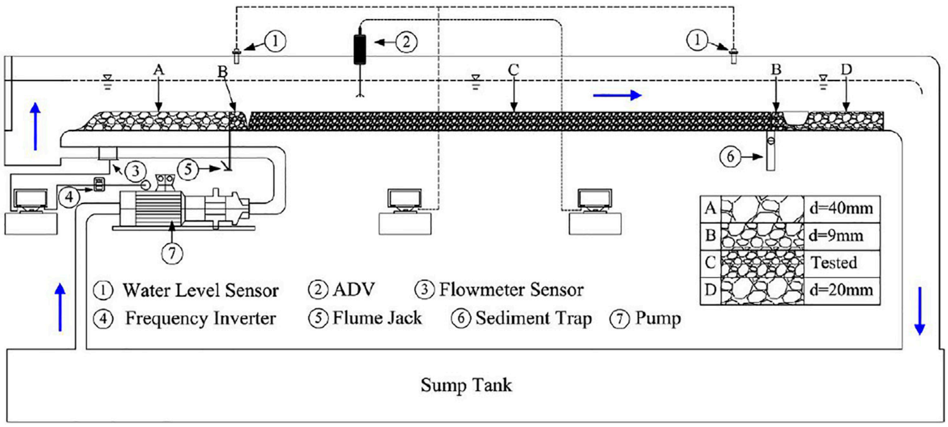

FIGURE 1 | Schematic representation of flume channel and experimental set-up.

indicates counterclockwise hysteresis (Mao, 2018). In nature, integrating the fractional bed load sediment rates along minimum and maximum flow is a representative of an overall sediment yield produced by either rising or falling limb. Here, the transport yield parameter W^*_{ti} is useful to provide information on the cumulative transport response of the graded sediment bed over the full hydrograph duration, in particular, a separative bed load yields attained during the rising and falling hydrograph limbs could be used as a direct surrogate to quantify sediment transport hysteresis in symmetrical hydrographs if a continuous measurement performed. As such, **Eq. 7** can be directly converted to the following form using limb-dependent bed load yields:

$$H = \psi_{ti} = \frac{W^*_{ti,r}}{W^*_{ti,f}} \tag{8}$$

where $W^*_{ti,r}$ and $W^*_{ti,f}$ represent fractional, non-dimensional bed-load yields measured during the rising and falling hydrograph limbs, respectively. Comparatively, **Eq. 8** is more convenient than **Eq. 7** in practical application.

EXPERIMENTAL MATERIALS AND METHODS

Flume Set-Up and Bed Sediments

Our experiments are conducted in a 22 m-long, 0.75 m-wide and 0.5 m-deep flow-recirculating, tilting flume channel (see **Figure 1**) in the Environmental Hydraulics Laboratory at Heriot-Watt University. The flume set-up and experimental operation are the same as described in Wang et al. (2019). The changing flow conditions in the channel were controlled by a pump frequency inverter capable of adjusting pump speed and producing repeatable, smooth hydrographs (where flow rates vary continually with time, see **Figure 2**) of any desired shape, and with a peak discharge up to 100 L s^{-1}. The unsteady hydrograph flows were monitored with a non-intrusive ultrasonic flow meter installed in the pipe delivering water to the channel inlet. A good match between prescribed design flows and the actual measured flows can be guaranteed by the sufficient measurement accuracy (±0.01 L s^{-1} typically), as well as minor statistical difference (i.e. 0.002 ± 0.28 L s^{-1}).

The graded sediment mixture employed in our experiments exhibits a fine-grained particle size distribution (31% sand–69% gravel, see **Figure 3**). Owing to the stochastic nature of sediment transport, especially for different grain sizes in a graded sediment mixture mobilized by unsteady flows, the interpretation of individual fractional sediment transport can sometimes be misleading. Thus, in order to reduce the uncertainties associated with the stochastic nature of size-dependent bed load transport, and obtain reliable knowledge of the dynamic response of graded sediment to varying flow conditions, a size classification approach proposed by Kuhnle and Southard (1988) and Frey et al. (2003) is employed here, whereby the experimental graded sediment mixture is subdivided into three distinct size classes or groupings, termed *fine*, *medium* and *coarse* (i.e., denoted as *F*, *M*, *C*). Specifically in terms of grain sizes *D*, the fine sediment class was defined as D = 1.0–2.8 mm, the medium grain size class as D = 2.8–6.3 mm, and the coarse size class as $D > 6.3$ mm. Within the undisturbed design sediment mixture, the relative proportion (by sieved weight) of these fine *F*, medium *M* and coarse *C* size classes is approximately 44, 38, 18%, respectively.

It should be noted that no additional sediment was supplied at the flume inlet or recirculated in the channel system over the duration of each experimental run. As such, the current experiments represent the typical low or limited sediment feed conditions usually encountered in regulated river reaches (e.g., downstream of a dam or reservoir). This upstream boundary setup helps simplify the experimental procedure between different runs, as well as our interpretation of bed load sediment transport hysteresis that is generally known to vary with many external factors (e.g., sediment feed mode, flow conditions, sediment type and grading, and bed conditions), as mentioned earlier.

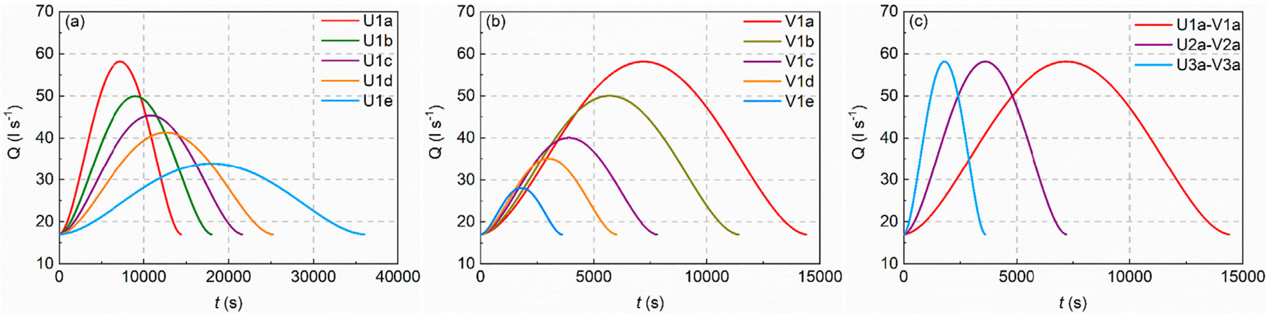

FIGURE 2 | Design flow hydrographs with varying **(A)** unsteadiness Γ_{HG} (group U1), **(B)** total water work W_k (group V1), and **(C)** unsteadiness Γ_{HG} and total water work W_k (group UV).

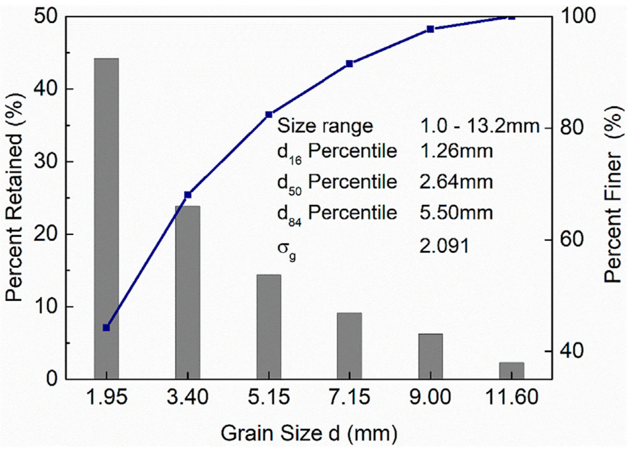

FIGURE 3 | Grain size distribution and percentiles for graded sediment mixture tested in the current study (Wang et al., 2021).

Experimental Procedure

Flume experiments were performed with an initial longitudinal bed slope S_0 of 0.002. At this slope, the base (antecedent) flow for $Q_b = 17.0$ L s^{-1} and $H_b = 0.059$ m was found to satisfy sub- and near-threshold conditions, as critical Shields stress parameter $\tau_{b,cr}{}^*$ for the fine F size class in the sediment mixture estimated to be $\tau_b{}^* = u_b{}^{*2}/(\gamma_s - \gamma) g d_{50} = 0.037$ with $u_b{}^* = (gH_b{\cdot}S_0)^{1/2} = 0.034$ m s^{-1}. By considering the sediment bed to be static and immobile during the base flow phase, the water surface slope S_f is approximately equivalent to bed slope S_0 and, as such, the base flow is deemed to be a steady, uniform flow condition.

The experimental configurations and protocols are exactly the same as described in Wang et al. (2021). The flume was segmented into three sections, including an effective working length covered with a uniform bed layer of the fine-grained sediment mixture, whereas the remaining part in the upstream and downstream flume channel were artificially roughened to prevent local scour and ensure the turbulent boundary layer is fully developed in the erodible test bed section. Our experiments are initiated by introducing a very low flow ($Q = 3.0$ L s^{-1}) into the channel to avoid any initial sediment bed disturbance and submerge the manually-placed sediment bed. The pump flow rate is then gradually increased to base flow condition Q_b. The sediment bed was then worked by the unsteady hydrograph flow after being subject to a base (antecedent) flow over a short period of 15 min. During the hydrograph flow conditions, the transported bed load sediments are collected at regular intervals (e.g., 5–30 min depending on hydrograph duration and magnitude) within a sediment trap located towards the downstream end of the erodible bed section. In all runs, the number of sampling time intervals were set to be identical on both limbs of the symmetrical hydrographs.

Hydrograph Flows

Three groups of design flow hydrographs were simulated in the current study, with full details of these hydrographs reported in the earlier work of Wang et al. (2021). In this study, we focus specifically on the bed load transport hysteresis under symmetrical hydrograph flows, for which hydrograph U1/V1/U1a-V1a (highlighted in **Table 1**) serves as a benchmark for the design of other hydrograph flow conditions tested. Hence, flow hydrographs in groups V1 and U1 are generated either by varying total water work W_k or unsteadiness Γ_{HG} (whilst holding the other parameter constant). In experimental group UV, both W_k and Γ_{HG} are varied whilst retaining a constant peak flow Q_p condition. The reduction in total hydrograph duration ΔT thus leads to the increase of Γ_{HG} and decrease of W_k from hydrograph U1a-V1a to U3a-V3a (see **Figure 2**).

As previously stated, hysteresis behaviour is observed between flow parameters such as flow depth, velocity, and flow rate in unsteady flows (e.g., Graf and Qu, 2004). Moreover, the water surface slope S_f can vary with respect to the bed slope S_0, Ghimire and Deng (2012) suggested that the following expression orignitated from the St Venant equations could be used to estimate the shear stress in unsteady flows,

$$\tau_b = \rho_f g R_b \left(S_f + \beta \frac{dQ}{dt} \right) \tag{9}$$

where ρ_f is the fluid density, R_b is the hydraulic radius of the bed, β [$= 1/(BgH)$] is a parameter related to the flood hydrograph slope

TABLE 1 | Unsteady hydrograph flow conditions employed in the present study (Wang et al., 2021).

Group	Run no	Q_p (l·s^{-1})	H_p (m)	ΔT_R (s)	ΔT_F (s)	ΔT (s)	Γ_{HG} (×10^{-4})	W_k	η
V1	V1a	58.0	0.1228	7,200	7,200	14,400	1.400	221.76	1.0
	V1b	52.0	0.1150	6,300	6,300	12,600	1.405	157.94	1.0
	V1c	46.0	0.1069	5,400	5,400	10,800	1.402	112.94	1.0
	V1d	40.0	0.0983	4,500	4,500	9,000	1.381	74.78	1.0
	V1e	35.0	0.0908	3,600	3,600	7,200	1.395	47.32	1.0
U1	U1a	58.0	0.1228	7,200	7,200	14,400	1.400	221.76	1.0
	U1b	50.0	0.1124	9,000	9,000	18,000	0.937	214.02	1.0
	U1c	45.0	0.1055	10,800	10,800	21,600	0.680	221.24	1.0
	U1d	41.0	0.0998	12,600	12,600	25,200	0.512	221.12	1.0
	U1e	34.0	0.0892	18,000	18,000	36,000	0.265	219.18	1.0
UV	U1a-V1a	58.0	0.1228	7,200	7,200	14,400	1.400	221.76	1.0
	U2a-V2a	58.0	0.1228	3,600	3,600	7,200	2.801	110.88	1.0
	U3a-V3a	58.0	0.1228	1,800	1,800	3,600	5.602	55.44	1.0

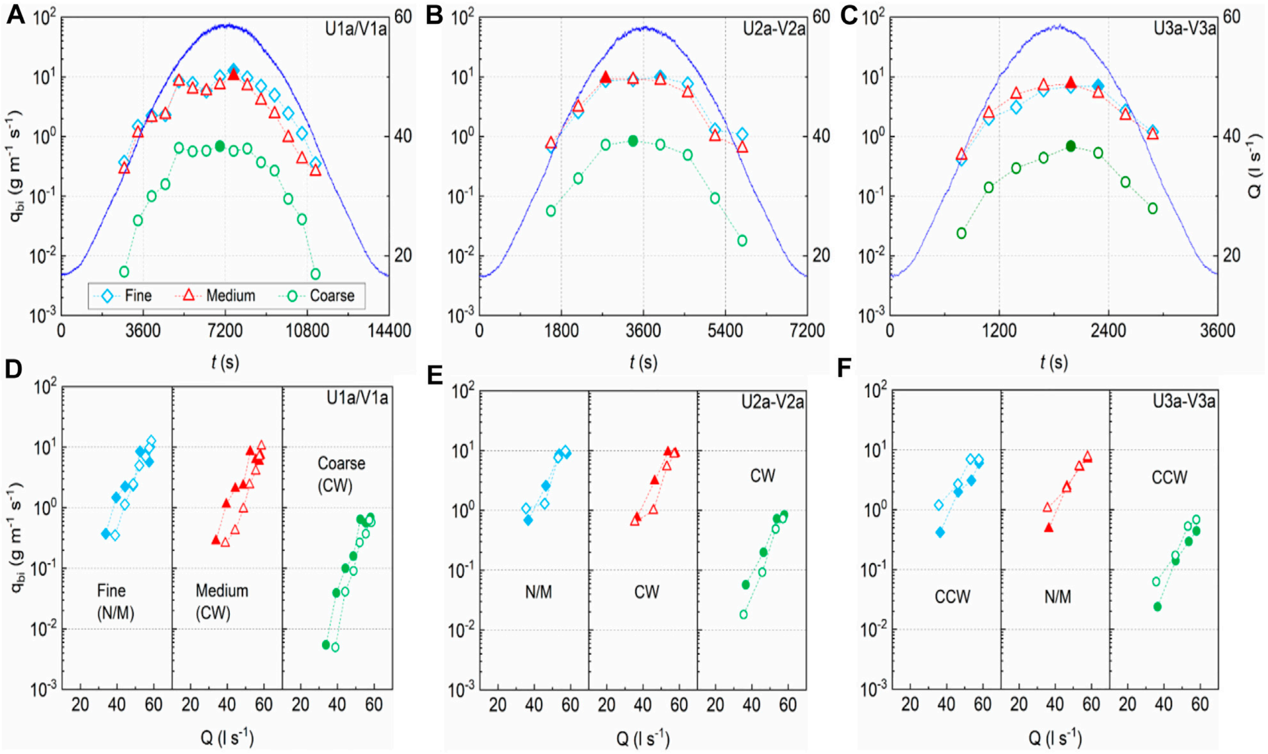

FIGURE 4 | (A–C) Illustrative plots showing temporal variation in flow rate *Q* and fractional bed load transport rates q_{bi} (for fine *F*, medium *M* and coarse *C* size classes), and **(D–F)** q_{bi}:*Q* phase plots showing representative hysteresis patterns for hydrograph runs **(A,D)** U1a (V1a); **(B,E)** U2a-V2a and **(C,F)** U3a-V3a (see **Table 1**).

with shear stress τ_b during the unsteady flow [in which *B* is the channel width and *H* is the flow depth], *Q* is the flow rate and *t* is the time. It is noted for the range of hydrographs considered in the present study, $\beta = 1.11\text{–}2.31\ \mathrm{m^{-3}\,s^2}$ and $dQ/dt = O\ (10^{-5}\text{–}10^{-6})\ \mathrm{m^3\,s^{-2}}$, indicating the additional shear stress exerted from flow gradient and hydrograph slope is relatively small, as such, **Eq. 9** could be reduced to $\tau_b = \rho_f g R_b S_f$ for predicting shear stress.

RESULTS

Bed Load Sediment Transport Hysteresis

In our experiments, we observed bed load sediment transport to have clockwise, no/mixed and counterclockwise hysteresis, with these different sediment hysteresis patterns particularly noticeable in experimental hydrograph group UV. More details on the temporal variations in fractional transport rates

$q_{b,i}$ in groups V1 and U1 can be found in Wang et al. (2021). Here, the size-class-dependent bed load transport rates q_b in this group UV are presented in **Figures 4A–C** for illustrative purposes. As expected, the temporal variations in measured bed load transport rates q_b for three defined size classes are largely shown to increase and decrease during the rising and falling hydrograph limb, respectively. However, closer examination indicates that the three size classes *C*, *M* and *F* tend to attain their peak bed load transport rates $q_{b,max}$ at different time instants around the peak flow phase $Q_{\max}$. Specifically, the coarse size class *C* attains its peak $q_{b,max}$ value at earlier elapsed times than the fine size class *F*, while the timing of peak $q_{b,max}$ for the medium size class coincides with either the coarse size class *C* (U3a-V3a, **Figure 4C**) or the fine size class *F* (U1a-V1a, **Figure 4A**), or is significantly earlier for hydrograph flow U2a-V2a (**Figure 4B**). It is also noted that the temporal lag between $q_{b,max}$ values appears to be consistent for the coarse *C* and fine *F* size classes, but varies for the medium *M* size class between hydrographs. This temporal lag effect was also found for fractional peak $q_{b,max}$ in a previous smaller scale study investigating the response of uni-modal and bimodal sediments to unsteady hydrograph flows under different experimental configurations (Wang et al., 2015).

In addition to differential response of varying size classes to changing flows in terms of temporal lag effect between their peak bed load transport rates $q_{b,max}$ and peak flow $Q_{\max}$, direct phase plot of fractional q_{bi} rates versus flow *Q* provides a more holistic approach to identify and categorise particular hysteretic behaviour in bed load transport for each hydrograph flow condition tested. These plots, for the same experimental group UV runs, are presented in **Figures 4D–F**. In the majority of cases, the q_b:*Q* phase plots reveal noticeable differences in the bed load sediment transport rates monitored during both hydrograph limbs, either in the form of clockwise (CW) or counterclockwise (CCW) loops. For runs where clear hysteresis is less evident, a no/mixed (N/M) hysteresis category is introduced to encompass all other hysteresis types [i.e., the single-valued, single-valued plus a loop and figure-8 shaped loop, see Wang et al. (2019)]. Moreover, it is apparent that coarse *C* and fine *F* size classes display contrasting hysteretic behaviour, with the coarse *C* size class presenting CW hysteresis in long-duration hydrographs U1a-V1a, U2a-V2a (**Figures 4D,E**) and CCW hysteresis in short-duration hydrograph U3a-V3a (**Figure 4F**). By contrast, the fine size *F* class varies from N/M to CCW hysteresis in hydrographs U1a-V1a → U3a-V3a (**Figures 4D–F**). This is, in essence, consistent with previously observed temporal lag effect of peak bed load transport rate $q_{b,max}$ for the coarse *C* and fine *F* size classes. By contrast, the hysteretic patterns of medium *M* size class is largely similar to coarse *C* size class in longer duration hydrographs, but unexpectedly demonstrates distinct N/M hysteresis for the shortest duration hydrograph (i.e., U3a-V3a, **Figure 4F**) in this study. Overall, it is noted that this size-dependent hysteretic behaviour agrees well with the fractional hysteretic response of bimodal bed load sediment to the symmetrical triangular and smooth hydrographs of Guney et al. (2013) and Wang et al. (2015), respectively.

Thresholds and Hysteresis of Sediment Motion

As stated before, it has commonly been assumed that the critical flows for sediment motion are of equivalence on the rising and falling limbs of a hydrograph flow (e.g., Plumb et al., 2020). In fact, this assumption inherently violates the principle of hysteretic behaviour, particularly when considering clockwise and counterclockwise loops that have been reported extensively for bed load sediment transport in a wide range of single-peaked hydrograph flows including in the current study. In addition, it has been found from our earlier studies (e.g., Wang et al., 2019; 2021) that the difference between bed load transport rates on both limbs decreased with increasing flows, implying that the difference tends to be more pronounced during more rapidly-changing (low) flow conditions (i.e., where $dQ/dt > 0$ on the rising limb and $dQ/dt < 0$ on the falling limb) than either side of the peak flow condition (i.e. where $dQ/dt \approx 0$). On this basis, it is informative to analyze the potential changes in threshold flow conditions that define the initiation and cessation of sediment motion during the rising and falling limbs, respectively.

Following the method of Parker et al. (1982), the reference shear stress $\tau_{ri}{}^*$ for the bed load incipient motion was defined as the shear stress that corresponds to a reference dimensionless bed load transport rate $W_i{}^* = 0.002$. This is obtained by plotting $W_i{}^*$ for each size class (i.e., *C*, *M* and *F*) against their normalized shear stresses $\tau_i{}^*$ and obtaining $\tau_{ri}{}^*$ from the best-fit regression at $W_i{}^* = 0.002$. As such, the size-dependent reference shear stresses $\tau_{ri}{}^*$ on the rising and falling limbs of hydrographs in experimental group UV are graphically determined in **Figure 5** and listed in **Table 2**. It is immediately apparent that the rising limb $\tau_{ri}{}^*$ values are smaller than their falling limb counterparts for the *M* and *C* size classes that display CW hysteresis (**Figures 5A,B**). However, this trend is reversed for the coarse *C* and fine *F* size classes displaying CCW hysteresis (**Figure 5C**). Even accounting for the sediment transport rates with N/M hysteresis, the values of $\tau_{ri}{}^*$ are shown to still vary significantly on both hydrograph limbs. This corroborates the hypothesis that this difference manifests itself in the different levels of stream power required at the thresholds for the initiation and cessation of sediment motion during the rising and falling hydrograph limbs, resepectively (Reid et al., 1985), as opposed to the common assumption of a fixed, critical shear stress condition on both limbs. Furthermore, the representative hysterestic patterns (and particularly the CW and CCW loops) appear to have strong association with the threshold flows associated with sediment mobilisation on the two hydrograph limbs. As bed load transport rates are generally higher on the rising limb than on the falling limb for CW hysteresis, this suggests that a lower shear stress condition is required to trigger sediment motion on the rising limb than the equivalent shear stress condition required for the cessation of sediment motion during the falling limb. The opposite is corrent for sediment transport with a CCW hysteresis, as a series of

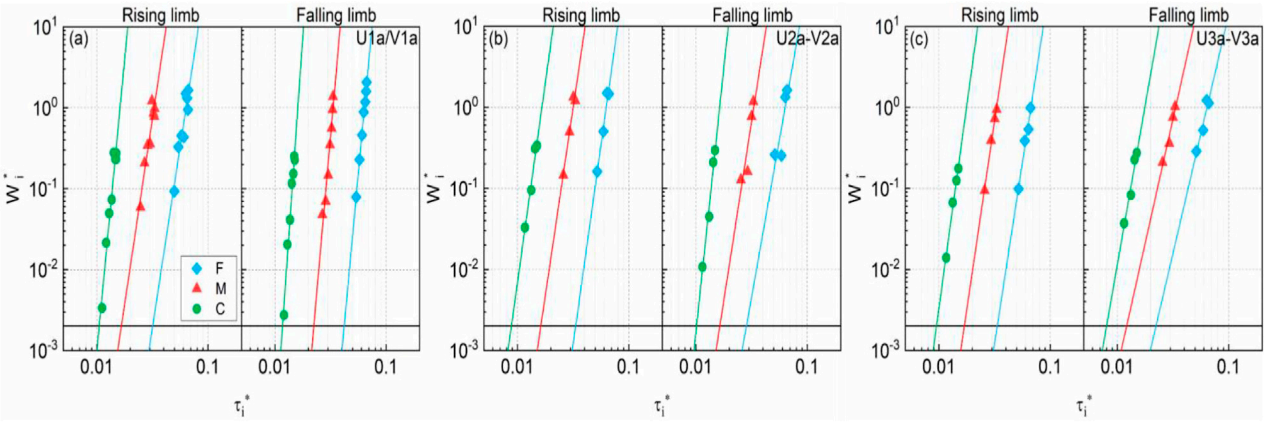

FIGURE 5 | Illustrative examples showing the reference shear stress τ_{ri}* for fine *F*, medium *M* and coarse *C* size classes on rising and falling limbs for representative hydrograph runs **(A)** U1a (V1a), **(B)** U2a-V2a, and **(C)** U3a-V3a (see **Table 1**) using threshold transport criterion W_i* = 0.002.

TABLE 2 | Reference shear stress τ_{ri}* obtained for fine *F*, medium *M* and coarse *C* size classes on rising limb (RL) and falling limb (FL) for the same experimental runs as shown in **Figure 5**.

Size class	**U1a-V1a**			**U2a-V2a**			**U3a-V3a**		
	Hysteresis Mode	**RL τ_{ri}***	**FL τ_{ri}***	**Hysteresis mode**	**RL τ_{ri}***	**FL τ_{ri}***	**Hysteresis Mode**	**RL τ_{ri}***	**FL τ_{ri}***
Fine	N/M	0.03193	0.04207	N/M	0.03347	0.02587	CCW	0.03347	0.02234
Medium	CW	0.01667	0.02234	CW	0.01628	0.01647	N/M	0.01696	0.01215
Coarse	CW	0.01054	0.01173	CW	0.00885	0.01019	CCW	0.00955	0.00802

higher sediment transport rates are observed on the falling hydrograph limb compared to the rising limb (e.g., **Figure 4C**). By comparision, sediment transport with N/M hysteresis behaviour tends to result in greater variability in threshold shear stresses for sediment motion on both limbs. However, in nature, the generation of high (or low) critical flow conditions, whether during the rising or falling hydrograph limbs, also depends on the relative overall magnitude of bed load transport rates monitored on corresponding limbs, as indicated by CW and CCW hysteretic conditions.

It can also be detected by comparision of the τ_{ri}* values from hydrograph run U1a-V1a to the equivalent values for hydrograph U3a-V3a (see details in **Figure 5** and **Table 2**) that the fractional τ_{ri}* values appear to reduce as both total water work W_k reduces and unsteadiness Γ_{HG} increases, particularly on the falling hydrograph limbs. To obtain a comprehensive view of these dependencies, all fractional τ_{ri}* values are plotted against the total water work to unsteadiness ratio W_k/Γ_{HG} for each hydrograph condition in **Figure 6**, illustrated separately for both limbs. (Note: a high and low W_k/Γ_{HG} value in experimental group UV corresponds to hydrograph runs U1a-V1a and U3a-V3a, respectively). It is important to note that the fractional reference shear stresses τ_{ri}* are computed for size class dependent sediment transport measured separately in each run, instead of being derived from the overall, rising and falling limb bed load transport datasets, combined from all runs as previously presented in Wang et al. (2021). This separate treatment of run-dependent transport data should provide greater detail and facilitate improved interpretation of the impact of hysteresis on limb-depedent sediment threshold motion within unsteady hydrograph flows.

It is evident that the fractional reference shear stress τ_{ri}* values tend to increase by a varying extent when a combined hydrograph descriptor W_k/Γ_{HG} was increased (see **Figure 6**). This may arise due to a gradual reduction in the sediment response to slower changing flows with reducing unsteadiness Γ_{HG} (i.e. $\Gamma_{HG} = 5.6 \times 10^{-4} \rightarrow 0.265 \times 10^{-4}$ for runs U3a-V3a → U1e, see **Table 1**). This effect is invoked by the limited sediment supply condition and becomes more evident for the initial and final sediment grain motion during longer duration hydrographs with higher W_k/Γ_{HG} values (i.e. $\Delta T = 3600 \rightarrow 36000$ s for runs U3a-V3a → U1e, see **Table 1**). It is also shown that the initial motion of grains from the coarse *C* size class are less sensitive to the different accelerating hydrograph flows (see **Figure 6A**). This is due to the general exposure of coarse *C* particles at bed surface, making them more responsive to flow changes at the beginning of each run (as indicated by the lower τ_{ri}* values in **Figure 6A**). By contrast, the reference shear stress τ_{ri}* for fine *F* size class are generally much higher and tend to change significantly on both limbs when the ratio W_k/Γ_{HG} is varied (see **Figures 6A,B**). This higher magnitude and variability in τ_{ri}* values for the fine *F* size class is obtained

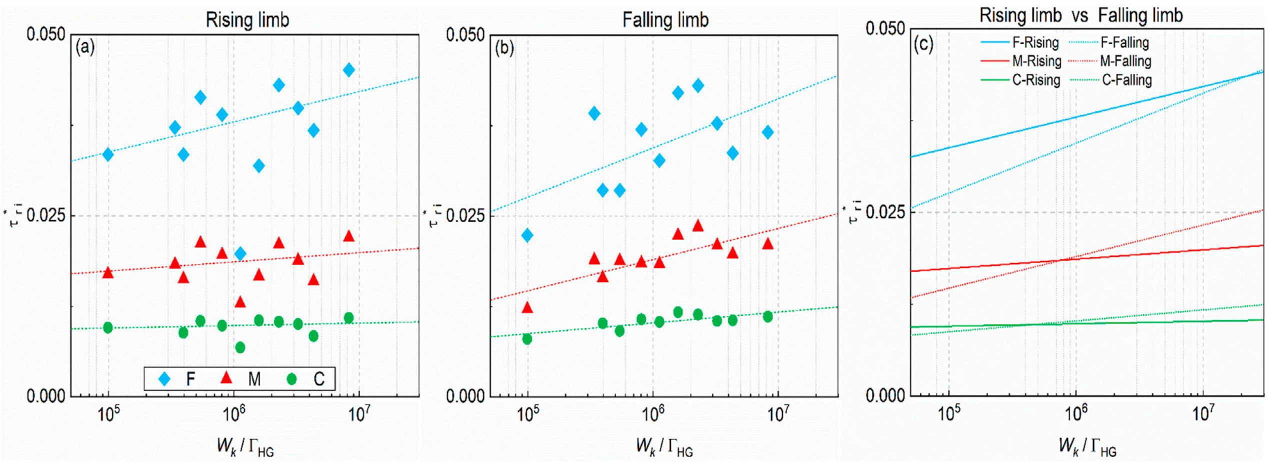

FIGURE 6 | Dimensionless reference shear stresses for fine *F*, medium *M* and coarse *C* size classes, grouped by rising **(A)** and falling limbs **(B)** and their fitted trend curves taken together **(C)** in all symmetrical hydrograph flows with varying W_k/Γ_{HG} values. Note: bed load transport rates measured over rising limb in run V1b is an outlier and excluded for best-fit regression (This outlier is attributable to an exceptional, unstable bed surface that leads to substantial sediment mobilisation at the beginning of this run).

mainly due to sheltering or hiding effects (i.e. the transport of fine sediment is suppressed significantly by the presence of coarse grains, especially when these coarse particles readily come to rest on the bed in a long-lasting receding flow limb and form static structural matrix as an impediment for fine sediment motion). Note: the small proportion of coarse *C* grains in the design sediment mixture, along with the no upstream sediment feed condition, results in a rapid depletion in the coarse sediment transport during the flow-sediment interactions. This consequently increases the $\tau_{ri}{}^*$ value of the final motion of coarse sediment transport during the long falling flow limb, compared to the equivalent $\tau_{ri}{}^*$ value for the initiation of motion on the rising limb. For the medium *M* sized grains, the variability in $\tau_{ri}{}^*$ with W_k/Γ_{HG} appears to lie between fine *F* and coarse *C* sediment size classes on both limbs, as shown in **Figures 6A,B**.

We can synthesize the effects of sediment transport hysteresis on the size-dependent reference shear stress $\tau_{ri}{}^*$ through plotting all fractional, limb-dependent best fit lines in **Figure 6C**. Over the range of $W_\mathrm{k}/\Gamma_{\mathrm{HG}}$ values tested in the study, we observe a greater increase of fractional $\tau_{ri}{}^*$ values on the falling limbs with increasing $W_\mathrm{k}/\Gamma_{\mathrm{HG}}$, compared to on the rising limbs. More importantly, it has been found that the CW and N/M hysteresis modes characterise predominantly the transport of the coarse *C* size class in the current hydrograph flows (Wang et al., 2021), as indicative of higher bed load transport rates of coarse sediment taking place during the rising limb compared to the falling limb. Thus, the critical flow condition required to initiate coarse sediment motion on rising limb is relatively small, while higher reference stresses $\tau_{ri}{}^*$ were obtained primarily on falling limb when the hydrograph $W_\mathrm{k}/\Gamma_{\mathrm{HG}}$ ratio increases (i.e., $W_\mathrm{k}/\Gamma_{\mathrm{HG}} > 5.0 \times 10^5$ for coarse sediment motion, **Figure 5C**). By contrast, the transport of fine *F* particles, that primarily featured displayed CCW and N/M hysteresis (Wang et al., 2021), means that higher bed load transport rates were obtained during the falling limb compared to on the rising limb. As such, this typically resulted in higher $\tau_{ri}{}^*$ values being obtained on the rising hydrograph limb over the range of $W_\mathrm{k}/\Gamma_{\mathrm{HG}}$ values studied. Clearly, the relative magnitudes of the $\tau_{ri}{}^*$ values identified for the three size classes *C*, *M* and *F* on both limbs are largely consistent with their respective temporal lag effects and hysteresis modes discussed earlier. In addition, the hydrograph $W_\mathrm{k}/\Gamma_{\mathrm{HG}}$ values that correspond to equivalence in the $\tau_{ri}{}^*$ values on both limbs appear to increase with decreasing grain size (i.e. $C \rightarrow M \rightarrow F$ sediment size classes, see **Figure 6C**). The marginal difference in $\tau_{ri}{}^*$ values for the coarse *C* sediment transport on both limbs over the full range of $W_\mathrm{k}/\Gamma_{\mathrm{HG}}$ values considered in the study is shown to correspond to a similar variation in $\tau_{ri}{}^*$ values for the medium *M* size class, but over a much narrower $W_\mathrm{k}/\Gamma_{\mathrm{HG}}$ range ($W_\mathrm{k}/\Gamma_{\mathrm{HG}} = 3 \times 10^5 – 2 \times 10^6$, **Figure 6C**).

The hysteretic implication of bed load transport on the initial and final sediment motion represented by reference shear stress derived on both limbs is graphically demonstrated in **Figure 7**. Here, a corresponding ratio ψ_{ri} is given to measure the magnitude of reference shear stress obtained on both limbs (i.e., $\psi_{ri} = \tau_{ri,r}{}^*/\tau_{ri,f}{}^*$, see **Figure 7A**). As previously stated, it is generally shown that fine *F* size class ratio $\psi_{ri} > 1$ for most hydrograph runs, meaning that $\tau_{ri,r}{}^* > \tau_{ri,f}{}^*$ in most cases. By contrast, the opposite situation, i.e. $\psi_{ri} < 1$, is again found for coarse *C* size class transport, with $\tau_{ri,r}{}^* < \tau_{ri,f}{}^*$ in most cases. More interestingly, a significant implication of the size-dependent sediment transport hysteresis is shown on the relative magnitude of corresponding reference shear stress used to define the thresholds of sediment motion of each size class on two limbs. It is apparent from **Figure 7B** that the cases with $\psi_{ri} > 1.0$ and $\psi_{ri} < 1.0$ correlate well with CCW and CW hysteresis, respectively, and are primarily attributed to sediment transport of the fine *F* and coarse *C* size class in the present study. By contrast, the cases in which $\psi_{ri} \approx 1.0$ correspond well with fractional sediment transport with

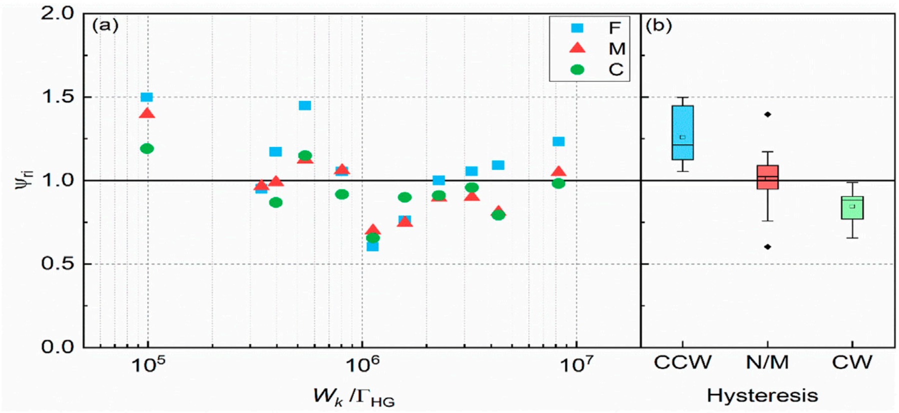

FIGURE 7 | Summary of **(A)** fractional stress threshold-motion ratio ψ_{ri} values for all symmetrical hydrographs for fine *F*, medium *M* and coarse *C* size classes, and **(B)** corresponding hysteretic modes compiled separately on the basis of bed load rates q_{bi} under CW, N/M and CCW hysteresis behaviour.

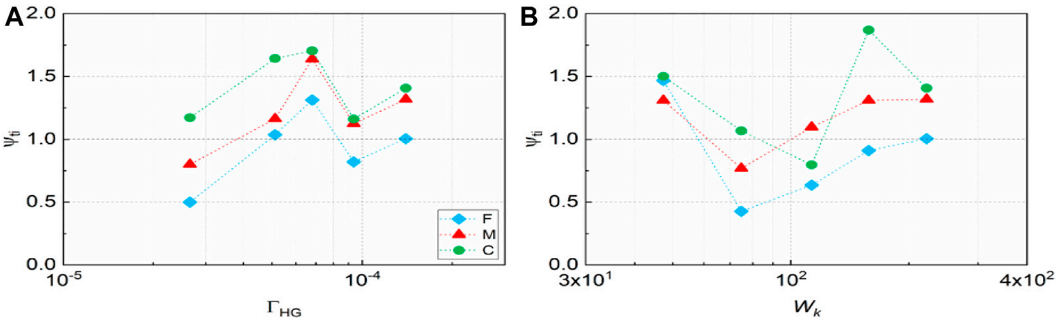

FIGURE 8 | Bed load yield ratios ψ_{ti} for fine *F*, medium *M* and coarse *C* size classes obtained plotted in **(A)** Γ_{HG}-varying (i.e., group U1, **Table 1)** and **(B)** W_k-varying **(**i.e., group V1, **Table 1)** hydrograph flows.

N/M hysteresis patterns that typically resulted from fine *F* and medium *M* size classes.

Bed Load Yields and Hysteresis of Sediment Motion

As stated previously, there is often a time lag between the arrival of peak bed load rates $q_{b,max}$ for the different grain size classes during the passage of a hydrograph. Again, bed load transport hysteresis reveals an overall, differential response of a particular size class in a graded sediment bed to the increasing and decreasing flow phases in a hydrograph. As such, **Eq. 8** is proposed to quantitively describe the hysteresis of bed load sediment transport within a symmetrical hydrograph. According to **Eq. 8**, the variability in bed load yield ratio ψ_{ti} for the coarse *C*, medium *M* and fine *F* size classes under experimental flow groupings V1 and U1 are presented in **Figure 8**. This figure indicates that there is little or no clear correlation between ψ_{ti} and either hydrograph unsteadiness Γ_{HG} (**Figure 8A**) or total water work W_k (**Figure 8B**). However, further comparison between size class dependent ψ_{ti} values shows that, in the majority of hydrograph runs, the hierarchy of the magnitude of ψ_{ti} values is coarse *C* size class ψ_{ti} > medium *M* size class ψ_{ti} > fine *F* size class ψ_{ti}. This, again, substantiates a more preferential response of the coarse *C* grains to changing flow over the rising limb of the simulated flood event, as partially reflected by an earlier appearance of peak transport rate q_{bi} for coarse *C* size class, compared to the fine *F* size class. Moreover, total water work W_k appears to display some degree of control on the difference of ψ_{ti} values among the three size classes, with differences shown to be comparatively subtle [i.e., $\Delta\psi_{ti} = \max(\psi_{ti}) - \min(\psi_{ti}) = 0.191$] when W_k is very low (i.e., $W_k = 47.32$ for hydrograph V1e, **Table 1**). It also results in a far more complex variation in the individual ψ_{ti} values for three size classes in experimental group UV, as evidenced by the total water work in hydrograph U3a-V3a (i.e., $W_k = 55.44$) which is only a quarter of the W_k value (i.e., $W_k = 221.76$) in hydrograph U1a-V1a, while the variation in ψ_{ti} values only reduce by a quarter (i.e., $\Delta\psi_{ti} = 0.40 \rightarrow 0.310$) over this range.

Our earlier tests using quasi-uniform sediments (Wang et al., 2019), indicated that the variation of the bed load yield ratio ψ_t with the combined hydrograph parameter W_k/Γ_{HG} follows a Boltzmann-type function. Therefore, all fractional ψ_{ti} values

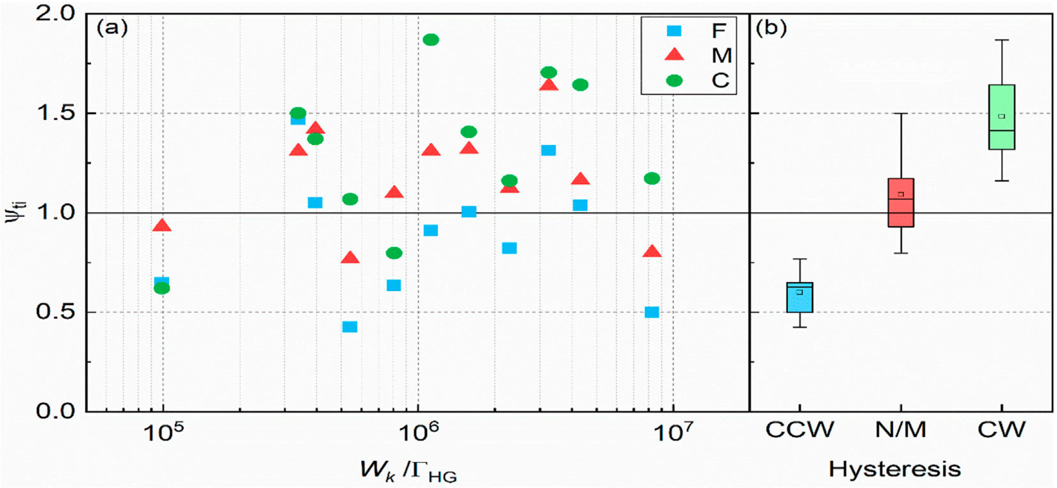

FIGURE 9 | Summary of **(A)** fractional bed load yield ratios ψ_{ti} in all symmetrical hydrographs for fine *F*, medium *M* and coarse *C* size classes, and **(B)** corresponding hysteretic mode compiled on the basis of their bed-load rates q_{bi} under CW, N/M and CCW hysteresis behavior.

with corresponding W_k/Γ_{HG} ratios are compiled along with sediment transport hysteresis patterns and presented in **Figure 9**. Again, while there is no explicit dependence of the fractional bed load yield ratio ψ_{ti} on the hydrograph parameter W_k/Γ_{HG}, a consistent hierarchy is found between fine *F*, medium *M*, and coarse *C* size class for symmetrical hydrographs with $W_k/\Gamma_{HG} > 10^6$ (i.e., for hydrographs with relatively large W_k and/or relatively small Γ_{HG} values). Within these hydrographs, with relatively low peak flows and long durations, it is suggested that the slowly-evolving flow conditions allow sufficient time for the varying grain sizes to adapt their transport rates under the bed limited sediment supply condition. As such, the temporal differences in the response of varying grain sizes to these slowly-changing hydrograph flows become more apparent and their hysteresis modes are more readily identified.

Furthermore, it is informative to apply the size-class dependent bed load yield ratios ψ_{ti} to characterise the basic hysteresis modes, as defined for the transport of the three size classes *C*, *M* and *F* in this study. In this regard, **Figure 9B** is plotted to illustrate the fractional bed load transport datasets with CW, N/M, and CCW hysteresis, along with their corresponding ψ_{ti} values. It is immediately apparent that the ψ_{ti} values are largely hysteresis interlinked, as expected. Specifically, the overall magnitude of ψ_{ti} values in the data showing CW and CCW hysteresis are much larger and smaller than unity, respectively, while the ψ_{ti} values in the data showing N/M hysteresis are closer to unity whilst exhibiting some overlap with those in CW hysteresis data. This indicates, by definition, good correspondence is expected between CW and CCW hysteresis patterns and bed load yield ratio ψ_{ti} values for symmetrical hydrograph flows, while our interpretation of the inter-relationship between N/M hysteresis data and their corresponding ψ_{ti} values is more complicated by the fluctuations of ψ_{ti} values that overlap with other hysteretic modes of bed load transport.

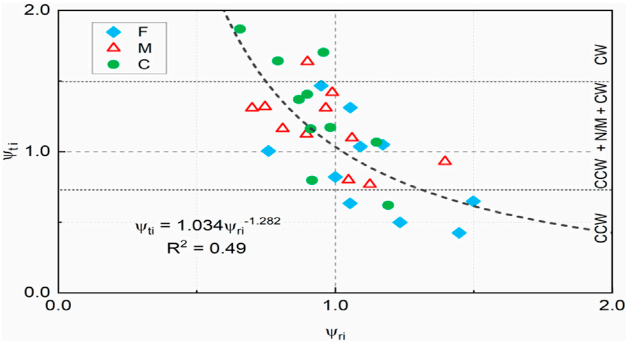

FIGURE 10 | Ratio of dimensionless reference shear stress for fine *F*, medium *M* and coarse *C* size classes in the rising limb over its counterpart in the falling limb (ψ_{ri}) plotted as a function of the corresponding ratios defined for size-specific bed load yields (ψ_{ti}).

Correlation Between Threshold Stress ψ_{ri} and Bed Load Yield ψ_{ti} Ratios

Our studies have demonstrated the linkage of size-dependent sediment transport hysteresis with their threshold motion deduced from limb-grouped transport data and corresponding ratio ψ_{ri} values. On the other hand, bed load yield ratios ψ_{ti}, comparing the bed load transport masses accumulated during both hydrograph limbs, can also be used as a good indicator to quantify the hysteresis of bed load sediment transport in symmetrical hydrographs, as described above. Considering the fact that bed load sediment transport hysteresis patterns are closely interconnected with both ratios of threshold stresses ψ_{ri} and bed load yields ψ_{ti} during the rising and falling hydrograph limbs (see **Figures** 7, **9**), it is reasonable to expect some form of functional relationship to exist between ψ_{ri} and ψ_{ti} that is determined by the relative fractional sediment transport characteristics arising within the individual hydrograph limbs.

In this regard, the plot of threshold stress ratio ψ_{ri} against bed load yield ratio ψ_{ti} is shown in **Figure 10**, as expected, a power relationship can be established between these transport properties through regression analysis, such that

$$\psi_{ti} = 1.034\left(\frac{1}{\psi_{ri}}\right)^{1.282} \tag{10}$$

It is shown from size class dependent datasets presented in **Figure 10** (and from **Eq. 10** above) that the ratios ψ_{ti} and ψ_{ri} are inversely correlated (R^2 = 0.49). This again corroborates our earlier finding that a smaller reference shear stress for the threshold motion of bed load sediment transport, either on the rising or falling limb, usually corresponds to cases characterised by larger sediment yields transported on that same limb during the passage of symmetrical hydrographs. Specifically, as in the case of sediment transport in significant CW hysteresis, the bed-load yields generated during rising limbs are much larger than those collected during falling limbs, with the reference shear stress for sediment initial motion on the rising limb obviously smaller than its corresponding value for sediment final motion on falling limb. This type of behaviour is mainly reflected in the transport of coarse *C* and medium *M* sediment size classes. By contrast, for the case of sediment transport with strong CCW hysteresis, bed load yields produced on the rising limb is much lower, while the reference shear stress for sediment motion on this limb is relatively large. This bed load transport scenario is primarily evidenced in the transport of the fine *F* sediment size class. Further, the bed load yields ratio ψ_{ti} generally decreases with an increase in the threshold stress ratio ψ_{ri} in CW → CCW hysteretic transitions in bed load transport, also shown in **Figure 10**. As such, it could be useful to employ **Eq. 10** in the prediction of limb-dependent sediment transport properties in unsteady hydrograph flows.

DISCUSSION

Implication of Hysteresis on Bed Load Transport Prediction

For graded sediment transport in symmetrical hydrographs, **Eq. 10** can potentially be used to estimate bed load yields and sediment threshold motion during both hydrograph limbs. It is also important to consider the prediction of sediment transport rates during hydrograph flows using existing transport models. As introduced previously, Waters and Curran (2015) employed **Eq. 4** to assess the non-dimensional sediment transport rates for entire datasets over the whole hydrograph, as well as limb-separated datasets. Here, we employed this method to quantify and analyse the graded sediment transport rates measured during our experiments. For the entire datasets, the best fit curve for graded sediment transport data is plotted in **Figure 11A**, along with similar curve given by Waters and Curran (2015) according to their measured bulk sediment transport rates under stepped hydrograph flows. It is shown that, for a given high W^*_i value in our datasets, the Waters and Curran (2015) curve tends to underestimate the specific Shields stress ratio τ_i^*/τ_{ri}^*. This appears somewhat associated with the higher reference stresses τ_{ri}^* for bed load transport under incremental steady flows within the stepped hydrograph case [e.g., τ_{ri}^* = 0.055–0.080 for sand fraction within the 70–30% sand-gravel mixture of Waters and Curran (2015)] than those obtained in the present study of continuously varying flows (e.g., τ_{ri}^* = 0.020–0.045 for the sand-gravel mixture in **Figure 3**). This implies that graded sediments are more likely to be entrained under smooth hydrograph flows than under stepped flow conditions. **Figure 11B** also plots the twin power curves using the separate-limb based method, outlined by Waters and Curran (2015), which provides a fairly good fit to the limb-specific transport rates, compared to considering the overall bulk transport data (e.g., **Figure 11A**), as indicated by the correlation coefficients listed in **Table 3**. From a process-based perspective, the separate-limb method is shown to have the merit of accounting for differences in the sediment transport rates during rising and falling limb of unsteady hydrograph flows, when compared to the bulk method (see **Figures 11A,B**).

However, these best-fit curves for bed load transport in the separate limbs are shown to have only marginal difference, caused by 1) relatively low bed load transport intensities for the graded sediment mixture tested under the range of hydrograph flow conditions (i.e., with most $W^*_i < 1.0$), when compared with quasi-uniform sediment transport experiments by Wang (2016) and by Waters and Curran (2015), and 2) bed load transport with CW, N/M and CCW hysteresis for fine *F*, medium *M* and coarse *C* size classes in the graded sediment bed, when taken together, mask the differential response of size-class dependent sediment transport to accelerating and decelerating flows on both hydrograph limbs. The hysteresis patterns, particularly in CW and CCW modes, are primarily responsible for the overall difference between all bed load transport rates on the rising and falling limbs. This suggests that prediction of bed load transport during unsteady, symmetrical hydrograph flows could be improved by considering fully the flow characteristics (i.e. rising and falling limbs specified in separated method), as well as the bed load transport hysteretic properties (i.e. CW, N/M and CCW hysteresis). On this basis, bed load sediment transport rates displaying either CW, N/M and CCW hysteresis during the rising-to-falling hydrograph limbs are fitted separately with power curves and plotted in **Figures 11C–E**. It is generally shown that the correlation coefficients (R^2 values, **Table 3**) for the fitted curves are reasonably increased if they also account for bed load transport hysteresis when applying the separate-limb method, under the following criteria: 1) case I - Rising-limb $W^*_i <$ falling-limb W^*_i for CW bed load transport hysteresis employing separate-limb method (**Figure 11C**); and 2) case II - Rising-limb $W^*_i >$ falling-limb W^*_i for CCW bed load transport hysteresis employing separate-limb method (**Figure 11E**). However, for case III where Rising-limb $W^*_i \approx$ falling-limb W^*_i in N/M bed load transport hysteresis, it is still recommended to use the bulk method (**Figure 11D**).

Boundary Conditions

The hydrograph flows simulated in the present flume experiments are all symmetrical (i.e., η = 1.0) with smooth

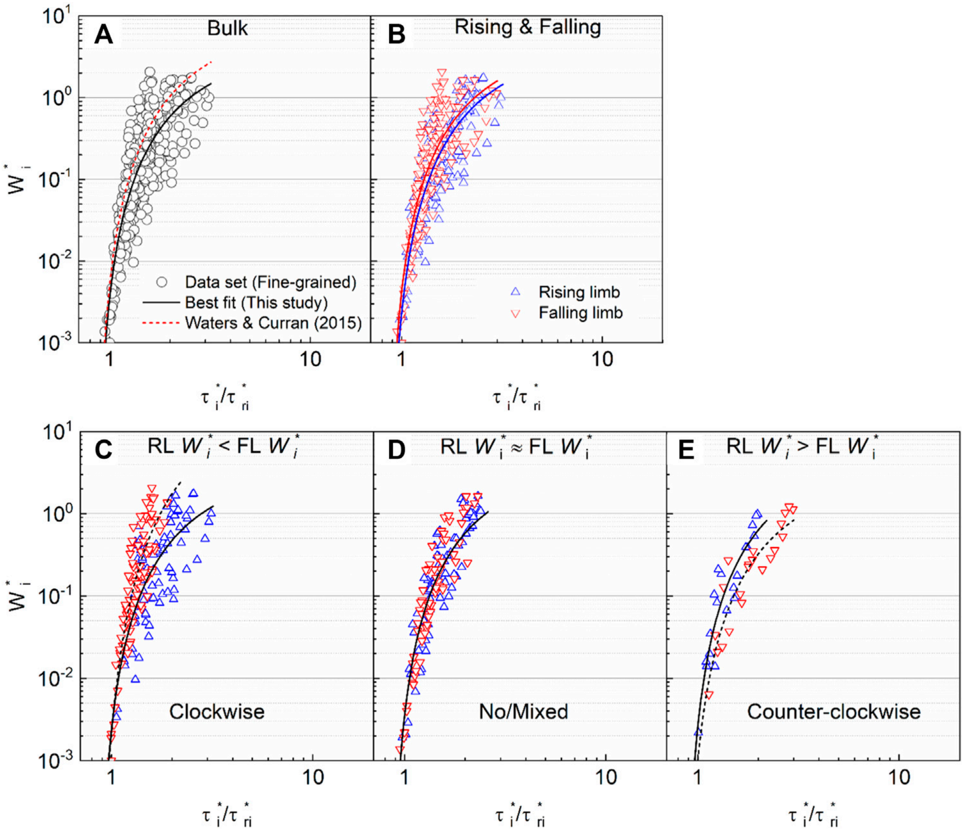

FIGURE 11 | Functional relationship between dimensionless bed load transport W_i^* and Shields stress ratio τ_i^*/τ_{ri}^* developed for **(A)** bulk transport dataset (i.e., represented by black solid and dashed line), **(B)** separate-limb dataset (i.e., all transport data on separate rising and falling limbs), **(C)** datasets where rising-limb (RL) W_i^* values < falling-limb (FL) W_i^* values (i.e., all transport data for CW hysteresis), **(D)** datasets where rising-limb (RL) W_i^* values ≈ falling-limb (FL) W_i^* values (i.e. all transport data with N/M hysteresis), and **(E)** rising-limb (RL) W_i^* values > falling-limb (FL) W_i^* values (i.e. all transport data with CCW hysteresis).

TABLE 3 | Values of parameters *m, n* and the correlation coefficient R^2 for the best-fit curve when applying **Eq. 4** to standard bulk and limb-separated datasets (i.e., **Figures 11A,B**) and our hysteretic mode-separated datasets (**Figures 11C–E**), in which sediment transport hysteresis modes are also taken into account (Note: RL for rising limb; FL for falling limb).

Data set	Bulk (Figure 11A)	RL and FL (Figure 11B)		RL W_i^* < FL W_i^* (Figure 11C)		RL W_i^*≈ FL W_i^* (Figure 11D)	RL W_i^* > FL W_i^* (Figure 11E)	
		Rising limb	Falling limb	Rising limb	Falling limb		Rising limb	Falling limb
M	4.74	5.03	5.61	4.12	27.22	4.68	6.04	3.47
N	3.75	4.00	3.75	3.90	4.95	3.75	4.06	4.26
R^2	0.74	0.75	0.76	0.62	0.80	0.84	0.85	0.85

triangular shaped profile (**Figure 2**). Under these unsteady flow boundary conditions, the bed load yield ratio ψ_{ti} is shown to be successful in describing bed-load sediment transport hysteresis modes (i.e., $\psi_{ti} > 1.0$ for CW hysteresis; $\psi_{ti} \approx 1.0$ for N/M hysteresis; and $\psi_{ti} < 1.0$ for CCW hysteresis). However, natural hydrographs are commonly non-symmetrical with shorter duration rising limbs, meaning that bed load yield ratios ψ_{ti} should be adjusted accordingly to quantify the hysteresis based on the hydrograph shape alone, such as considering cases where $\psi_{ti} > \eta$, $\psi_{ti} \approx \eta$, and $\psi_{ti} < \eta$, as indicative of CW, N/M and CCW hysteresis, respectively, for sediment transport under non-symmetrical hydrographs. Alternatively, those indexes already developed to characterise hysteresis for suspended sediment transport in flood hydrographs could also be considered when studying hysteretic behaviour in bed load sediment transport, such as **Eq. 7** proposed by Langlois et al. (2005) for suspended sediment and more recently employed by Mao (2018) to study bed load transport.

It has been specified in our study that no sediment is supplied from the upstream flume inlet over the duration of the experiment. This prescribed sediment boundary condition is typically representative of managed river channels, usually encountered in river reaches immediately downstream of dams or reservoirs, where longitudinal flow and sediment connectivity were disrupted (Cao et al., 2016; Li et al., 2018). As the magnitude of sediment transport in our experiment is relatively low, and the bed scour/erosion occurs primarily at the upstream end of the channel test section, the in-channel bed sediment supply from upstream compensates for the loss of bed sediments from more downstream sections, adjacent to the sediment trap. Nevertheless, it is shown that CW hysteresis is predominant characterizing feature of the observed bed load transport in our study (see **Figure 11C**) due to the lack of an upstream sediment supply. This effect has also been verified by previous related studies with zero upstream sediment feed (e.g., Hassan et al., 2006), while the impact of varying the sediment supply boundary condition (from limited to unlimited supply) on the resulting bed load transport hysteresis, more details can be found in other similar studies (e.g., Guney et al., 2013; Mao et al., 2014).

CONCLUSION

Our experimental study is undertaken to fully reveal the significant implications of hysteretic patterns on bed load sediment transport in terms of limb-dependent stress thresholds, size-dependent sediment transport rates and bed load yields that are generated by symmetrical hydrograph flows under a zero upstream sediment feed condition. Based on this study, the following conclusions can be drawn:

Typical clockwise (CW), no/mixed (N/M) and counter-clockwise (CCW) hysteresis modes are found to characterise graded (sand-gravel) bed load sediment transport in a series of symmetrical smooth triangular shaped hydrograph flows within the present study. The bed load transport hysteresis mode is found to be strongly dependent on the grain size class and hydrograph flow duration. Coarse *C* (gravel) sized sediment generally exhibits CW and N/M hysteresis, while fine *F* (sand) sized sediments usually displays N/M or CCW hysteresis, with medium *M* sized sediments varying in between. It is also shown that the dominant hysteresis mode generally changes from CW to CCW hysteresis as the hydrograph flow duration is decreased.

These hysteretic modes also have important implications for sediment threshold motion, as quantified by the reference bed shear stress. Due to the existence of hysteresis modes, especially CW and CCW modes, it is found that the reference shear stress (or critical flow rate) for the initiation and termination of sediment motion on both limbs is not likely to be identical in most experimental runs. This difference in limb-dependent reference shear stresses becomes significant for the fine *F* size class, while appearing to reduce for the coarse *C* size class. Moreover, the reference shear stress for coarse *C* sediment grains is generally smaller on the rising limb due to their relative exposure at the bed surface, responding preferentially to the changing (increasing) flow conditions (CW hysteresis), whereas fine sediment grains tend to obtain lower reference shear stress on the falling limb due to their delayed active response during receding flow conditions on the falling limb (CCW hysteresis).

These hysteretic modes also imply the existence of difference in size-dependent sediment transport rates on both limbs, especially those with CW and CCW hysteresis, as manifested through low bed load transport on both limbs. For this reason, a separate (or bimodal) limb method appears to perform well in predicting sediment transport rates generated during each limb in symmetric hydrograph flows compared to using a bulk method with the entire transport data. However, we believe that the hysteresis modes should be incorporated into the separate-limb method through which the relative magnitude of bed load transport rates measured during both limbs could be well identified, particularly for CW and CCW transport hysteresis modes (meaning the separate-limb or bimodal method should be considered individually for CW and CCW transport hysteresis modes), whereas the bulk method seems to perform reasonably well for the N/M bed load transport hysteresis.

Both bed load yield and stress threshold ratios (i.e. ψ_{ti} and ψ_{ri}) are developed to quantify the relative magnitude of bed load yields and reference shear stresses on both limbs of symmetrical hydrographs. As coarse *C* and fine *F* sediment transport in these hydrographs is generally characterised by CW (and N/M) and CCW hysteretic behaviour, respectively, the bed load yield ratio ψ_{ti} values for coarse *C* sediments are generally larger than for the fine *F* sediments. By contrast, the threshold stress ratio ψ_{ri} values for coarse *C* sediments are usually lower than for the fine *F* sediments. As such, bed load yield ψ_{ti} and threshold stress ψ_{ri} ratios are shown to be inversely correlated and follow a general power law (as expressed by **Eq. 10**), demonstrating a reasonable level of correlation.

DATA AVAILABILITY STATEMENT

The original contributions presented in the study are included in the article/Supplementary Materials, further inquiries can be directed to the corresponding authors.

AUTHOR CONTRIBUTIONS

LW: Conceptualisation, Methodology, Formal Analysis, Investigation, Writing – Original Draft; DW: Conceptualisation, Writing, Revision; AC: Conceptualisation, Writing – Original Draft, Project Administration, Supervision; DZ: Suggestions, Writing – Original Draft; GP: Conceptualisation, Supervision.

FUNDING

This work was supported financially by National Natural Science Foundation of China (Grants No. 52009041), the Project of International Cooperation and Exchanges NSFC (Grant No. 52061135104), the Fundamental Research Funds for the Central Universities (Grant No. 2020MS024), and the Scientific Program of China Institute of Water Resources and Hydropower Research (Grant No. SE 110145B0022021).

REFERENCES

Ahanger, M. A., Asawa, G. L., and Lone, M. A. (2008). Experimental Study of Sediment Transport Hysteresis. *J. Hydraulic Res.* 46 (5), 628–635. doi:10.3826/jhr.2008.3185

Aich, V., Zimmermann, A., and Elsenbeer, H. (2014). Quantification and Interpretation of Suspended-Sediment Discharge Hysteresis Patterns: How Much Data Do We Need? *Catena* 122, 120–129. doi:10.1016/j.catena.2014.06.020

American Society of Civil Engineers (2008). Sedimentation Engineering Manuals and Reports on Engineering Practice 110.

Bombar, G., Elçi, Ş., Tayfur, G., Güney, M. Ş., and Bor, A. (2011). Experimental and Numerical Investigation of Bed-Load Transport under Unsteady Flows. *J. Hydraul. Eng.* 137 (10), 1276–1282. doi:10.1061/(ASCE)HY.1943-7900.0000412

Camporese, M., Penna, D., Borga, M., and Paniconi, C. (2014). A Field and Modeling Study of Nonlinear Storage-Discharge Dynamics for an Alpine Headwater Catchment. *Water Resour. Res.* 50 (2), 806–822. doi:10.1002/2013WR013604

Cao, Z.-x., Hu, P., Pender, G., and Liu, H.-h. (2016). Non-capacity Transport of Non-uniform Bed Load Sediment in Alluvial Rivers. *J. Mt. Sci.* 13 (3), 377–396. doi:10.1007/s11629-015-3710-8

Curran, J. C., Waters, K. A., and Cannatelli, K. M. (2015). Real Time Measurements of Sediment Transport and Bed Morphology during Channel Altering Flow and Sediment Transport Events. *Geomorphology* 244, 169–179. doi:10.1016/j.geomorph.2015.03.009

Einstein, H. A. (1942). Formulas for the Transportation of Bed Load. *T. Am. Soc. Civ. Eng.* 107 (1), 561–577. doi:10.1061/taceat.0005468

Frey, P., Ducottet, C., and Jay, J. (2003). Fluctuations of Bed Load Solid Discharge and Grain Size Distribution on Steep Slopes with Image Analysis. *Experiments in Fluids* 35 (6), 589–597. doi:10.1007/s00348-003-0707-9

Gaeuman, D., Andrews, E. D., Krause, A., and Smith, W. (2009). Predicting Fractional Bed Load Transport Rates: Application of the Wilcock-Crowe Equations to a Regulated Gravel Bed River. *Water Resour. Res.* 45 (6). doi:10.1029/2008WR007320

Gaeuman, D. (2010). "Mechanics of Bedload Rating Curve Shifts and Bedload Hysteresis in the Trinity River, California," in *Proceedings of the 9th Federal Interagency Sedimentation Conference* (Nev: Las Vegas).

Ghimire, B., and Deng, Z. Q. (2012). Event Flow Hydrograph–Based Method for Modeling Sediment Transport. *J. Hydrol. Eng.* 18 (8), 919–928. doi:10.1061/(ASCE)HE.1943-5584.0000710

Graf, W. H., and Qu, Z. (2004). Flood Hydrographs in Open Channels. *Proc. Inst. Civil Eng. - Water Manag.* 157 (1), 45–52. doi:10.1680/wama.2004.157.1.45

Graf, W. H., and Suszka, L. (1985). "Unsteady Flow and its Effect on Sediment Transport," in *Proc. 21st IAHR Congress* (Mel-bourne, Australia, 1–5.

Guney, M. S., Bombar, G., and Aksoy, A. O. (2013). Experimental Study of the Coarse Surface Development Effect on the Bimodal Bed-Load Transport under Unsteady Flow Conditions. *J. Hydraul. Eng.* 139 (1), 12–21. doi:10.1061/(asce)hy.1943-7900.0000640

Gunsolus, E. H., and Binns, A. D. (2018). Effect of Morphologic and Hydraulic Factors on Hysteresis of Sediment Transport Rates in Alluvial Streams. *River Res. Applic* 34 (2), 183–192. doi:10.1002/rra.3184

Hassan, M. A., Egozi, R., and Parker, G. (2006). Experiments on the Effect of Hydrograph Characteristics on Vertical Grain Sorting in Gravel Bed Rivers. *Water Resour. Res.* 42 (9), 1–15. doi:10.1029/2005WR004707

Humphries, R., Venditti, J. G., Sklar, L. S., and Wooster, J. K. (2012). Experimental Evidence for the Effect of Hydrographs on Sediment Pulse Dynamics in Gravel-Bedded Rivers. *Water Resour. Res.* 48, W01533. doi:10.1029/2011WR010419

Kuhnle, R. A. (1992). Bed Load Transport during Rising and Falling Stages on Two Small Streams. *Earth Surf. Process. Landforms* 17 (2), 191–197. doi:10.1002/esp.3290170206

Kuhnle, R. A., and Southard, J. B. (1988). Bed Load Transport Fluctuations in a Gravel Bed Laboratory Channel. *Water Resour. Res.* 24 (2), 247–260. doi:10.1029/WR024i002p00247

Langlois, J. L., Johnson, D. W., and Mehuys, G. R. (2005). Suspended Sediment Dynamics Associated with Snowmelt Runoff in a Small Mountain Stream of Lake Tahoe (Nevada). *Hydrol. Process.* 19 (18), 3569–3580. doi:10.1002/hyp.5844

Lee, K. T., Liu, Y.-L., and Cheng, K.-H. (2004). Experimental Investigation of Bedload Transport Processes under Unsteady Flow Conditions. *Hydrol. Process.* 18 (13), 2439–2454. doi:10.1002/hyp.1473

Li, Z., Qian, H., Cao, Z., Liu, H., Pender, G., and Hu, P. (2018). Enhanced Bed Load Sediment Transport by Unsteady Flows in a Degrading Channel. *Int. J. Sediment Res.* 33 (3), 327–339. doi:10.1016/j.ijsrc.2018.03.002

Mano, V., Nemery, J., Belleudy, P., and Poirel, A. (2009). Assessment of Suspended Sediment Transport in Four alpine Watersheds (France): Influence of the Climatic Regime. *Hydrol. Process.* 23 (5), 777–792. doi:10.1002/hyp.7178

Mao, L., Dell'Agnese, A., Huincache, C., Penna, D., Engel, M., Niedrist, G., et al. (2014). Bedload Hysteresis in a Glacier-Fed Mountain River. *Earth Surf. Process. Landforms* 39 (7), 964–976. doi:10.1002/esp.3563

Mao, L. (2018). The Effects of Flood History on Sediment Transport in Gravel-Bed Rivers. *Geomorphology* 322, 196–205. doi:10.1016/j.geomorph.2018.08.046

Martin, R. L., and Jerolmack, D. J. (2013). Origin of Hysteresis in Bed Form Response to Unsteady Flows. *Water Resour. Res.* 49 (3), 1314–1333. doi:10.1002/wrcr.20093

Moog, D. B., and Whiting, P. J. (1998). Annual Hysteresis in Bed Load Rating Curves. *Water Resour. Res.* 34 (9), 2393–2399. doi:10.1029/98wr01658

Mrokowska, M. M., Rowiński, P. M., Książek, L., Strużyński, A., Wyrębek, M., and Radecki-Pawlik, A. (2018). Laboratory Studies on Bedload Transport under Unsteady Flow Conditions. *J. Hydrol. Hydromech.* 66 (1), 23–31. doi:10.1515/johh-2017-0032

Parker, G., Klingeman, P. C., and McLean, D. G. (198219837). Bedload and Size Distribution in Paved Gravel-Bed Streams. *J. Hydr. Div.* 108109 (4), 5445–5571. doi:10.1061/(ASCE)0733-942910.1061/jyceaj.0005854

Phillips, C. B., Hill, K. M., Paola, C., Singer, M. B., and Jerolmack, D. J. (2018). Effect of Flood Hydrograph Duration, Magnitude, and Shape on Bed Load Transport Dynamics. *Geophys. Res. Lett.* 45 (16), 8264–8271. doi:10.1029/2018GL078976

Phillips, J. D. (2003). Sources of Nonlinearity and Complexity in Geomorphic Systems. *Prog. Phys. Geogr. Earth Environ.* 27 (1), 1–23. doi:10.1191/0309133303pp340ra

Piedra, M. M., Haynes, H., and Hoey, T. B. (2012). The Spatial Distribution of Coarse Surface Grains and the Stability of Gravel River Beds. *Sedimentology* 59 (3), 1014–1029. doi:10.1111/j.1365-3091.2011.01290.x

Plumb, B. D., Juez, C., Annable, W. K., McKie, C. W., and Franca, M. J. (2020). The Impact of Hydrograph Variability and Frequency on Sediment Transport Dynamics in a Gravel-bed Flume. *Earth Surf. Process. Landforms* 45 (4), 816–830. doi:10.1002/esp.4770

Poff, N. L., Allan, J. D., Bain, M. B., Karr, J. R., Prestegaard, K. L., Richter, B. D., et al. (1997). The Natural Flow Regime. *BioScience* 47 (11), 769–784. doi:10.2307/1313099

Redolfi, M., Bertoldi, W., Tubino, M., and Welber, M. (2018). Bed Load Variability and Morphology of Gravel Bed Rivers Subject to Unsteady Flow: A Laboratory Investigation. *Water Resour. Res.* 54 (2), 842–862. doi:10.1002/2017WR021143

Reesink, A., Parsons, D., Ashworth, P., Hardy, R., Best, J., Unsworth, C., et al. (2013). The Response and Hysteresis of Alluvial Dunes under Transient Flow Conditions. *Mar. River Dunes 2013, Conf. Proc.* 220, 215.

Reid, I., Frostick, L. E., and Layman, J. T. (1985). The Incidence and Nature of Bedload Transport during Flood Flows in Coarse-Grained Alluvial Channels. *Earth Surf. Process. Landforms* 10 (1), 33–44. doi:10.1002/esp.3290100107

Spence, C. (2010). A Paradigm Shift in Hydrology: Storage Thresholds across Scales Influence Catchment Runoff Generation. *Geogr. Compass* 4 (7), 819–833. doi:10.1111/j.1749-8198.2010.00341.x

Suszka, U. L. (1987). *Sediment Transport at Steady and Unsteady Flow*. Lausanne: EPFL.

Vericat, D., Batalla, R. J., and Garcia, C. (2006). Breakup and Reestablishment of the armour Layer in a Large Gravel-Bed River below Dams: The Lower Ebro. *Geomorphology* 76, 122–136. doi:10.1016/j.geomorph.2005.10.005

Wang, L. (2016). *Bedlaod Sediment Transport and Bed Evolution in Steady and Unsteady Flows*. Edinburgh: Heriot-Watt University.

Wang, L., Cuthbertson, A. J. S., Pender, G., and Cao, Z. (2015). Experimental Investigations of Graded Sediment Transport under Unsteady Flow Hydrographs. *Int. J. Sediment Res.* 30 (4), 306–320. doi:10.1016/j.ijsrc.2015.03.010

Wang, L., Cuthbertson, A. J. S., Zhang, S. H., Pender, G., Shu, A. P., and Wang, Y. Q. (2021). Graded Bed Load Transport in Sediment Supply Limited Channels under Unsteady Flow Hydrographs. *J. Hydrol.* 595, 126015. doi:10.1016/j.jhydrol.2021.126015

Wang, L., Cuthbertson, A., Pender, G., and Zhong, D. (2019). Bed Load Sediment Transport and Morphological Evolution in a Degrading Uniform Sediment Channel under Unsteady Flow Hydrographs. *Water Resour. Res.* 55, 5431–5452. doi:10.1029/2018WR024413

Waters, K. A., and Curran, J. C. (2015). Linking Bed Morphology Changes of Two Sediment Mixtures to Sediment Transport Predictions in Unsteady Flows. *Water Resour. Res.* 51 (4), 2724–2741. doi:10.1002/2014WR016083

Williams, G. P. (1989). Sediment Concentration versus Water Discharge during Single Hydrologic Events in Rivers. *J. Hydrol.* 111 (1-4), 89–106. doi:10.1016/0022-1694(89)90254-0

Yen, C.-I., and Lee, K. T. (1995). Bed Topography and Sediment Sorting in Channel bend with Unsteady Flow. *J. Hydraulic Eng.* 121 (8), 591–599. doi:10.1061/(ASCE)0733-9429(1995)121:8(591)

Zuecco, G., Penna, D., Borga, M., and Van Meerveld, H. J. (2016). A Versatile index to Characterize Hysteresis between Hydrological Variables at the Runoff Event Timescale. *Hydrol. Process.* 30 (9), 1449–1466. doi:10.1002/hyp.10681

Conflict of Interest: The authors declare that the research was conducted in the absence of any commercial or financial relationships that could be construed as a potential conflict of interest.

frontiers in Environmental Science

ORIGINAL RESEARCH
published: 03 January 2022
doi: 10.3389/fenvs.2021.792289

Side Tributary Distribution of Quasi-Uniform Iterative Binary Tree Networks for River Networks

Keyi Wang[1], **Li Zhang**[2,3]*, **Tiejian Li**[3,4], **Xiang Li**[3,5], **Biyun Guo**[3,6], **Guoxin Chen**[3,4], **Yuefei Huang**[3,4] **and Jiahua Wei**[3,4]

[1]College of Transportation and Environment, Shenzhen Institute of Information Technology, Shenzhen, China, [2]School of Civil and Hydraulic Engineering, Huazhonng University of Science and Technology, Wuhan, China, [3]State Key Laboratory of Plateau Ecology and Agriculture, Qinghai University, Xining, China, [4]State Key Laboratory of Hydroscience and Engineering, Tsinghua University, Beijing, China, [5]State Key Laboratory of Simulation and Regulation of Water Cycle in River Basin, China Institute of Water Resources and Hydropower Research, Beijing, China, [6]Marine Science and Technology College, Zhejiang Ocean University, Zhoushan, China

Self-similarity and plane-filling are intrinsic structure properties of natural river networks. Statistical data indicates that most natural river networks are Tokunaga trees. Researchers have explored to use iterative binary tree networks (IBTNs) to simulate natural river networks. However, the characteristics of natural rivers such as Tokunaga self-similarity and plane-filling cannot be easily guaranteed by the configuration of the IBTN. In this paper, the generator series and a quasi-uniform iteration rule are specified for the generation of nonstochastic quasi-uniform iterative binary tree networks (QU-IBTNs). First, we demonstrate that QU-IBTNs definitely satisfy self-similarity. Second, we show that the constraint for a QU-IBTN to be a Tokunaga tree is that the exterior links must be replaced in the generator series with a neighboring generator that is larger than the interior links during the iterative process. Moreover, two natural river networks are examined to reveal the inherent consistency with QU-IBTN at low Horton-Strahler orders.

Keywords: horton-strahler (H-S) order, tokunaga tree, generator series, side tributary distribution, self-similarity, iterative binary tree network

Edited by:
Jaan H. Pu,
University of Bradford,
United Kingdom

Reviewed by:
Haiyun Shi,
Southern University of Science and Technology, China
Songdong Shao,
Dongguan University of Technology, China

***Correspondence:**
Li Zhang
lizhangpig@gmail.com

Specialty section:
This article was submitted to Freshwater Science,
a section of the journal
Frontiers in Environmental Science

Received: *10 October 2021*
Accepted: *12 November 2021*
Published: *03 January 2022*

Citation:
Wang K, Zhang L, Li T, Li X, Guo B, Chen G, Huang Y and Wei J (2022) Side Tributary Distribution of Quasi-Uniform Iterative Binary Tree Networks for River Networks.
Front. Environ. Sci. 9:792289.
doi: 10.3389/fenvs.2021.792289

INTRODUCTION

River networks are typically considered to be dendritic, self-similar, and plane-filling in plane shape (Horton, 1945; Tokunaga, 1966; Mandelbrot, 1982; Peckham, 1995b). With this in mind, their scalings have been comprehensively studied. The first method for quantifying the scale of streams in a river network was given by Horton (1945), and then modified by Strahler (1952) to create what is now known as the Horton-Strahler (H-S) ordering method. This method gives every stream an H-S order according to its position in the confluencing structure of a river network. It has become one of the most basic concepts in river network topology. Furthermore, the Horton ratios, which are the bifurcation ratio R_B, the length ratio R_L, and the area ratio R_A, have been well established and verified (Horton, 1945; Strahler, 1952). These ratios reflect the self-similarity of a river network by approximately formed geometric sequences.

Tokunaga (1966), Tokunaga (1978) introduced a bivariate stream ordering method based on the H-S method. The Tokunaga ordering method quantifies different confluences by using the H-S order in pairs to describe the flow of a tributary into its main stem. The mean ratio of the number of streams with H-S order ω to the number of streams with H-S order $\omega+k$, which are the streams that

H-S order ω streams flow into, is defined as the side-branching ratio T_k. Furthermore, Tokunaga (1978, 1984) recognized that the side-branching ratio characterizes the self-similar structure of a binary tree river network. Therefore, a strict constraint for a binary tree network to be a Tokunaga tree is that T_k varies geometrically with k but independently with ω. By using this constraint of side-branching ratios, large natural river networks have been proved to be Tokunaga trees (Tokunaga, 1978; Peckham, 1995a; Mantilla et al., 2010; Zanardo et al., 2013; Gupta and Mesa, 2014).

Additionally, studies on similarity and fractals have made the synthetic generation of iterative networks an efficient tool for simulating real systems with self-similarity. Some of these synthetic iterative networks have been used for hydrological simulations of their analogous natural river networks (Claps et al., 1996; Menabde et al., 2001; Veitzer and Gupta, 2001; Wang and Wang, 2002; Hung and Wang, 2005). Furthermore, recursive replacement networks have been introduced to show that the Horton laws are well predicted (Peckham, 1995a; Veitzer and Gupta, 2000; Mcconnell and Gupta, 2008). Synthetic trees generated by the Tokunaga model have been used to statistically evaluate the Tokunaga self-similarity, and have been compared with natural river networks (Zanardo et al., 2013). Besides the iterative replacement networks, the diffusion-limited aggregation (DLA) model using random walk as synthetic mechanism can also be used for river network generation, and is similar to natural river networks (Masek and Turcotte, 1993). However, none of these synthetic networks have been proved to be self-similar or Tokunaga trees, either mathematically or theoretically. Therefore, it is unreasonable to use them to capture the properties of natural river networks.

Using synthetic iterative networks to simulate natural river networks has limitations that need to be overcome, mainly in two aspects. First, a commonly accepted and rigorous mathematical definition of generators for river networks is needed. The lack of a rigorous definition of generators (Wang and Wang, 2002; Troutman, 2005) results in an inability to guarantee the basicness and completeness of the generator population. A basic and complete binary generator series has been specially and explicitly defined and graphed by Zhang et al. (2009), and has been proved to be effective and fundamental by means of comparison with data from China and the United States (Zhang et al., 2009). Second, the constraints of Tokunaga trees should be strictly added during the generation of synthetic iterative networks.

The main objectives of this paper involve specifying a common mathematical framework so as to 1) reemphasize the standard generator series for iterative networks; 2) generate an iterative binary tree network using the generator series and iteration rules; and 3) find the appropriate constraint that guarantees a synthetic iterative network to be a Tokunaga tree.

This paper is organized as follows. *Materials and Method* briefly reviews the rules and definitions of the H-S method, Tokunaga ordering method, Tokunaga tree, Generators and rules for the iterative binary tree networks (IBTNs). In *Results*, the mathematical derivations of side tributary distribution are shown recursively and graphically for quasi-uniform iterative binary tree networks (QU-IBTNs). The sufficient and necessary conditions for a QU-IBTN to be a Tokunaga tree are discussed in *Discussion*. Two natural river networks are given as examples to verify the feasibility of QU-IBTNs.

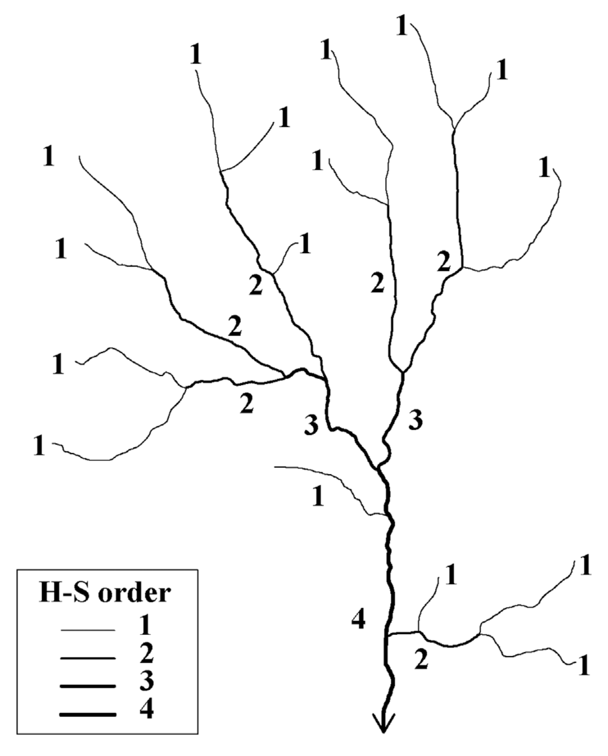

FIGURE 1 | H-S ordering method schematic diagram for the illustrated river network with H-S order 4. There are 16 streams with H-S order 1, 6 streams with H-S order 2, 2 streams with H-S order 3, and 1 stream with H-S order 4. The arrow at the bottom is the outlet of this river network.

MATERIALS AND METHOD

Tokunaga Tree

Horton (1945) and Strahler (1952) defined the classification method for the hierarchical structure of a river network by means of stream order as follows:

1) every source channel has an H-S order 1;
2) two streams with the same order, ω, confluence to a stream ordered $\omega + 1$; and
3) two streams with different orders, $u, v\,(u < v)$, confluence to a stream with ordered v.

The H-S order of the whole network, Ω, is defined as the highest order of all streams. The H-S ordering method is shown in **Figure 1**.

Tokunaga (1966) proposed an extended ordering method based on the H-S order. The Tokunaga ordering method reflects the topological relation of a side-branching tributary flowing into another stream with a higher order. His work

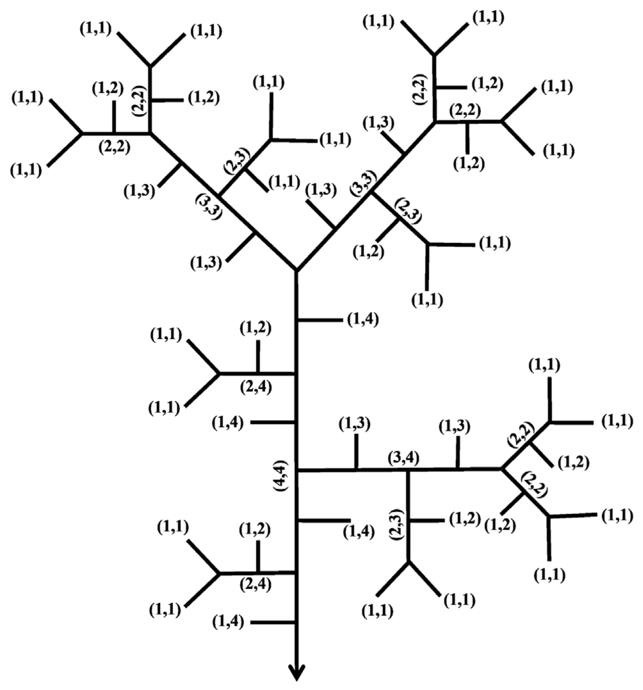

FIGURE 2 | Schematic diagram for the Tokunaga ordering method for a binary tree (from Zhang et al., 2009).

plays an important role in analyzing the topology of river networks because it represents the inherent self-similarity of a river network.

A stream with H-S order ω as a side-branching tributary flowing into a stream ordered ω' is assigned a Tokunaga order (ω, ω'), for which $\omega < \omega'$. A pair of streams as sources of a stream ordered $\omega + 1$ is assigned a Tokunaga order (ω, ω). **Figure 2** shows the Tokunaga ordering method applied to an example binary tree.

For a binary tree network, the Tokunaga stream number matrix $\boldsymbol{N}$ specifies the number of streams with Tokunaga order (ω, ω'), $N_{\omega,\omega'}$, as:

$$\boldsymbol{N} = \begin{pmatrix} N_{1,1} & N_{1,2} & N_{1,3} & \cdots & N_{1,(\Omega-1)} & N_{1,\Omega} \\ & N_{2,2} & N_{2,3} & \cdots & \cdots & N_{2,\Omega} \\ & & & \cdots & \cdots & \cdots \\ & & & & N_{(\Omega-1),(\Omega-1)} & N_{(\Omega-1),\Omega} \\ & & & & & N_{\Omega,\Omega} \end{pmatrix} \quad (1)$$

For example, the Tokunaga stream number matrix of the binary tree in **Figure 2** is:

$$\boldsymbol{N} = \begin{pmatrix} 22 & 11 & 6 & 4 \\ & 6 & 3 & 2 \\ & & 2 & 1 \\ & & & 1 \end{pmatrix} \quad (2)$$

Eq. 2 defines the ordering method in **Figure 2**, which shows 22 streams with Tokunaga order (1,1), 11 streams with Tokunaga order (1,2), and so on.

The Tokunaga side-branching ratio $T_{\omega,\omega+k}$ $(1 \le k \le \Omega - \omega)$, which is determined in terms of the ratio of the number of streams with the H-S order ω flowing into streams with the H-S order $\omega + k$ to the number of streams with the H-S order $\omega + k$, is defined as:

$$T_{\omega,\omega+k} = \frac{N_{\omega,\omega+k}}{N_{\omega+k}} = \frac{N_{\omega,\omega+k}}{\sum_{i=\omega+k}^{\Omega} N_{\omega+k,i}}, \; 1 \le k \le \Omega - \omega \quad (3)$$

An upper triangular matrix $\boldsymbol{T}$, which is calculated in terms of the Tokunaga stream number matrix $\boldsymbol{N}$ by **Eq. 3**, is defined as the side-branching ratio matrix with a dimension of $\Omega - 1$. The side-branching ratio matrix of the binary tree in **Figure 2** is:

$$\boldsymbol{T} = \begin{pmatrix} 1 & 2 & 4 \\ & 1 & 2 \\ & & 1 \end{pmatrix} \quad (4)$$

The necessary condition for a network to be self-similar is that the side-branching ratio T_k is independent of ω (Peckham, 1995a), that is:

$$T_{\omega,\omega+k} = T_k \quad (5)$$

For a network to be a Tokunaga tree in a statistical sense, the side-branching ratio must satisfy the constraint (Peckham, 1995a):

$$T_k = ac^{k-1} \quad (6)$$

Here, a is the average number of streams of H-S order ω flowing into streams of order $\omega + 1$, and c is the average rate of increase of the side-branching ratios of side tributaries with different order.

In **Figure 2**, $T_1 = 1, T_2 = 2, T_3 = 4$, and consequently $T_k = 2^{k-1}$, which means that the binary tree in **Figure 2** is a Tokunaga tree with $a = 1$ and $c = 2$.

Iterative Binary Tree Networks

The basic elements of a synthetic iterative network are 1) the generators, which are the smallest units of an iterative network, and 2) the iteration rules, which specify the growth pattern of the network using the generators. Different combinations of generators and iteration rules result in different networks. Iterative network models must be based on a series of generators. Each generator should be unique, and the generator series should be complete (Zhang et al., 2009; Mantilla et al., 2010).

Generator Series

Self-similarity has been considered to be an inherent characteristic of river networks since Mandelbrot first described their fractal nature (Mandelbrot, 1982; Peckham, 1995b). Since then, various methods to create synthetic networks have been proposed based on generator iteration (Veitzer and Gupta, 2000; Wang and Wang, 2002; Hung and Wang, 2005; Zhang et al., 2009; Mantilla et al., 2010). However, generators are not sequential and complete until they are cataloged by their topological structure (Zhang et al., 2009;

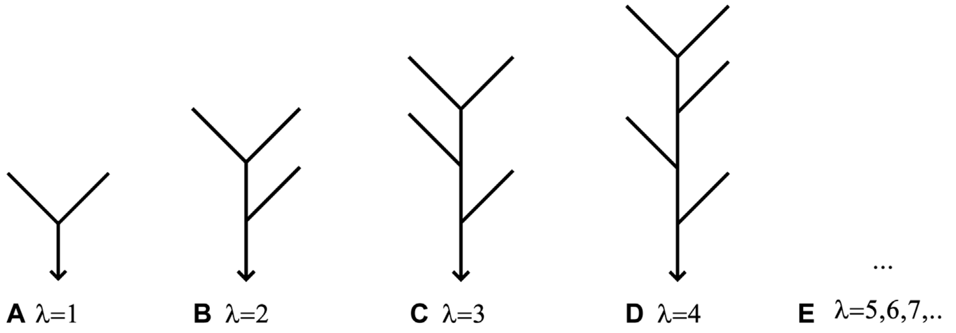

FIGURE 3 | Diagrammatic infinite generator series for the topological structure of iterative binary tree networks. Here, λ is the index of each generator [revised from Zhang et al. (2009)].

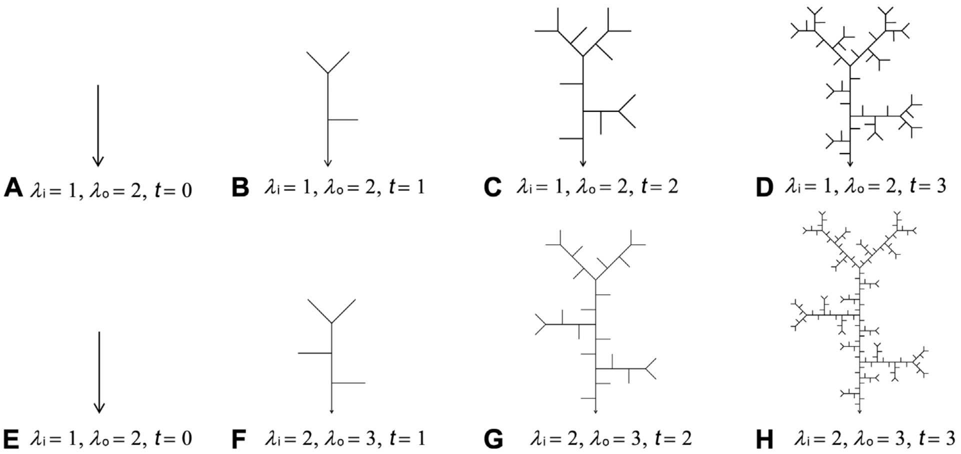

FIGURE 4 | QU-IBTNs **(A)** and **(E)**: initial cases ($t = 0$); **(B–D)**: generator $\lambda_i = 1$ and $\lambda_o = 2$ after 1, 2, and 3 iteration steps; **(F–H)**: generator $\lambda_i = 2$ and $\lambda_o = 3$ after 1, 2, and 3 iteration steps.

Mantilla et al., 2010). **Figure 3** shows the first four generators in a generator series. Each generator in the series can be denoted by an index λ, which is a positive integer in sequential order. The generator series in **Figure 3** is the basis of the iterative networks discussed in this paper.

Iteration Rule

The generation of a synthetic iterative network, specifically an ITBN, is based on iteration definitions and rules. First, we give some basic definitions for an iterative network. An exterior link is an unbroken section of stream that extends from a source to the first junction, and corresponds to a stream with H-S order 1, whereas an interior link connects two successive junctions or the last junction with the outlet (Shreve, 1966). The generators for the replacement of interior and exterior links are chosen from the series in **Figure 3** and are denoted by λ_i and λ_o, respectively. Both interior and exterior links are replaced by the interior generator λ_i and exterior generator λ_o, respectively, in each step of the iterative process. The length of each link is assumed to be 1 in this paper. We use one link as the initial case ($t = 0$), and then the exterior generator λ_o as the first iterative step ($t = 1$).

The iteration rule discussed in this paper is taking λ_i as the constant interior generator and λ_o as the constant exterior generator in each step of the iterative process. This iteration rule is quasi-uniform because of the consistent generators in every iterative step. Therefore, the iterative network generated by this rule is defined as a QU-IBTN. **Figure 4** shows two examples of how to generate QU-IBTNs using $\lambda_i = 1, \lambda_o = 2$ (**Figures 4A–D**) and $\lambda_i = 2$, $\lambda_o = 3$ (**Figures 4E–H**), respectively.

The invariance of generators in each iterative step for QU-IBTNs is strictly consistent with the definition of self-similarity. However, although the relevant iterative processes must not only have the sequentially and mathematically expressible generator series, but must also agree with the explicit given iteration rule, whether the QU-IBTN is a Tokunaga tree has never been examined graphically and recursively using a mathematical method.

Side Tributary Distribution of QU-IBTNs

The generation of a QU-IBTN begins with one link, the interior generator λ_i, and the exterior generator λ_o (i.e. the QU-IBTN is λ_o itself when $t = 1$). According to the iteration rule and Tokunaga

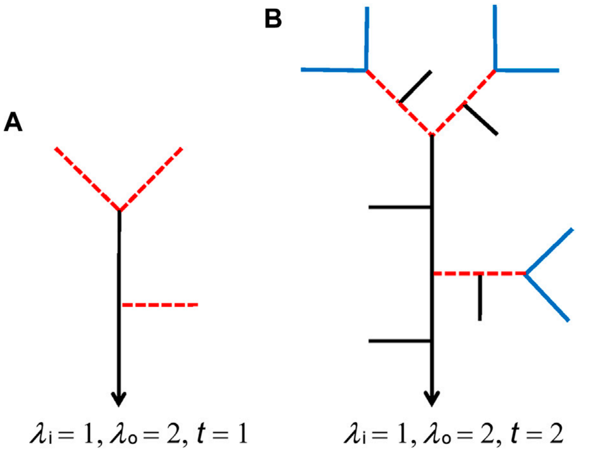

FIGURE 5 | Generation of sources in the iterative process. The sources at the second step are generated by the exterior links at the first step. The red dotted lines in both **(A)** and **(B)** are the exterior links of QU-IBTNs at the first step in **(A)**. The blue lines in **(B)** are the sources at the second step that are generated by the red dotted lines.

ordering method, there are five stream number generating laws that must be obeyed during the iterative process.

The components of the generating law equations are defined as follows:

$N_{t,\omega}$ is the number of streams with H-S order ω at the tth iterative step;
$N_{t,(\omega,\omega')}$ is the number of streams (ω, ω') at the tth iterative step;
M_t^{o} is the number of exterior links at the tth iterative step; and
M_t^{i} is the number of interior links at the tth iterative step.

Law 1: H-S Order Law

The H-S order of the QU-IBTN is $\Omega = t + 1$ after the tth iterative step, that is:

$$N_{t,\omega} = \sum_{\omega'=\omega}^{\Omega} N_{t,(\omega,\omega')} = \sum_{\omega'=\omega}^{t+1} N_{t,(\omega,\omega')} \tag{7}$$

Law 1 serves to replace the upper bound of the H-S order with the iterative step number in the calculations.

Law 2: Iteration Unchanging Law

The H-S orders of every stream and the entire network increase by 1 from the $(t-1)$th iterative step to the tth iterative step. Therefore, the number of streams (ω, ω') in the tth iterative step (i.e., $N_{t,(\omega,\omega')}$) equals the number of streams $(\omega - 1, \omega' - 1)$ in the $(t-1)^{\text{th}}$ iterative step, that is:

$$N_{t,(\omega,\omega')} = N_{t-1,(\omega-1,\omega'-1)} \tag{8}$$

By recursion from the $(t-k)$th iterative step to the tth iterative step, the relationship between the numbers of streams is found to be:

$$N_{t,(\omega,\omega')} = N_{t-k,(\omega-k,\omega'-k)} \tag{9}$$

Law 2 ensures that the corresponding equality relationship between the number of streams in the different iterative steps is satisfied.

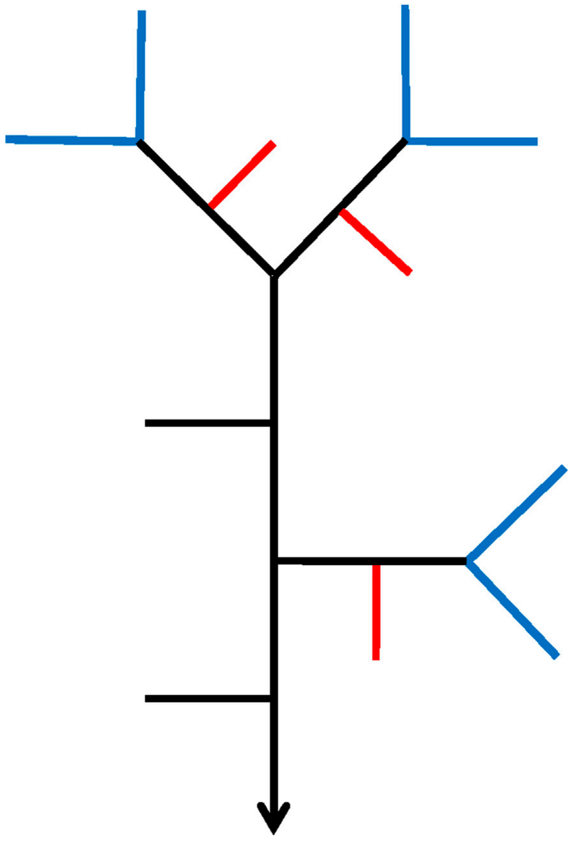

FIGURE 6 | The QU-IBTN generated by $\lambda_i = 1$, $\lambda_o = 2$, $t = 2$ at the second step. The red lines are the streams with Tokunaga order (1,2) and the blue lines are the sources, which are the streams with Tokunaga order (1,1).

Law 3: The Source Stream Law

Every pair of source streams with order $(1, 1)$ at the tth iterative step comes from one exterior link at the $(t-1)$th iterative step, which is shown as an example of QU-IBTNs by the choices $\lambda_i = 1$, and $\lambda_o = 2$ in **Figure 5**.

Figure 5 shows the generation of sources in **Figure 5B** from exterior links in **Figure 5A**. Consequently, the relationship between the sources at the tth step and the exterior links in the $(t-1)$th step is found to be:

$$N_{t,(1,1)} = 2N_{t-1,1} = 2\sum_{\omega'=1}^{t} N_{t-1,(1,\omega')} \tag{10}$$

According to **Eq. 9** in Law 2 and **Eq. 10**, the number of streams with order (k, k) in the tth step can be determined by the number of exterior links at the $(t-k+1)$th step:

$$N_{t,(k,k)} = N_{t-k+1,(1,1)} \tag{11}$$

Law 4: The Neighbor-Ordered Side-branch Law

In every iterative step, the relationship between the number of streams with Tokunaga order (1,1) and order (1,2) that depend on the exterior generator λ_o is:

$$N_{t,(1,2)} = \frac{\lambda_o - 1}{2} N_{t,(1,1)} \tag{12}$$

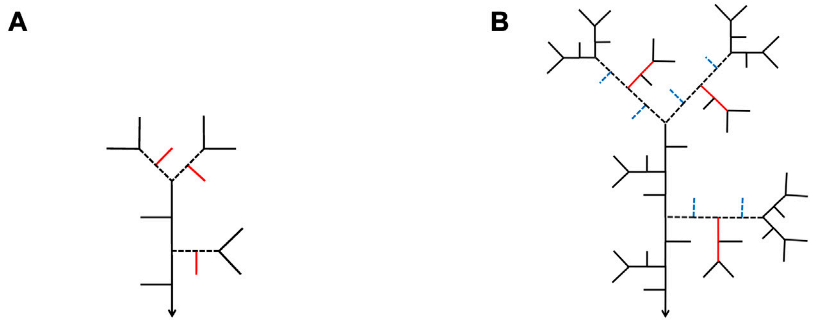

$\lambda_i = 1, \lambda_o = 2, t = 2$. The red lines are the three streams with Tokunaga order (1,2), and the black dotted lines are the six interior links.

$\lambda_i = 1, \lambda_o = 2, t = 3$. The blue dotted lines are the six streams with Tokunaga order (1,3) generated on the six black dotted lines.

FIGURE 7 | Streams with Tokunaga order (1,3) in QU-IBTNs are generated using $\lambda_i = 1$, $\lambda_o = 2$ from the second step in **(A)** to third iterative step in **(B)**.

Figure 6 shows a ratio of 3/6 for the number of streams with the order (1,2) and the number of streams with the order (1,1) in the QU-IBTN generated by the choices $\lambda_i = 1, \lambda_o = 2$ at the second iterative step.

According to **Eq. 9** in Law 2 and **Eq. 12**, the number of side branches that flow into streams that are 1 order greater (i.e., $(k, k+1)$) is:

$$N_{t,(k,k+1)} = N_{t-k+1,(1,2)} = \frac{\lambda_o - 1}{2} N_{t-k+1,(1,1)} \tag{13}$$

Law 5: The Greater-Ordered Side-branch Law

1) The streams with Tokunaga order (1,3) at the tth iterative step are generated by the $\frac{\lambda_o}{\lambda_o - 1} N_{t-1,(1,2)}$ interior links between the streams with Tokunaga order (1,2) at the $(t-1)$th iterative step. Additionally, each interior link produces λ_i streams with Tokunaga order (1,3). Therefore, the number of streams with Tokunaga order (1,3) is:

$$N_{t,(1,3)} = \left(\frac{\lambda_o}{\lambda_o - 1} N_{t-1,(1,2)}\right)\lambda_i = \frac{\lambda_i \lambda_o}{\lambda_o - 1} N_{t-1,(1,2)} \tag{14}$$

According to **Equation 9** and **14**, the number of side branches that flow into streams that are 2 orders greater [i.e., $(k, k+2)$] is:

$$N_{t,(k,k+2)} = N_{t-k+1,(1,3)} = \frac{\lambda_i \lambda_o}{\lambda_o - 1} N_{t-k,(1,2)} \tag{15}$$

Figure 7 shows the generation of streams with Tokunaga order (1,3) in the QU-IBTN with $\lambda_i = 1, \lambda_o = 2$, from the second to third iterative step.

2) The streams with Tokunaga order $(1, \omega' + 1), \omega' \geq 3$ at the tth iterative step are generated by the $(\frac{\lambda_i + 1}{\lambda_i} N_{t-1,(1,\omega')})$ interior links between streams with Tokunaga order $(1, \omega')$ at the $(t-1)$th iterative step. Each interior link produces λ_i streams with Tokunaga order $(1, \omega' + 1)$. Therefore, the number of streams with Tokunaga order $(1, \omega' + 1)$ is:

$$N_{t,(1,\omega'+1)} = \left(\frac{\lambda_i + 1}{\lambda_i} N_{t-1,(1,\omega')}\right)\lambda_i = (\lambda_i + 1) N_{t-1,(1,\omega')}, \omega' \geq 3 \tag{16}$$

Figure 8 shows the generation of streams with Tokunaga order (1,4) in the QU-IBTN with $\lambda_i = 1, \lambda_o = 2$ from the second to third iterative step.

According to **Equation 9** and **16**, the number of side branches that flow into streams that are ω' orders greater (i.e. $(k, k + \omega')$) is:

$$N_{t,(k,k+\omega')} = N_{t-k+1,(1,\omega'+1)} = (\lambda_i + 1) N_{t-k,(1,\omega')}, \omega' \geq 3 \tag{17}$$

Tokunaga Matrix N_t of IBTNs

During the tth iterative step, $(\lambda_o + 1)$ exterior links grow from the M_{t-1}^o exterior links and λ_i exterior links grow from the M_{t-1}^i interior links. Additionally, λ_o interior links grow from the M_{t-1}^o exterior links and $(\lambda_i + 1)$ interior links grow from the M_{t-1}^i interior links. **Figure 9** shows the numerical relationship of the exterior and interior links between the $(t-1)$th step and tth step.

Eq. 18 describes the relationship for increase of exterior and interior links between the $(t-1)$th and tth iterative step, illustrated in **Figure 9**, as:

$$\begin{cases} M_t^o = (\lambda_o + 1) M_{t-1}^o + \lambda_i M_{t-1}^i \\ M_t^i = \lambda_o M_{t-1}^o + (\lambda_i + 1) M_{t-1}^i, \qquad t \geq 2 \\ M_t^o = M_t^i + 1 \end{cases} \tag{18}$$

For the initial condition $t = 1$, we have $M_1^o = \lambda_o + 1$, and $M_1^i = \lambda_o$.

From **Eqs 10**, **Eqs 18**, it is clear that the number of exterior links at the $(t-1)$th step M_{t-1}^o and the number of streams with order (1,1) at the tth step $N_{t,(1,1)}$ are:

$$N_{t,(1,1)} = 2M_{t-1}^o = \left(2\lambda_o + 1 + \frac{\lambda_o - \lambda_i}{\lambda_o + \lambda_i}\right)(\lambda_o + \lambda_i + 1)^{t-1} + \frac{2\lambda_i}{\lambda_o + \lambda_i} \tag{19}$$

The Tokunaga matrix $\boldsymbol{N_t}$ of the QU-IBTN, which is generated by the interior generator λ_i and the exterior generator λ_o at the tth step, follows Law 1 through Law 5. Its diagonal elements, $\boldsymbol{N_t}(k, k)$, are calculated using **Eqs 11**, **18** in Law 3. The elements $\boldsymbol{N_t}(k, k+1)$ next to the diagonal elements come from **Eq. 13** in Law 4. The farther elements $\boldsymbol{N_t}(k, k+2)$ and $\boldsymbol{N_t}(k, k+\omega')$, in which $\omega' \geq 3$, are from **Eqs 15**, **17** in Law 5. The initial conditions are $N_{1,(1,1)} = 2$, $N_{1,(1,2)} = \lambda_o - 1$, and $N_{1,(2,2)} = 1$. The dimension of the matrix $\boldsymbol{N_t}$is $\Omega \times \Omega$ (i.e., $(t+1) \times (t+1)$).

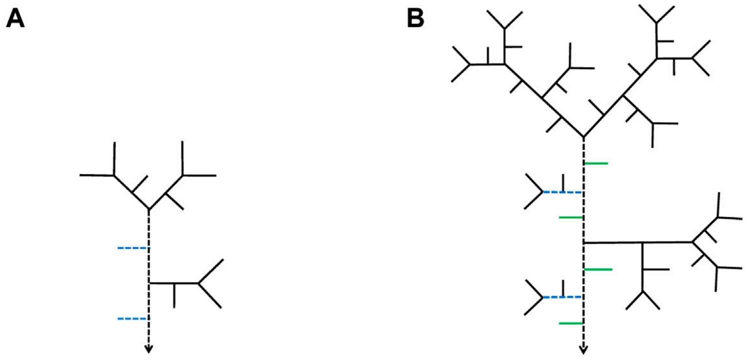

$\lambda_i = 1, \lambda_o = 2, t = 2$. The blue dotted lines are the two streams with Tokunaga order (1,3) and the black dotted lines are the four interior links between them.

$\lambda_i = 1, \lambda_o = 2, t = 3$. The green lines are the four streams with Tokunaga order (1,4) generated on the four black dotted lines.

FIGURE 8 | Streams with Tokunaga order (1,4) in QU-IBTNs are generated using $\lambda_i = 1$, $\lambda_o = 2$ from the second step in **(A)** to third iterative step in **(B)**.

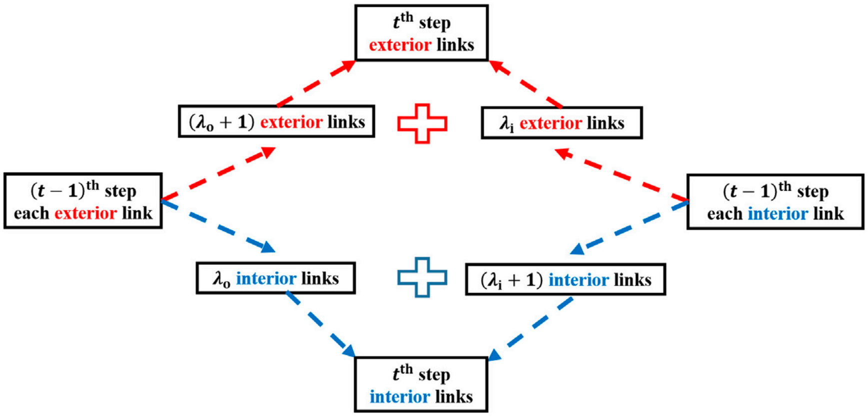

FIGURE 9 | The generation of each interior and exterior link from the $(t-1)$th to the tth iterative step.

Using the first row of $\boldsymbol{N_t}$ as an example, we find that:

$$\begin{aligned}
&\left(N_{t,(1,1)} \quad N_{t,(1,2)} \quad N_{t,(1,3)} \quad N_{t,(1,4)} \quad N_{t,(1,5)} \cdots \right)\\
&= \Bigg(N_{t,(1,1)} \quad \frac{\lambda_o - 1}{2} N_{t,(1,1)} \quad \frac{\lambda_i \lambda_o}{\lambda_o - 1} N_{t-1,(1,2)}\\
&\quad \times (\lambda_i + 1) N_{t-1,(1,3)} \; (\lambda_i + 1) N_{t-1,(1,4)} \; \cdots \Bigg)\\
&= \Bigg(N_{t,(1,1)} \quad \frac{\lambda_o - 1}{2} N_{t,(1,1)} \quad \frac{\lambda_i \lambda_o}{2} N_{t-1,(1,1)}\\
&\quad \times (\lambda_i + 1) \frac{\lambda_i \lambda_o}{\lambda_o - 1} N_{t-2,(1,2)} \; (\lambda_i + 1)^2 N_{t-2,(1,3)} \cdots \Bigg)\\
&= \Bigg(N_{t,(1,1)} \quad \frac{\lambda_o - 1}{2} N_{t,(1,1)} \quad \frac{\lambda_i \lambda_o}{2} N_{t-1,(1,1)}\\
&\quad \times (\lambda_i + 1) \frac{\lambda_i \lambda_o^2}{2} N_{t-2,(1,1)} \, (\lambda_i + 1)^2 \frac{\lambda_i \lambda_o}{2} N_{t-3,(1,1)} \cdots \Bigg)
\end{aligned} \tag{20}$$

In the following equations, $\hat{a} = \frac{\lambda_o - 1}{2}$, $\hat{b} = \frac{\lambda_i \lambda_o}{\lambda_o - 1}$, and $\hat{c} = \lambda_i + 1$. The matrix $\boldsymbol{N_t}$ is in the form of the general terms $m_{i,j}$ $(1 \le i, j \le t + 1 = \Omega)$ as follows:

In the first column of $\boldsymbol{N_t}$:

$$m_{1,1} = N_{t,(1,1)} \tag{21}$$

In the second column of $\boldsymbol{N_t}$:

$$m_{1,2} = \hat{a} m_{1,1}, \; m_{2,2} = N_{t-1,(1,1)} \tag{22}$$

In the third column of $\boldsymbol{N_t}$:

$$m_{1,3} = \hat{b} \hat{a} m_{2,2}, \; m_{2,3} = \hat{a} m_{2,2}, \; m_{3,3} = N_{t-2,(1,1)} \tag{23}$$

In the j^{th} column $(4 \le j \le t)$, the parameter $\hat{c}$ appears in the terms shown below:

$$\begin{aligned}
m_{j,j} = N_{t-j+1,(1,1)}, \; m_{j-1,j} = \hat{a} m_{j-1,j-1},\\
m_{i,j} = \hat{c}^{j-i-2} \hat{b} \hat{a} m_{j-1,j-1}, \; 1 \le i \le j-2
\end{aligned} \tag{24}$$

In the $(t+1)^{th}$ column, the exterior generator λ_o affects the elements as follows:

$$\begin{aligned}
m_{t+1,t+1} = 1, \; m_{t,t+1} = \hat{a} m_{t,t} = \lambda_o - 1,\\
m_{i,t+1} = \hat{c}^{t-1-i} \hat{b} \hat{a} m_{t,t} = \lambda_o \lambda_i \hat{c}^{t-1-i}, \; 1 \le i \le t-1
\end{aligned} \tag{25}$$

The recursion of elements in **Eqs 21–25** form the matrix $\boldsymbol{N_t}$as:

$$\boldsymbol{N_t} = \begin{pmatrix} m_{1,1} & \hat{a}m_{1,1} & \hat{b}\hat{a}m_{2,2} & \hat{c}\,\hat{b}\hat{a}m_{3,3} & \dots & \dots & \hat{c}^{t-3}\hat{b}\hat{a}m_{t-1,t-1} & \hat{c}^{t-2}\hat{b}\hat{a}m_{t,t} \\ & m_{2,2} & \hat{a}m_{2,2} & \hat{b}\hat{a}m_{3,3} & \dots & \dots & \hat{c}^{t-4}\hat{b}\hat{a}m_{t-1,t-1} & \hat{c}^{t-3}\hat{b}\hat{a}m_{t,t} \\ & & m_{3,3} & \hat{a}m_{3,3} & \dots & \dots & \dots & \dots \\ & & & \dots & \dots & \dots & \dots & \dots \\ & & & & m_{t-2,t-2} & \hat{a}m_{t-2,t-2} & \hat{b}\hat{a}m_{t-1,t-1} & \hat{c}\hat{b}\hat{a}m_{t,t} \\ & & & & & m_{t-1,t-1} & \hat{a}m_{t-1,t-1} & \hat{b}\hat{a}m_{t,t} \\ & & & & & & m_{t,t} & \hat{a}m_{t,t} \\ & & & & & & & 1 \end{pmatrix} \tag{26}$$

The sum of the $(k+1)^{\text{th}}$ row in the matrix $\boldsymbol{N_t}$ is the number of streams with H-S order 1at the $(t-k)^{\text{th}}$ iterative step, which is also essentially the number of the exterior links. The number of exterior links at the $(t-k)^{\text{th}}$ iterative step is:

$$M^{\text{o}}_{t-k} = \sum\nolimits_{\boldsymbol{j=k+1}}^{\boldsymbol{t+1}} \boldsymbol{N_t}(k+1, j) \tag{27}$$

Furthermore, the number of streams (1,1) at the $(t-k+1)^{\text{th}}$ iterative step (i.e., $N_{t-k+1,(1,1)}$) is twice the number of the exterior links at the $(t-k)^{\text{th}}$ iterative step (i.e., M^{o}_{t-k}) for any $1 \le k \le t-1$ according to **Eq. 10** in Law 3. Therefore:

$$\frac{N_{t-k+1,(1,1)}}{M^{\text{o}}_{t-k}} = \frac{m_{k,k}}{M^{\text{o}}_{t-k}} = \frac{m_{k,k}}{\sum_{\boldsymbol{j=k+1}}^{\boldsymbol{t+1}} \boldsymbol{N_t}(k+1, j)} = 2,\ 1 \le k \le t-1 \tag{28}$$

Side-Branching Ratio Matrix $\boldsymbol{T_t}$ of IBTNs

The side-branching ratio matrix $\boldsymbol{T_t}$ is composed of the side-branching ratio $T_{i,k+1}$ as its element $\boldsymbol{T_t}(i,k)$. According to the definition of $T_{i,k+1}$ in **Eq. 3**, the expression for $T_{i,k+1}$ is:

$$\boldsymbol{T_t}(i,k) = T_{i,k+1} = \frac{\boldsymbol{N_t}(i,k+1)}{\sum_{\boldsymbol{j=k+1}}^{\boldsymbol{t+1}} \boldsymbol{N_t}(k+1, j)} = \frac{\boldsymbol{N_t}(i,k+1)}{m_{k,k}/2} \tag{29}$$

We can get the expression for $\boldsymbol{N_t}(i,k+1)$ in $\boldsymbol{N_t}$ as:

$$\boldsymbol{N_t}(i,k+1) = \begin{cases} \hat{a}m_{k,k}, & i = k \\ \hat{c}^{k-i-1}\hat{b}\hat{a}m_{k,k}, & i \le k-1 \end{cases} \tag{30}$$

We modify the form of $\boldsymbol{N_t}(i,k+1)$ in **Eq. 29** using **Eq. 30**; therefore, the final form for $\boldsymbol{T_t}(i,k)$ is:

$$\boldsymbol{T_t}(i,k) = \begin{cases} 2\hat{a}, & i = k \\ 2\hat{c}^{k-i-1}\hat{b}\hat{a}, & i \le k-1 \end{cases} \tag{31}$$

By combining **Eq. 3** and the condition $\boldsymbol{N_t}(t+1, t+1) = 1$ in the t^{th} column of the matrix $\boldsymbol{T_t}$, we get:

$$\boldsymbol{T_t}(i,t) = T_{i,t+1} = \frac{\boldsymbol{N_t}(i,t+1)}{\boldsymbol{N_t}(t+1,t+1)} = \boldsymbol{N_t}(i,t+1) \tag{32}$$

Using **Eqs 31**, **32**, we get the matrix $\boldsymbol{T_t}$ as follows:

$$\boldsymbol{T_t} = \begin{pmatrix} \lambda_{\text{o}}-1 & \lambda_{\text{i}}\lambda_{\text{o}} & \lambda_{\text{i}}\lambda_{\text{o}}(\lambda_{\text{i}}+1) & \dots & \lambda_{\text{i}}\lambda_{\text{o}}(\lambda_{\text{i}}+1)^{t-3} & \lambda_{\text{o}}\lambda_{\text{i}}(\lambda_{\text{i}}+1)^{t-2} \\ & \lambda_{\text{o}}-1 & \lambda_{\text{i}}\lambda_{\text{o}} & \dots & \lambda_{\text{i}}\lambda_{\text{o}}(\lambda_{\text{i}}+1)^{t-4} & \lambda_{\text{o}}\lambda_{\text{i}}(\lambda_{\text{i}}+1)^{t-3} \\ & & \dots & \dots & \dots & \dots \\ & & & \lambda_{\text{o}}-1 & \lambda_{\text{i}}\lambda_{\text{o}} & \lambda_{\text{o}}\lambda_{\text{i}}(\lambda_{\text{i}}+1) \\ & & & \cdot & \lambda_{\text{o}}-1 & \lambda_{\text{o}}\lambda_{\text{i}} \\ & & & \cdot & & \lambda_{\text{o}}-1 \\ & & & \cdot & & \end{pmatrix} \tag{33}$$

The efficient and necessary condition to be a self-similar network is that $\boldsymbol{T_t}$ must to be a Toeplitz matrix according to **Eq. 5**. The QU-IBTNs with the interior generator λ_{i} and exterior generator λ_{o} are definitely self-similar because the elements on the diagonal are equal in **Eq. 33**, which is a Toeplitz matrix. This is also shown in terms of the results for side-branching ratios:

$$T_1 = \lambda_{\text{o}} - 1,\ T_k = \lambda_{\text{i}}\lambda_{\text{o}}(\lambda_{\text{i}}+1)^{k-2},\ 2 \le k \le t \tag{34}$$

For strict Tokunaga self-similarity, the elements in $\boldsymbol{T_t}$ must satisfy **Eq. 6**. Therefore, the necessary condition for a QU-IBTN to be a Tokunaga tree is:

$$\lambda_{\text{o}} = \lambda_{\text{i}} + 1 \tag{35}$$

No matter which values of λ_{o} and λ_{i} are selected to generate a QU-IBTN, this QU-IBTN must be self-similar. However, a QU-IBTN is a Tokunaga tree only when $\lambda_{\text{o}} = \lambda_{\text{i}} + 1$. This means that when we use QU-IBTNs to simulate natural river networks, which are Tokunaga trees, we need to generate a QU-IBTN with the special condition that $\lambda_{\text{o}} = \lambda_{\text{i}} + 1$.

To demonstrate the constraints on self-similarity versus Tokunaga self-similarity, we provide the following two examples.

Example 1: $\lambda_o = \lambda_i$

When the generators $\lambda_{\text{o}} = \lambda_{\text{i}}$, the side-branching ratios given by **Eq. 34** are:

$$T_1 = \lambda_{\text{o}} - 1, T_k = \lambda_{\text{o}}^2(\lambda_{\text{o}}+1)^{k-2},\ 2 \le k \le t \tag{36}$$

The side-branching ratio T_k $(1 \le k)$ contains different constants, but does not define a geometric series. Therefore, the QU-IBTN with $\lambda_{\text{o}} = \lambda_{\text{i}}$ is self-similar but not a Tokunaga tree, as pointed out by Peckham (1995a).

Example 2: $\lambda_o = \lambda_i + 1$

When the exterior link generator and the interior link generator satisfy the condition $\lambda_{\text{i}} = \lambda_{\text{o}} - 1$, the side-branching ratios given by **Eq. 34** are:

$$T_k = (\lambda_{\text{o}} - 1)\lambda_{\text{o}}^{k-1},\ k \ge 1 \tag{37}$$

According to **Eq. 37**, this QU-IBTN is a Tokunaga tree with $a = \lambda_{\text{o}} - 1$ and $c = \lambda_{\text{o}}$. Based on statistics, the necessary condition for a QU-IBTN to be a Tokunaga tree in **Eq. 37** is consistent with the result presented by Veitzer and Gupta (2000).

RESULTS

Natural River Networks

In the following, we use the Yellow River in China (H-S order 11) and the Amazon River in South America (H-S order 12) as examples to verify whether or not they follow the rules of QU-IBTNs and the constraint of a Tokunaga tree. **Figure 10** shows the river networks extracted from digital elevation model (DEM) data with a 30 m resolution (Li et al., 2018; Li et al., 2020).

Supplementary Table S1 (shown in Supplementary Material) shows the Tokunaga matrices of the stream numbers $N_{\omega,\omega'}$ for both the Yellow River and the Amazon River.

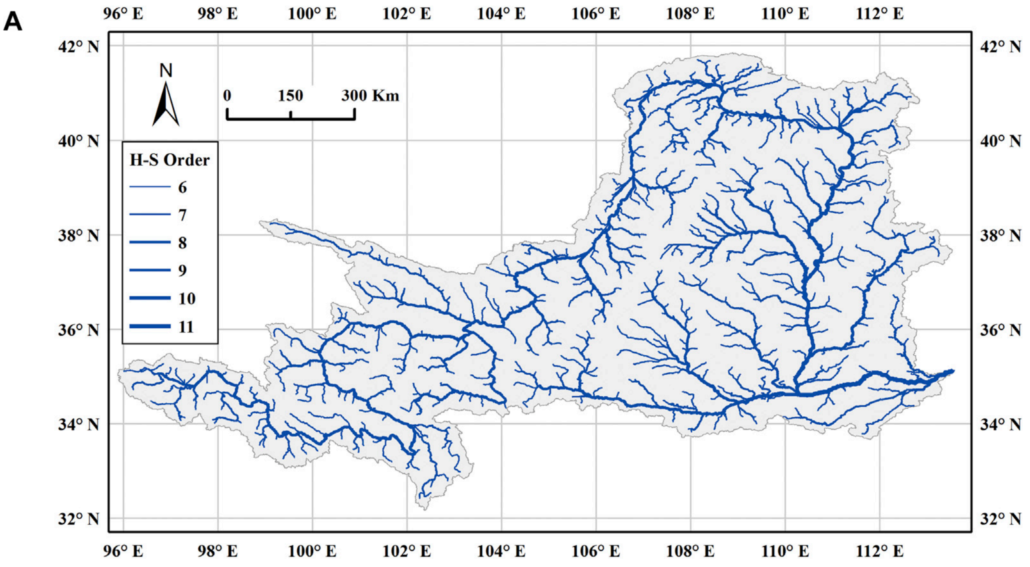

River networks of the Yellow river with Ω = 11. Streams of H-S orders 7 to 11 are depicted.

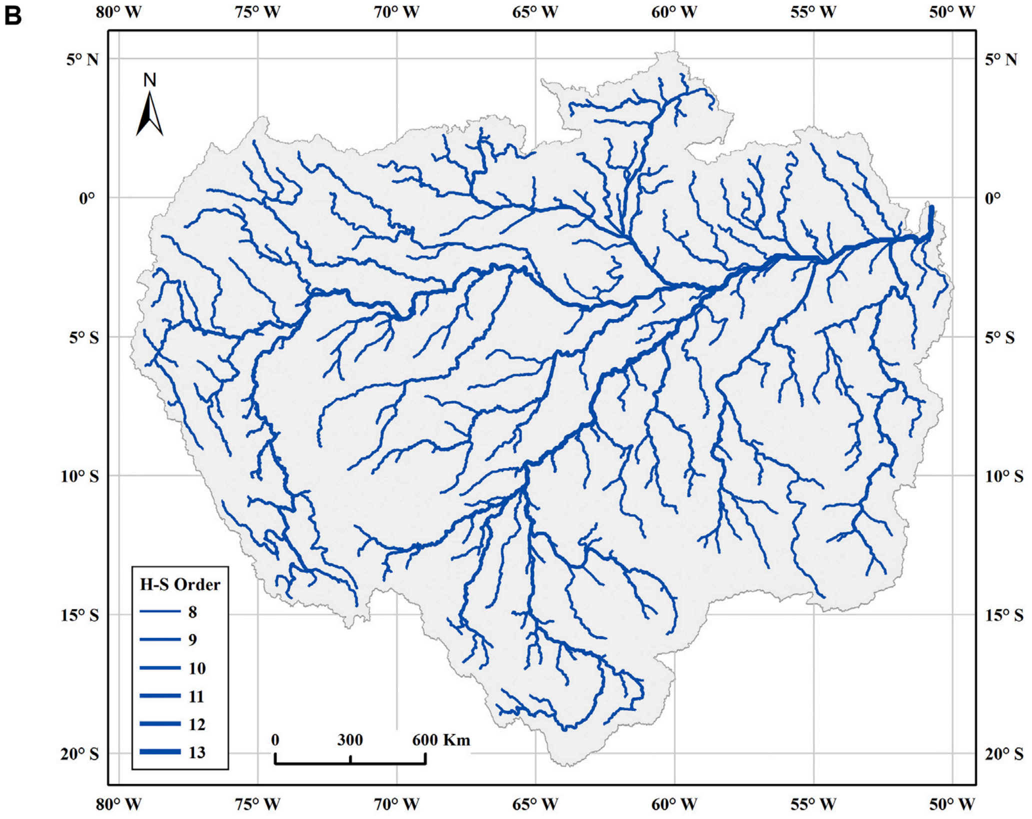

River networks of the Amazon River with Ω = 12. Streams of H-S orders 8 to 12 are depicted.

FIGURE 10 | River networks of the Yellow River and the Amazon River with streams of no less than an H-S order 7 are shown in the figure.

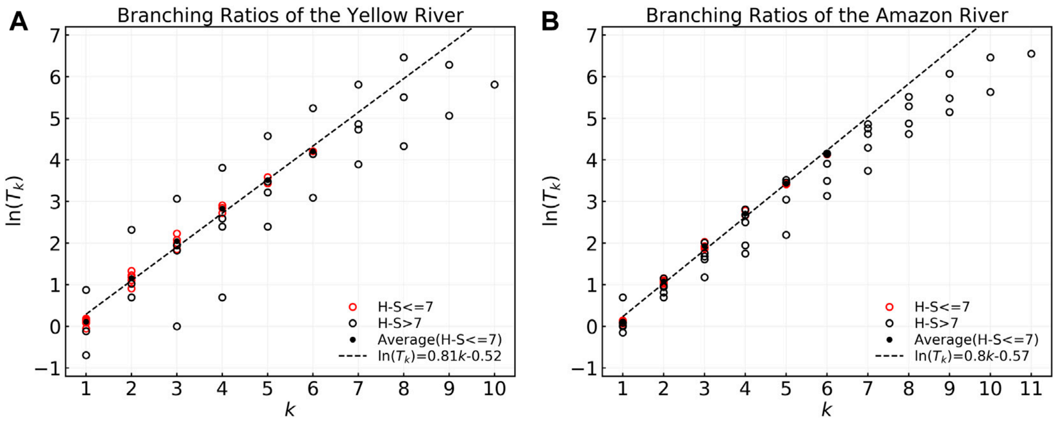

FIGURE 11 | Branching ratios, T_k, of the Yellow River and theAmazon River for every k. The black circles are the branching ratios shown in the shaded sections of the matrices of **Supplementary Table S2**. The red circles are the remaining data in the matrices. The black points are the average values of the black circles. The dotted black line is the fit of the black points using the least squares regression method.

The similarities Between Natural River Networks and Tokunaga Trees

Supplementary Table S2 (shown in Supplementary Material) shows the side-branching ratio matrices for the side-branching ratios $T_{i,j}$ based on **Eq. 3** for the two rivers.

Supplementary Table S2 also shows that the branching ratio values have large fluctuations for main stems with large H-S orders, as shown in **Figure 11**.

The statistical side-branching ratio matrices of the two rivers in **Supplementary Table S2** and **Figure 11** show that the statistical results of T_k vary greatly compared with the theoretic self-similarity derivation, which is uniform for a fixed k. The black circles in **Figure 11** denote the T_k data in the shaded sections of **Supplementary Table S2** that are less affected by local geomorphology and terrain, and therefore are more concentrated in their distribution. The red circles in **Figure 11** are the T_k data excluding the shaded sections of **Supplementary Table S2**; these are seen to scatter far away from each other. We now use streams with H-S orders 1 to 7 (i.e., the shaded sections of **Supplementary Table S2** and the black circles in **Figure 11**) to analyze the Tokunaga self-similarity of the two natural river networks. The values of the black points in **Figure 11**, which are the statistical average values, $\overline{T_k}$, of T_k for each k $(1 \le k \le 6)$, are $(1.11, 3.19, 7.76, 16.91, 33.53, 67.09)$ for the Yellow River and $(1.11, 2.93, 6.90, 14.97, 30.86, 62.41)$ for the Amazon River.

The side-branching ratio series in **Figure 11** were verified to satisfy as $1.34 \times 2.25^{k-1}$ and $1.26 \times 2.23^{k-1}$ using the least squares method, as shown in **Figure 11** in terms of the dotted black lines with coefficients of determination $R^2 > 0.99$.

Therefore, the Tokunaga parameters can be evaluated using $a_{\text{Yellow}} \cong 1.34$, $c_{\text{Yellow}} \cong 2.25$ and $a_{\text{Amazon}} \cong 1.26$, $c_{\text{Amazon}} \cong 2.23$.

The Similarities Between Natural River Networks and QU-IBTNs

We construct $\boldsymbol{N\_R_t}$ matrices with the same dimension of $\boldsymbol{N_t}$ in **Supplementary Table S1** in terms of:

$$\boldsymbol{N\_R_t}(k,k+1) = \frac{\boldsymbol{N_t}\ (k,k+1)}{\boldsymbol{N_t}\ (k,k)},\quad 1 \le k \le \Omega - 1 \tag{38}$$

$$\boldsymbol{N\_R_t}(k,k+2) = \frac{\boldsymbol{N_t}\ (k,k+2)}{\boldsymbol{N_t}\ (k+1,k+2)},\quad 1 \le k \le \Omega - 2 \tag{39}$$

and

$$\boldsymbol{N\_R_t}(i,k) = \frac{\boldsymbol{N_t}\ (i,k)}{\boldsymbol{N_t}\ (i+1,k)},\quad 1 \le i \le k-3,\ 4 \le k \le \Omega \tag{40}$$

The $\boldsymbol{N\_R_t}$ matrices for the Yellow River and the Amazon River using **Eqs 38–40** are listed in **Supplementary Table S3** (shown in Supplementary Material).

According to the standard form of the Tokunaga matrix $\boldsymbol{N_t}$ in **Eq. 26**, $\hat{a}$ values are expressed in **Eq. 38** by the ratios of $\boldsymbol{N_t}\ (k,k+1)$ to $\boldsymbol{N_t}\ (k,k)$ $(1 \le k \le \Omega - 1)$; $\hat{b}$ values are expressed in **Eq. 39** by the ratios of $\boldsymbol{N_t}\ (k,k+2)$ to $\boldsymbol{N_t}\ (k+1,k+2)$ $(1 \le k \le \Omega - 2)$; and $\hat{c}$ values are expressed in **Eq. 40** by the ratios of $\boldsymbol{N_t}(i,k)$ to $\boldsymbol{N_t}(i+1,k)$ $(1 \le i \le k-3,\ \ 4 \le k \le \Omega)$.

We calculate λ_{o} and λ_{i} for each iterative step from every row of the matrix $\boldsymbol{N\_R_t}$ in **Supplementary Table S3**, as shown in the Methods section. The matrices of the λ_{o} and λ_{i} values are defined as $\boldsymbol{N\_\lambda_t}$ in **Supplementary Table S4** (shown in Supplementary Material).

In the $\boldsymbol{N\_\lambda_t}$ matrices in **Supplementary Table S4**, the first element in each row is the value of the exterior generator λ_{o} for each iterative step, and the following elements in the row are the interior generators λ_{i} for each corresponding iterative step. **Figure 12** shows the values of the generators λ_{o} and λ_{i} for each iterative step in **Supplementary Table S4** for both the Yellow River and the Amazon River.

1) The exterior generators λ_{o} (i.e., the gray solid points) vary slightly for the higher iterative steps (greater than 6) in **Supplementary Table S4** and **Figure 12**. At the higher iterative steps, the streams are closer to the source streams, which allows them to evolve freely according to the same formative mechanism because they have enough space to

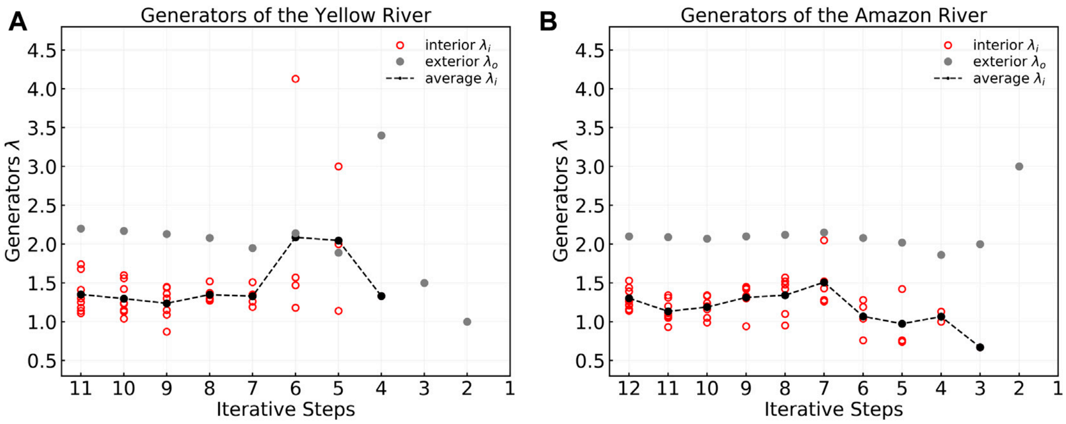

FIGURE 12 | Generators of the Yellow River and the Amazon River for each iterative step. The gray solid points are the exterior generators λ_o. The black circles are the interior generators λ_i. The dotted black line corresponds to the average value of the interior generators λ_i for each row, excluding those in the last column of **Supplementary Table S4**. Analysis and Conclusions for **Supplementary Table S4** and **Figure 12**.

grow. Freedom and space allows streams between different iterative steps in a river network, and even for different river networks, to be uniform and similar, which can be seen in terms of the uniformity of the generators λ_o.

2) The interior generators λ_i (i.e., the black circles) are concentrated and approaching uniform for the higher iterative steps in **Supplementary Table S4** and **Figure 12**. The last column in the Yellow River $\boldsymbol{N\_\lambda_t}$ matrix in **Supplementary Table S4** shows the interior generators for the main stem of the Yellow River basin. The changes in this column are results from the geomorphology and terrain, which constrain the generators on the main stems. The Amazon River $\boldsymbol{N\_\lambda_t}$ matrix also shows the same changes in this column. For the lower iterative steps, the generators shown in **Supplementary Table S4** are generators for streams with high H-S orders, which are also influenced by the geomorphology and terrain. To satisfy the conditions of uniformity of generators and similarity of the river networks, we need to exclude the streams that are heavily constrained by the geomorphology and terrain.
3) The interior generators λ_i (i.e., the black circles) vary slightly at iterative steps 7 to 11 for the Yellow River, and steps 8 to 12 for the Amazon River, as shown in **Supplementary Table S4** and **Figure 12**. The average values for each iterative step (i.e., the dotted black line) are almost stable between iterative steps 7 and 11 for the Yellow River and steps 8 and 12 for the Amazon River. The exterior generators λ_o are consistent at these iterative steps. The stability and consistency of the generators λ_o and λ_i at high iterative steps confirms that the two natural river networks follow the rules of QU-IBTNs in a statistical sense. We use the average values of λ_o and λ_i in the shaded section in **Supplementary Table S4** from iterative steps 7–11 and 8–12 separately to evaluate the generator of the Yellow River and the Amazon River. The calculations for the generators are provided in the Methods section. The statistical averages for the exterior generator and the interior generator are evaluated using $\lambda_{o-\text{Yellow}} \cong 2.11$, $\lambda_{i-\text{Yellow}} \cong 1.34$ for the Yellow River and $\lambda_{o-\text{Amazon}} \cong 2.10$, $\lambda_{i-\text{Amazon}} \cong 1.26$ for the Amazon River.

TABLE 1 | The generators (λ_i, λ_o) and Tokunaga parameters (a,c) for the Yellow River and the Amazon River.

Rivers	(λ_i, λ_o)	(a, c)	$\lambda_o - \lambda_i$	c − a
Yellow River	(1.34, 2.11)	(1.33, 2.25)	0.77	0.91
Amazon River	(1.26, 2.10)	(1.26, 2.23)	0.84	0.97

Table 1 lists the generators and Tokunaga parameters for the Yellow River and the Amazon River.

Analysis and conclusions for **Table 1**:

1) In our analysis, we have removed the main stems with high H-S orders at the low iterative steps, as these are controlled by the local geomorphology and terrain. The QU-IBTN rules and Tokunaga self-similarity are well demonstrated using the Yellow River and the Amazon River in terms of the uniformity and equality of the generators and branching ratios for streams with low H-S orders at high iterative steps.
2) According to the sufficient and necessary condition for a QU-IBTN to be a Tokunaga tree in **Eq. 35**, we should have $a = \lambda_i$, $c = \lambda_o$ and $\lambda_o - \lambda_i = c - a = 1$. However, from **Table 1**, there is a difference between c and λ_o because of the different data and methods used for calculation.

DISCUSSION

The QU-IBTNs proposed above illustrate how to generate iterative binary tree networks simulating natural river networks. The complete mathematic iterative steps with graphic deduction are demonstrated in iterative orders. The iterative process is sustained by the self-similarity theory. The synthetic QU-IBTNs are close to the natural river networks in similarity characteristics parameters by two examples.

When generated by exterior generator $\lambda_o = 2$ and interior generator $\lambda_i = 1$, the QU-IBTN is equivalent to the Shreve model (Shreve, 1966), for which the bifurcation ratio is $R_B = 4$ and the Tokunaga parameters are $a = 1$, $c = 2$ (Peckham, 1995a). This is the only case of a plane-filling IBTN (Zhang et al., 2009). Therefore, only the Shreve model can generate a plane-filling Tokunaga tree, and only the IBTN plane-filling Tokunaga tree fits the Shreve model.

Although in theory the Shreve model should be the most ideal topology network that approaches natural river networks because it is a Tokunaga tree and plane-filling, there is an obvious contradiction that topological parameters such as $R_B = 4$, $a = 1$, and $c = 2$ of the Shreve model are far from those of natural river networks [Average values of R_B, a and c are around 4.4, 1.1 and 2.5 (Peckham, 1995a; Dodds and Rothman, 1999; Dodds, 2000; Pelletier and Turcotte, 2000; Mantilla et al., 2010; Zanardo et al., 2013; Wang et al., 2016)]. Furthermore, the entire natural river network is determined not only by topological characteristics (such as stream number, R_B and Tokunaga parameters), but also geometrical characteristics (such as stream length and confluence angle) that depend on the energy conservation and the relation between sediment and water discharge. Consequently, the Shreve model is an ideal model to simulate the topology of river networks, but it is an unsatisfactory model for simulating the geometrical properties of natural river networks. Furthermore, a layout for an ideal plane-filling Tokunaga tree is still needed.

We have supposed that the hypothesis of the uniformity of link length in the IBTN may lead to differences in the bifurcation ratio as compared with natural river networks under the condition of plane-filling. The link length and confluence angles of IBTNs should be redefined according to the values of the stream length ratios of natural river networks when considering plane-filling.

Some aspects of the linkages between the structure of river networks and the processes that shape them remain somewhat unclear and difficult to understand (Abrahams, 1984; Montgomery and Dietrich, 1992; Perron et al., 2012; Seybold et al., 2017). A considerable body of research is available on the topologic structure associated with stream numbers and self-similarity of river networks (Peckham, 1995a; Dodds, 2000; Pelletier and Turcotte, 2000; Veitzer and Gupta, 2000; Mcconnell and Gupta, 2008; Mantilla et al., 2010; Zanardo et al., 2013). Recently, confluence angles (also referred to as junction angles) of a number of natural river networks, which represent a geometric component of river network structure, have been statistically evaluated and shown to depend on the climatic setting (Devauchelle et al., 2012; Seybold et al., 2017). These treatments of confluence angles may provide important clues in further studies to explore the following two questions: 1) where does a stream emerge from an unchannelized region? and 2) how far downstream does this stream extend until it merges into another stream?

CONCLUSION

In this paper we provide a complete mathematical and graphical deduction of QU-IBTNs with specified generator series and iteration rule. Our conclusions are as follows:

1) For the QU-IBTN generated by the generator series and iteration rule in this paper, five intrinsic stream number laws—which determine the distribution of source streams and side-branches following into streams of greater orders—are graphically and recursively analyzed and satisfied.
2) As defined in this paper, the QU-IBTN are demonstrated to be self-similar.
3) The sufficient and necessary constraint for a QU-IBTN to be a Tokunaga tree is that the exterior links must be replaced with a neighboring generator in the generator series that is larger than the interior links during the iterative process. This defines a generation method for a simulated network that is identical to a natural river network in topology.
4) Two natural river networks, i.e. the Yellow River, China and the Amazon River, South America, are shown to be Tokunaga trees and QU-IBTNs within specified H-S order scales.

The self-similarity of river networks is a classical topic, and there are many researchers working on this topic using varied methods, including mathematicians who are good at fractal theory (Kovchegov and Zaliapin, 2020). Other researchers might use random and mathematical foundations in their own research. Our manuscript here is an intuitive, accessible and understandable initial tool to measure the self-similarity of river networks. The advance of generator series, the integer iterative rules showing directly by graphs, and the corresponding mathematical derivations are new and different from others' methods. The QU-IBTNs are built just in a few finite iterative steps as shown in the figures. QU-IBTNs in random scales will be generated by coding in the future. However, to some extent we are doing the same thing as other researchers-just find a way to demonstrate the self-similarity and Tokunaga property of river networks. This is what we think we can share with other researchers, and help make progress in river network simulations in the future.

METHODS

The Method for Calculating λ_o and λ_i From the Matrix N_R_t

For the k^{th} row in matrix $\boldsymbol{N\_R_t}$, $\Omega - k + 1$ is the corresponding iterative step. The matrix $\boldsymbol{N\_\lambda_t}$ expresses the generators λ_o and λ_i. The exterior generator at the $(\Omega - k + 1)^{\text{th}}$ iterative step is:

$$\lambda_o(\Omega - k + 1) = \boldsymbol{N\_\lambda_t}(k, k+1) = 2 \times \boldsymbol{N\_R_t}(k, k+1) + 1,\ 1 \le k \le \Omega - 1 \quad \text{(M1)}$$

The interior generators in the k^{th} row (i.e., the $(\Omega - k + 1)^{\text{th}}$ iterative step) are:

$$\lambda_{\mathrm{i\_1}}(\Omega - k + 1) = \boldsymbol{N\_\lambda_t}(k, k+2) = \frac{\lambda_{\mathrm{o}}(k) - 1}{\lambda_{\mathrm{o}}(k)} \times \boldsymbol{N\_R_t}(k, k+2),\ 1 \le k \le \Omega - 2 \quad \text{(M2)}$$

and

$$\boldsymbol{N\_\lambda_t}(k, i) = \frac{\lambda_{\mathrm{i\_1}}(\Omega - k + 1)}{\lambda_{\mathrm{i\_1}}(\Omega - k)} \times \boldsymbol{N\_R_t}(k, i),\ 1 \le k \le i - 3,\ 4 \le i \le \Omega \quad \text{(M3)}$$

In the matrix $\boldsymbol{N\_R_t}$, the elements $\boldsymbol{N\_\lambda_t}(k, k+1)$ $(1 \le k \le \Omega - 1)$ in Equation (M1) correspond to the exterior generator at the $(\Omega - k + 1)$th iterative step. The elements $\boldsymbol{N\_\lambda_t}(k, k+2)$ and $\boldsymbol{N\_\lambda_t}(k, i)$ $(k + 3 \le i \le \Omega)$ are the interior generators at the $(\Omega - k + 1)$th iterative step.

For the Yellow River and the Amazon River, the statistically averaged values for $\lambda_{\mathrm{o-Yellow}}$ and $\lambda_{\mathrm{o-Amazon}}$ are:

$$\lambda_{\mathrm{o-Yellow}} = \frac{\sum_{k=1}^{5} \lambda_{\mathrm{o}}(12 - k)}{5} = \frac{\sum_{k=1}^{5} \boldsymbol{N}_{\lambda t}(k, k+1)}{5} = 2.11 \quad \text{(M4)}$$

and

$$\lambda_{\mathrm{o-Amazon}} = \frac{\sum_{k=1}^{5} \lambda_{\mathrm{o}}(13 - k)}{5} = \frac{\sum_{k=1}^{5} \boldsymbol{N}_{\lambda t}(k, k+1)}{5} = 1.34 \quad \text{(M5)}$$

For the Yellow River and the Amazon River, the statistically averaged values for $\lambda_{\mathrm{i-Yellow}}$ and $\lambda_{\mathrm{i-Amazon}}$ are:

$$\lambda_{\mathrm{i-Yellow}} = \frac{\sum_{k=1}^{5} \sum_{i=k+2}^{10} \boldsymbol{N}_{\lambda t}(k, i)}{5} = 2.10 \quad \text{(M6)}$$

and

$$\lambda_{\mathrm{i-Amazon}} = \frac{\sum_{k=1}^{5} \sum_{i=k+2}^{11} \boldsymbol{N}_{\lambda t}(k, i)}{5} = 1.26 \quad \text{(M7)}$$

DATA AVAILABILITY STATEMENT

The original contributions presented in the study are included in the article/**Supplementary Material**, further inquiries can be directed to the corresponding author.

AUTHOR CONTRIBUTIONS

LZ, the corresponding author, did all the mathematics derivations. KYW organized the manuscript. TJL did the derivations and provided the data. XL, BYG, and GXC collected the data and plot figures. JHW and YFH processed the data and revised the manuscript.

FUNDING

This paper is supported by the State Key laboratory of Plateau Ecology and Agriculture, Qinghai Univerisity (2021-KF-10), National Natural Science Foundation of China (52109092), and Huazhong University of Science and Technology (3004242101).

ACKNOWLEDGMENTS

Data supporting **Figure 10** and **Supplementary Table S1** in this study were obtained from a digital elevation model (DEM) data with a 30 m resolution. I would like to thank Rina Schumer and Gary Parker for their useful comments and revisions of the manuscript.

SUPPLEMENTARY MATERIAL

The Supplementary Material for this article can be found online at: https://www.frontiersin.org/articles/10.3389/fenvs.2021.792289/full#supplementary-material

Supplementary Table S1 | The Tokunaga matrices $\boldsymbol{N_t}$ for the Yellow River and the Amazon River.

Supplementary Table S2 | The side-branching ratio matrices $\boldsymbol{T_t}$ for the Yellow River and the Amazon River.

Supplementary Table S3 | The $\boldsymbol{N\_R_t}$ matrices for the Yellow River and the Amazon River.

Supplementary Table S4 | The $\boldsymbol{N\_\lambda_t}$ matrices of generators λ_{o} and λ_{i} for the Yellow River and the Amazon River.

REFERENCES

Abrahams, A. D. (1984). The Development of Tributaries of Different Sizes along Winding Streams and Valleys. *Water Resour. Res.* 20, 1791–1796. doi:10.1029/wr020i012p01791

Claps, P., Fiorentino, M., and Oliveto, G. (1996). Informational Entropy of Fractal River Networks. *J. Hydrol.* 187, 145–156. doi:10.1016/s0022-1694(96)03092-2

Devauchelle, O., Petroff, A. P., Seybold, H. F., and Rothman, D. H. (2012). Ramification of Stream Networks. *Proc. Natl. Acad. Sci.* 109, 20832–20836. doi:10.1073/pnas.1215218109

Dodds, P. S. (2000). Geometry of River Networks. Ph.D. Thesis. Massachusetts Institute of Technology.

Dodds, P. S., and Rothman, D. H. (1999). Unified View of Scaling Laws for River Networks. *Phys. Rev. E* 59, 4865–4877. doi:10.1103/PhysRevE.59.4865

Gupta, V. K., and Mesa, O. J. (2014). Horton Laws for Hydraulic-Geometric Variables and Their Scaling Exponents in Self-Similar Tokunaga River Networks. *Nonlin. Process. Geophys.* 21, 1007–1025. doi:10.5194/npg-21-1007-2014

Horton, R. E. (1945). Erosional Development of Streams and Their Drainage Basins; Hydrophysical Approach to Quantitative Morphology. *Geol. Soc. Am. Bull.* 56 (3), 275–370. doi:10.1130/0016-7606(1945)56[275:edosat]2.0.co;2

Hung, C.-P., and Wang, R.-Y. (2005). Coding and Distance Calculating of Separately Random Fractals and Application to Generating River Networks. *Fractals* 13 (1), 57–71. doi:10.1142/S0218348X05002738

Kovchegov, Y., and Zaliapin, I. (2020). Random Self-Similar Trees: A Mathematical Theory of Horton Laws. *Probab. Surv.* 17, 1–213. doi:10.1214/19-PS331

Li, J., Li, T., Liu, S., Shi, H., and Shi, H. Y. (2018). An Efficient Method for Mapping High-Resolution Global River Discharge Based on the Algorithms of Drainage Network Extraction. *Water* 10 (4), 533. doi:10.3390/w10040533

Li, J. Y., Li, T. J., Zhang, L., Bellie, S., Fu, X. D., Huang, Y. F., et al. (2020). A D8-Compatible High-Efficient Channel Head Recognition Method. *Environ. Model. Softw.* 125, 104624. doi:10.1016/j.envsoft.2020.104624

Mandelbrot, B. B. (1982). *The Fractal Geometry of Nature*. New York: W. H. Freeman.

Mantilla, R., Troutman, B. M., and Gupta, V. K. (2010). Testing Statistical Self-Similarity in the Topology of River Networks. *J. Geophys. Res.* 115, 1–12. doi:10.1029/2009JF001609

Masek, J. G., and Turcotte, D. L. (1993). A Diffusion-Limited Aggregation Model for the Evolution of Drainage Networks. *Earth Planet. Sci. Lett.* 119, 379–386. doi:10.1016/0012-821x(93)90145-y

Mcconnell, M., and Gupta, V. K. (2008). A Proof of the Horton Law of Stream Numbers for the Tokunaga Model of River Networks. *Fractals* 16 (3), 227–233. doi:10.1142/S0218348X08003958

Menabde, M., Veitzer, S., Gupta, V., and Sivapalan, M. (2001). Tests of Peak Flow Scaling in Simulated Self-Similar River Networks. *Adv. Water Resour.* 24, 991–999. doi:10.1016/S0309-1708(01)00043-4

Montgomery, D. R., and Dietrich, W. E. (1992). Channel Initiation and the Problem of Landscape Scale. *Science* 255, 826–830. doi:10.1126/science.255.5046.826

Peckham, S. D. (1995b). Self-similarity in the Three-Dimensional Geometry and Dynamics of Large River Basins. Ph.D.Thesis. USA: University of Colorado.

Peckham, S. D. (1995a). New Results for Self-Similar Trees with Applications to River Networks. *Water Resour. Res.* 31 (4), 1023–1029. doi:10.1029/94WR03155

Pelletier, J. D., and Turcotte, D. L. (2000). Shapes of River Networks and Leaves: Are They Statistically Similar? *Phil. Trans. R. Soc. Lond. B* 355, 307–311. doi:10.1098/rstb.2000.0566

Perron, J. T., Richardson, P. W., Ferrier, K. L., and Lapôtre, M. (2012). The Root of Branching River Networks. *Nature* 492, 100–103. doi:10.1038/nature11672

Seybold, H., Rothman, D. H., and Kirchner, J. W. (2017). Climate's Watermark in the Geometry of Stream Networks. *Geophys. Res. Lett.* 44 (5), 2272–2280. doi:10.1002/2016gl072089

Shreve, R. L. (1966). Statistical Law of Stream Numbers. *J. Geol.* 74 (1), 17–37. doi:10.1086/627137

Strahler, A. N. (1952). Hypsometric (Area-altitude) Analysis of Erosional Topography. *Geol. Soc. Am. Bull.* 63, 1117–1142. doi:10.1130/0016-7606(1952)63[1117:haaoet]2.0.co;2

Tokunaga, E. (1978). Consideration on the Composition of Drainage Networks and Their Evolution, Geograph. *Rep* 13, 1–27.

Tokunaga, E. (1984). Ordering of divide Segments and Law of divide Segment Numbers. *Trans. Jpn. Geomorphol. Union* 5 (2), 71–77.

Tokunaga, E. (1966). The Composition of Drainage Network in Toyohira River basin and Valuation of Horton's First Law (In Japanese with English Summary). *Geophys. Bull. Hokkaido Univ.* 15, 1–19.

Troutman, B. M. (2005). Scaling of Flow Distance in Random Self-Similar Channel Networks. *Fractals* 13, 265–282. doi:10.1142/S0218348X05002945

Veitzer, S. A., and Gupta, V. K. (2000). Random Self-Similar River Networks and Derivations of Generalized Horton Laws in Terms of Statistical Simple Scaling. *Water Resour. Res.* 36 (4), 1033–1048. doi:10.1029/1999WR900327

Veitzer, S. A., and Gupta, V. K. (2001). Statistical Self-Similarity of Width Function Maxima with Implications to Floods. *Adv. Water Resour.* 24, 955–965. doi:10.1016/S0309-1708(01)00030-6

Wang, G. Q., Li, T. J., Zhang, L., et al. (2016). *River basin Geometry*. Beijing, China: Science Press, 133–138. (in Chinese).

Wang, P.-J., and Wang, R.-Y. (2002). A Generalized Width Function of Fractal River Network for the Calculation of Hydrologic Responses. *Fractals* 10 (2), 157–171. doi:10.1142/S0218348X02001038

Zanardo, S., Zaliapin, I., and Foufoula-Georgiou, E. (2013). Are American Rivers Tokunaga Self-Similar? New Results on Fluvial Network Topology and its Climatic Dependence. *J. Geophys. Res. Earth Surf.* 118, 1–18. doi:10.1002/jgrf.2002910.1029/2012jf002392

Zhang, L., Dai, B., Wang, G., Li, T., and Wang, H. (2009). The Quantization of River Network Morphology Based on the Tokunaga Network. *Sci. China Ser. D-Earth Sci.* 52 (11), 1724–1731. doi:10.1007/s11430-009-0176-y

Conflict of Interest: The authors declare that the research was conducted in the absence of any commercial or financial relationships that could be construed as a potential conflict of interest.

GLOSSARY

ω H-S order [-]

N_ω the number of streams with H-S order ω [-]

$R_\mathbf{B}$ bifurcation ratio (i.e. the ratio of the number of streams [-])

(ω, ω') a stream as a side-branching tributary with H-S order ω that flows into a stream ordered ω', assigned by a Tokunaga order (ω, ω') [-]

$N_{\omega,\omega'}$ the number of streams with Tokunaga order (ω, ω') [-]

$\boldsymbol{N}$ Tokunaga stream number matrix composed by $N_{\omega,\omega'}$ [-]

$T_{\omega,\omega+k}$ the ratio of the number of streams with the H-S order ω that flow into streams with the order $(\omega+k)$ to the number of streams with the H-S order $(\omega+k)$ [-]

$\boldsymbol{T}$ Tokunaga side-branching ratio matrix composed by $T_{\omega,\omega+k}$ [-]

T_k the side-branching ratio [-]

a the average number of streams with the H-S order ω that flow into streams ordered $\omega+1$[-]

c the average increasing rate of the side-branching ratio of side tributaries with a different order [-]

λ, $\lambda_\mathbf{o}, \lambda_\mathbf{i}$ generator, exterior generator, interior generator [-]

t iterative steps [-]

$M_t^\mathbf{o}, M_t^\mathbf{i}$ the number of exterior links and interior links at the tth iteration step [-]

$N_{t,(\omega,\omega')}, N_{t,\omega}$ the number of streams with Tokunaga order $(\omega, \omega^{'})$ and H-S order ω at the tth iterative step [-]

$\boldsymbol{N_t}$, $\boldsymbol{T_t}$ Tokunaga matrix and side-branching ratio matrix of the QU-IBTN, which is generated by the interior generator λ_i and the exterior generator λ_o at the tth step [-]

N_R_t, N_λ_t a transformation of $\boldsymbol{N_t}$; a transformation of $\boldsymbol{N\_R_t}$ and represents the $\boldsymbol{\lambda_o}$ and λ_i values [-]

Frontiers in Environmental Science

TYPE Original Research
PUBLISHED 12 October 2022
DOI 10.3389/fenvs.2022.991969

OPEN ACCESS

EDITED BY
Songdong Shao,
Dongguan University of Technology,
China

REVIEWED BY
Can Huang,
North China University of Technology,
China
Xiaodong Yu,
Hohai University, China

*CORRESPONDENCE
Qingzhi Hou,
qhou@tju.edu.cn

SPECIALTY SECTION
This article was submitted to
Freshwater Science,
a section of the journal
Frontiers in Environmental Science

RECEIVED 12 July 2022
ACCEPTED 29 July 2022
PUBLISHED 12 October 2022

CITATION
Liu W, Hou Q, Lei X, Lian J and Dang J
(2022), SPH modeling of substance
transport in flows with
large deformation.
Front. Environ. Sci. 10:991969.
doi: 10.3389/fenvs.2022.991969

SPH modeling of substance transport in flows with large deformation

Wanying Liu[1], Qingzhi Hou[2]*, Xiaohui Lei[3], Jijian Lian[2] and Jianwu Dang[4]

[1]School of Marine Science and Technology, Tianjin University, Tianjin, China, [2]State Key Laboratory of Hydraulic Engineering Simulation and Safety, Tianjin University, Tianjin, China, [3]State Key Laboratory of Simulation and Regulation of Water Cycle in River Basin, China Institute of Water Resources and Hydropower Research, Beijing, China, [4]College of Intelligence and Computing, Tianjin University, Tianjin, China

The velocity field in coastal and oceanic currents is mostly non-uniform, which will result in irregular particle distribution when the fluid is represented by an amount of moving discrete particles as in smoothed particle hydrodynamics (SPH). When the non-uniformity of the flow is big, i.e., with large deformation, the conventional SPH method can hardly solve the associated advection-diffusion process (e.g., substance transport). To accurately simulate the substance transport in flows with large deformation, two types of particle shifting techniques (PSTs) are incorporated into the conventional SPH in this paper. One is based on current particle distance, and the other is based on Fick's law. In the second type, the repulsive force (RF) term for suppressing the paring instability that occurs in particle shifting technique (PST) is studied and the effect of the kernel function is examined. By introducing a particle disorder measurement, the simulated results of SPH with the two types of PSTs and their modifications are evaluated and the influence of the shifting magnitude is analyzed. The suggestions for how to set reasonable parameters in PSTs are provided by a systematic parametric study. For further illustration, the simulation of the anisotropic diffusion is also examined. To give reliable reference solutions, the high-resolution modified total variation diminishing Lax Friedrichs scheme with Superbee limiter (MTVDLF-Superbee) with fine mesh is also implemented. The validated Lagrangian particle model with optimized PST is applied to a practical application.

KEYWORDS

smoothed particle hydrodynamics, anisotropic diffusion, particle shifting technique, particle disorder measurement, MTVDLF-Superbee

1 Introduction

Substances (including sediment, salt and soluble pollutants, etc.) transport in surface and subsurface water is modeled by the advection-diffusion equation, for which various numerical methods have been developed (Finlayson, 1992; Ewing and Wang, 2001; Wang and Hutter, 2001; Alhumaizi, 2004). The difficulties to obtain good solutions for advection-diffusion equation mainly exist in two aspects. One is the treatment of the advection term, especially when the problem is advection dominated, and the other is that there exist steep fronts in the solution. Compared with Eulerian methods, the major advantage of the Lagrangian methods is that the advective term is not involved in the Lagrangian form of the advection-diffusion equation, so that the numerical problems of both spurious oscillations and diffusion error caused by spatial discretization of the advection can be easily eliminated, leading to accurate solutions (Zimmermann et al., 2001; Liu and Liu, 2006; Devkota and Imberger, 2009). Compared with mesh-based Eulerian methods, the smoothed particle hydrodynamics (SPH) is more competitive and attractive due to its good properties of Lagrange and meshfree. It is considered to have the competence to tackle intractable problems in the CFD field, such as big deformation, free-surface and multi-phase flows (Monaghan and Kocharyan, 1995; Kum et al., 2003; Larbe and Price, 2012; Monaghan, 2012; Ye et al., 2019; Gu et al., 2022).

However, SPH has two inherent drawbacks, i.e., boundary deficiency and particle inconsistency, which are still the key issues for research and application in the SPH society (Monaghan, 2000; Kum et al., 2003; Ye et al., 2019; Gu et al., 2022). To solve the governing partial differential equations (PDEs) using SPH, there are two main procedures. One is the kernel approximation in continuous form, and the other is the particle approximation in discretization form. To obtain reasonable solutions, the kernel needs to satisfy some requirements, such as normalization of kernel integration, symmetry of the kernel and anti-symmetry of kernel gradients (Violeau, 2012). These properties can be well preserved in the procedure of particle approximation when the particles maintain regularly spaced, otherwise numerical instability and accuracy degradation cannot be fully avoided. The conventional SPH has second-order accuracy for organized particles, while it cannot even achieve first order as the particles become disorganized (Ye et al., 2019). This is known as particle inconsistency, which mainly results from the discrepancy between kernel approximation and particle approximation when the particles are irregularly spaced.

SPH is applicable in solving the advection-diffusion and heat conduction equations, to which some studies have devoted (Cleary and Monaghan, 1999; Monaghan, 2005; Aristodemo et al., 2010; Bai et al., 2018; Wang et al., 2019). Noticing that both of them have identical form in Lagrangian frame, the discrepancy between them is the zero advection in heat conduction problems, while attention also needs to be paid to particle inconsistency when heat conduction couples with the large deformation flows (Cleary and Monaghan, 1999). Arising from advection, particle disorder affects the simulation of the diffusion process. Chaniotis et al. (2002) approximated the diffusion terms by directly discretizing the second-order derivatives, but this approach is sensitive to particle disorder, then particle remeshing schemes have to be added. Most of the studies (Cleary and Monaghan, 1999; Shao and Lo, 2003; Aristodemo et al., 2010; Ryan et al., 2010; Chang and Chang, 2017; Zheng et al., 2018) adopted a scheme that can be regarded as the hybrid of SPH and difference method. In this scheme, the simulation of diffusion terms merely includes the first-order derivative approximation of SPH. Via this hybrid scheme, Cleary and Monaghan (1999), Aristodemo et al. (2010), Chang and Chang (2017) expressed the diffusion coefficient in a symmetric form to ensure continuity of the flux when the diffusion coefficient is discontinuous and to reduce the influence of particle disorder. Ryan et al. (2010) also used the hybrid scheme to handle the diffusion terms in flows with small deformation, and the focus was on the treatment of the complicated boundary conditions. Recently, Alvarado-Rodríguez et al. (2019) improved the consistency of SPH *via* setting smoothing length and the number of neighboring particles relevant to the total number of particles, aiming to simulate the anisotropic diffusion with irregular particle distribution. In this paper, the SPH format for diffusion terms differs from the two methods mentioned above. It is a complete SPH form and does not directly approximate the second-order derivatives.

To restore particle consistency, many high-order SPH methods have been proposed, which are known as corrective SPH schemes. To enhance the approximation accuracy, the reproducing kernel particle method (RKPM) modifies the kernel function by a correction function (Liu et al., 1995; Liu and Jun, 1998). The corrective smoothed particle method (CSPM) (Chen et al., 1999; Chen and Beraun, 2000) improves the conventional SPH on the basis of Taylor series expansion, whose discretization form is equivalent to the normalization for the function and its first derivatives. Based on CSPM, the finite particle method (FPM) was put forward by Liu and Liu (2006), which approximates the function and its first derivatives simultaneously and has higher order accuracy than CSPM. The kernel gradient correction (KGC) (Bonet and Lok, 1999; Shao et al., 2012) method corrects the kernel gradient by multiplying the original kernel gradient with an invertible matrix. This method is easy to code on account of retaining the structure of conventional SPH. For the ease of choosing kernel function, the kernel gradient free (KGF) SPH method was proposed (Huang et al., 2015), whose corrective matrix is invertible even if the particles are highly disordered, because the corrective matrix is symmetric. Recently, the decoupled finite particle method (DFPM) (Zhang and Liu, 2018) was developed, in which the corrective matrix is diagonally dominant and it is not necessary to calculate the inverse matrix particle by particle, so it becomes less sensitive to the particle disorder. In fact, the high-order SPH methods mentioned above correct the conventional SPH by some kernel properties which are satisfied only when the particle distribution is regular. On that account, the accuracy of these algorithms will degrade to some extent when particles are disordered.

Apart from the corrective SPH methods, some other ones, namely particle regularization techniques, are also capable of restoring particle consistency. The XSPH scheme (Monaghan, 1988; Shahriari et al., 2013; Ye et al., 2019) uses the adjacent particles to calculate the local velocity, by which the movement of particles tends to mitigate. However, this method may result in non-physical solutions especially when large velocity gradient exists. To improve particle consistency, Monaghan (2000) adopted a repulsive force (RF) term in the equation of motion to avoid the clumping of particles. Similar to RF, Tsuruta et al. (2013) employed a stabilizing force to prevent interparticle penetration. In this work, the same RF term as that of Monaghan (2000) is brought into particle shifting techniques (PST) to redistribute particles. The state of the art PSTs gained much attention in recent years (Nestor et al., 2009; Xu et al., 2009; Lind et al., 2012; Skillen et al., 2013; Antuono et al., 2014; Khorasanizade and Sousa, 2016; Huang et al., 2018). They try to make the particles distribute as uniformly as possible according to certain rules. Xu et al. (2009) brought the PST proposed originally in the finite volume particle method (Nestor et al., 2008; Nestor et al., 2009) into SPH. They applied this technique to simulate incompressible flows by coupling with incompressible SPH (ISPH) method. This PST depends on the calculation of particle distance to decide the shifting of particles. Lind et al. (2012) proposed another type of method on the basis of Fick's law aiming at the incompressible flows too. Several improvements (Skillen et al., 2013; Khorasanizade and Sousa, 2016; Huang et al., 2018) for Xu et al. (Xu et al., 2009) and Lind et al. (Lind et al., 2012) methods are suggested in succession to stabilize the PSTs. In this paper, we contribute to the parameter optimization and stabilities improvement for the PSTs. The purpose of studying PSTs in this paper is to solve the particle cavity problem which leads to the failure of the simulation of advection-diffusion process.

The rest of the paper is organized as follows. Section 2 presents the governing equation and the SPH-based Lagrangian particle transport model. In Section 3, to deal with substance transport in large deformation flows, several typical PSTs are presented. An evaluation method for the degree of particle disorder is also described. In Section 4, the Lagrangian particle transport model based on SPH combined with PSTs is applied to the isotropic and anisotropic diffusion problems in flows with large deformation, and the results are compared with the exact and reference solutions. The performance of different PSTs and the effect of involved parameters are also evaluated. In Section 5, the SPH method with optimized PST is applied to a case study to show its applicability to practical problems. Section 6 summarizes the concluding remarks.

2 Lagrangian particle transport model

2.1 Governing equations

The governing equation for substance transport adopted in this paper is the two-dimensional (2D) advection-diffusion equation

$$\frac{\partial C}{\partial t} + u\frac{\partial C}{\partial x} + v\frac{\partial C}{\partial y} = k\left(\frac{\partial^2 C}{\partial x^2} + \frac{\partial^2 C}{\partial y^2}\right) \tag{1}$$

where $C(x, y)$ is the concentration of the substance; u and v are the velocity of the flow field; k is the coefficient for isotropic diffusion; x and y are the spatial coordinates and t is time. In coastal flow, the physical process of diffusion should consider the longitudinal dispersion and turbulent diffusion at least, i.e., behaves as anisotropic diffusion. To denote the anisotropic diffusion, the mixed second-order derivatives should be included in Eq. 1 as

$$\frac{\partial C}{\partial t} + u\frac{\partial C}{\partial x} + v\frac{\partial C}{\partial y} = \frac{\partial}{\partial x}\left(k_{11}\frac{\partial C}{\partial x}\right) + \frac{\partial}{\partial x}\left(k_{12}\frac{\partial C}{\partial y}\right) + \frac{\partial}{\partial y}\left(k_{21}\frac{\partial C}{\partial x}\right) + \frac{\partial}{\partial y}\left(k_{22}\frac{\partial C}{\partial y}\right) \tag{2}$$

where the diffusion coefficients can be symbolized by a tensor $\boldsymbol{K}$ $(\boldsymbol{K} = k_{ij}\ (i, j = 1, 2))$.

Note that Eqs 1, 2 are derived for incompressible fluid and hence the divergence of the velocity is zero. The given velocity field in Section 4 is consistent with this assumption. The velocities of the flow field can either be given analytically or numerically calculated by any suitable methods, which are supposed to be known here.

With the definition of the material derivative $\frac{d}{dt} = \frac{\partial}{\partial t} + u\frac{\partial}{\partial x} + v\frac{\partial}{\partial y}$, the Lagrangian form of Eq. 1 is expressed as

$$\frac{\mathrm{d}C}{\mathrm{d}t} = k\left(\frac{\partial^2 C}{\partial x^2} + \frac{\partial^2 C}{\partial y^2}\right) \tag{3}$$

on the moving coordinate system

$$\frac{\mathrm{d}x}{\mathrm{d}t} = u \text{ and } \frac{\mathrm{d}y}{\mathrm{d}t} = v \tag{4}$$

The Lagrangian form of Eq. 2 can be constructed following the same way.

2.2 SPH-based Lagrangian particle model

The SPH method is introduced briefly in this section, the foundation of which is the interpolation theory (Violeau, 2012). The kernel approximation in continuous form and the particle approximation in discretization form are its two main ingredients.

There are three typical approximation forms for second derivatives in SPH. They can be directly approximated via the second derivatives of the kernel (Monaghan, 2005) as

$$\langle \frac{\partial^2 C}{\partial x^2} \rangle_a = \sum\nolimits_b C_b \frac{\partial^2 W_{ab}}{\partial x^2} \frac{m_b}{\rho_b} \tag{5}$$

where m_b and ρ_b are the mass and density of particle b; C_b is the concentration at position $\boldsymbol{x}_b$; $W_{ab} = W(|\boldsymbol{x}_a - \boldsymbol{x}_b|, h)$ is the kernel function and h stands for the smoothing length. The formulation (5) is sensitive to irregular particle distribution and may lead to numerical results inconsistent with physics due to instability of the second derivative of the kernel (Monaghan, 2005).

To circumvent the weakness of Eq. 5, other forms approximating the second derivatives are developed, among which the hybrid scheme and the approach presented in this work have been widely used. By the hybrid scheme (Cleary and Monaghan, 1999; Monaghan, 2005), the diffusion term can be discretized as

$$\langle \frac{\partial^2 C}{\partial x^2} \rangle_a = \sum\nolimits_b (k_a + k_b)(C_a - C_b) \frac{x_a - x_b}{|x_a - x_b|^2} \frac{\partial W_{ab}}{\partial x} \frac{m_b}{\rho_b} \tag{6}$$

in which only the first derivative of kernel is contained. The formulation (6) can be considered as the hybrid of SPH and finite difference (Cleary and Monaghan, 1999), hence its stability and accuracy is vulnerable to be effected by the finite difference part.

In this paper, another scheme for approximating diffusion terms is applied, in which only first-order derivatives need to be treated (Jeong et al., 2003; Liu et al., 2020). By this scheme, Eq. 1 can be rewritten by the diffusive flux $\boldsymbol{q}$ (Liu et al., 2020)

$$\begin{cases} \boldsymbol{q} = -k\nabla C \\ \dfrac{\mathrm{d}C}{\mathrm{d}t} = -\nabla \cdot \boldsymbol{q} \end{cases} \tag{7}$$

Again k needs to be changed into $\boldsymbol{K}$ for anisotropic diffusion. With this form, the diffusion terms can be solved by approximating the first-order derivative twice. It is easy to code and converted flexibly between isotropic and anisotropic diffusion codes. Better yet, it is a totally SPH based model. The kernel approximation of the concentration gradient in SPH is (Liu et al., 2020)

$$\langle \nabla C_a \rangle = \int_\Omega C(\boldsymbol{x}) \nabla_a W d\boldsymbol{x} \tag{8}$$

where $\nabla_a W$ is the kernel gradient with respect to the position of particle a. To make the discretization form of (8) less sensitive to particle distribution, the anti-symmetry property of the kernel gradient (Violeau, 2012)

$$\int_\Omega \nabla_a W d\boldsymbol{x} = 0 \tag{9}$$

can be used to extend Eq. 8 as

$$\langle \nabla C_a \rangle = \int_\Omega C(\boldsymbol{x}) \nabla_a W d\boldsymbol{x} - C_a \int_\Omega \nabla_a W d\boldsymbol{x} \tag{10}$$

The particle discretization form of Eq. 10 is

$$\langle \nabla C_a \rangle = \sum\nolimits_b (C_b - C_a) \nabla_a W_{ab} \frac{m_b}{\rho_b} \tag{11}$$

Note that Eq. 11 can mitigate the particle inconsistency problem to some degree, although the discretization of Eq. 9 is only true for regularly distributed particles.

Applying Eq. 11 to the first-order derivatives in Eq. 7, the semi-discretization form of the substance transport equation is derived as (Liu et al., 2020)

$$\begin{cases} \dfrac{\mathrm{d}C_a}{\mathrm{d}t} = \sum\nolimits_b \dfrac{m_b}{\rho_b} (\boldsymbol{q}_b - \boldsymbol{q}_a) \cdot \nabla_a W_{ab} \\ \boldsymbol{q}_a = k \sum\nolimits_b \dfrac{m_b}{\rho_b} (C_b - C_a) \nabla_a W_{ab} \end{cases} \tag{12}$$

Note that a similar formulation can be obtained for anisotropic diffusion, which eases the coding of anisotropic diffusion process (Liu et al., 2020). Since the diffusive flux is included, it is also easy to handle Neumann type boundary. The accuracy of Eq. 12 is the same order as that of Eq. 6 when particles are regularly spaced (Fatehi and Manzari, 2011). Together with a time integration algorithm, the above semi-discretization form and the change of the coordinate can be integrated. For simplicity, the first-order one-step Euler method is used here, which gives accurate results if the used time step is sufficiently small.

Equation 12 has been derived in Liu et al. (2020) with more details. In that work, the capability of the Lagrangian particle transport model to handle the grid anisotropic problem, dominated advection, pure advection and discontinuity have been validated in the flows with small deformation. Its accuracy, efficiency and stability were compared with the mesh-based Eulerian method, and the particle cavity problem was also recognized. In this work, the SPH-based model is further applied to substance transport problem in flows with large deformation. Since the model given by Eq. 12 cannot simulate the diffusion process when particles are in cavity state, the PSTs for eliminating particle cavities need to be incorporated, which is presented below.

3 Particle shifting techniques

When the particles become disordered due to non-uniform velocity field, SPH cannot accurately approximate the first- and second-order derivatives (Monaghan, 2000; Xu et al., 2009; Lind et al., 2012), and PSTs are good remedies. PSTs can be categorized into two classes. One is based on the distance between particles (Xu's approach and its modified ones), and the other is based on the Fick's law of diffusion (Lind's approach and its modified ones). The latter ones are more feasible for free surface flow. In this section, the representative PSTs and their modified ones are presented. Moreover, a measurement to evaluate the degree of particle disorder is introduced.

3.1 PST of Xu (Xu et al., 2009)

In Xu's approach, the particles are shifted in terms of the distance between the center particle and its neighbors (those in the support domain of the kernel). On the basis of Tailor series expansion, the concentration in the new position is interpolated by

$$C_{a'} = C_a + \delta \boldsymbol{r}_{aa'} \cdot (\nabla C)_a + O\left(\delta r_{aa'}^2\right) \tag{13}$$

where $C_{a'}$ denote the concentration of particle a at the new position $\boldsymbol{x}_{a'}$, $\delta \boldsymbol{r}_{aa'}$ is the distance vector between $\boldsymbol{x}_{a'}$ and $\boldsymbol{x}_a$, and $\delta r_{aa'}$ is the distance between the two positions. Note that Eq. 13 will be adopted to interpolate the concentration in all the PSTs demonstrated in this paper.

In Xu's approach, the regulation directing particle redistribution is given by

$$\delta \boldsymbol{r_a} = -A\alpha \boldsymbol{R}_a \tag{14}$$

$$\boldsymbol{R}_a = \sum\nolimits_{b=1}^{N_a} \frac{\boldsymbol{r}_{ab}}{r_{ab}^3} \bar{r}_a^2 \tag{15}$$

$$\bar{r}_a = \frac{1}{N_a} \sum\nolimits_{b=1}^{N_a} r_{ab} \tag{16}$$

where A is a constant ranging from 0.01 to 0.1, and $\alpha = U_{max}\mathrm{d}t$ is the shifting magnitude which is assigned to be the maximum advection distance. N_a is the number of neighbors of particle a , $\boldsymbol{r}_{ab} = \boldsymbol{x}_a - \boldsymbol{x}_b$, $r_{ab} = |\boldsymbol{r}_{ab}|$, and $\bar{r}_a$ is the averaged distance between particle a and its neighbors. The anisotropic features of particles are achieved by the summation of unit distance vector $\boldsymbol{r}_{ab}/r_{ab}$ in Eq. 15 and the term $\bar{r}_a^2/r_{ab}^2$ decreases the influence of particles in far distance. The parameter A should be properly chosen to restrict the shifting magnitude to a reasonable range, because it affects both the interpolation accuracy of the concentration and the degree of particle disorder.

3.2 Modified Xu's algorithm

In Xu's approach, U_{max} in the shifting magnitude is the global maximum velocity, which increases the shifting distance of particles with lower velocities. To solve this problem, Khorasanizade and Sousa (2016) introduced the local maximum velocity. For the purpose of obtaining appropriate shifting magnitude, i.e., the product of A and α in Eq. 14, they proposed a set of algebraic equations, by which the shifting magnitude was determined ultimately. Replacing $A\alpha$ with A', the whole set algebraic equations is given by

$$\begin{cases} a_1 = U_{max} dtA \\ a_2 = U_{max,a}^{local} dtA \\ b = C_F \bar{r}_a \\ d = max\ (a_2, b) \\ A' = min\ (a_1, d) \end{cases} \tag{17}$$

where $U_{max,a}^{local}$ stands for the local maximum velocity related to particle a; C_F is a constant with the best choice of 0.001. The anisotropic degree of particles is determined by the parameter d, and the maximum advection distance is still a limitation for particle shifting in this modified approach. Its main contribution is the introduction of the local maximum velocity, which regulates the shifting distance of slower particles to be moderate. Due to the ambiguous description of $U_{max,a}^{local}$ (Khorasanizade and Sousa, 2016), it is assigned to be the same as U_a in Eq. 24 in this work.

3.3 Lind's approach

In Lind's approach, the movement of particles is determined by the gradient of particle concentration. To distinguish the diffusion process of pollutant concentration in *Lagrangian Particle Transport Model Section* from that of particle number concentration in this section, we use D to represent the particle number concentration and K for its diffusion coefficient. The diffusion flux can be presumed to be the number of particles crossing the unit area in unit time, which means that the flux is directly proportional to the particle shifting velocity. Define P_s as the proportional scale between the flux and the shifting velocity $\boldsymbol{v}_a$, then the relation is given by

$$-K\nabla D_a = P_s \boldsymbol{v}_a \tag{18}$$

Colagrossi et al. (2012) showed that $-\nabla D$ can direct particles to move along the maximum anisotropic direction.

Substituting Eq. 18 into the shifting displacement of particle a, i.e., $\delta \boldsymbol{r}_a = \boldsymbol{v}_a dt$, yields

$$\delta \boldsymbol{r}_a = -K/P_s \mathrm{d}t \nabla D_a \tag{19}$$

The gradient of particle concentration can be discretized by SPH as (Lind et al., 2012)

$$\nabla D_a = \sum\nolimits_b \mathrm{V}_b \nabla_a W_{ab} \tag{20}$$

where $\mathrm{V}_b = m_b/\rho_b$ is the volume of the neighboring particle b.

Monaghan (2000) showed that when Eq. 20 is applied, the kernel gradient deviates from its physical meaning and will result in unphysical solution. For instance, the gradient of the cubic spline is zero in the origin, which will impose unphysical influence on the results when particle b is close enough to particle a. Physically speaking, the kernel gradient is supposed to increase with the decrease of particle distance. To make up for this kernel deficiency, Monaghan (2000) employed the term of RF (in fluid dynamics, it is regarded as artificial

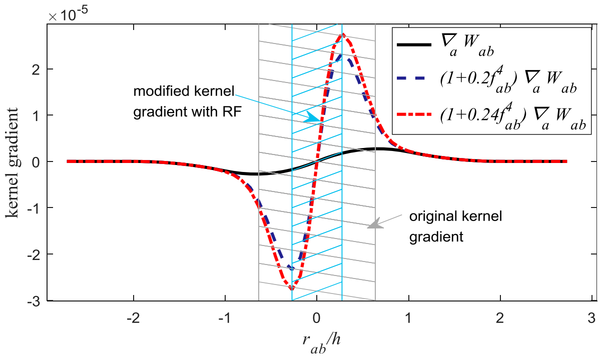

FIGURE 1
Comparison of the original kernel gradient (cubic spline kernel, solid line) with the modified ones by adding RF.

pressure) to eliminate the tensile instability. The expression for the RF is

$$f_{ab} = \frac{W(r_{ab})}{W(\mathrm{d}x_0)} \tag{21}$$

where $\mathrm{d}x_0$ is the initial particle spacing. In Lind's approach, Eq. 21 is employed to calculate the gradient of particle concentration and Eq. 20 is then modified as

$$\nabla D_a = \sum\nolimits_b V_b\left(1 + Rf_{ab}^n\right)\nabla_a W_{ab} \tag{22}$$

The parameters R and n are suggested to be 0.2 and 4, respectively (Monaghan, 2000). Via the modification, the kernel gradient is in better agreement with its physical meaning. For details, Figure 1 can be referred.

Using the symbol $K' = K/P_s$ to stand for integration of the scaling constants, the coefficient K' has similar meaning as parameter A' in Eq. 17 and is of great importance to decide the shifting magnitude. Its value is determined on the basis of von Neumann stability theory with the expression (Lind et al., 2012)

$$K' \le L_p h^2 \big/ dt \tag{23}$$

where L_p is taken as a constant of 0.5 by Lind et al. (2012), but it can be different values as tested in Section 4. Note that as the shifting distance has the possibility to exceed the smoothing length, Lind et al. (2012) gave an upper limit for it with the value of $0.2h$.

3.4 Modified Lind's algorithms

Skillen et al. (2013) improved Lind's approach via the CFL condition for the purpose of bringing in the local velocity which makes a similar sense as $U_{max,a}^{local}$ in Eq. 17. According to the CFL condition, the time step should satisfy

$$\mathrm{d}t \le \frac{h}{U_a} \tag{24}$$

in which U_a is the velocity magnitude of particle a. Taking $\mathrm{d}t = 0.5h/U_a$ and $L_p = 0.5$, and substituting them into Eq. 23 yields

$$K' \le hU_a \tag{25}$$

Then the local velocity can be used to control the shifting magnitude. In fact, there should be a dimensionless parameter as L_p to adjust the shifting magnitude. For the sake of distinction, this parameter is symbolized by S_p. As the upper limit is not necessary to be set, the shifting of all the particles satisfies the Fick's law, while the shifting distance of some particles is clipped by $0.2h$ in Lind's approach.

Recently, by using the maximum advection distance to replace one h in Eq. 23 and slightly changing the constant R, Huang et al. (2018) derived a new formula as

$$\delta \boldsymbol{r}_a = U_{max}\mathrm{d}t\frac{h}{2}\sum\nolimits_b V_b\left(1 + 0.24f_{ab}^4\right)\nabla_a W_{ab} \tag{26}$$

Note that although these PSTs do not strictly preserve momentum, they are still valuable in solving the particle inconsistency problem because they have good features in convergence, accuracy and stability (Lind et al., 2012).

In Figure 1, the original kernel gradient (derivative with respect to x_a) is compared with those with added RF. As demonstrated above, the portion between the two inflexions (see Figure 1) does not conform to its physical meaning. If possible, the smoothing length h should be chosen properly to make the nearest neighboring particle outside the misleading portion, otherwise particle clustering will be resulted (Lind et al., 2012). Physically speaking, the repulsive force between two particles should become larger when they get closer, while the kernel gradient indicating that the repulsive force shows the opposite effect. After the RF term is added, the improper zone gets narrower and the curve becomes much steeper (see Figure 1), which implies a larger shifting distance and a more flexible selection of h. In theory, a larger shifting distance can lead to more regular particle distribution.

3.5 Particle disorder measurement

For judging the performance of different PSTs and the effect of related parameters, a measurement to evaluate the degree of particle disorder is presented in this section. The algorithm proposed by Antuono et al. (2014) is adopted here to figure out the best choice of parameters in different schemes and to appraise which scheme can lead to the best consequence in the simulation of the advection-diffusion process.

In the evaluation of particle consistency, there are two main steps. The first step is to search the neighbors of particle a in its support domain Ω_a (see Figure 2), and the second is to find the

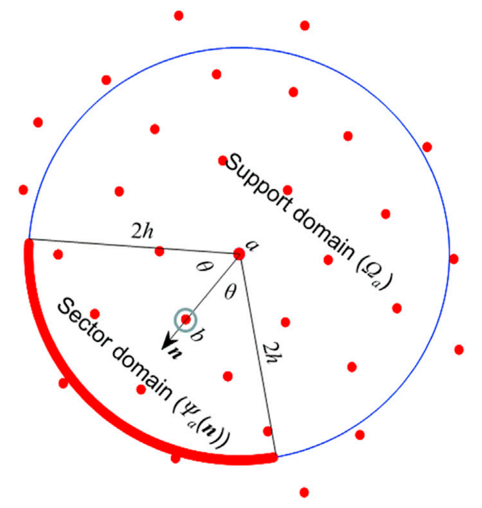

FIGURE 2
The schematic of particle disorder measurement.

maximum nearest distance among all the sectors which partition the support domain by specific rules (see Figure 2). In the first step, the minimum distance r_{min} between particles a and b is calculated by

$$r_{min} = \min_{b\in\Omega_a}\|\boldsymbol{x}_a - \boldsymbol{x}_b\| \tag{27}$$

In the second step, the sector domain $\Psi_a(\boldsymbol{n})$ is defined firstly, where $\boldsymbol{n}$ is the unit vector to denote its direction. In terms of proper angle θ (see Figure 2) and sector numbers suggested by Antuono et al. (2014), $\theta = 7\pi/18$ and eight sectors are used to divide the support domain. For the ease of segmentation, the first sector direction is determined by the vector $\boldsymbol{r}_{min} = \boldsymbol{x}_a - \boldsymbol{x}_b{}^{min}$, where $\boldsymbol{x}_b{}^{min}$ symbolizes the nearest neighboring particle in Ω_a. The next sector direction needs to plus $\pi/4$ since eight sectors are used. It means that there are certain areas are overlapped between two adjacent sectors. In every sector region, the nearest neighboring particle to the center particle a is searched by

$$r_{min}(\boldsymbol{n}) = \min_{b\in\Psi_a(\boldsymbol{n})}\|\boldsymbol{x}_a - \boldsymbol{x}_b\| \tag{28}$$

Accordingly, the maximum value R_{min} among the eight minimum distances $r_{min}(\boldsymbol{n})$ is obtained, which is compared with r_{min} to judge the anisotropic degree of particles.

The function for quantitating particle disorder is given by

$$\lambda_a = \frac{R^a_{min} - r^a_{min}}{R^a_{min} + r^a_{min}} \tag{29}$$

Then the effect of particle inconsistency can be evaluated by averaging all of λ_a as

$$\Lambda = \frac{\sum_{a=1}^{N}\lambda_a}{N} \tag{30}$$

where N is the total number of particles in the computational domain. If the distribution of particles is regular, the index Λ is equal to zero, which means that the closer Λ is to zero, the more regular the particles are. For more details, one is referred to Antuono et al. (2014).

4 Numerical results and discussion

In this section, we aim to confirm the feasibility of SPH coupled with PST in solving the advection-diffusion process when particle cavity problem occurs. An anisotropic rotation flow field with strong deformation (Pudykiewicz and Staniforth, 1984) is used for validation. The pure advection simulation is carried out firstly to illustrate the cavity phenomenon, which still exists even a large number of particles are used. Under this circumstance, the diffusion terms cannot be accurately approximated. For eliminating the cavity problem and regulating the particle distribution, PSTs are added to the Lagrangian particle transport model (Liu et al., 2020) and a series of tests are then conducted. Through the numerical experiments, the efficiency of different PSTs is compared, the factors affecting the stability of PSTs are optimized, and the accuracy is examined by comparing with the reference solution of MTVDLF-Superbee. The performances of PSTs are discussed in detail to guide their possible application to real engineering problems. The anisotropic diffusion simulations are also performed to further state the feasibility of the particle model.

In this test, the flow field is given by the streamline function

$$\psi = -\frac{LV_{max}}{4}\left(1 - \frac{4x^2}{L^2}\right)\cos\left(\frac{\pi y}{L}\right) \tag{31}$$

Then the velocities in x and y directions are

$$u = \frac{\mathrm{d}x}{\mathrm{d}t} = -\psi_y = -\frac{\pi V_{max}}{4}\left(1 - \frac{4x^2}{L^2}\right)\sin\left(\frac{\pi y}{L}\right) \tag{32}$$

$$v = \frac{\mathrm{d}y}{\mathrm{d}t} = \psi_x = 2V_{max}\frac{x}{L}\cos\left(\frac{\pi y}{L}\right) \tag{33}$$

where $V_{max} = 3$ m/s is used herein. The absolute velocity and the velocity vector are shown in Figure 3. It is a circulating non-uniform flow. The computational domain is $0 \le x, y \le 3200$ m.

The initial distribution of pollutant is given by the Gaussian as

$$C(x, y, 0) = \exp\left(-\frac{(x - x_0)^2}{2\sigma_x^2} - \frac{(y - y_0)^2}{2\sigma_y^2}\right) \tag{34}$$

where (x_0, y_0) is the center of the pollutant, and $(x_0, y_0) = (1000\,\text{m}, 1700\text{m})$ is set in this test; σ_x and σ_y are the variance in the x and y direction, respectively, and $\sigma_x = \sigma_y = 100$ are assigned here. The initial value of the concentration is from 0 mg/L to 1 mg/L, which is assigned for all the numerical experiments in Section 4 except for the anisotropic case.

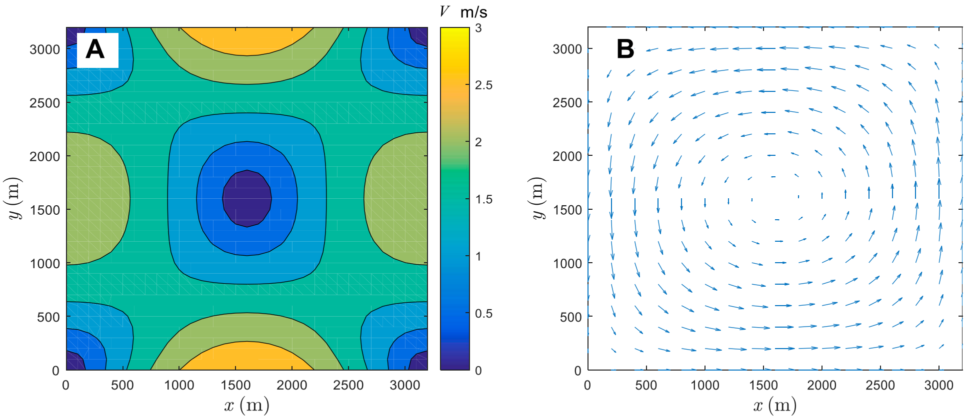

FIGURE 3
The absolute velocity **(A)** and velocity vector **(B)** for the large deformation flow.

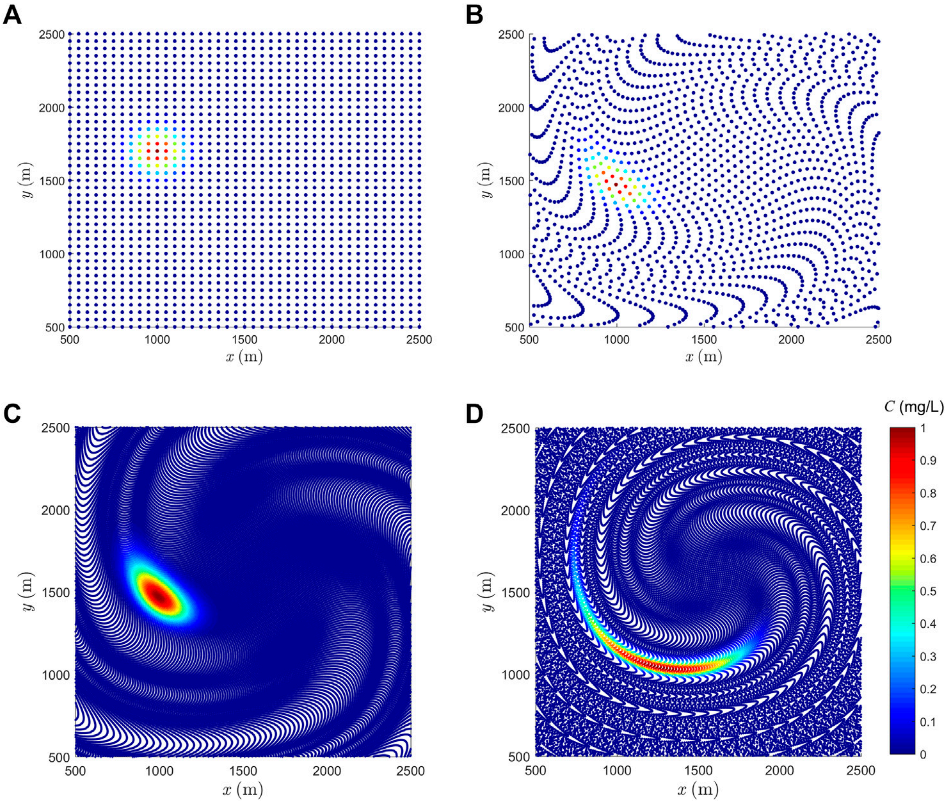

FIGURE 4
Pure advection simulation by SPH: concentration and particle distribution. **(A)** t = 0 s and 4096 particles, **(B)** t = 3400 s (roughly one rotation) and 4096 particles, **(C)** t = 3400 s and 102400 particles and **(D)** t = 6800 s and 102400 particles.

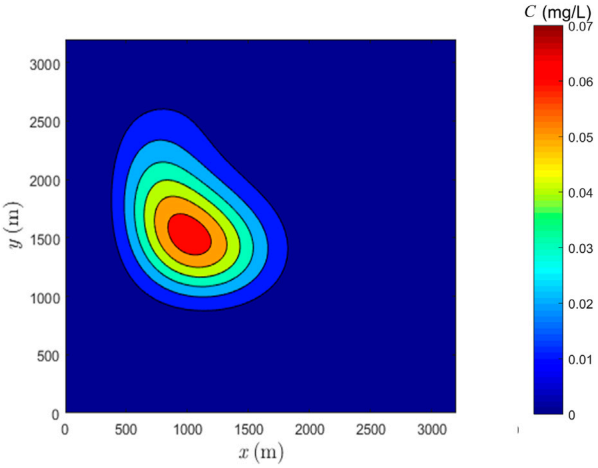

FIGURE 5
Reference solution obtained by MTVDLF-Superbee with grid number 400 by 400 and dt = 0.005 s.

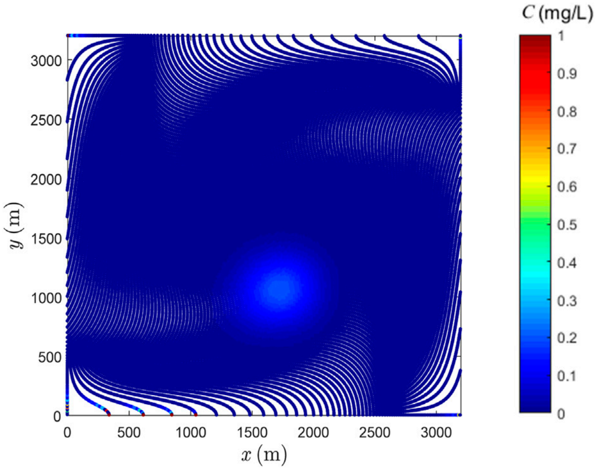

FIGURE 6
Simulation result of advection-diffusion by SPH without PSTs.

4.1 Advection-diffusion simulation without PSTs

The pure advection case is simulated to verify the existence of cavity problem even a large number of particles are used. First, particles with a uniform spacing of 50 m (4096 particles) are distributed in the domain (see Figure 4A). The time step is 2.5 s and the simulation time is 3400 s, which approximately equals to the time needed for one rotation. As shown in Figure 4B, after one rotation, the particle distribution becomes highly irregular and some cavities appear, which is also shown in (Liu et al., 2020). Note that in the following figures, the color bar means pollutant concentration unless otherwise mentioned.

A uniform spacing of 10 m (102,400 particles) is then applied. The results after one rotation are presented in Figure 4C, where the cavity problem is still evident. After two rotations, the particle cavity phenomenon gets worse (see Figure 4D). They indicate that increasing particle number does not help to remove the cavity problem and higher computational cost will be caused.

For the advection-diffusion process in the given flow field, there is no exact solution available. To provide a good reference solution for comparison and evaluation, MTVDLF-Superbee method is implemented. In this case, the initial concentration distribution is smooth and no steep front forms within the simulation time, for which MTVDLF-Superbee can achieve second-order accuracy (Wang and Hutter, 2001). As the diffusion coefficient is assigned to be 20 m^2/s, this is a diffusion dominated case, for which MTVDLF-Superbee gives good reference solutions (Liu et al., 2020). The grid number is 400 by 400 and the time step is 0.005 s. The reference solution after one rotation is shown in Figure 5. On a laptop machine (Core i7-5600U, 2.6 GHz), the CPU time for MTVDLF-Superbee is roughly 6 h.

In the SPH-based model, 160 by 160 particles are used to test its performance without PSTs. The smoothing length of $h = 1.5dx$ is set for the purpose of sufficient neighboring particles and the time step is 1 s. As the cubic spline kernel is used, the searching radius is $2h$. The simulated result after 1000 s is shown in Figure 6, where incorrect concentrations have appeared at the boundary region. The solution at one rotation cannot be obtained due to the breakdown of the calculation caused by particle cavities. Therefore, to obtain correct results for substance transport in natural flows where both longitudinal dispersion and turbulent diffusion play a vital role, PST-like measures have to be taken.

4.2 Advection-diffusion simulation with PSTs

As it is not necessary to arrange a large number of particles in view of applying PSTs, the particle number is set to be 64 by 64 for all the tests in this section. For SPH combined with PSTs, the CPU time is about half an hour. In general, Lind's PST needs one-third more time than Xu's PST because it is based on SPH approximations, whereas Xu's PST is just based on a set of algebraic expressions.

To quantitatively evaluate the SPH results, the L_2 norm error is taken here to measure the discrepancy between the solution of SPH with PST and the one of MTVDLF-Superbee with finer grids.

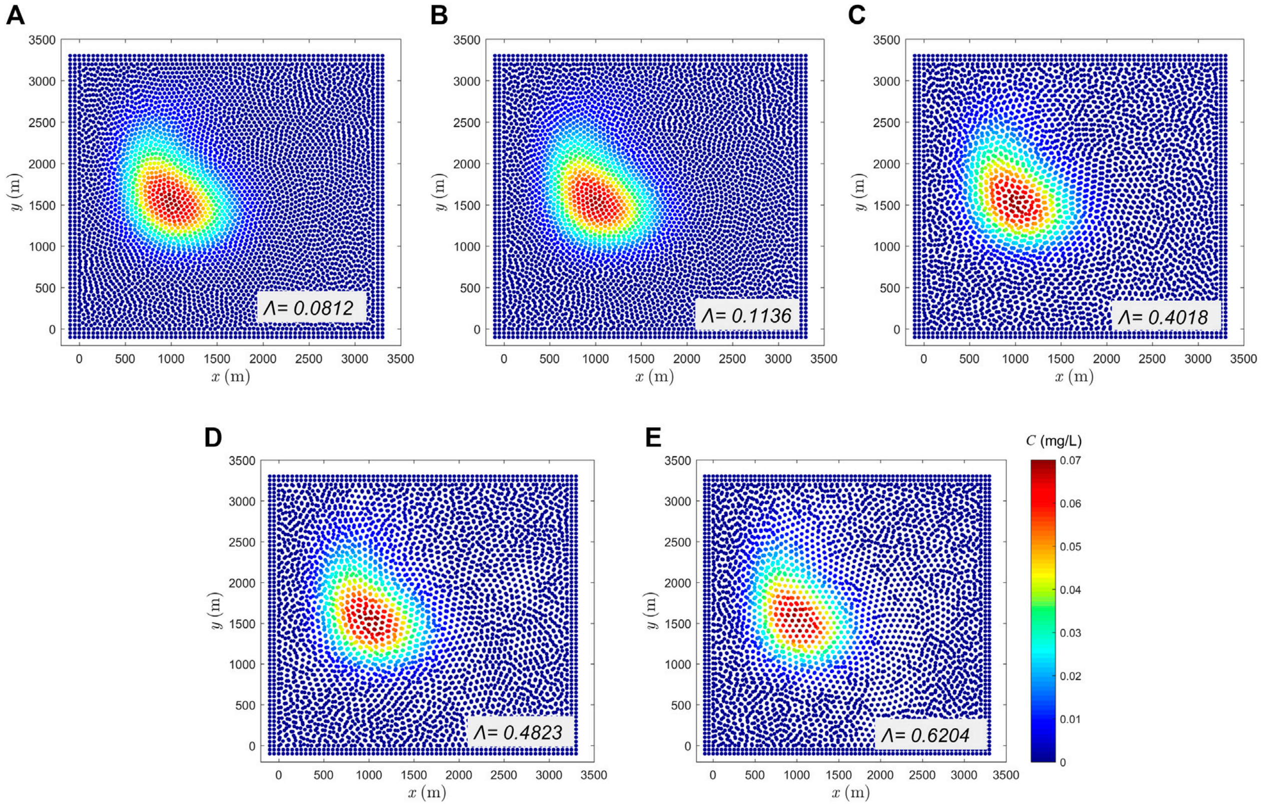

FIGURE 7
Simulation results for one rotation by Lind's PST with cubic spline kernel without RF in different smoothing length. **(A)** $h = 1.1dx$, **(B)** $h = 1.2dx$, **(C)** $h = 1.33dx$, **(D)** $h = 1.4dx$ and **(E)** $h = 1.5dx$.

$$L_2 = \frac{\left[\sum_{a=1}^{N} \left(C_a^e - C_a^n\right)^2\right]^{1/2}}{\left[\sum_{a=1}^{N} \left(C_a^e\right)^2\right]^{1/2}} \tag{35}$$

where c_a^e is the exact solution and c_a^n is the numerical solution; N is the total number of particles.

Moreover, the irregularity index Λ presented in Section 3.5 is used to judge which method can achieve more regular particle distribution. For a numerical solution, if both the value of the L_2 norm error and the index Λ are the minimum among those for comparison, it can be judged as the best one. However, they are used herein mainly to evaluate the performance of PSTs and to optimize the involved parameters.

4.2.1 Factors affecting the stability of PSTs

1) Paring instability affected by kernel types in Lind's PST

In Lind's PST, the paring instability often occurs. To avoid it, the smoothing length h should be chosen carefully, unless the RF term is added. Without adding RF, the SPH results with Lind's PST are compared in Figure 7 for cases with different smoothing lengths. Note that the different smoothing length set here is used only in PSTs, while $h = 1.33dx$ is adopted for the discretization of the diffusion terms. The pairing instability phenomenon gets more evident with the increase of h. On the other hand, when the RF is added, no matter what h is chosen, no pairing instability appears;see Figure 8. It means that adding RF can avoid pairing instability.

As mentioned in Section 3.4, the misleading portion of the kernel gradient should be narrow to alleviate the paring instability, from which aspect the Wendland type kernel (see Figure 9) is termed to be a better option (Dehnen and Aly, 2012; Alvarado-Rodríguez et al., 2019). Since the paring instability only occurs in PST and the simulation of diffusion is free of it, only the cubic spline kernel is replaced by Wendland. For ease of comparison, the same smoothing length with that in Figure 8E is used. In the solution obtained with the Wendland kernel without RF, paring instability has been completely resolved; see Figure 10. The value of Λ is 0.0622 for Figure 8E and it is 0.0702 for Figure 9, which means that the performance of the Wendland kernel without

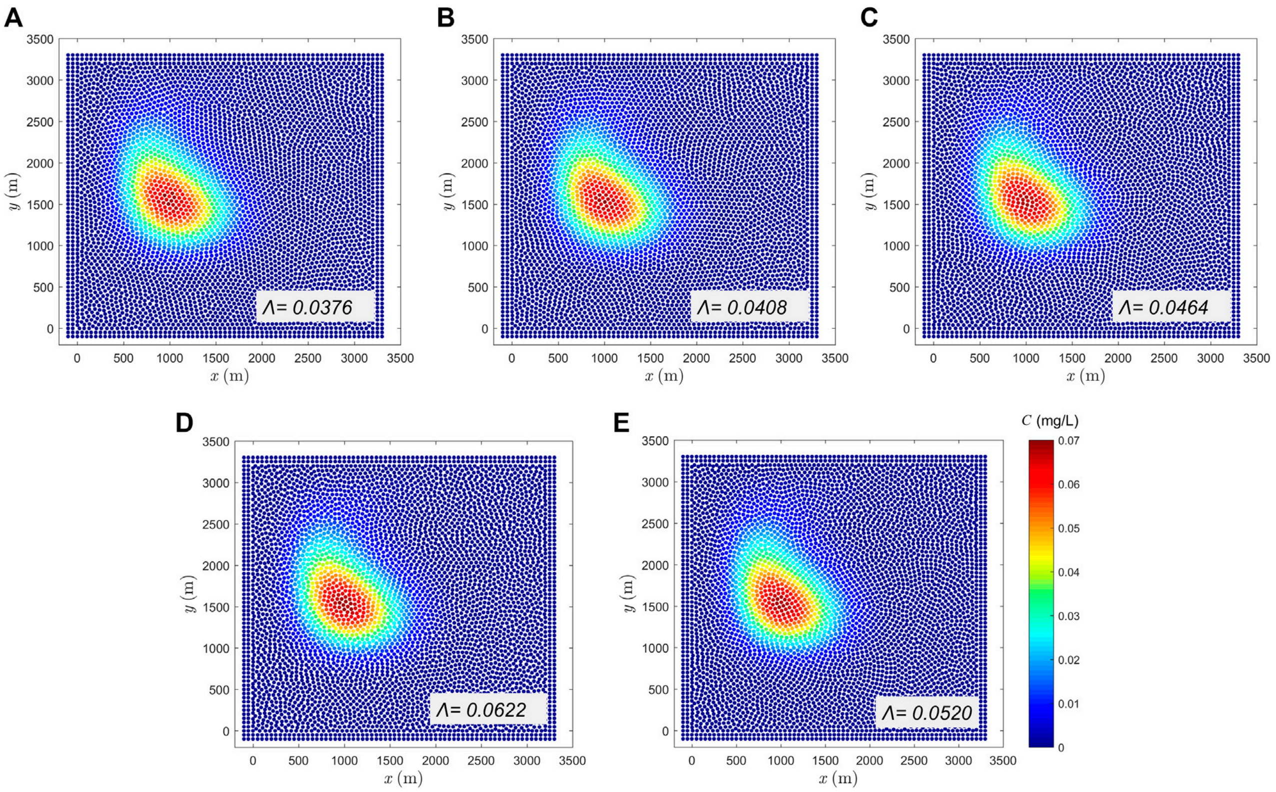

FIGURE 8
Simulation results for one rotation by Lind's PST with cubic spline kernel with RF in different smoothing length. **(A)** $h = 1.1dx$, **(B)** $h = 1.2dx$, **(C)** $h = 1.33dx$, **(D)** $h = 1.4dx$ and **(E)** $h = 1.5dx$.

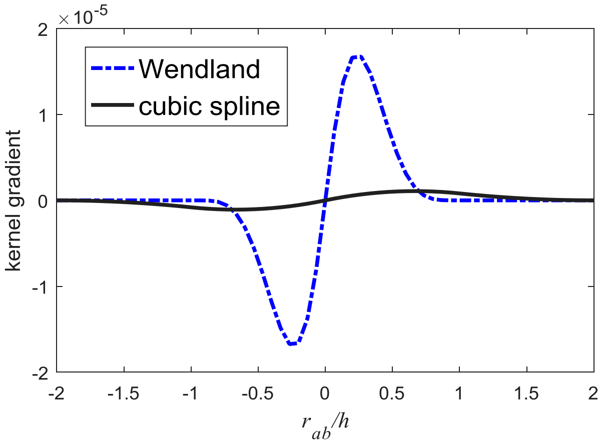

FIGURE 9
Gradient comparison between Wendland kernel and cubic spline kernel.

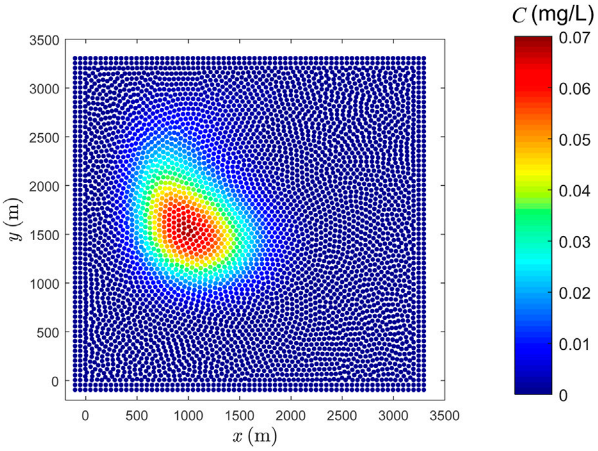

FIGURE 10
Simulation results for one rotation by Lind's PST with Wendland kernel without RF.

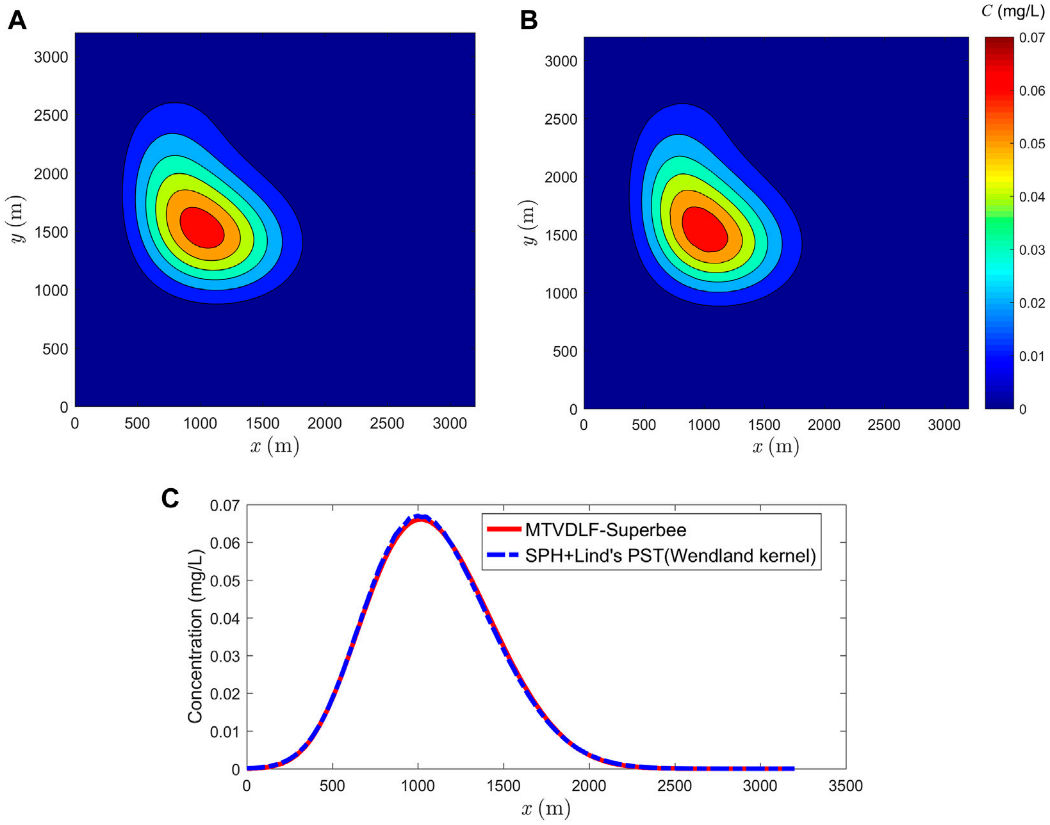

FIGURE 11
Comparison between reference solution and the result obtained by SPH combined with Lind's PST. **(A)** Reference solution yielded by MTVDLF-Superbee, **(B)** solution of particle scheme (Lind's PST with Wendland kernel) and **(C)** concentrations along $y = 1500$ m.

RF is more or less the same as that of the cubic spline kernel with RF. Furthermore, when the Wendland kernel is used, R and n in Eq. 22 and in the modified methods can be removed, which simplifies the algorithm to some extent.

In Figure 11, the contours of simulated result by Lind's PST with Wendland kernel are compared with the reference solution. For clearness, the concentration profiles along $y = 1500$ m are also compared in Figure 11C. The good agreement demonstrates that the SPH combined with Lind's PST can perfectly simulate the advection-diffusion process in flows with large deformation.

In summary, when the cubic spline kernel is adopted, paring instability appears, unless small smoothing length is applied or the RF term is added. While when the Wendland kernel is employed, there is no need to add RF to avoid paring instability, even a large smoothing length is used.

2) Parameters controlling the shifting amplitude

In Lind's approach, the shifting magnitude depends on the value of L_p whose range can be determined by the von Neumann stability analysis as presented in Section 3.3, and the recommended value is 0.5 (Lind et al., 2012). In Table 1, with changing L_p, the variation of the indicator Λ for particle inconsistency and the L_2 norm error are listed. The smoothing length for PST is taken as $h = 1.1dx$, $1.33dx$ and $1.5dx$, respectively. In this section, h is also $1.33dx$ for the discretization of diffusion terms. When $h = 1.1dx$ and $L_p \leq 0.7$, its effect on particle disorder and numerical accuracy is not significant, while when $L_p > 0.7$, the numerical accuracy decreases rapidly and the degree of particle disorder largely increases. Whereas, the limit becomes $L_p = 1.3$ when $h = 1.33dx$ and $L_p = 1.8$ when $h = 1.5dx$. Based on the results shown in Table 1, it can be concluded that the reasonable range of L_p is related to the smoothing length h, and it expands as h becomes larger.

To visually show whether the results are stable or not, several simulations with different L_p and h are exhibited in Figure 12. When $L_p = 1$, the concentration distribution has become distorted for $h = 1.1dx$, but it is still satisfactory for $h = 1.33dx$.

TABLE 1 Influence of L_p on particle inconsistency and numerical error in Lind's PST.

$h = 1.1dx$	L_p	0.3	0.4	0.5	0.6	0.7	0.8	0.9	1.0
	Λ	0.0419	0.0396	0.0376	0.0326	0.0363	0.0718	0.0867	0.0920
	L_2(%)	2.88	2.90	2.95	2.82	2.88	22.34	36.35	43.62
$h = 1.33dx$	L_p	0.9	1	1.1	1.2	1.3	1.4	1.5	1.6
	Λ	0.0379	0.0370	0.0344	0.0341	0.0380	0.0777	0.1033	0.1126
	L_2(%)	2.82	2.85	2.71	2.71	2.67	22.09	46.05	61.53
$h = 1.5dx$	L_p	1.5	1.6	1.7	1.8	1.9	2.0	2.1	2.2
	Λ	0.0507	0.0521	0.0515	0.0526	0.0623	0.0818	0.1184	0.1283
	L_2(%)	2.89	2.86	2.87	2.96	3.20	14.38	51.08	

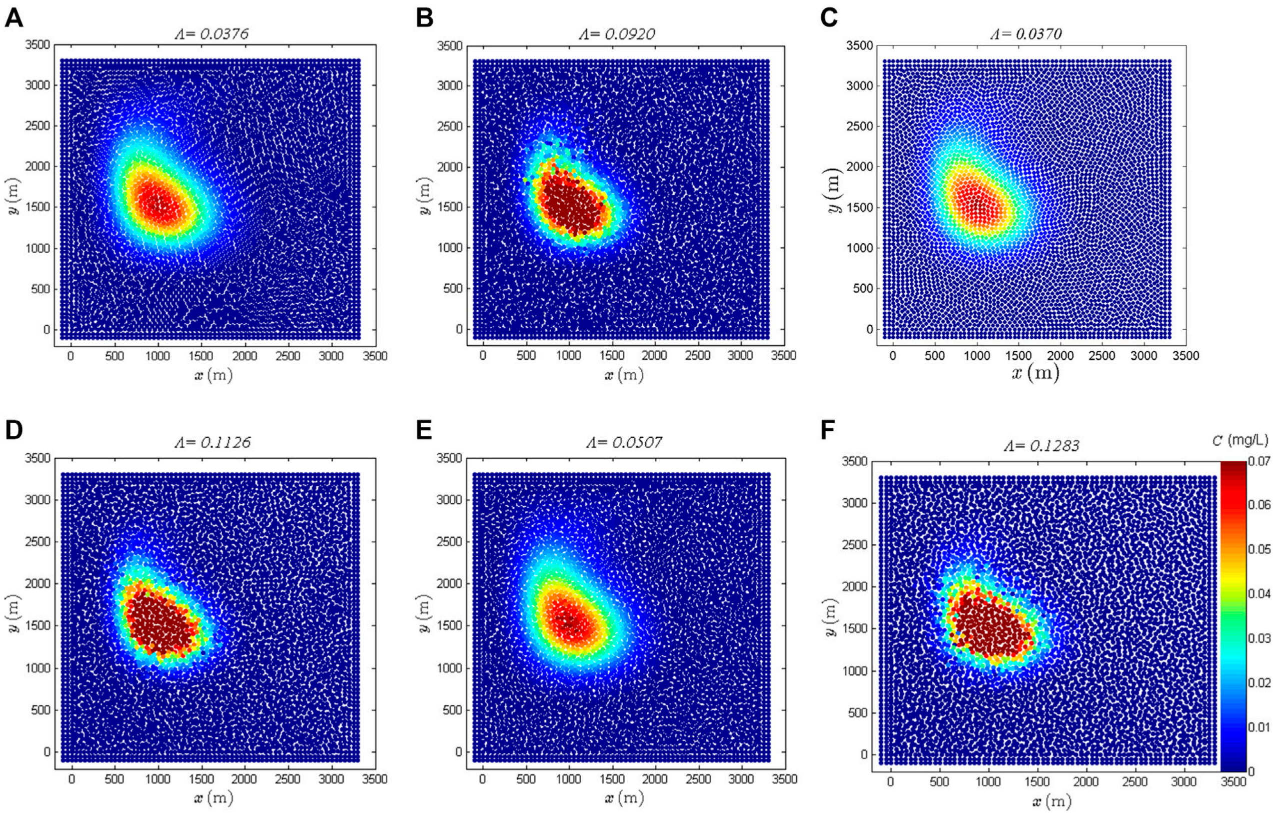

FIGURE 12
Simulation results of SPH combined with Lind's PST with RF in different smoothing length and different L_p. **(A)** $h = 1.1dx$ and $L_p = 0.5$, **(B)** $h = 1.1dx$ and $L_p = 1$, **(C)** $h = 1.33dx$ and $L_p = 1$, **(D)** $h = 1.33dx$ and $L_p = 1.6$, **(E)** $h = 1.5dx$ and $L_p = 1.6$ and **(F)** $h = 1.5dx$ and $L_p = 2.2$.

In Xu's approach, the shifting magnitude relies on parameter A, the range of which is suggested to be 0.0Γ0.1 and 0.04 is considered to be the best choice (Xu et al., 2009). This is tested for the concerned case. The variation of the indicator Λ for particle inconsistency and the L_2 norm error are listed in Table 2, which shows that no matter $h = 1.1dx$ or $h = 1.33dx$ is taken, the results are nearly equivalent. That is to say, A is independent of the smoothing length h. The indicator Λ tends to be smaller when A gets bigger and the L_2 norm error in all the cases shows subtle distinction. It demonstrates that the influence of A is not so significant as that of L_p in Lind' PST.

TABLE 2 Influence of *A* on particle distribution and numerical error in Xu's PST.

A		0.01	0.02	0.03	0.04	0.05	0.06	0.07	0.08	0.09	0.1
$h = 1.1dx$	Λ	0.1178	0.0975	0.0875	0.0838	0.0771	0.0765	0.0735	0.0741	0.0715	0.0702
	L_2(%)	3.76	3.76	3.62	3.43	3.33	3.13	3.05	3.23	3.34	2.97
$h = 1.33dx$	Λ	0.1124	0.0927	0.0866	0.0835	0.0805	0.0773	0.0774	0.0755	0.0767	0.0749
	L_2(%)	3.81	3.58	3.51	3.48	3.49	3.43	3.39	3.34	3.22	3.15

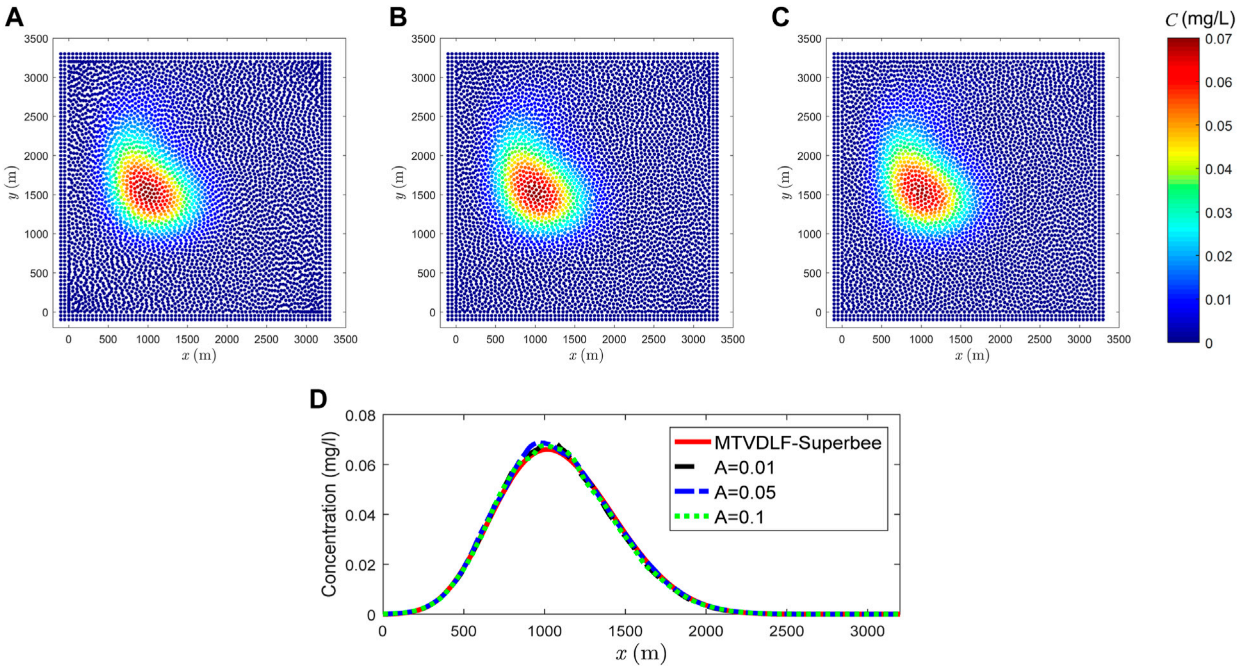

FIGURE 13
Simulation results by Xu's PST with different A. **(A)** *A* = 0.01, **(B)** *A* = 0.05, **(C)** *A* = 0.1 and **(D)** concentration profiles along y = 1500 m.

TABLE 3 Comparison of numerical results of different PSTs.

PST	Xu	Khorasanizade & sousa	Lind with RF		Skillen		Huang
	$A = 0.4$	$A = 0.4$	$L_p = 1.2$	$S_p = 1$	$S_p = 6$	$S_p = 10$	
Λ	0.0835	0.0940	0.0341	0.0786	0.0461	0.0407	0.0742
L_2 (%)	3.48	3.73	2.71	3.30	2.84	2.80	3.20

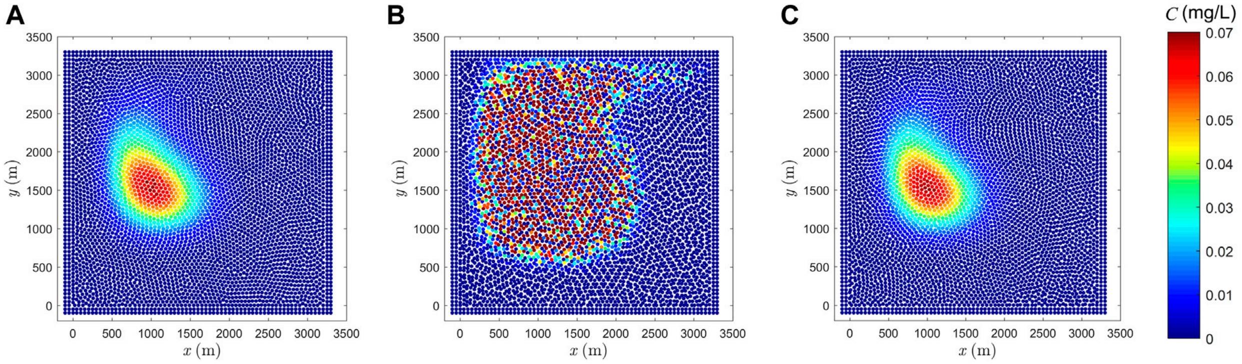

FIGURE 14
Simulation results by SPH with PST using **(A)** mixed particle position n_p and n_a and L_p = 0.4, **(B)** advected particle position n_a and L_p = 0.4, and **(C)** advected particle position n_a and L_p = 0.3.

The concentration for three typical values of A are shown in Figure 13. For all the cases, the particle distribution is reasonable. In Figure 13D, the concentration profiles for different A along y = 1500 m are compared with that of MTVDLF-Superbee. The three curves with $A = 0.01$, $A = 0.05$ and $A = 0.1$ show almost the same difference from the solution of MTVDLF-Superbee, which is consistent with the error analysis shown in Table 3.

According to the numerical results, it is seen that the solution of Lind's PST within stable range is more accurate and has more regular particle distribution, while Xu's PST is more stable. For the key parameter L_p in Lind's PST with RF, its stable range is related to the smoothing length h, and it should be set according to the value of h, otherwise distorted results might be generated.

3) Encoding details for mixed particle position

The test in this section is only for Lind's PST. In the above simulations, the PST is executed after the advection process, which means that the particle position needs to be updated twice in each time step. For illustration, two symbols are used to distinct the particle positions in the current time step n. The one is n_a denoting the position after advection, and the other is n_p standing for the position after PST. If a particle has been shifted in the PST, its position n_p will be updated. When it is searched as a neighbor, its position n_p should be used to shift the position of the center one, while for a particle (belong to the neighboring particles) whose position has not been shifted, n_a will be used. All the results shown above are obtained by using the mixed particle positions of both n_p and n_a.

Note that the PST can be done by solely using n_a, but it is not as stable as that using the mixed n_p and n_a. This is illustrated below. In Figure 14, the results are obtained by using Lind's approach (with RF) with $h = 1.1dx$. In Figure 14A, n_p and n_a are mixed to carry out the PST with L_p = 0.4, while only n_a is used to shift particles in Figure 14B with L_p = 0.4. The latter result is seriously distorted and is not correct. Meanwhile, if L_p is set to be smaller than 0.4, acceptable results can still be obtained by using n_a only (see Figure 14C). As shown in Table 1, when mixed particle positions are used, good results are still obtained for L_p up to 0.7. This implies that by using mixed particle position in the PST, the stable range of L_p can be enlarged. In addition, when mixed particle positions are used, in theory, computation sequence of the particles decided by the identity number might affect the final solution, i.e., different ways of ordering particles could lead to different results in PST. It is because the particles are shifted one by one in a certain time step according to the identity number and the shifting distance depends on the position of their neighboring particles. However, numerical experiments showed that this effect can be neglected.

In terms of the results presented in this section, mixed particle positions after both advection and PST should be used, otherwise the solution will become less stable, if only particle positions after advection are used.

4.2.2 Results of modified PSTs

To better control the shifting distance, the local velocity of particles or the maximum advection distance is introduced in the modified PSTs, which stabilizes the original algorithms and deletes the upper limit for the shifting magnitude. In this section, the results of the modified PSTs presented in Section 3 are compared with those of the original ones. The smoothing length h for all the PSTs is still taken as $1.33dx$.

In the PST of Skillen et al. (2013) (modified Lind), numerical results with three different S_p are computed. In the PST of Huang et al. (2018), the computation directly follows Eq. 23. In the PST of Khorasanizade and Sousa (2016) (modified Xu), the same A is assigned as that in Xu's PST. Together with the solutions of the original PSTs of Xu and Lind, results of the modified ones are listed in Table 3. Although all the results are not better than those of

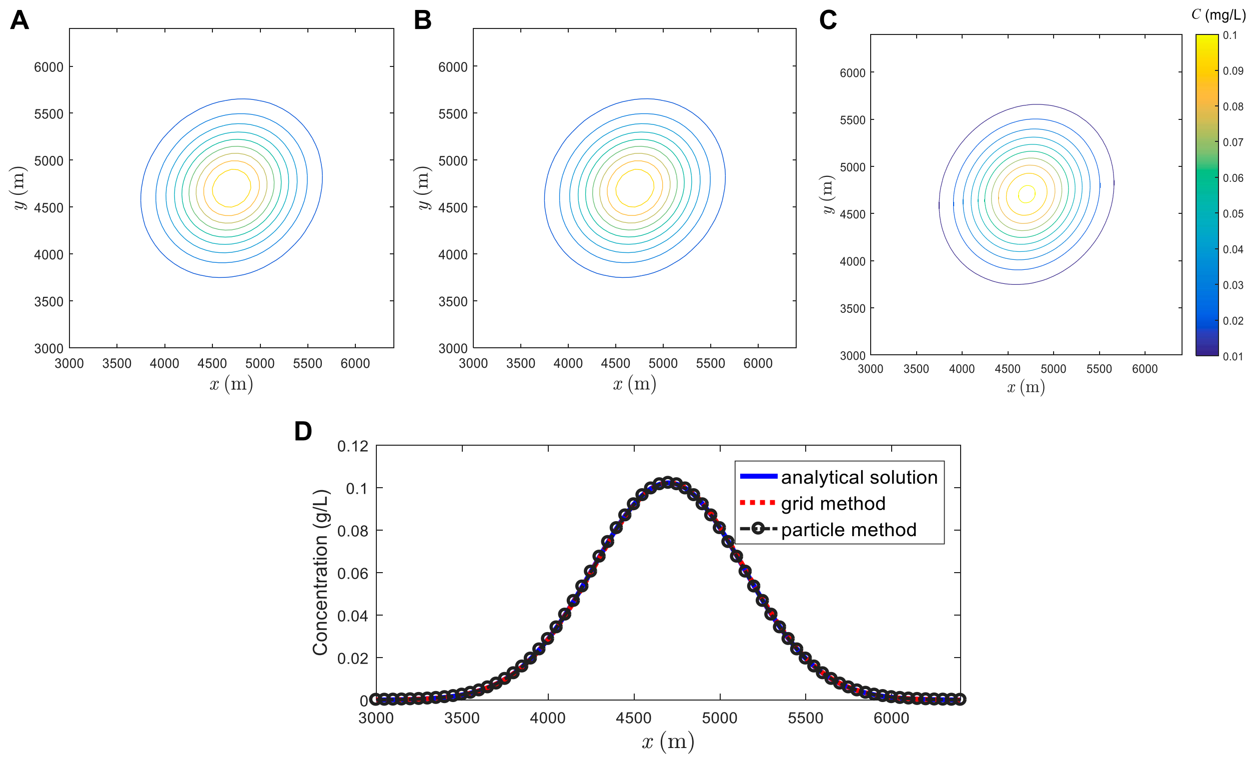

FIGURE 15
Results of the anisotropic diffusion under condition of $k_{11}k_{22} - k_{12}^2 < 0$. **(A)** Analytical solution, **(B)** particle solution, **(C)** grid solution and **(D)** comparison of concentration profiles along *y = 4700* m.

the original ones, they are all acceptable and the merits of the modified PSTs stated in Section 3 are still reasonable from the aspect of theoretical basis.

4.3 Simulation of anisotropic diffusion

Different from the isotropic diffusion cases studied above, the anisotropic diffusion process brings two mixed derivatives. In this section, the capability of the developed particle scheme to simulate the anisotropic diffusion process with different $\boldsymbol{K}$ is tested.

4.3.1 Transport in uniform flow

The ability of the SPH-based transport model (Eq. 12) to solve the anisotropic diffusion process is firstly verified by simulating an example with analytical solution.

The initial distribution of the concentration is also the Gaussian type and the exact solution is

$$C(x,y,t) = \frac{\Delta M}{2\pi\sqrt{4t^2\left(k_{11}k_{22} - k_{12}^2\right) + \varepsilon^4 + 2\varepsilon^2 t\left(k_{11} + k_{22}\right)}} \exp\left[\frac{-x^2\left(2tk_{22} + \varepsilon^2\right) - y^2\left(2tk_{11} + \varepsilon^2\right) + xy4tk_{12}}{8t^2\left(k_{11}k_{22} - k_{12}^2\right) + 2\varepsilon^4 + 4\varepsilon^2 t\left(k_{11} + k_{22}\right)}\right] \tag{36}$$

where ΔM is the total mass of the substance; ε is related to the distribution range of the concentration. The coefficient k_{21} disappears as it equals to k_{12}.

In this case, ΔM is set to be 125,000 g and ε is 400 m; the computational domain is $0 \le x,\ y \le 6400$ m; the central point of concentration is initially located at $(x_0,\ y_0) = (3200\,\text{m}, 3200\,\text{m})$; the flow velocity is $u = v = 1$m/s; and the simulation time is 1500 s. In MTVDLF, the grids are set to be 256 by 256 and dt is 0.025 , while in the particle method, the number of particles is 128 by 128 and dt is 25 s. Two groups of $\boldsymbol{K}$ are assigned to test the discrepancy between the particle model and the grid method. One is that the diffusivity of the mixed derivative terms is less than that of the remaining two terms, i.e., $k_{11}k_{22} - k_{12}^2 > 0$, and the other is $k_{11}k_{22} - k_{12}^2 < 0$. For the first group, $k_{11} = k_{22} = 12\text{m}^2/\text{s}$, $k_{12} = k_{21} = 8\,\text{m}^2/\text{s}$, and for the second one, $k_{11} = k_{22} = 8\,\text{m}^2/\text{s}$, $k_{12} = k_{21} = 12\,\text{m}^2/\text{s}$. The two occasions denoted the different degree of anisotropic. Since the mesh method is prone to produce unstable results, such as

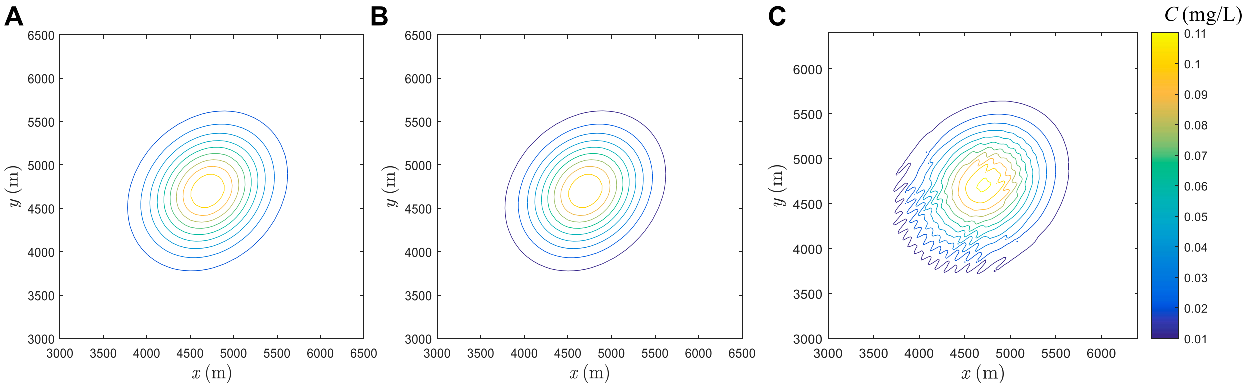

FIGURE 16
Results of the anisotropic diffusion under condition of $k_{11}k_{22} - k_{12}^2 > 0$. **(A)** Analytical solution, **(B)** particle solution, and **(C)** grid solution.

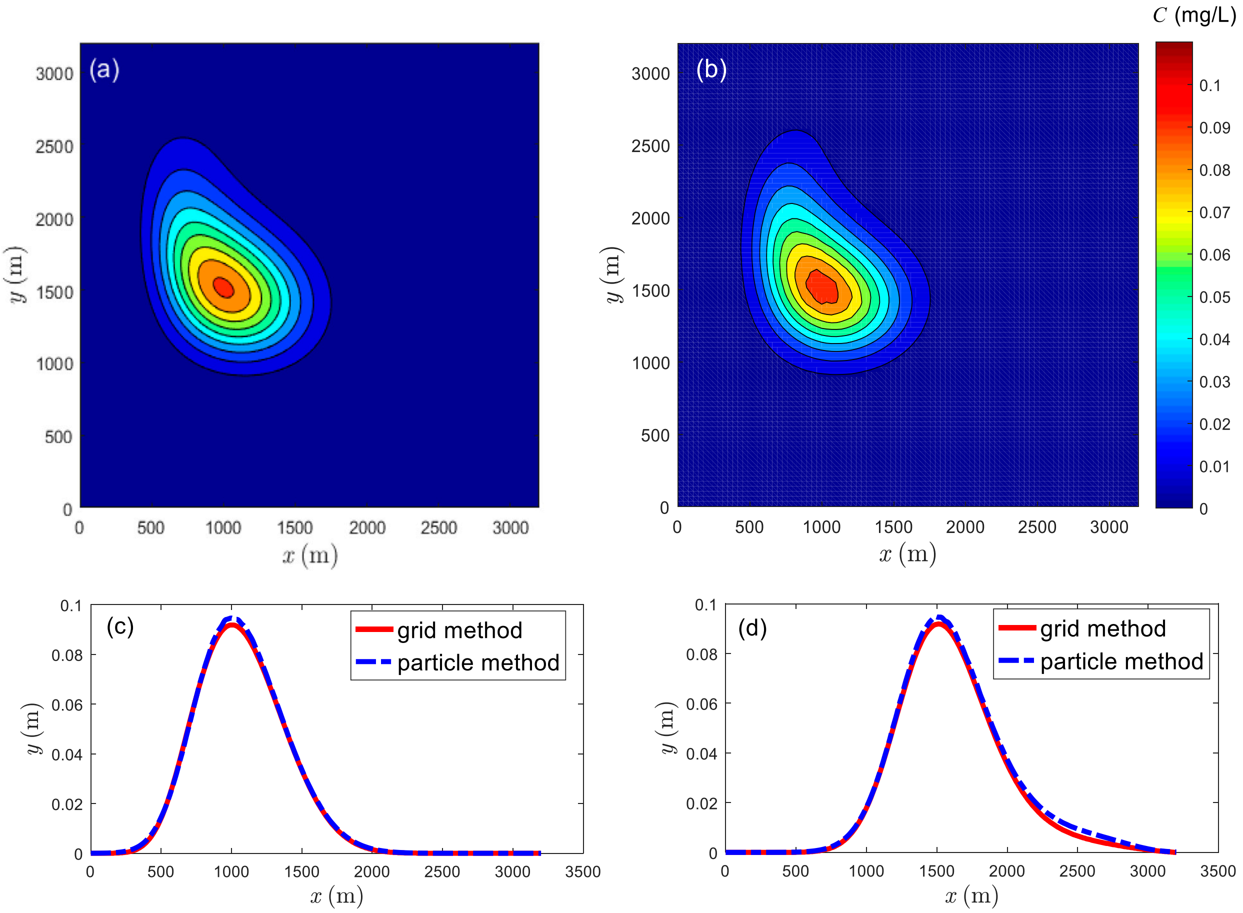

FIGURE 17
Simulations of anisotropic diffusion in flow with cavities by **(A)** grid method and **(B)** particle method and comparison of concentration profiles along **(C)** *y* = *1500* m and **(D)** *x* = *1000* m.

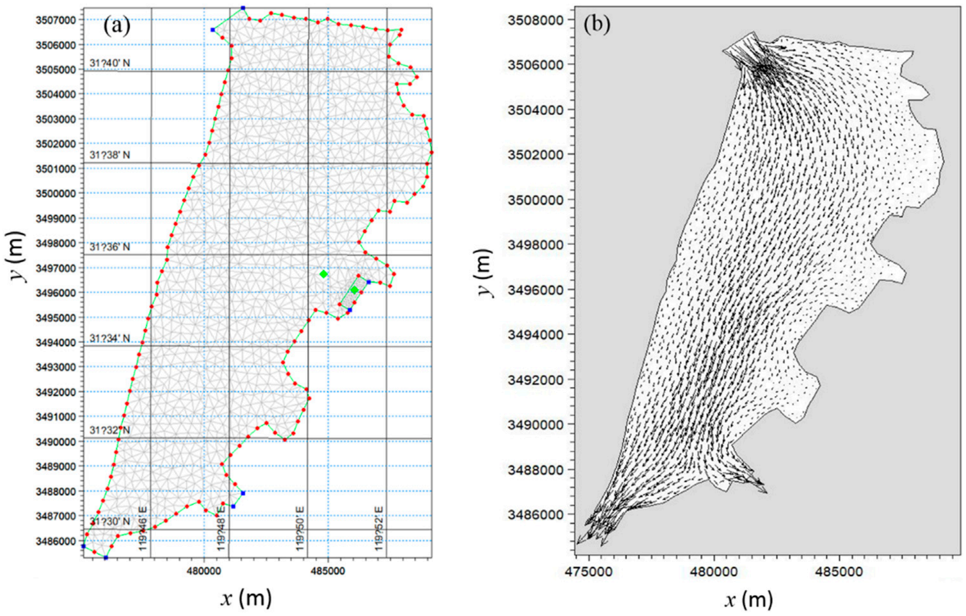

FIGURE 18
The geometry of Gehu Lake discretized with triangular meshes **(A)** and calculated flow velocity **(B)**.

negative concentration and artificial mixing (Nordbotten and Aavatsmark, 2005; Mlacnik and Durlofsky, 2006; Yuan and Sheng, 2008; Dehnen and Aly, 2012), especially when the degree of anisotropic diffusion is large, we want to verify whether the SPH-based model is susceptible to tensor $\boldsymbol{K}$.

The numerical results of the first group are shown in Figure 15, where the results of both the particle and grid methods agree well with the analytical solution. For more clearness, all of them are compared through the concentration profiles along y = 4700 m; see Figure 15D. With regard to the second group (see Figure 16), the result of the particle method still agrees well with the analytical solution (Figure 16B), while that of the grid method loses stability (Figure 16C).

4.3.2 Transport in cavity problem

The flow field is still that with large deformation given by Eq. 31 and the initial concentration distribution is identical with that shown in Figure 4A. For the reference solution obtained by the grid method, the parameters are consistent with those used in the isotropic case in Section 4.1. In SPH the particles are 64 by 64 and the time step is 2.5 s. The simulation time is 3400 s. The diffusion coefficients $k_{11} = 20\,\mathrm{m}^2/\mathrm{s}, k_{22} = 8\,\mathrm{m}^2/\mathrm{s}$, and $k_{12} = k_{21} = 10\,\mathrm{m}^2/\mathrm{s}$ are set, giving the condition of $k_{11}k_{22} - k_{12}^2 > 0$, under which the grid method gives accurate and stable solutions as shown in Section 4.3.1.

As shown in Figure 17, although a slight discrepancy still exists, good agreements between particle solution and reference solution are observed. That is, the developed particle model can also give reliable solutions for the anisotropic diffusion in the cavity problem.

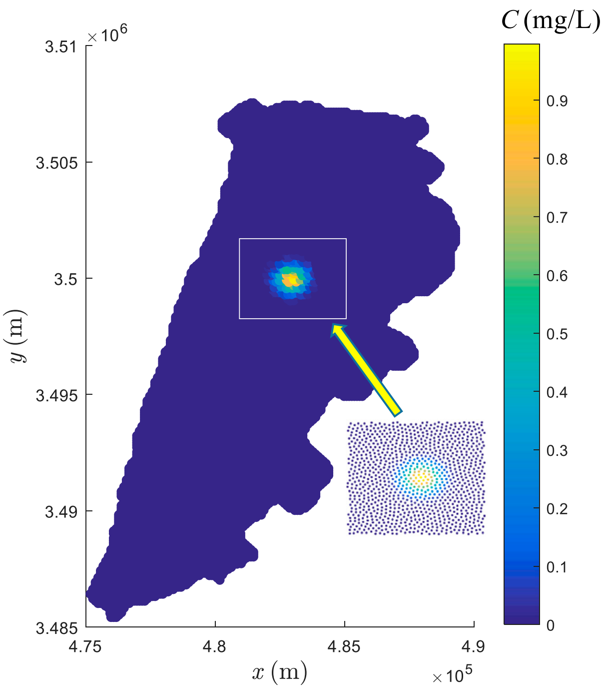

FIGURE 19
The initial distribution of particles and pollutant.

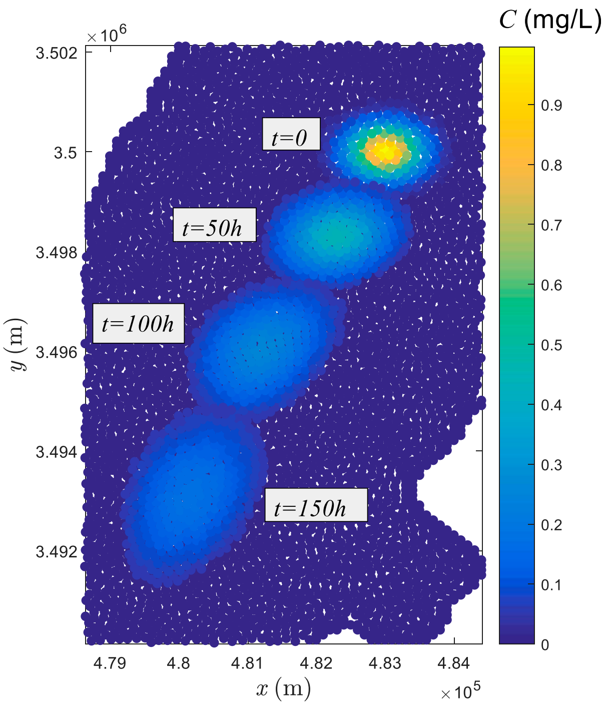

FIGURE 20
The concentration distribution at different time.

5 Case study

To show the capacity of the developed model for real problems, an engineering case study is presented in this section. The Gehu Lake is an artificial lake located in Jiangsu Province, China, the area of which is about 164 square kilometers. Its geometry is shown in Figure 18. To meet the ecological and landscape needs, the renewal time of the water body has to be determined. As the maximum water depth is only 4 m, the horizontal scale is much larger than the vertical scale. Meanwhile, the calculation of water renewal time involves the convection and diffusion of substances in the water. Therefore, this case study can be simplified into a problem of substance transport in 2D space. With the given shoreline, topography, outlet water level and inlet flow velocity, the flow field is firstly calculated by solving the shallow water equation on triangular meshes (see Figure 18A). As seen from the calculated velocity shown in Figure 18B, the flow is governed by the inlet and the two outlets.

Different from the idealized case with given analytical velocity field (e.g., Figure 3), the velocity distribution in this real case is known only on the nodes of the triangular meshes (see Figure 18A). To interpolate the velocity of particles moving through the grids, the symmetric smoothed particle hydrodynamics (SSPH) method (Batra and Zhang, 2008) is used, which is third order accurate when up to third-order derivatives are remained in the Taylor's expansion. Since the computational domain is irregular, the triangular mesh is adopted for initial particle distribution. In this case, as the transportation of pollutants along the central axis of this lake is the main concern, the zero concentration for the dummy particles is applied. For the PST, sufficient dummy particles are needed to prevent fluid particles clustering near the boundary or escaping from the computational domain.

To determine how substances transport in this lake and how long they cross the lake, the Gaussian type pollutant given by Eq. 34 is supposed to be released into the water instantaneously at the upstream (See Figure 19), for which the maximum concentration value is 1 mg/L. Initially 9000 fluid particles are set at the triangular mesh point with a spacing of 100 m. An enlarged view of the area around the pollutants shows that initially the particles are more or less uniformly distributed. The time step can be assigned with a large value, up to 3000 s, which still satisfies the stability condition due to the slow velocity. A constant diffusion coefficient of $k = 10\,\mathrm{m}^2/\mathrm{s}$ is applied. As shown in Figure 20, when the simulation starts, the pollutant moves downstream gradually and is still along the central axis. As a result of diffusion, the area of the pollutant goes broader and the concentration is diluted. Since Lind' PST is added, the particles remain uniform all the time. When the pollutant is close to the first outlet, it takes roughly 150 h, and it takes roughly 10 days for all the pollutants flowing out of the lake. In this work, we only discussed the transportation along the central axis, for which the pollutant can be expelled from the lake and its impact on the water body is diminished because of diffusion. If they were released near the boundary, how long it would take to get out of the lake would be a challenging problem.

6 Conclusion

The SPH method under Lagrangian frame has advantages in solving the advection-diffusion problems. It can well handle the advection-dominated transport problems with discontinuity which are tough for mesh-based Eulerian methods, and has characters of high efficiency and precision (Liu et al., 2020). However, when complicated velocity field is encountered, the particle distribution will become disordered and even forms particle cavities. On this condition, the simulation of the diffusion process easily fails because the insufficient or asymmetry of neighboring particles leads to inaccuracy of kernel approximation. To settle this problem, the particle shifting techniques (PSTs) are introduced to eliminate the particle cavities and make the Lagrangian particle transport model run accurately and smoothly. It can well resolve both the isotropic and anisotropic diffusion process in large deformation flow. Reasonable results are obtained when it is applied in practical flow. The stability, efficiency and accuracy of different PSTs are compared. Lind's approach gives more regular particle distribution and hence higher accuracy, while Xu's PST is more stable and its efficiency is higher. When Lind's approach is adopted, to prevent paring instability, the Wendland kernel is a better choice than the cubic spline, since the RF term is not needed. In addition, to carry out the PST for a given particle, the updated positions of its neighbors after both advection and PST should be applied, otherwise instability might be induced if only the advected positions are used. Comparing with the original PSTs of Xu and Lind, the modified ones do not show noticeable improvements, at least for the cases studied in this work.

The flow field in the present work, either steady in the real case or straightly given by the streamline function, is relatively simple. How the developed scheme performs in the more practical problems, e.g., in the complicated and time-variant ocean flow field (Luo et al., 2021), should be further explored. The involvement of irregular boundaries could be more intractable, which has not been fully discussed in this work. The PST introduced intents to make the particle method available in the transportation simulation of real flows. We will focus on promoting the capability of the proposed numerical model in solving the practical problems in future.

Data availability statement

The original contributions presented in the study are included in the article/Supplementary material, further inquiries can be directed to the corresponding author.

Author contributions

WL: methodology, investigation, simulation, visualization, validation, analysis, and writing original draft. QH: supervision, conceptualization, methodology, analysis, investigation and writing, review and editing. XL: conceptualization, supervision, review and editing. JL: supervision, review and editing. JD: supervision, review and editing.

Funding

This study was supported by the National Key Research and Development Program of China (No. 2020YFC1807905), National Natural Science Foundation of China (No. 52079090) and Basic Research Program of Qinghai Province (No. 2022-ZJ-704).

Conflict of interest

The authors declare that the research was conducted in the absence of any commercial or financial relationships that could be construed as a potential conflict of interest.

Publisher's note

References

Alhumaizi, K. (2004). Comparison of finite difference methods for the numerical simulation of reacting flow. *Comput. Chem. Eng.* 28, 1759–1769. doi:10.1016/j.compchemeng.2004.02.032

Alvarado-Rodríguez, C. E., Sigalotti, L. D. G., and Klapp, J. (2019). Anisotropic dispersion with a consistent smoothed particle hydrodynamics scheme. *Adv. Water Resour.* 131, 103374. doi:10.1016/j.advwatres.2019.07.004

Antuono, M., Bouscasse, B., Colagrossi, A., and Marrone, S. (2014). A measure of spatial disorder in particle methods. *Comput. Phys. Commun.* 185, 2609–2621. doi:10.1016/j.cpc.2014.06.008

Aristodemo, F., Federico, I., Veltri, P., and Panizzo, A. (2010). Two-phase SPH modelling of advective diffusion processes. *Environ. Fluid Mech.* 10, 451–470. doi:10.1007/s10652-010-9166-z

Bai, B., Rao, D. Y., Xu, T., and Chen, P. P. (2018). SPH-FDM boundary for the analysis of thermal process in homogeneous media with a discontinuous interface. *Int. J. Heat. Mass Transf.* 117, 517–526. doi:10.1016/j.ijheatmasstransfer.2017.10.004

Batra, R. C., and Zhang, G. M. (2008). SSPH basis functions for meshless methods, and comparison of solutions with strong and weak formulations. *Comput. Mech.* 41, 527–545. doi:10.1007/s00466-007-0209-3

Bonet, J., and Lok, T. S. L. (1999). Variational and momentum preservation aspects of smooth particle hydrodynamic formulations. *Comput. Methods Appl. Mech. Eng.* 180, 97–115. doi:10.1016/s0045-7825(99)00051-1

Chang, Y. S., and Chang, T. J. (2017). SPH simulations of solute transport in flows with steep velocity and concentration gradients. *Water* 9, 132. doi:10.3390/w9020132

Chaniotis, A. K., Poulikakos, D., and Koumoutsakos, P. (2002). Remeshed smoothed particle hydrodynamics for the simulation of viscous and heat conducting flows. *J. Comput. Phys.* 182, 67–90. doi:10.1006/jcph.2002.7152

Chen, J. K., and Beraun, J. E. (2000). A generalized smoothed particle hydrodynamics method for nonlinear dynamic problems. *Comput. Methods Appl. Mech. Eng.* 190, 225–239. doi:10.1016/s0045-7825(99)00422-3

Chen, J. K., Beraun, J. E., and Carney, T. C. (1999). A corrective smoothed particle method for boundary value problems in heat conduction. *Int. J. Numer. Methods Eng.* 46, 231–252. doi:10.1002/(sici)1097-0207(19990920)46:2<231::aid-nme672>3.0.co;2-k

Cleary, P. W., and Monaghan, J. J. (1999). Conduction modelling using smoothed particle hydrodynamics. *J. Comput. Phys.* 148, 227–264. doi:10.1006/jcph.1998.6118

Colagrossi, A., Bouscasse, B., Antuono, M., and Marrone, S. (2012). Particle packing algorithm for SPH schemes. *Comput. Phys. Commun.* 183, 1641–1653. doi:10.1016/j.cpc.2012.02.032

Dehnen, W., and Aly, H. (2012). Improving convergence in smoothed particle hydrodynamics simulations without pairing instability. *Mon. Not. R. Astron. Soc.* 425, 1068–1082. doi:10.1111/j.1365-2966.2012.21439.x

Devkota, B. H., and Imberger, J. (2009). Lagrangian modeling of advection-diffusion transport in open channel flow. *Water Resour. Res.* 45 (12406), 1–14. doi:10.1029/2009wr008364

Ewing, R. E., and Wang, H. (2001). A summary of numerical methods for time-dependent convection-dominated partial differential equations. *J. Comput. Appl. Math.* 128 (1-2), 423–445. doi:10.1016/S0377-0427(00)00522-7

Fatehi, R., and Manzari, M. T. (2011). Error estimation in smoothed particle hydrodynamics and a new scheme for second derivatives. *Comput. Math. Appl.* 61, 482–498. doi:10.1016/j.camwa.2010.11.028

Finlayson, B. A. (1992). *Numerical methods for problems with moving fronts*. Seattle: Ravenna Park Publishing.

Gu, S., Zheng, W., Wu, H., Chen, C., and Shao, S. (2022). DualSPHysics simulations of spillway hydraulics: A comparison between single- and two-phase modelling approaches. *J. Hydraulic Res.* 60, 835–852. doi:10.1080/00221686.2022.2064343

Huang, C., Lei, J. M., Liu, M. B., and Peng, X. Y. (2015). A kernel gradient free (KGF) SPH method. *Int. J. Numer. Meth. Fluids* 78, 691–707. doi:10.1002/fld.4037

Huang, C., Zhang, D. H., Shi, Y. X., Si, Y. L., and Huang, B. (2018). Coupled finite particle method with a modified particle shifting technology. *Int. J. Numer. Methods Eng.* 113, 179–207. doi:10.1002/nme.5608

Jeong, J. H., Jhon, M. S., Halow, J. S., and van Osdol, J. (2003). Smoothed particle hydrodynamics: Applications to heat conduction. *Comput. Phys. Commun.* 153, 71–84. doi:10.1016/s0010-4655(03)00155-3

Khorasanizade, S., and Sousa, J. M. M. (2016). An innovative open boundary treatment for incompressible SPH. *Int. J. Numer. Meth. Fluids* 80, 161–180. doi:10.1002/fld.4074

Kum, O., Hoover, W. G., and Hoover, C. G. (2003). Smooth-particle boundary conditions. *Phys. Rev. E* 68, 017701. doi:10.1103/physreve.68.017701

Larbe, G., and Price, D. J. (2012). Dusty gas with smoothed particle hydrodynamics–II. Implicit time stepping and astrophysical drag regimes. *Mon. Not. R. Astron. Soc.* 420 (3), 2365–2376. doi:10.1111/j.1365-2966.2011.20201.x

Lind, S. J., Xu, R., Stansby, P. K., and Rogers, B. D. (2012). Incompressible smoothed particle hydrodynamics for free-surface flows: A generalised diffusion-based algorithm for stability and validations for impulsive flows and propagating waves. *J. Comput. Phys.* 231, 1499–1523. doi:10.1016/j.jcp.2011.10.027

Liu, M. B., and Liu, G. R. (2006). Restoring particle consistency in smoothed particle hydrodynamics. *Appl. Numer. Math.* 56, 19–36. doi:10.1016/j.apnum.2005.02.012

Liu, W., Hou, Q., Lian, J. J., Zhang, A. M., and Dang, J. W. (2020). Coastal pollutant transport modeling using smoothed particle hydrodynamics with diffusive flux. *Adv. Water Resour.* 146, 103764. doi:10.1016/j.advwatres.2020.103764

Liu, W. K., and Jun, S. (1998). Multiple-scale reproducing kernel particle methods for large deformation problems. *Int. J. Numer. Methods Eng.* 41, 1339–1362. doi:10.1002/(sici)1097-0207(19980415)41:7<1339::aid-nme343>3.0.co;2-9

Liu, W. K., Jun, S., and Zhang, Y. (1995). Reproducing kernel particle methods. *Int. J. Numer. Meth. Fluids* 20, 1081–1106. doi:10.1002/fld.1650200824

Luo, M., Khayyer, A., and Lin, P. (2021). Particle methods in ocean and coastal engineering. *Appl. Ocean Res.* 114, 102734. doi:10.1016/j.apor.2021.102734

Mlacnik, M. J., and Durlofsky, L. J. (2006). Unstructured grid optimization for improved monotonicity of discrete solutions of elliptic equations with highly anisotropic coefficients. *J. Comput. Phys.* 216, 337–361. doi:10.1016/j.jcp.2005.12.007

Monaghan, J. J. (1988). An introduction to SPH. *Comput. Phys. Commun.* 48 (1), 89–96. doi:10.1016/0010-4655(88)90026-4

Monaghan, J. J., and Kocharyan, A. (1995). SPH simulation of multi-phase flow. *Comput. Phys. Commun.* 87 (1-2), 225–235. doi:10.1016/0010-4655(94)00174-z

Monaghan, J. J. (2005). Smoothed particle hydrodynamics. *Rep. Prog. Phys.* 68, 1703–1759. doi:10.1088/0034-4885/68/8/r01

Monaghan, J. J. (2012). Smoothed particle hydrodynamics and its diverse applications. *Annu. Rev. Fluid Mech.* 44, 323–346. doi:10.1146/annurev-fluid-120710-101220

Monaghan, J. J. (2000). SPH without a tensile instability. *J. Comput. Phys.* 159, 290–311. doi:10.1006/jcph.2000.6439

Nestor, R., Basa, M., Lastiwka, M., and Quinlan, N. (2009). Extension of the finite volume particle method to viscous flow. *J. Comput. Phys.* 228, 1733–1749. doi:10.1016/j.jcp.2008.11.003

Nestor, R., Basa, M., and Quinlan, N. (2008). Moving boundary problems in the finite volume particle method. in Proceedings of 3rd International SPHERIC Workshop, Lausanne, Switzerland, 4-6 June 2008. 109–114.

Nordbotten, J. M., and Aavatsmark, I. (2005). Monotonicity conditions for control volume methods on uniform parallelogram grids in homogeneous media. *Comput. Geosci.* 9 (1), 61–72. doi:10.1007/s10596-005-5665-2

Pudykiewicz, J., and Staniforth, A. (1984). Some properties and comparative performance of the semi-Lagrangian method of Robert in the solution of the advection-diffusion equation. *Atmosphere-Ocean* 22 (3), 283–308. doi:10.1080/07055900.1984.9649200

Ryan, E. M., Tartakovsky, A. M., and Amon, C. (2010). A novel method for modeling Neumann and Robin boundary conditions in smoothed particle hydrodynamics. *Comput. Phys. Commun.* 181, 2008–2023. doi:10.1016/j.cpc.2010.08.022

Shahriari, S., Hassan, I. G., and Kadem, L. (2013). Modeling unsteady flow characteristics using smoothed particle hydrodynamics. *Appl. Math. Model.* 37 (3), 1431–1450. doi:10.1016/j.apm.2012.04.017

Shao, J. R., Li, H. Q., Liu, G. R., and Liu, M. B. (2012). An improved SPH method for modeling liquid sloshing dynamics. *Comput. Struct.* 100-101, 18–26. doi:10.1016/j.compstruc.2012.02.005

Shao, S. D., and Lo, E. Y. M. (2003). Incompressible SPH method for simulating Newtonian and non-Newtonian flows with a free surface. *Adv. Water Resour.* 26, 787–800. doi:10.1016/s0309-1708(03)00030-7

Skillen, A., Lind, S., Stansby, P. K., and Rogers, B. D. (2013). Incompressible smoothed particle hydrodynamics (SPH) with reduced temporal noise and generalised Fickian smoothing applied to body–water slam and efficient wave–body interaction. *Comput. Methods Appl. Mech. Eng.* 265, 163–173. doi:10.1016/j.cma.2013.05.017

Tsuruta, N., Khayyer, A., and Gotoh, H. (2013). A short note on dynamic stabilization of moving particle semi-implicit Method. *Comput. Fluids* 82, 158–164. doi:10.1016/j.compfluid.2013.05.001

Violeau, D. (2012). *Fluid mechanics and the SPH method: The theory and applications*. Oxford: Oxford University Press.

Wang, J. Q., Hu, W., Zhang, X. B., and Pan, W. X. (2019). Modeling heat transfer subject to inhomogeneous Neumann boundary conditions by smoothed particle hydrodynamics and peridynamics. *Int. J. Heat. Mass Transf.* 139, 948–962. doi:10.1016/j.ijheatmasstransfer.2019.05.054

Wang, Y. Q., and Hutter, K. (2001). Comparisons of numerical methods with respect to convectively dominated problems. *Int. J. Numer. Meth. Fluids* 37, 721–745. doi:10.1002/fld.197

Xu, R., Stansby, P., and Laurence, D. (2009). Accuracy and stability in incompressible SPH (ISPH) based on the projection method and a new approach. *J. Comput. Phys.* 228, 6703–6725. doi:10.1016/j.jcp.2009.05.032

Ye, T., Pan, D. Y., Huang, C., and Liu, M. B. (2019). Smoothed particle hydrodynamics (SPH) for complex fluid flows: Recent developments in methodology and applications. *Phys. Fluids* 31, 1–41. doi:10.1063/1.5068697

Yuan, G., and Sheng, Z. (2008). Monotone finite volume schemes for diffusion equations on polygonal meshes. *J. Comput. Phys.* 227, 6288–6312. doi:10.1016/j.jcp.2008.03.007

Zhang, Z. L., and Liu, M. B. (2018). A decoupled finite particle method for modeling incompressible flows with free surfaces. *Appl. Math. Model.* 60, 606–633. doi:10.1016/j.apm.2018.03.043

Zheng, X., Ma, Q. W., and Shao, S. D. (2018). Study on SPH viscosity term formulations. *Appl. Sci.* 8, 249. doi:10.3390/app8020249

Zimmermann, S., Koumoutsakos, P., and Kinzelbach, W. (2001). Simulation of pollutant transport using a particle method. *J. Comput. Phys.* 173 (1), 322–347. doi:10.1006/jcph.2001.6879

frontiers | Frontiers in Environmental Science

ORIGINAL RESEARCH
published: 13 April 2022
doi: 10.3389/fenvs.2022.889526

Numerical Investigation of Pollutant Transport in a Realistic Terrain with the SPH-SWE Method

Lirong Tian [1,2,3], *Shenglong Gu* [1,2,3]*, *Yushuai Wu* [1,2,3], *Haitao Wu* [1,2,3] *and Chi Zhang* [4]*

[1] *School of Water Resources and Electric Power, Qinghai University, Xining, China,* [2] *Laboratory of Ecological Protection and High Quality Development in the Upper Yellow River, Xining, China,* [3] *Key Laboratory of Water Ecology Remediation and Protection at Headwater Regions of Big Rivers, Ministry of Water Resources, Xining, China,* [4] *TUM School of Engineering and Design, Technical University of Munich, Munich, Germany*

A large amount of wastewater from industrial and urban residents enters rivers and lakes through the sewage outlet, causing a deterioration of water quality near the sewage outlet. The smoothed particle hydrodynamics (SPH) formulation based on the open-source Fortran code SPHysics is extended to solve the advective diffusion for the evolution of the pollution distribution with the shallow water equation (SWE). Several numerical cases, such as the uniform flow and dam-break flows in one and two dimensions, are studied to verify the accuracy of the present SPH-SWE diffusion model. The results are in good agreement with the analytical solutions. The concentration of the negative value and oscillation could be avoided. It demonstrates that the current SPH-SWE diffusion model has good stability and reliability for solving the pollutant transport equation. The actual terrain case is also simulated to predict the concentration distribution of the river. The concentration is distributed in the center of the Nanmenxia River, where the flow velocity is relatively high. The simulation results are reasonable, implying that it has a high potential in predicting the diffusion process of pollutants in the actual terrain.

Keywords: SPH, advection-diffusion, transport equation, shallow water equation, dam break

Edited by:
Manish Pandey,
National Institute of Technology
Warangal, India

Reviewed by:
Xing Zheng,
Harbin Engineering University, China
PengNan Sun,
Sun Yat-sen University, China

***Correspondence:**
Shenglong Gu
sl.gu@qhu.edu.cn
Chi Zhang
c.zhang@tum.de

Specialty section:
This article was submitted to
Freshwater Science,
a section of the journal
Frontiers in Environmental Science

Received: *04 March 2022*
Accepted: *11 March 2022*
Published: *13 April 2022*

Citation:
Tian L, Gu S, Wu Y, Wu H and Zhang C (2022) Numerical Investigation of Pollutant Transport in a Realistic Terrain with the SPH-SWE Method. Front. Environ. Sci. 10:889526. doi: 10.3389/fenvs.2022.889526

1 INTRODUCTION

The numerical study of spread behavior and pollutant prediction has always been the focus and difficulty of the water environment. The water pollution problem is one of the base components of ecological water environmental protection. The governing equation of the pollution transport processing with water as the carrier is strongly non-linear and non-definite. Therefore, an analytical solution may be impossible to be obtained for the most complicated cases. However, numerical methods provide suitable tools for solving problems of pollutant transportation. In recent years, as a meshfree method, smoothed particle hydrodynamics (SPH) has been widely applied in the numerical simulation of fluids and solids due to the advantages of its Lagrangian properties. The SPH method was first proposed by Lucy (1977) and Gingold and Monaghan (1977) for astrophysics applications. Since then, Monaghan (1994) first extended the SPH method to the hydrodynamic simulation of free surface rolling and breaking. It serves as a pioneering application of the SPH method in hydrodynamics with free surfaces. The SPH method could track the movement of each particle, and these particles could move freely without being restricted by the traditional mesh-based method in the computational domain. With the rapid development of the SPH method, its advantages in computational fluid dynamics (CFD) have emerged, and its application fields have expanded to many aspects, e.g., free surface flow Colagrossi and Landrini (2003); Li et al. (2012); Zhang C. et al. (2017), fluid-structure coupling dynamics Long et al. (2017); Zhang A.-m. et al. (2017); Liang et al. (2017); Zhang et al. (2021a), multiphase flow Rezavand et al. (2020), and reaction–diffusion problem with Zhang et al. (2021c), Zhang et al. (2021b).

Concerning the application of the SPH method for solving the shallow-water equation, Ata and Soulaïmani (2005) introduced a new scheme based on the Riemann solver to improve the numerical stability. With an improved shock wave capturing accuracy, this scheme can produce better and more reliable results. To further improve the numerical accuracy, Rodriguez-Paz and Bonet (2005) proposed a shallow-water formulation with a variable smoothing length. This new system of equations is based on the variational SPH formulation presented by Bonet and Lok (1999), which contains new treatments for the terrain, as it allows more general terrains to be considered. It demonstrated the potential to simulate geophysical flows such as dam breaks, collapses, mudslides, avalanches, and tsunamis with robustness and stability. Vacondio (2010) applied the modified virtual particle method to improve the fixed-wall boundary conditions of the SPH method. The shock capture scheme is used to improve the resolution of the small water depth problem and treat the open boundary condition with the Riemann solver. Chang et al. (2011) presented a SPH methodology to investigate shallow-water dam breaks in one-dimensional open channels. They adopted the concept of sliced water particles (SWP) in the SPH-SWE formulation, which produces a suitable SWP value and variable smooth length in one-dimensional wet and dry river bed dam-break flows. This method can capture shock discontinuities, shock front motion, and other special phenomena, offering a powerful new tool for the numerical investigation of dam-break flows. Pu et al. (2012) proposed integrating the so-called surface gradient upwind method (SGUM) with the source term treatment in the inviscid discretization scheme to further improve the performance of the surface gradient method. Xia et al. (2013) discussed the balance problem caused by the slope source term when using the standard SPH method to solve the SWE and derived a new SPH algorithm, which could be used to investigate different types of actual shallow flow problems. Gu et al. (2017) developed a SPH-SWE model to simulate the problem of obstacles encountered for the two-dimensional dam-break flow and explored the dam-break simulation of the actual terrain. Capecelatro (2018) proposed the SPH-SWE model for simulating shallow water flow on the surface of a rotating sphere, which extends the most advanced method of classical SPH calculation. To improve the computational efficiency, Wu et al. (2020) modified the framework of the SPH-SWE open-source code with OpenMP parallel calculations.

Similarly, many scholars have expanded the SPH method to study the diffusion of pollutants in fluids. Cleary and Monaghan (1999) proposed an SPH conduction formulation and adopted the energy conservation equation to ensure the continuity of heat flux, especially between materials with different densities such as water and air. The calculation error of heat conduction will neither propagate nor increase and will be relatively attenuated. Then, Zhu and Fox (2001) investigated the transport of solutes in porous media and conducted further studies. It provides a reference for the calculation of non-dimensional diffusion coefficients for the simulation of solute transport in real porous media. Tartakovsky et al. (2007) proposed a reactive transport model based on the SPH method, which was successfully used to study some complex coupling phenomena, such as flow, reactive transport, and precipitation in porous and fractured media. Hirschler et al. (2016) used the open-source DualSPHysics code to simulate the spread and attenuation process of radio nuclear pollution. These numerical results are in good agreement with analytical solutions and other SPH results. Later, Chang and Chang (2017) established a SPH-SWE-ADE model, which could ensure the conservation of the pollutant concentration and mass in the simulation of the pure convection–diffusion process, and there is no physical oscillation and negative concentration value in the simulation of the rapid velocity gradient and concentration gradient. Bai et al. (2018) used the SPH-FDM method to study the thermal diffusion process of discontinuous interface media. Nguyen et al. (2018) established an ISPH model of natural convection heat conversion based on the analytical kernel renormalization factor. It is possible to simulate the motion of non-Darcy porous media in a square cavity under different thermal conduction boundary conditions without virtual particles, which is highly consistent with the comparison of the finite element results. Liu et al. (2020) applied the SPH method to solve the two-dimensional average convection–diffusion equation, introducing diffusion flux to reduce the second-order equation of the diffusion term into two first-order equations. The problem of grid anisotropy could be solved effectively without grid division. Even if the streamline is oblique and curved, its performance is good. Rao and Bai (2020) used the SPH method to simulate the three-dimensional soil column and then introduced curve fitting to obtain the diffusion tortuosity of the porous medium and determine the effective diffusion coefficient. Notwithstanding the fact that the SPH-based method has been widely applied in the numerical study of shallow-water flows and convection–diffusion phenomena, its applications in studying pollutant transport in a realistic terrain are still not fully addressed. On the other hand, pollutant transport has been the subject of tremendous studies in the community. However, its multi-physics coupling with hydrodynamics phenomena in the realistic terrain is still not fully addressed.

In this study, we present an SPH-SWE diffusion model to study pollutant transport in the realistic terrain by integrating an SWE formulation with an advection–diffusion model in the SPH framework. The present model is devoted to solving the advection–diffusion equation for the evolution of the concentration field coupled to the fluid dynamic with complex geometry in the realistic terrain. Applying an SPH-based method for studying pollutant transport takes advantage of multi-physics coupling with the hydrodynamics phenomenon. However, high accurate and complex boundary treatment is still in its infancy. Therefore, we applied the virtual particles to deal with boundary conditions. Also, the computational code for the present model is written in open-source SPHysics code and is available by request, allowing its further availability and possible modification. Finally, several numerical examples are investigated to verify the accuracy of the SPH-SWE diffusion model against analytical solutions. The present SPH-SWE formulation can be applied to simulate and predict the migration of conservation pollution in actual terrain. This study is organized as follows: **Section 2** presents the latest numerical development progress of the SPH method in shallow water flow and pollutant diffusion simulation. **Section 3** then employs several numerical cases to verify the accuracy of the SPH-SWE results of the pollutant transport equation against the analytical solutions. In **section 4**, the SPH-SWE diffusion model is applied to study the diffusion and distribution processes of pollutants on actual terrain. The last section draws the conclusions and suggests further studies.

2 SPH METHODOLOGY

The discrete process of the SPH method includes two steps: kernel function interpolation and particle approximation, which involves using a set of particles to represent the problem domain and then obtaining the field variable information of these particles. Considering that a computational domain is filled with a group of particles distributed randomly, these particles could be a concentrated particle group initially generated by an existing mesh generation tool or a central particle initially generated by using a certain spatial discretization model. Similarly, these particles could be used for integration, interpolation, difference, and representing materials.

Particles have mass m and density ρ, and the corresponding volume could also be replaced by the ratio of the mass to the density m/ρ. A given function $f(x)$ is appropriated in terms of the value of the function at a number of the neighboring particles and a kernel function W as

$$\langle f(\mathbf{x}_i)\rangle = \sum_{j=1}^{N} \frac{m_j}{\rho_j} W\left(\mathbf{x}_{ij}, h\right), \tag{1}$$

where $\langle \cdot \rangle$ represents particle approximation, $\mathbf{x}$ represents the position, i and j represent, respectively, the central particle and the neighboring particle, and N is the total number of neighboring particles, which are measured by the smooth length h. The kernel function approximation of the gradient of the function $\nabla \cdot f(\mathbf{x}_i)$ could also be obtained by

$$\langle \nabla \cdot f(\mathbf{x}_i)\rangle = \sum_{j=1}^{N} \frac{m_j}{\rho_j} f(\mathbf{x}_i) \cdot \nabla W\left(\mathbf{x}_{ij}, h\right), \tag{2}$$

where $\nabla W(\mathbf{x}_{ij}, h) = \frac{\mathbf{x}_{ij}}{|\mathbf{x}_{ij}|}\frac{\partial W}{\partial x}$, indicating the gradient value of $f(\mathbf{x}_i)$ could also be approximately discrete by summing the gradient values of the adjacent particles in the support domain. The B-spline kernel function is selected herein, and it shows better accuracy when the particles are disordered Liu and Liu (2003). The SPH method uses particle approximate integration, which is a simple key approximation that could avoid the use of grids for numerical integration and is also a key factor affecting its accuracy.

2.1 Continuity Equation

The area density of fluid particles in two-dimensional shallow water is redefined to connect the water depth and volume density. By introducing ρ to represent the area density and $\rho_w 1000\ \mathrm{Kg} \cdot \mathrm{m}^{-3}$ to represent the density of water, we obtained

$$\rho = \rho_w d, \tag{3}$$

where d is the water depth. Then, the continuity equation in shallow water is derived as

$$\frac{\mathrm{d}\rho}{\mathrm{d}t} = -\rho \nabla \cdot \bar{\mathbf{v}}, \tag{4}$$

where t is time, $\bar{\mathbf{v}} = \frac{1}{h}\int_0^d \mathbf{v} dz$ the velocity vector of the integrated depth average in the vertical direction, which has a horizontal component $\bar{u}$ and a longitude component$\bar{v}$, with z denoting the vertical direction.

The classic density dispersion formula and variable smoothing length calculation formula are calculated as

$$\begin{cases} \rho = \sum_{j=1}^{N} \dfrac{m_j}{\rho_j} W\left(\mathbf{x}_{ij}, h\right) \\ h = h_0 \left(\dfrac{\rho_0}{\rho}\right)^{1/d_m} \end{cases}, \tag{5}$$

where d_m is the number of dimension, ρ_0 and h_0 are the initial density and smooth length, respectively. The Newton–Raphson iteration method is used to solve the fluid particle density and smooth length as **Eq. 5** has implicit function relations. Then, the water depth d of the fluid particles is calculated by **Eq. 3**.

2.2 Momentum Equation

The Lagrangian form of the momentum equation for the shallow-water reads

$$\frac{\mathrm{d}\bar{\mathbf{v}}}{\mathrm{d}t} = -\frac{\mathbf{g}}{\rho_w}\nabla\rho + \mathbf{g}\left(-\nabla b + S_f\right), \tag{6}$$

where $\mathbf{g} = 9.81\ \mathrm{m\ s}^{-2}$ is the acceleration gravity, ∇b is the gradient of riverbed elevation, $S_f = n^2 \mathbf{g}\bar{\mathbf{v}}|\bar{\mathbf{v}}|/d$ is the source term of riverbed friction, n is the Manning coefficient, and $n_i = \sum_j^{N_b} n_j^b \nabla_i W_{ij} V_j$,with N_b denoting the total number of bed particles in the adjacent search range.

The SPH formulation of the momentum equation is described as follows:

$$\frac{\mathrm{d}\bar{\mathbf{v}}}{\mathrm{d}t} = -\frac{\mathbf{g} + \bar{\mathbf{v}}_i \cdot k_i \bar{\mathbf{v}}_i + t_i \cdot \nabla b_i}{1 + \nabla b_i \cdot \nabla b_i}\nabla b_i - t_i, \tag{7}$$

where $k_i = \nabla(\nabla b_i)$ is the curvature tensor of the bottom elevation, $t_i = T_i/m_i$ is the internal force which is obtained using the continuity equation and the internal energy expressed in terms of energy per unit mass, and T_i is defined as

$$T_i = -\sum_j^N m_i m_j \frac{\mathbf{g}}{2\rho_w}\left(\frac{\alpha_i + \alpha_j}{\alpha_i \alpha_j} + \Pi_{ij}\right)\nabla_i W_{ij}, \tag{8}$$

where

$$\alpha_i = -\frac{1}{\rho_i m_i d_m} \sum_j^N m_j \frac{x_{ij}^2}{x_{ij}} \nabla_i W_{ij}. \tag{9}$$

The additional numerical viscosity Π_{ij} is used to preserve the numerical stability.

$$\Pi_{ij} = \begin{cases} -\alpha \bar{c}_{ij} \mu_{ij} + \beta \bar{c}_{ij} \mu_{ij}^2 & if \quad \bar{\mathbf{v}}_{ij} \cdot \mathbf{x}_{ij} < 0 \\ 0 & otherwise \end{cases}, \tag{10}$$

where $\alpha \in [0.01, 0.1]$, $\beta = 0$, $c = \sqrt{gd}$ the speed of sound, $\mu_{ij} = \frac{\bar{h}_{ij} \bar{\mathbf{v}}_{ij} \cdot \mathbf{v}_{ij}}{|\mathbf{x}_{ij}|^2 + 0.01\ h^2}$, $\bar{h}_{ij} = \frac{h_i + h_j}{2}$, $\bar{c}_{ij}$ and $\bar{\rho}_{ij}$ are calculated in the same way.

To improve the accuracy of river elevation interpolation, the SPH formula of the river bed height and its gradient are modified by using the Shepard correction and kernel gradient correction Randles and Libersky (1996); Bonet and Lok (1999), respectively.

2.3 Transport Equation

Ignoring the source, sink terms, and biochemical reactions of pollutants in the water body, the Lagrangian form of the pollutant transport equation is described by Fickle's law (Zhu and Fox (2001); Monaghan (2005)) as

$$\frac{\mathrm{d}C}{\mathrm{d}t} = \frac{1}{\rho} \nabla \cdot (D \nabla C), \tag{11}$$

Combining the finite difference and SPH methods for the discrete solution, the corresponding discrete formula reads

$$\frac{\mathrm{d}C_i}{\mathrm{d}t} = \sum_j^N \frac{m_i}{\rho_i \rho_j} \left(D_i + D_j \right) \frac{\mathbf{x}_{ij} \cdot \nabla_i W_{ij}}{\mathbf{x}_{ij}^2 + \eta^2}, \tag{12}$$

where C_i and D_i are, respectively, the pollutant concentration and the concentration diffusion coefficient. It assumes that the pollutant is a dilute solution in the water body so that the concentration field does not affect the hydrodynamic field. When the concentration of pollutants is discontinuous or the complex fluid that simulates the multiphase flow is encountered in the calculation, $D_i + D_j$ could be replaced by $\frac{4 D_i D_j}{D_i + D_j}$, and the diffusion coefficient D could also be partial derivatives D_{xx}, D_{xy}, D_{yx}, and D_{yy}. Zhu and Fox (2001) have successfully applied the SPH method to solve the second-order diffusion equation to the diffusion of pollutants in porous media. Their results provide a reference for the determination of the concentration diffusion coefficient in actual porous media.

2.4 Boundary Condition

The treatment of the solid wall boundary adopts the non-slip boundary condition. The smooth kernel function interpolation formula of the SPH method determines that the particle's influence field is truncated at the boundary, leading to truncation errors. Therefore, virtual particles could be set at the boundary to prevent particle penetration. The velocity of the virtual particle is the same as the velocity of the central particle, and its direction is the opposite. The other physical values of the virtual particles are the same as the physical attributes of the central fluid particle, such as the concentration, density, mass, and water depth. In this study, the modified virtual particle method of Vacondio (2010) is used to treat the closed boundary. Note that the boundary treatment with a higher accuracy can be achieved by introducing moving-least-square interpolation, which induces excessive computational effort. The method is a modification of the virtual boundary particle method of Lastiwka et al. (2009). Since the concentration of pollutants on the solid wall in this study does not consider the absorption and adhesion of the boundary and since there is no pollution source term, it is a completely reflective boundary, so there is no flux through the closed wall. The treatment of open boundaries has experienced great developments in particle-based methods. The study of open boundary problems is a key element of any shallow water numerical model. In the traditional grid-based methods, the inlet and outlet boundaries are fixedly set at the boundary of a series of (usually straight or flat) grids, and a layer of virtual grids is arranged on the other side of the boundary to set the inflow or outflow velocity. It is relatively convenient and direct to impose boundary conditions on the inflow and outflow of information. In the SPH method, the particles move with time during the simulation process, and the position of the particles could not be restricted. Therefore, the particles could be inserted and removed. In addition, the approximate nature of SPH interpolation makes it more difficult to achieve this boundary condition. Lastiwka et al. (2009) introduced permeability and non-reflective boundary conditions in the gas-dynamic SPH model. Ramos-Becerra et al. (2009) applied the ISPH model to the inflow and outflow boundary conditions. For the open boundary condition, the inflow and outflow boundary implement the buffer zone. The inflow and outflow of particles are in the form of single particles moving in and out. The inflow and outflow particle parameter values are calculated by the critical conditions of the inflow and outflow, which are described in detail in the literature by Vacondio et al. (2012). The concentration value of the inflow particles is given a specific value and enters the flow field.

2.5 Time Integration

In this study, an explicit leapfrog time integration scheme (Vacondio et al. (2012); Hernquist and Katz (1989)) is applied for time integration. The velocity is updated every half step, and the position is updated every step. The pollutant concentration is updated accordingly. The integral time item is calculated by

$$\begin{cases} \mathbf{v}_i^{n+1/2} = \mathbf{v}_i^{n-1/2} + \Delta t \dfrac{\mathrm{d}\mathbf{v}_i}{\mathrm{d}t}^n \\ \mathbf{x}_i^{n+1} = \mathbf{x}_i^n + \Delta t \mathbf{v}_i^{n+1/2} \\ \mathbf{v}_i^{n+1} = \mathbf{v}_i^{n+1/2} + 0.5 \Delta t \dfrac{\mathrm{d}\mathbf{v}_i}{\mathrm{d}t}^n \end{cases}, \tag{13}$$

where n is an instantaneous moment, $n + 1/2$ is half of a time step, $n + 1$ is the new time step, and the time step size is Δt. The calculation of the time step needs to consider the Courant condition and diffusion condition.

$$\Delta t = \min \left\{ C_{CFL} \frac{h}{\max (c_i + |\mathbf{v}_i|)}, 0.125 \frac{h^2}{D} \right\}, \tag{14}$$

where C_{CFL} is the Courant number. The aforementioned equation is the SPH-SWE formula, the discrete formula of the pollutant transport equation, and the basic theoretical knowledge of boundary processing and time integration. The open-source code based on the SPH variational scheme to solve the shallow water wave equation is adopted in this study. This program is suitable for SPH-based simulation of deep average shallow water flow. It is a numerical method developed by the teamwork of Dr. Renato Vacondio, Professor P.K. Steinsby, and Dr. Ben Rogers. The main innovation of this algorithm is that it could simulate floods under actual water depth conditions, the boundary conditions of inflow and outflow, and particle splitting to increase the necessary resolution. Finally, the formula for the stability term has been improved. This study extends the source code and adds the pollutant concentration calculation code. The analytical solution is used to compare and verify the calculation results of the concentration solution code, and the SPH-SWE diffusion model is applied to the pollutant diffusion process on the actual terrain. The SPH-SWE diffusion model is obtained by solving the shallow water wave equation and the corresponding migration diffusion equation.

3 NUMERICAL RESULTS FOR VALIDATION

In this part, uniform flow and dam break cases in 1-D or 2-D are simulated to verify the accuracy of the SPH-SWE formula for the migration and diffusion of pollutants. The results illustrate that the numerical solution of the present method is reasonable and reliable. It also simulates the migration and diffusion processes of pollutants in the current terrain and predicts the diffusion distribution of pollutant concentrations in the Nanmenxia Reservoir.

3.1 Uniform Flows in One Dimension

This section simulates the diffusion of finitely distributed and time-continuously distributed sources in one-dimensional uniform flow. Six numerical experiments are simulated to verify the accuracy of the results obtained with different pollution sources and diffusion coefficients. In this test, we considered a rectangular flat-bottomed tank of a length of 10,000 m with a water depth of 1 m discretized by 10,000 fluid particles and 10,000 bottom particles. The diffusion process of pollutants is simulated when D_x is 0, 5 and 50 $m^2\ s^{-1}$. The inflow and outflow boundary conditions are used. The particle velocity and water depth of the inflow and outflow of the instantaneous finite distribution source and the time-continuous source are set to 1 m and 2 m s^{-1}, and the pollutant concentrations are set to 0 and 1 Kg m^{-3}, respectively. The initial fluid fills the computational domain, and the initial velocity and depth of the flow field are the same as the outflow and inflow particles. The initial concentration distribution of the time-continuous source is that when time $t = 0$ s, the diffusible concentration everywhere along the X-axis is 0. When time $t > 0$ s, the point source is continuously released. The initial concentration distribution of a finitely distributed source is a function of C.

$$C(x,0) = \begin{cases} 1, & 2500 < x < 3500 \\ 0, & \text{otherwise} \end{cases}. \tag{15}$$

The analytical solution of 1D finite distributed source reads

$$C(x,t) = \frac{C_0}{2}\left[\operatorname{erf}\left(\frac{x + x_1 - ut}{\sqrt{4D_x t}}\right) - \operatorname{erf}\left(\frac{x - x_1 - ut}{\sqrt{4D_x t}}\right)\right], \tag{16}$$

and of 1D time-continuous source reads

$$C(x,t) = \frac{C_0}{2}\left[1 - \operatorname{erf}\left(\frac{x - ut}{\sqrt{4D_x t}}\right)\right], \tag{17}$$

where C_0 is the initial concentration and x_1 is the range of concentration at the location.

The diffusion process of the 1-D instantaneous finite distributed source and the time-continuous source is simulated, respectively, to verify the reliability of the 1-D SPH-SWE diffusion model with different diffusion coefficients.

Figure 1 presents the three finite pollution source cases with $D_x = 0$, 5, and 50 $m^2\ s^{-1}$ at time $t = 2{,}600$ s; the velocity and depth of the water flow in the entire calculation area are 1 m and 2 m s^{-1}, respectively (**Figure 1A**). When simulating different diffusion coefficients, the concentration calculation results of the SPH-SWE formula are highly consistent with the analytical solution, as shown in **Figures 1B–D**. For the same diffusion coefficient, the concentration results of the SPH-SWE formula are in good agreement with the analytical solutions at different times. For the time-continuous source case, as shown in **Figure 2**, when the time $t = 1{,}300$ s (**Figure 2A**) and 2, 600 s (**Figure 2B**), the SPH-SWE results of the pollutants are highly consistent with the analytical solution. The simulation results for different diffusions are also in good agreement with the analytical solutions. For the aforementioned six cases, the numerical results are consistent with the analytical ones. It is concluded that the SPH-SWE diffusion model simulates the pollutant diffusion process with reliable results, and the obtained diffusion coefficient does not affect the numerical results.

3.2 Dam-Break Flow

The case of pure convective diffusion ignoring gradient diffusion in dry and wet dam-break flows is simulated in this part with the diffusion coefficient of 0 $m^2\ s^{-1}$. The computational domain is a rectangular flat-bottomed river bed with a length of 2000 m. The particle spacing of the dry river bed is taken as 10 m and that of the upper reaches of the wet river bed is 10 m, and the downstream is 20 m.

The upstream water depth and pollutant concentration of the wet river bed are 10 m and 0.7 Kg m^{-3}, and the downstream water depth and pollutant concentration are 5 m and 0.5 Kg m^{-3}, respectively. The water depth and pollutant concentration upstream of the dry riverbed are the same as the initial parameters of the wet riverbed, and there is no water downstream. The migration process of the pollutant concentration is simulated for dry and wet river bed dam breaks, and the results of the SPH-SWE formula are compared with the analytical solution (Stoker, 1948) for verification. The SPH-SWE result of the dam break on the dry river bed is shown in **Figure 3**. It could be seen from **Figure 3A** that when time $t = 50$ s, the upstream water depth is 10 m, and near 450 m, the water depth decreases with a small

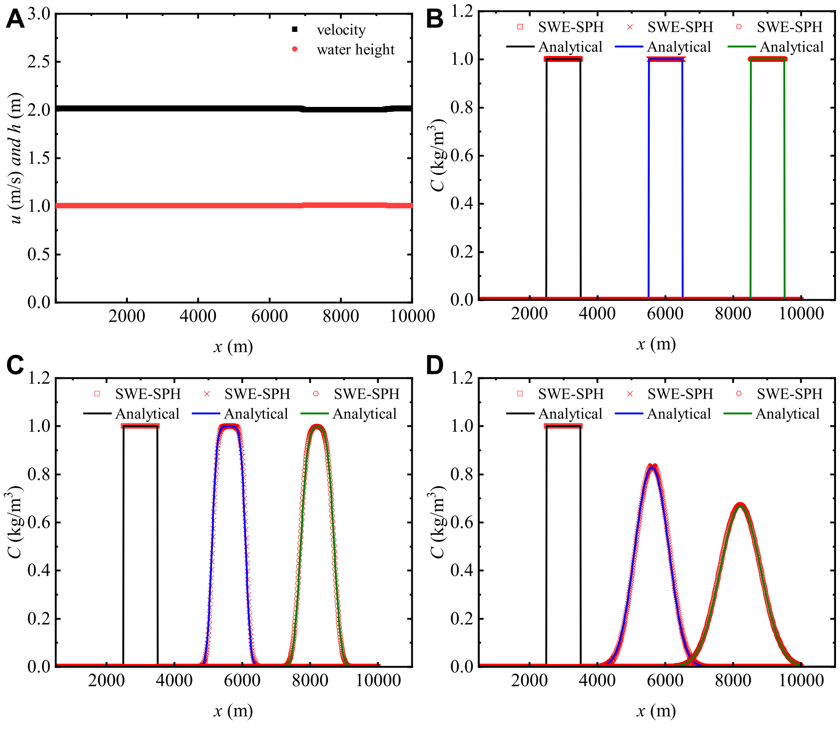

FIGURE 1 | Comparison of analytical solutions and SPH-SWE simulation results of 1-D finitely distributed sources **(A)** Velocity and water height along the *x*-axis (t = 1,300 s), **(B–D)** Concentration distribution (t = 0 s, 1,300 s, and 2,600 s respectively).

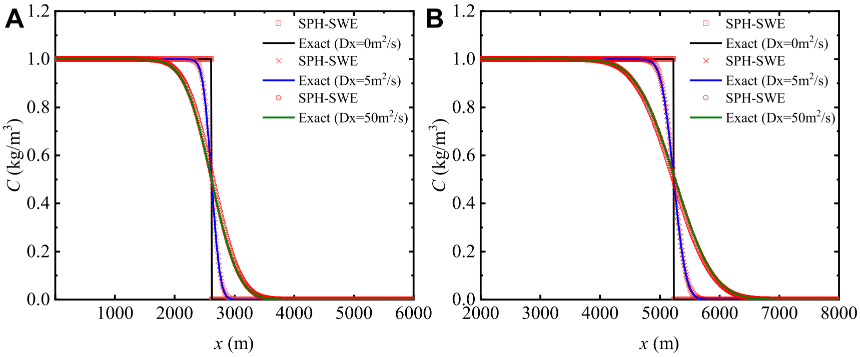

FIGURE 2 | Comparison of analytical solutions and SPH-SWE simulation results of a 1-D time-continuum distribution source. **(A,B)** Concentration distribution (t = 1300 s and 2600 s respectively).

curvature. The result is continuous and smooth. The water depth gradient of the initial conditions at the intermediate position is relatively large, but there is no numerical oscillation, and the result is relatively stable. In **Figure 3B**, since the gradient diffusion effect is not considered, the pollutant concentration value is always 0.7 Kg m^{-3}, and the calculation result is reasonable.

The simulation results of dam breaks with the wet bed are shown in **Figure 4**. **Figures 4A, B**, respectively, present the water depth and concentration distribution of the wet river bed dam break at time $t = 50$ s. In **Figure 4A**, it could be seen that the water depth at the upstream and downstream positions is 10 and 5 m, respectively. The result of the water depth is close to the analytical solution, and there is no numerical oscillation at the discontinuity. The simulation result of the SPH-SWE formula is smoother than the analytical solution. In **Figure 4B**, it could be seen that the concentration drops abruptly when the horizontal displacement is close to 1,200 m, from the upstream concentration value of 0.7 Kg m^{-3} to the downstream value of 0.5 Kg m^{-3}. The numerical results are consistent with the analytical ones. It is further verified that the 1-D SPH-SWE diffusion model is reasonable and has good numerical stability.

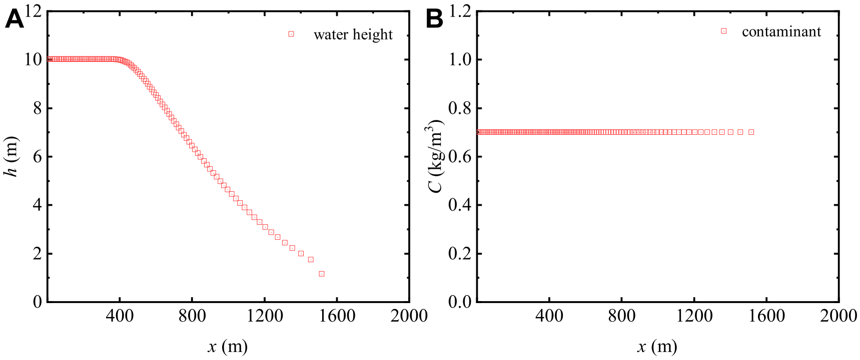

FIGURE 3 | Calculation results of a dry bed *t* = 50 s: water depth **(A)** and concentration **(B)**.

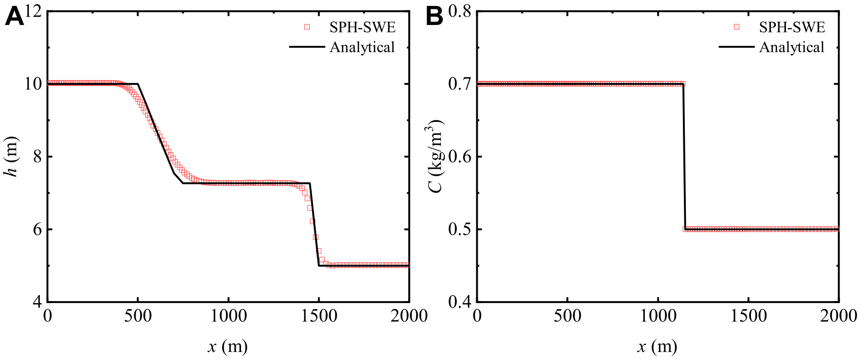

FIGURE 4 | Calculation results of a wet bed *t* = 50 s: water depth **(A)** and concentration **(B)**.

3.3 Uniform Flow in Two Dimensions

The computational domain of the two-dimensional uniform flow is a rectangular upside-slope channel with a size of 1,200 × 400 m and a slope value of 0.001m discretized by the fluid particle spacing of 1 m. Then, the initial velocity and water depth are set to 2.9 m s^{-1} and 5 m, respectively. Open boundary and closed boundary conditions are encountered in the simulation, and no-slip boundary conditions are set for the closed boundary on the left and right banks. The fluid movement direction of the two-dimensional uniform flow sets the inflow and outflow boundaries. The particle velocity, water depth, and concentration of the inflow and outflow are 2.9 m s^{-1}, 5 m, and 0 Kg m^{-3} , respectively. The migration and diffusion law distribution of circular instantaneous pollution non-point sources with pollutant diffusion coefficients of 0 and 10,000 m^2 s^{-1} are studied. **Figure 5** shows the numerical results of the SPH-SWE formula for the circular instantaneous non-point source pollutant concentration at different time instants without considering the diffusion effect. The blue area in **Figure 5** represents that the concentration of pollutants in the fluid is 0 Kg m^{-3}. It could be seen that the pollutant is red in the movement of the fluid with time, and the concentration value is 1 Kg m^{-3}. It shows that the diffusion effect is not involved in the process of pollutant dissemination, and the distance from the instantaneous surface source diffusion to the rightmost edge position (the red dotted line in the figure) is the product of the speed of the 2-D uniform flow and the time *t*, $x = x_0 + ut$, corresponding to the different positions. It could explain the rationality of the present numerical results.

With the diffusion coefficient D = 10,000 m^2 s^{-1}, **Figure 6** shows the results of the circular instantaneous non-point source pollutant concentration at the different time instants. By comparing the results of **Figures 5**, **6**, it could be seen that the center of the circular instantaneous non-point source pollutant in **Figure 6** is at the same position as the center of the circle in **Figure 5**. Due to the gradient diffusion effect, at time *t* = 50, 120, 200, and 300 s, the distance from the center of the pollutant circle to the diffusion edge in **Figure 6** is farther than that in **Figure 5**. The concentration value changes with time; the concentration value is less than 1 Kg m^{-3} and the edge positions (the red dotted line in the figure) are, respectively. The concentration value near the center of the pollution source is always at its peak state, and its concentration value decreases from the center of the circle to the edge position, satisfying the law of concentration diffusion. Reasonable results verify that the SPH-SWE diffusion model also has reasonable capturing of pollutants in the two-dimensional fluid movement. It proves that the SPH-SWE formula has advantages in simulating the migration and

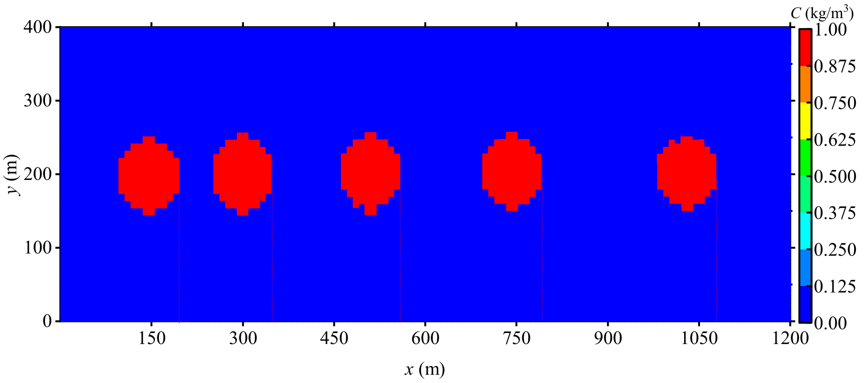

FIGURE 5 | Calculation result of the two-dimensional uniform flow condition $D = 0\ m^2s^{-1}$.

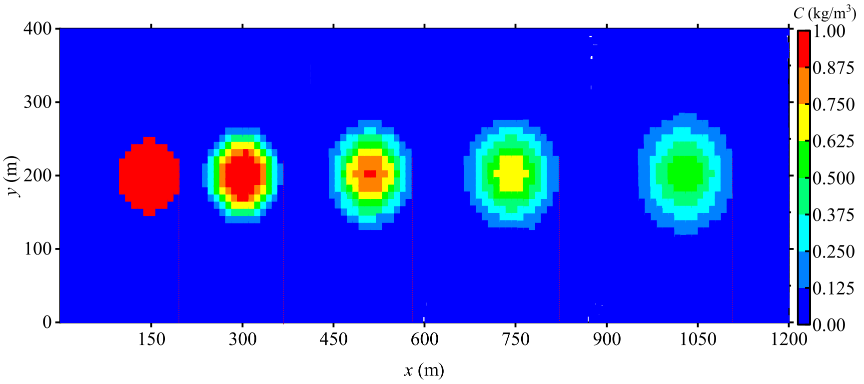

FIGURE 6 | Calculation result of the two-dimensional uniform flow condition $D = 10{,}000\ m^2s^{-1}$.

diffusion processes of conservative pollutants, and there is no need to consider the solution of the migration term in the transport equation. Only using the numerical discretization technique of the SPH method to approximate the diffusion term with the second-order derivative could simulate and predict the diffusion process of pollutants, showing that the SPH-SWE method has good advantages in simulating the diffusion of conservative pollutants.

4 APPLICATION

This part explains the Nanmenxia Reservoir in Huzhu County, Qinghai Province. The elevation of the reservoir's total area is above 2, 700 m, and the area is about 218 Km^2. The maximum dam height is 27.50 m, the crest length is 467 m, and the crest elevation is 2, 772.5 m. The topographic map is shown in **Figure 7**. Here, *X*, *Y*, and *Z* are the three-dimensional coordinates of the topographic data of the Nanmenxia Reservoir.

Zheng (2017) has carried out a numerical study of the dam-break flow in the Nanmenxia Reservoir area, simulating the full-break (breaking width of 467 m) and partial-break (breaking width of 117 m) conditions. The fluid-particle spacing is 10, 15, and 20 m, respectively. The water levels and velocities at different locations are discussed, and a convergence analysis is conducted. Through the analysis of the numerical data, it is concluded that the SPH-SWE model is convergent and reasonable. The present study mainly conducts an extended study of this case. When the simulated diffusion coefficient is taken as $0\ m^2\ s^{-1}$, the variable diffusion coefficient and the migration and diffusion process of pollutants in the watershed are calculated after the Nanmenxia Reservoir breaks instantaneously. The rest of the initial conditions of water movement and parameter settings are the aforementioned parameters. The simulation area of the Nanmenxia Reservoir shows that the riverbed gradient is 0.012, and the roughness is 0.024. The initial fluid area is arranged between the x coordinate of 1800 m–2,500 m and the y coordinate of 8,200 m–9,000 m. The fluid-particle spacing is 20 m, with a total of 2,664 fluid particles. The initial water depth and velocity are 0.15 m and $0\ m\ s^{-1}$, respectively, and the particle spacing of the river bed is also taken as 30 m, with a total of 89,167 river bed particles. The initial position of the contaminants is a circular area source with x and y coordinates of 2, 450 m and 9, 255 m and a radius of 100 m. The

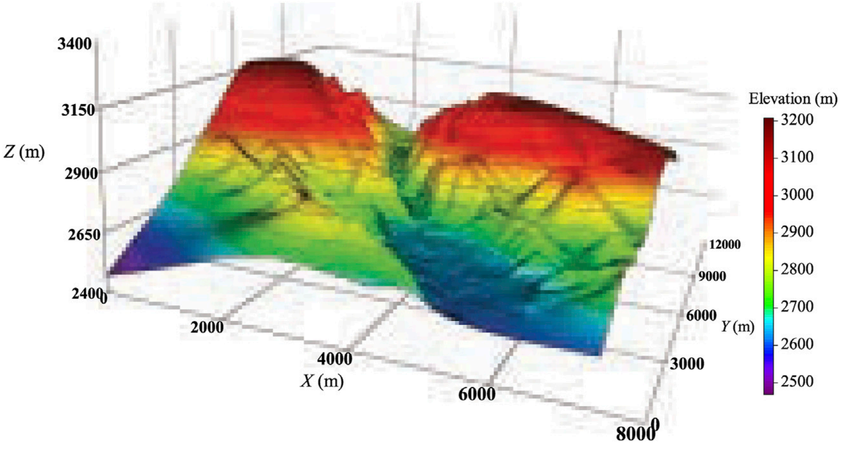

FIGURE 7 | Topographic map of the Nanmenxia Reservoir.

concentration is 1 Kg m^{-3}, and the initial concentration in the remaining areas is 0 Kg m^{-3}. The total simulation time is taken as 600 s. A detailed discussion on the water flow movement process of the Nanmenxia Reservoir dam break has been made, and it was verified that the particle spacing of 20 m is feasible. This study focuses on the study of the distribution of pollutant concentration fields in the calculation area of the Nanmenxia Reservoir during the instantaneous total collapse. The simulation results of the pollutant concentration of the Nanmenxia Reservoir with $D = 0\ m^2\ s^{-1}$ and variable diffusion coefficients are discussed as follows. The variable diffusion coefficient formula is as follows:

$$\begin{cases} D_L = 6.09 \times u^* \times d \\ D_T = 0.6 \times u^* \times d \end{cases}, \tag{18}$$

and the second-order tensors D_{xx}, D_{xy}, D_{yx}, and D_{yy} corresponding to the diffusion coefficient are

$$\begin{cases} D_{xx} = D_T + (D_L - D_T)\dfrac{\bar{u}^2}{V^2} \\ D_{xy} = D_{yx} = (D_L - D_T)\dfrac{\bar{u}\bar{v}}{V^2} \\ D_{yy} = D_T + (D_L - D_T)\dfrac{\bar{u}^2}{V^2} \end{cases}. \tag{19}$$

where D_L and D_T are the lateral and longitudinal diffusion coefficients, respectively, and u^* is the frictional velocity of the river bed, which could be calculated according to the river bed gradient and water depth; $V = \sqrt{\bar{u}^2 + \bar{v}^2}$ is the square root of the velocity.

Figure 8 shows the migration and diffusion results of the concentration of pollutants in the dam break of the Nanmenxia Reservoir when the diffusion coefficient is set to 0 $m^2\ s^{-1}$ at time $t = 600$ s. It shows that when the simulation time reaches 600 s, the fluid has entered the wide plain area downstream. The pollutants are located in the middle of the river, against the direction of the water flow, such as the red area with the larger velocity. The red area of the concentration distribution already occupies about 1/3 of the fluid area at time $t = 600$ s, and its shape is roughly the same as the curved shape of the river, indicating that the uneven terrain will also affect the spread of pollutants. It could be found that the pollutants in the research basin are mainly related to the velocity of the water flow. The premise of this case assumes that the diffusion coefficient is 0 $m^2\ s^{-1}$, implying that the pollutant is only related to the trajectory of the fluid particles in the transportation process, that is to say, only the migration process of the pollutant is considered. As it is assumed that water in the dam of Nanmenxia Reservoir collapses instantly, and with the ups and downs of the topography, the concentration of pollutants will be discontinuous. Because the diffusion coefficient is assumed to be zero, the concentration is not continuous. In actual situations, the spreading and diffusion process of pollutants in water bodies will be related to factors such as the concentration diffusion coefficient and attenuation coefficient of the river and such discontinuities will not occur in the concentration of pollutants.

It could be found from **Eqs. 18, 19** that the variable diffusion coefficient is calculated based on the river bed gradient, fluid velocity, and water depth. Therefore, each fluid particle in the study area has its own diffusion coefficient. The diffusion process of pollutants is researched and analyzed by solving the variable diffusion coefficient. **Figure 9** and **Figure 10** show the numerical results of the pollutant concentration with the variable diffusion coefficient at time $t = 600$ s. It could be noted that there is a large red area in the middle of the river channel with a peak concentration of 0.076 Kg m^{-3}, and a small red area in the middle of the downstream river channel with a peak concentration of 0.068 Kg m^{-3}. It could be seen that regardless of whether the larger red area or the smaller red area, the concentration value is continuous, the concentration value decreases sequentially from large to small, and there is no jump-type discontinuous distribution of the pollutant concentration. The density values on the left and right sides of the density value of each color gradation are the density values of the adjacent color gradations. Generally divided into four situations, in the downstream plain area, the left is high

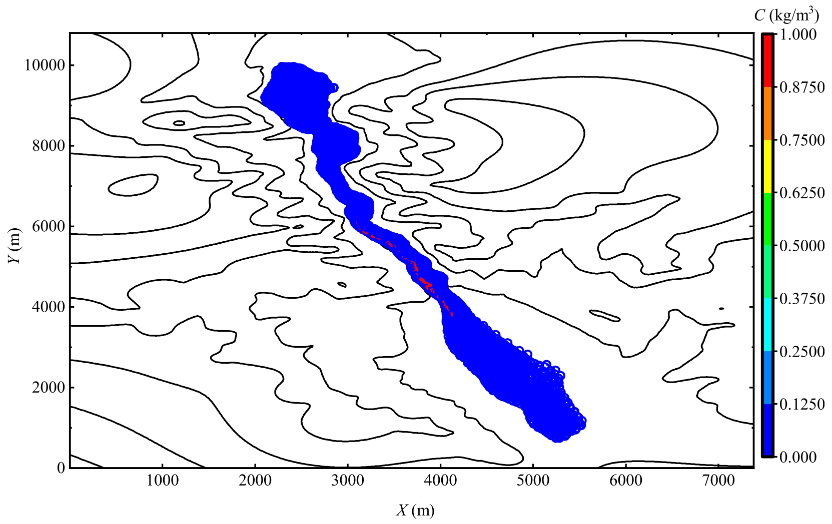

FIGURE 8 | Pollutant concentration distribution map after the Nanmenxia dam break (D = 0 m^2 s^{-1}).

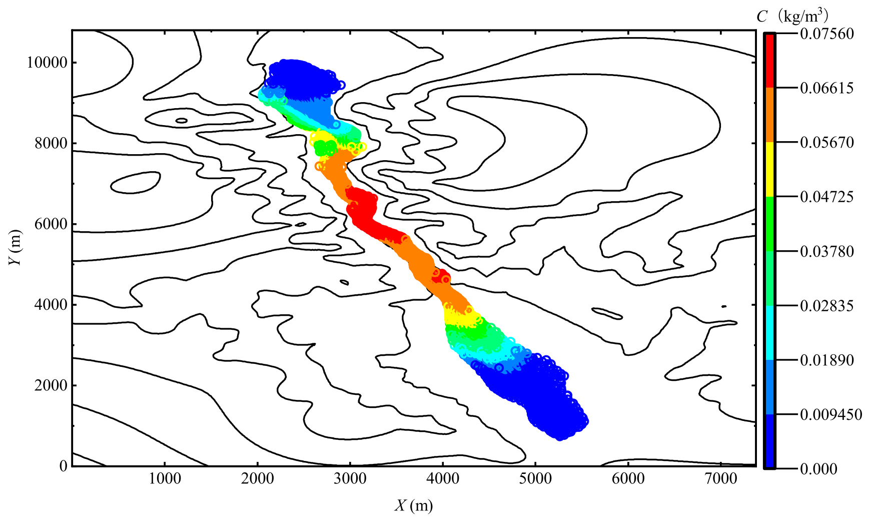

FIGURE 9 | Pollutant concentration distribution map after the Nanmenxia dam break under variable diffusion coefficients.

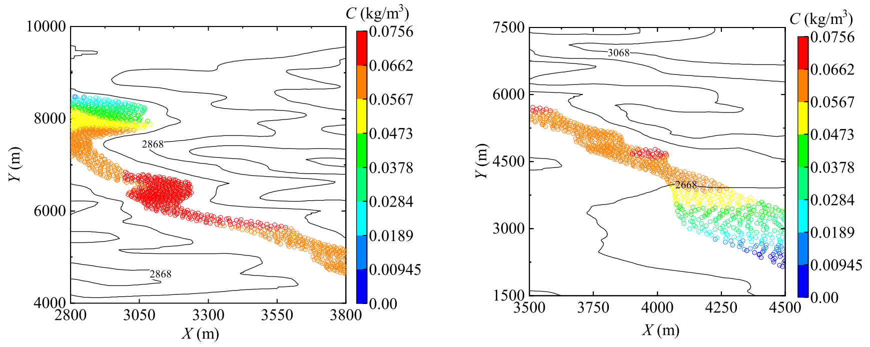

FIGURE 10 | Peak contaminant concentration area.

and the right is low; in the upstream reservoir area, the left is low and the right is high; in the middle area of the river channel, the left and the right are low; and in the yellow area surrounded by two red areas, the left and the right are high and the middle is low. Second, there is no numerical singularity of the pollutant concentration in the whole calculation process, which ensures the non-negativity of the concentration value. The calculation result is stable, and the simulation result conforms to the migration and diffusion laws of pollutants in the actual river.

Since the variable diffusion coefficient is related to topography, water flow velocity, and water depth, it more truly describes the migration and diffusion process of soluble conservative pollutants in the actual wide and shallow water flow, verifying that the SPH-SWE diffusion model simulates the pollutants in the actual terrain. Concentration diffusion has good stability, and the SPH-SWE method has a high research value in the prediction of the pollutant transportation process.

5 CONCLUSION

Cleary and Monaghan (1999) proposed a SPH heat conduction model, which provides a mature numerical format for the discrete solution of the second-order diffusion term in the heat conduction formula. Based on the previous work, this article further expands the application of the SPH-SWE formula. The simulation of the migration and diffusion of pollutants in shallow water is realized, and the diffusion process of soluble inert pollutants in the river is simulated and predicted. The research results of this article are summarized as follows:

- Adding the transport equation for conservative pollutants in the open-source program, uniform flow and classic dam-break flows are simulated in 1 D and 2 D. The numerical results are highly consistent with the analytical solutions, which prove the accuracy of the SPH-SWE model in predicting the propagation process of pollutants in rivers with actual terrain.
- The SPH-SWE formula is used to study the migration laws of soluble and insoluble pollutants in rivers. In the simulation process, negative concentration values could be avoided, which verifies the stability of the model and the rationality of the pollutant numerical results. It proves that the SPH-SWE method has great potential in simulating the spread of pollutants.

The open-source code is used to study the migration and diffusion of soluble conservative pollutants in shallow water, which expands the application fields of the SPH-SWE method. However, the problems of boundary and calculation efficiency are not considered in detail. In the boundary treatment, the concentration diffusion effect near the solid wall boundary is not fully considered. Second, Wu et al. (2020) performed parallel processing on the open-source shallow water code, but we have not added parallel computing. The next step is to add parallel computing to further improve its efficiency. The content of this research has some shortcomings, but we hope to provide some experience for the future related research study. It should be noted that the initial pollutants in the present simulation are simple, and they are much more complex in real life. Complex and realistic pollution sources will be taken into consideration in future research.

DATA AVAILABILITY STATEMENT

The original contributions presented in the study are included in the article/Supplementary Material, further inquiries can be directed to the corresponding authors.

AUTHOR CONTRIBUTIONS

LT: methodology, visualization, validation, formal analysis, investigation, writing—original draft, and writing—review and editing; SG: supervision, investigation, and writing—review and editing; YW: investigation; HW: investigation; CZ investigation and writing—review and editing.

FUNDING

This research work was supported by the National Natural Science Foundation of China (No. 51869025) and the Open Research Fund Program of the State Key Laboratory of Hydroscience and Engineering, Tsinghua University (No. SKLHSE-2021-B-04).

REFERENCES

Ata, R., and Soulaïmani, A. (2005). A Stabilized Sph Method for Inviscid Shallow Water Flows. *Int. J. Numer. Meth. Fluids* 47, 139–159. doi:10.1002/fld.801

Bai, B., Rao, D., Xu, T., and Chen, P. (2018). Sph-fdm Boundary for the Analysis of thermal Process in Homogeneous media with a Discontinuous Interface. *Int. J. Heat Mass Transfer* 117, 517–526. doi:10.1016/j.ijheatmasstransfer.2017.10.004

Bonet, J., and Lok, T.-S. L. (1999). Variational and Momentum Preservation Aspects of Smooth Particle Hydrodynamic Formulations. *Comp. Methods Appl. Mech. Eng.* 180, 97–115. doi:10.1016/s0045-7825(99)00051-1

Capecelatro, J. (2018). A Purely Lagrangian Method for Simulating the Shallow Water Equations on a Sphere Using Smooth Particle Hydrodynamics. *J. Comput. Phys.* 356, 174–191. doi:10.1016/j.jcp.2017.12.002

Chang, T.-J., Kao, H.-M., Chang, K.-H., and Hsu, M.-H. (2011). Numerical Simulation of Shallow-Water Dam Break Flows in Open Channels Using Smoothed Particle Hydrodynamics. *J. Hydrol.* 408, 78–90. doi:10.1016/j.jhydrol.2011.07.023

Chang, Y.-S., and Chang, T.-J. (2017). Sph Simulations of Solute Transport in Flows with Steep Velocity and Concentration Gradients. *Water* 9, 132. doi:10.3390/w9020132

Cleary, P. W., and Monaghan, J. J. (1999). Conduction Modelling Using Smoothed Particle Hydrodynamics. *J. Comput. Phys.* 148, 227–264. doi:10.1006/jcph.1998.6118

Colagrossi, A., and Landrini, M. (2003). Numerical Simulation of Interfacial Flows by Smoothed Particle Hydrodynamics. *J. Comput. Phys.* 191, 448–475. doi:10.1016/s0021-9991(03)00324-3

Gingold, R. A., and Monaghan, J. J. (1977). Smoothed Particle Hydrodynamics: Theory and Application to Non-spherical Stars. *Monthly notices R. astronomical Soc.* 181, 375–389. doi:10.1093/mnras/181.3.375

Gu, S., Zheng, X., Ren, L., Xie, H., Huang, Y., Wei, J., et al. (2017). Swe-sphysics Simulation of Dam Break Flows at South-Gate Gorges Reservoir. *Water* 9, 387. doi:10.3390/w9060387

Hernquist, L., and Katz, N. (1989). TREESPH - A Unification of SPH with the Hierarchical Tree Method. *ApJS* 70, 419–446. doi:10.1086/191344

Hirschler, M., Säckel, W., and Nieken, U. (2016). On Maxwell-Stefan Diffusion in Smoothed Particle Hydrodynamics. *Int. J. Heat Mass Transfer* 103, 548–554. doi:10.1016/j.ijheatmasstransfer.2016.07.061

Lastiwka, M., Basa, M., and Quinlan, N. J. (2009). Permeable and Non-reflecting Boundary Conditions in Sph. *Int. J. Numer. Meth. Fluids* 61, 709–724. doi:10.1002/fld.1971

Li, J., Liu, H., Gong, K., Tan, S. K., and Shao, S. (2012). Sph Modeling of Solitary Wave Fissions over Uneven Bottoms. *Coastal Eng.* 60, 261–275. doi:10.1016/j.coastaleng.2011.10.006

Liang, D., Jian, W., Shao, S., Chen, R., and Yang, K. (2017). Incompressible Sph Simulation of Solitary Wave Interaction with Movable Seawalls. *J. Fluids Structures* 69, 72–88. doi:10.1016/j.jfluidstructs.2016.11.015

Liu, G.-R., and Liu, M. B. (2003). Smoothed Particle Hydrodynamics: A Meshfree Particle Method *(World Scientific)*.

Liu, W., Hou, Q., Lian, J., Zhang, A., and Dang, J. (2020). Coastal Pollutant Transport Modeling Using Smoothed Particle Hydrodynamics with Diffusive Flux. *Adv. Water Resour.* 146, 103764. doi:10.1016/j.advwatres.2020.103764

Long, T., Hu, D., Wan, D., Zhuang, C., and Yang, G. (2017). An Arbitrary Boundary with Ghost Particles Incorporated in Coupled FEM-SPH Model for FSI Problems. *J. Comput. Phys.* 350, 166–183. doi:10.1016/j.jcp.2017.08.044

Lucy, L. B. (1977). A Numerical Approach to the Testing of the Fission Hypothesis. *astronomical J.* 82, 1013–1024. doi:10.1086/112164

Monaghan, J. J. (1994). Simulating Free Surface Flows with Sph. *J. Comput. Phys.* 110, 399–406. doi:10.1006/jcph.1994.1034

Monaghan, J. J. (2005). Smoothed Particle Hydrodynamics. *Rep. Prog. Phys.* 68, 1703–1759. doi:10.1088/0034-4885/68/8/r01

Nguyen, M. T., Aly, A. M., and Lee, S.-W. (2018). Isph Modeling of Natural Convection Heat Transfer with an Analytical Kernel Renormalization Factor. *Meccanica* 53, 2299–2318. doi:10.1007/s11012-018-0825-3

Pu, J. H., Cheng, N.-S., Tan, S. K., and Shao, S. (2012). Source Term Treatment of Swes Using Surface Gradient Upwind Method. *J. hydraulic Res.* 50, 145–153. doi:10.1080/00221686.2011.649838

Ramos-Becerra, G., Moulinec, C., Emerson, D., and Gu, X. (2009). "Inlet-outlet Boundary Conditions and Truly Incompressible Sph," in Proc 4th ERCOFTAC SPHERIC workshop, Nantes, France, 226–231.

Randles, P. W., and Libersky, L. D. (1996). Smoothed Particle Hydrodynamics: Some Recent Improvements and Applications. *Comp. Methods Appl. Mech. Eng.* 139, 375–408. doi:10.1016/s0045-7825(96)01090-0

Rao, D., and Bai, B. (2020). Study of the Factors Influencing Diffusive Tortuosity Based on Pore-Scale Sph Simulation of Granular Soil. *Transp Porous Med.* 132, 333–353. doi:10.1007/s11242-020-01394-0

Rezavand, M., Zhang, C., and Hu, X. (2020). A Weakly Compressible Sph Method for Violent Multi-phase Flows with High Density Ratio. *J. Comput. Phys.* 402, 109092. doi:10.1016/j.jcp.2019.109092

Rodriguez-Paz, M., and Bonet, J. (2005). A Corrected Smooth Particle Hydrodynamics Formulation of the Shallow-Water Equations. *Comput. Structures* 83, 1396–1410. doi:10.1016/j.compstruc.2004.11.025

Stoker, J. J. (1948). The Formation of Breakers and Bores the Theory of Nonlinear Wave Propagation in Shallow Water and Open Channels. *Comm. Pure Appl. Math.* 1, 1–87. doi:10.1002/cpa.3160010101

Tartakovsky, A. M., Meakin, P., Scheibe, T. D., and Eichler West, R. M. (2007). Simulations of Reactive Transport and Precipitation with Smoothed Particle Hydrodynamics. *J. Comput. Phys.* 222, 654–672. doi:10.1016/j.jcp.2006.08.013

Vacondio, R., Rogers, B. D., Stansby, P. K., and Mignosa, P. (2012). Sph Modeling of Shallow Flow with Open Boundaries for Practical Flood Simulation. *J. Hydraul. Eng.* 138, 530–541. doi:10.1061/(asce)hy.1943-7900.0000543

Vacondio, R. (2010). *Shallow Water and Navier-Stokes Sph-like Numerical Modelling of Rapidly Varying Free-Surface Flows*.

Wu, Y., Tian, L., Rubinato, M., Gu, S., Yu, T., Xu, Z., et al. (2020). A New Parallel Framework of Sph-Swe for Dam Break Simulation Based on Openmp. *Water* 12, 1395. doi:10.3390/w12051395

Xia, X., Liang, Q., Pastor, M., Zou, W., and Zhuang, Y.-F. (2013). Balancing the Source Terms in a Sph Model for Solving the Shallow Water Equations. *Adv. Water Resour.* 59, 25–38. doi:10.1016/j.advwatres.2013.05.004

Zhang, A.-m., Sun, P.-n., Ming, F.-r., and Colagrossi, A. (2017a). Smoothed Particle Hydrodynamics and its Applications in Fluid-Structure Interactions. *J. Hydrodyn* 29, 187–216. doi:10.1016/s1001-6058(16)60730-8

Zhang, C., Hu, X. Y., and Adams, N. A. (2017b). A Weakly Compressible Sph Method Based on a Low-Dissipation Riemann Solver. *J. Comput. Phys.* 335, 605–620. doi:10.1016/j.jcp.2017.01.027

Zhang, C., Rezavand, M., and Hu, X. (2021a). A Multi-Resolution Sph Method for Fluid-Structure Interactions. *J. Comput. Phys.* 429, 110028. doi:10.1016/j.jcp.2020.110028

Zhang, C., Rezavand, M., Zhu, Y., Yu, Y., Wu, D., Zhang, W., et al. (2021b). Sphinxsys: An Open-Source Multi-Physics and Multi-Resolution Library Based on Smoothed Particle Hydrodynamics. *Comp. Phys. Commun.* 267, 108066. doi:10.1016/j.cpc.2021.108066

Zhang, C., Wang, J., Rezavand, M., Wu, D., and Hu, X. (2021c). An Integrative Smoothed Particle Hydrodynamics Method for Modeling Cardiac Function. *Comp. Methods Appl. Mech. Eng.* 381, 113847. doi:10.1016/j.cma.2021.113847

Zheng, X. P. (2017). *The application of the sph method in dam-break water flow simulation*. Qinghai Provence, China: Qinghai University.

Zhu, Y., and Fox, P. J. (2001). Smoothed particle hydrodynamics model for diffusion through porous media. *Transport in Porous Media* 43, 441–471. doi:10.1023/a:1010769915901

Conflict of Interest: The authors declare that the research was conducted in the absence of any commercial or financial relationships that could be construed as a potential conflict of interest.

frontiers
in Environmental Science

ORIGINAL RESEARCH
published: 01 March 2022
doi: 10.3389/fenvs.2022.858692

Numerical Simulation of Alpine Flash Flood Flow and Sedimentation in Gullies With Large Gradient Variations

Yufei Ding, Xingnian Liu and Ridong Chen*

State Key Laboratory of Hydraulics and Mountain River Engineering, College of Water Resource and Hydropower, Sichuan University, Chengdu, China

Compared with floods occurring over plains, alpine flash floods are formed over scattered locations with complex terrain and data is often lacking regarding the land topography, flow and sedimentation, causing difficulties when developing mathematical models to predict flash floods. The existing flash flood models mainly focus on the influence of water flow, such as the sharp increase in flow discharge caused by convergence at steep slopes, disregarding the sediment load carried by the water flow. However, under the effect of high-intensity sediment transport, the sedimentation in gullies may lead to surges in water level, causing the phenomenon of "great disasters resulting from minor flooding". In this study, an efficient and accurate water-sediment coupling model was established with a Godunov-type finite volume method based 2D flow model, and a sediment module and OPENMP parallel computing module were added as well. Firstly, a common gully in mountainous area with large gradient variations was used as a generalized model to explore the impact of sedimentation on the flow field of the gully and compared with the physical model. Then, the alpine flash flood incident in Gengdi Village was simulated with the computer model. The calculation results show that the high-intensity sedimentation significantly increased the magnitude of alpine flash floods. Calculated by this mathematical model, the research results verified that this mathematic model can efficiently, accurately and concisely predict the occurrence of flash floods in gullies with large gradient variations. The model also provides a flow and sediment modeling method that incorporates the effect of high-intensity sediment transport into the traditional flash flood flow model. Thus, this model can be a powerful tool for detecting flash floods.

Keywords: flash flood, high-intensity sediment transport, 2D flow and sediment simulation, gully with large gradient variations, Gengdi village

Edited by:
Jaan H. Pu,
University of Bradford,
United Kingdom

Reviewed by:
Jiarui Lei,
National University of Singapore,
Singapore
Saiyu Yuan,
Hohai University, China

****Correspondence:***
Ridong Chen
chenridong1984@163.com

Specialty section:
This article was submitted to
Freshwater Science,
a section of the journal
Frontiers in Environmental Science

Received: *20 January 2022*
Accepted: *31 January 2022*
Published: *01 March 2022*

Citation:
Ding Y, Liu X and Chen R (2022)
Numerical Simulation of Alpine Flash
Flood Flow and Sedimentation in
Gullies With Large Gradient Variations.
Front. Environ. Sci. 10:858692.
doi: 10.3389/fenvs.2022.858692

1 INTRODUCTION

Short-term high-intensity rainfall may cause flash flooding in mountainous regions, bringing large amounts of sediment (Reid et al., 1998). The situation can rapidly evolve into natural disasters such as landslides and mudslides, causing huge destructions such as the collapse of bridges, damage to buildings, traffic interruptions, and casualties (Hapuarachchi et al., 2011). Flood waters mixed with large amounts of sediment flows into the gully, absorbing energy from the flow which leads to increased flow resistance. Meanwhile, the sediment load in the flash flood is greater than the sediment-carrying capacity of the water flow. As a result, sediment deposits and quickly builds up in certain areas, resulting in an increase in water level, which endangers the buildings on the river bank,

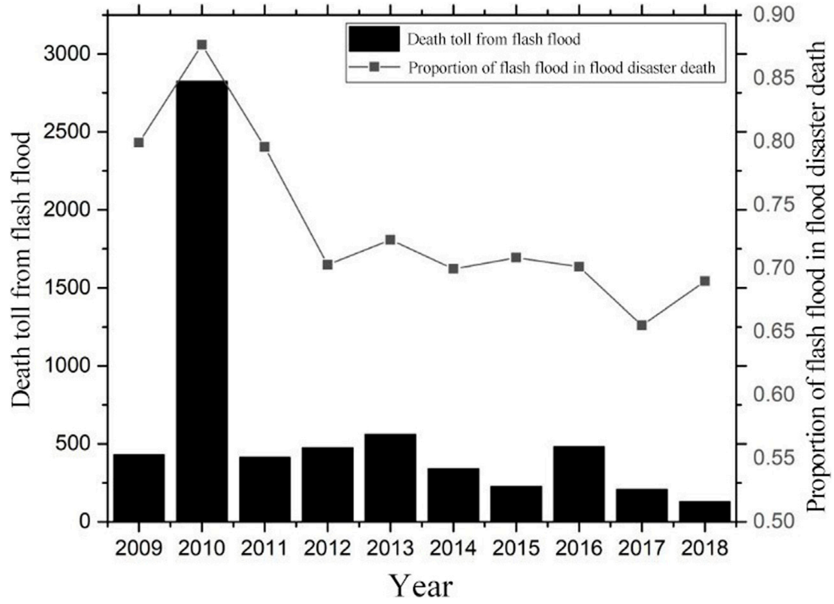

FIGURE 1 | The number of people affected by flash floods during 2009–1018.

leading to the phenomenon that minor floods can cause great disasters. Every year in China, the loss of life and property caused by flash floods accounts for about 40% of the total loss caused by natural disasters. As shown in **Figure 1**, the annual average death toll from flash floods during 2009–2018 was 608, accounting for 78.1% of the death toll from floods. In 2010, the catastrophic debris flow disaster in Zhouqu, Gansu caused 1,744 deaths and a direct economic loss of 0.4 billion CNY (Ministry of water resources of the people's republic of China, 2018). As flash floods often occur suddenly in remote mountainous regions that are lacking in observational data, there is a great degree of technical difficulty and uncertainty in evaluating pre-disaster risk, or for monitoring, providing early alerts and planning for post-disaster emergency rescue. The key to lessening the destruction caused by flash floods is to provide accurate and early alerts in time to take remedial actions and respond to the disaster.

America, Britain, Australia and China have taken the lead in studying the mechanism of flash floods and forecasting their occurrence (Penning-Rowsell et al., 2000; Handmer, 2001; Liu et al., 2018; Shan et al., 2018). As more knowledge was gained regarding the mechanism, it became clear that establishing an efficient and reliable flash flood numerical model is of great significance for the accurate forecasting of flash floods. The current trend is to establish a 1D or 2D hydraulic model for areas vulnerable to flash flooding. The hydraulic model is mainly based on shallow water equations and uses the Saint-Venant equations for fluid calculations (Piotrowski et al., 2006). Norbiato et al. (2007) used the CARIMA 1D unsteady flow model to reproduce the catastrophic flash floods that occurred in the Gard region of France in September 2002, and they calculated the peak flow at each key station during the flash flooding. Kobold and Brilly (2006) used a 1D numerical model to evaluate the impact of open-channel flash floods on riverbeds and dams in mountainous areas. Om (1976) used clear water scouring and high-intensity sediment input to carry out 1D numerical simulations on alpine rivers with steep slopes, and they analyzed the post-flood longitudinal deposition form. Compared with 2D models, 1D models require less data, calculation time and computer memory. However, 1D models cannot accurately calculate the hydraulic elements when there are large and irregular changes in the terrain of the alpine rivers. As a result, the results from flash floods simulations have been poor (Sirdaş and Şen, 2007).

2D models can provide some calculations for river channel flow fields under flash flooding, such as the flow depth and velocity vector at each grid point, and the flow field can also be accurately simulated with high accuracy without the need to interpolate by refining the grid. The finite element method and the finite volume method are numerical modeling methods commonly used for 2D water flow simulations. In the finite element method, there is freedom to choose the basic functions that will be used, and elements of various shapes can be used to fit the complex geometric shapes. In addition, simulation accuracy can be improved by establishing higher-order polynomials in a numerically discrete process (Aizinger, 2004). The finite element method mainly uses implicit algorithms and the calculation efficiency is relatively fast. However, self-adaptation and stability problems have always plagued the development of continuous finite element methods. Therefore, the accuracy of the algorithm is poor for fluids dominated by convection. Since only the net flux balance on the domain boundary can be guaranteed, we can therefore only guarantee local conservation and not global conservation.

Finite element methods can work well to model rivers in plain regions, but they often become invalid when they are used to model alpine flash floods. This is because intermittent flow of shallow water often occurs in the flooding process, causing abrupt changes in the water level and flow rate. Meta-methods often fail to solve discontinuous problems. In recent years, Godunov-type finite volume methods are often used to solve hyperbolic conservation equations, such as shallow water equations, due to their unique built-in mechanisms to capture shock. Starting from differential equations in integral form, this method uses the principles of the Riemann problem to solve the equations, which makes this method suitable for solving discontinuous problems (Li, 2006). The solution domain is divided into multiple non-overlapping sub-domains, and the design variables are assumed to be constant in the sub-domains, such that the Riemann problem is formed at the interface of the sub-domains. By solving the Riemann problem at the interface, the flux through the interface can be calculated to determine the flux passing through the interface (Chen et al., 2015). The intermittent flooding process simulated in this method not only correctly simulates the discontinuous propagation velocity, but also simulates the sharp discontinuous shape and essentially solves the non-physical oscillation problem of the high-order precision differential scheme near the discontinuity. This method has become the main method for solving the water flow in mountainous rivers and gullies with large gradient variations (Li, 2006).

Based on the finite volume method theory, Wang et al. (2009) adopted the second-order WAF-TVD scheme to effectively capture spatial shock waves. They also adopted the first-order Runge-Kutta method, and utilized an adaptive time step to satisfy the numerical stability requirement. In this way, their model was able to maintain high calculation efficiency when dealing with complex landforms and quantifying the critical rainfall conditions of alpine flash floods. Juez et al. (2013) first established a global coordinate system and a local coordinate system. Subsequently, they used an approximate Riemann solver to simulate flash flood events for slopes with varying degrees of steepness in mountainous regions. They obtained good results with this method. El Kadi Abderrezzak et al. (2009) developed Rubar20, a 2D hydraulic model, based on the second-order Godunov format Monotonic Upstream Schemes for Conservation Laws (MUSCL), and they verified the accuracy of this model through generalization experiments. Simulations of the conditions for two different terrains were used to verify the influence of terrain on flood propagation. Liang et al. (2016) et al. used a GPU-accelerated High-Performance Integrated Hydrodynamic Modeling System (HiPIMS) to simulate the flash flooding processes in the Glasgow region of Scotland and the Haltwhistle watershed in England based on local precipitation information. They modified the bottom slope source term to prevent the Godunov's algorithm from generating incorrect water depths.

The current research on the mechanism of alpine flash floods mainly focuses on studying the sharp increase in water flow during flash flooding caused by the convergence at steep slopes in mountainous rivers (Weishuai, 2013). In certain cases, flash flooding may occur even though the flood flow does not exceed the standard water flow. High-intensity sediment transport and the unique features of alpine rivers, such as slopes with high degrees of steepness, river widths that alternate between wide and narrow, and a high number of tributaries, lead to a strange phenomenon in the evolution of the river bed. When a large amount of sediment is transported downstream, deposition builds-up on the frontal surface and begins to extend in reverse upstream, causing the water level to increase to many times greater than the normal level. In this way, even minor flooding can lead to great disasters.

Regarding the additional damage caused by high-intensity sediment transport during flash floods, Zheng et al. (2019) used a 2D bed flow model to simulate the dynamic and hydraulic processes of a steep river channel with varying degrees of steepness, and under conditions of sufficient sediment replenishment. They proposed the critical triggers for retrograde deposition in alpine gullies during flash floods. Guan et al. (2013) simulated the alpine flash flooding process based on a 2D flow and sediment coupling model. They found that the water flow has a high sediment-carrying capacity at flood peak, leading to reduced deposition in the river bed. A large amount of siltation increases the roughness of the river bed, thereby reducing the flow rate and promoting deposition. Yuntian et al. (2019) reproduced the "7.21" flash flood in Hongluogu Gully of Beijing by using a hydrologic and hydrodynamic sediment transport model and discovered that sediment transport has a significant impact on the spatial distribution of flood eigenvalues, such as the maximum flood level and flow rate. Under the combined action of changes in resistance and riverbed erosion and deposition, the maximum flood level of each section increased globally versus the fixed bed state. Pu et al. (2014) proposed a time-varying approach to simulate the sediment erosion-deposition rate, this method improved the simulation accuracy for fast moving flows in the gullies. Roca et al. (2009) conducted a field investigation and 2D numerical simulation study on a 90° confluence area in the Mediterranean region. They found that in flash flooding, the addition of sediment created an interesting effect in the flood movement; not only did the surface roughness of the tributary streams increase, but the sediment transport also determined the topographical changes in the confluence area.

It can be seen that there exist some limitations in the current alpine flash flood models, such as lack of research on the sediment modules, lack of data on the hydrological and topographical conditions of alpine rivers, and low efficiency of explicit algorithms for Godunov-type hyperbolic equations. Therefore, a new set of models is proposed in this paper to efficiently and accurately simulate the dynamic water flow and sedimentation processes during alpine flash flooding events in gullies with large varying gradients and high-intensity sediment transport.

The reliability of this mathematical model was verified with data from a variable-slope gully model and the flash flood event in Gengdi Village. When the boundary conditions, such as the water flow, sedimentation and topographical features were missing (such as in the flash flood event in Gengdi Village), the flow discharge in the disaster area was forecasted based on a Geomorphologic Instantaneous Unit Hydrograph (GIUH) model, the rainfall data at the actual location of occurrence and time of flash flooding, and the DEM data of a 12 m local grid. The flow and sediment model adopted the standard

Godunov method to solve the shallow water equation that splits the source term of shear stress. Next, the second-order weighted average flux (WAF) method with TVD format was used to calculate the flux of unit interface, where the Riemann solver was an HLL solver and the WAF limit function was Van Leer's limit function (Zhou et al., 2001). In order to eliminate the iterative error in the calculation of the source term, the surface gradient method was used to solve the source term, where the surface elevation of each point was used instead of the water depth. The sediment module includes calculations for the suspended load and bed load. The upwind method was used to calculate the suspended load content in flash floods, and Zhang Ruijin's improved formula was used to calculate the sediment-carrying capacity of the water flow. Next, the saturated sediment transport model was used to calculate the bed load and sediment transport rate, and finally the deformation of the river bed was predicted. Furthermore, an OPENMP interface was added to the model based on the flow and sediment modules to perform multi-core parallel calculations of the flash flooding process, which greatly improved the calculation efficiency compared with conventional serial computation methods.

2 MATERIALS AND METHODS

2.1 Flow Model

2.1.1 2D Shallow Water Equation

During flash floods, the water flow movement and the load transported by the flow generally behave like 3D flow, and the mathematical model should simulate the hydrodynamic process in 3D form in order to fully reflect its features. However, due to the complexity of 3D water flow, many research studies have often simplified the flow of shallow water by averaging the moving elements in the direction of water depth, thus transforming the 3D problem into a 2D problem.

Given the assumption that vertical acceleration can be ignored and the water pressure is distributed as hydrostatic pressure along the direction of water depth, an average value was introduced in the direction of water depth in the Cartesian coordinate system, and viscous stress was ignored. Based on NS equation, the 2D shallow water equation can be derived.

$$\frac{\partial \boldsymbol{U}}{\partial \boldsymbol{t}} + \nabla \cdot \boldsymbol{F} = \boldsymbol{S} \tag{1}$$

In the equation, U is the vector of conserved variables; F is the vector flux; and S is the source term vector. U and $F\ (U)$ are calculated as follows:

$$\boldsymbol{U} = \begin{pmatrix} \phi \\ \phi u \\ \phi v \end{pmatrix} \tag{2}$$

$$\boldsymbol{F} = \begin{pmatrix} \phi V \\ \phi u V + \frac{1}{2}\phi^2 i \\ \phi v V + \frac{1}{2}\phi^2 j \end{pmatrix} \tag{3}$$

In the equations, $\phi = gh$ is the gravitational potential; u is the flow rate in the x direction; v is the flow rate in the y direction; $V = ui + vj$ represents the velocity vector; $g = 9.81 m^2/s$ is the acceleration of gravity; and h is the water depth.

In many engineering applications, the source term S includes components such as the geostrophic deflecting force, wind force, and bottom friction. For the simulations performed in this research, the source term S is composed of the bottom slope source term S_b and the bottom friction source term S_f, namely $S = S_b + S_f$, where S_b and S_f can be expressed as follows:

$$\boldsymbol{S_b} = \begin{pmatrix} 0 \\ g\phi \frac{\partial \boldsymbol{H}}{\partial \boldsymbol{x}} \\ g\phi \frac{\partial \boldsymbol{H}}{\partial \boldsymbol{y}} \end{pmatrix} \tag{4}$$

$$\boldsymbol{S_f} = \begin{pmatrix} 0 \\ -\frac{\boldsymbol{g}}{\boldsymbol{\rho}}\boldsymbol{\tau_{fx}} \\ -\frac{\boldsymbol{g}}{\boldsymbol{\rho}}\boldsymbol{\tau_{fy}} \end{pmatrix} \tag{5}$$

$$\boldsymbol{\tau_{fx}} = \boldsymbol{\rho g n^2 u}\sqrt{\boldsymbol{u}^2 + \boldsymbol{v}^2}\ \frac{1}{\boldsymbol{R}^{\frac{1}{3}}} \tag{6}$$

$$\boldsymbol{\tau_{fy}} = \boldsymbol{\rho g n^2 v}\sqrt{\boldsymbol{u}^2 + \boldsymbol{v}^2}\ \frac{1}{\boldsymbol{R}^{\frac{1}{3}}} \tag{7}$$

In the equations, H is the difference between the fixed horizontal base level and the bottom elevation; ρ is density; τ_{fx} and τ_{fy} are the friction stresses of the river bed in the x and y directions; n is the roughness coefficient; and R is the hydraulic radius, which is used to approximate the water depth, h, in the open channel.

2.1.2 Godunov-type Method

The shallow water equation is a nonlinear hyperbolic partial differential equation and calculating the grid interface flux is an important step in solving the hyperbolic equation. The first-order algorithm has too much dissipation when it uses the unit average to calculate the flux of the interface, smoothing out what should be a steep shock wave (Roe, 1997). Therefore, higher-order formats, such as the second-order TVD method, are favored by researchers around the world. For higher-order Godunov problems, the second-order format is usually obtained using piecewise linear reconstruction of the local variables in the center of the grid.

Due to the existence of non-zero source terms (bottom slope source term and shear stress source term), the non-homogeneous partial differential **Eq. 1** can be separated and decomposed into the homogeneous partial differential, **Eq. 8**, and the ordinary differential **Eq. 9**, using only the bottom slope source term and the shear stress source term. The equations were solved in two steps: estimation and correction. Namely, the estimation step with a step size of $(\Delta t)/2$ was first used to solve the source term U; then, the solved U was substituted into the correction step with step size of Δt.

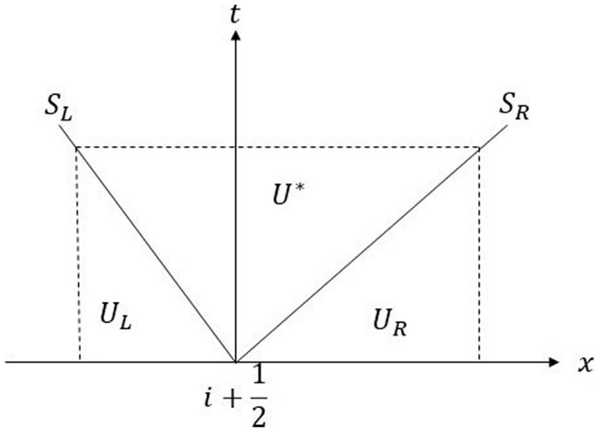

FIGURE 2 | Approximate Riemann solver of HLL scheme.

$$\frac{\partial \boldsymbol{U}}{\partial \boldsymbol{t}} + \nabla \cdot \boldsymbol{F} = 0 \tag{8}$$

$$\frac{\boldsymbol{dU}}{\boldsymbol{dt}} = \boldsymbol{S_b} + \boldsymbol{S_f} \tag{9}$$

When the source term of the bottom slope is 0 and the viscosity of the water is ignored; the water depth h can be used to accurately calculate the gravitational potential gradient $\delta\phi_i$. However, the impact from changes in the river bed surface should be considered during an actual flash flood. Hence, the water depth at the unit interface cannot be accurately determined if the gravitational potential is taken as the conserved term. This is because the depth gradient cannot reproduce true water depth variations. So various numerical methods have been developed to improve the treatment of source terms in the shallow water equations (Pu et al., 2012). The surface gradient upwind method (SGUM) proposed by Hui Pu et al. (2013) and surface gradient method (SGM) proposed by Zhou et al. (2001) proved that the hyperbolic equation is conserved when using surface elevation instead of water depth for gradient calculations. Therefore, the algorithm subtracts the river bottom elevation from the surface elevation η_i of each point, instead of using the water depth, h_i, to calculate the conservation term, ϕ, thereby ensuring the conservation of the bottom slope source term.

In this paper, to solve the **Eq. 8**, the numerical solution consists of two steps: prediction and correction, and they are shown, respectively, in **Eqs 10**, **11**.

$$(\boldsymbol{AU})_i^{n+\frac{1}{2}} = (\boldsymbol{AU})_i^n - \frac{\Delta \boldsymbol{t}}{2}\left(\sum_{m=1}^{M} \boldsymbol{F}(\boldsymbol{U_m})^n \cdot \boldsymbol{L_m}\right) \tag{10}$$

$$(\boldsymbol{AU})_i^{n+1} = (\boldsymbol{AU})_i^n - \Delta \cdot \boldsymbol{t}\left(\sum_{m=1}^{M} \boldsymbol{F}\left(\boldsymbol{U}_m^L, \boldsymbol{U}_m^R\right)^{n+\frac{1}{2}} \cdot \boldsymbol{L_m}\right) \tag{11}$$

where, A is the area of the grid; $\boldsymbol{L_m}$ is the side vector of the grid, which is defined as the cell edge length multiplied by the outward-pointing unit normal vector; M is the number of cell edges; $F(\boldsymbol{U_m})^n$ is the unit interface flux of the m-th side of each grid at the n-th time; $F(\boldsymbol{U}_m^L, \boldsymbol{U}_m^R)^{n+\frac{1}{2}}$ is the m-th edge unit grid interface flux of the correction step after the prediction step.

The computational workload required to solve the equations is relatively large; hence, approximate Riemann solutions in formats such as Roe, Osher, and HLL are often used to reduce the processing time. In this paper, the WAF method and HLL format were used to calculate the interface flux. The WAF interface flux (Cao et al., 2004) can be written as follows:

$$\boldsymbol{F}_{i+\frac{1}{2}} = \frac{1}{2}\left(\boldsymbol{F_i} + \boldsymbol{F}_{i+1} - \frac{1}{2}\sum_{k=1}^{N} \boldsymbol{c_k} \Delta \boldsymbol{F}_{i+\frac{1}{2}}^{(k)}\right) \tag{12}$$

where, c_k is the Courant number corresponding to the velocity S_k of the k-th train wave.

$$\boldsymbol{c_k} = \frac{\Delta \boldsymbol{t} \boldsymbol{S_k}}{\Delta \boldsymbol{x}} \tag{13}$$

The HLL scheme (Hubbard and Dodd, 2002) is a two-wave train model. The Riemann problem is simplified into three conserved regions separated by two waves, S_L and S_R. The interfaces of the three regions are as shown in **Figure 2**.

In **Figure 2**, U_L and U_R represent the conservation vectors on the left and right sides of the interface; U^* represents the intra-interface vector; while S_L and S_R represent the velocities of waves on the left and right sides of the interface. The HLL scheme can be calculated using the following formula:

$$\boldsymbol{F}_{i+\frac{1}{2}}^{hll} = \begin{cases} \boldsymbol{F_L} & 0 \le \boldsymbol{S_L} \\ \dfrac{\boldsymbol{S_R F_L} - \boldsymbol{S_L F_R} + \boldsymbol{S_L S_R}(\boldsymbol{U_R} - \boldsymbol{U_L})}{\boldsymbol{S_R} - \boldsymbol{S_L}} & \boldsymbol{S_L} \le 0 \le \boldsymbol{S_R} \\ \boldsymbol{F_R} & 0 \ge \boldsymbol{S_R} \end{cases} \tag{14}$$

where, S_L and S_R (Toro, 1992) can be estimated as:

$$\boldsymbol{S_L} = \boldsymbol{min}\left(\boldsymbol{u_i} - \sqrt{\phi_i}, \boldsymbol{u_s} - \sqrt{\phi_s}\right), \ \boldsymbol{S_R} = \boldsymbol{max}\left(\boldsymbol{u}_{i+1} + \sqrt{\phi_{i+1}}, \boldsymbol{u_s} + \sqrt{\phi_s}\right) \tag{15}$$

$$\boldsymbol{u_s} = \frac{1}{2}(\boldsymbol{u}_{i+1} + \boldsymbol{u_i}) + \sqrt{\phi_i} - \sqrt{\phi_{i+1}} \tag{16}$$

$$\sqrt{\phi_s} = \frac{\sqrt{\phi_i} + \sqrt{\phi_{i+1}}}{2} + \frac{\boldsymbol{u_i} - \boldsymbol{u}_{i+1}}{4} \tag{17}$$

The wave velocity algorithm described above is applicable for wet boundaries. For dry and wet mesh boundaries, Da Silva (2017) proposed a corrected model. When the left river bed is dry, the following calculation can be used:

$$\boldsymbol{S_L} = \boldsymbol{u_i} - \sqrt{\phi_i}, \qquad \boldsymbol{S_R} = \boldsymbol{u_i} + 2\sqrt{\phi_i} \tag{18}$$

When the right river bed is dry:

$$\boldsymbol{S_L} = \boldsymbol{u}_{i+1} - 2\sqrt{\phi_{i+1}}, \qquad \boldsymbol{S_R} = \boldsymbol{u}_{i+1} + \sqrt{\phi_{i+1}} \tag{19}$$

After the homogeneous equations were corrected, the total differential **Eq. 9** was decomposed, and the estimation step discrete equation of S_b is determined as follows:

$$\boldsymbol{S_b} = \boldsymbol{g}\phi\frac{\partial \boldsymbol{H}}{\partial \boldsymbol{x}} = \frac{\partial}{\partial \boldsymbol{x}}\left(\frac{1}{2}\phi^2\right) \tag{20}$$

$$(\boldsymbol{AU})_i^{n+\frac{1}{2}} = (\boldsymbol{AU})_i^n + \frac{\Delta \boldsymbol{t}}{2}\sum_{m=1}^{M}\left(\frac{1}{2}\phi^2\right)^n \cdot \boldsymbol{L_m} \tag{21}$$

For S_f, the algorithm adopted a forward difference scheme to solve the final flux $(AU)_i^{n+\frac{1}{2}}$ of the estimation step; then the final flux was substituted into **Eq. 11** before iteration of the correction step. Finally, Δt was used as the step size to calculate $(AU)_i^{n+1}$ in the total differential equation.

In order to ensure the stability of the numerical scheme, the display algorithm needs to adjust the time step Δt at each calculation step to reduce the deviation in the propagation of the source term along the characteristic line, thereby ensuring the stability of the algorithm and the accuracy of the numerical solution. The Courant number CFL should satisfy the following condition (LeVeque, 2002):

$$0 \le CFL \le 1 \tag{22}$$

In this paper, the value of CFL was assumed to be 0.9 to ensure the stability of the algorithm. Step Δt was calculated as per the following formula:

$$\Delta t = CFL\frac{\Delta x}{max\, 1 \le i \le M\left(\left|u_i - \sqrt{\phi_i}\right|, \left|u_{i+1} - \sqrt{\phi_{i+1}}\right|\right)} \tag{23}$$

2.2 Sediment Model

Flash floods are a type of disaster that can occur suddenly, and not only do they carry small-sized sediments, but they can also carry large-sized sediments, such as pebbles and gravel. This ability to carry large-sized sediments is a unique feature of alpine rivers and the rivers are subjected to long-term coarsening. Large calculation errors will occur if the sediments are assumed to be uniform. Therefore, the calculation of the grouped sediment transport capacity of non-uniform sediments is one of the key issues to be resolved in the mathematical modelling of river sediment. The idea of a grouped sediment model was first proposed by Einstein. Based on Einstein's initial idea, Misri, Chiodi et al. established and verified a grouped sediment transport model (Misri et al., 1984; Chiodi et al., 2014). In this research study, the sediments were grouped and arranged by particle size, from small to large. The median size of each sediment group was used for detailed calculations.

The sediment settling velocity was used as the basis for the sediment calculation module. Zhang Ruijin's formula was used in this research study, and the formula is as follows (Tan et al., 2018):

$$\omega = \sqrt{\left(13.95\frac{\nu_t}{d_i}\right)^2 + 1.09\frac{\gamma_s - \gamma}{\gamma}gd_i} - 13.95\frac{\nu_t}{d_i} \tag{24}$$

where, ν_t is the horizontal eddy viscosity coefficient; and d_i is the median size of a sediment group.

The sediment transport model consists of the sediment transport equation and the river bed deformation equation. The sediments can be divided into bed load and suspended load according to their particle size. The basic equations of the 2D sediment model are as follows:

$$\frac{\partial hS}{\partial t} + \frac{\partial uhS}{\partial x} + \frac{\partial vhS}{\partial y} = \frac{\partial}{\partial x}\left(h\nu_t\frac{\partial S}{\partial x}\right) + \frac{\partial}{\partial y}\left(h\nu_t\frac{\partial S}{\partial y}\right) + \alpha\omega\left(S^* - S\right) \tag{25}$$

$$(1-\lambda)\frac{\partial z_b}{\partial t} + \frac{\partial g_{bx}}{\partial x} + \frac{\partial g_{by}}{\partial y} = \frac{\alpha\omega}{\rho_s}\left(S - S^*\right) \tag{26}$$

In the above equations, ω is the deposition velocity, S^* and S are the suspended load carrying capacity and the suspended load content, respectively; and α is the scouring coefficient. When deposition is obvious, $\alpha = 0.25$; when scouring and deposition are alternated, $\alpha = 0.5$; when scouring is obvious, $\alpha = 1$. z_b is the thickness of the movable layer; λ is the porosity; g_{bx} and g_{by} are the bed load transport rates.

Liu et al. (1991) proposed the Rz number to differentiate the particle sizes of the suspended load and bed load, where:

$$Rz = \frac{\omega}{ku^*} \tag{27}$$

In the above equation, $k = 0.41$ is the Karman constant and u^* is the friction velocity. When $Rz > 4.166$, the sediment is in the bed load, and when $Rz \le 4.166$, the sediment is in the suspended load.

2.1.3 Suspended Load Calculation

The key to calculating the suspended load is to determine the suspended matter content, S, and sediment-carrying capacity, S^*, of the river. S was calculated using the finite volume method with a first-order upwind finite volume method. The regions upstream and downstream of the adjacent grids were judged according to the flux in the normal direction of the common grid interface, and the sediment flux at each interface of the grid was calculated. Furthermore, the sediment flux at each interface was integrated at the specified time step to obtain the suspended load content of the grid. This algorithm can unconditionally guarantee the stability of the suspended load content calculations.

There has not been much research on the sediment-carrying capacity of 2D water flow. Therefore, the sediment-carrying capacity of most 2D mathematic models is usually calculated directly using a 1D sediment-carrying capacity formula or a modified formula. Since the suspended load particles are small, the sediment particles were divided into finer groups in the algorithm. The median size of each group of particles is directly used to calculate the sediment-carrying capacity for the suspended load group. The most commonly used formula is the one developed by Zhang Ruijin, which is given below (Tan et al., 2018):

$$S^* = k\left(\frac{\sqrt{u^2 + v^2}}{gh\omega}\right)^m \tag{28}$$

In the above equation, k and m are the empirical constants of the model's sediment-carrying capacity, which were derived based on the experimental data collected from the Yangtze River, the Yellow River, several reservoirs, and indoor water channels. Hence, the empirical constants have a high degree of universality. Theoretically, Zhang Ruijin's indexless formula can be coordinated with Bagnold's energy formula; and by improving

Zhang Ruijin's formula, the comprehensive coefficient K_1 can be obtained as shown below:

$$\boldsymbol{\Phi} = \boldsymbol{K}_1 \frac{\gamma_m}{\gamma_s - \gamma_m} \frac{\sqrt{\boldsymbol{u}^2 + \boldsymbol{v}^2}}{\boldsymbol{gh}\omega} \tag{29}$$

$$\boldsymbol{K}_1 = 0.102\left(\frac{\sqrt{\boldsymbol{u}^2 + \boldsymbol{v}^2}}{\boldsymbol{gh}\omega}\right)^{0.6346-0.21611\boldsymbol{lg}\left(\frac{\sqrt{\boldsymbol{u}^2+\boldsymbol{v}^2}}{\boldsymbol{gh}\omega}\right)} \tag{30}$$

In the above formula, γ_m and γ_s are the bulk densities of clear water and sediment, respectively; and Φ is the sediment-carrying capacity, which is equivalent to the S^* term in **Eq. 28**.

In flash floods, the finest and coarsest sediments can differ by more than 100 times, resulting in differences of thousands of times for the settling velocity. Therefore, the mathematical model should calculate the sediment-carrying capacity per group. The sediment-carrying capacity needs to be considered in the transport of sediments suspended in the water and the erosion of the river bed. When the sediment-carrying capacity is greater than the sediment content in the water, the bed surface is eroded. The sediment movement should be considered when calculating the erosion sediment-carrying capacity. The sediment can only be scoured when the flood flow rate exceeds the sediment starting velocity. Hence, **Eq. 29** can be improved as follows:

$$\boldsymbol{\Phi}' = \boldsymbol{K}_1 \frac{\gamma_m}{\gamma_s - \gamma_m} \frac{\left(\sqrt{\boldsymbol{u}^2 + \boldsymbol{v}^2} - \boldsymbol{U}_c\right)\left(\boldsymbol{u}^2 + \boldsymbol{v}^2\right)}{\boldsymbol{gh}\omega} \tag{31}$$

In the above formula, U_c is the initial particle size for the group. The formula from the School of Water Resources and Hydropower Engineering of Wuhan University was applied as follows (Tan et al., 2018):

$$\boldsymbol{U}_c = \left(\frac{\boldsymbol{D}}{\boldsymbol{d}_i}\right)^{0.14}\left(17.6\frac{\gamma_s - \gamma_m}{\gamma_m}\boldsymbol{d}_i + 0.000000605\frac{10 + \boldsymbol{D}}{\boldsymbol{d}_i^{0.72}}\right)^{\frac{1}{2}} \tag{32}$$

Therefore, the total carrying rate ϕ_i of the grouped sediment group is as follows (taking the i-th sediment group as an example):

$$\phi_i = \phi_i^s + \phi_i^e = \boldsymbol{\sigma P}_i \Phi(\boldsymbol{\omega}_s) + (1 - \boldsymbol{\sigma})\boldsymbol{p}_{bi}^{'}\phi^{'}(\omega_i) \tag{33}$$

$$\boldsymbol{\sigma} = \boldsymbol{min}[S/\boldsymbol{\Phi}(\boldsymbol{\omega}_s)] \tag{34}$$

$$\boldsymbol{\omega}_s = \boldsymbol{P}_i\boldsymbol{\omega}_i \tag{35}$$

In the above formula, ϕ_i^s is the sediment-carrying capacity of the water flow used for transporting sediment in the water; ϕ_i^e is the sediment-carrying capacity of the water flow used for activating the sediment bed; P_i is the mass ratio of the suspended sediment with this particle size versus the total suspended sediment content; σ is the weight coefficient; and $p_{bi}^{'}$ is the effective gradation of the sediment bed.

The key to solving **Eq. 33** is to calculate the effective gradation of the sediment bed, which is affected by many factors. First, the scouring energy remaining in the water is fully distributed along the water depth so the height of suspended sediments that can be scoured is limited. When the sediments cannot be suspended, the scouring energy that exists in the local water body cannot be used for scouring. Hence, the small sediment transport invariant used for scouring should be related to the suspended height of the scoured sediments. Moreover, the effective gradation of the sediment bed is also greatly affected by how the coarse bed sediments conceal the finer sediments, the effective action of the current drag along the sediment bed surface, and the action of the shear stress on the bed surface (Yang et al., 2020).

Based on the above factors, the effective gradation of the sediment bed can be expressed as follows:

$$\boldsymbol{p}_{bi}^{e} = \frac{\boldsymbol{\eta}_i\boldsymbol{\delta}_i\boldsymbol{P}_i}{\boldsymbol{d}_i\sum\boldsymbol{\eta}_j\boldsymbol{\delta}_j\frac{\boldsymbol{P}_j}{\boldsymbol{d}_j}} \tag{36}$$

In the above formula, δ_i is the suspended sediment height; and η_i is the concealment coefficient. These two values were calculated using the formulas proposed by Lane and Kalinske (1941) and Wu et al. (2000).

2.1.4 Bed Load Calculation

The model utilizes the Mayer-Peter formula to calculate the bed load for particle sizes greater than 0.2 mm and the Sharmov's formula is used to calculate the bed load when particle sizes are less than 0.2 mm.

The Mayer-Peter formula (Chien and Wan, 1999):

$$\boldsymbol{q}_{bx} = 8\sqrt{(\boldsymbol{G} - 1)\boldsymbol{G}\boldsymbol{d}_i^3}\ \frac{\boldsymbol{U}}{\sqrt{\boldsymbol{U}^2 + \boldsymbol{V}^2}}\boldsymbol{max}\left(\boldsymbol{\tau}_* - \boldsymbol{\tau}_{*,c}, 0\right)^{1.5} \tag{37}$$

$$\boldsymbol{q}_{by} = 8\sqrt{(\boldsymbol{G} - 1)\boldsymbol{G}\boldsymbol{d}_i^3}\ \frac{\boldsymbol{V}}{\sqrt{\boldsymbol{U}^2 + \boldsymbol{V}^2}}\boldsymbol{max}\left(\boldsymbol{\tau}_* - \boldsymbol{\tau}_{*,c}, 0\right)^{1.5} \tag{38}$$

$$\boldsymbol{\tau}_* = \frac{\boldsymbol{n}^2\left(\boldsymbol{U}^2 + \boldsymbol{V}^2\right)^{1.5}}{(\boldsymbol{G} - 1)\boldsymbol{d}_i\boldsymbol{D}^{\frac{1}{3}}} \tag{39}$$

In the formula, G is the relative weight of sediment to water; τ_* is the drag force; $\tau_{*,c} = 0.047$ is the initial drag force; and n is the roughness coefficient.

According to Sharmov's formula, U_{OH} is critical maximum velocity of the sediment.

$$\boldsymbol{q}_{bx} = 0.95\sqrt{\boldsymbol{d}_i}\left(\frac{\boldsymbol{U}}{\boldsymbol{U}_{OH}}\right)^3(\boldsymbol{U} - \boldsymbol{U}_{OH})\left(\frac{\boldsymbol{d}_i}{\boldsymbol{D}}\right)^{0.25} \tag{40}$$

$$\boldsymbol{q}_{by} = 0.95\sqrt{\boldsymbol{d}_i}\left(\frac{\boldsymbol{V}}{\boldsymbol{U}_{OH}}\right)^3(\boldsymbol{U} - \boldsymbol{U}_{OH})\left(\frac{\boldsymbol{d}_i}{\boldsymbol{D}}\right)^{0.25} \tag{41}$$

$$U_{OH} = 3.83\boldsymbol{d}_i^{\frac{1}{3}}\boldsymbol{D}^{\frac{1}{6}} \tag{42}$$

2.1.5 River Bed Deformation Calculation

The river bed deformation calculation includes the elevation changes caused by scouring and deposition of bed and suspended matter. **Eq. 26** adopts the time forward difference and integrates the spaces in the grid. Next, the Gaussian deformation was calculated as per the following equation:

$$\int_{\Delta S}(1 - \boldsymbol{\lambda})\frac{\boldsymbol{z}_{\boldsymbol{b}_{new}} - \boldsymbol{z}_{\boldsymbol{b}_{old}}}{\boldsymbol{\Delta t}}\boldsymbol{ds} + \int_{\Delta l}\vec{\boldsymbol{g}}_b\boldsymbol{d}\vec{\boldsymbol{l}} = \int_{\Delta S}\frac{\boldsymbol{\alpha\omega}}{\boldsymbol{\rho}_s}(\boldsymbol{S} - \boldsymbol{S}^*) \tag{42}$$

Namely,

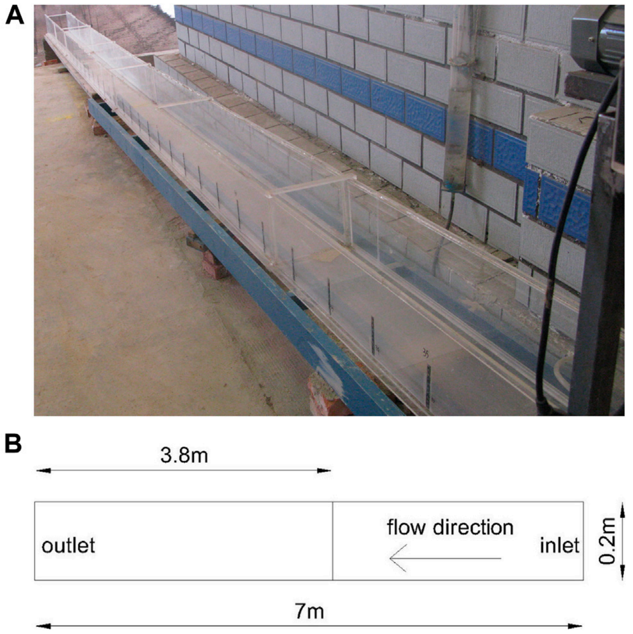

FIGURE 3 | (A) Actual image of the variable slope water channel **(B)** Planar dimensions of the variable slope water channel.

$$z_{b_{new}} = z_{b_{old}} - \frac{\Delta t}{\Delta S}\frac{1}{1-\lambda}\sum\nolimits_{1}^{m} g_{ni}\,dl_i + \frac{\Delta t}{1-\lambda}\frac{\alpha\omega}{\rho_s}\left(S - S^{*}\right) \tag{43}$$

In the equation, $z_{b_{old}}$ and $z_{b_{new}}$ represent the thickness of the movable layer before and after this step, respectively; Δt is the time step; m is the number of grid interface edges; g_{ni} is the single-width sediment transport rate perpendicular to the element interface, which is positive when pointing outwards, i is the interface serial number, 1~m; ΔS is the grid; Δt is the time step; dl_i is the unit interface length, where i is the unit interface serial number, 1~m.

3 RESULTS AND DISCUSSION

3.1 Verification by Generalized Models

After a large amount of sediment enters an alpine gully with large gradient, the frontal deposition can develop quickly and in retrograde, potentially causing the water level to increase to twice the normal level with clear water. Such a situation can lead to the phenomenon where minor floods can cause great disasters. In this section, the sharp increase in water level that is typical in alpine gullies with large gradient variations and sediment-carrying capacities is reproduced in combination with experiments on physical models and mathematic models. The purpose is to study the laws of sediment transport, investigate how sediments deposit and extend upstream due to changes in the sediment-carrying capacity of the water flow, and to verify the accuracy of the algorithm.

Since alpine gullies are steep upstream and gentle downstream, an experiment was conducted at the State Key Laboratory of Hydraulics and Mountain River Engineering of Sichuan University using a water channel with varying gradients, as shown in **Figure 3A**. For the water channel, the upstream slope was designed to 5% (length: 3.2 m) and the downstream slope was 2% (length: 3.8 m). Considering that there will be some influence from local mixing after the addition of sediment at the inlet, the effective test section was set to 6.5 m above the water channel outlet. The water channel was made of Plexiglas, with a width of 20 cm and a depth of 30 cm. The upstream water was controlled by a measuring weir, and a self-designed sediment feeding machine was used to add the sediment. The parameters of the mathematical model are shown in **Figure 3B** and the calculation area was composed of 9,292 triangular meshes. To optimize the drawing effect, the numerical results of this model were drawn as a 2D representation of the water channel with a horizontal scale of 5:1. The upstream flow rate for the experiment was 4.48 L/s; the downstream flow was allowed to discharge freely; the water channel had a rectangular cross-section, with a roughness factor of 0.035; the sediment content at the inlet boundary was 0.343 kg/s, with particle size of 0.5 mm. In the mathematical model, there is no sediment in the water channel before experiment, only the supplement of sediment at the inlet contributed to the change in bed form.

Figure 4 presents the actual images of sediment deposition and water level changes in the physical model experiments. At the beginning of the test, the upstream and downstream water flows at the slope break point were approximately the same as uniform flow, and only the location near the slope break point showed any local changes in water level (**Figure 4A**). When sediment was added upstream, the sediment-laden water flowed steadily in the steep slope section; however, after entering the downstream section with a slope of 2%, sediment deposits began to form and extend upstream. As the intensity of deposition began to increase, the depth of sediment deposition on the bed surface increased, and the water level at the frontal surface of the deposition increased significantly (**Figure 4B**). When the deposition extended to the variable slope, the unaffected upstream jet stream velocity was relatively higher, and the hydraulic jumps in the front of the deposition became more obvious (**Figure 4C**). When the water flow entered the downstream section of the water channel with slope of 5%, the retrograde deposition and increases in water level progressed stably. However, after further retrogradation upstream, the hydraulic jump at the retrograde sediment wave front gradually became unstable, and even resulted in breakage, followed by unsteady fluctuations in the river bed in the frontal section of the retrograde sediment wave (**Figure 4D**).

The calculated results from the mathematical model are similar to the experimental results from the physical model. At first, sediment was not added to the upstream inlet until the water flow in the entire water channel became stable. **Figure 5** shows a diagram of the water levels produced from the mathematical model when the clear water is at steady-state. When the water flow was clear, the upstream water depth at the slope break point was 0.015 m; the water level at the slope break point increased and gradually stabilized at 0.021 m. Although the water depth in the downstream 2% slope section was larger than that in the upstream, the impact of the backwater did not transmit upstream.

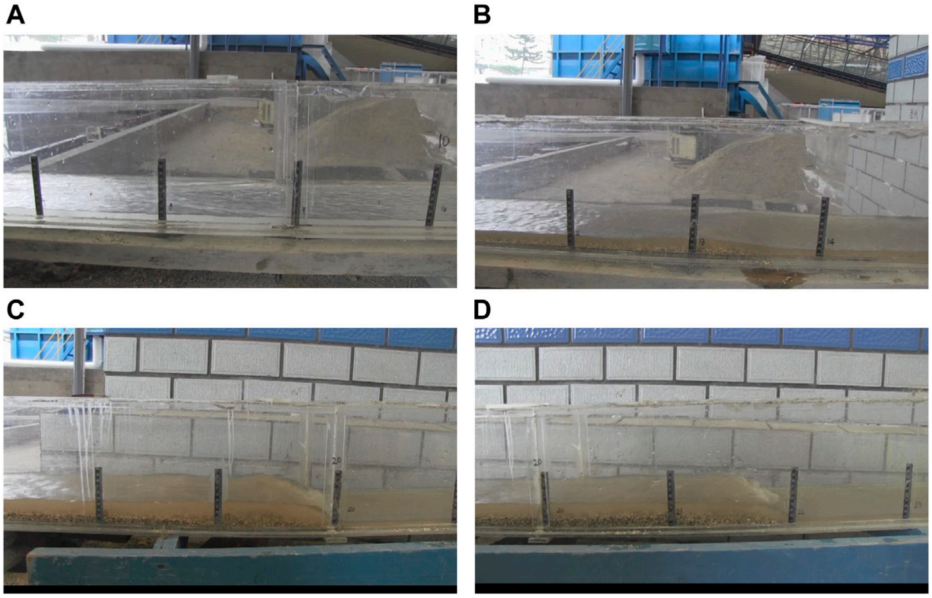

FIGURE 4 | Actual images of the physical model at different times: **(A)** flow state without added sediments; **(B)** state at the start of deposition (at a slope of 2%); **(C)** deposition with gradient variations; **(D)** deposition in the section with 5% slope.

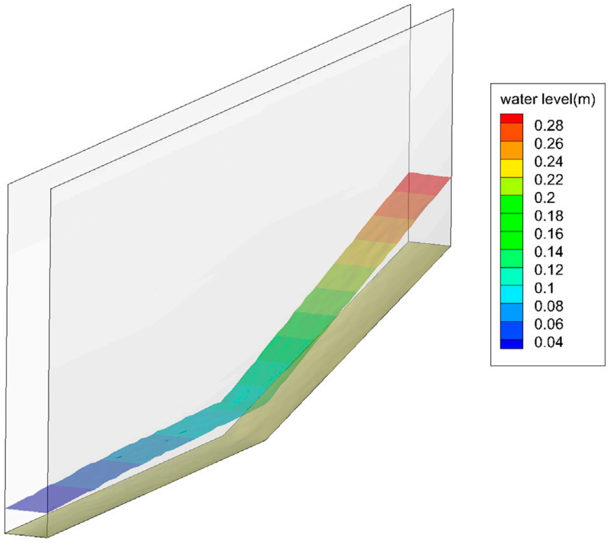

FIGURE 5 | Hydrograph of clear water flow.

Figure 6 presents the water level distribution and sediment deposition in the water channel at different times after sediment was added in the channel. After the sediment-laden water left the 5% slope section and entered the 2% slope section, the slope decreased and the sediment deposition caused interference, leading to reductions in water flow energy and flow discharge. Accordingly, the sediment-carrying capacity of the water flow also decreased. When the sediment-carrying capacity was lower than the actual sediment content in the water flow, sediment began to build-up at about 1.8 m behind the slope break point for the first time (**Figure 6A**). The deposition not only increased the bed resistance but also caused a decrease in the local slope of the bed. The combination of these two effects further reduced the hydraulic conditions of the water flow at the deposition site. When the upstream flow passed through the deposition front, the high flow rate caused the water to flow downstream along the surface of the deposited sandbank. As a result, the actual water level at the deposition location was far higher than the normal water depth of the upstream water flow. Furthermore, sediment from upstream would continue to be deposited here. With the constant deposition at this downstream location, the water level in the local area gradually increased, the water flow energy consumed by the hydraulic jump also increased. The sediment carrying capacity of the water flow was significantly reduced, and serious deposition occurred at the deposition front, and extended upstream continuously. In turn, the hydraulic jumps extended upstream, first reaching the slope break point (**Figure 6B**) and then the upstream section with slope of 5% (**Figure 6C**). Due to the high sediment content, deposition occurred at the upstream surface, while the downstream surface was scoured. The sediment scoured in this area was deposited on the upstream surface of the next sediment ridge. As the deposition extended, a continuous retrograde sand dune was formed, causing multiple reverse hydraulic jumps downstream (**Figure 6D**).

Graphs of the water level and water depth along the central axis of flow are shown in **Figure 7**. Processes 1–5 in the figure represent the calculated results of the mathematic model at different time. For clear water discharge, the model produced a section of backwater starting from the slope break point, and the water depth was stable at 0.021 m from the from the backwater to a distance of 1.8 m from the outlet. With the addition of sediment,

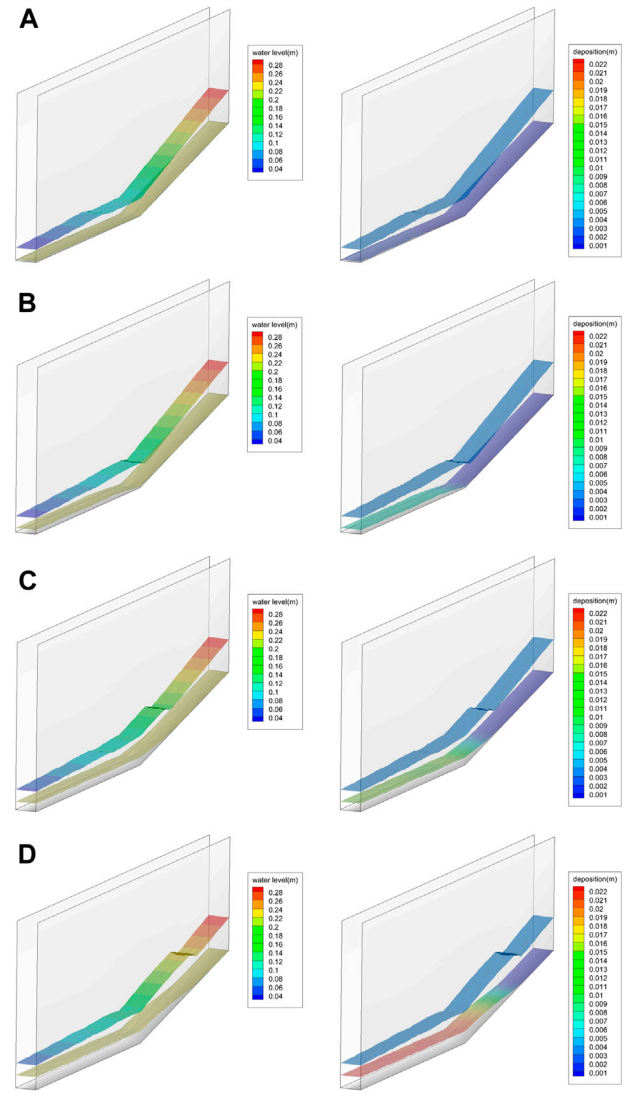

FIGURE 6 | Water level distribution (left part) and sediment deposition (right part) at different times: **(A)** deposition begins; **(B)** extension to slope break point; **(C)** extension to the section with slope of 5%; **(D)** extension to the inlet.

the downstream water depth increased rapidly from the deposition starting point, and dynamic hydraulic jumps gradually appeared and extended upstream. With the continual deposition of sediments on the upstream face, the depth of the dynamic hydraulic jumps increased. The water depth rose from 0.014 m in clear water to 0.029 m when the dynamic hydraulic jump reached 5.8 m from the outlet. As the water depth increased, the water level increased as well due to the continuing deposition of sediments, which aggravated the disaster effect caused by minor flooding.

The model results showed that under the action of high-intensity sediment transport and retrograde deposition with large variations in slope, a sharp increase in water depth occurs at each cross section along the gully. In areas unaffected by the retrograde deposition, the water flow state and water depth are also not affected. During deposition, the most drastic changes in water depth occurs at the deposition front, and the increase in water depth is mainly due to the superposition effect of uplift of the river bed caused by sediment deposition on the river bed and the hydraulic jumps in the junction of local rapid and subcritical flow areas. In other words, the relative reduction of power is the premise for the rapid silting up of the river bed, and the frontal surface of deposit forms the basis for subsequent deposition.

3.2 Applying the Model in a Case Study

On 8 August 2017, heavy rainfall caused a flash flood in Gengdi Village, Liangshan Yi Autonomous Prefecture, Sichuan Province (**Figure 8**), resulting in 24 deaths. Upstream of the village is a middle mountain area in Yanyuan County, Xichang City, with serious soil erosion. There are two erosion gullies on the mountain, with average longitudinal slope reaching 365%. The right gully, Shaba Gully, abruptly becomes flat after reaching the residential area, causing disasters in the affected area. The left gully, Guangjiahe Gully, is deep and the slope is relatively small, which prevents flood waters from submerging the residential area, avoiding disasters. Due to poor vegetation cover in this area, the heavy rainfall resulted in the convergence of a large amount of sediment entering the gully, and heavy deposition appeared in the left gully, causing water blockage. After the flood waters entered the downstream residential area with the small slope, severe flooding occurred from the small flow in the gully, and the sediment heavy water flowed beyond the protective barriers and submerged the houses, causing a catastrophic flash flood event.

Due to the lack data on the actual flow, water level, and incoming sediment load, the model first forecasted the flow discharge of the two gullies in the disaster area based on the GIUH model, the rainfall data at the actual occurrence place and time of the flash flood, and the DEM data of the local 12 m grid. The time curve of flow discharge at the gully inlet is shown in **Figure 9**. The inlet of Shaba Gully is 1,840 m away from the disaster area, while that of Tangjiahe Gully is 1,637 m from the disaster area. Zemu River is the outlet, and water flowed freely to the outlet. The DEM data was used to create an irregular grid terrain with a grid length of 4 m, and the number of irregular grids is 210209. Besides, the roughness factor is 0.035 along the gully. The model calculation area is presented in **Figure 10**. As the DEM terrain data was coarse, the calculation area was larger than the actual drainage area of the gullies. For the hydrodynamic calculations, if the water depth at the grid was less than 0.01 m, it was judged as dry mesh and not included in the calculations. No additional sediment was added at the entrance of the model, and the sediment bed that was formed by the ditch erosion was used as the supply of silt and sand to the disaster area. The gradation of the sediment bed sediment is shown in **Table 1**.

Figure 11 shows the water depth diagram of the disaster area at certain times under the flow duration curve. In the numeric calculations, the rainfall start time was regarded as the starting point, 0 h. At 0 h, the rainfall volume gradually increased and formed a flash flood, which entered the gully inlet and gradually flowed to the disaster area. At 1.5 h, the flash flood was 1 km from

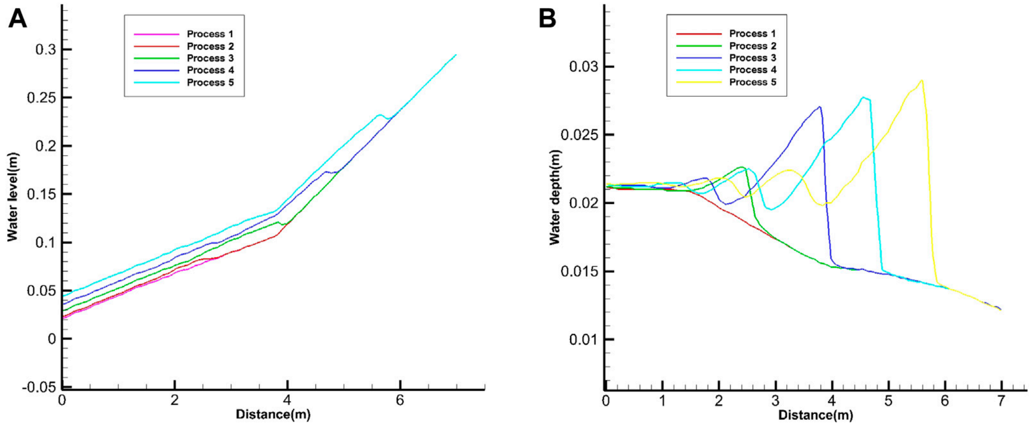

FIGURE 7 | Hydraulic factors on the central axis of the water channel at different times: **(A)** water level; **(B)** water depth. Processes 1–5 in the figure represent the calculated results of the mathematic model for clear water discharge, start of sediment deposition, and the hydraulic jumps at the slope break point, at the upstream section with 5% slope and in the area near the inlet.

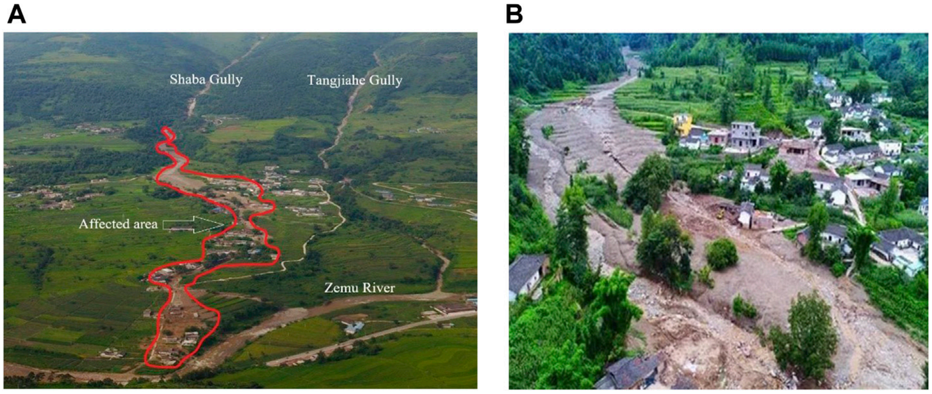

FIGURE 8 | Actual images of the flash flood event in Gengdi village: **(A)** position of the affected area; **(B)** post-disaster situation in the affected downstream area.

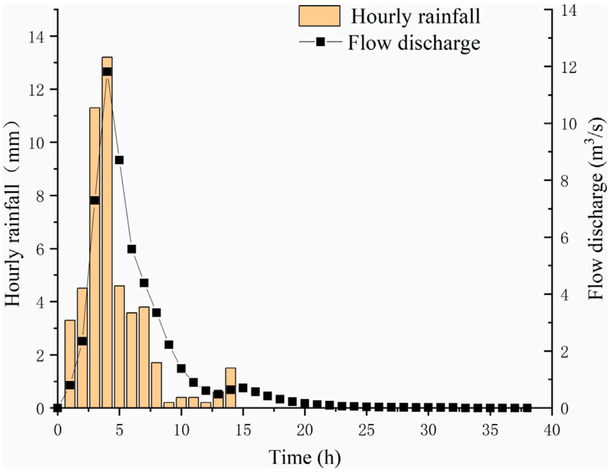

FIGURE 9 | Time-lapse curve of flow at the gully inlet.

the disaster area (**Figure 11A**). At 2 h, the flood reached Gengdi Village. As the gully slope decreased, the drainage area widened, the flow rate decreased, and sediment began to deposit in the disaster area (**Figure 11B**). At 2.5 h, the flash flood passed through the entire village. As the rainfall volume continued to increase, and the flow discharge gradually increased as well (**Figure 11C**). At 4 h, the flow discharge reached a peak and the residential area adjacent to Shaba Gully was submerged. The maximum water depth in the disaster area exceeded 3 m (**Figure 11D**). After passing through the two gullies, the floods converged at Zemu River.

Figure 12 illustrates the water depth and sediment deposition distribution in the affected area of Gengdi Village at 2, 4, 6 and 12 h. It can be seen that during the flash flood, high-intensity sediment transport and the presence of slopes with large gradient variations greatly affected the sediment transport, which aggravated the destructive force of the flood. When the peak flow discharge reached 11.84 m^3/s, the flood flowing from Shaba Gully to Gengdi Village passed through an area with gradient

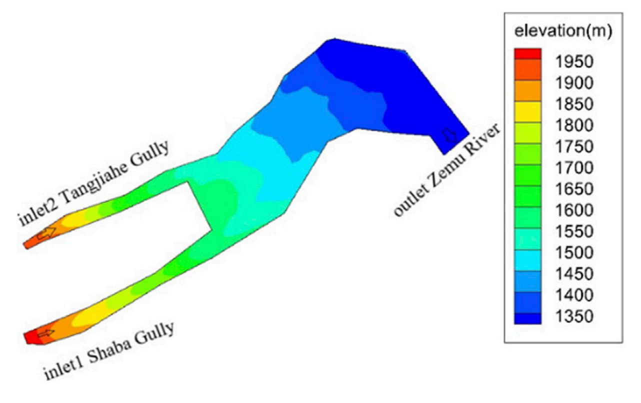

FIGURE 10 | Calculation area of the model.

TABLE 1 | Sediment Gradation for the Gengdi village flash flood model.

Diameter, in mm	>50	10–50	1–10	0.2–1	0.035–0.2	<0.035
Percentage, in %	0.3	16.8	19.8	27.5	25.4	10.2

variations, from steep slopes to the gentler slopes in the river section. In this area, the flow slowed down, followed by an increase in water level, resulting in a great decrease in the sediment-carrying capacity of the water flow. Sediment rapidly deposited in the gully and enlarged the flooded area. At the flood peak, the water depth in the residential area of the disaster area near the gully exceeded 3 m, with maximum deposition reaching 2.71 m. Due to the sharp increase in water level and heavy sediment content, the houses close to the gully were seriously damaged. In contrast, the Tangjiaba Gully in Gengdi Village is deep and the slope variations are low. Hence, the flood in Tangjiaba Gully flowed closely along the mountain, then downstream to converge with Zemu River. At the flood peak, the maximum water depth and deposition were 1.52 and 0.81 m respectively, which was not enough to extend to the residential area (**Figure 12B**). With the decrease in rainfall volume during the retreat of the flash flood, the water level in the disaster area decreased gradually, but the deposition continued and reached a maximum of 5.06 m after 12 h. At this time, the gully was filled with sediment (**Figure 12D**).

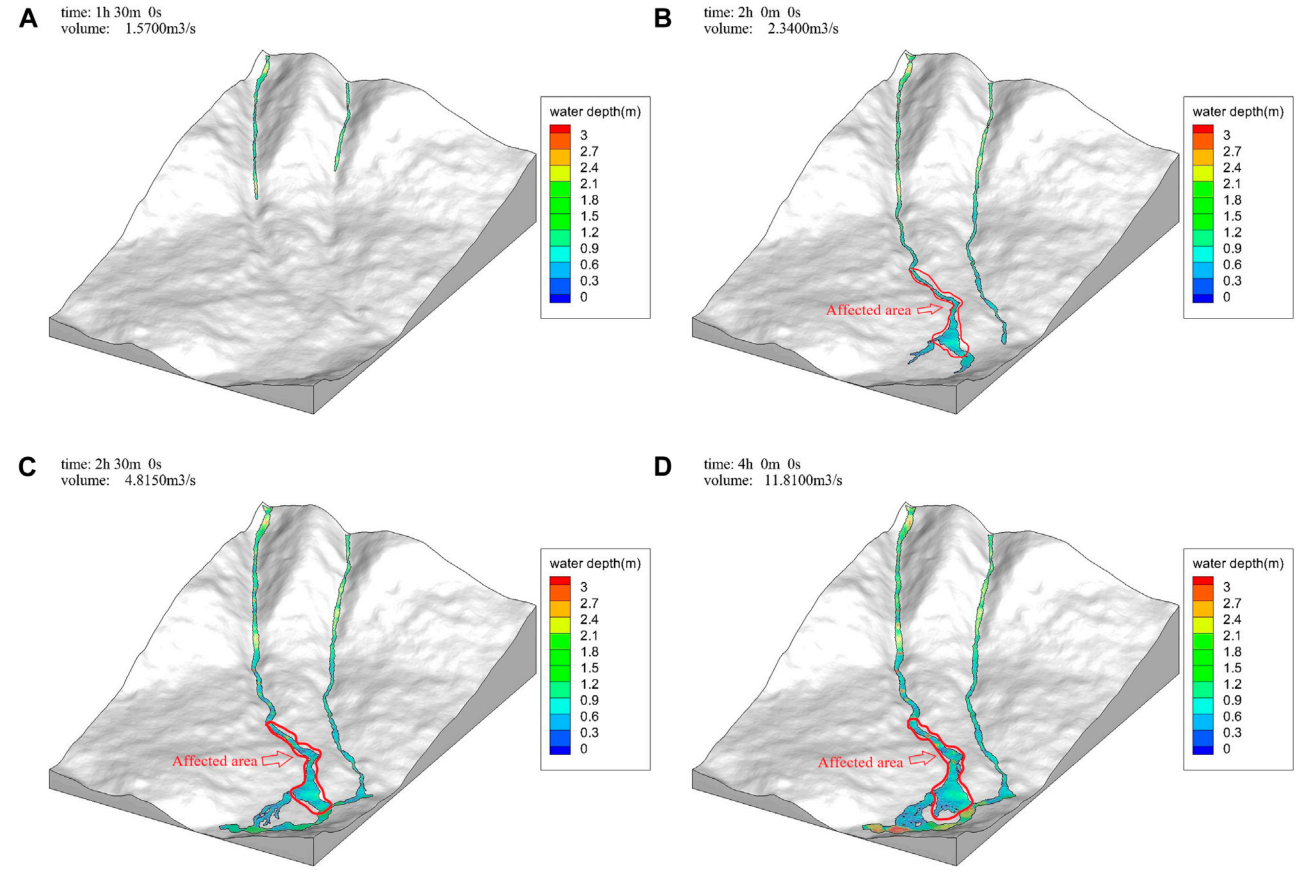

FIGURE 11 | Model calculated water levels at different times: **(A)** 1.5 h; **(B)** 2 h; **(C)** 2.5 h; **(D)** 4 h.

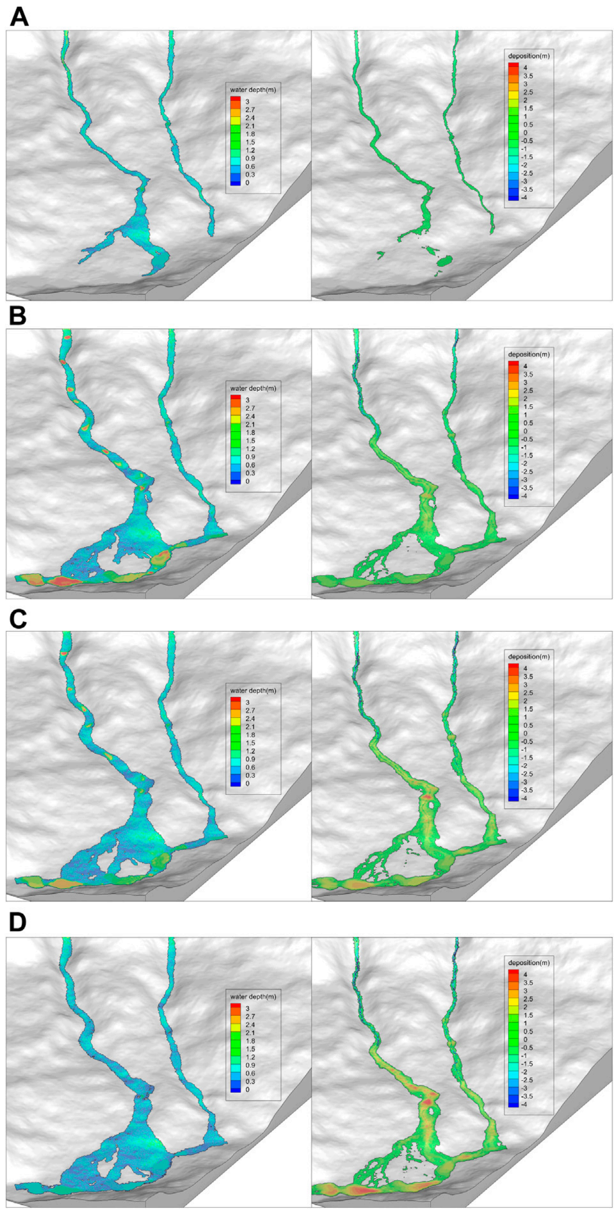

FIGURE 12 | Water level distribution (left part) and sediment deposition (right part) in the disaster area at different times: **(A)** 2 h; **(B)** 4 h; **(C)** 6 h; **(D)** 12 h

4 CONCLUSION

In this paper, the finite volume method with Godunov scheme was used to calculate the flow discharge of flash floods in alpine regions with large slope variations, and SGM was used to eliminate the error caused by the source term of the bottom slope. The sediment module was then added over this foundation to explore how the river flow field will change under the action of high-intensity sediment transport and an OPENMP parallel calculation module was incorporated to improve the calculation efficiency. An efficient and accurate flash flood flow and sediment coupling model was established and verified using a generalized experimental model and the actual water level, flow rate and deposition data of the flow field. Finally, the following major conclusions were obtained:

1) Through the physical model experiments and the results from the mathematical model, it was verified that under the action of high-intensity sediment transport, sedimentation will form at the slope break point, leading to an increase in water level and a decrease in the sediment-carrying capacity of the water flow. As a result, sediment quickly accumulated in that location and gradually extended upstream. Eventually the water flow was impacted and hydraulic jumps formed at the interface between rapid and slow flowing waters, causing a sharp increase in water level. Finally, the water depth at the hydraulic jumps near the inlet section increased to more than twice the initial water depth.
2) The flash flood in Gengdi Village was reproduced accurately. Due to the lack of terrain and flow discharge data, a GIUH model was established based on DEM data of a 12 m local grid and the actual rainfall volume during the event to predict the flow discharge in the disaster area and simulate the disaster range and process for average rainfall conditions in the village. The results revealed Shaba Gully experienced a large flooded area, a high amount of sediment deposition and high water levels. The maximum water depth at peak flooding exceeded 3 m, which seriously affected the safety of the residential area.

All the computations were carried out on a workstation equipped with Intel(R) Xeon(R) Platinum 8280 CPU: 28 cores, 56 threads, 2.7 GHz, and 384 GB memory. It cost 40 min of CPU time for 24 h of water and sediment simulation in **section 3.2**.

DATA AVAILABILITY STATEMENT

The raw data supporting the conclusion of this article will be made available by the authors, without undue reservation.

AUTHOR CONTRIBUTIONS

YD carried out the model simulations and result analysis as well as writing of the manuscript. XL took the leadership of whole project and participated in the discussion and decision-making process. RC developed and tested the numerical code. All the authors participated and contributed to the final manuscript.

FUNDING

This research work was supported by National Natural Science Foundation of China (No. U2040219).

REFERENCES

Aizinger, V. (2004). *A Discontinuous Galerkin Method for Two-And Three-Dimensional Shallow-Water Equations*. Austin, USA: The University of Texas at Austin.

Cao, Z., Pender, G., Wallis, S., and Carling, P. (2004). Computational Dam-Break Hydraulics over Erodible Sediment Bed. *J. Hydraul. Eng.* 130 (7), 689–703. doi:10.1061/(asce)0733-9429(2004)130:7(689)

Chen, R., Shao, S., and Liu, X. (2015). Water-sediment Flow Modeling for Field Case Studies in Southwest China. *Nat. Hazards* 78 (2), 1197–1224. doi:10.1007/s11069-015-1765-z

Chien, N., and Wan, Z. (1999). *Mechanics of Sediment Transport*. Reston, VA, USA: ASCE Press.

Chiodi, F., Claudin, P., and Andreotti, B. (2014). A Two-phase Flow Model of Sediment Transport: Transition from Bedload to Suspended Load. *J. Fluid Mech.* 755, 561–581. doi:10.1017/jfm.2014.422

Da Silva, D. A. D. O. (2017). Experimental and Numerical Assessment of Reinforced Concrete Joints Subjected to Shear Loading. Dissertation thesis. (Do Porto(Portugal): Universidade Do Porto.

El Kadi Abderrezzak, K., Paquier, A., and Mignot, E. (2009). Modelling Flash Flood Propagation in Urban Areas Using a Two-Dimensional Numerical Model. *Nat. Hazards* 50 (3), 433–460. doi:10.1007/s11069-008-9300-0

Guan, M., Wright, N., and Sleigh, P. (2013). "Modelling and Understanding Multiple Roles of Sediment Transport in Floods," in Proceedings of the 35th IAHR World Congress, Chengdu, China, September 8-13, 2013 (Tsinghua University Press).

Handmer, J. (2001). Improving Flood Warnings in Europe: A Research and Policy Agenda. *Glob. Environ. Change B: Environ. Hazards* 3 (1), 19–28. doi:10.1016/s1464-2867(01)00010-9

Hapuarachchi, H. A. P., Wang, Q. J., and Pagano, T. C. (2011). A Review of Advances in Flash Flood Forecasting. *Hydrol. Process.* 25 (18), 2771–2784. doi:10.1002/hyp.8040

Hubbard, M. E., and Dodd, N. (2002). A 2D Numerical Model of Wave Run-Up and Overtopping. *Coastal Eng.* 47 (1), 1–26. doi:10.1016/s0378-3839(02)00094-7

Hui Pu, J., Shao, S., Huang, Y., and Hussain, K. (2013). Evaluations of SWEs and SPH Numerical Modelling Techniques for Dam Break Flows. *Eng. Appl. Comput. Fluid Mech.* 7 (4), 544–563. doi:10.1080/19942060.2013.11015492

Juez, C., Murillo, J., and García-Navarro, P. (2013). 2D Simulation of Granular Flow over Irregular Steep Slopes Using Global and Local Coordinates. *J. Comput. Phys.* 255, 166–204. doi:10.1016/j.jcp.2013.08.002

Kobold, M., and Brilly, M. (2006). The Use of HBV Model for Flash Flood Forecasting. *Nat. Hazards Earth Syst. Sci.* 6 (3), 407–417. doi:10.5194/nhess-6-407-2006

Lane, E. W., and Kalinske, A. A. (1941). Engineering Calculations of Suspended Sediment. *Trans. AGU* 22 (3), 603–607. doi:10.1029/tr022i003p00603

LeVeque, R. J. (2002). *Finite Volume Methods for Hyperbolic Problems*. Cambridge, UK: Cambridge University Press.

Li, Wei. (2006). *Roe-Upwind Finite Volume Model and Numerical Simulation of Hydrodynamic Mechanism of Tidal Bore. Dissertation Thesis*. Nanjing: Hohai University.

Liang, Q., Xia, X., and Hou, J. (2016). Catchment-scale High-Resolution Flash Flood Simulation Using the GPU-Based Technology. *Proced. Eng.* 154, 975–981. doi:10.1016/j.proeng.2016.07.585

Liu, X., Zhou, Q., Huang, S., Guo, Y., and Liu, C. (2018). Estimation of Flow Direction in Meandering Compound Channels. *J. Hydrol.* 556, 143–153. doi:10.1016/j.jhydrol.2017.10.071

Liu, X., Chen, Y., and Chen, J. (1991). Study of the Distribution of Total Sediment Concentration. *Prog. Nat. Sci. Commun. State. Key Laboratories China (Chinese)* 05, 405–414.

Ministry of water resources of the people's republic of China (2018). Bulletin on Flood and Drought Disasters in China of 2018. Available at: http://www.mwr.gov.cn/sj/tjgb/zgshzhgb/ (Accessed July, , 2019).

Misri, R. L., Garde, R. J., and Ranga Raju, K. G. (1984). Bed Load Transport of Coarse Nonuniform Sediment. *J. Hydraulic Eng.* 110 (3), 312–328. doi:10.1061/(asce)0733-9429(1984)110:3(312)

Norbiato, D., Borga, M., Sangati, M., and Zanon, F. (2007). Regional Frequency Analysis of Extreme Precipitation in the Eastern Italian Alps and the August 29, 2003 Flash Flood. *J. Hydrol. -Amsterdam-* 345 (3-4), 149–166. doi:10.1016/j.jhydrol.2007.07.009

Om, S. B. (1976). Development and Application of a Conceptual Runoff Model for Scandinavian Catchments. Report RH07.

Penning-Rowsell, E. C., Tunstall, S. M., Tapsell, S. M., and Parker, D. J. (2000). The Benefits of Flood Warnings: Real but Elusive, and Politically Significant. *Water Environ. J* 14 (1), 7–14. doi:10.1111/j.1747-6593.2000.tb00219.x

Piotrowski, A., Napiórkowski, J. J., and Rowiński, P. M. (2006). Flash-flood Forecasting by Means of Neural Networks and Nearest Neighbour Approach - A Comparative Study. *Nonlin. Process. Geophys.* 13 (4), 443–448. doi:10.5194/npg-13-443-2006

Pu, J. H., Cheng, N.-S., Tan, S. K., and Shao, S. (2012). Source Term Treatment of SWEs Using Surface Gradient Upwind Method. *J. hydraulic Res.* 50 (2), 145–153. doi:10.1080/00221686.2011.649838

Pu, J. H., Hussain, K., Shao, S.-d., and Huang, Y.-f. (2014). Shallow Sediment Transport Flow Computation Using Time-Varying Sediment Adaptation Length. *Int. J. Sediment Res.* 29 (2), 171–183. doi:10.1016/s1001-6279(14)60033-0

Reid, I., Laronne, J. B., and Powell, D. M. (1998). Flash-flood and Bedload Dynamics of Desert Gravel-Bed Streams. *Hydrol. Process.* 12 (4), 543–557. doi:10.1002/(sici)1099-1085(19980330)12:4<543:aid-hyp593>3.0.co;2-c

Roca, M., Martín-Vide, J., and Moreta, P. (2009). Modelling a Torrential Event in a River confluence. *J. Hydrol.* 364 (3-4), 207–215. doi:10.1016/j.jhydrol.2008.10.020

Roe, P. L. (1997). Approximate Riemann Solvers, Parameter Vectors, and Difference Schemes. *J. Comput. Phys.* 135 (2), 250–258. doi:10.1006/jcph.1997.5705

Shan, Y., Huang, S., Liu, C., Guo, Y., and Yang, K. (2018). Prediction of the Depth-Averaged Two-Dimensional Flow Direction along a Meander in Compound Channels. *J. Hydrol.* 565, 318–330. doi:10.1016/j.jhydrol.2018.08.004

Sirdaş, S., and Şen, Z. (2007). Determination of Flash Floods in Western Arabian Peninsula. *J. Hydrologic Eng.* 12 (6), 676–681. doi:10.1061/(ASCE)1084-0699(2007)12:6(676)

Tan, G., Fang, H., Dey, S., and Wu, W. (2018). Rui-Jin Zhang's Research on Sediment Transport. *J. Hydraul. Eng.* 144 (6), 02518002. doi:10.1061/(asce)hy.1943-7900.0001464

Toro, E. F. (1992). Riemann Problems and the WAF Method for Solving the Two-Dimensional Shallow Water Equations. *Phil. Trans. R. Soc. Lond. Ser. A: Phys. Eng. Sci.* 338 (1649), 43–68. doi:10.1098/rsta.1992.0002

Wang, X., Cao, Z., and Tan, G. (2009). Shallow Water Hydrodynamic Modelling of Rainfall Induced Flash Flooding. *Eng. J. Wuhan Univ.* 42 (4), 413–416.

Weishuai, C. (2013). A Review of Rainfall Thresholds for Triggering Flash Floods. *Adv. Water Sci. (Chinese)* 24 (6), 901–908. doi:10.14042/j.cnki.32.1309.2013.06.012

Wu, W., Wang, S. S. Y., and Jia, Y. (2000). Nonuniform Sediment Transport in Alluvial Rivers. *J. hydraulic Res.* 38 (6), 427–434. doi:10.1080/00221680009498296

Yang, F., Ni, Y., Huang, W., and Liu, J. (2020). Numerical Modelling of Dam-Break Floods in Chushandian Reservoir. *Yellow River* 42 (1), 27–36. doi:10.3969/j.issn.1000-1379.2020.01.006

Yuntian, S., Xin, Z., Yu, Z., Chenge, A., Meihong, M., and Xudong, F. (2019). Effect of Sediment Transport on the Temporal and Spatial Characteristics of Flash Floods: A Case Study of "7.21" Flood in Beijing. *J. Tsinghua Univ. (Science Technology)* 59 (12), 990–998. doi:10.16511/j.cnki.qhdxxb.2019.26.023

Zheng, X.-g., Chen, R.-d., Luo, M., Kazemi, E., and Liu, X.-n. (2019). Dynamic Hydraulic Jump and Retrograde Sedimentation in an Open Channel Induced by Sediment Supply: Experimental Study and SPH Simulation. *J. Mt. Sci.* 16 (8), 1913–1927. doi:10.1007/s11629-019-5397-8

Zhou, J. G., Causon, D. M., Mingham, C. G., and Ingram, D. M. (2001). The Surface Gradient Method for the Treatment of Source Terms in the Shallow-Water Equations. *J. Comput. Phys.* 168 (1), 1–25. doi:10.1006/jcph.2000.6670

Conflict of Interest: The authors declare that the research was conducted in the absence of any commercial or financial relationships that could be construed as a potential conflict of interest.

frontiers | Frontiers in Environmental Science

TYPE Original Research
PUBLISHED 14 October 2022
DOI 10.3389/fenvs.2022.981680

Computational fluid dynamics simulation of rough bed open channels using openFOAM

Yun-Hang Cho[1,2]*, My Ha Dao[1] and Andrew Nichols[2]

[1]Department of Fluid Dynamics, Institute of High Performance Computing, Agency for Science, Technology, and Research, Singapore, Singapore, [2]Sheffield Water Center, Department of Civil and Structural Engineering, University of Sheffield, Sheffield, United Kingdom

OPEN ACCESS

EDITED BY
Jiaye Li,
Dongguan University of Technology,
China

REVIEWED BY
Shenglong Gu,
Qinghai University, China
Yan Zhou,
University of Liverpool, United Kingdom
Huabin Shi,
University of Macau, Macau SAR, China

*CORRESPONDENCE
Yun-Hang Cho,
yun-hang.cho@sheffield.ac.uk

SPECIALTY SECTION
This article was submitted to Freshwater Science,
a section of the journal
Frontiers in Environmental Science

RECEIVED 29 June 2022
ACCEPTED 20 September 2022
PUBLISHED 14 October 2022

CITATION
Cho Y-H, Dao MH and Nichols A (2022), Computational fluid dynamics simulation of rough bed open channels using openFOAM.
Front. Environ. Sci. 10:981680.
doi: 10.3389/fenvs.2022.981680

With increased flood risk due to climate change, population expansion and urbanisation; robust waterway design and management are critical. One common type of waterway used to gather and transport ground water is the open channel. Most simulations do not account for the physical roughness of the bed, instead using a roughness coefficient. This means that only the turbulent energy content can be modelled whilst physical turbulent eddies and vortices cannot. Furthermore, many past studies assume the free surface is a rigid lid. This could affect the way that turbulent structures near the free surface behave. Computational Fluid Dynamics simulation of an open channel with a rough bed and rigid lid are conducted using OpenFOAM. Results show good correlation with experimental tests. It can be visually observed that turbulent structures generated from the rough bed do interact with the free surface and thus a rigid lid is perhaps not a great approximation. This is supported by an apparent decrease in the Reynolds shear stress from the free surface and 30% of the flow depth immediately beneath.

KEYWORDS

open channel, computational fluid dynamics, openFOAM, rough bed channels, free surface

1 Introduction

Shallow open channels are one of the most commonly used geometries for water transport; examples being man-made aqueducts, canals and other natural waterways with a water-air interface. Many of these waterways form key water infrastructure to prevent flooding and deliver clean water. It has been shown experimentally that the patterns and behaviour of the water surface are correlated with some underlying flow properties (e.g. flow velocity) as well as physical properties (e.g. bed roughness) (see e.g. Lamb, 1993; Savelsberg and van de Water, 2008; Horoshenkov et al., 2013). Horoshenkov et al. (2013) looked at spatial correlation of water surface waves generated in shallow water flows over a gravel bed without appreciable bed forms. It was shown that a mathematical function could be used to correlate the spatial correlation radius, lag and characteristic period to the depth-averaged flow velocity, the vertical velocity profile, bed roughness, hydraulic roughness and the flow Reynolds number. These were explored further experimentally by Nichols et al. (2013) who proposed further relationships, however more research needs to be conducted to develop more generalised knowledge of the mechanisms behind these relationships. Muraro et al. (2021) provides a good review of all the current state of research. If a reliable correlation can be established, it may be possible to use the latest innovations in 3D scanning (e.g. LIDAR) and digital signal processing to remotely assess the water surface and deduce key performance characteristics of the waterway such as water carrying capacity (see e.g. Horoshenkov et al., 2016; Nichols and Rubinato, 2016; Nichols et al., 2020). This could be critical in identifying early warning signs of flooding such as increasing depth of flow. Given the unpredictability of climate change, this could become a vital tool.

Much of the existing literature on open channel Computational Fluid Dynamics (CFD) simulations use a smooth bed with some wall function to estimate the amount of turbulent energy that would be in the flow if a real material with physical roughness were used (Tan et al., 2015). Whilst this can represent the average energies, it cannot replicate transient effects such as the generation of vortex structures at the bed (Komori et al., 1989), their movement within the flow, interaction with other turbulent structures (Kline et al., 1967; Adrian et al., 2000) and ultimately, their breakdown and eventual dissipation (Grass, 1971; Roy et al., 2004). Part of the reason is due to the existence of a roughness boundary layer near the bed which is heavily dependent on the bed geometry. The variability of the bed geometries makes artificial modelling of the roughness boundary layer a challenge (Jimenez, 2004). Using a physically rough bed instead of wall functions would resolve this however, this requires a very high quality mesh which imposes a very high computational cost. The computational power that was available in the past was low (Moore's law dictates the number of transistors on a microchip doubles about every two years) so computational power 20 years ago is almost a thousand times less than modern capabilities (see e.g. Burg and Ausubel, 2021)).

Some numerical studies of open channel flow with physical bed roughness do exist. Singh et al. (2007) performed Direct Numerical Simulation (DNS) on a hexagonal closed packed bed of spheres to study the nature of the flow near the bed. Good agreement with experimental results are seen for the mean velocity, turbulence intensities, and Reynolds stress. A Large Eddy Simulation (LES) was initially run for around 30T (where $T = d/u_\tau$ is the large-eddy turnover time) to obtain a fully developed turbulent field. This was then mapped onto a DNS simulation. The depth of flow has been taken as four times the diameter of the spheres. This was achieved using a simulation domain of $4\sqrt{3}d \times 4d \times d$ (streamwise × spanwise × depth) although the actual values of the sphere diameters was never revealed. Furthermore, a rigid lid free surface was used and claimed to be appropriate due to small surface deformations.

Another study by Stoesser and Rodi (2007) used spheres of 22 mm in diameter in a hexagonal closed packed bed formation to simulate flow over a rough bed using LES code MGLET. The results showed excellent agreement with the measured data of Detert (2005) and conformity with the log law for rough walls. However, it should be noted that the experimental data was unpublished. The depth of flow was $h = 94$ mm relative to the top of the spheres. The domain was $5h$ in streamwise, $2h$ in spanwise and $1h$ in vertical directions. In total, 46 million mesh points were used. The grid spacing in terms of wall units were $\Delta x^+ = 5$ in the streamwise direction and $\Delta z^+ = 7$ in the spanwise direction. In the vertical direction the grid spacing was kept at a constant value of $\Delta y^+ = 2.5$ at the bed and then stretched towards free surface. Periodic boundary conditions were applied in the streamwise and spanwise directions with a constant pressure gradient driving the flow. The free surface was not discussed at all.

Bomminayuni and Stoesser (2011) also repeated a similar LES simulation but using hemi-spheres. They state that a $2\pi H \times \pi H \times H$ domain size for smooth bed flows is commonly accepted. A common theme is that periodic boundary conditions are used in the streamwise direction to reduce the size of the computational domain. Once again, the free surface was not modelled with the claim that a rigid lid was sufficient.

Alfonsi et al. (2019) used LES to simulate flow over rocks with a median size of 70 mm. OpenFOAM was used with Wall-Adapting-Local-Eddies (WALE) wall modelling. WALE is a sub-grid scale closure model first proposed by Nicoud and Ducros (1999) as a new sub-grid model for complex geometries. The model is able to simulate near wall eddy viscosity and accounts for the effects of the strain and the rotation in the smallest resolved turbulent fluctuations. This was also used by Adrian et al. (2000) in OpenFOAM. Unlike the previous studies, Alfonsi et al. (2019) used the interFOAM approach to capture the free surface using a Volume of Fluid (VoF) method. Results were compared to ADV measurements of laboratory flows in terms of turbulence statistics and turbulent laws, showing a good agreement and demonstrating that OpenFOAM was able to simulate open channel flows with rough beds.

Table 1, 2 summarises some of the key studies discussed. It can be seen that whilst there are some advances in free surface modelling Kazemi et al. (2020), many studies claim a rigid lid is an appropriate simplification of the simulation (see e.g. Satoru et al., 1982; Borue et al., 1995; Nagaosa, 1999; Nagaosa and Handler, 2003). This is understandable as a significant number of cells are required to capture the free surface interface properly, especially if the surface fluctuations are small (Dao et al., 2018). Mesh also cannot be refined suddenly at the free surface and a gradual gradient is required which further increases mesh difficulty. However, few studies provide actual evidence that the turbulent structures which are generated from the rough bed are not affected by the rigid lid simplification. The aim of this paper is to investigate the effect of a rigid lid approximation on the flow. To achieve this, a rough bed simulation is designed. The next section uses the information gathered during the literature review and presents the final setup of the CFD simulation.

TABLE 1 Summary of rough bed simulations and domain ratio used.

References	Author(s)	Title	Domain ratio[a]	Software	Simulation Method
Xie et al. (2021)	Z. Xie, B. Lin, R. A. Falconer, A. Nichols, S. J. Tait & K. V. Horoshenkov	Large-eddy simulation of turbulent free surface flow over a gravel bed	10H x 1.75H x 5H	Xdolphin3D	LES
Alfonsi et al. (2019)	G. Alfonsi, D. Ferraro, A. Lauria, and R. Gaudioa	Large-eddy simulation of turbulent natural-bed flow	5.6H x 2H x 0.8H	OpenFOAM	LES
Singh et al. (2007)	K. M. Singh, N. D. Sandham, and J. J. R. Williams	Numerical Simulation of Flow over a Rough Bed	6.9H x H x 4H	CgLes	DNS
Stoesser and Rodi (2007)	T. Stoesser, W. Fröhlich, and J. Rodi	Large Eddy Simulation of Open-Channel Flow Over and Through Two Layers of Spheres	5H x H x 2H	MGLET	LES
Bomminayuni and Stoesser. (2011)	S. Bomminayuni and T. Stoesser	Turbulence Statistics in an Open-Channel Flow over a Rough Bed	6.12H x H x 3.06H	Hydro3D-GT	LES
Yue et al. (2003)	W.S. Yue, C. L. Lin, and V. C. Patel	Numerical Investigations of Turbulent Free Surface Flows Using Level Set Method and Large Eddy Simulation	2.86H x H x H	Not stated	LES

[a](Streamwise x Vertical x Spanwise)

TABLE 2 Summary of rough bed simulations and CFD parameters.

References	Depth based Reynolds number	Roughness elements	Relative submergence	y^+	x^+	z^+	Vertical elements across free surface	Total mesh size[a]
Xie et al. (2021)	14,448	median grain size = 4.4 mm	0.11	0.5–10.0	$\Delta x^+ = 2.1\Delta y^+$	$\Delta z^+ = 2.1\Delta y^+$	10.5	$256 \times 96 \times 128$ (3.14×10^6)
Alfonsi et al. (2019)	46,500	median size = 70 mm	0.38	$\Delta y^+ = 1$	20	20	Not stated, hyperbolic tangent used near bed and free surface	$1024 \times 160 \times 512$ (84×10^6)
Singh et al. (2007)	3,112	Spheres unknown diameter	0.25	$\Delta y^+ = 3.6$	$\Delta x^+ = 4.2$	$\Delta z^+ = 4.2$	Not modelled	$1024 \times 128 \times 512$ (67.1×10^6)
Stoesser and Rodi. (2007)	40,000	Hexagonal packed 22 mm dia spheres	0.23	$\Delta y^+ = 2.5$	$\Delta x^+ = 5$	$\Delta z^+ = 7$	Not modelled	$800 \times 180 \times 320$ (46×10^6)
Bomminayuni and Stoesser (2011)	13,680	Square packed hemi-spheres	0.29	$\Delta y^+ = 2.6$	$\Delta x^+ = 6.6$	$\Delta z^+ = 6.6$	Not modelled	$1200 \times 126 \times 600$ (91×10^6)
Yue et al. (2003)	57,000	Dunes	0.14	Unknown	Unknown	$\Delta z^+ = 4.0$	Not modelled	$80 \times 32 \times 64$ (1.64×10^5)

[a](Streamwise x Vertical x Spanwise)

2 Materials and methods

The simulation is split into two stages. The first stage uses a coarse mesh and a wider computational domain with RANS calculation to stabilise and obtain time averaged statistics comparable to the experimental results. The second stage takes these results and uses the *MapFields* utility in OpenFOAM to map them onto a finer mesh with a smaller computational domain. LES calculation with the Wall-Adapting-Local-Eddies (WALE) method is then used to develop transient turbulent effects for closer analysis.

The simulation uses a rigid lid to purposefully and artificially remove the effect of the free surface. This means that unlike in real life, the water surface is not allowed to fluctuate. It is anticipated that the turbulent structures which grow from the bed and propagate upwards will hit the surface and deform. This would suggest that without a flexible lid, the response of the structure to the free surface would be different (the analogy being a solid object landing on a trampoline vs. landing on concrete ground).

2.1 Validation against experimental tests

Experiments were conducted at the University of Sheffield's water laboratory for validation of the CFD model. The tests were

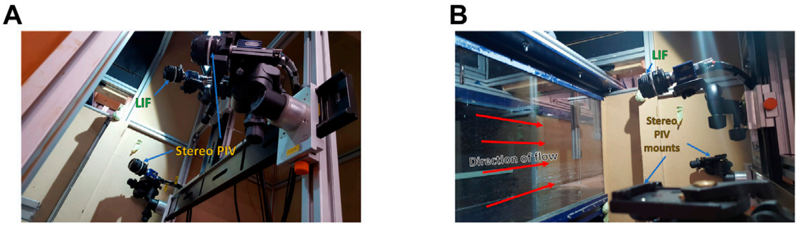

Imager MX cameras setup, two PIV cameras in stereo setup and one LIF camera (unused - topmost)

Imager MX camera view of the flume (PIV cameras not shown)

FIGURE 1
PIV camera setup for experimental flow validation. **(A)** Imager MX cameras setup, two PIV cameras in stereo setup and one LIF camera (unused - topmost) **(B)** Imager MX camera view of the flume (PIV cameras not shown).

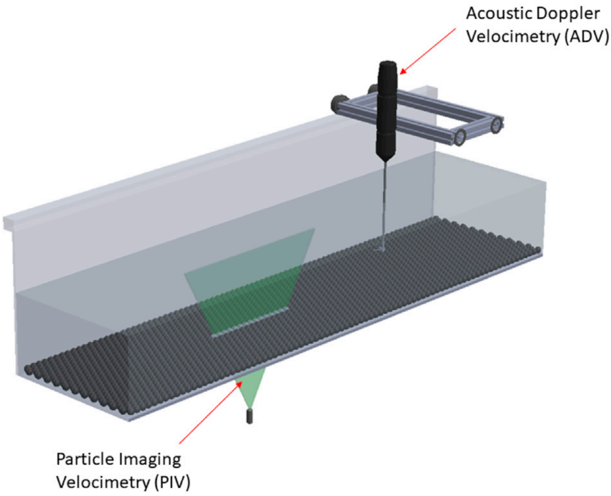

FIGURE 2
Experimental setup. The Particle Imaging Velocimetry (PIV) and Acoustic Doppler Velocimetry (ADV) were used to measure flow properties. Properties.

carried out using a 15 m long recirculating flume with a width of 500 mm. A full bed of spheres with a 24 mm diameter was used in a hexagonal close packing pattern.

Particle Imaging Velocimetry (PIV) techniques were applied 10 m from the upstream inlet to obtain a velocity field along the flume's centerline. A flat laser light sheet illuminated the tracer particles in the measurement region from beneath the rough bed. Two cameras were calibrated using a two level 309–15 calibration grid from LaVision. These operated at 100 Hz to capture snapshots of the particles moving. By comparing the position of the particles in each snapshot, the velocity of the particles (and hence the surrounding flow), could be estimated. The dual-camera stereo setup enabled some capture of the transverse velocity within the plane (Figure 1).

Acoustic Doppler Velocimetry (ADV) sensing was used at 7, 8 and 9 m from the upstream inlet to ensure the flow was fully developed prior to the PIV measurement section. At each streamwise position, the ADV probe was placed at 4 mm vertical intervals inside the flow and measured the velocity at 100 Hz. Once the ADV was used to check the flow was fully developed, the probe was removed to avoid disturbance of the flow entering the PIV measurement section. ADV data collected from the 9 m location was used to compare against the PIV results.

Figure 2 shows the sensors used in the experimental tests.

2.2 CFD setup

2.2.1 Bed geometry and mesh creation

A bed of physical roughness elements was created using hexagonal packed spheres with a radius, r of 12 mm.

Since the majority of the turbulence generation occurs from the upper half of the spheres, in the CFD simulation only the upper parts are used. As shown in Figure 3A, the spheres touch at a tangential point which causes issues with the mesh. To allow a small distance between each sphere ($d_2 = 0.5\,mm$), the spheres are further sunken into the bed. This assists in creating a good mesh without requiring infinitesimally small elements. By using Pythagoras' theorem, Eq. 2 was used to calculate the distance, t which the hemi-spheres need to be sunk into the bed.

$$d_1 = r - \frac{d_2}{2} \tag{1}$$

$$t = \sqrt{r^2 - (d_1)^2} = 4.8734 \text{ mm} \tag{2}$$

Figure 3B provides a visual comparison of the flow depth between the CFD domain (D_{CFD}) and the laboratory flume experiments (D_{EXP}). To move between the computational domain and the experimental domain, Eq. 3 can be used.

$$D_{CFD} = D_{EXP} - (r + t) \tag{3}$$

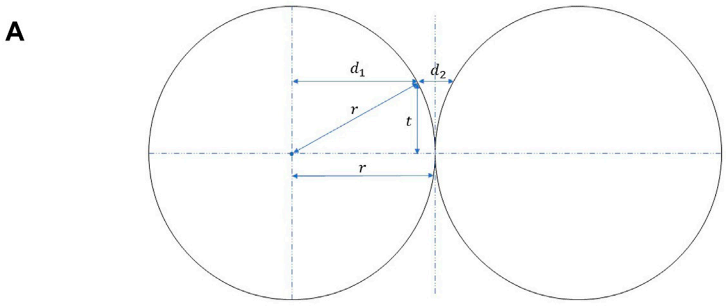

Close up view of the spheres

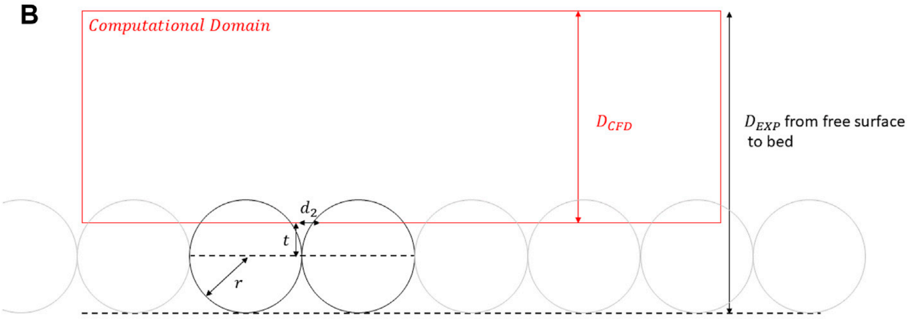

Computational Domain compared to real life experiments. D_{CFD} represents the depth of the CFD domain whilst D_{EXP} represents the depth of the experimental tests

FIGURE 3
Diagram showing the submergence of the virtual bed below the bed of spherical roughness elements. r is the radius of the spherical roughness element, d_2 is the distance between the spherical roughness elements at a given distance t above the centerline of the spheres and d_2 is the adjacent length of the right angle triangle formed by the sides makred r and t. Eq. 2 states geometric relations between these variables to enable calculation of t. **(A)** Close up view of the spheres **(B)** Computational Domain compared to real life experiments. D_{CFD} represents the depth of the CFD domain whilst D_{EXP} represents the depth of the experimental tests.

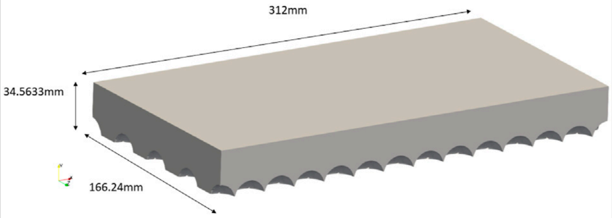

FIGURE 4
Computational domain for stage 1 of the simulation (only 4 spherical cap roughness elements are shown).

For stage 1, the computational domain was 312 mm in the streamwise direction (13 sphere diameters), 166.24 mm in the transverse direction (8 sphere diameters in hexagonal close packed configuration) and a flow depth of 33 mm (Figure 4). For stage 2, the computational domain was shrunk to 96 mm in the streamwise direction (4 sphere diameters in hexagonal close packed configuration) and 82 mm in the transverse direction (4 spheres). This can be seen in Figure 6. The depth of flow was not changed.

To create the mesh, several steps are taken. Firstly, the general computational domain without the rough bed is created using blockMesh.

Secondly, the rough bed is saved as an STL file and imported into OpenFOAM. This is used by the SnappyHexMesh utility to generate a mesh of the rough bed. The edges of the hemi-spheres are extracted and used to refine the mesh around the physical roughness elements. Mesh points which are located inside the physical roughness elements are removed, elements are moved to conform to the bed geometry and additional layers are added around the hemi-spheres to improve near bed performance. The minimum mesh size was originally determined by the desired y + to capture near wall effects. However, it was later discovered that the mesh needed to be much finer than this minimum requirement due to the complex bed geometry. Therefore, the mesh was dictated by the quality of the mesh around these complex bed features. Notably in the second stage of the simulation, the fine mesh is able to fully capture the curvature

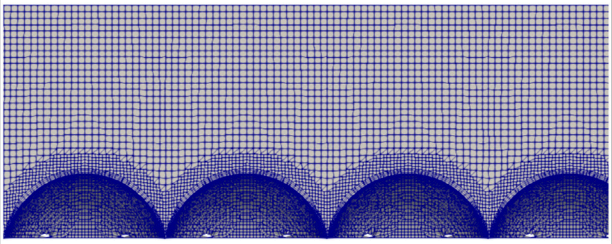

FIGURE 5
Mesh for stage 1 of the simulation, small section of 4 spheres shown.

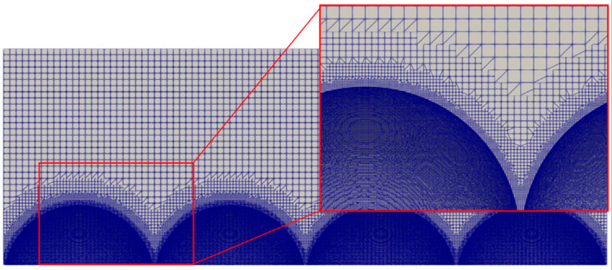

FIGURE 6
Mesh for stage 2 of the simulation (mesh has been refined as shown in the close up view).

of the spherical caps even in the small gaps between the spherical cap elements.

Figure 4 and Figure 5 show the computational domain and the mesh created respectively for the stage 1 simulation. Figure 6 shows the refined mesh used for the second stage of the simulation.

2.3 Boundary conditions

The same boundary conditions were applied to both stages of the CFD simulation.

Cyclic (also known as periodic) boundary conditions are applied to the upstream and downstream faces. Any fluid that exits the computational domain immediately re-enters *via* the upstream face.

As the flow conditions were classified as shallow and the channel's width is sufficiently larger than the water depth, the sides of the open channel have minimal effect on the center of the flow. Hence, symmetrical conditions were imposed on the side walls of the truncated CFD model. Periodic boundary conditions were considered but not selected to minimise any artificial transverse velocity errors from being propagated and magnified. Based on the conservation of mass, there should be no time averaged net movement of fluid across the open channel in the transverse direction.

A no-slip condition was applied to the bed and the spheres. As discussed above, the free surface was modelled as a rigid lid with symmetry boundary condition applied.

The force applied to the fluid ensures an average velocity of 0.08 m/s (the same as the experimental tests). According to literature, 130 depths are needed for entrance length to develop the flow (Lien et al., 2004). With an effective depth of 25 mm, that would translate to 3.25 m if using the stage 2 smaller computational domain. This would correspond to 3,250 mm/96 mm = 34 FTP. At a bulk flow rate of 0.08 m/s, the time taken is 3.25/0.08 = 40.6 s. However, as the stage 1 RANS simulation is used to initialise the stage 2 LES simulation, the time to reach stabilisation can be reduced slightly.

The first stage RANS simulation was run for 43 s. Monitoring of the local and global residuals was carried out to check for stabilisation and convergence of the simulation whilst comparison to experiments were conducted in the second stage to assess real world compatibility.

The second stage of the simulation using LES was run for a further 50 s before the data was extracted to analyse flow statistics such as velocity, turbulence intensity and Reynolds shear stress.

2.4 Solver

Within OpenFOAM, the pimpleFoam algorithm is used, this combines the PISO (Pressure-Implicit with Splitting of Operators) and SIMPLE (Semi-Implicit Method for Pressure Linked Equations) algorithms. PimpleFoam solves the general momentum equations and is intended for incompressible, single-phase, transient flows (Holzmann, 2019). In this simulation, the *momentumPredictor* is enabled with *nOuterCorrectors* = 1 (equivalent to PISO mode), *nCorrectors* = 2, and *nNonOrthogonalCorrectors* = 1. A maximum Courant number of 1 was used.

2.5 Computational resources

The simulation was run using OpenMPI at the National Supercomputing Centre in Singapore. ASPIRE-1 (Advanced Supercomputer For Petascale Innovation Research and Enterprise) is a national facility with a 1 PFLOPS System, 1,288 nodes (dual socket, 12 cores/CPU E5-2690v3), 128 GB DDR4 RAM/node and 10 large memory nodes (1x6TB, 4x2TB, 5x1TB). It has a total of 13 PB Storage using GPFS and Lustre File Systems and an I/O bandwidth up to 500 GB/s 6 jobs of 24 h each were submitted using 96 processors across 4 nodes.

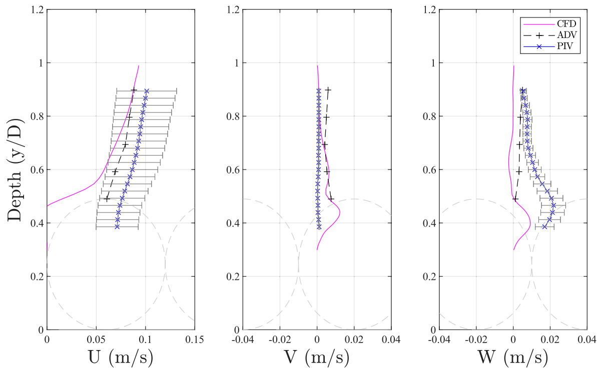

FIGURE 7
Comparison of mean velocity profile. Rough bed has been added in for visual effect only. U is the velocity in the streamwise direction, V is the velocity in the vertical direction and W is velocity in the transverse or spanwise direction.

Communication within the cluster is achieved with an Infiniband Interconnection EDR (100Gbps) Fat Tree with full bisectional bandwidth.

3 Results and discussion

3.1 Validation

The CFD data was extracted every 0.01 s using the *singleGraph* function in OpenFOAM. This extracts a line of data within the flow field for further analysis. Figure 7 shows a comparison between the time-averaged streamwise, transverse and vertical velocity profiles from the CFD simulation against PIV and ADV measurements.

The PIV data shown in Figure 7 was extracted in a single vertical line and not spatially averaged. The ADV measurements used for validation in this section were taken at 9 m downstream from the inlet. ADV and PIV methods have different types of errors. For example, the PIV method is affected by the image quality which influences the accuracy of the vector field calculation. Error bars have been added to the PIV to demonstrate the expected uncertainty of the velocity. It can be seen that in the streamwise direction, the CFD and the ADV data is within the PIV measurement margin of error.

Figure 8 shows a similar comparison for turbulence intensity, *TI*. This was calculated using Eq. 4 where U' is the instantaneous velocity fluctuation in the streamwise direction and U_{shear} is the shear velocity.

$$TI = \sqrt{\overline{U'^2}} \Big/ U_{shear} \tag{4}$$

Here, it can be observed that the turbulence is very large between the spherical caps. This cannot be validated using the experimental data because the PIV and ADV are only able to provide reliable data above the spheres. The PIV cameras do not have line of sight to see deep in between the spheres and the ADV probe and its sampling volume is too large to fit in between the spheres. The position of the bed (d2) in the CFD domain is virtual with the actual bed (from the experiments) located at the bottom of the spheres (which is outside the computational domain and not modelled). Therefore, it is possible that the no-slip condition on the virtual bed caused a magnification of the shear gradient which was not present in the same position compared to the experimental tests. Note that the focus here is on the free surface, however future work should use a slip condition to minimise potential effects. Figure 9 shows a comparison with the Reynolds' shear stress calculated using Eq. 7 where RS_i is the Reynolds' shear stresses with subscript i being the different cross products. ρ is the density of water, V' and W' are the vertical and transverse velocity fluctuations respectively.

The ADV method is affected by vibration of the flume apparatus due to the operation of the water pump. Therefore it was not used for validation of the higher order flow statistics.

$$RS_{uv} = \rho\overline{U'V'} \Big/ U_{shear} \tag{5}$$

$$RS_{uw} = \rho\overline{U'W'} \Big/ U_{shear} \tag{6}$$

$$RS_{vw} = \rho\overline{V'W'} \Big/ U_{shear} \tag{7}$$

Whilst the CFD and the experimental tests follow similar trends, the Reynolds shear stresses near the rigid lid free surface are subdued. The rigid lid imposes zero vertical fluctuation as a boundary, therefore, the vertical velocity fluctuation at the rigid lid will always be zero. Referring back to Figure 7, this can also be observed as the CFD vertical velocity profile (middle pane), ends with zero velocity at the free surface. Since the equation for RS_{uv} includes the term V', it is a mathematical inevitability that RS_{uv} near the free surface is reduced to zero. This effect is evident in Figure 9 from a normalised depth from 1 to 0.7 (Y = 49 mm to Y = 34.3 mm) suggesting that the turbulence data in this region is inaccurate. This would affect any sediment transportation effects and possibly wider turbulent structure interaction. Figure 10 shows the power spectra analysis of the streamwise velocity fluctuation taken at $X = 0$, $Y = 32$ mm, $Z = 0$. The nonparametric, periodogram Welch method by Welch (1967) was used. Kolmogorov's -5/3 power law is also shown to indicate the turbulent dissipation across the energy spectrum. Data was extracted every 0.01 s (100 Hz). As can be seen from the power spectra, most of the energy is concentrated in the low frequency region of the spectra which suggests that the sampling interval is sufficient. The results show a reasonable capture of the

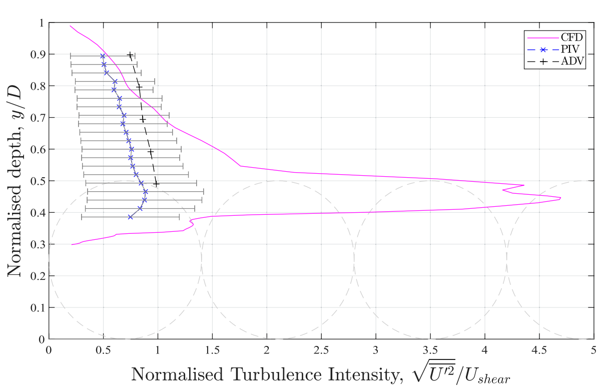

FIGURE 8
Comparison of Turbulence Intensity profile. Rough bed has been added in for visual effect only.

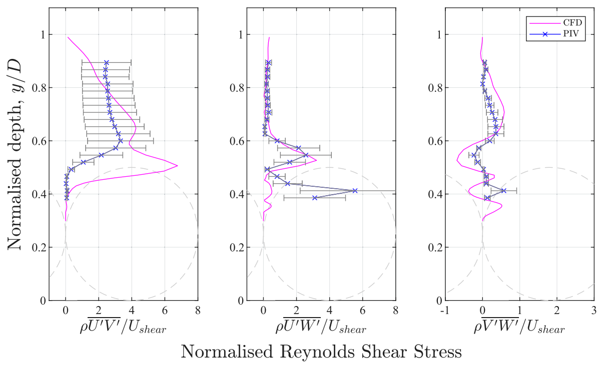

FIGURE 9
Comparison of Reynolds Stress profile. Rough bed has been added in for visual effect only.

turbulent energy cascade within the CFD simulation. This suggests that the turbulence energies are simulated correctly.

3.2 Vortex analysis

Time series analysis was conducted by visual observation of flow snapshots and identifying the movement of coherent structures.

Figure 11A uses the Q-criterion method with a threshold of 40. Proposed by Hunt et al. (1988), Q-criterion is a variable which describes the main motion pattern of a fluid element. For $Q > 0$, the rotation motion dominates, whilst for $Q < 0$, the deformation motion dominates. The vortex flow has the character of $Q > 0$, but not all regions with $Q > 0$ are vortex flow regions. Previous studies such as Nagaosa and Handler (2003); Miura and Kida (1997); Jeong and Hussain (1995); Tanaka and Kida (1998) have demonstrated that a manual selection a non-zero threshold can visualise more appropriate structures in flow. The same approach is utilised here with different thresholds tested to assess the number of structures identified. Using a Q-criteron threshold of 40, it can be seen that numerous vortex-like structures are present within the flow. A similar analysis was carried out using the Lambda2 vortex detection method. The same time step is shown in Figure 11B. This method was proposed by Jeong and Hussain (1995) and is essentially a vortex core line detection algorithm which defines a vortex in terms of eigenvalues of the symmetric tensor. It captures the pressure minimum in a plane perpendicular to the vortex axis at high Reynolds numbers. Furthermore, unlike a pressure-minimum criterion, the lambda2 method claims to accurately define vortex cores at low Reynolds numbers. This is important for the current application as the flow is not highly turbulent. Seddighi et al. (2015) was able to use the lambda2 method for identifying vortices in channel flows with regular pyramidal roughness elements.

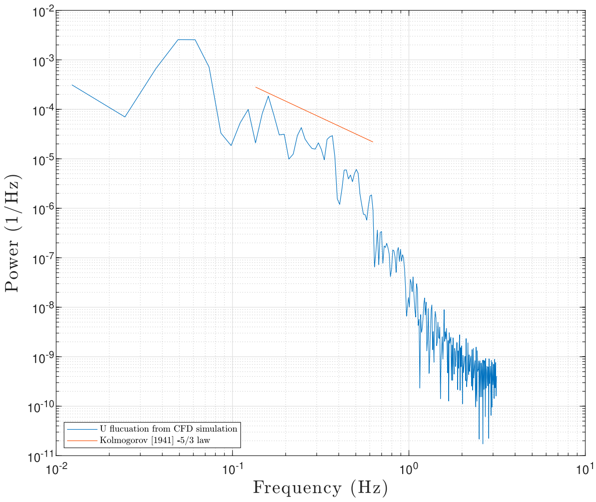

FIGURE 10
Power Spectra Analysis of streamwise velocity fluctuation taken at spanwise centerline, 2.5 mm below the free surface (X = 0, Y = 0.032, Z = 0).

In both figures, it can be observed that the vortices identified are similar in number, scale and shape. For both methods, the threshold value has been selected to identify vortices near the bed. Lowering the Q-criteron threshold enables more of the flow to be identified as a vortex. A frame by frame analysis using a lower Q-criteron is shown in Figure 12. Time steps of 0.1 s are shown from 36.1 s to 36.4. It can be seen that the vortices are clearly rising from the bed whilst being deformed in the streamwise direction by the bulk flow. From 36.1 to 36.3 s, the effect of the turbulent structure hitting the rigid lid water surface can also be observed. These

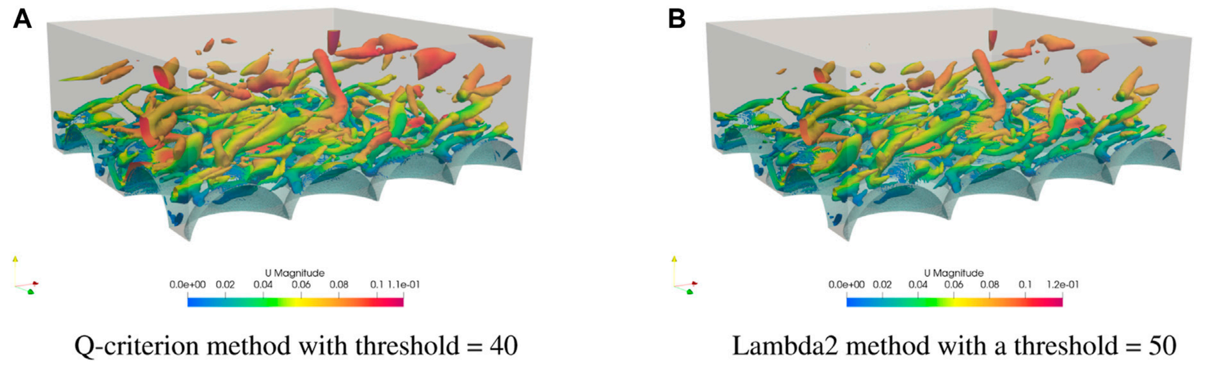

Q-criterion method with threshold = 40

Lambda2 method with a threshold = 50

FIGURE 11
Vortex Detection methods at 89.54 s. **(A)** Q-criterion method with threshold = 40 **(B)** Lambda2 method with a threshold = 50.

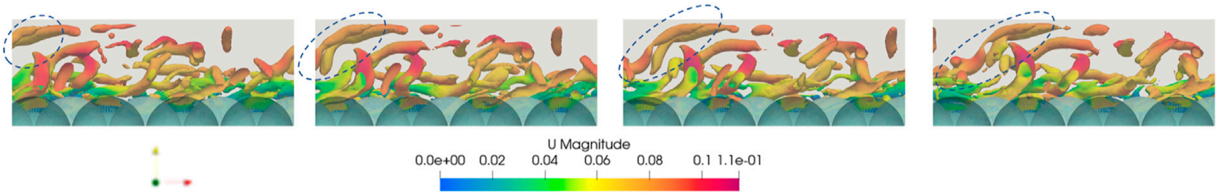

FIGURE 12
Consecutive frames from 36.1 to 36.4 at 0.1 s intervals using Q-criteron with threshold = 20. Only structures in a 0.02 m slice section are shown (taken from −0.01 m to 0.01 m in the spanwise direction).

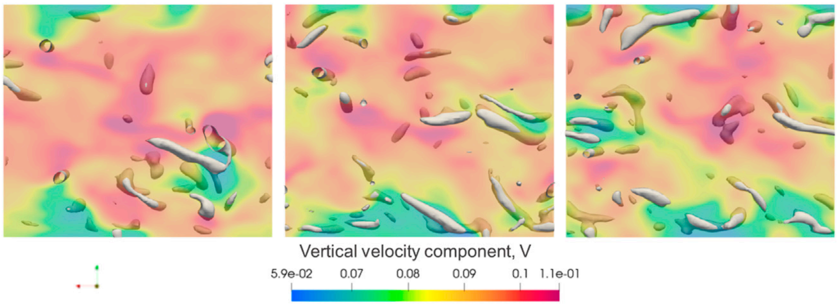

FIGURE 13
Top view using Lambda with threshold = 10. Selected frames at 23.68, 36.0 and 36.9 s from left to right. Coloured by vertical velocity. Horizontal plane taken 2.5 mm below the free surface. Areas of vertical velocity appear to correlate with the presence of local turbulent structures.

coherent structures clearly hit the underside of the water surface before being propagated in the streamwise direction with the bulk flow.

Assessing this further, Figure 13 shows the simulation domain with a top view using Lambda2 with threshold = 10. A horizontal flat plane is taken 2.5 mm below the free surface with the colours representing the velocity in the vertical direction. It can be observed that the presence of turbulent structures often coincides with the green coloured regions. This suggests that 1) turbulent structures move with a different vertical velocity to the bulk flow and 2) will hit the free surface (given the proximity of the horizontal plane with the free surface).

By studying the creation and movement of turbulent structures using different Q-criteron thresholds, it is clear that the turbulent structures that are generated at the bed do occasionally grow to enough magnitude to break through the near surface water layer and impinge on the water surface above. Since a rigid lid has very different properties to a flexible lid, it can be said that the rigidity of the lid will lead to an unrealistic response of the turbulent structure as it impacts the free surface. The impingement of the turbulent structures on a free surface would be expected to generate at least some upwards deformation of the free surface shortly followed by a downwards deformation due to the gravitational force and surface tension pulling the flexible lid back downwards. The fluctuation of the free surface would likely transmit some force or pressure onto the coherent structure possibly causing it to re-enter the central part of the flow and possibly triggering new bursts at the bed to restart the cycle again.

Conceptually, if the flow is visualised “upside-down” such that the free surface becomes the “bed”, then should be clear that the underside of the water-air interface is also dynamically “rough”. When the bulk flow attempts to move past this turbulent rough movement, it is inevitable that the bulk flow is affected by the underside of the free surface. In wave propagation theory, a wave is referred to as “smooth” if its wavelength is considered “long” with respect to the turbulence length scales. However, if the length scale of wave is similar to eddy length scales, from the perspective of the flow, the surface appears very rough. In the framework proposed by Brocchini and Peregrine (2001), they suggest that these specific shallow flow conditions create small surface fluctuations. Based on the Reynolds’ number, empirical turbulent sub-layer studies and analysis conducted in the present study, it is clear that the dominant turbulent scales are also relatively small and of similar scale to the free surface fluctuation. Therefore, the use of a rigid lid will certainly have a noticeable effect on the re-distribution of turbulent energies from coherent structures as they impinge on the free surface.

Unlike experiments, CFD time steps can be saved and restarted to obtain the same results. These time step files can also be used in a different simulation with little loss in accuracy. Therefore a logical future step could be to take a timestep containing large vortex before it impacts the free surface (e.g. 36 s into the simulation). A new simulation with a flexible free surface could be started using this time step to compare the response of the structure with and without a rigid lid. Results from a free surface simulation can further investigate the hypothesis that roughness on the free surface is generated and determine if rigid lids could still be used in future simulations.

4 Conclusion

CFD simulations have been developed to study the effect of rigid lids on turbulent structures in open channel flows with a rough bed. A two stage approach was used whereby a coarse mesh was created for an initial RANS simulation to develop flow statistics before a second stage used a fine mesh with LES to develop transient turbulent structures. Both the time averaged velocity profiles and the turbulent intensities simulated correlate well with experimental results. However, Reynolds’ shear stresses associated with the vertical velocity fluctuation are artificially reduced to zero near the rigid lid. This is due to the boundary condition forcing zero vertical velocity at the rigid lid leading to no vertical fluctuations. This was shown to affect the flow from a normalised depth of 1 (at the free surface) to 0.7 (30% below the free surface).

Finally, it was visually shown that turbulent structures that are generated at the bed can impinge on the rigid lid. Once this occurs, the structure is then pinned at the lid and dragged along by the bulk flow until the structure dissipates. Were the lid to be flexible and representative of a real free surface, the response of the turbulent structures are expected to be different. It is believed that the findings are applicable to a range of similar flows (shallow). More work is necessary to repeat the simulation with different depths and flow rates to confirm this. Future steps should take a time step with a large turbulent structure rising towards the free surface and run a flexible free surface simulation to directly compare the differences in the response of the coherent structure after contact with the rigid/flexible free surface.

Data availability statement

The original contributions presented in the study are publicly available. This data can be found and generated using code here: https://github.com/Yun-HangCho/-Computational-Fluid-Dynamics-Simulation-of-Rough-Bed-Open-Channels-Using-OpenFOAM.

Author contributions

Y-HC developed the CFD model and wrote the paper. MD and AN supervised and edited the paper.

Funding

The computational work for this article was (fully/partially) performed on resources of the National Supercomputing Centre, Singapore (https://www.nscc.sg) (Accessed via the Institute of High Performance Computing at the Agency for Science, Technology and Research (ASTAR).

Acknowledgments

Many thanks to the ASTAR Graduate Academy and the University of Sheffield for their funding of this research. Sincere appreciation to Arthur Hajaali at UCL for the technical support and advice.

Conflict of interest

The authors declare that the research was conducted in the absence of any commercial or financial relationships that could be construed as a potential conflict of interest.

Publisher's note

References

Adrian, R., Meinhart, C., and Tomkins, C. (2000). Vortex organization in the outer region of the turbulent boundary layer. *J. Fluid Mech.* 422, 1–54. doi:10.1017/S0022112000001580

Alfonsi, G., Ferraro, D., Lauria, A., and Gaudio, R. (2019). Large-eddy simulation of turbulent natural-bed flow. *Phys. Fluids* 31, 085105. doi:10.1063/1.5116522

Bomminayuni, S., and Stoesser, T. (2011). Turbulence statistics in an open-channel flow over a rough bed. *J. Hydraul. Eng.* 137, 1347–1358. doi:10.1061/(ASCE)HY.1943-7900.0000454

Borue, V., Orszag, S. A., and Staroselsky, I. (1995). Interaction of surface waves with turbulence: Direct numerical simulations of turbulent open-channel flow. *J. Fluid Mech.* 286, 1–23. doi:10.1017/S0022112095000620

Brocchini, M., and Peregrine, D. H. (2001). The dynamics of strong turbulence at free surfaces. Part 1. Description. *J. Fluid Mech.* 449, 225–254. doi:10.1017/S0022112001006012

Burg, D., and Ausubel, J. H. (2021). Moore's law revisited through intel chip density. *PLOS ONE* 16, 02562455–e256318. doi:10.1371/journal.pone.0256245

Dao, M. H., Chew, L. W., and Zhang, Y. (2018). Modelling physical wave tank with flap paddle and porous beach in openfoam. *Ocean. Eng.* 154, 204–215. doi:10.1016/j.oceaneng.2018.02.024

Grass, A. J. (1971). Structural features of turbulent flow over smooth and rough boundaries. *J. Fluid Mech.* 50, 233–255. doi:10.1017/S0022112071002556

Holzmann, T. (2019). *Mathematics, numerics, derivations and OpenFOAM® (holzmann CFD).*

Horoshenkov, K. V., Nichols, A., Tait, S. J., and Maximov, G. A. (2013). The pattern of surface waves in a shallow free-surface flow. *J. Geophys. Res. Earth Surf.* 118, 1864–1876. doi:10.1002/jgrf.20117

Horoshenkov, K. V., Van Renterghem, T., Nichols, A., and Krynkin, A. (2016). Finite difference time domain modelling of sound scattering by the dynamically rough surface of a turbulent open channel flow. *Appl. Acoust.* 110, 13–22. doi:10.1016/j.apacoust.2016.03.009

Hunt, J., Wray, A., and Moin, P. (1988). "Eddies stream, and convergence zones in turbulent flows," in *Proceedings of the 1988 summer program.*

Jeong, J., and Hussain, F. (1995). On the identification of a vortex. *J. Fluid Mech.* 285, 69–94. doi:10.1017/S0022112095000462

Jimenez, J. (2004). Turbulent flows over rough walls. *Annu. Rev. Fluid Mech.* 36, 173–196. doi:10.1146/annurev.fluid.36.050802.122103

Kazemi, E., Koll, K., Tait, S., and Shao, S. (2020). Sph modelling of turbulent open channel flow over and within natural gravel beds with rough interfacial boundaries. *Adv. Water Resour.* 140, 103557. doi:10.1016/j.advwatres.2020.103557

Kline, S., Reynolds, W., Schraub, F., and Runstadler, P. (1967). The structure of turbulent boundary layers. *J. Fluid Mech.* 30, 741–773. doi:10.1017/s0022112067001740

Komori, S., Murakami, Y., and Ueda, H. (1989). The relationship between surface-renewal and bursting motions in an open-channel flow. *J. Fluid Mech.* 203, 103–123. doi:10.1017/S0022112089001394

Lamb, H. (1993). *Hydrodynamics*. New York: Cambridge University Press.

Lien, K., Monty, J., Chong, M., and Ooi, A. (2004). "The entrance length for fully developed turbulent channel flow," in 15th Australasian Fluid Mechanics Conference.

Miura, H., and Kida, S. (1997). Identification of tubular vortices in turbulence. *J. Phys. Soc. Jpn.* 66, 1331–1334. doi:10.1143/JPSJ.66.1331

Muraro, F., Dolcetti, G., Nichols, A., Tait, S. J., and Horoshenkov, K. V. (2021). Free-surface behaviour of shallow turbulent flows. *J. Hydraulic Res.* 59, 1–20. doi:10.1080/00221686.2020.1870007

Nagaosa, R. (1999). Direct numerical simulation of vortex structures and turbulent scalar transfer across a free surface in a fully developed turbulence. *Phys. Fluids* 11, 1581–1595. doi:10.1063/1.870020

Nagaosa, R., and Handler, R. (2003). Statistical analysis of coherent vortices near a free surface in a fully developed turbulence. *Phys. Fluids (1994).* 15, 375–394. doi:10.1063/1.1533071

Nichols, A., Rubinato, M., Cho, Y., and Wu, J. (2020). Optimal use of titanium dioxide colourant to enable water surfaces to be measured by kinect sensors. *Sensors (Basel).* 20, 3507–3517. doi:10.3390/s20123507

Nichols, A., and Rubinato, M. (2016). *Remote sensing of environmental processes* via *low-cost 3D free-surface mapping*. Liege, Belgium: 4th IHAR Europe Congress, 27.

Nichols, A., Tait, S., Horoshenkov, K., and Shepherd, S. (2013). A non-invasive airborne wave monitor. *Flow Meas. Instrum.* 34, 118–126. doi:10.1016/j.flowmeasinst.2013.09.006

Nicoud, F., and Ducros, F. (1999). Subgrid-scale stress modelling based on the square of the velocity gradient tensor. *Flow. Turbul. Combust.* 62, 183–200. doi:10.1023/A:1009995426001

Roy, A., Buffin-Belanger, T., Lamarre, H., and Kirkbride, A. D. (2004). Size, shape and dynamics of large-scale turbulent flow structures in a gravel-bed river. *J. Fluid Mech.* 500, 1–27. doi:10.1017/s0022112003006396

Satoru, K., Hiromasa, U., Fumimaru, O., and Tokuro, M. (1982). Turbulence structure and transport mechanism at the free surface in an open channel flow. *Int. J. Heat Mass Transf.* 25, 513–521. doi:10.1016/0017-9310(82)90054-0

Savelsberg, R., and van de Water, W. (2008). Turbulence of a free surface. *Phys. Rev. Lett.* 100, 034501. doi:10.1103/PhysRevLett.100.034501

Seddighi, M., He, S., Pokrajac, D., O'Donoghue, T., and Vardy, A. E. (2015). Turbulence in a transient channel flow with a wall of pyramid roughness. *J. Fluid Mech.* 781, 226–260. doi:10.1017/jfm.2015.488

Singh, K. M., Sandham, N. D., and Williams, J. J. R. (2007). Numerical simulation of flow over a rough bed. *J. Hydraul. Eng.* 133, 3864–4398. doi:10.1061/(asce)0733-9429(2007)133:4(386)

Stoesser, T., and Rodi, W. (2007). *Large eddy simulation of open-channel flow over spheres*. Springer Berlin Heidelberg. doi:10.1007/978-3-540-36183-1_23

Tan, S. K., Cheng, N.-S., Xie, Y., and Shao, S. (2015). Incompressible sph simulation of open channel flow over smooth bed. *J. Hydro-environment Res.* 9, 340–353. doi:10.1016/j.jher.2014.12.006

Tanaka, M., and Kida, S. (1998). Characterization of vortex tubes and sheets. *Phys. Fluids A Fluid Dyn.* 5, 2079–2082. doi:10.1063/1.858546

Welch, P. D. (1967). The use of fast Fourier transform for the estimation of power spectra: A method based on time averaging over short, modified periodograms. *IEEE Trans. Audio Electroacoust.* 15, 70–73. doi:10.1109/TAU.1967.1161901

Xie, Z., Lin, B., Falconer, R. A., Nichols, A., Tait, S. J., and Horoshenkov, K. V. (2021). Large-eddy simulation of turbulent free surface flow over a gravel bed. *Jornal Hydraulic Reserach* 60, 205. doi:10.1080/00221686.2021.1908437

Yue, W., Lin, C.-L., and Patel, V. (2003). *Numerical investigation of turbulent free surface flows using level set method and large eddy simulation*. Hydroscience & Engineering College of Engineering, The University of Iowa. Ph.D. thesis.

frontiers in Environmental Science

ORIGINAL RESEARCH
published: 08 December 2021
doi: 10.3389/fenvs.2021.802091

ISPH Simulation of Solitary Waves Propagating Over a Bottom-Mounted Barrier With *k*–ε Turbulence Model

Dong Wang[1,2,3,4], **Sheng Yan**[5]*, **Chen Chen**[6], **JianGuo Lin**[1], **Xupeng Wang**[7] and **Ehsan Kazemi**[8]

[1]College of Environmental Science and Engineering, Dalian Maritime University, Dalian, China, [2]State Key Laboratory of Hydraulic Engineering Simulation and Safety, Tianjin University, Tianjin, China, [3]State Key Laboratory of Coastal and Offshore Engineering, Dalian University of Technology, Dalian, China, [4]Department of Civil and Environmental Engineering, National University of Singapore, Singapore, Singapore, [5]College of Transport Engineering, Dalian Maritime University, Dalian, China, [6]State Key Laboratory of Hydroscience and Engineering, Tsinghua University, Beijing, China, [7]Hebei Changli Gold Coast National Nature Reserve Management Centre, Changli, China, [8]Department of Civil and Structural Engineering, The University of Sheffield, Sheffield, United Kingdom

Edited by:
Jaan H. Pu,
University of Bradford,
United Kingdom

Reviewed by:
Hongjie Wen,
South China University of Technology,
China
Songdong Shao,
Dongguan University of Technology,
China

***Correspondence:**
Sheng Yan
yansheng20210039@dlmu.edu.cn

Specialty section:
This article was submitted to
Freshwater Science,
a section of the journal
Frontiers in Environmental Science

Received: 26 October 2021
Accepted: 16 November 2021
Published: 08 December 2021

Citation:
Wang D, Yan S, Chen C, Lin J, Wang X
and Kazemi E (2021) ISPH Simulation
of Solitary Waves Propagating Over a
Bottom-Mounted Barrier With k–ε
Turbulence Model.
Front. Environ. Sci. 9:802091.
doi: 10.3389/fenvs.2021.802091

Solitary wave propagating over a bottom-mounted barrier is simulated using the Incompressible Smoothed Particle Hydrodynamics (ISPH) method in order to study the generation and transport of turbulence associated with flow separation around submerged structures. For an accurate capture of turbulence characteristics during the wave propagation, rather than employing the standard sub-particle scale (SPS) model, the *k*-ε turbulence model is coupled with the numerical scheme. The results of the numerical model are compared with experimental data, and good agreement is observed in terms of mean velocity, free surface elevation, vorticity fields and turbulent kinetic energy. The numerical model is then employed to investigate the effects of wave non-linearity and geometrical size of the submerged barrier on the flow separation; and calculate the reflection, dissipation and transmission coefficients to evaluate the importance of energy dissipation due to the generation of vortices. The results of this study show that the developed ISPH method with the *k*-ε turbulence closure model is capable of reproducing the velocity fields and the turbulence characteristics accurately, and thus can be used to perform predictions of comprehensive hydrodynamics of flow-structure interactions in the urban hydro-environment systems.

Keywords: solitary wave, barrier, reflection, dissipation, transmission, flow separation

1 INTRODUCTION

The impacts of hazards such as tsunami or flash floods on the coastal communities are critical for the economic and social activities of coastal cities. Tsunami or flash floods can result in serious destruction of coastal structures. The interaction of fluid flow with structures involves many complex processes, such as displacement of the free surface, flow separation, vortex shedding, and turbulence generation. In recent years, several laboratory experiments have been conducted to study these processes. Wu et al. (2012) used the particle image velocimetry (PIV) technique to observe the vortex and turbulence generated by flow separation and wave breaking of a solitary wave propagating over a bottom-mounted barrier. In order to investigate the effects of flow depth and velocity on cities, Soares-Frazão and Zech (2008) conducted experimental studies on the transient flow of the dam-break wave in a square city layout of 5 × 5 buildings in both horizontal and oblique directions. Zhang (2009) carried out a three-dimensional (3D) experiment to study a tsunami interacting with single and multiple cylinders, and measured water surface elevation, water particle velocity, horizontal force, and overturning moment on the cylindrical structure.

In recent years, the particle methods, such as Smoothed Particle Hydrodynamics (SPH), have shown promising capacities in simulating the impacts of waves and currents on solid (impermeable) structures (e.g., Wu et al., 2013; Albano et al., 2016; Farmani et al., 2019; Ren et al., 2019) as well as porous structures (e.g., Kazemi et al., 2020a). Although significant improvements have been achieved with regards to the accuracy of the numerical schemes in the estimation of large deformation of the free surface boundaries and the pressures acting on the structures, the applicability of the method for simulating turbulence and vortices still needs careful attention.

The commonly used turbulence model in ISPH is the sub-particle scale turbulence model (e.g., in Gotoh et al., 2001; Issa et al., 2005; Wang et al., 2016; Shi et al., 2017; Wang et al., 2018), in which the eddy viscosity is determined by the Smagorinsky subgrid model (Smagorinsky, 1963), or the mixing length theory (Kazemi et al., 2020b). The poorly designed Large Eddy Simulations (LES) in the early ISPH models using the SPS closure model for turbulence was still sufficient for the problems studied by them; however, for problems such as the one simulated in this study, i.e., when flow is characterised by significant flow separations, it is hard to capture the correct turbulent characteristics by the SPS model, especially when the numerical resolution is insufficient. Kazemi et al. (2020b) showed that the SPS model cannot correctly estimate the effect of turbulence when the flow is highly sheared and computational resolution is coarse. For situations like this, coupling the ISPH method with the *k*-*ε* turbulence model could be a useful alternative, an issue which is investigated in this study.

Only a few researchers have attempted coupling the particle methods with the *k*-*ε* model for modelling turbulence. For example, Shao (2006) introduced the two-equation *k*–*ε* model into the ISPH method and showed that this combination provides a useful tool to investigate the surf zone dynamics. However, only simple numerical results of modelled turbulence were shown, mainly on the kinetic energy distributions during wave breaking on a plane beach. Other examples of the application of the *k*–*ε* model with particle methods are Kolahdoozan et al. (2014), Napoli et al. (2015), and Leroy et al. (2016). A benchmark review of particle turbulence models in coastal and ocean field was documented by Luo et al. (2021). However, only limited results of turbulence intensity were compared with experiment data. Wang and Liu (2020) presented the first comprehensively validated two dimensional (2D) ISPH model with the *k*–*ε* turbulence closure. They simulated two laboratory experiments, a non-breaking solitary wave propagating over a bottom-mounted barrier and a solitary wave breaking on a 1 on 50 slope and presented a detailed discussion on the effects of initial seeding of turbulent kinetic energy. In the present study, the model developed in Wang and Liu (2020) is employed to estimate free surface elevation, velocity field, and turbulence intensity; and then applied to investigate the effects of wave non-linearity and geometrical size of submerged impermeable structure on the flow separation. To fully evaluate the benefits of the proposed *k*–*ε* modelling technique, two comparative computations based on the SPS and non-turbulence models are also carried out for a comparison. Furthermore, the reflection, dissipation and transmission coefficients are calculated, and their variations are analysed to assess the importance of the energy dissipation due to the generation of vortices.

The present paper is organised as follows. **Section 2** introduces the ISPH model equations and relevant Lagrangian transport equations of turbulent kinetic energy *k* and dissipation rate *ε*; **Section 3** presents the ISPH model validation by experimental results of solitary wave propagating over a bottom mounted barrier; **Section 4** discusses the effects of wave non-linearity and the various geometrical sizes of submerged structure on the vortices around the structure and the coefficients of wave reflection, transmission, dissipation; and finally, **Section 5** summarizes the findings of the study.

2 GOVERNING EQUATIONS AND NUMERICAL METHODOLOGY

The governing equations include the ensemble averaged mass and momentum conservation equations, which can be expressed as

$$\nabla \cdot \mathbf{u} = 0 \tag{1}$$

$$\frac{D\mathbf{u}}{Dt} = -\frac{1}{\rho_0}\nabla p + \mathbf{g} + \nu_0\nabla^2\mathbf{u} + \frac{1}{\rho_0}\nabla\cdot\vec{\boldsymbol{\tau}} \tag{2}$$

where t is the time; D/Dt denotes the total derivative; ρ_0 is the density of fluid; $\mathbf{u}$ is the ensemble averaged velocity; p is the pressure; g is the gravitational acceleration; and ν_0 is the kinematic viscosity. $\vec{\boldsymbol{\tau}}$ is the turbulent stress tensor, which can be calculated by the Boussinesq eddy viscosity assumption as

$$\frac{\vec{\boldsymbol{\tau}}}{\rho_0} = 2\nu_t\vec{\mathbf{S}} - \frac{2}{3}k\vec{\mathrm{I}}, \tag{3}$$

where ν_t is the turbulent eddy viscosity; $\vec{\mathbf{S}}$ is the strain rate tensor; k is the turbulent kinetic energy; and $\vec{\mathrm{I}}$ is the identical matrix in tensor form. The turbulent eddy viscosity for each particle can be evaluated as

$$\nu_t = C_\mu\frac{k^2}{\varepsilon}, \tag{4}$$

where ε is the energy dissipation rate; and C_μ is an empirical constant (Launder and Spalding, 1974).

The standard *k*-*ε* model is used to account for the turbulence scale smaller than the particle size. The equations of kinetic energy and dissipation rate take the following advection–diffusion forms

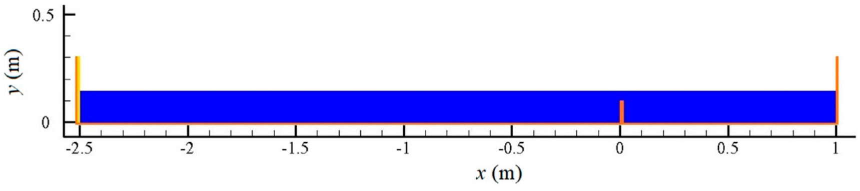

FIGURE 1 | Initial setup of the numerical model.

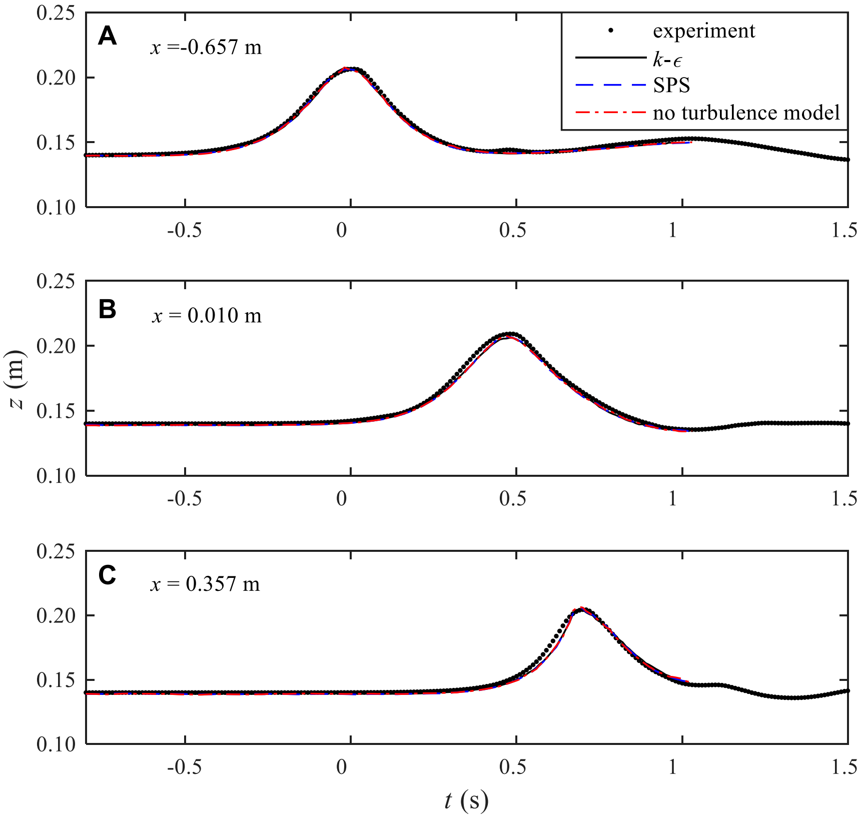

FIGURE 2 | Comparisons of time series of the free surface elevations between experimental and numerical results at three locations of **(A)** x = −0.657 m; **(B)** 0.010 m; and **(C)** 0.357 m.

$$\frac{Dk}{Dt} = \nabla\cdot\left(\frac{\nu_t}{\sigma_k}\nabla k\right) + P - \varepsilon, \tag{5}$$

$$\frac{D\varepsilon}{Dt} = \nabla\cdot\left(\frac{\nu_t}{\sigma_\varepsilon}\nabla\varepsilon\right) + C_{\varepsilon1}\frac{P\varepsilon}{k} - C_{\varepsilon2}\frac{\varepsilon^2}{k}, \tag{6}$$

The production of kinetic energy P acts as a source term, while the dissipation ε is a sink term. The source and sink terms have the relation $P/\varepsilon = C_\mu\,(Sk/\varepsilon)^2$ (Pope, 2000), which can be written as

$$P = \nu_t S^2 \tag{7}$$

with

$$S = \sqrt{2\left|\vec{S}\right|^2} \tag{8}$$

referring to the scalar mean rate-of-strain. The set of constant values recommended by Launder and Spalding (1974) were used in the present simulations ($C_\mu = 0.09$; $\sigma_k = 1.0$; $\sigma_\varepsilon = 1.3$; $C_{\varepsilon1} = 1.44$; and $C_{\varepsilon2} = 1.92$).

The adopted ISPH model is based on the numerical scheme proposed by Khayyer and Gotoh (2011). The most important feature of this version is the use of a higher-order error compensating term for the pressure Poisson equation (PPE). The two-step projection approach, i.e., prediction and correction, is used for the time implementation. The model has been demonstrated to maintain the particle/pressure stability through the validation of several benchmark tests. 2D and 3D versions of the model were employed by Wang et al. (2016, 2018) for the simulation of scouring around coastal

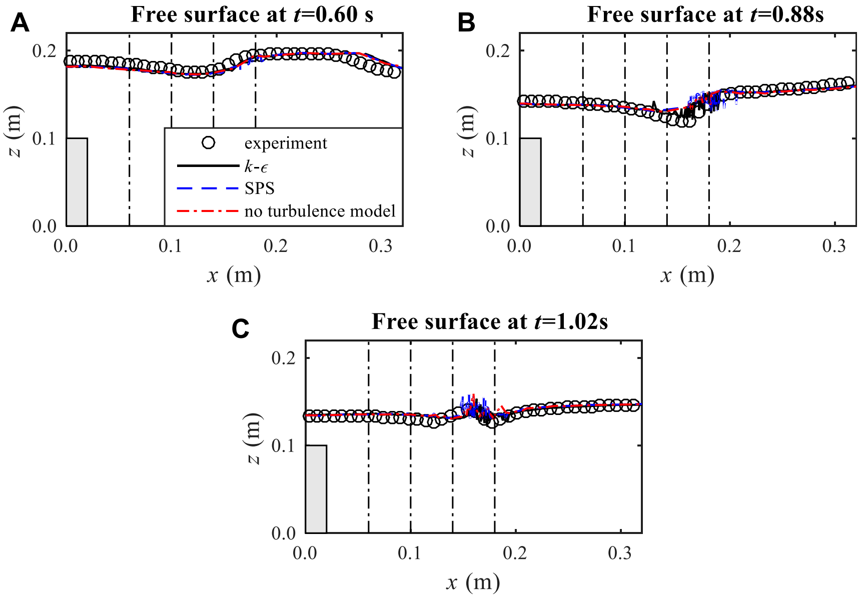

FIGURE 3 | Comparisons between experimental data and numerical results for the free surface elevations at three times t = **(A)** 0.60 s; **(B)** 0.88 s; and **(C)** 1.02 s.

structures. The ISPH model is modified by substituting the original SPS turbulence model with the standard k-ε turbulence model for the present simulations. The numerical discretization of the above equations, boundary and initial conditions, and solution procedure can be found in Wang and Liu (2020).

3 NUMERICAL SIMULATION OF SOLITARY WAVE PROPAGATING OVER A BOTTOM MOUNTED BARRIER

In this section, the turbulence and energy dissipation associated with flow separation around the submerged structures caused by solitary waves are simulated and the results of the model are compared with benchmark experiments as follows.

3.1 Experiment Setup

The experiments were conducted in a glass-walled wave flume (22 m long, 0.5 m wide and 0.76 m deep) in Tainan Hydraulics Laboratory, National Cheng Kung University (Wu et al., 2012). A vertical rectangular barrier with height of d = 10 cm and thickness of w = 2 cm was mounted on the bottom and located in the middle of the wave flume. A solitary wave with a wave height H = 7.0 cm in a constant water depth of h = 14.0 cm was generated by a piston-type wavemaker at one end of the wave flume using Goring (1978) method. The surface wave elevations were measured by six capacitance-type wave gauges and the velocity fields in the vicinity of the barrier were measured using a dual-cameras PIV system. The origin of the coordinate system (x, z) = (0, 0) was defined at the intersection of the left side of the vertical barrier and the flume bottom. The details of the experimental set-up and apparatus layouts can be found in Figure 1 of Wu et al. (2012).

3.2 Numerical Model Setup

The ISPH model setup (see **Figure 1**) followed that of the experiments, except that the length of the flume was reduced to 3.5 m to accommodate the computing expenses. As a result, the barrier was located 2.5 m far from the numerical wave paddle.

The SPH particle spacing is set to D = 2 mm, and a total of 135,419 particles are employed in this simulation. Adaptive scheme is used, and the time step range is between $\Delta t_{\min} = 10^{-5}$ s and $\Delta t_{\max} = 10^{-2}$ s with a Courant number (Cr) of 0.1. The number of time intervals is 16,737 for a physical test duration of 3 s. The computation for this test took about 1 h using 96-cores on the National Supercomputing Centre Singapore (NSCC).

3.3 Model Validation on Generated Solitary Wave

To verify the wave generation of solitary waves, time series of the free surface elevations of the numerical and experimental models are compared and shown in **Figure 2**. Three measured wave gauge data at x = −0.657 m, 0.010 and 0.357 m (respectively, at upstream, middle, and downstream of the barrier) are chosen to compare with the numerical results. The time at which the crest of the solitary wave arrives at x = −0.657 m is defined as t = 0 s. The numerical results fit quite well with the experiment data for the main wave form and the small undulating tails of the incident waves (**Figure 2A**), reflected waves (**Figure 2A**) and transmitted waves (**Figures 2B,C**).

To demonstrate the benefit of the proposed k–ε model, two comparative tests including one without any turbulence model, and another with k–ε being replaced by the SPS turbulence model, have been carried out. The results are shown together in

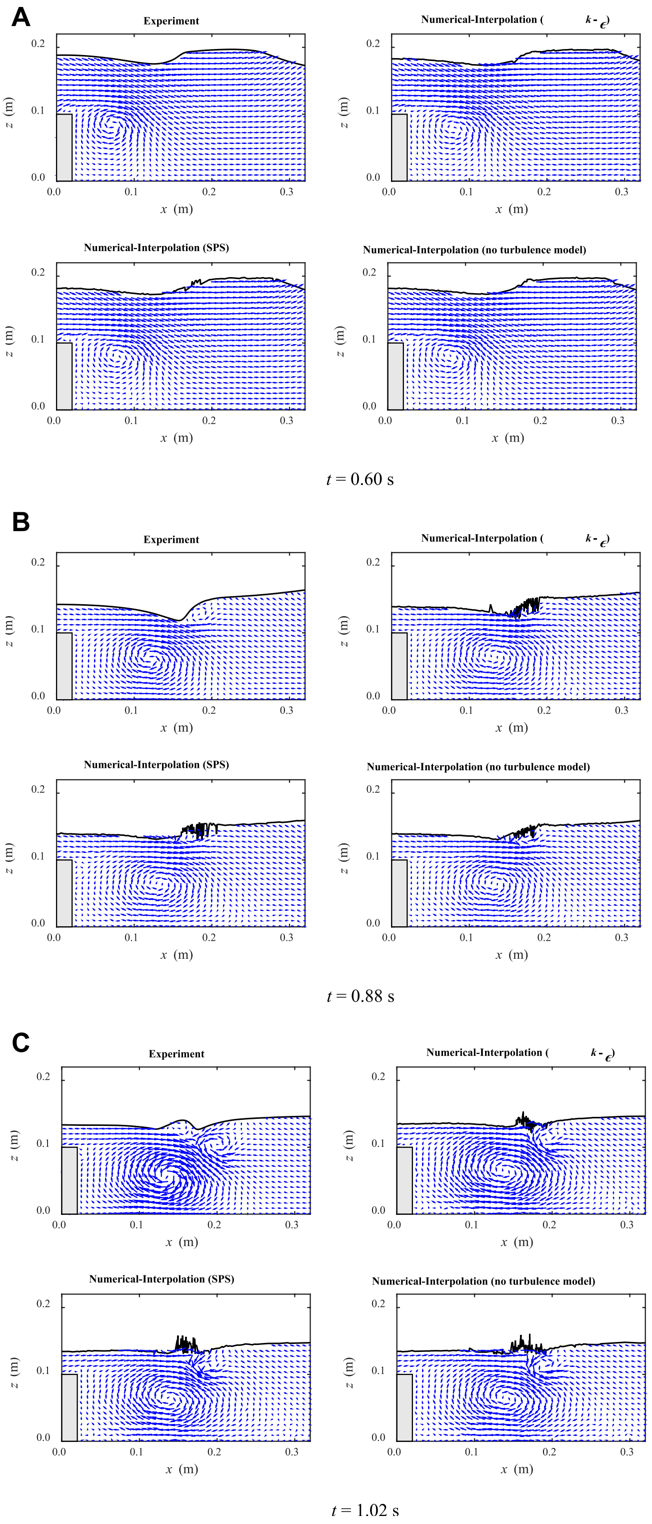

FIGURE 4 | Comparisons between experimental data and numerical results for the velocity fields at three times *t* = **(A)** 0.60 s; **(B)** 0.88 s; and **(C)** 1.02 s.

Figure 2A–C for a comparison. It shows very little differences in the time-dependent free surface profiles. It is shown that the lack of sufficient turbulence dissipation narrowed the wave profile as shown in **Figure 2C**. On the other hand, from the viewpoint of both k–ε and SPS turbulence modelling results, almost no tangible differences were found in the wave propagation profiles.

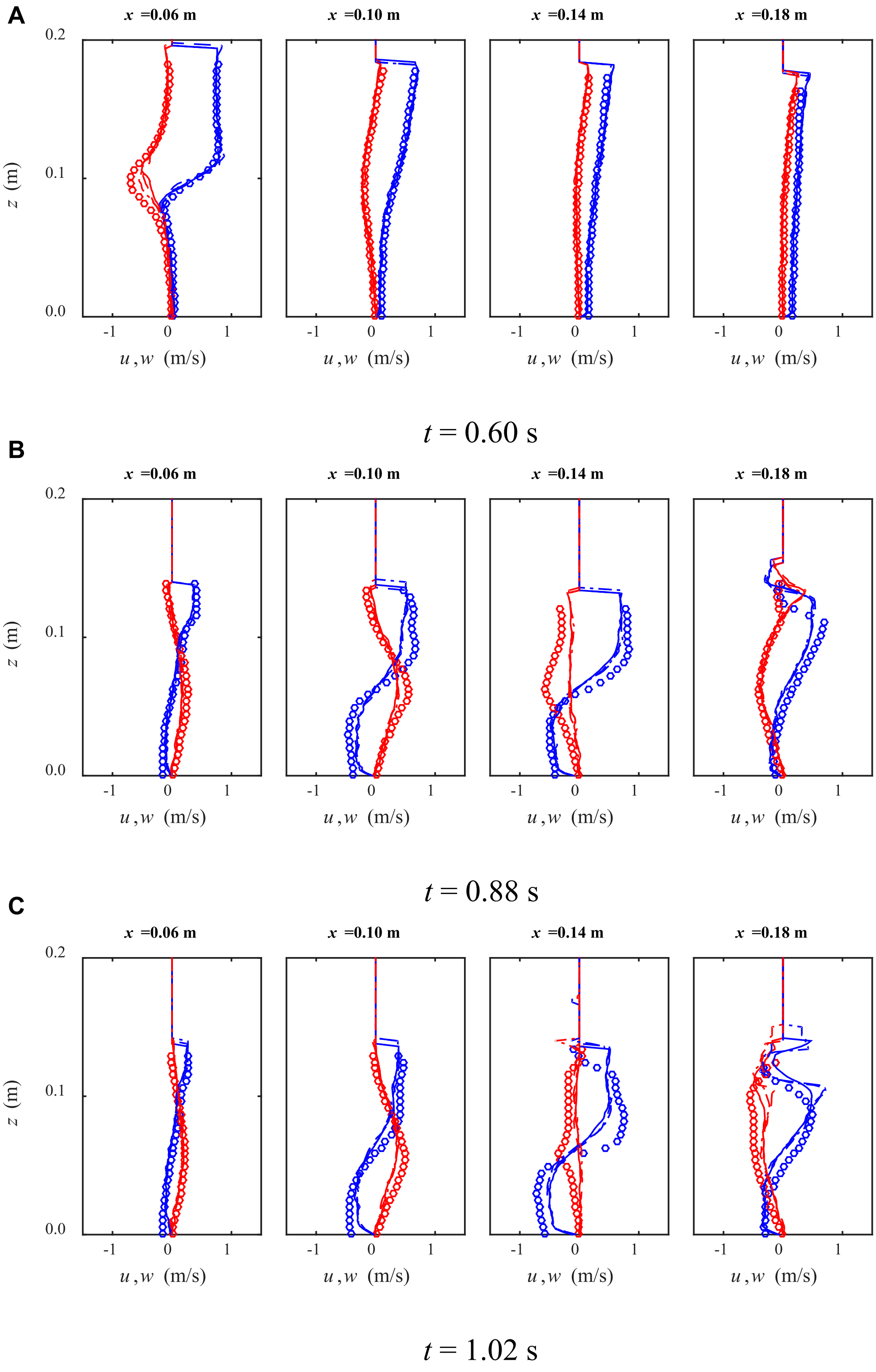

FIGURE 5 | Comparisons between experimental data (circles) and numerical results for the horizontal *u* (blue) and vertical *w* (red) velocity profiles, calculated by *k*-ε model (solid lines), SPS model (dashed lines) and non-turbulence model (dash-dotted lines) at three times *t* = **(A)** 0.60 s; **(B)** 0.88 s; and **(C)** 1.02 s.

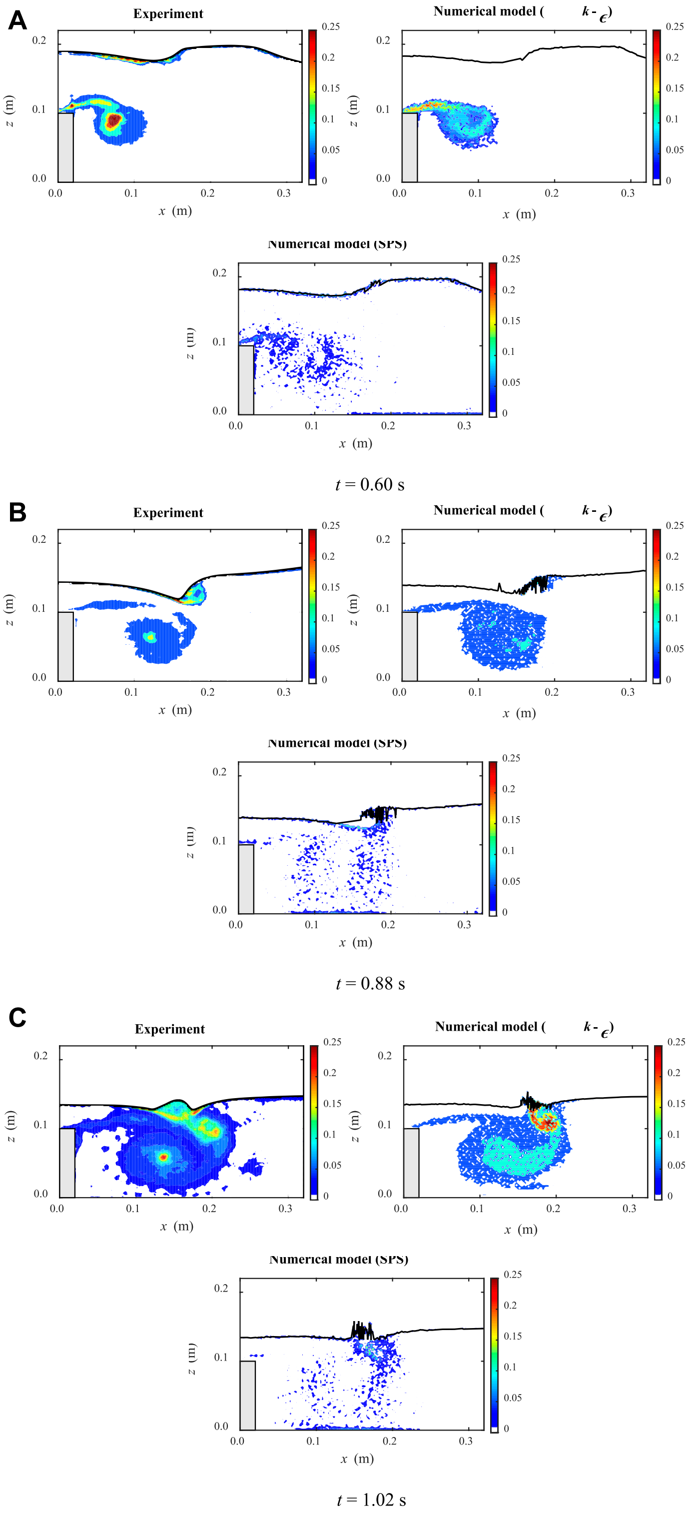

FIGURE 6 | Comparisons between experimental data and numerical results for the contours of turbulent intensity (m/s) at three times t = **(A)** 0.60 s; **(B)** 0.88 s; and **(C)** 1.02 s

3.4 Model Validation on Spatial Surface Displacements and Velocity Fields

Comparative snapshots of the spatial free surface displacements, velocity fields, and profiles of the horizontal and vertical velocities obtained from the laboratory measurements and the numerical simulations at three instants (t = 0.60 s, 0.88 s, 1.02 s) are shown, respectively, in **Figures 3A–C**, **Figures 4A–C**, **Figures 5A–C**, respectively.

Figures 3A–C show the spatial variations of free surface when the wave is passing over the vertical barrier. The fluctuations behind the barrier suggest that there are significant deformations due to the non-linear interactions with the barrier. Three different numerical results matched the experimental profiles quite well; but at the sharp wave dips in **Figure 3B** and wave tips in **Figure 3C**, both SPS and non-turbulence results showed some inaccuracies and numerical noise due to the inappropriate treatment of the turbulence effects. These places are where the local wave breaking occurs when the effect of turbulence must be well addressed. The benefit of the k–ε modelling indicated clear superiority in these areas.

Figure 4A–C provided the experimental and numerical velocity fields, computed with the k–ε model, LES-based SPS turbulence model and non-turbulence model, at the same time instants as the ones in **Figure 3**. All the numerical results well reproduced the existence of flow circulations immediately after the barrier and the whole flow structure. The three snapshots show that the numerical results realistically disclosed the characteristic events when the solitary wave propagates over the submerged barrier, which are the crest-crest exchange event (at t = 0.60 s), the backward breaker event (at t = 0.80 s), and the splash-up event (at t = 1.02 s).

No significant differences have been found for all the numerical results from different turbulence modelling approaches, except for the regions near the broken wave surface. This indicates that a turbulence model may not always be necessary for reproducing the macro flow field, and that a non-turbulence SPH can also achieve a satisfactory level of accuracy. The reason is related to the particle nature of the SPH method which makes it capable of reproducing a part of flow turbulence effect at the particle scale. This resolved effect is thus probably sufficient in the present case to replicate the average flow field of the experiment.

Figure 5A–C showed the comparisons for the profiles of horizontal and vertical velocities at four sections from x = 0.06 m to x = 0.20 m (with an identical interval of 0.04 m, shown by the dash-dotted lines in **Figure 3**). The velocity profiles were plotted by interpolating SPH particle velocities to the imaginary grid lines in the computational domain.

At times t = 0.60 and 0.88 s, almost no differences were observed for the numerical results of the three turbulence treatments as compared with the experimental data. However, at time t = 1.02 s as shown in **Figure 5C**, especially at section x = 0.18 m, the k–ε model results show better match with the experimental velocity profiles, not only in the velocity amplitude but also in the two turning points. This is the section where complex flow circulations and vortices are generated behind the barrier. From this, we can understand that an adequate turbulence model in SPH may not always improve the macro flow behaviours significantly, such as the flow surface and the average velocity structure in the present tests. However, for the micro flow details, such as the velocity or pressure profiles, the proposed k–ε model should demonstrate better advantages. This is due to the fact that a non-turbulence model cannot resolve the smaller flow structures below particle scale, mainly as a result of using coarse particle resolutions in the most SPH applications. On the other hand, also, the traditional SPS turbulence treatment (with the Smagorinsky model) cannot accurately capture these turbulence structures.

3.5 Model Validation on Turbulence Intensity

Figure 6A–C show the snapshots of the calculated turbulence intensity contours at three time instants corresponding to those of **Section 3.4** (i.e., at t = 0.60 s, 0.88 s, and 1.02 s). The experimental turbulent kinetic energy k was estimated as $k = 0.5\langle u'u' + w'w' \rangle_N$, in which the symbol < > represents the ensemble average, N is the number of repeated experiments (N = 35 in Wu et al. (2012)), and u' and w' denote the horizontal and vertical turbulent velocities, respectively. The numerical k was calculated from the k-$\boldsymbol{\varepsilon}$ equations and the SPS turbulence models (Gotoh et al., 2001).

The results show that the present ISPH model coupled with the k-$\boldsymbol{\varepsilon}$ turbulence closure satisfactorily reproduced the turbulence intensity, too, generated by the flow separations. Relatively large discrepancies appear in the core of the vortex, which might be related to the uncertainties of the repeated experiments during the ensemble averaged operation (Wu et al., 2012). On the other hand, the SPS turbulence model predicted somewhat unrealistic turbulence at very low levels, although the range of turbulence generations had been generally captured.

For a quantitative validation purpose, **Figure 7A–C** present the comparisons for the profiles of turbulence intensities at four sections from x = 0.06 m to x = 0.20 m (with an identical interval of 0.04 m, shown by the dash-dotted lines in **Figure 3**), at three instants of t = 0.60 s, 0.88 and 1.02 s, respectively. The turbulent intensity profiles were calculated by interpolating SPH particle quantities to the imaginary grid lines in the computational domain. It shows that the k-$\boldsymbol{\varepsilon}$ turbulence results agree with the experimental measurements in a very satisfactory manner, while the SPS model predicted very low turbulence levels at the scale of 10 times smaller. Therefore, we need to caution that the Smagorinsky-based SPS model may not be an appropriate tool for the prediction of turbulence quantities. Until the spatial resolution can become very refined, the k-$\boldsymbol{\varepsilon}$ turbulence model should still constitute an effective turbulence modelling technique in the SPH particle modelling applications. However, we should also note that the k-$\boldsymbol{\varepsilon}$ model tends to overpredict the experimental turbulence, especially at the later stage of wave separation such as at time t = 1.02 s, while SPS model is quite good at capturing small-scale turbulence.

4 EFFECT OF DIFFERENT GEOMETRICAL SIZES AND WAVE HEIGHTS

The validations in the previous section showed that the present ISPH method coupled with the k-$\boldsymbol{\varepsilon}$ turbulence model has a great capacity to simulate the fluid-structure interactions between the solitary wave and submerged structure.

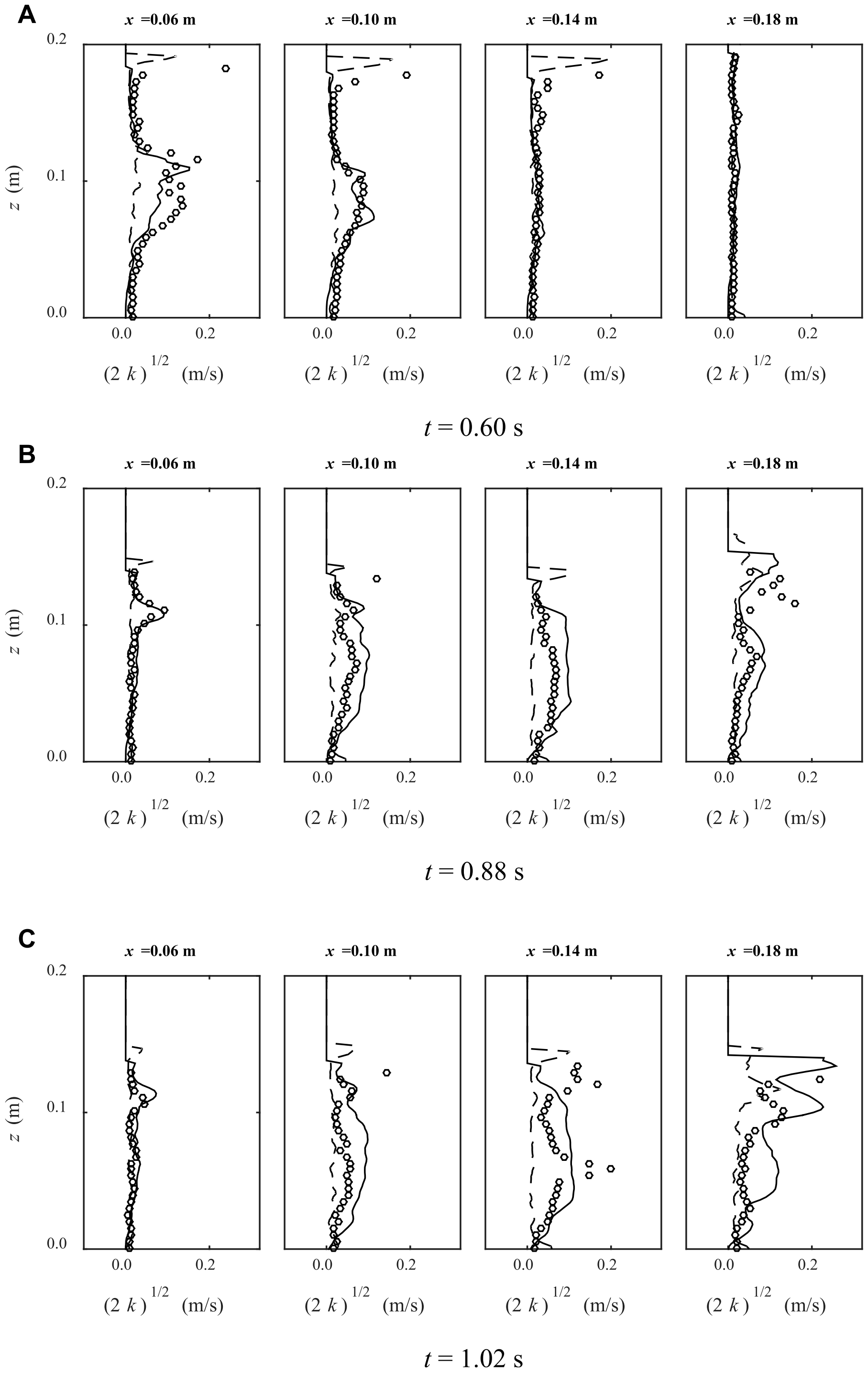

FIGURE 7 | Comparisons between experimental data (circles) and numerical results for the turbulence intensity (m/s) profiles, calculated by k-ε model (solid lines) and SPS model (dashed lines) at three times t = **(A)** 0.60 s; **(B)** 0.88 s; and **(C)** 1.02 s.

In this section, the effects of wave non-linearity and geometrical size of the submerged barrier on the flow separation are shown and discussed; and the reflection, dissipation, and transmission coefficients are also calculated to assess the importance of energy dissipation which is due to the generation of vortices.

4.1 Effects on Flow Separation

To investigate the effect of various geometrical sizes of the submerged barrier on the flow separation, detailed numerical experiments are performed using the validated model. In these simulations, the horizontal width and vertical height

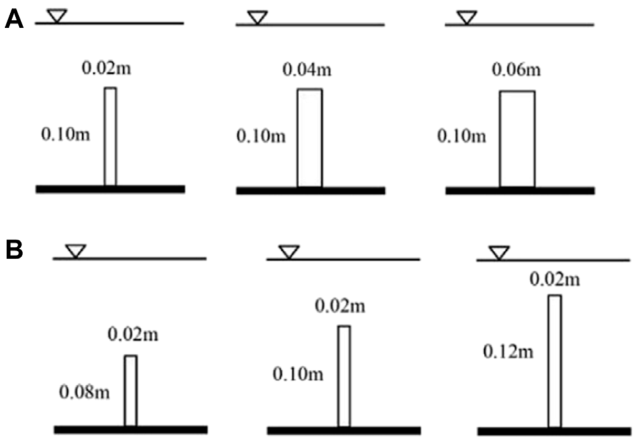

FIGURE 8 | Schematic view of the submerged barrier of different geometrical sizes: **(A)** setup for different widths (*W* = 0.02 m, 0.04 m, 0.06 m) with a fixed height (*L* = 0.1 m); and **(B)** setup for different heights (*L* = 0.08 m, 0.10 m, 0.12 m) with a fixed width (*W* = 0.02 m).

of the submerged structure are selected uniformly with an interval of 0.02 m. The range of the horizontal width (W) of the barrier was chosen to be 0.02–0.06 m (W/h = 0.14–0.42), and the range of the vertical height (L) was set to be 0.08–0.12 m (L/h = 0.57–0.85). A schematic view of the setup of the structure sizes is presented in **Figure 8A,B** (in total, five geometrical sizes were considered with three widths and three heights). The wave conditions corresponding to the previous section, that is, the water depth of h = 0.14 m and wave height of H/h = 0.5 were adopted.

Figure 9 shows the calculated velocity fields for different horizontal widths of the barrier at different times. It is shown that for the wider barriers, the distance between the vortex and the barrier becomes smaller. **Figure 10** shows the calculated velocity fields for different barrier heights. For the highest barrier (0.12 m), the main vortex transports further from it, and a larger secondary anticlockwise vortex in the downstream direction is generated. Due to the stronger breaking of free surface for the highest barrier, the secondary vortex transports into the deeper water. For the lowest barrier (0.08 m), the

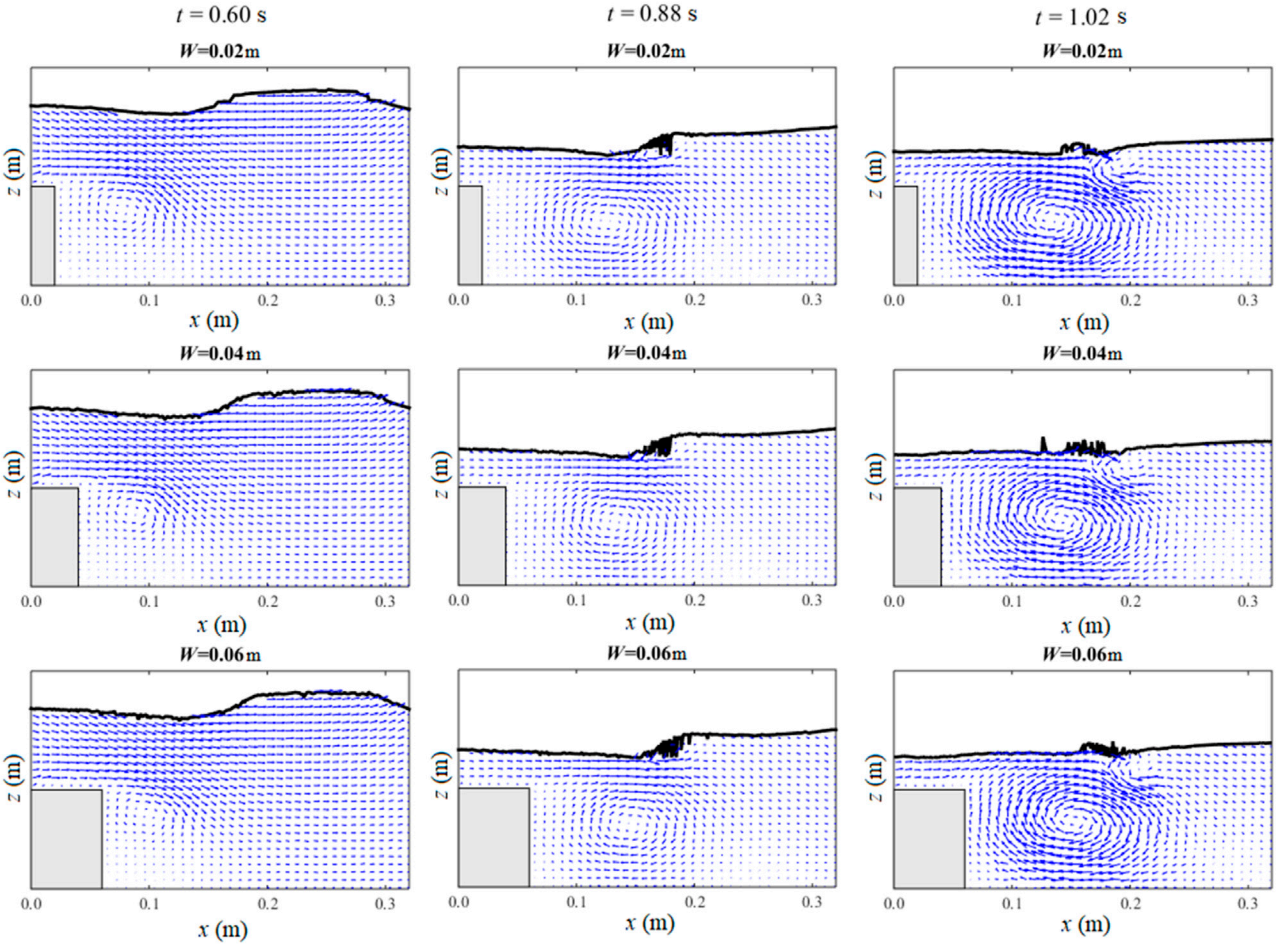

FIGURE 9 | Comparisons of calculated velocity vector fields for different horizontal widths of the barrier.

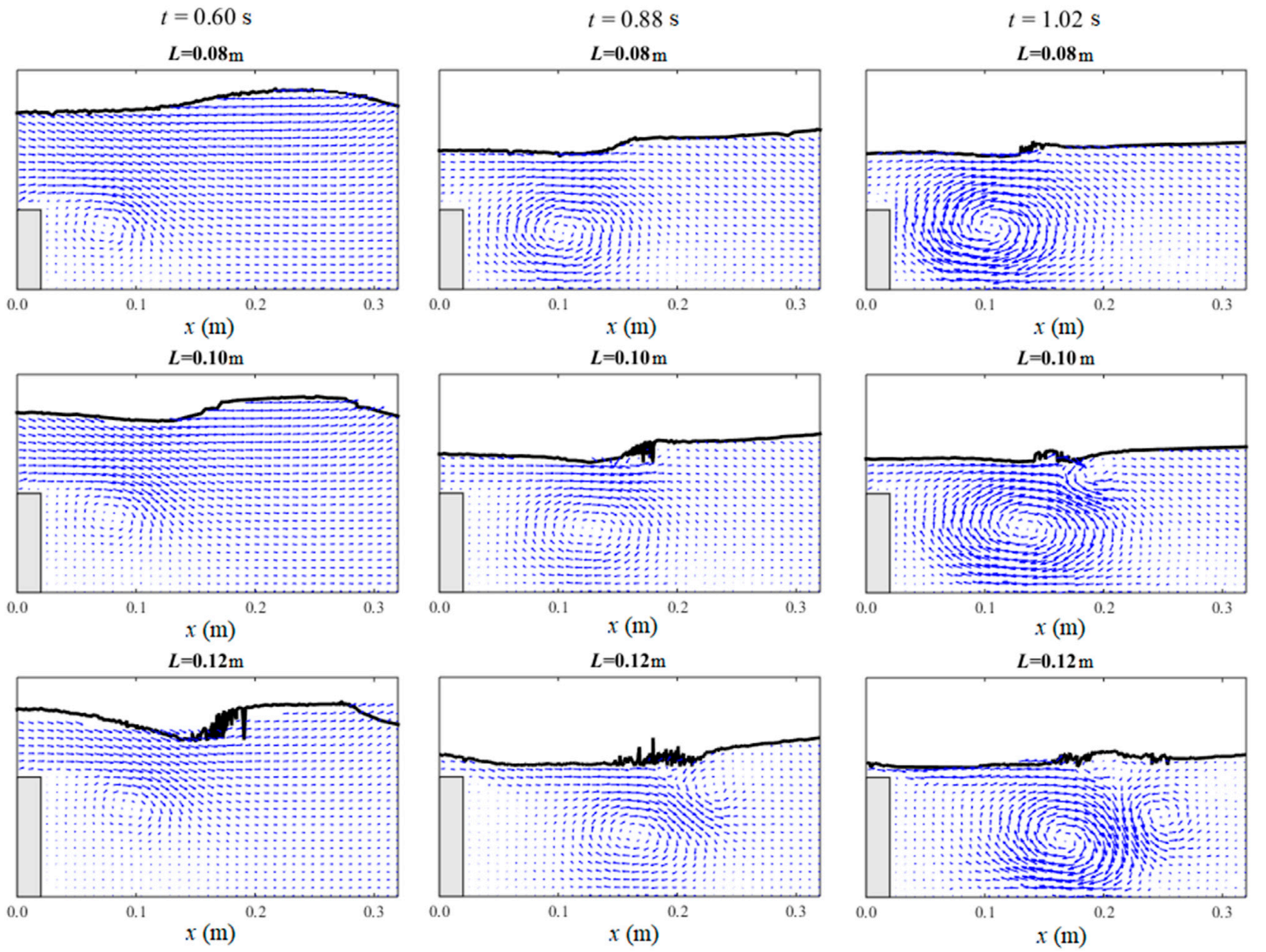

FIGURE 10 | Comparisons of calculated velocity vector fields for different vertical lengths of the barrier.

secondary vortex is not generated at all because the breaking near the free surface is very small in this case. The behaviour of the vortex behind the barrier with moderate height (0.10 m) has a situation between the other two.

4.2 Effects on Energy Transmission, Reflection and Dissipation Coefficients

Due to the wave-structure interaction under the processes of vortex shedding and wave separation, the energy coefficients will be influenced by the wave non-linearity and the geometrical sizes of structure. The effects of different values of wave non-linearity ($H/h = 0.1, 0.25, 0.35, 0.5, 0.6$, $h = 0.14$ m) and various geometrical sizes (the same as in **Figures 9**, **10**) of the submerged barrier on the reflection, dissipation and transmission coefficients are calculated in this section to evaluate the importance of energy dissipation due to the generation of vortices.

Figure 11A–F presents the time series of the free surface elevation at $x = -1.5$ m (upstream of the barrier) and $x = 0.5$ m (downstream of the barrier), simulated by the model, for different barrier geometrical sizes. The wave non-linearity is fixed at $H/h = 0.5$ ($h = 0.14$ m). The reference time ($t = 0$ s) is defined when the crest of the solitary wave arrives at $x = -0.657$ m (similar to Wu et al., 2012). **Figure 12A–E** shows the time series of the free surface elevation at $x = -1.5$ and 0.5 m for different incident wave heights, while the vertical height and the horizontal width of the barrier are fixed at 0.1 and 0.02 m, respectively. The results present the profiles of the incident and reflected waves recorded at $x = -1.5$ m, and the transmissive waves recorded at $x = 0.5$ m.

In order to provide a clear description of the characteristics of the solitary wave transformation over the barrier, the calculated values of the energy coefficients in terms of energy reflection (C_R), transmission (C_T), and dissipation (C_D) against different barrier width W, height L and incident wave height H, are illustrated in **Figure 13A–C**, respectively. Note all these indicators are normalized by the water depth h. The method proposed by Lin (2004) is adopted to calculate these coefficients for the sake of engineering applications.

According to the model results, the energy reflection coefficients increase rapidly as the barrier heights increase from 0.08 to 0.12 m ($L/h = 0.57–0.85$), but it keeps nearly constant for the different values of the barrier width (0.02–0.06 m, corresponding to $W/h = 0.14–0.42$). The energy transmission coefficient decreases with an

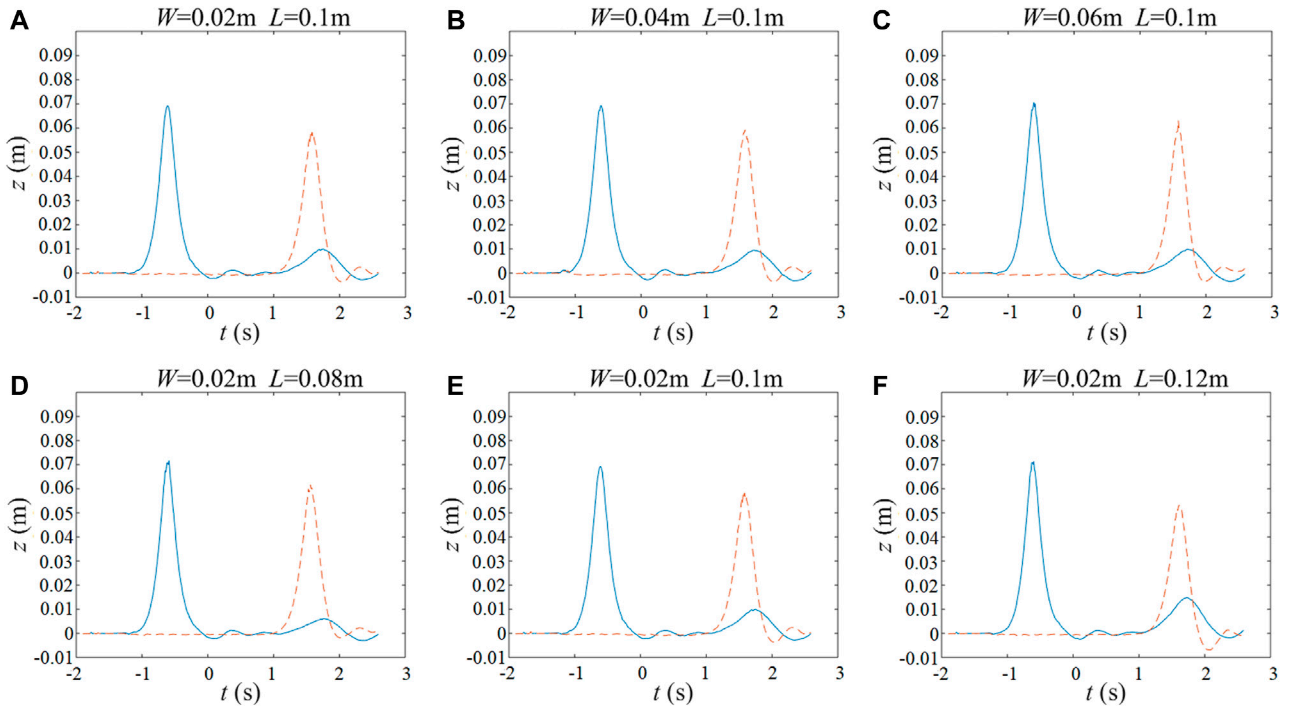

FIGURE 11 | (A–E) Time series of free surface elevation at $x = -1.5$ m (blue solid Q19 lines) and $x = 0.5$ m (orange dashed lines) for different barrier geometrical sizes.

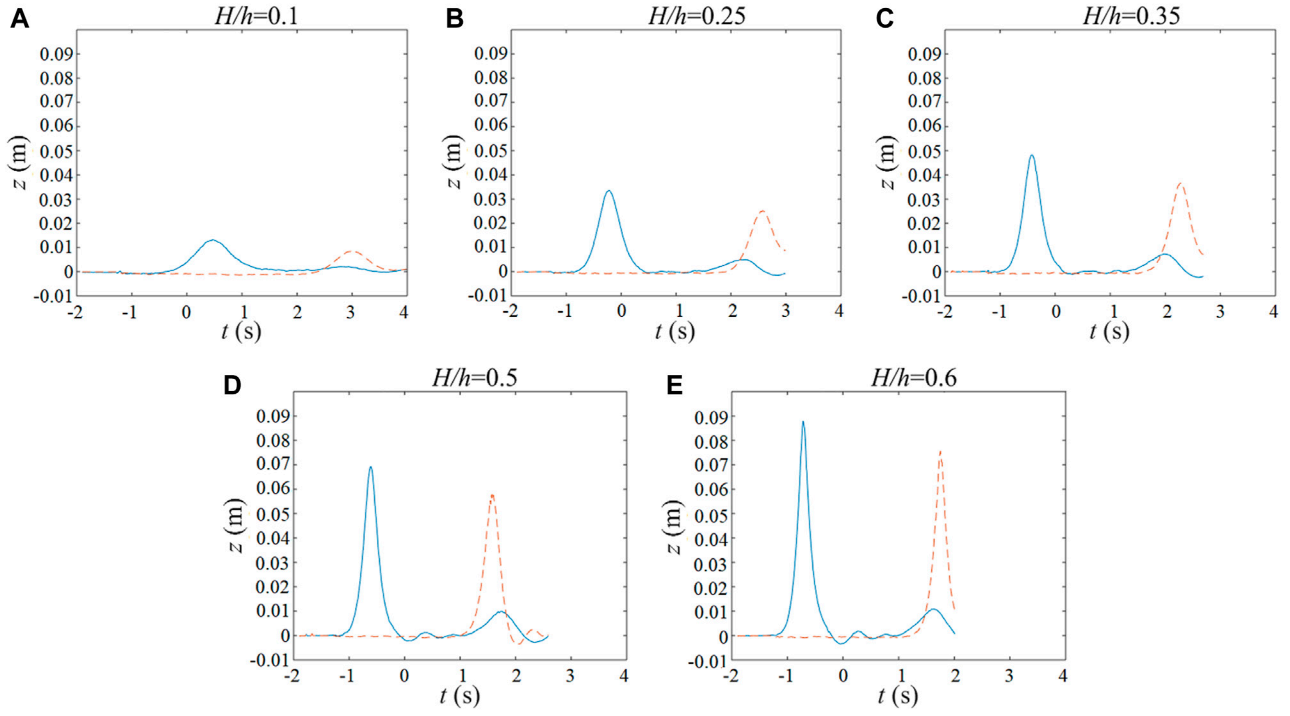

FIGURE 12 | (A–E) Time series of free surface elevation at $x = -1.5$ m (blue solid Q19 lines) and $x = 0.5$ m (orange dashed lines) for different incident wave heights.

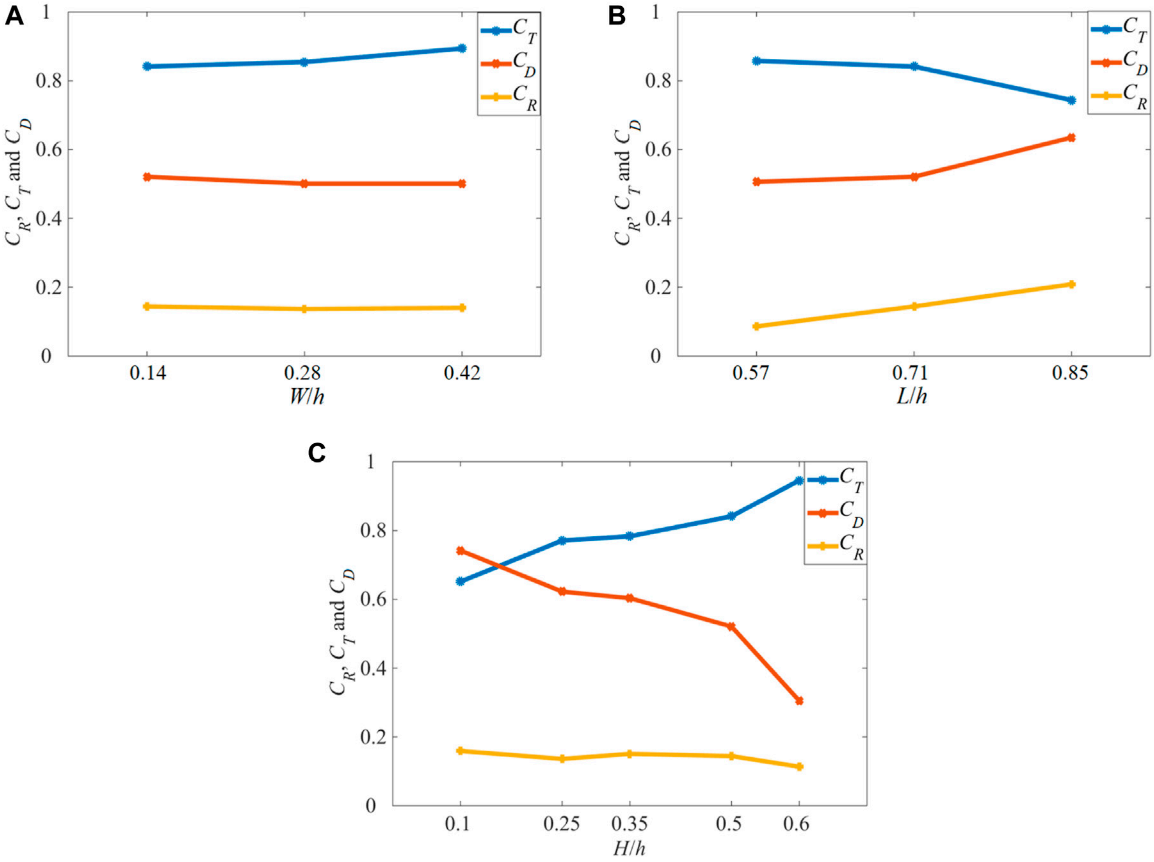

FIGURE 13 | Coefficients of wave reflection C_R, transmission C_T, and dissipation C_D vs different barrier **(A)** width *W*; **(B)** height *L*; and **(C)** incident wave height *H*.

increase in the barrier height, while it slightly goes up when a larger barrier width is used. On the other hand, the energy dissipation coefficient shows an opposite trend. It goes up with the increase of the barrier height and reduces slightly when the barrier width increases. Variations of these coefficients with the increase of wave non-linearity (*H/h*, from 0.1 to 0.6) show an increase in the transmission coefficient, an opposite behaviour in the dissipation coefficient (i.e., a decline), and small fluctuations (with a small decreasing trend) in the energy reflection coefficient.

5 CONCLUSION

In this paper, a validated ISPH method coupled with *k*-*ε* turbulence model was presented and applied to simulate the propagation of a solitary wave over the submerged bottom-mounted barrier. Through detailed comparisons with the experimental data, it was shown that the coupled model is capable of simulating the main features of the flow (i.e., free surface profile and velocity field) as well as the dynamics of the induced turbulent intensity with a good degree of accuracy. The model was then employed to study the effects of wave non-linearity and geometrical sizes of submerged barrier on the flow separations (which is often a difficult and expensive task to do in the laboratory or field). The variations of the coefficients of wave reflection, dissipation, and transmission with these factors were comprehensively investigated.

With regards to the two different turbulence modelling techniques applied in this study, i.e., the *k*-*ε* turbulence model and the Smagorisnky-based SPS model, the following understandings can be obtained. The *k*-*ε* model is usually employed with the time-averaged (Reynolds–averaged) Navier–Stokes (NS) equations to model the effects from the unresolved temporal fluctuations. However, its application with the SPH method in the present study indicates a LES type of turbulence modelling. This is because the equations are defined based on spatial average of flow quantities due to the use of SPH formulation. Therefore, in the present simulations, a part of turbulence effect is already resolved by the SPH discretisation itself, and a part of it is modelled by either the *k*-*ε* or the SPS models. Total turbulence in a LES context is composed of the resolved and the modelled parts. The resolved component can be calculated from the spatial deviations of the numerically estimated velocity with respect to its average over an averaging volume, and the modelled one is obtained from the relevant turbulence models, i.e., *k*-*ε* or SPS. In both cases, the resolved part of turbulence should be nearly the same. Also, because the resolved parts are expected to be quite small (see e.g., Kazemi et al., 2017; Kazemi et al., 2020b), it would be quite appropriate that the modelled parts be compared directly. Thus, a comparison was made between the modelled turbulence effects in this study, and it was shown that the *k*-ε model provides higher accuracy than the SPS model, when coupled with the ISPH method. In order to improve the applicability of the model, extension of it to 3D flow simulations is recommended.

DATA AVAILABILITY STATEMENT

The raw data supporting the conclusion of this article will be made available by the authors, without undue reservation.

AUTHOR CONTRIBUTIONS

DW and SY contributed to conception and design of the study. DW and SY organized the database. DW performed the statistical analysis and wrote the first draft of the manuscript. SY, CC, JL, XW and EK wrote sections of the manuscript. All authors contributed to manuscript revision, read, and approved the submitted version.

FUNDING

This work was supported by the National Natural Science Foundation of China (Grant No. 52101299 and 52001042), Fundamental Research Funds for the Central Universities of China (Grant No. 3132021163 and 3132019304), Open Funds of State Key Laboratory of Hydraulic Engineering Simulation and Safety (Tianjin University, Grant No. HESS-2113) and State Key Laboratory of Coastal and Offshore Engineering (Dalian University of Technology, Grant No. LP 2007) and Dalian Supports High-Level Talent Innovation and Entrepreneurship Project (Grant No. 2020RQ005).

ACKNOWLEDGMENTS

We are very grateful to Professor Philip Li-Fan Liu for his constructive comments during the establishment of the ISPH and the *k*–ε closure model, and Dr. Yun-Ta Wu of Tamkang University for providing the experimental data.

REFERENCES

Albano, R., Sole, A., Mirauda, D., and Adamowski, J. (2016). Modelling Large Floating Bodies in Urban Area Flash-Floods *via* a Smoothed Particle Hydrodynamics Model. *J. Hydrol.* 541, 344–358. doi:10.1016/j.jhydrol.2016.02.009

Farmani, S., Barani, G., Ghaeini-Hessaroeyeh, M., and Memarzadeh, R. (2019). Numerical Modeling of Flood Waves in a Bumpy Channel with Different Boundary Conditions. *Sci. Iran.* 26, 667–677. doi:10.24200/sci.2017.4582

Goring, D. G. (1978). *Tsunamis - the Propagation of Long Waves onto a Shelf,*. KH-R-38. Berkley: University of California, Keck Lab Rep. PhD thesis.

Gotoh, H., Shibahara, T., and Sakai, T. (2001). Sub-particle-scale Turbulence Model for the MPS Method-Lagrangian Flow Model for Hydraulic Engineering. *Comput. Fluid Dyn. Jour.* 9, 339–347.

Issa, R., Violeau, D., and Laurence, D. (2005). "A First Attempt to Adapt 3D Large Eddy Simulation to the Smoothed Particle Hydrodynamics Gridless Method," in Proc. Int. Conf. Comput. and Experimental Engng. and Sc., 1st Symposium on Meshless Methods, Stara-Lesna, Slovakia, June 2005.

Kazemi, E., Tait, S., and Shao, S. (2020a). SPH-based Numerical Treatment of the Interfacial Interaction of Flow with Porous media. *Int. J. Numer. Meth Fluids* 92, 219–245. doi:10.1002/fld.4781

Kazemi, E., Koll, K., Tait, S., and Shao, S. (2020b). SPH Modelling of Turbulent Open Channel Flow over and within Natural Gravel Beds with Rough Interfacial Boundaries. *Adv. Water Resour.* 140, 103557. doi:10.1016/j.advwatres.2020.103557

Kazemi, E., Nichols, A., Tait, S., and Shao, S. (2017). SPH Modelling of Depth-Limited Turbulent Open Channel Flows Over Rough Boundaries. *Int. J. Numer. Methods Fluids* 83, 3–27. doi:10.1002/fld.4248

Khayyer, A., and Gotoh, H. (2011). Enhancement of Stability and Accuracy of the Moving Particle Semi-implicit Method. *J. Comput. Phys.* 230, 3093–3118. doi:10.1016/j.jcp.2011.01.009

Kolahdoozan, M., Ahadi, M., and Shirazpoor, S. (2014). Effect of Turbulence Closure Models on the Accuracy of Moving Particle Semi-implicit Method for the Viscous Free Surface Flow. *Sci. Iran.* 21, 1217–1230.

Launder, B. E., and Spalding, D. B. (1974). The Numerical Computation of Turbulent Flows. *Comput. Methods Appl. Mech. Eng.* 3, 269–289. doi:10.1016/0045-7825(74)90029-2

Leroy, A., Violeau, D., Ferrand, M., Fratter, L., and Joly, A. (2016). A New Open Boundary Formulation for Incompressible SPH. *Comput. Math. Appl.* 72, 2417–2432. doi:10.1016/j.camwa.2016.09.008

Lin, P. (2004). A Numerical Study of Solitary Wave Interaction with Rectangular Obstacles. *Coastal Eng.* 51, 35–51. doi:10.1016/j.coastaleng.2003.11.005

Luo, M., Khayyer, A., and Lin, P. (2021). Particle Methods in Ocean and Coastal Engineering. *Appl. Ocean Res.* 114, 102734. doi:10.1016/j.apor.2021.102734

Napoli, E., De Marchis, M., and Vitanza, E. (2015). PANORMUS-SPH. A New Smoothed Particle Hydrodynamics Solver for Incompressible Flows. *Comput. Fluids* 106, 185–195. doi:10.1016/j.compfluid.2014.09.045

Pope, S. B. (2000). *Turbulent Flows*. Cambridge: Cambridge University Press.

Ren, Y., Luo, M., and Lin, P. (2019). Consistent Particle Method Simulation of Solitary Wave Interaction with a Submerged Breakwater. *Water* 11, 261. doi:10.3390/w11020261

Shao, S. (2006). Simulation of Breaking Wave by SPH Method Coupled with K-∊ Model. *J. Hydraulic Res.* 44, 338–349. doi:10.1080/00221686.2006.9521686

Shi, H., Yu, X., and Dalrymple, R. A. (2017). Development of a Two-phase SPH Model for Sediment Laden Flows. *Comput. Phys. Commun.* 221, 259–272. doi:10.1016/j.cpc.2017.08.024

Smagorinsky, J. (1963). General Circulation Experiments with the Primitive Equations. *Mon. Wea. Rev.* 91, 99–164. doi:10.1175/1520-0493(1963)091<0099:gcewtp>2.3.co;2

Soares-Frazão, S., and Zech, Y. (2008). Dam-break Flow through an Idealised City. *J. Hydraul. Res.* 46, 648–658. doi:10.3826/jhr.2008.3164

Wang, D., and Liu, P. L.-F. (2020). An ISPH with K–ε Closure for Simulating Turbulence under Solitary Waves. *Coast. Eng.* 157, 1–28. doi:10.1016/j.coastaleng.2020.103657

Wang, D., Li, S., Arikawa, T., and Gen, H. (2016). ISPH Simulation of Scour behind Seawall Due to Continuous Tsunami Overflow. *Coast. Eng. J.* 58, 1–23. doi:10.1142/s0578563416500145

Wang, D., Shao, S., Li, S., Shi, Y., Arikawa, T., and Zhang, H. (2018). 3D ISPH Erosion Model for Flow Passing a Vertical cylinder. *J. Fluids Struct.* 78, 374–399. doi:10.1016/j.jfluidstructs.2018.01.003

Wu, Y.-T., Hsiao, S.-C., Huang, Z.-C., and Hwang, K.-S. (2012). Propagation of Solitary Waves over a Bottom-Mounted Barrier. *Coastal Eng.* 62, 31–47. doi:10.1016/j.coastaleng.2012.01.002

Wu, J., Zhang, H., and Dalrymple, R. A. (2013). "Simulating Dam-Break Flooding with Floating Objects through Intricate City Layouts Using GPU-Based SPH Method," in *Lecture Notes in Engineering Computer Science. 3 LNECS*, 1755–1760.

Zhang, W. (2009). *An Experimental Study and a Three-Dimensional Numerical Wave basin Model of Solitary Wave Impact on a Vertical cylinder*. Corvallis: Ocean Engineering Program, Oregon State University. MSc Thesis.

Conflict of Interest: The authors declare that the research was conducted in the absence of any commercial or financial relationships that could be construed as a potential conflict of interest.

frontiers | Frontiers in Environmental Science

TYPE Original Research
PUBLISHED 05 September 2022
DOI 10.3389/fenvs.2022.976271

OPEN ACCESS

EDITED BY
Prashanth Reddy Hanmaiahgari,
Indian Institute of Technology
Kharagpur, India

REVIEWED BY
Ming He,
Tianjin University, China
Zhihua Xie,
Cardiff University, United Kingdom

*CORRESPONDENCE
Jiahua Wei,
weijiahua@tsinghua.edu.cn

SPECIALTY SECTION
This article was submitted to Freshwater Science,
a section of the journal
Frontiers in Environmental Science

RECEIVED 23 June 2022
ACCEPTED 01 August 2022
PUBLISHED 05 September 2022

CITATION
Liu R, Wei J, Wang Z, Zhang B and Zhang C (2022), Model integration methods for hydro-model platform under cloud computing environments.
Front. Environ. Sci. 10:976271.
doi: 10.3389/fenvs.2022.976271

Model integration methods for hydro-model platform under cloud computing environments

Ronghua Liu[1,2], Jiahua Wei[2,3]*, Zhongjing Wang[2], Bingyu Zhang[1] and Chi Zhang[4]

[1]China Institute of Water Resources and Hydropower Research, Beijing, China, [2]State Key Laboratory of Hydroscience and Engineering, Department of Hydraulic Engineering, Tsinghua University, Beijing, China, [3]State Key Laboratory of Plateau Ecology and Agriculture, Laboratory of Ecological Protection and High-Quality Development in the Upper Yellow River, School of Water Resources and Electric Power, Qinghai University, Xining, China, [4]TUM School of Engineering and Design, Technical University of Munich, Garching, Germany

Computing platforms providing cloud simulation services have raised new challenges on the model integration. Unlike calls to the model programs (components) in traditional simulation software, here the models should be dynamically integrated in the "plug and play" mode regardless of the differences in model type and developer. To this end two integration methods have been proposed, i.e., coarse-grained EXE integration and interactive integration. In an EXE integration method, the simulation program is directly called and thus only a data conversion interface is needed while rewriting of the model source code is not required. In contrast, an interactive integration method wraps the model components using the standard wrapper with communication interfaces, and therefore, it can communicate and exchange data with the platform in a real time. The first method is suitable for the integration of legacy models, while the second one can control the progress of simulation schemes and facilitate the scheduling of computing resources. Examples of the model integration and platform application have been presented in hydraulics/hydrodynamics to demonstrate the effectiveness of the integration method and the cloud computing platform.

KEYWORDS

hydromp, model integration, dynamic model management, cloud computing, hydraulics, hydrodynamics

1 Introduction

Real-time sophisticated water resource and hydro-environment management as well as decision-making are relying more and more on the simulation-based multi-scenario analysis, which imposes a challenging requirement on the simulation accuracy, reliability and computing speed. For example, in situations such as the optimal operation of long-distance water pipelines, emergency responses to the water pollution disaster and calibrations of the model parameters, decision-makers and researchers usually would like to select an optimized plan through the comparisons of a large number of optional schemes. On the other hand, it is common to use multiple simulation models to improve the prediction reliability of water management due to the stochastic nature and uncertainty of the fundamental hydrological process. Therefore, large amount of models and heavy computing resources are needed to achieve fast and various multi-scenario analyses. Meanwhile, as some of the computing resources are not always required, it would be more supportive to the decision-makers and economically viable if these could be provided when needed, so as to make the use of computing resources more effective. To satisfy such a requirement, one simulation service platform should have the following two characteristics: 1) it can provide flexible and pay-as-you-go hydro-environment simulation services based on its elastic and use-on-demand computing resources; 2) it can integrate and manage a large amount of different simulation models and thus the end users could have the options to select the most optimal one to achieve their multi-purpose tasks.

Cloud computing is an effective way of providing elastic computing resources. Studies and practices on the water resource management based on the cloud computing originated in 2012. For example, the Environmental Decision Support System (EDSS) used such cloud services as Google Drive and Google Fusion Table and obtained quite promising results Sun, (2013). Bürger et al. (2012) provided hydrological simulation cloud computing services using a platform named ParFlow with high performance clusters. Liu et al. (2013) built a platform “MODFLOWOnAzure” for ground water simulations based on the elastic computing resources of Windows Azure and they also got satisfactory speed up ratios as well. These applications have provided cloud computing services from different aspects or for a certain modeling tool. However, as far as our knowledge is concerned, it is still yet to develop a platform that could dynamically integrate the multiple models and provide simulations (Harris et al., 2021; Zhang et al., 2021; Gu et al., 2022; Gabreil et al., 2022) as a service.

Another difficulty in developing such a platform lies in the robust method of dynamic integrations. However, this is not a brand-new topic, since in literatures many integration methods for single-purpose information management and decision-making systems have been available. Wei et al. (2003) developed a groundwater simulation system based on Map Objects (MO) components and object-oriented technology, where a full integration between the Geographic Information Systems (GIS) and numerical groundwater models was achieved. In MIKE SHE developed by the Danish Hydraulic Institute (DHI, 2004; DHI, 2005), each physical process of the hydrological cycle was modeled and computed individually, and different hydrological cycles were simulated via the data exchange between the multiple models. Each model was wrapped as a component and each sub-process as a module. Based on the river network coding, the digital watershed model (Wang et al., 2007; Li et al., 2009) integrated the runoff, convergence and other simulation processes into a modeling platform, from which the hydrological simulation of the entire basin could be performed. In Peng et al. (2011), a relational database with pre-processing and post-processing modules was used to integrate the Environmental Fluid Dynamics Code (EFDC) Model and the Geographical Information System (GIS) Platform to develop a system with more efficient data processing, organization and analysis. Welsh et al. (2013) developed an integrated river management system, in which different processes such as basin runoff, river network/submergence analysis, water quality, scheduling, irrigation management, and other models were integrated into a simulation and regulation system to evaluate the water quantity and quality in the river basin. The open modeling interface (OpenMI) was used to provide the inter-operations between the model components, such as definition of the exchanged data and drive method. Gregersen et al. (2007) developed a method to integrate platforms and models in a single-process mode, where the single-step boundary definition method was adopted to provide good reference for the model integrations in a cloud platform. Besides, it has been reported by Peckham et al. (2013) and Overeem et al. (2013) that the Community Surface Dynamics Modeling System (CSDMS) also aimed to couple different simulation models with the HPC resources using the modularized method, while Rahman et al. (2004) and David et al. (2013) found that the Object Model System (OMS) and Integrated Customer Management System (ICMS) have the ability to integrate the multiple models which have been developed in an object-oriented language and component-based programming. Most of the above model integration methods use the concept of tight coupling and focus on the integration of models within the platform, which makes it difficult for the models to function independently among the HPC environment. Different with the tight coupling mode, where two programs interoperate by calling each other’s interfaces for data transfer and computation driving, and the same public variables are even used between the two model programs, the loose coupling mode does not call the interfaces directly, but achieve interoperation through third-party platforms. Tight coupling mode is relatively easier to implement as it does not need to consider the interface defined by the platform, and the developer can write the program to realize the data exchange and mutual invocation between the models accordingly. The platform is responsible for defining the standardized interface and calling the model program to achieve data transfer and interoperation, mainly focusing on the definition of the standardized interface and the data exchange and interoperation relationship between the model program, without the need to deeply understand the specific implementation of the model program. The model program does not need to consider the calls and data exchange with other model programs. Compared with tight coupling, the loose coupling mode is more suitable for cloud computing environment, especially for the integration of various complex program call relationship models and large system construction. Platforms such as CSDMS and OMS have achieved the loose coupling and provided useful information on the model integrations as proposed in this paper. However, dynamic integration of models in a cloud computing environment still faces a number of challenging issues, such as the plug-and-play and real-time interactions.

In this paper, two methods of the model integration are proposed, i.e., the EXE integration and interactive integration method. For the legacy models, non-destructive integration to the platform is required so the coarse-grained EXE integration method is proposed. With this method, the source code of the original model does not need to be changed and only a DLL file for data exchange between the model and the platform needs to be developed. On the other hand, for the open-source code models, real-time control on the simulation cases is needed and thus an interactive integration method is preferred. To carry out interactive integration, a standard model wrapper is constructed and the original model code needs to be converted to the model component satisfying the process requirement of the standard model wrapper. In addition, interface files for data exchange between the model component and the platform also need to be developed. With interactive integration, real-time communications between the models and the platform, such as pause, restart and information extraction during the simulation process can be achieved through the named pipes. Both EXE and interactive integration methods use loose coupling, i.e. the models and the platform belong to different processes, which makes the multi-scenario simulation and plug-and-play convenient. Through effective model management, they can be registered, go online or get offline without the need to stop and re-compile the platform. Both integration methods have been implemented on the Hydrological/Hydraulic Modeling Platform (HydroMP) in the work of Liu et al. (2017). It is worth noting that Liu et al. (2017) mainly introduced the architecture, brief technology and application of the cloud computing-based hydrology and hydrodynamic simulation platform HydroMP, while the present paper mainly focuses on the integration technology between the hydrological and hydrodynamic algorithm and the platform, and introduces the details of the integration technology of the model in detail.

This paper will present in details the model integration methods, including the model rewriting, data exchange, inter-process communication and model management. The structure of the paper is as follows: The second section introduces HydroMP and the platform architecture. The third and fourth sections describe the EXE and interactive integration methods, respectively. The fifth section describes the dynamic model management and the sixth section presents examples of the integrated method in hydro-environment applications. Finally the seventh section concludes the paper and discusses future research initiatives. Besides, technical details of the system implementation are provided in a separate Supplementary Appendix File.

2 HydroMP

HydroMP is a hydrological/hydraulic simulation service platform based on the cloud computing, developed to provide elastic and pay-as-you-go water environment simulation service to the decision makers. It is also the platform where the proposed two model integration methods are implemented. HydroMP provides cloud services using the SaaS (Software as a Service) mode (Mell and Grance, 2011) and adopts hybrid cloud architecture. As shown in Figure 1, it includes a HydroMP Center and a number of multiple dynamic HydroMP Servers. The HydroMP Server can be dynamically built into a public or private cloud HPC Cluster and registered in the HydroMP Center. The HydroMP Center deploys the computing resources for each HydroMP Server through a load balancer, thereby providing computing power of theoretically unlimited scalability. In the test environment of present paper, a single HydroMP Server is deployed on the Windows Azure commercial cloud platform to construct elastic HPC clusters through the expansion of virtual machines. Note that HydroMP uses the . Net Framework, which is more compatible with Windows than Linux.

The HydroMP Server performs scenario simulation, model/progress query, result acquisition, and other services through the web service interfaces. Each HydroMP Server integrates a large number of computing resources and hydraulic models. The computing resources are managed through a Windows HPC Server. The HydroMP Server calls the application programming interface (API) provided by the Windows HPC Server to use computing resources. With the proposed model integration methods, HydroMP can dynamically realize the registration, cancellation and information management of the models that meet the requirement of the interface, and the end-users can select appropriate models according to their applicability, accuracy and other indicators. HydroMP is a cloud computing platform for hydrological/hydraulic modeling tools that integrates the computing resources and models to provide scalable model computing capability. Any user terminal can submit a scenario to the cloud and select appropriate models for the specified scenario.

In the structure of HydroMP Sever, platform and computing nodes are distributed in the LAN. When the web service receives simulation requests, the API of the HPC Cluster is called to initiate the simulation processes. Each computing scenario corresponds to one simulation process and all of the simulation processes are randomly assigned to different computing nodes in the cluster. Platform management and scenario simulation can be considered as different processes running on different machines in the LAN. The logical structure of the platform, HPC Cluster and integrated simulation models are shown in Figure 2.

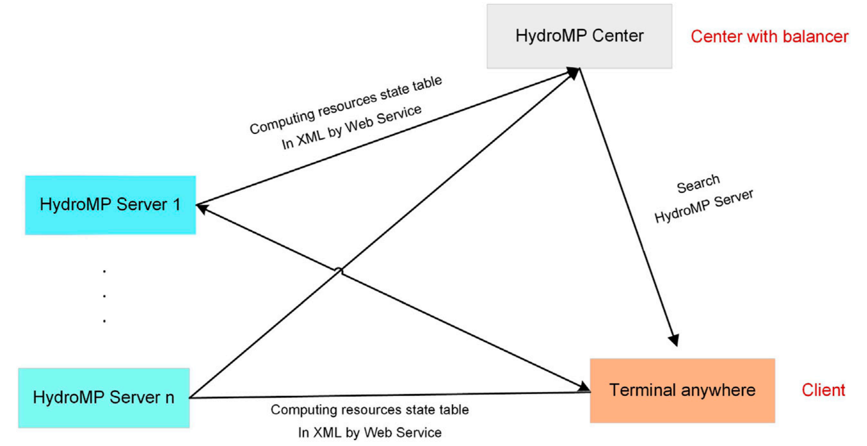

FIGURE 1
The structure of HydroMP platform.

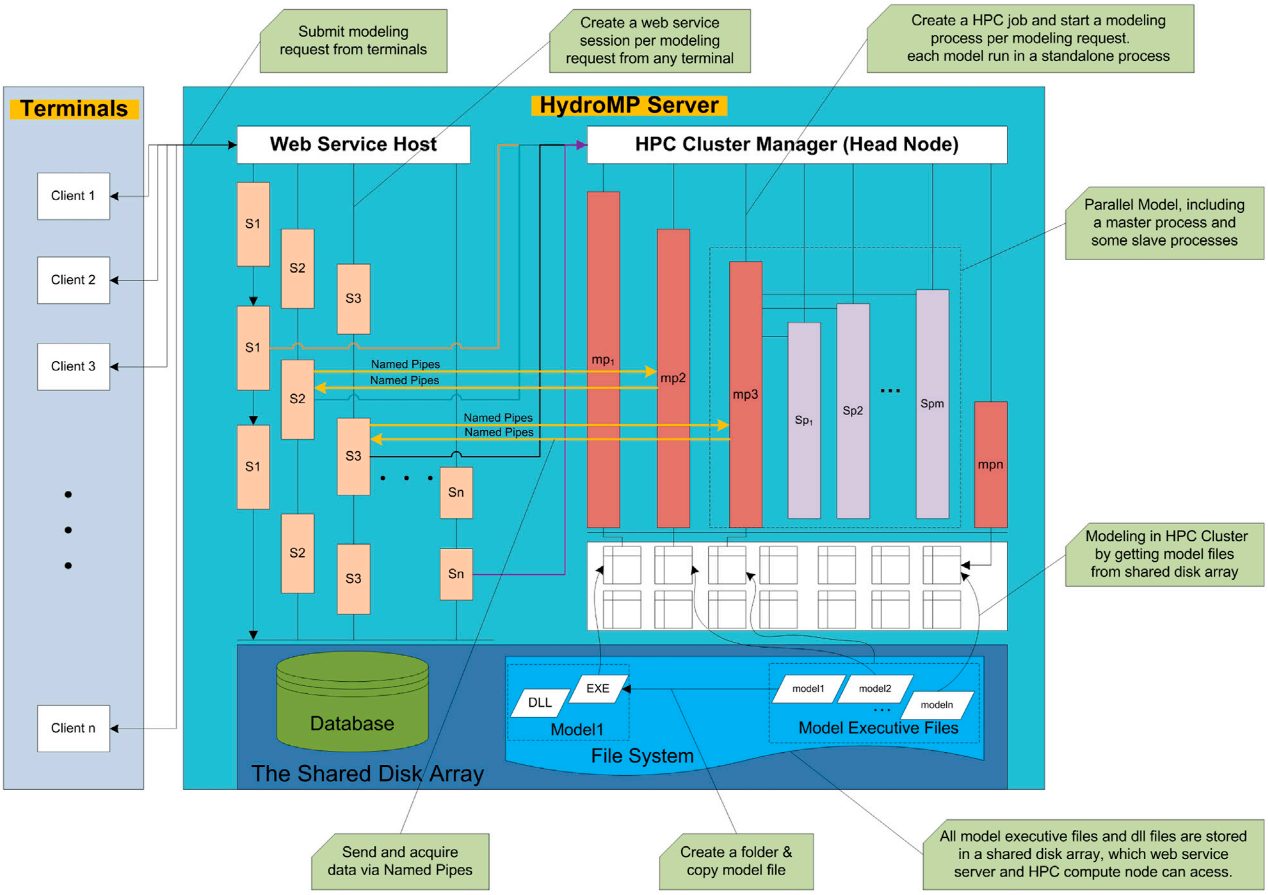

FIGURE 2
Logical hierarchy of the platform and model process in cloud computing environment.

3 EXE integration

Research on a large number of hydraulic models revealed that although these models differ in algorithm and handling of specific problems, the majority of them have the same basic requirements with regard to the system boundary and type of data (Fang and Wang, 2000; DHI, 2004; DHI, 2005; Hu et al., 2009; USACE, 2010; Zhu et al., 2011). For example, all one-dimensional hydrodynamic models of the river network require data on the topology, cross section, boundary condition, simulation parameter and initial conditions. The same calculation conditions across different models make the reuse of the models possible. With the multiple models being integrated in one platform, the users can select the appropriate model by its characteristics and suitability to perform particular tasks and call the interfaces through the Web, so as to enable sharing and reuse of the models. A coarse-grained, non-invasive model integration method (EXE) could be used, where the users do not need to understand the model process or change the model code for model integration.

This method has three characteristics: 1) the original process and code of the model do not need to be changed, and only the input and output file formats should be known. 2) if the integrated model sends output to a file during the simulation, the platform can access the simulation progress in real time using the file size. 3) the input files of the integrated model include all the variables that are parameterized. After the platform starts the simulation process, through real-time monitoring of the output file size, the data exchange can be performed immediately after the scenario simulation finishes. This will meet the real-time requirement of the platform on the model integration. The disadvantage of the method is that, during the running process the platform cannot communicate with the model process directly and thus it cannot control the running process of the model, i.e., the platform cannot pause or resume the simulations once started.

3.1 Method overview

EXE integration focuses on the conversion between the platform and model data structures, calls of the model program by the platform, and the relevant data communications. EXE integration is achieved via the following several steps: 1) by referencing to the Simulation Class provided by HydroMP and implementing the reserved InputFileCreate and OutputFileRead interfaces, the input and output file sets of a particular model are generated. 2) the executable file (EXE file) of the model and the generated input file set are copied, and the System. Diagnostics.Process method is used to run the EXE program. 3) the simulation progress is estimated by using real-time reading of the size of the model output file, thereby implementing the GetComprocess interface. The whole EXE model integration process and its interaction with the platform are shown in Figure 3, which demonstrates the interaction between the platform and DLL and EXE files.

3.2 Interface implementation and file management

The main purpose of the interface InputFileCreate is to generate model input files and start the simulation. The interface GetComprocess estimates the simulation progress by reading the size of the output file. This method applies only to the models running in the simulating-while-outputting mode but not to the models that output the results when the simulation is completed. For the models with constant output step and time intervals, the size of the main output file has a linear relationship with the simulation progress.

The interface OutputfileRead is called once the simulation is completed. Before calling this, it must be determined whether the simulation has been completed or not. Three criteria are used during this process, i.e., simulation progress, file size and any possible error message. The method of reading the output results is opposite to that of generating the input file. The main task is to convert the format of each model output file into the data format required by the platform. After the reading, the file folder generated in Step (1) as illustrated above is deleted.

3.3 Requirements of model integration

The platform scheduler is used to generate the input file and read the output file by calling the unified data conversion interfaces during the running of the model program, and the process management method in the . NET framework is called to initiate the running of the model. Therefore, models that can be integrated using this method must meet certain requirements: 1) data structures and character encoding of the input and output files must be open and clear; and 2) the compiled EXE file must be able to run on Windows platforms. The greatest advantage of EXE integration is that there is no need to rewrite the model source code. However, the platform cannot control or schedule the running of the model, and therefore cannot guarantee real-time access to the model's progress and results.

4 Interactive integration

4.1 Method overview

In an interactive integration, the model can interact with the platform in real time while running, which enables the features such as model process control, progress acquisition, error messaging, and result acquisition. In HydroMP the platform

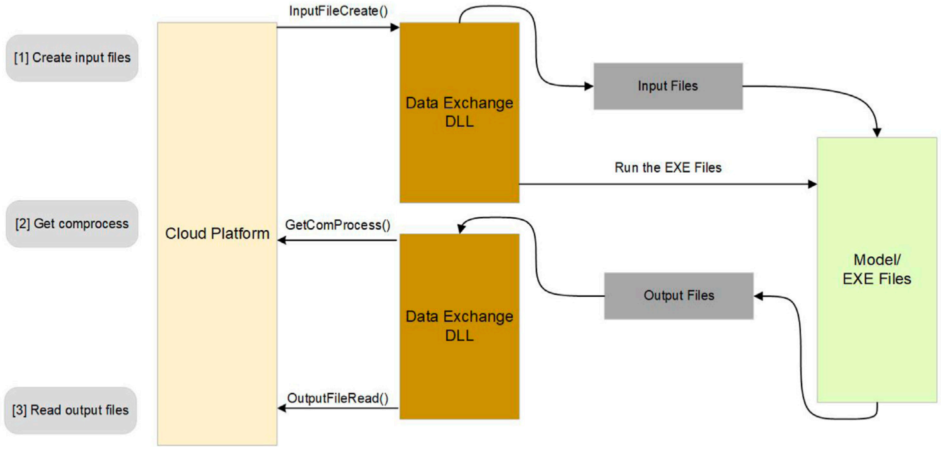

FIGURE 3
Running process of the model in EXE integration mode.

and model programs run independently on different operating systems in the LAN. Their interactions are thus cross-platform inter-process communication on the same network segment. In general, there are three approaches for the inter-process communications: clipboards, anonymous pipes and named pipes. The clipboard approach is the fastest, but it can only realize communication of the processes running on the same machine. The anonymous pipe approach is used for local communication between the parent and child processes, while the named pipes approach facilitates two-way communications across the networks with the advantages of having simple interface and logical clarity.

Based on the relative locations and dependency relationships of the platform and the model, Named Pipes are used for communication in the proposed interactive model integration. To do this, the named pipes are established between the platform and the model programs, and a set of simple and practical communication rules are defined. The header information on the message string serves as a flag for the identification of communication types, which facilitates rapid parsing of the data at both ends of the pipe once the message is received. A two-layer integration mode is used to speed up the integration and reduce the amount of model code rewriting required. Firstly, a standard wrapper is developed to serve as the middleware between the platform and the models, which can communicate with the platform via named pipes. Secondly, the standard wrapper integrates the models by referencing to the model components and calling the corresponding interfaces. This two-layer integration mode, as shown in Figure 4, reduces the difficulty of integration process since there is no need to consider the communications during the model rewriting. In general, the interactive integration approach includes four steps, namely, rewriting of the model code, implementation of the data conversion interface, generation of the new model executable file using the standard wrapper, and registering the model.

4.2 Standard wrapper

The standard wrapper provides a standard program for the communication between the integrated model and the platform, and it communicates with the platform using named pipes. For messages from the platform to the standard wrapper, there are five categories of identifiers, namely, model initialization, initiation of simulation, pausing of simulation, progress acquisition, and result acquisition, which corresponds to the identifiers as Initialize, Start, Pause, Progress, and Result, respectively. There are four categories of messages sent from the standard wrapper to the platform: simulation progress, results of simulation, simulation completion, and pause completion.

The flow chart of the standard wrapper is shown in Figure 5. There are five steps: pipe creation, initialization, data parsing, scenario simulation, and simulation completion. In the initialization step, the wrapper receives the scenario data sent by the platform and obtains a serialized XML byte stream. In the data-parsing step, it desterilizes the byte stream of the scenario into arrays of the wrapper, calls the interface in the data conversion component to generate input file byte streams, and then executes corresponding interfaces in the model component. The scenario simulation step includes the operations such as single-step execution, boundary update, and result acquisition. With the step length parameter, the single-step execution interface performs simulation for a single time step and automatically updates the initialization condition of the model when the simulation is completed. The parameter for the

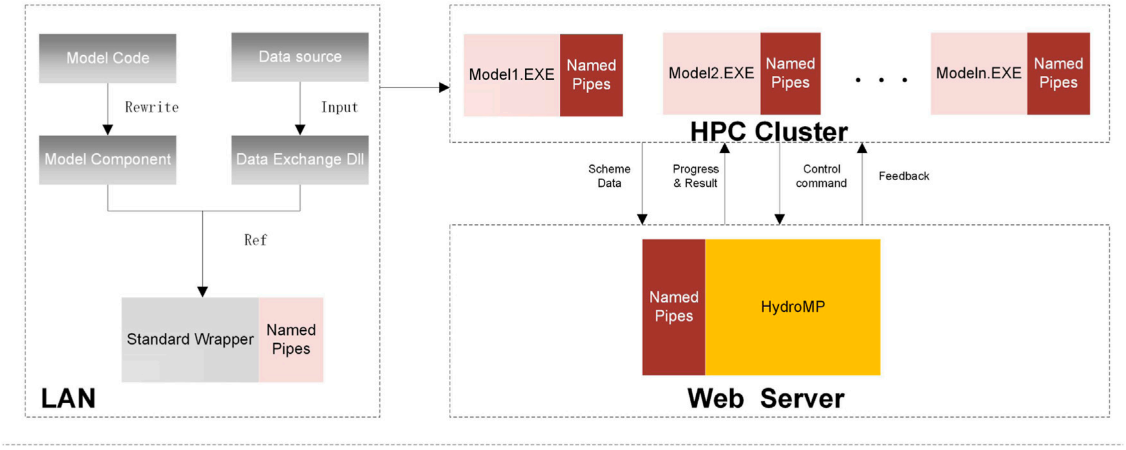

FIGURE 4
Interactive process between platform, model wrapper and DLL files.

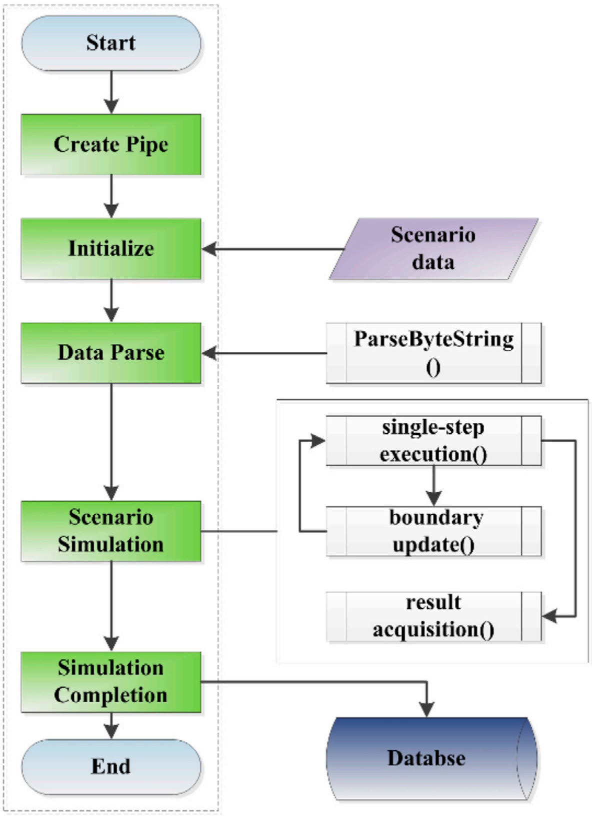

FIGURE 5
Process of the standard model wrapper.

boundary update interface is the boundary condition array in the next time step that includes all the required boundary conditions. The parameter for the single-step result acquisition interface is the time step and the return parameter is a string that needs to be parsed by the data conversion component interface and then attached to the result set array SimulationOut of the wrapper.

4.3 Methods of rewriting the model

The model wrapper serves as a bridge for communication between the model and the platform. In addition to processing various requests and parsing data sent by the platform, another important role of the model wrapper is to directly integrate the model program (component), call the model interface to execute the simulation, and control the simulation process. In order to integrate a model program into the standard wrapper, the model program must be rewritten and exported in a manner as required by the standard wrapper, forming a model component DLL file. To illustrate the communication between the standard wrapper and the platform and the integration of the model component, the pseudo-code of a standard wrapper is shown in the Supplementary Appendix File.

As shown from the pseudo-code, the standard wrapper needs to call two DLL files: the model component DLL file and the data conversion component DLL file. According to the format of the input files, output files, and single-step boundary data of the model, the data conversion component implements the data conversion interface that converts the data structure of the wrapper into the byte stream format as required by the model component. A new model program is generated by replicating the standard wrapper, referencing the model component DLL file and the data conversion DLL file in this wrapper, and recompiling. After registration, this generated model program can be dynamically called by the platform and there is no need for the platform to recompile and restart.

4.4 Data exchange procedure and method

4.4.1 Exchange of simulation scenario

The scenario string in the wrapper contains three segments of characters—basic information, data set information, and array information, so as to implement data exchange between the wrapper and the platform. Because the format of the input files differ largely between the models, it is not possible to use structured data for the data exchange. A common feature of the input files is that they are a number of text files, although the number of files and data (variables) stored in each file could vary between the models. Based on this, the interactive integration method uses the same number of byte streams as the input files to transmit the scenario string in the wrapper to the model component.

4.4.2 Exchange of result set

The result set of the wrapper includes five different arrays. The first array is of digital type and defines the number of time-series data points; the second array is of length L and defines the type and unit of the output data; the third array defines the serial numbers of the output objects and is an integer array of length M; the fourth array is of length N and defines the time of each data with the format of YYYYMMDDHHMMSS, which is 14 characters long; and the fifth array is of length L*M*N, defining the simulation objects, time points and data types.

4.4.3 Exchange of single-step boundary condition

The single-step boundary conditions, as part of the simulation control, facilitate the data exchange in the scheduler for subsequent integration of the multiple models. The string parameters of single-step boundary function include all the boundary conditions that need to be updated for the model to enter the simulation in the next time step, including the number of boundaries, the serial numbers of boundary objects, the types of boundary conditions, and the numeric values of boundary conditions. For one-dimensional hydrodynamic simulations, it includes the parameters such as Water Level, Discharge, and Lateral Q. The water level—flow discharge relationship is a boundary that does not need to be updated and is thus beyond the scope of single-step boundary conditions.

5 Dynamic model management

The model program generated using either integration approach as described in Sections 3, 4 includes an executable EXE file, a dependent DLL file, and a data conversion DLL file. The platform manages the models by recording the location of the files, model name, model type, model status, and other parameters. Model management includes the operations such as model registration, model cancelation, information editing, and model deletion. All registration information is stored in the model table RegisterModel, the structure of which is shown in Table 1.

TABLE 1 Structure of model management table.

No.	Field Name	Field Type	Description
1	ModelName	Char (30)	Model Name
2	ModelType	Char (10)	Model Type
3	ModelDIR	Char (70)	Model path
4	DataExcDIR	Char (70)	Convert file path
5	ModelState	Number (1)	Model state

In the RegisterModel, ModelType consists of 10 characters. The first two specify the type of the model, e.g., hydrological model, hydrodynamic model, or water quality model. The 3rd and 4th characters indicate whether the model is empirical or physical. The 5th and 6th characters denote the dimension of the model, namely, one-dimensional, two-dimensional, or three-dimensional. The 7th and 8th characters denote the type of model integration, namely EXE integration, interactive integration, or OpenMI standard components. The last 9th and 10th characters are the reserved bits.

Model management involves the addition, deletion, modification, and inquiry of the model table. The HydroMP Server provides web service interfaces for the model management, including ModelRegister, ModelEdit, ModelDelete, and ModelUnavailable. When registering a model, the platform administrator needs to store the model name, model path, and data conversion interface file path into the model table.

6 Example of model integration and application

6.1 Example of model integration

Two one-dimensional hydrodynamic models of river networks, CE-QUAL-RIV1 (Dortch et al., 1990) and JPWSPC (Zhu et al., 2011), were used as examples to describe the integration process of different model integration methods. The CE-QUAL-RIV1 model is a 1D hydrodynamic model developed early by the US Army Corps, including a hydraulics module and a pollutant module. It is a legacy model and thus the EXE integration method will be used. The JPWSPC model uses the joint point water stage prediction-correction method to solve the hydrodynamic process of complex river networks. This model will be integrated into the platform using the interactive integration approach.

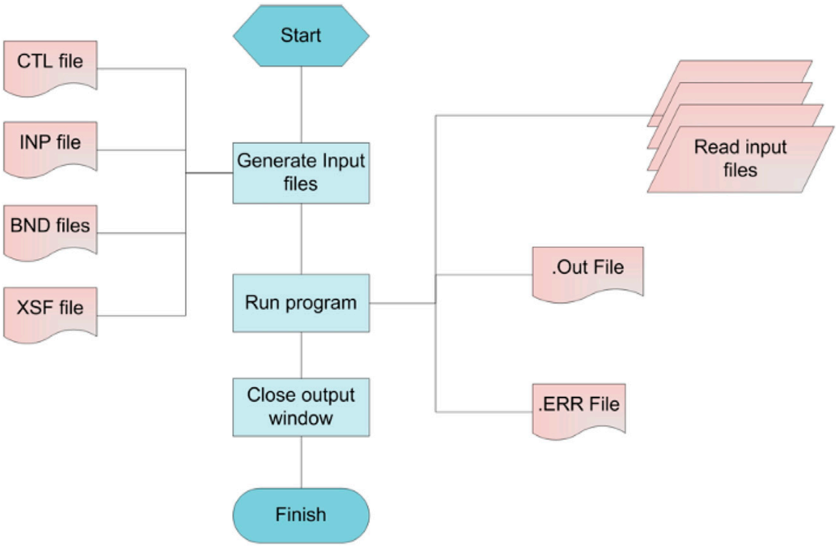

FIGURE 6
Running process of CE-QUAL-RIV1.

The input files of the CE-QUAL-RIV1 model include CTL, INP, XSF, BND, and LAT files, representing the control file, main input file, cross section file, boundary file, and lateral inflow file, respectively. The control file gives the names of the subsequent files. The main input file includes the basic river network information, topology, initial conditions, regular cross section, and coefficient of roughness. The cross section file gives the information of irregular cross sections, corresponding to the micro-segments in the INP file through the names of the cross sections. The boundary file gives the time series values of the unsteady upstream and downstream boundaries, which correspond to the river network structure through numbering of the branches. The lateral inflow file documents the unsteady lateral inflow data at different micro-segments. To run the simulation program, one needs to first generate these five files and then double-click the EXE program. The EXE program outputs the results into the OUT file in accordance with the output interval settings defined in the input file while running, until the completion of the simulation. A flow chart of the running process is shown in Figure 6. The CE-QUAL-RIV1 model is integrated by using the coarse-grained, non-invasive integration method, which includes the class referencing, input files Creating interface implementation, Get computing process interface implementation and Output File Reading interface implementation. The details are also shown in Supplementary Appendix SA.

The interactive integration approach is used for the integration of JPWSPC model. The original program is rewritten into four functions: Initialize, PerformTimeStep, BndConditionUpdate, and GetStepResult. These functions are then wrapped into the JPWSPC_Model.DLL file. The main function of Initialize is to read the byte streams and parse them into different arrays in the model. The BndConditionUpdate is to update the double-precision boundary data arrays in the model according to the numbering of the boundaries. With PerformTimeStep, one time step of simulation is performed based on the current initialization conditions and boundary conditions to obtain the properties of each micro-segment in this time step. With GetStepResult, the results of single-step simulation of the model are packaged into a byte stream for output.

By comparing the data structure of the wrapper with that of the JPWSPC model, the data structure conversion DLL file JPWSPC_DataExchange.DLL is generated according to the format requirement of the model file, the encoding format of the result byte stream and the sequence format of the boundary condition. Finally, the new executable file JPWSPC-SC. EXE is generated by referencing the JPWSPC_Model.DLL and JPWSPC_DataExchange.DLL files in the standard wrapper. Besides the two models describe above, a number of models including the hydrodynamic model of canal control (Zhang et al., 2007) and the sedimentation model (Zhong et al., 2004) have also been integrated into HydroMP.

6.2 Model application in middle route of South-North water diversion project

In this section the HydroMP with integrated models is applied to the scheduling policy study in the middle route of

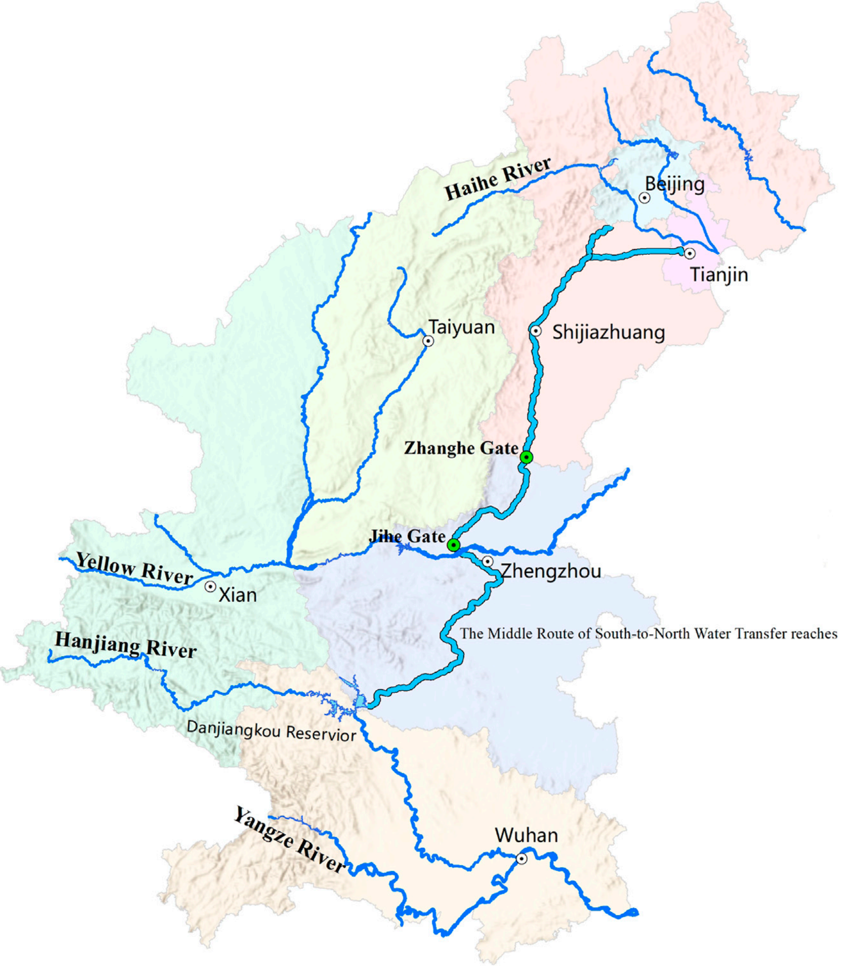

FIGURE 7
The middle route of South-North Water Diversion project.

South-North Water Diversion project (SNWD). The middle route of SNWD is an extra-long water diversion project in China with 1753 cross-sectional structures along the river path, including 61 control gates and 141 diversion gates, which have a total length of 1277 km. A schematic view of the route of SNWD is shown in Figure 7. The operation practice of keeping constant water level in front of the control gate is commonly used to ensure the gate safety. The control and regulation of the main channel are achieved through the coordination of the control gates, diversion gates and outlet gates. The maintenance of constant water level at the control gates becomes much more complicated under the emergency conditions (e.g., a control gate must be closed in a short time in case of the pollution incident). To get an effective control scenario, massive simulations must be concurrently performed and compared to analyze the influence of different regulation factors.

The canal segment between the Jihe Gate (chainage of 493.138 km) and Zhanghe Gate (chainage of 731.527 km) is taken here as the study segment. Assuming that the upstream canal encounters an emergency, all the control gates in this canal segment must be closed imminently. Different operation scenarios are designed to simulate the response of the flows. The initial conditions are set as follows. The upstream flow has the designed discharge value of 265 m^3/s and the downstream water level is set to the designed value of 91.971 m. Two sets of scenarios are designed to analyze the individual influence of the speed and magnitude of gate movement. For each gate movement, five values are specified. With ten control gates and two 1D hydrodynamic models, there are 200 scenarios in total. These scenarios are concurrently submitted to the HydroMP and the simulation results are obtained in a real time. The simulation results show that the range of gate movement is a key factor to affect the flow and water level stability in front of the control gate. Also, it is found that the movement range of different gates should be adjusted according to the distance between the gate and the emergency location. Generally, a gate closer to the emergency location should be set a larger movement range in the beginning phase.

With HydroMP, 11 min were consumed to perform the simulation of 200 scenarios, where 40 virtual machines with 8 cores in Windows Azure were employed to construct the HPC Cluster. The process included scenario group submission, scenario simulation and simulation result acquisition. To verify the efficiency of cloud computing, all the scenarios were simulated sequentially using a single machine and it took nearly 4 h. The speedup ratio of parallel computing is up to nearly 22 times. Note that the parallel efficiency is 0.068. It is found that the main reason for the low parallel efficiency is that the network bandwidth is not enough, which leads to a long waiting time for job submission.

The scalable computing resources provided by HydroMP built in the cloud environment can greatly improve the efficiency of scheduling policy analysis. Moreover, comparison and validation of simulation results using the multiple models are much more convenient because the models integrated into HydroMP can use the same data structure *via* the data exchange interface in the DLL files. For the end users, both parallel computing and multi-model simulation can be performed on HydroMP platform without extra work.

7 Conclusion

Compared with model integration within a stand-alone system, one difficulty of model integration in cloud computing environments is that the simulation platform and model processes are running on different computers in the LAN of the HPC Cluster. Moreover, the requirements of “plug and play” and universality further increase the difficulty of model integration. According to the characteristics of legacy models and the requirements of multi-model coupling, the EXE integration method and interactive integration method are proposed. The integration processes, requirements on the models, and respective advantages and disadvantages of each method are presented. The details of model rewriting and calling, data exchange, and communications involved in the model integration are described. Model management and classification by the platform are also briefly introduced. The integration processes of two different 1D hydrodynamic models are given as examples to illustrate the practical application of these integration methods. Until now five different hydraulic and sedimentation models, viz. CE-QUAL-RIV1, JPWSPC-SC, JPWSPC-PC, Zhang-Model, THU-SEDIMENTS, have been integrated into HydroMP. These models can be accessed by the end-users anywhere and can be driven by the platform to perform real simulations. The integrated HydroMP framework has the capability of coupling 1D and 2D models, focuses on the boundary condition treatment and date process and transfer. In the interactive integration method, real-time data exchange between different models at a single time step is realized, solving the problem of data transfer and boundary condition treatment. In this case, users can use the inheritance mechanism in the software to write different processing methods.

From the examples of platform application, it was found that the platform can run steadily while concurrently performing 200 scenario simulations using different models and the simulation results can be acquired in real time when the model is integrated in the interactive mode, which demonstrates the effectiveness of the proposed model integration methods and their “plug and play” property. The speedup ratio of about 22 shows the practical efficiency of HydroMP in the cloud computing environment. Meanwhile, it can also be seen that the concurrent simulations of multiple scenarios by using different models can be achieved in a cloud environment. This has significantly increased the simulation efficiency, which has a more prominent speedup effect for the computationally intensive applications.

Future work could include the following aspects. 1) The multi-model coupling interface reserved in the interactive integration method requires further verification. 2) Currently, text files and Named Pipes are used as the message passing channel. Further study should be conducted to use relational databases as the communication media in cloud computing environments. 3) The universality of the proposed model integration methods should be tested on two-dimensional, three-dimensional, and distributed hydrological models. 4) The startup and shutdown of virtual machine should be executed automatically based on the real-time computational needs by calling the scripts by Windows Azure. 5) Simulation interface based on the WebGIS would be more favorable than the currently adopted Terminal + Cloud mode. Furthermore, the proposed model integration methods, although having been designed for cloud computing environments, are also applicable to the stand-alone systems. System designers and developers can choose an appropriate model integration method as per communication cost and complexity of the integrated systems.

Data availability statement

The raw data supporting the conclusion of this article will be made available by the authors, without undue reservation.

Author contributions

RL: investigation, writing—original draft, writing—review and editing; JW: supervision, investigation, writing—review and editing; ZW, BZ, and CZ: investigation, writing—review and editing.

Funding

This work has been sponsored in part by the National Key Technology Research and Development Program of the Ministry of Science and Technology of China (No. 2019YFC1510605), Science and Technology Program of Qinghai (No. 2020-GX-ZL 15) and Program of Joint Research Institute of Tsinghua University—Ningxia Yinchuan for the Internet of Water and Digital Governance (Nos SKL-IOW-2020TC 2004 and SKL-IOW-2022TC2201).

Acknowledgments

We would also like to thank all our sponsors and other members of the HydroMP and Cloud Computing Research Group at the State Key Laboratory of Hydroscience and Engineering.

Conflict of interest

The authors declare that the research was conducted in the absence of any commercial or financial relationships that could be construed as a potential conflict of interest.

Publisher's note

Supplementary material

The Supplementary Material for this article can be found online at: https://www.frontiersin.org/articles/10.3389/fenvs.2022.976271/full#supplementary-material

References

Bürger, C. M., Kollet, S., Schumacher, J., and Bösel, D. (2012). Short note: Introduction of a web service for cloud computing with the integrated hydrologic simulation platform parflow. *Comput. Geosciences* 48, 334–336. doi:10.1016/j.cageo.2012.01.007

David, O., Ascough, J. C., II, Lloyd, W., Green, T. R., Rojas, K., Leavesley, G. H., et al. (2013). A software engineering perspective on environmental modeling framework design: The object modeling system. *Environ. Model. Softw.* 39, 201–213. doi:10.1016/j.envsoft.2012.03.006

DHI (2004). *Mike she user guide.* Hørsholm, Denmark: Danish Hydraulic Institute.

DHI (2005). *Mike ii: A modeling system for rivers and channels reference manual (r).* Hørsholm, Denmark: Danish Hydraulic Institute.

Dortch, M., Schneider, T., Martin, J., Zimmerman, M., and Griffin, D. (1990). *CE-QUAL-RIV1: A dynamic, one-dimensional (longitudinal) water quality model for streams.* User's Manual. Tech. rep.. Vicksburg, MS (United States): Army Engineer Waterways Experiment Station Vicksburg Ms Environmental Lab.

Fang, H.-W., and Wang, G.-Q. (2000). Three-dimensional mathematical model of suspended-sediment transport. *J. Hydraul. Eng.* 126, 578–592. doi:10.1061/(asce)0733-9429(2000)126:8(578)

Gregersen, J., Gijsbers, P., and Westen, S. (2007). Openmi: Open modelling interface. *J. hydroinformatics* 9, 175–191. doi:10.2166/hydro.2007.023

Gu, S., Zheng, W., Wu, H., Chen, C., and Shao, S. (2022). Dualsphysics simulations of spillway hydraulics: A comparison between single-and two-phase modelling approaches. *J. Hydraulic Res.*. doi:10.1080/00221686.2022.2064343

Gabreil, E., Wu, H., Chen, C., Li, J., Rubinato, M., Zheng, X., et al. (2022). Three-dimensional smoothed particle hydrodynamics modeling of near-shore current flows over rough topographic surface. *Front. Mar. Sci.* 9. doi:10.3389/fmars.2022.935098

Harris, L., Liang, D., Shao, S., Zhang, T., and Roberts, G. (2021). Mpm simulation of solitary wave run-up on permeable boundaries. *Appl. Ocean Res.* 111, 102602. doi:10.1016/j.apor.2021.102602

Hu, D., Zhang, H., and Zhong, D. (2009). Properties of the eulerian–Lagrangian method using linear interpolators in a three-dimensional shallow water model using z-level coordinates. *Int. J. Comput. Fluid Dyn.* 23, 271–284. doi:10.1080/10618560902736475

Li, T., Wang, G., Huang, Y., and Fu, X. (2009). Modeling the process of hillslope soil erosion in the loess plateau. *J. Environ. Inf.* 14, 1–10. doi:10.3808/jei.200900148

Liu, R., Wei, J., Ren, Y., Liu, Q., Wang, G., Shao, S., et al. (2017). Hydromp–a computing platform for hydrodynamic simulation based on cloud computing. *J. Hydroinformatics* 19, 953–972. doi:10.2166/hydro.2017.140

Liu, Y., Sun, A. Y., Nelson, K., and Hipke, W. E. (2013). Cloud computing for integrated stochastic groundwater uncertainty analysis. *Int. J. Digital Earth* 6, 313–337. doi:10.1080/17538947.2012.687778

[Dataset] Mell, P., and Grance, T. (2011). The nist definition of cloud computing draft. special publication 800-145. Available at: http://www.nist.gov/itl/cloud/index.cfm (accessed 08 12, 2022).

Overeem, I., Berlin, M. M., and Syvitski, J. P. (2013). Strategies for integrated modeling: The community surface dynamics modeling system example. *Environ. Model. Softw.* 39, 314–321. doi:10.1016/j.envsoft.2012.01.012

Peckham, S. D., Hutton, E. W., and Norris, B. (2013). A component-based approach to integrated modeling in the geosciences: The design of csdms. *Comput. Geosciences* 53, 3–12. doi:10.1016/j.cageo.2012.04.002

Peng, S., Fu, G., Zhao, X., and Moore, B. C. (2011). Integration of environmental fluid dynamics code (efdc) model with geographical information system (gis) platform and its applications. *J. Environ. Inf.* 17, 75–82. doi:10.3808/jei.201100189

Rahman, J. M., Seaton, S. P., and Cuddy, S. M. (2004). Making frameworks more useable: Using model introspection and metadata to develop model processing tools. *Environ. Model. Softw.* 19, 275–284. doi:10.1016/s1364-8152(03)00153-1

Sun, A. (2013). Enabling collaborative decision-making in watershed management using cloud-computing services. *Environ. Model. Softw.* 41, 93–97. doi:10.1016/j.envsoft.2012.11.008

USACE (2010). *HEC-RAS river analysis system Hydraulic reference manual.* Version 4.1. Tech. rep.. Davis, CA: Hydrologic Engineering Center Davis CA.

Wang, G., Wu, B., and Li, T. (2007). Digital yellow river model. *J. Hydro-Environment Res.* 1, 1–11. doi:10.1016/j.jher.2007.03.001

Wei, J.-h., Li, C.-j., Wang, G.-q., Shao, J.-l., and Li, S.-l. (2003). Study on the integration of groundwater numeric model and component gis. *J. Jilin Univ. Sci. Ed.* 33, 534–538. doi:10.1007/BF02873153

Welsh, W. D., Vaze, J., Dutta, D., Rassam, D., Rahman, J. M., Jolly, I. D., et al. (2013). An integrated modelling framework for regulated river systems. *Environ. Model. Softw.* 39, 81–102. doi:10.1016/j.envsoft.2012.02.022

Zhang, C., Fu, X., and Wang, G.-q. (2007). One-dimensional numerical model for unsteady flows in long-route open channel with complex inner boundary conditions. *South-to-North Water Transfers Water Sci. Technol.* 5, 16–20.

Zhang, C., Rezavand, M., Zhu, Y., Yu, Y., Wu, D., Zhang, W., et al. (2021). Sphinxsys: An open-source multi-physics and multi-resolution library based on smoothed particle hydrodynamics. *Comput. Phys. Commun.* 267, 108066. doi:10.1016/j.cpc.2021.108066

Zhong, D.-y., Yang, P., and Zhang, H. (2004). Unsteady one-dimensional numerical model for alluvial rivers with heavy sediment load and its applications. *Adv. Water Sci.* 15, 706–710.

Zhu, D., Chen, Y., Wang, Z., and Liu, Z. (2011). Simple, robust, and efficient algorithm for gradually varied subcritical flow simulation in general channel networks. *J. Hydraul. Eng.* 137, 766–774. doi:10.1061/(asce)hy.1943-7900.0000356

frontiers | Frontiers in Environmental Science

ORIGINAL RESEARCH
published: 11 May 2022
doi: 10.3389/fenvs.2022.905499

Hydrodynamic Process of Partial and en Masse Dam Failure Induced Debris Flows

Anping Shu[1]*, Le Wang[2], Fuyang Zhu[3], Jiapin Zhu[1], Chengling Pi[1], Ziru Zhang[1] and Huarez Christian[1]

[1]School of Environment, Key Laboratory of Water and Sediment Sciences of MOE, Beijing Normal University, Beijing, China, [2]School of Water Resources and Hydropower Engineering, North China Electric Power University, Beijing, China, [3]Power China ZhongNan Engineering Corporation Limited, Chang Sha, China

Because of landslides, seismic events, and/or unregulated human activities, a massive amount of loose solid materials are sometimes deposited at the confluence between the branch valley and stem stream, or blocked at the lateral channel contraction section in a river channel. Immersion of these granular materials in naturally-generated reservoirs tend to cause mass failure and even induce debris flow. However, the majority of previous studies primarily focused on post-event processes (i.e. flow hydraulics such as flood flow hydrographs, sediment transport or erosion, and river morphological changes) following dam failure. In this study, our attention is restricted to hydro-sediment dynamic processes that control unconsolidated dam failure as well as subsequent debris flow. This objective is achieved by conducting a series of experiments in a tilting flume and selecting the overtopping flows, vertical grading configurations, dam heights, and channel gradients as causative factors responsible for chain disaster in the form of dam failure and debris flow. We found that all experimental dams are either subject to partial failure through a gradual breach development or suddenly collapsed in en masse failure mode, debris flows induced by partial dam failures are likely to take place in the conditions of low overtopping flow and shallow channel slope. On the contrary, debris flows originated from en masse dam failures are shown to develop well in the opposite conditions. Also, the critical shear stresses for sediment entrainment under en masse dam failure cases are generally higher if compared with partial dam-failure equivalents. Moreover, the relative proportion of clear water to erodible solid materials is also related to dam failure mode, which will eventually determine debris-flow properties. These findings have strong implications for predicting and mitigating natural disasters of these kinds usually encountered in nature.

Keywords: overtopping flow, hydro-sediment dynamic process, dam failure, debris flow, chain disaster

Edited by:
Prashanth Reddy Hanmaiahgari,
Indian Institute of Technology
Kharagpur, India

Reviewed by:
Huabin Shi,
University of Macau, China
Zhijing Li,
Changjiang River Scientific Research
Institute (CRSRI), China

Correspondence:
Anping Shu
shuap@bnu.edu.cn

Specialty section:
This article was submitted to
Freshwater Science,
a section of the journal
Frontiers in Environmental Science

Received: *27 March 2022*
Accepted: *06 April 2022*
Published: *11 May 2022*

Citation:
Shu A, Wang L, Zhu F, Zhu J, Pi C,
Zhang Z and Christian H (2022)
Hydrodynamic Process of Partial and
en Masse Dam Failure Induced
Debris Flows.
Front. Environ. Sci. 10:905499.
doi: 10.3389/fenvs.2022.905499

1 INTRODUCTION

Debris flows, as a typical water-driven as well as gravitational erosion process within which both liquid water and solid sediment are fully mixed and mobilised at an unexceptionally high velocity, have become more frequent and devastating in recent decades due to global climate change (i.e. extreme hydrological events) and extensive anthropogenic disturbances (He et al., 2017; Ruan et al., 2021). Over the past decades, a huge number of check dams were built in China to trap sediment and their effectiveness in soil as well as water conversation are well recognized. However, more and more dams in the gullies are gradually filled with sediment and fully exposed with low vegetation cover, these check dams are progressively collapsed at an accelerating scour rate and tend to increase the risk of erosional hazards (Kang et al., 2021; Li et al., 2021; Zhu et al., 2021) like dam failures and subsequent debris flows (Song and Choi 2021). For example, the debris flow event that took place on 8 August 2010 in Zhouqu county, Gansu province, China, caused 1765 fatalities and significant damages. It was found that the loose material trapped upslope of the dams was incorporated into the debris flow, the flow volume was amplified (Fang et al., 2019) and wreaked a terrible cost in human life and property.

Debris flow is well recognized as an important category of natural and destructive hazards. Following a landslide, earthquake, inappropriate human activities, or their coupled influence, a large volume of loose solid material could accumulate at the confluence between the branch valley and stem stream or the lateral channel contraction section. Both temporal and spatial concentration of these materials usually facilitate a sudden formation of unconsolidated granular dams to temporarily block the running flow course. As the time elapsed with these materials within a newly developed dam partially or fully immersed in a gradual rising flow stage forced by a continuous flow supply from upstream. Therefore, a naturally-formed dam of this kind could eventually become destabilized and breached as a result of overtopping, seepage, or piping, and the accompanying erosion of the dam body. According to the study of Takahashi and Nakagawa (1993), the majority of dam failures are caused by the water overtopping rather than by other forms of dam collapse due to either flow piping or seepage, and many dam failures at steep slopes could induce debris flows (Capart et al., 2001; Zech and Spinewine 2002; Zech et al., 2008; Xia et al., 2010).

In this context, an outburst of medium or large-scale dam-break induced debris flows can potentially turn out to be a catastrophic and pressing issue as the associated processes are highly transient and thus provide limited time for the rapid evacuation to operate downstream. As such, there have been continuing efforts to enhance our understanding of the consequences of dam break-type flows in the following three aspects over the past decades (Cao et al., 2004). That is, dam-break flows were viewed as an active agent of uncompacted sediment transfer in mountainous areas (Caine 1980; Cao et al., 2004; Godt and Coe 2007; Xia et al., 2010; Othman et al., 2019), as a transitory process involving hydraulic changes in conjunction with steep slopes in a channel (Chen and Simons 1979; Zech and Spinewine 2002; Cao et al., 2004; Carrivick 2010; Xia et al., 2010; Carrivick et al., 2011; Pu et al., 2012); and as a rapid reconstruction of landscape topography along the impacted downstream reach through erosion and deposition that is generally documented in the far field (Chen and Simons 1979; Brooks and Lawrence 1999; Capart et al., 2001; Zech and Spinewine 2002; Cao et al., 2004; Chen et al., 2004; Soares-Frazão et al., 2007; Zech et al., 2008). Obviously, many of these previous studies are comparatively more general and not specifically focused on the problem of dam-break debris flows, this might be due to the fact the formative mechanism and rheological proprieties of debris flows are more complex than a flood or even sediment-laden flow owing to high concentration of solid particles contained in the mixture and its intricate interactions with liquid flow. Also, these works are primarily devoted to flow changes (e.g. hydraulic jump and wave propagation), sediment transport, and/or morphological evolutions following the dam failures rather than those physical processes that intrinsically control the dam break and subsequent formation of debris flows; this is quite understandable because the flood or debris flows following the dam failure appear to constitute a direct and imminent threat to the infrastructures and human lives immediately downstream.

However, as dam-break debris flows usually occur in remote mountainous areas, it is prohibitively dangerous and difficult to implement the field observations due to their sudden occurrence, short lifespan, and powerful destruction (Cui 1992; Carrivick 2010). Although some field studies and interpretations of geological legacy mainly take place some time following the event (e.g. Brooks and Lawrence 1999; Chen et al., 2004), and this effort still cannot directly link outburst flood processes with products like sedimentary deposits (Carrivick et al., 2011). To overcome this, there are quite a few works particularly dedicated to studying the dam-break induced debris flows using experimental and numerical methods (Chen and Simons 1979; Takahashi and Nakagawa 1993; Visser 2000; Capart et al., 2001; Morris and Hassan 2002; Zech and Spinewine 2002; Spinewine et al., 2004; Sarno et al., 2013). Currently, there are still some major limitations associated with numerical treatments, such as 1) reliable data for model validation and calibration are still scarce and far from complete (Visser 2000; Morris and Hassan 2002; Shao and Lo 2003); 2) most available models are heavily dependent on crude assumptions, such as gradually varied shallow flow and constant sediment concentration (Zech and Spinewine 2002; Spinewine et al., 2004); and 3) most models are one-dimensional and cannot fully describe the dam failure triggered debris flows that significantly featured with two- and three-dimensional dynamic behaviours (Xia et al., 2010; Shi et al., 2018). In contrast, flume-based experiments offer the advantage to provide a detailed, mechanistic understanding of dam-break processes responsible for generating debris flows and producing satisfactory data sets that are of direct use to numerical code developments. Also, in the present study, some important causative factors, such as dam heights, channel slopes, water volume etc., can be controlled more precisely in a tilting flume to examine their relative influence on debris flows originating from various dam failure modes, and the dam breach and subsequent debris flow moving processes can be continuously observed over a short duration with the aid of an image tracking, acquisition, and analysis technique. Further, a general review of the state-of-the-art studies from the literature has shown that there are two representative experimental arrangements in the earlier research works. Because the typical study case with a gate positioned behind the dam body was carried out to study the post-dam-failure process by suddenly removing or lifting the gate, their results cannot be used to predict onset times of debris flow caused by the failure, which is critically indispensable for managing the disaster and reducing potential damage (Chen

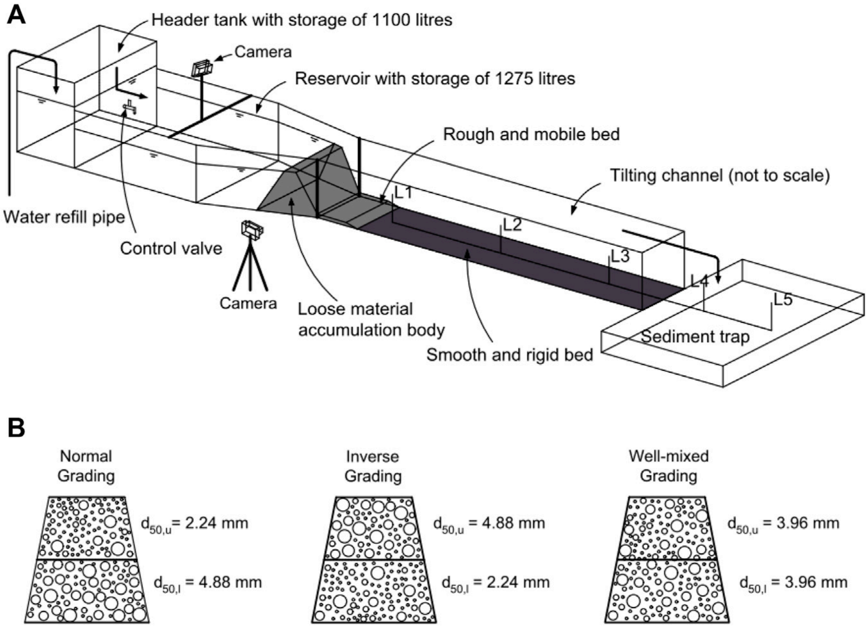

FIGURE 1 | Schematics of experimental arrangement **(A)** and three vertical grading structures originated from corresponding configurations with lower layer medium grain size d_{50} being coarser, finer, or nearly equivalent to the upper layer d_{50} within artificial dam **(B)**.

and Simons 1979; Takahashi and Nakagawa 1993). As for a complete, physical process from dam failure to debris flows, the latter case with water and dam body separated by a gate represents an ideal configuration to match well with natural analogue and will be adopted in the current experiments.

2 EXPERIMENTAL SET UP

2.1 Experimental Facility

Our experiments were conducted in a flume consisting of an upstream header tank, a reservoir, a mid-stream channel, and a downstream sediment trap (see **Figure 1A**). Specifically, the header tank at the upstream end was close to a meter cube (i.e. 1.0 m long, 1.0 m wide, 1.1 m high) and used to store clear water. A specific volume of water was gradually supplied to the reservoir by means of carefully controlling a valve, and the reservoir was split into two lengthy segments: the rectangular section (i.e. 2.0 m long, 1.0 m wide, 0.5 m deep) and the laterally as well as vertically contracted section (i.e. 1.0 m in length, 1.0 m → 0.3 m in width, 0.5 m → 0.4 m in height), where an artificial dam was constructed and located in the lower contraction section. In the middle reach, the flume is geometrically rectangular and can be tilted within a wide range (i.e. 15° → 35°) to mobilize water-sediment mixture. At the downstream end, a trap was set up to mainly collect sediment particles. Also, two high-speed cameras (50 fps) were positioned in a forward and side-looking perspective respectively to record the dynamic behaviors that involved from dam break to debris flow motion, and three piezometer sensors were buried vertically within the dam body to measure the pore-fluid pressure.

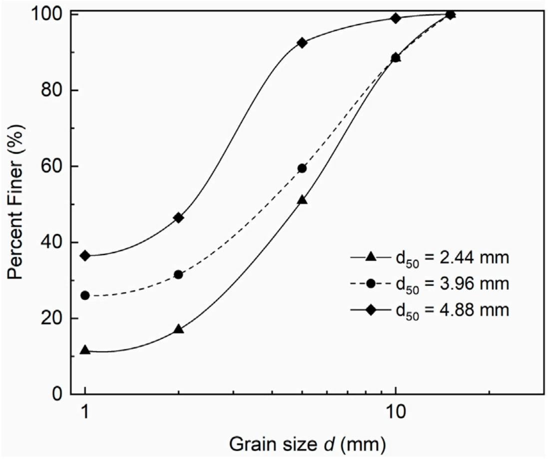

FIGURE 2 | Grain size distributions of three loose sediment mixtures employed for producing artificial dams with varying vertical grading structures in the present experiment.

2.2 Experimental Conditions

In order to fully examine the impact of impounded flow on dam break and successive debris flow transport, our major experimental controls are considered to include steady flow condition, dam properties, and channel slope. According to previous studies regarding the effect of dam-related parameters on dam break (e.g. Cao et al., 2004; Carrivick 2010), both dam materials and dam height are highlighted to represent the main dam properties in the present study. As for the dam materials, we consider the vertical stratifications possibly developed from

TABLE 1 | Summary of experimental conditions in this study.

Run No.	Q (m^3/h)	H_d (m)	ψ	S (°)
1	2.4	0.35	1.00	35
2	13.1	0.35	1.00	35
3	2.4	0.25	1.00	35
4	13.1	0.25	1.00	35
5	2.4	0.35	2.18	35
6	13.1	0.35	2.18	35
7	2.4	0.25	2.18	35
8	13.1	0.25	2.18	35
9	2.4	0.35	0.46	35
10	13.1	0.35	0.46	35
11	2.4	0.25	0.46	35
12	13.1	0.25	0.46	35
13	2.4	0.35	1.00	25
14	13.1	0.35	1.00	25
15	2.4	0.25	1.00	25
16	13.1	0.25	1.00	25
17	2.4	0.35	2.18	25
18	13.1	0.35	2.18	25
19	2.4	0.25	2.18	25
20	13.1	0.25	2.18	25
21	2.4	0.35	0.46	25
22	13.1	0.35	0.46	25
23	2.4	0.25	0.46	25
24	13.1	0.25	0.46	25

multiple discrete debris flows or distinct grading pattern resulting from a single event (e.g. Naylor 1980; Major 1997; Larcan et al., 2006; Starheim et al., 2013) as the basic guidance to generate three vertical structures for an artificial dam, namely, normal grading, inverse grading, and well-mixed grading that are illustrated in **Figure 1B**, these typical vertical grading configurations were produced by using three mixtures characterised by the same range of grain size considered (i.e. grain diameter d = 1.0 mm → 15.0 mm, see **Figure 2**) and different median grain size (i.e. d_{50} = 2.24, 3.96, and 4.88 mm). It is noted that the original sediment mixture with d_{50} = 3.96 mm were directly collected from the field loose materials legacy that contributes to frequent occurrence of debris flow in the mountainous region adjacent to Dongchuan Debris Flow Research Station, China, also widely known as the debris flow museum. The remaining two contrasting sediment mixtures with d_{50} = 2.24 mm, 4.88 mm were created by adding finer or coarser grains into the original mixture. Further, an artificial dam was constructed with one of these mixtures piled up within the bottom layer and another one within the top layer, which is clearly exemplified in **Figure 1B**. That is, for the vertical profile of the dam characterised by normal grading, the mixtures with d_{50} = 4.88 mm, 2.24 mm were placed in the bottom and top layer, respectively; the dam with inverse grading structure was in the opposite sediment setting; whereas the original mixture is adopted to create the well-mixed grading dam. In addition to the sediment materials, the second dam-related parameter is the dam height. Considering the minimum depth associated with the contracted section within the reservoir (i.e. 0.4 m), we have constructed the dams with 0.35 and 0.25 m in height, which corresponds to 157 and 90 kg in mass, respectively.

Regarding the flow condition, our attentions are primarily focused on the elapsed time for water flowing over the dam structure at a given flow rate to initiate the dam break and debris flow mobilization after the reservoir pre-filled with clear water from the header tank. The inflow rates of Q = 2.4 m^3/h and 13.1 m^3/h were achieved by controlling the valve with an accuracy of ±8%. Channel slope is also an important factor in affecting the dam break as well as debris flow transport (e.g. Chen et al., 2004). Herein, the tilting channel was inclined at S = 35° and 25°, respectively, where S = 35° represents the maximum slope that can be adjusted by the current flume facility.

Summarising basic experimental conditions in this study that encompass normal, inverse, and well-mixed vertical grading structure within artificial dams; dam height H_d = 0.35 m, 0.25 m; flow rate Q = 2.4 m^3/h, 13.1 m^3/h; and channel slope S = 35°, 25° (see **Table 1**). According to the basic principle of factor combination, there are 24 runs in total which should be carried out according to orthogonal design principle (Cui et al., 2017).

2.3 Experimental Procedure

Prior to each test, the header tank was filled with clear water through a pump, and the sediment dam was manually built using the specific mixtures according to the prescribed criteria of vertical grading configuration and dam height. All the sediment materials are placed in the lower converging section within the reservoir and extended over a 0.4 m distance downstream in 5.0 mm thickness. Three piezometer sensors are buried vertically in the vertical locations of 0.3 m (Sensor V1), 0.2 m (Sensor V2), and 0.1 m (Sensor V3) from the dam base to measure the pore pressure. It is noted that 1) Sensor V1 is employed only for a high dam with H_d = 0.35 m; 2) Sensors labelled as V1 and V2 are always placed in the upper sediment sublayer; and 2) Sensor V3 is buried in the lower sediment sublayer within the high dam or coincides with the interface between upper and lower sediment sublayer within the low dam (see **Figure 3**). These sensors are positioned along the vertical centerline in order to successfully capture the hydrodynamic changes and internal erosions associated with the dam failing process. After dam construction was completed, two high-speed cameras were installed in a side-looking and downslope-looking position, respectively, and ensured with high definition to cover the spatial distance from the dam location to the downstream sediment trap.

The experiment was launched by opening the valve and delivering clear water to the reservoir at a flow rate of Q = 2.4 m^3/s for each run. At the same time, the wire piezometer sensors and high-speed cameras were initiated to obtain a continuous record of tempo-spatial variabilities associated with dam failure and debris flow propagation, all measurements extracted from the cameras are interpreted with the aid of a regular grid with cell size (0.05 × 0.10 m) marked on the right side-wall glass. Following a gradual rise of water level in the reservoir, a large volume of white plastic beads was placed upstream of the dam and used as tracers to track the surface velocity in the dam-failure process and flow-sediment mixture displacement along the slope. It should be noted here that the opening of the valve was adjusted to generate the designated flow rate (i.e. Q = 2.4 m^3/s or 13.1 m^3/s) immediately after the reservoir was filled with water. Samples are taken in the

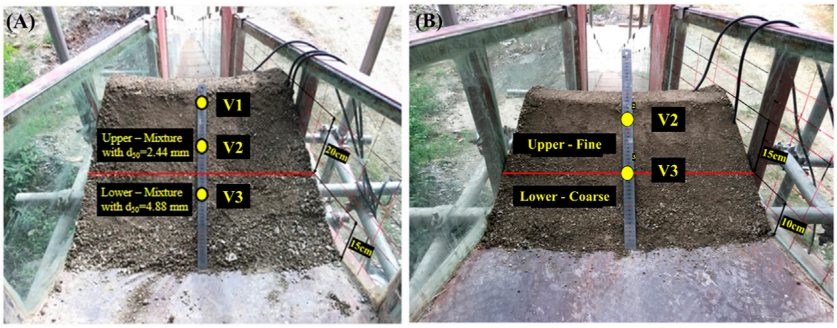

FIGURE 3 | Piezometer sensors positioned in equal spacing locations along the vertical centerline of high (left) and low (right) artificial dam before test. Note: all three sensors are used for high-elevation dam **(A)** and two sensors are employed for low-elevation dam **(B)**.

successive points L1, L2, L3 once the debris flow formed and subsequently passed through the tilting channel (i.e. Measurement Points L1, L2, L3 located at 1.0, 3.0, 5.0 m downstream from the tilting channel inlet, see **Figure 1A**). It should be emphasized here that our experiment was terminated if no flow-sediment mixing materials rapidly developed into debris flow following either a partial or complete dam failure, the remaining flow in the reservoir was then released through the sediment trap. Additional samples collected from the points L4, L5 at the centerline were used to analyse the depositional behaviour of debris flows [i.e. these points L4, L5 are set at 0.5 m, 2.5 m downstream from the contacting interface between the channel outlet and sediment trap, see **Figure 1A**). After the experiment was completed, all sediment samples were subsequently dried in an oven, weighed, and sieved.

3 THEORETICAL CONSIDERATIONS

3.1 Quantification of Vertical Grading Structure

To quantitatively characterize vertical grading configurations in the dam structure, we have proposed a vertical grading coefficient that is expressed in the following form (e.g. Shu et al., 2017)

$$\psi = \frac{d_{50-u}}{d_{50-l}} \tag{1}$$

where $d_{50\text{-}u}$ and $d_{50\text{-}l}$ represent the median grain size of the non-uniform sediment mixture placed within the upper and lower layer in the entire sediment column, therefore, the vertical grading coefficient for the corresponding vertical structures in an artificial shown in **Figure 1B** can be specified as $\psi = 0.46$ for the normal grading, $\psi = 2.18$ for the inverse grading, and $\psi = 1.00$ for the well-mixed grading, respectively.

3.2 Impact of Flow Shear Stress on Sediment Transport

In an open channel flume, bed shear stress can be calculated using the depth-slope product,

$$\tau = \gamma h S_0 \tag{2}$$

where γ denotes the specific gravity for sediment and water, h is the flow depth. An accurate prediction of debris flows is always challenging due to the more complex processes involved. Also, the sediment entrainment has been considered as a fundamental issue. It has long been known that the incipient motion of loose sediment can be predicted by using Shields stress. Considering the non-uniform sediment mixture employed in the current experiment, a modified version of Shields' relationship is given as

$$\tau_c = 0.054\frac{(\gamma_s - \gamma)d}{\mathrm{Re}_*}\left(\frac{8.8 + \mathrm{Re}_*^{1.6}}{3.6 + \mathrm{Re}_*^{1.6}}\right) \tag{3}$$

where τ_c is the dimensional Shields stress for initiating sediment motion (N/m^2), γ_s is the specific gravity for sediment and water, respectively, d is grain size in diameter and replaced by d_{50} for performing the present calculations suggested by Wilcock (1988), Re_* is the particle's Reynolds number and written as

$$\mathrm{Re}_* = \frac{u_* d}{\upsilon} \tag{4}$$

in which u_* is the shear velocity ($u_* = \sqrt{gRS_0}$ where R is the hydraulic radius, g is the gravitational acceleration, S_0 is the water surface slope), ν represents the kinematic fluid viscosity.

Sediment entrainment is likely to take place once the shear stress of flow exceeds the particle's critical Shields stress, namely, the ratio of τ/τ_c is larger than unity (Shu et al., 2017), reflecting the impact of flow intensity on sediment transport.

4 EXPERIMENTAL RESULTS

4.1 Characteristics of Debris Flows Induced by Dam Failures

In our experiments, an instantaneous dam failure followed by the debris flow was observed to exclusively evolve in two dominant modes. The first mode of dam failure induced debris flow is characterized by the following features, that is, 1) Stage I: the overtopping flow inundated the dam and sediment on the dam crest was entrained by the overspill flow, small rills then formed

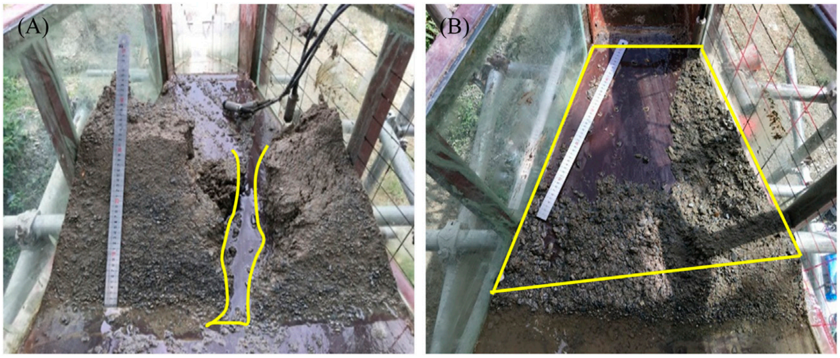

FIGURE 4 | Post-experiment legacy to demonstrate partial **(A)** and en masse **(B)** dam failure mode observed in the present research.

through headcutting and progressively developed laterally and vertically into a significant breach through which the water was concentrated to flow; 2) Stage II: Following the continuous scouring of the dam body by the concentrated flow, erodable banks of the breach collapsed and then dammed the flow pathway; and 3) Stage III: As the static flow pressure from the blocked flow increased and built up to a critical level, all flow-sediment mixing materials in the breach were instantly and fully collapsed, this process eventually resulted in partial dam collapse and formation of (immature) debris flows (see **Figure 4**).

In contrast, the second mode consisted of shared features that can be described as, 1) Stage I: A significant hydraulic jump formed through the flow overtopping of a steep granular slope under gravity effects, this resulted in massive sediment movement taking place at the toe of the downstream slope; 2) Stage II: As sediment transport occurred along the downstream slope, bed erosion was simultaneously found to migrate upstream and contributed to retrogressive slope failure; 3) Stage III: when retrogressive erosion was near the dam and coupled with bed erosion happened on the dam crest, then the dam height was reduced and its longitudinal profile became flattened with time, after a period of time along with dam becoming fully saturated as well as an increase of pore-fluid pressure, a macro instability occurred and contributed to en masse dam collapse that was closely followed by debris flow (see **Figure 4**).

Such dynamic behaviours of dam failure induced debris flow are intrinsically linked to flow conditions, loose sediment materials, and channel slopes, which jointly determined the extent of flow infiltration, the tempo-spatial variations of pore-fluid pressure, the way in which the dam collapsed, a debris flow formed and move towards downstream. Herein, all flume-based runs are fully detailed and summarised in **Table 2** in terms of experimental conditions and main results obtained.

TABLE 2 | Summary of experimental results.

Run No.	U (m/s)	h_d (m)	γ_m	τ_c	τ	T (s)
1	2.21	0.05	1.848	3.26	50.59	162
2	2.60	0.08	1.753	3.27	67.45	68
3	1.93	0.04	1.723	3.26	56.21	134
4	2.76	0.06	1.650	3.28	84.32	54
5	2.42	0.05	1.814	4.04	50.59	201
6	2.71	0.06	1.452	4.06	67.45	95
7	2.31	0.02	1.588	4.05	56.21	177
8	2.88	0.07	1.512	4.07	84.32	75
9	2.51	0.07	1.617	1.79	44.97	121
10	2.72	0.09	1.595	1.81	67.45	50
11	2.63	0.06	1.598	1.80	56.21	96
12	2.85	0.07	1.567	1.82	84.32	40
13	2.08	0.04	1.733	3.25	45.56	180
14	2.36	0.08	1.677	3.26	57.98	110
15	1.77	0.04	1.710	3.24	41.42	156
16	2.45	0.06	1.629	3.26	62.13	87
17	2.25	0.05	1.787	4.04	53.84	243
18	2.51	0.04	1.556	4.05	66.27	143
19	2.11	0.03	1.597	4.05	57.98	202
20	2.43	0.03	1.532	4.05	62.13	129
21	1.83	0.05	1.678	1.77	28.99	170
22	2.41	0.09	1.481	1.80	49.70	79
23	2.28	0.06	1.615	1.79	41.42	152
24	2.64	0.06	1.446	1.81	62.13	63

Note, *The green-shaded cells indicate that partical mode of dam failure induced debris flow occurred in these experimental runs, whereas other runs in non-shaded cells are associated with en masse failure mode.*

It is shown that partial mode of dam failure induced debris flow occurred in 11 runs, whereas those in en masse mode were observed in the remaining 13 cases (see **Table 1**). In order to analyse the impact of four basic controls on dam failure generated debris flow in two dynamic modes. The response of dam failure generated debris flow in two process-based modes to different values associated with these experimental controls is plotted in **Figure 5**. Among these factors, the number of dam failure generated debris flows under high and low dam height configuration is almost identical regardless of their dynamic modes. In contrast, the dam failure triggered debris flows are more sensitive to fluctuations in flow conditions for both failure modes, namely, the partial dam failure induced debris flows are prone to take place in the low overspill flow process, while those in en masse mode, on the contrary, are more likely to occur in high flows. Also, both channel slope and vertical grading coefficient are shown to have significant effects on dam collapse followed by debris flow. Obviously, more partial dam failure and resultant debris flow events appear to preferentially occur in the inverse grading configuration and along lower channel slopes, while en masse dam collapse seems more

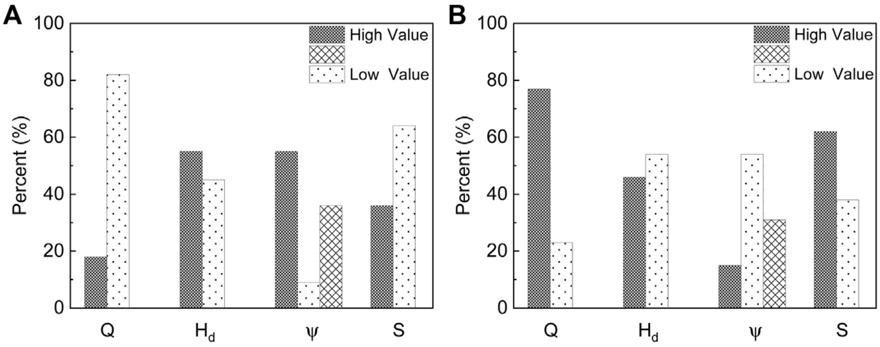

FIGURE 5 | Percent of partial **(A)** and en masse **(B)** dam failure induced debris flows under high, moderate (only for ψ), and low controls in the preset tests.

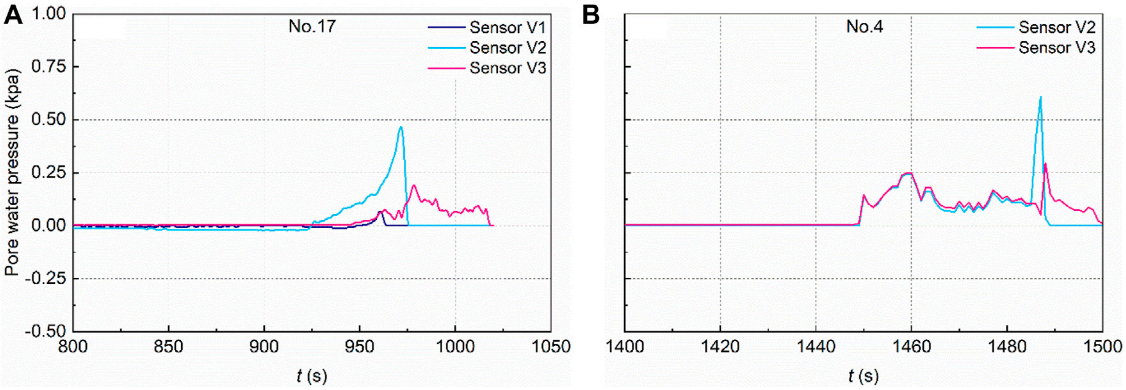

FIGURE 6 | Example plots showing temporal variation in pore pressure measured from the partial **(A)** and en masse **(B)** collapsed dam, respectively.

likely to result in debris flows in the opposite conditions featured with normal grading pattern and higher slopes.

4.2 Hydrodynamic Process of Dam Failures

A complete data set of temporal variations in pore water pressures measured within the dam could provide fundamental information for the interpretation of the failure mechanism (e.g. Gens and Alonso, 2006). As it has been found that the rates and styles of landslide are sensitive to pore-water pressure changes caused by changes in soil porosity accompanying shear deformation (Iverson et al., 2010), this equally holds true for the dam break induced debris flow, especially in partial and en masse failure mode. Also, the pore-fluid pressure, as an important indicator for internal dam stability assessment and significant triggering factor for the initiation of debris flow (e.g. Guo et al., 2018; Zhou et al., 2018), is highly sensitive to the hydraulic connectivity of loose sediment mixtures that we employed for constructing the model dams under different vertical grading configuration, which is found to have a significant impact on the dam failure mode in the present experiment. To better explain this, example plots of temporal variations in pore-fluid pressure measured in different dam failure mode with relative short and long duration are presented in **Figure 6**, respectively. In the partial dam failure, a noticeable temporal lag effect between measured peak pore pressure in three vertical locations are shown in **Figure 6A**. Specifically, the upper coarse sediment layer of the dam was observed to transiently reach a small peak piezometric head earlier, which is followed by the maximum piezometric head measured in the middle section of the dam, the peak piezometric head in the lower fine sediment layer of the dam were attained slightly later. It is important to understand that the unconsolidated materials within the dam body are brought to dilation because of the increase in pore water pressure caused by flow infiltration (Dai et al., 1999), thereby reducing the shear strength of dam materials (Chen et al., 2010) and consequently causing instability on dam structure (e.g. Iverson et al., 2010). This effect of pore pressure on vertical insataibility on the dam geotechnical structure is consistent with a rapid deepening (and enlargement) progress of breach from the dam head to the impervious, erosion-resistant bed in the partial dam failing process. As for the en masse dam failure illustrated through run No.4 (i.e. lower dam height, see **Table 2**), we observed a sudden and dramatic increase of pore water pressure in the upper bed layer, followed closely by the peak pore pressure attained for the lower sediment layer, this demonstrates a strong implication for the dam safety as internal dam instability originating from a

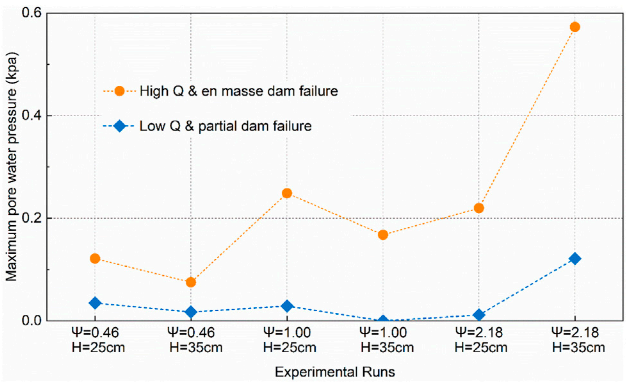

FIGURE 7 | Maximum pore water pressure measured for partial and en masse failed dam in comparative runs characterised with the same vertical grading parameter and dam height.

significant increase of pore water pressure is mainly initiated by a higher upstream discharge.

Our analysis is further extended for comparing the pore water pressure that contributes to internal dam instability in partial and en masse dam failure mode. **Figure 7** displays the magnitude of maximum pore water pressure measured for (low-Q) partial and (high-Q) en masse dam failure in comparative runs featured with the same vertical grading parameter (ψ) and dam height (H). In general, the maximum pore water pressure recorded for en masse dam failure is consistently greater than its partial failed counterpart, this well explains the critical role of flow rate upon inducing dam internal instability, because the high flow rate to penetrate into the dam body is responsible for generating high pore water pressure over a short duration, as a result, the resistant moment of a dam body is thus decreased by the increase of the water pressures and the resulting decrease of the intergranular pressures and the internal shearing resistance (Visser 2000), meanwhile, a high flow also leads to greater hydro-static and hydro-dynamic pressure for the upstream slope and dam crest, and a combination of pore water pressure, hydro-static, and hydro-dynamic pressure jointly causes external and internal dam instability and finally results in dam failure occurring in en masse mode. It is also noticeable that the pore water pressure seems to increase as vertical sediment grading (ψ) increases in a high-elevation dam (i.e. $H = 35$ cm), the main reason for this has been described earlier that a lower dam permeability is created by placing coarse sediment on the top of an artificial dam and lower bed layer therefore becoming more consolidated. Thus, an occurrence of dam collapse in an inverse grading configuration, regardless of partial or en masse dam failure mode, is basically initiated by a higher pore water pressure as presented in **Figure 7**.

4.3 Dynamic Process of Sediment Transport Associated With Dam Failures

It is statistically shown that the overtopping flow rate Q may have a critical role in determining whether debris flow formed in partial or en masse dam failure mode. This seems to be reasonable since a lower overtopping flow is more capable of entraining sediment and incising dam crest rather than forming a significant hydraulic jump on the downstream slope, this dam head cutting process continues to develop until outflow increases and finally equals to inflow, the flow depth in the reservoir therefore maintains a constant level below the dam crest and the overtopping flow is accordingly terminated. As the breach is incised to become wider and deeper, the flow depth tends to decrease with time, those bank geotechnical equilibrium characteristics are suddenly disrupted, such as the reduction in pore-fluid pressure (as discussed later) and weight of the ground, especially a rapid decline of the water level after a long lasting high water may endanger the dam stability (Visser 2000; Zech and Spinewine 2002), in such a way that micro-to-meso dam instability occurs along lower channel slopes. This consequently results in block-by-block bank failure and a rapid sediment accumulation within the breach. However, for en masse dam failure originated from high overtopping flows, retrogressive erosion dominantly occurs on the downstream slope and quickly proceeds from downstream toe to the upstream dam crest. In such a situation, the dam body was thoroughly inundated with an increased weight of the ground, especially when the channel slope is steeper. As a result, a macro-instability leads to an abrupt, complete dam failure, this is consistent with the effect of the high-intensity sprinkling on slope failure in Reid et al. (1997)'s work. Following the bulking of flow with eroded sediment, these partial or en masse dam failures somehow contribute to the formation of debris flows.

Also, we calculate the flow shear stress for both partial and en masse failure dam using **Eq. 4** with average flow depth, as can be seen from **Table 2**, the stress ratio τ/τ_c is far above unity, indicating that the experimental overflow, either in low or high level, is capable of triggering dam failure and inducing debris flow in the present investigation. However, as the partial and en masse dam failure are prone to take place under low and high overtopping flow conditions, respectively, the corresponding stress ratio τ/τ_c for dam failure in both modes are in the respective range of 12.53–17.24 and 16.64–46.38. Evidently, the stress ratio corresponds approximately to $\tau/\tau_c \approx 17.0$ could be used as a critical value to separate the distinct dam failures in partial and en masse behaviour. Again, due to the combined effect of high overflow rate (or shear stress) and severe erosion imposed upon a dam, the time elapsed from the beginning of flow overtopping to dam collapse is relatively shorter in en masse failure mode (Takahashi and Nakagawa 1993), that is, T = 40–152 s (see **Table 2**) if compared with those in partial failure mode (i.e. T = 129–243 s). This demonstrates that the overtopping flow not only determines the dam failure mode but also the timing of dam collapse, which is an important factor and must be accounted for in the dam failure predictions.

Compared to the effect of overflow rate Q on the dam failing behaviour, the vertical grading parameter ψ seems to have a secondary impact on the dam failure mode. It has been geotechnically identified that the coarser and finer sediment comprising loosely piled materials generally exhibit low and

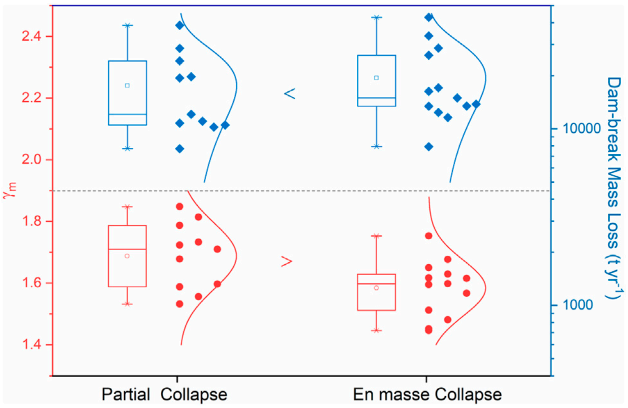

FIGURE 8 | Magnitude of solid materials eroded from dam structure and specific gravity for debris flows developed in partial and en masse dam failure mode.

high initial porosity, respectively (e.g. Esselburn et al., 2011). If considering the dam in an inverse grading pattern with coarser and finer sediment placed in the top and bottom layer, this implies that low porosity in the upper layer could somehow facilitate flow infiltration even seepage initially, thereby depressing the development of a significant hydraulic jump along the downstream slope; while for the bottom layer filled with finer particles, their void ratio or porosity could be further reduced as a result of the packing effect that caused by the added weight of coarse particles laid in the upper layer. Once the dam was overtopped by the rising flow in the reservoir, those particles exposed on the dam crest are easily entrained and rills are gradually formed. At the same time, a low permeability in the lower layer composed of finer sediment also assists in preventing the occurrence of macro-instability, especially at a lower slope. In a normal grading configuration, a significant moving-towards-upstream hydraulic jump is evolved due to low porosity of finer sediment in the upper layer as well as the reduced porosity of packing coarser sediment placed in the bottom layer. In this case, the downstream slope is more susceptible to be eroded than the dam crest, a long-term immersion of the dam body in high overtopping flow could trigger the dam failure in en masse mode, especially under a steeper slope (Takahashi and Nakagawa 1993).

4.4 Implications of Hydro-Sediment Dynamics for Dam-failure-induced Debris Flows

Further analysis of transported samples in the flume channel indicates that the specific density of debris flow originated from partial dam failure is generally higher than those resulted from en masse dam failure, as shown in **Table 2** and **Figure 8**. Similarly, a relevant analysis is also performed for the magnitude of dam-break-related mass as well as flow volume that collectively involved in debris-flow formation and transport. **Figure 8** shows the mass loss due to contrasting dam failures in en masse and partial mode, the ensemble mean mass mobilised in partial dam failure is slightly lower but still varied within the same magnitude of order if compared with those displayed in en masse dam failure mode. Meanwhile, it is stated earlier that the total flow volume responsible for producing partial dam failures is usually significantly lower than en masse dam failure cases (e.g. see **Figure 5**). Such differential proportion of solid mass (due to dam collapse) and liquid water (released from the header tank) in debris-flow composition within two dam failure modes can explain this difference in the debris-flow specific gravity (γ_m, see **Figure 8**). For debris flow induced by partial dam failures, solid materials are proportionally sufficient relative to total water volume in debris flows, this leads to higher debris-flow specific gravity γ_m. By contrast, although a large amount of solid materials was derived from dam and involved in debris flows, a higher volume of liquid flow become dominantly in shaping debris flows to be low sediment concentration with low specific gravity γ_m.

5 CONCLUSION

A flume-based study is conducted to determine the relative contribution of the overtopping flow rate (Q), dam height (H_d), vertical grading configuration (ψ), and channel slopes (S) to dam failure induced debris flows. After a series of tests by varying the values of these controls, the debris flows are shown to form under either partial or en masse dam failure mode. In the process of partial dam failure induced debris flows, small rills are initially formed through sediment transport on dam crest and subsequently resulted in a breach development through severe dam downcutting as well as lateral bank collapse, debris flow is thus formed by the bulking of flow and sediment in the breach evolved from partial dam failure. By contrast, a significant hydraulic jump formed on the downstream slope of a dam and migrated upstream as the time elapsed, thereby causing a retrogressive slope erosion and a reduction in dam height, with the dam relics fully saturated and pore pressure increased, macro dam stability was produced and contributed to a sudden, complete dam collapse.

We also found that the overtopping flow rate Q has a dominant control on the formation of debris flow in partial or en masse dam failure mode, the vertical grading parameter ψ appears to have a secondary impact; whereas the dam height H_d is shown to have a negligible influence. A detailed comparison clearly indicated that the partial dam failure induced debris flows are more likely to originate in the small overspill flow, inverse grading configuration, and lower channel slopes; while the en masse dam failure triggered debris flows are prone to occur in the opposite conditions. Under the effects of these controls considered, especially the overtopping flow, the following findings are drawn, 1) the characteristic time elapsed from the beginning of flow overtopping to en masse dam failure is relatively shorter than the time measured in partial failure process, and 2) the stress ratio τ/τ_c for dam failure induced debris flows in en masse dam failure is higher than in partial failure scenario, a critical stress ratio $\tau/\tau_c \approx 17.0$ can be used to separate the debris flows resulting from these contrasting dam failing behaviours.

The effect of vertical grading configuration on dam failure induced debris flows is intrinsically correlated with the temporal evolution of pore-fluid pressure in dam structure. In the partial dam failure mode, as the breach gradually developed from the dam head to lower layer, a noticeable temporal lag effect between peak pore pressure measured at three vertical locations was thus obtained. By contrast, the temporal response of pore pressure in an en masse dam failure was relatively shorter between measured sections and the corresponding pore pressure was found to attain a higher peak value, this creates a macro and internal instability that imposed upon the dam structure. As a result, the propagation velocity and flow depth for debris flow originated from en masse dam failure is generally larger than those from partial dam failure. A combined behaviour of en masse dam failure induced debris flows that took place in a shorter period of time and loaded with higher velocity demonstrates a strong implication that a more destructive debris flow tends to be developed under a complete dam failure, this fundamental knowledge is essential to predict and alleviate the dam-failure-initiated debris flows.

Within this study, solid materials eroded from the dam structure are in the same magnitude of order in both dam failure modes. However, a total volume of liquid water contributed to partial dam failure (and formation of debris flow) is generally lower than en masse dam failure cases. As a result, debris flows following partial dam failure tend to have a higher specific gravity than originated from en masse dam failure.

DATA AVAILABILITY STATEMENT

The original contributions presented in the study are included in the article, further inquiries can be directed to the corresponding author.

AUTHOR CONTRIBUTIONS

AS the corresponding author, organized and revised the paper. LW organized the manuscript. FZ conducted the experiments and analysed the data. JZ, CP, ZZ and HC analysed the data.

FUNDING

This work was also supported financially by the CRSRI Open Research Program (Program SN: CKWV2015225/KY), the Key Project of National Natural Science Foundation (Grant No. 52039001), the Natural Science Foundation of China (Grant No. 52009041) and the Fundamental Research Funds for the Central Universities (Grant No. 2020MS024).

REFERENCES

Brooks, G. R., and Lawrence, D. E. (1999). The Drainage of the Lake Ha!Ha! Reservoir and Downstream Geomorphic Impacts along Ha!Ha! River, Saguenay Area, Quebec, canada. *Geomorphology* 28, 141–167. doi:10.1016/s0169-555x(98)00109-3

Caine, N. (1980). The Rainfall Intensity: Duration Control of Shallow Landslides and Debris Flows. *Geogr. Ann. Ser. A, Phys. Geogr.* 62, 23–27. doi:10.2307/520449

Cao, Z., Pender, G., Wallis, S., and Carling, P. (2004). Computational Dam-Break Hydraulics over Erodible Sediment Bed. *J. Hydraul. Eng.* 130, 689–703. doi:10.1061/(asce)0733-9429(2004)130:7(689)

Capart, H., Young, D. L., and Zech, Y. (2001). "Dam-break Induced Debris Flow," in *Particulate Gravity Currents*, 149–156. doi:10.1002/9781444304275.ch11

Carrivick, J. L., Jones, R., and Keevil, G. (2011). Experimental Insights on Geomorphological Processes within Dam Break Outburst Floods. *J. Hydrol.* 408, 153–163. doi:10.1016/j.jhydrol.2011.07.037

Carrivick, J. L. (2010). Dam Break - Outburst Flood Propagation and Transient Hydraulics: A Geosciences Perspective. *J. Hydrol.* 380, 338–355. doi:10.1016/j.jhydrol.2009.11.009

Chen, Y. H., and Simons, D. B. (1979). An Experimental Study of Hydraulic and Geomorphic Changes in an Alluvial Channel Induced by Failure of a Dam. *Water Resour. Res.* 15, 1183–1188. doi:10.1029/wr015i005p01183

Chen, C.-Y., Chen, T.-C., Yu, F.-C., and Hung, F.-Y. (2004). A Landslide Dam Breach Induced Debris Flow ? a Case Study on Downstream Hazard Areas Delineation. *Env. Geol.* 47, 91–101. doi:10.1007/s00254-004-1137-6

Chen, N. S., Zhou, W., Yang, C. L., Hu, G. S., Gao, Y. C., and Han, D. (2010). The Processes and Mechanism of Failure and Debris Flow Initiation for Gravel Soil with Different Clay Content. *Geomorphology* 121, 222–230. doi:10.1016/j.geomorph.2010.04.017

Cui, Y.-f., Zhou, X.-j., and Guo, C.-x. (2017). Experimental Study on the Moving Characteristics of Fine Grains in Wide Grading Unconsolidated Soil under Heavy Rainfall. *J. Mt. Sci.* 14 (3), 417–431. doi:10.1007/s11629-016-4303-x

Cui, P. (1992). Study on Conditions and Mechanisms of Debris Flow Initiation by Means of Experiment. *Chin. Sci. Bull.* 12 (9), 759–763.

Dai, F., Lee, C. F., and Wang, S. (1999). Analysis of Rainstorm-Induced Slide-Debris Flows on Natural Terrain of Lantau Island, Hong Kong. *Eng. Geol.* 51, 279–290. doi:10.1016/S0013-7952(98)00047-7

Esselburn, J. D., Ritzi Jr, R. W., and Dominic, D. F. (2011). Porosity and Permeability in Ternary Sediment Mixtures. *Groundwater* 49 (3), 393–402.

Fang, Q., Tang, C., Chen, Z., Wang, S., and Yang, T. (2019). A Calculation Method for Predicting the Runout Volume of Dam-Break and Non-dam-break Debris Flows in the Wenchuan Earthquake Area. *Geomorphology* 327, 201–214. doi:10.1016/j.geomorph.2018.10.023

Gens, A., and Alonso, E. E. (2006). Aznalcóllar Dam Failure. Part 2: Stability Conditions and Failure Mechanism. *Géotechnique* 56 (3), 185–201.

Godt, J. W., and Coe, J. A. (2007). Alpine Debris Flows Triggered by a 28 July 1999 Thunderstorm in the Central Front Range, Colorado. *Geomorphology* 84, 80–97. doi:10.1016/j.geomorph.2006.07.009

Guo, X., Baroth, J., Dias, D., and Simon, A. (2018). An Analytical Model for the Monitoring of Pore Water Pressure inside Embankment Dams. *Eng. Struct.* 160, 356–365. doi:10.1016/j.engstruct.2018.01.054

He, S., Wang, D., Fang, Y., and Lan, H. (2017). Guidelines for Integrating Ecological and Biological Engineering Technologies for Control of Severe Erosion in Mountainous Areas - A Case Study of the Xiaojiang River Basin, China. *Int. Soil Water Conservation Res.* 5 (4), 335–344. doi:10.1016/j.iswcr.2017.05.001

Iverson, N. R., Mann, J. E., and Iverson, R. M. (2010). Effects of Soil Aggregates on Debris-Flow Mobilization: Results from Ring-Shear Experiments. *Eng. Geol.* 114, 84–92. doi:10.1016/j.enggeo.2010.04.006

Kang, C., Ren, D., Gao, X., Han, C., and Wang, Y. (2021). Study of Kinematic Characteristics of a Rock Avalanche and Subsequent Erosion Process Due to a Debris Flow in WenJia Gully, Sichuan, China. *Nat. Hazards* 106 (1), 937–964. doi:10.1007/s11069-021-04501-6

Larcan, E., Mambretti, S., and Pulecchi, M. (2006). A Procedure for the Evaluation of Debris Flow Stratification. *WIT Trans. Ecol. Environ.* 90, 81–88. doi:10.2495/deb060081

Li, Y., Hu, W., Wasowski, J., Zheng, Y., and McSaveney, M. (2021). Rapid Episodic Erosion of a Cohesionless Landslide Dam: Insights from Loss to Scour of Yangjia Gully Check Dams and from Flume Experiments. *Eng. Geol.* 280, 105971. doi:10.1016/j.enggeo.2020.105971

Major, J. J. (1997). Depositional Processes in Large-Scale Debris-Flow Experiments. *J. Geol.* 105, 345–366. doi:10.1086/515930

Morris, M., and Hassan, A. M. (2002). *Breach Formation through Embankment Dams & Flood Defense Embankments: A State of the Art Review*. Wallingford, United Kingdom: HR Wallingford. IMPACT-Project Workshop Paper.

Naylor, M. A. (1980). The Origin of Inverse Grading in Muddy Debris Flow Deposits: a Review. *J. Sediment. Res.* 50, 1111–1116. doi:10.1306/212f7b8f-2b24-11d7-8648000102c1865d

Othman, I. K., Jiang, Z., and Baldock, T. E. (2019). Influence of Grain Size on Sediment Transport during Initial Stages of Horizontal Dam Break-type Flows. *J. Waterw. Port. Coast. Ocean. Eng.* 145, 04019009. doi:10.1061/(asce)ww.1943-5460.0000510

Pu, J. H., Cheng, N.-S., Tan, S. K., and Shao, S. (2012). Source Term Treatment of SWEs Using Surface Gradient Upwind Method. *J. hydraulic Res.* 50 (2), 145–153. doi:10.1080/00221686.2011.649838

Reid, M. E., LaHusen, R. G., and Iverson, R. M. (1997). "Debris-flow Initiation Experiments Using Diverse Hydrologic Triggers," in *Debris-Flow Hazards Mitigation: Mechanics, Prediction and Assessment*, 1–11.

Ruan, H., Chen, H., Li, Y., Chen, J., and Li, H. (2021). Study on the Downcutting Rate of a Debris Flow Dam Based on Grain-Size Distribution. *Geomorphology* 391, 107891. doi:10.1016/j.geomorph.2021.107891

Sarno, L., Carravetta, A., Martino, R., and Tai, Y.-C. (2013). Pressure Coefficient in Dam-Break Flows of Dry Granular Matter. *J. Hydraul. Eng.* 139, 1126–1133. doi:10.1061/(asce)hy.1943-7900.0000772

Scotton, P., and Deganutti, A. M. (1997). *Phreatic Line and Dynamic Impact in Laboratory Debris Flow Experiments*. New York: ASCE, 777–786.

Shao, S., and Lo, E. Y. M. (2003). Incompressible SPH Method for Simulating Newtonian and Non-newtonian Flows with a Free Surface. *Adv. water Resour.* 26 (7), 787–800. doi:10.1016/S0309-1708(03)00030-7

Shi, Y., Li, S., Chen, H., He, M., and Shao, S. (2018). Improved SPH Simulation of Spilled Oil Contained by Flexible Floating Boom under Wave-Current Coupling Condition. *J. Fluids Struct.* 76, 272–300. doi:10.1016/j.jfluidstructs.2017.09.014

Shu, A., Wang, L., Zhang, X., Ou, G., and Wang, S. (2017). Study on the Formation and Initial Transport for Non-homogeneous Debris Flow. *Water* 9, 253. doi:10.3390/w9040253

Soares-Frazão, S., Le Grelle, N., Spinewine, B., and Zech, Y. (2007). Dam-break Induced Morphological Changes in a Channel with Uniform Sediments: Measurements by a Laser-Sheet Imaging Technique. *J. Hydraulic Res.* 45, 87–95. doi:10.1080/00221686.2007.9521835

Song, P., and Choi, C. E. (2021). Revealing the Importance of Capillary and Collisional Stresses on Soil Bed Erosion Induced by Debris Flows. *J. Geophys. Res. Earth Surf.* 126 (5), e2020JF005930. doi:10.1029/2020jf005930

Spinewine, B., Delobbe, A., Elslander, L., and Zech, Y. (2004). "Experimental Investigation of the Breach Growth Process in Sand Dikes," in Second IAHR international conference on fluvial hydraulics, Napoli, Italy, 983–991. doi:10.1201/b16998-126

Starheim, C. C. A., Gomez, C., Harrison, J., Kain, C., Brewer, N. J., Owen, K., et al. (2013). Complex Internal Architecture of a Debris-Flow Deposit Revealed Using Ground-Penetrating Radar, Cass, New Zealand. *N. Z. Geog* 69, 26–38. doi:10.1111/nzg.12002

Takahashi, T., and Nakagawa, H. (1993). Flood and Debris Flow Hydrograph Due to Collapse of a Natural Dam by Overtopping. *Proc. Hydraulic Eng.* 37, 699–704. doi:10.2208/prohe.37.699

Visser, P. J. (2000). *Breach Growth in Sand-Dikes*. Delft University of Technology.

Wilcock, P. R. (1988). Methods for Estimating the Critical Shear Stress of Individual Fractions in Mixed-Size Sediment. *Water Resour. Res.* 24, 1127–1135. doi:10.1029/wr024i007p01127

Xia, J., Lin, B., Falconer, R. A., and Wang, G. (2010). Modelling Dam-Break Flows over Mobile Beds Using a 2D Coupled Approach. *Adv. Water Resour.* 33, 171–183. doi:10.1016/j.advwatres.2009.11.004

Zech, Y., and Spinewine, B. (2002). "Dam-break Induced Floods and Sediment Movement-State of the Art and Need for Research," in First Workshop of the EU Project IMPACT (HR Wallingford).

Zech, Y., Soares-Frazão, S., Spinewine, B., and Le Grelle, N. (2008). Dam-break Induced Sediment Movement: Experimental Approaches and Numerical Modelling. *J. Hydraulic Res.* 46 (2), 176–190. doi:10.1080/00221686.2008.9521854

Zhou, Z.-H., Ren, Z., Wang, K., Yang, K., Tang, Y.-J., Tian, L., et al. (2018). Effect of Excess Pore Pressure on the Long Runout of Debris Flows over Low Gradient Channels: A Case Study of the DongYueGe Debris Flow in Nu River, China. *Geomorphology* 308, 40–53. doi:10.1016/j.geomorph.2018.01.012

Zhu, L., He, S., Qin, H., He, W., Zhang, H., Zhang, Y., Jian, J., Li, J., and Su, P. (2021). Analyzing the Multi-Hazard Chain Induced by a Debris Flow in XiaoJinChuan River, Sichuan, China. *Eng. Geol.* 293, 106280. doi:10.1016/j.enggeo.2021.106280

Conflict of Interest: FZ is employed by the company Power China ZhongNan Engineering Corporation Limited. The remaining authors declare that the research was conducted in the absence of any commercial or financial relationships that could be construed as a potential conflict of interest.

frontiers
in Environmental Science

ORIGINAL RESEARCH
published: 16 February 2022
doi: 10.3389/fenvs.2022.840653

Applicability of Flow Resistance Formulae for Sand-Bed Channels: An Assessment Using a Very Large Data Set

Hao Peng[1,2], *He Qing Huang*[1,2]*, *Guoan Yu*[1] *and Hongwu Zhang*[3]

[1]*Key Laboratory of Water Cycle and Related Land Surface Processes, Institute of Geographic Sciences and Natural Resources Research, Chinese Academy of Sciences, Beijing, China,* [2]*University of Chinese Academy of Sciences, Beijing, China,* [3]*State Key Laboratory of Hydro Science and Engineering, Tsinghua University, Beijing, China*

Among numerous flow resistance formulae for sand-bed channels, this study selected five for evaluation and in order to cover flow conditions in sand-bed river channels as widely as possible, a total of 1,636 sets of field measures were collected from the hydrological stations of two large river systems of China—the Yellow and Yangtze Rivers, in addition to the data compiled by Brownlie. The performance of the selected formulae in yielding the values of Manning resistance coefficient *n* was evaluated against the total of 6,805 datasets. In many cases, the formula of Ma et al. yielded unreasonable *n* values of <0, while that of Deng et al. and formulae 1 and 2 of Zhang et al. yielded *n* values with large errors. The formula of Wu and Wang yielded *n* values varying within the scope only in the case of *n* < 0.04. By dividing the absolute relative errors (AREs) from the selected formulae into six groups of 0–0.05, 0.05–1, 0.1–0.2, 0.2–0.5, 0.5–1, and >1, it can be found that, for all five selected formulae, ARE occurred in the group 0.2–0.5 occupied the largest percentage, while in each of the adjacent groups of 0.5–1 and 0.1–0.2 it also occupied a very large percentage. Hence, all five formulae still need to improve their predicting ability.

Keywords: flow resistance, sand-bed channel, large dataset, Manning roughness coefficient, bedforms, error analysis

Edited by:
Jaan H. Pu,
University of Bradford,
United Kingdom

Reviewed by:
Ming He,
Tianjin University, China
Le Wang,
North China Electric Power University,
China

***Correspondence:**
He Qing Huang
huanghq@igsnrr.ac.cn

Specialty section:
This article was submitted to
Freshwater Science,
a section of the journal
Frontiers in Environmental Science

Received: *21 December 2021*
Accepted: *06 January 2022*
Published: *16 February 2022*

Citation:
Peng H, Huang HQ, Yu G and Zhang H (2022) Applicability of Flow Resistance Formulae for Sand-Bed Channels: An Assessment Using a Very Large Data Set.
Front. Environ. Sci. 10:840653.
doi: 10.3389/fenvs.2022.840653

INTRODUCTION

There are a plethora of flow resistance formulae available for sand-bed river channels, but river scientists and engineers have been facing the very difficult problem of selecting a convincing one in practical problem solving (Zhang et al., 2020). Although the following Manning resistance formula (Manning, 1890; Herschel, 1897) was developed a long time ago to calculate the resistance to flow in fixed-bed open channels, it still is widely applied to determine the flow resistance of sand-bed river channels:

$$V = \frac{1}{n} R^{2/3} J^{1/2} \tag{1}$$

where V is the average velocity of channel flow, R is the hydraulic radius of the channel, J is the energy slope of flow, and n is the Manning roughness coefficient.

Because the roughness of a riverbed can be reflected by the size of the sediments composing the bed, the Manning roughness coefficient n in **Eq. 1** has frequently been determined using the following relationship:

TABLE 1 | Comparisons of *A* and *D* for different investigators.

Parameter	Meyer-Peter and Müller (1948)	Jaeger (1961)	Maynord (1991)		Wu and Wang (1999)
D	D_{90}	D_{50}	D_{50}	D_{90}	D_{50}
A	26	21.1	21.6	22.8	20

$$n = D^{1/6}/A \tag{2}$$

where *D* and *A* are a representative bed sediment size and a roughness parameter, respectively.

The sediments composing a riverbed, however, are hardly uniform, and there has been no consensus of opinions on what size of the non-uniform sediments can represent the role of *D* in **Eq. 2**. While the study by Chang (1939) granted support to the use of D_{50}, nevertheless, Meyer-Peter and Muller (1948) argued that it is more appropriate to use D_{90} to represent *D* and consequently found $A = 26$. However, Maynord (1991) used a large number of flume data collected from various sources and identified that the use of particle size D_{90} gave slightly better results than the use of D_{50}, with *A* taking 21.6 and 22.8 respectively for D_{50} and D_{90}. In the reformulation of the Meyer-Peter and Muller (1948) equation, Huang (2010) also discovered that utilizing D_{50} or D_{90} had no effect on the accuracy of flow resistance calculations.

The roughness of a channel can be divided into grain roughness and form roughness for a riverbed with bedforms (Einstein, 1952; Engelund, 1961). While it has been assumed that a representative size of riverbed sediments, such as D_{90} or D_{65}, may accurately reflect the grain roughness of a flat riverbed (Engelund and Hansen, 1967; van Rijn, 1982; Kamphuis, 1974; Zhang et al.,2012a; Zhang et al., 2012b; Niazkar et al., 2019), form roughness is closely related to the strength of flow acting on a channel bed, usually reflected with the Shields parameter (Yalin, 1963; van Rijn, 1984). Using data from the Compendium of Solids Transport Data compiled by Brownlie (1981), nevertheless, Peterson and Peterson (1988) made a comparison of the bed roughness values between observational data and the results calculated from different flow resistance formulae and commented that the commonly applied formulae with the Shields parameter as the sole factor were insufficient. Importantly, they demonstrated that the roughness of a mobile bed is also a function of the Froude number (*Fr*) and a dimensionless settling velocity (Zhang et al., 1998). On the basis of both physical reasoning and dimensional analysis, Wu and Wang (1999) proposed a relationship to determine the roughness of a mobile bed by relating the roughness parameter *A* in **Eq. 2** to a non-dimensional shear stress parameter and *Fr*. Importantly, they tested the relationship with a large number of data observed in experimental flumes and fields collected from different sources and demonstrated that the values of *n* computed using their relationship yielded results consistent with the measured data at a much higher level than when using the other methods. **Table 1** presents the selection of a representative sediment size *D* and the corresponding value of roughness parameter *A* by different investigators.

In contrast to the approach of selecting a representative sediment size *D* in **Eq. 2**, many studies determined the value of the Manning roughness coefficient *n* in **Eq. 1** directly from a statistical analysis of field observations. Using field observations from the lower Yellow River, Chien and Wan (1983) analyzed the variation of *n* at various flow and sediment conditions and consequently recognized that *n* is closely related to both of the relative strength of tractive force and sediment size D_{65}. Zhao and Zhang (1997) presented a detailed physical analysis of the effects of the rough thickness of channel bed on flow velocity, and a relationship expressing *n* as a complex function of flow depth, sediment size D_{50}, and *Fr* received a high level of validation with a larger number of field observations obtained from the lower reach of the Yellow River. By reanalyzing the flume experimental data provided by Guy et al. (1966) and field observations at stations located in the middle and lower reaches of the Yellow River, however, Deng et al. (2007) identified that *n* had a poor relationship with flow discharge and depth, but increased initially and then decreased with an increase in sediment concentration. Importantly, they found that *n* had a good relationship with *Fr* and that a power function was shown to be fitting the collected data well.

Using 64 sets of data observed in experimental flumes and more than 1,000 sets of data measured during 1958–1959 at six hydrological stations located in the lower reach of the Yellow River, Ma et al. (2017) evaluated the performance of three roughness formulae proposed respectively by van Rijn (1984), Zhao and Zhang (1997), and Qin et al. (1995). They identified that the formula of Zhao and Zhang fitted best the observations from natural rivers, while the van Rijn formula performed well in laboratory flumes. In addition, Ma et al. (2017) reanalyzed the collected data, and their statistical regression results demonstrated that *n* showed a very close relationship with *Fr*. Recently, Zhang et al. (2020) presented a systematic review of the progress on the determination of the roughness of a moving bed channel and highlighted the need to treat *Fr* as a primary parameter in the establishment of a practically useful flow resistance formula. Consequently, they proposed two formulae to determine *n*. The first formula is in a relatively simple form considering the effect of *Fr* only, while the second formula is in a comprehensive form taking into account the effects of *Fr*, sediment size D_{50}, roughness parameter *A*, and the von Kármán constant that reflects the effect of sediment concentration on flow energy consumption. While complex in form, the second formula had a much higher level of accuracy. The validation of the two roughness formulae clearly showed that the results generated by both were in a good agreement with a large number of data measured from natural rivers, although deviating slightly from observations in experimental flumes.

It is apparent that most flow resistance formulae were derived with reference to the data observed from experimental flumes and/or from natural rivers collected or conducted by original author(s), supplemented with some data obtained by one or several other researchers. Furthermore, the performance of a formula has often been assessed tentatively based on its agreement with a limited amount of data collected. In addition, there is considerable overlap of the data employed in the development of many formulae, with data incorporated in the subsequent evaluations of their performance. All of these contributed to the proliferation rather than the consolidation of flow resistance formulae for mobile-bed channels (Mark Powell, 2014; Ferro, 2018a; Ferro, 2018b; Di Stefano et al., 2020; Carollo and Ferro, 2021; Nicosia et al., 2021; Yadav et al., 2022). So far, none of the previously developed formulae has been either universally accepted or recognized as being especially appropriate for practical application. Although the performance of many formulae had been evaluated under a relatively wide range of hydraulic conditions, either from laboratory and/or from the field (e.g., Huang et al., 2004; Zhang, 2012a; Zhang, 2012b; Zhang et al., 2020), a collection of more observational datasets has become possible recently, and it is necessary to evaluate which flow resistance formula can give better predictions. For this purpose, this study selected flow resistance formulae for mobile-bed channels that have been most quoted in the literature and collected observational data wide in varying ranges and large in number from various sources. A set of statistical indicators was then used to evaluate the performance of the selected formulae against a large observational dataset collected in this study.

SELECTION OF FORMULAE

The selection of formulae for evaluation in this study was mainly in terms of popularity and the number and range of data used for developing them. From a detailed literature review of the progress on the development of the formulae, those developed by Wu and Wang (1999), Deng et al. (2007), Ma et al. (2017), and Zhang et al. (2020) satisfied these criteria and so were selected.

The flow resistance formula developed by Wu and Wang (1999) takes a form of:

$$\lg \frac{A}{g^{1/2} F^{1/3}} = 0.911 - 0.273 \lg T - 0.051 \left(\lg T\right)^2 + 0.135 \left(\lg T\right)^3 \quad (3)$$

where g is the acceleration due to gravity, Fr is the Froude number ($= V/\sqrt{gh}$, where h is the flow depth), and T is the non-dimensional shear stress of flow acting on the riverbed sediments.

To obtain the value of T in **Eq. 3**, the following relationships need to be applied:

$$T = \tau' \big/ \tau_{c50}; \quad \tau' = \left(\frac{n'}{n}\right)^{3/2} \tau; \quad n' = \frac{D_{50}^{1/6}}{20}; \quad \tau = gRJ \quad (4)$$

where τ', τ_{c50}, n', and τ are respectively the shear stress of flow acting on the riverbed sediments, the critical shear stress with D_{50} representing the size of bed sediments, the grain roughness coefficient, and the shear stress of flow acting on the channel boundary, in which the critical shear stress τ_{c50} was determined from the following relationships given by Chien and Wan (1983) after their modification of the Shields curve:

$$\frac{\tau_{c50}}{(\gamma_s - \gamma) D_{50}} = 0.126 D_*^{-0.44}; \quad D* = D_{50} \left(\frac{\gamma_s - \gamma}{\gamma} \frac{g}{\nu^2}\right)^{1/3} \quad (5)$$

where ν is the kinematic viscosity coefficient in square centimeters per second cm^2/s.

By reanalyzing the flume experimental data provided by Guy et al. (1966) and field observations at stations located in the middle and lower reaches of the Yellow River, Deng et al. (2007) obtained the following power–function relationship between n and Fr by using a statistical regression method:

$$n = 0.005 Fr^{-0.7336} \quad (6)$$

Using 64 sets of data observed in experimental flumes and more than 1,000 sets of data measured during 1958–1959 at six hydrological stations located in the lower reach of the Yellow River, based on data from both experimental flumes and field measurements in the Lower Yellow River, Ma et al. (2017) developed the following regression formula:

$$n = -0.0124 \ln Fr + 0.0009 \quad (7)$$

Zhang et al. (2020) proposed two flow resistance relationships: the simple one, referred to as formula 1 of Zhang et al. in this study, takes the form

$$n = \frac{0.01}{0.1 + 1.85 Fr} \quad (8)$$

When the influences of bed materials and sediment concentration on flow energy expenditure were taken into account, Zhang et al. (2020) presented a more comprehensive formula, referred to as formula 2 of Zhang et al. in this study, taking the form

$$n = \frac{0.9 D_{50}^{1/6} (\kappa/\kappa_0)^{1/5}}{A_{50} (0.1 + 1.85 Fr)} \quad (9)$$

where κ is the Karman coefficient of flow, $\kappa_0 = 0.4$. κ has a relationship with sediment concentration S_V in the form

$$\kappa = \kappa_0 \left(1 - 4.2 \sqrt{S_V}\, (0.365 - S_V)\right) \quad (10)$$

The sources and other details pertaining to the development of the five formulae selected above are summarized in **Table 2**.

DATA SOURCES

Laboratory and Field Data Compiled by Brownlie (1981)

The datasets compiled by Brownlie (1981) contained 7,027 records (5,263 laboratory records and 1,764 field records) in 77 data files. All of the records were collected from various studies conducted during the 20th century and provide a historically

TABLE 2 | The flow resistance formulae investigated in this study.

Formula	Data source	Number of data		
		Flume	Field	Total
Wu and Wang (1999)	Gilbert (1914), Meyer-Peter and Muller (1948), East Parkistan Water and Power Development Authority (1967), Taylor (1971), Samaga et al. (1986), Liu (1986), Kuhnle (1993), Wilcock and McArdell (1993), Black Susitna River, Mississippi River, hydrological data of the Yellow River basin	375	436	811
Deng et al. (2007)	Summary of alluvial channel data from flume experiments, 1956–1961 by Guy et al. (1966), hydrological data of the Yellow River basin	230	110	340
Ma et al. (2017)	Flume experiments of Wang (1990), hydrological data of the Yellow River basin	64	1,121	1,185
Formulas 1 and 2 of Zhang et al. (2020)	Hydrological data of the Yellow River basin, hydrological data of the Yangtze River basin	0	2,334	2,334
This study	Laboratory data and field data by Brownlie (1981), hydrological data of the Yellow River basin, hydrological data of the Yangtze River basin	3,623	3,182	6,805

TABLE 3 | Datasets used in this study.

Data source	*N*	*Q* (m^3/s)	*V* (m/s)	*Fr*	*B* (m)	*H* (m)	*J* (10^{-4})	D_{50} (mm)	*S* (kg/m^3)
Laboratory data of Brownlie	3,623	0.01–2.21	0.10–2.35	0.08–3.51	0.08–2.44	0.01–0.86	0.019–36.7	0.011–20.20	0–111
Field data of Brownlie	1,546	0.06–28,825.68	0.19–3.32	0.04–1.05	3.05–1,109.47	0.04–17.28	0.003–12.6	0.083–76.11	0–11.4
Data from the Yellow and Yangtze Rivers	1,636	12.9–46,600	0.074–3.33	0.0001–0.71	0.19–3.33	0.45–18.70	0.11–6.33	0.027–0.712	0–320

complete set of alluvial channel observations. This data collection was inspired by the data compendium of Peterson and Howells (1973), and in comparison with previous data compendiums, this compendium corrected early errors, completed omissions, and added about 2,500 new records consisting of 10 basic hydraulic parameters. If no data were available, it was recorded as −1.

TABLE 4 | Statistical parameters and expressions.

Statistical parameters	Expression
Root mean square error	$\mathrm{RMSE} = \sqrt{\frac{\sum_{i=1}^{N}(P_i - O_i)^2}{N-1}}$
Correlation coefficient	$\mathrm{CD} = \frac{\sum_{i=1}^{N}(O_i - \bar{O})(P_i - \bar{P})}{\sum_{i=1}^{N}(O_i - \bar{O})^2 \sum_{i=1}^{N}(P_i - \bar{P})^2}$
Nash coefficient	$\mathrm{NA} = 1 - \frac{\sum_{i=1}^{N}(P_i - O_i)^2}{\sum_{i=1}^{N}(O_i - \bar{O})^2}$
Absolute relative error	$\mathrm{ARE} = \frac{100}{N}\sum_{i=1}^{N}\frac{\lvert P_i - O_i\rvert}{O_i}$
Relative error	$\mathrm{RE} = \frac{100}{N}\sum_{i=1}^{N}\frac{P_i - O_i}{O_i}$

Data From the Yellow and Yangtze Rivers

In the drainage basins of the Yellow and Yangtze Rivers, numerous hydrological stations have been set up by the state government of China since the 1950s, and the measured data have been made available in hydrological almanacs, including flow discharge, slope, sediment concentration, average velocity, channel width, flow depth, median size of bed material, and the Manning resistance coefficient (Ma and Huang, 2016; Yellow River hydrological almanac, 2019). This study collected the measured data from the hydrological stations at Huayuankou, Jiahetan, Gaocun, Sunkou, Luokou, Tuchengzi, and Lijin in the Lower Yellow River, at Shizuishan (II), Bayan Gaole, and Toudaoguai in the upper reach of the Yellow River, and at Xianyang (II), Lintong, and Huaxian in the main tributary of the Weihe River. In the Yangtze River basin, the data collected were from the hydrological stations at Yichang, Luoshan, Datong, Jianli, Chenjiawan, and Xinchang in the trunk river and at Buhe, Hanjiang, Xincheng, and Guchen in the main tributaries.

In the following evaluation of the performance of the five selected formulae, datasets that lacked any of D_{50}, gradient, water temperature, and sediment concentration and had a value of <6 for the width/depth ratio were removed from the original data in order to maintain consistency with the studies by van Rijn (1984) and Peterson and Peterson (1988). As a result, 3,327 datasets (3,623 from experimental flumes and 1,546 from the field) compiled by Brownlie (1981) and 958 field datasets from the Yellow and Yangtze Rivers were selected. The sources and varying ranges of the parameters used in this study are provided in **Table 3**. All datasets are presented in **Supplementary Data Sheet S1**.

In a comparison of the information presented in **Tables 2** and **3**, it is clearly seen in **Table 2** that the datasets used in this study are larger than those used in the development and validation of each of the five flow resistance formulae selected. In the following analysis, each of the five formulae was examined in light of all datasets collected. Except for minor amendments, which have been discussed in the computational procedure of

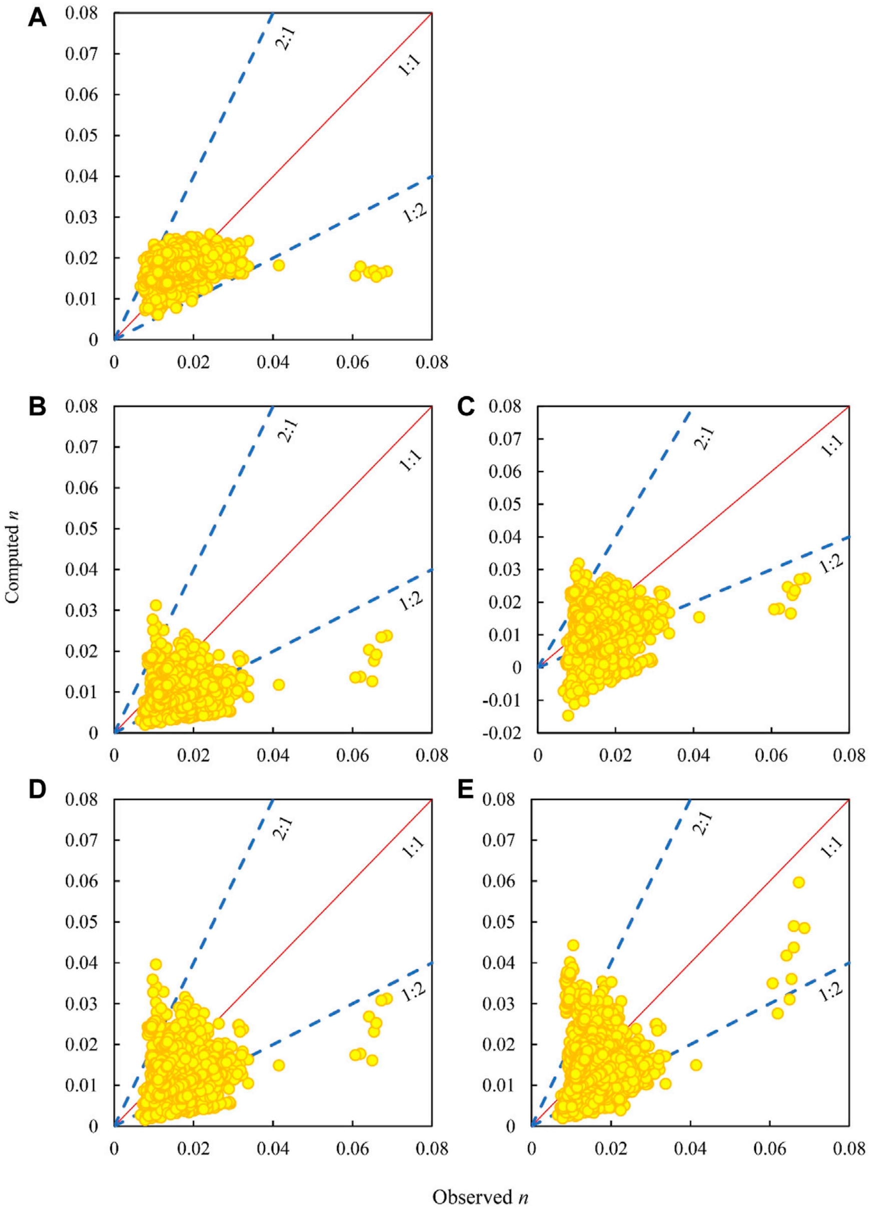

FIGURE 1 | Computed *n* values against the observed *n* valued for the laboratory data of Brownlie. **(A)** Wu and Wang formula. **(B)** Deng et al. formula. **(C)** Ma et al. formula. **(D)** Formula 1 of Zhang et al. **(E)** Formula 2 of Zhang et al.

the Ma et al. (2017) formula, each formula was applied in a precise manner specified by the original author(s).

METHOD OF EVALUATION

To evaluate the performance of the five formulae against the large datasets collected in this study, several statistical parameters were adopted in this study. **Table 4** shows the expressions of these parameters. RMSE is the root mean square error between the observed data and computed results, CD is the square of Pearson's correlation coefficient that reflects the proportion of the total variance in the observed data, and NA is the Nash coefficient that evaluates the agreement between the computed and observed values, with $NA = 1$ indicating perfect agreement between the computed and observed values. Furthermore, ARE (absolute relative error), computed as the ratio of the absolute error between the prediction and observation results to the observed value, was used to depict whether the predicted value was overestimated or underestimated. RE (relative error) was also used, and an $MSE = 0$ means that the computed value agreed perfectly with the observed value on the whole, while $RE > 0$ or $RE < 0$ indicate respectively that an overestimation or an underestimation occurred. Moreover, the percentages of data with

TABLE 5 | Statistical results for the laboratory data of Brownlie.

Formula	RMSE	CD	NA	P_{25} (%)	P_{50} (%)	POE (%)	ARE (%)	RE (%)
Wu and Wang (1999)	0.005	0.351	0.005	52.36	82.86	77.73	29.18	22.08
Deng et al. (2007)	0.008	0.253	−1.564	24.70	66.74	8.50	41.32	−35.46
Ma et al. (2017)	0.009	0.257	−1.940	33.98	65.33	20.12	44.37	−29.94
Formula 1 of Zhang et al. (2020)	0.007	0.255	−1.112	35.05	74.28	18.99	36.74	−22.39
Formula 2 of Zhang et al. (2020)	0.007	0.224	−1.063	39.11	78.19	33.70	37.60	−7.12

RMSE, *root mean square error;* CD, *square of Pearson's correlation coefficient;* NA, *Nash coefficient;* P_{25}, *percentage of the data with a relative error of 25%;* P_{50}, *percentage of the data with a relative error of ≤50;* POE, *percentage of the data with an overestimated error;* ARE, *absolute relative error;* RE, *relative error.*

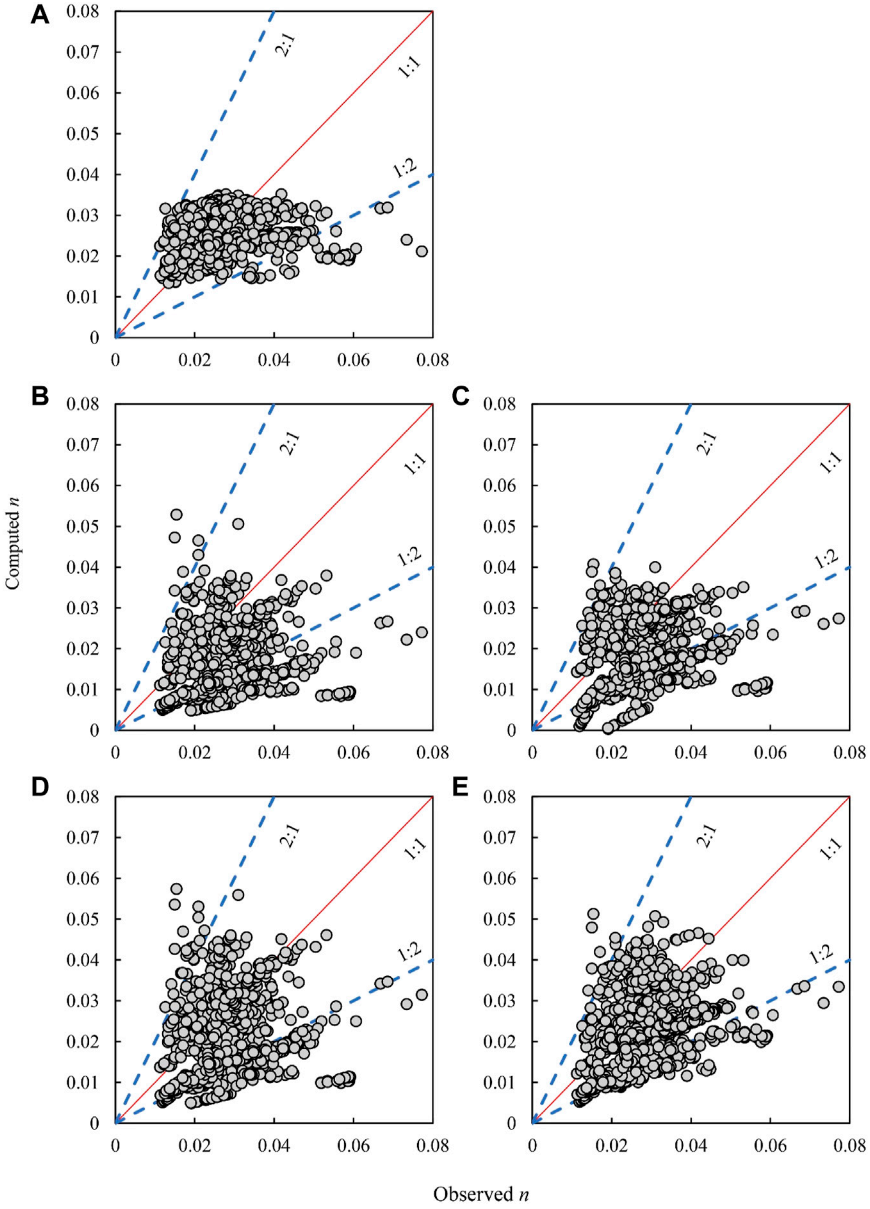

FIGURE 2 | Computed *n* values against the observed *n* values for the field data of Brownlie. **(A)** Wu and Wang formula. **(B)** Deng et al. formula. **(C)** Ma et al. formula. **(D)** Formula 1 of Zhang et al. **(E)** Formula 2 of Zhang et al.

TABLE 6 | Statistical results for the field data of Brownlie.

Formula	RMSE	CD	NA	P_{25} (%)	P_{50} (%)	POE (%)	ARE (%)	RE (%)
Wu and Wang (1999)	0.009	0.181	−0.189	59.06	92.30	43.34	23.50	−1.70
Deng et al. (2007)	0.015	0.154	−2.391	24.26	47.35	9.31	44.60	−39.10
Ma et al. (2017)	0.013	0.216	−1.444	34.22	66.36	19.34	37.10	−28.00
Formula 1 of Zhang et al. (2020)	0.014	0.165	−1.6	30.72	62.87	25.36	38.90	−22.60
Formula 2 of Zhang et al. (2020)	0.011	0.333	−0.744	40.49	81.37	26.33	31.40	−16.60

RMSE, *root mean square error;* CD, *square of Pearson's correlation coefficient;* NA, *Nash coefficient;* P_{25}, *percentage of the data with a relative error of 25%;* P_{50}, *percentage of the data with a relative error of ≤50;* POE, *percentage of the data with an overestimated error;* ARE, *absolute relative error;* RE, *relative error.*

relative errors of ≤50% and 25% (P_{50} and P_{25}, respectively) and the percentages of the data with an overestimated error (POE) were also deployed (Nash and Sutcliffe, 1970; Bjerklie et al., 2005; López et al., 2007).

PERFORMANCE OF THE SELECTED FORMULAE IN DIFFERENT DATASETS

Laboratory Data of Brownlie

In terms of the laboratory data compiled by Brownlie (1981), the values of n computed from the five selected formulae against the observed counterparts are presented in **Figure 1**. It can be seen from **Figures 1A–E** that the differences between the computed and the observed values of n varied beyond the range of 2:1–1:2 (ratio of the computed to the observed). In many cases, the Ma et al. formula even yielded unreasonable results of <0, as shown in **Figure 1C**. Relatively speaking, nevertheless, the values of n computed using the formula of Wu and Wang were closer to the observed counterparts, typically when n was <0.04.

The statistical results on the correlation of the values of n computed from the five formulae against the observed counterparts in terms of the laboratory data of Brownlie are provided in **Table 5**. The correlation coefficient (CD) of the results computed using the formula of Wu and Wang was 0.351, the highest among the five formulae, while the other four yielded correlation coefficient results of generally <0.3. Among the NA values of the five formulae, only that by Wu and Wang yielded results with NA > 0, manifesting that the results were generally closer to the average level of the observations; that is, the points in **Figure 1A** are much more evenly distributed on both sides of the 1:1 line. All of these indicated that the formula of Wu and Wang outperformed the other four equations in Brownlie's laboratory data.

Field Data of Brownlie

Using the field data compiled by Brownlie (1981), the values of n computed from each formula against the observed n values are presented in **Figures 2A–E**. It can be noticed from **Figure 2** that the differences between the computed and the observed values of n varied beyond the range of 2:1–1:2 (ratio of the computed to the observed). Relatively speaking, nevertheless, the distribution of the n values computed using the Wu and Wang formula against the observed n values was much less scattered than those computed using the other four formulae.

The performance of the five selected formulae in the field data of Brownlie is summarized in **Table 6**. The CD computed using formula 2 of Zhang et al. was 0.333, which is the highest among the five formulae, while the CD values of the other four formulae were <0.3. Although the AREs of the results computed using formula 2 of Zhang et al. and the formula of Wu and Wang took smaller values of 31.4% and 23.5%, respectively, their P_{50} values were respectively 92.3% and 81.37%, indicating that the results computed using the Wu and Wang formula and formula 2 of Zhang et al. fitted the observed values at respective degrees of 92.3% and 81.37% within an error of 50%. Hence, the Wu and Wang formula yielded results best fitting the observed values among the five selected formulae.

Data From the Yellow and Yangtze Rivers

Using data collected from the hydrological stations in the main tributaries and the trunk reach of the Yellow and Yangtze Rivers, the values of n computed from the five selected formulae against the observed values of n are presented in **Figures 3A–E**. It can be seen that, except for the results computed using the Wu and Wang formula, the differences between the values of n computed from the other four formulae and the observed n varied within the range of 2:1–1:2 (ratio of the computed to the observed). Relatively speaking, nevertheless, the values of n computed using formula 1 of Zhang et al. were distributed more uniformly on both sides of the 1:1 line and so fitted the observations to the highest level among the five selected formulae.

The statistical results of the performance of the five formulae in the data collected from the drainage basins of the Yellow and Yangtze Rivers are shown in **Table 7**. The CD values of the results computed using the Deng et al. formula, Ma et al. formula, and formulae 1 and 2 of Zhang et al. were all very high, respectively 0.87, 0.871, 0.88, and 0.896, and the AREs of the results computed using the four formulae were no larger than 22.3%. In addition, the NA and P_{50} of the results computed using the four formulae were all larger than 0.6% and 95%, respectively. On the contrary, the results computed using the Wu and Wang formula only had values of 0.679 for CD, 51.83% for ARE, 0.173 for NA, and 57.46% for P_{50}. Except for the Wu and Wang formula, hence, the other four selected formulae were all able to yield results best fitting the observed values.

All Datasets

In terms of the laboratory and field data compiled by Brownlie (1981) and the data collected from the hydrological stations in the main tributaries and the trunk reach of the Yellow and Yangtze

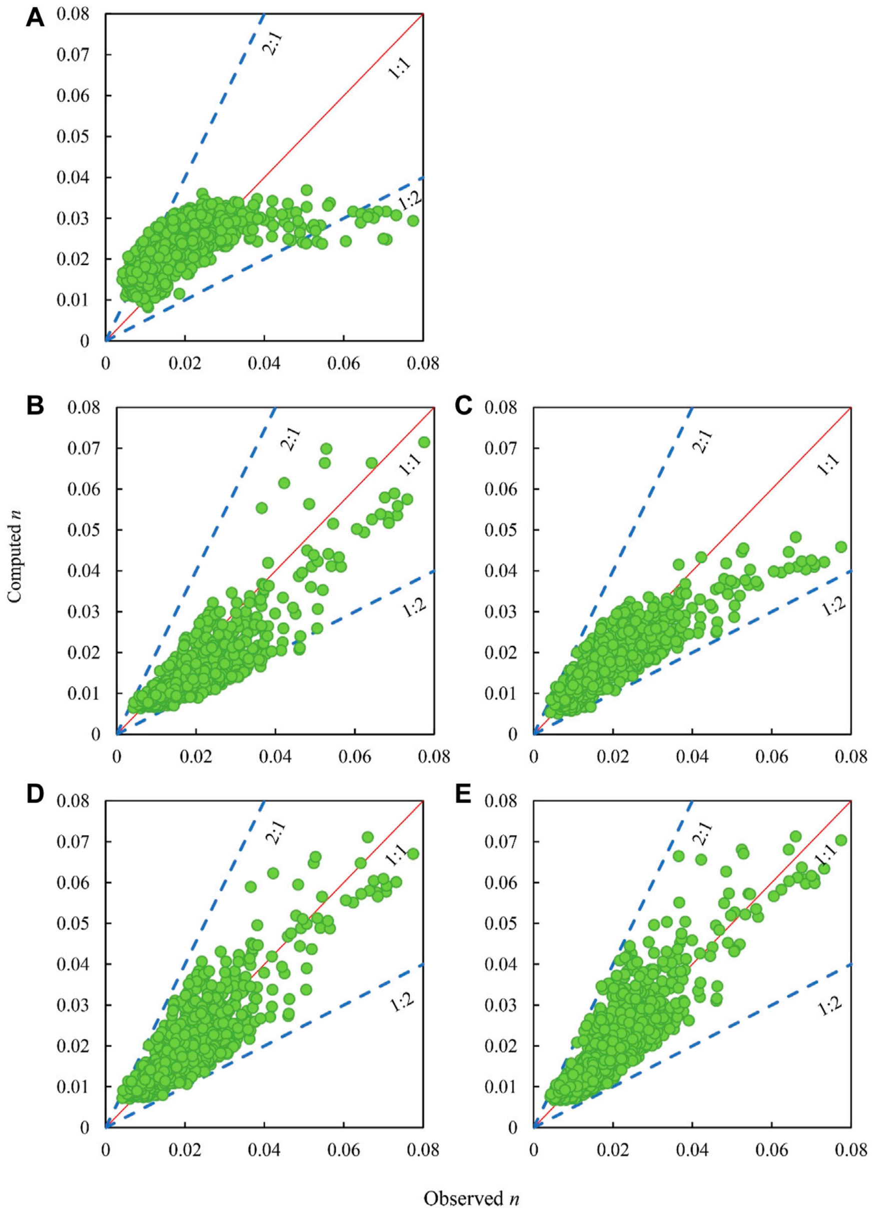

FIGURE 3 | Computed *n* values against the observed *n* values for the data from the Yellow and Yangtze Rivers. **(A)** Wu and Wang formula. **(B)** Deng et al. formula. **(C)** Ma et al. formula. **(D)** Formula 1 of Zhang et al. **(E)** Formula 2 of Zhang et al.

TABLE 7 | Statistical results for data from the Yellow and Yangtze Rivers.

Formula	RMSE	CD	NA	P_{25} (%)	P_{50} (%)	POE (%)	ARE (%)	RE (%)
Wu and Wang (1999)	0.009	0.679	0.173	33.25	57.46	85.57	51.83	47.68
Deng et al. (2007)	0.006	0.87	0.605	58.99	97.37	18.64	22.30	−16.98
Ma et al. (2017)	0.005	0.871	0.726	34.22	97.74	30.26	18.78	0.63
Formula 1 of Zhang et al. (2020)	0.004	0.88	0.776	70.17	96.39	52.08	19.32	2.91
Formula 1 of Zhang et al. (2020)	0.004	0.896	0.782	75.79	95.54	53.30	17.96	4.84

RMSE, *root mean square error;* CD, *square of Pearson's correlation coefficient;* NA, *Nash coefficient;* P_{25}, *percentage of the data with a relative error of 25%;* P_{50}, *percentage of the data with a relative error of ≤50;* POE, *percentage of the data with an overestimated error;* ARE, *absolute relative error;* RE, *relative error.*

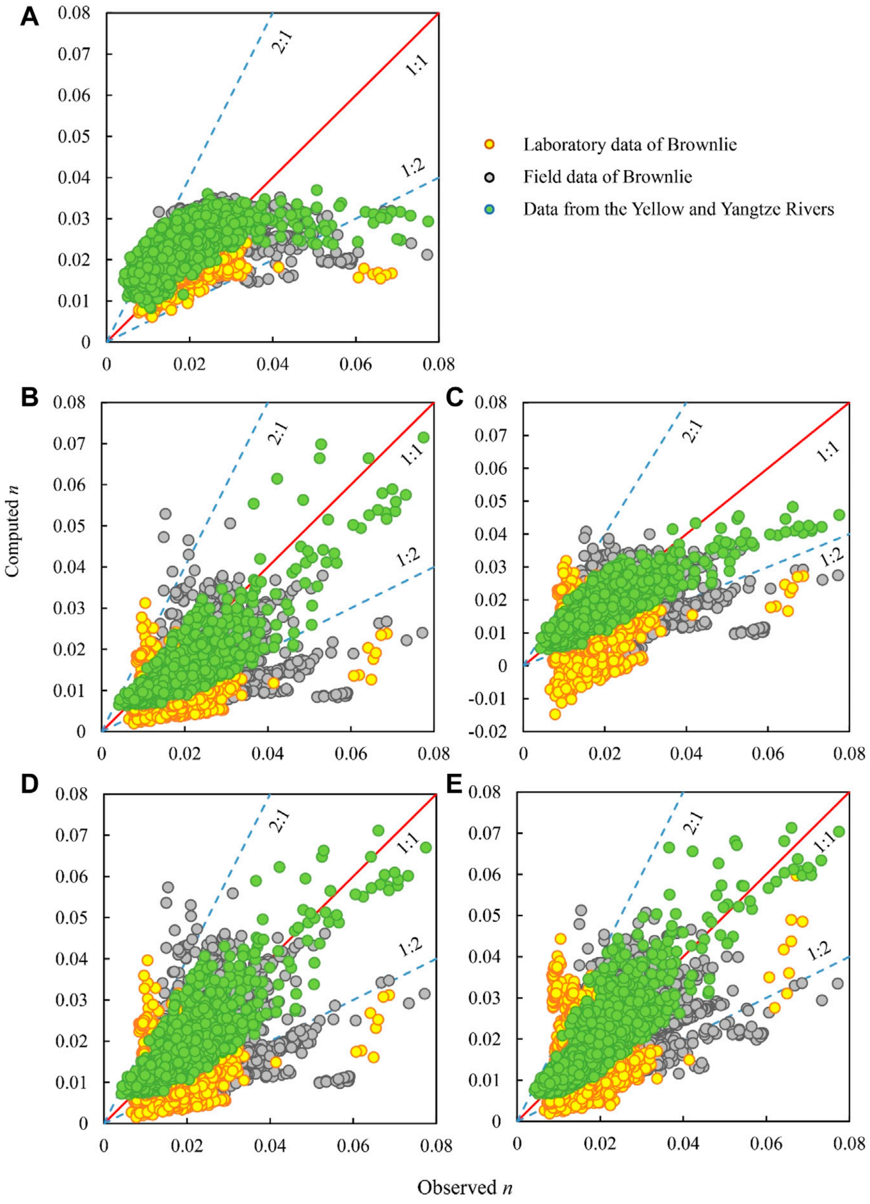

FIGURE 4 | Computed *n* values against observed *n* values for all datasets. **(A)** Wu and Wang formula. **(B)** Deng et al. formula. **(C)** Ma et al. formula. **(D)** Formula 1 of Zhang et al. **(E)** Formula 2 of Zhang et al.

TABLE 8 | Statistical results for all datasets.

Formula	RMSE	CD	NA	P_{25} (%)	P_{50} (%)	POE (%)	ARE (%)	RE (%)
Wu and Wang (1999)	0.002	0.597	0.310	49.29	50.71	71.80	33.35	22.67
Deng et al. (2007)	0.010	0.579	-0.300	32.84	67.16	11.12	37.49	–31.91
Ma et al. (2017)	0.009	0.551	-0.126	42.63	57.37	26.61	36.57	–22.18
Formula 1 of Zhang et al. (2020)	0.009	0.578	0.001	42.51	57.49	28.39	33.04	–16.41
Formula 2 of Zhang et al. (2020)	0.008	0.620	0.196	48.24	51.76	36.74	31.46	–6.45

RMSE, *root mean square error;* CD, *square of Pearson's correlation coefficient;* NA, *Nash coefficient;* P_{25}, *percentage of the data with a relative error of 25%;* P_{50}, *percentage of the data with a relative error of ≤50;* POE, *percentage of the data with an overestimated error;* ARE, *absolute relative error;* RE, *relative error.*

TABLE 9 | Distribution of the prediction ratios

Data source	Distribution of (Computed – Observed)/Observed						ARE (%)
	0.00–0.05 (%)	0.05–0.1 (%)	0.1–0.2 (%)	0.2–0.5 (%)	0.5–1 (%)	>1 (%)	
Formula of Wu and Wang							
Laboratory data of Brownlie	6.13	6.13	9.63	60.97	16.12	1.02	29.18
Field data of Brownlie	4.46	11.77	23.29	43.08	7.24	6.27	23.50
Yellow River and Yangtze River	6.66	6.42	14.12	30.26	27.87	14.67	51.83
Formula of Deng et al.							
Laboratory data of Brownlie	1.08	0.97	2.32	62.38	32.46	0.80	41.32
Field data of Brownlie	4.46	4.53	8.60	29.75	52.26	6.21	44.60
Yellow River and Yangtze River	11.67	11.86	25.00	48.84	2.63	0.00	22.30
Formula of Ma et al.							
Laboratory data of Brownlie	2.13	2.57	4.53	56.11	26.00	8.67	44.37
Field data of Brownlie	5.76	8.21	15.59	36.80	33.25	6.21	37.10
Yellow River and Yangtze River	16.93	15.10	26.41	39.30	2.20	0.06	18.78
Formula 1 of Zhang et al.							
Laboratory data of Brownlie	1.90	2.26	4.72	65.39	23.93	1.79	36.74
Field data of Brownlie	8.93	6.73	10.09	37.13	35.58	7.37	38.90
Yellow River and Yangtze River	16.20	13.88	28.73	37.59	3.55	0.06	19.32
Formula 2 of Zhang et al.							
Laboratory data of Brownlie	2.43	2.68	5.58	67.51	18.11	3.70	37.60
Field data of Brownlie	10.16	10.03	12.81	48.38	17.98	6.47	31.40
Yellow River and Yangtze River	17.18	16.87	30.75	30.75	4.40	0.06	17.96

Rivers in this study, the values of n computed from each selected formula against the observed n values are presented in **Figures 4A–E**. It can be seen that the formula of Ma et al. yielded an unreasonable result of $n < 0$ in many cases (**Figure 4C**). While the formula of Deng et al. and formulae 1 and 2 of Zhang et al. yielded results varying significantly beyond the range of 2:1–1:2 (ratio of the computed to the observed), the formula of Wu and Wang yielded results varying mostly within the scope, typically in cases of $n < 0.04$.

Statistical results of the performance of the five selected formulae in all datasets used in this study are shown in **Table 8**. The CD values of the results computed using all five formulae were not very high and varied within the small range of 0.551–0.62. The AREs of the results computed using the five formulae were considerably small and also varied within the small range of 31.46%–37.49%. However, the NA values of the results computed using the Deng et al. formula, the Ma et al. formula, and formula 1 of Zhang et al. were negative or very close to 0, while the NA values of the results computed using the formula of Wu and Wang and formula 2 of Zhang et al. were positive, with the Wu and Wang formula yielding a much larger NA of 0.31. All of these demonstrated that formula 2 of Zhang et al. and the formula of Wu and Wang were the most appropriate in all datasets, despite their low calculation accuracy.

DISTRIBUTION OF RELATIVE ERRORS AND PERFORMANCE RANKING

The AREs of n (computed n – Observed n)/Observed n) by all five selected formulae were computed for the three datasets, i.e., the laboratory data and field data compiled by Brownlie (1981) and the data from the drainage basins of the Yellow and Yangtze Rivers collected in this study. The distribution of AREs in the six groups of 0–0.05, 0.05–1, 0.1–0.2, 0.2–0.5, 0.5–1, and >1 is presented in **Table 9** and shown in **Figure 5**. In the laboratory data of Brownlie, the AREs in the group 0.2–0.5 by all five selected formulae occupied around 60%, and there was a very small difference among the percentages in the group for the five formulae. The AREs in the group 0.5–1 occupied around 20%, while the AREs of each of the other groups occupied a very small percentage (**Figure 5A**).

In the field data of Brownlie, however, the AREs in the groups of 0.2–0.5 and 0.5–1 by all five formulae occupied large and nearly equal percentages of around 35%, while those in each of the other groups occupied only a very small percentage (**Figure 5B**). In the data from the Yellow and Yangtze Rivers, the AREs in the two groups of 0.1–0.2 and 0.2–0.5 by all five formulae occupied large and nearly equal percentages of slightly larger than 30%, while the AREs in the two groups of 0.05–0.1 and <0.05 occupied nearly equal percentages of about 18% (**Figure 5C**). Overall, it was obvious that the relative errors in the range of 0.2–0.5 accounted for the biggest percentage, with each of the nearby groups of 0.5–1 and 0.1–0.2 accounting for a sizable portion as well. This clearly manifests that the AREs by all five flow resistance formulae occupied a very large percentage almost in the same range of 0.1–1; hence, the five formulae needed to improve their predicting ability. Importantly, it is noticeable from **Table 9** and **Figure 5** that the AREs by each of the five selected flow resistance formulae were considerably large among the three datasets used.

The formula of Wu and Wang performed better in the laboratory and field data of Brownie, with ARE <30%. In the data from the Yellow and Yangtze Rivers, nevertheless, ARE >50% and the group of ARE >100% still accounted for 14.67% of the total. The formula of Deng et al. considerably yielded large values of 41.3% and 44.6% for ARE in the laboratory data and

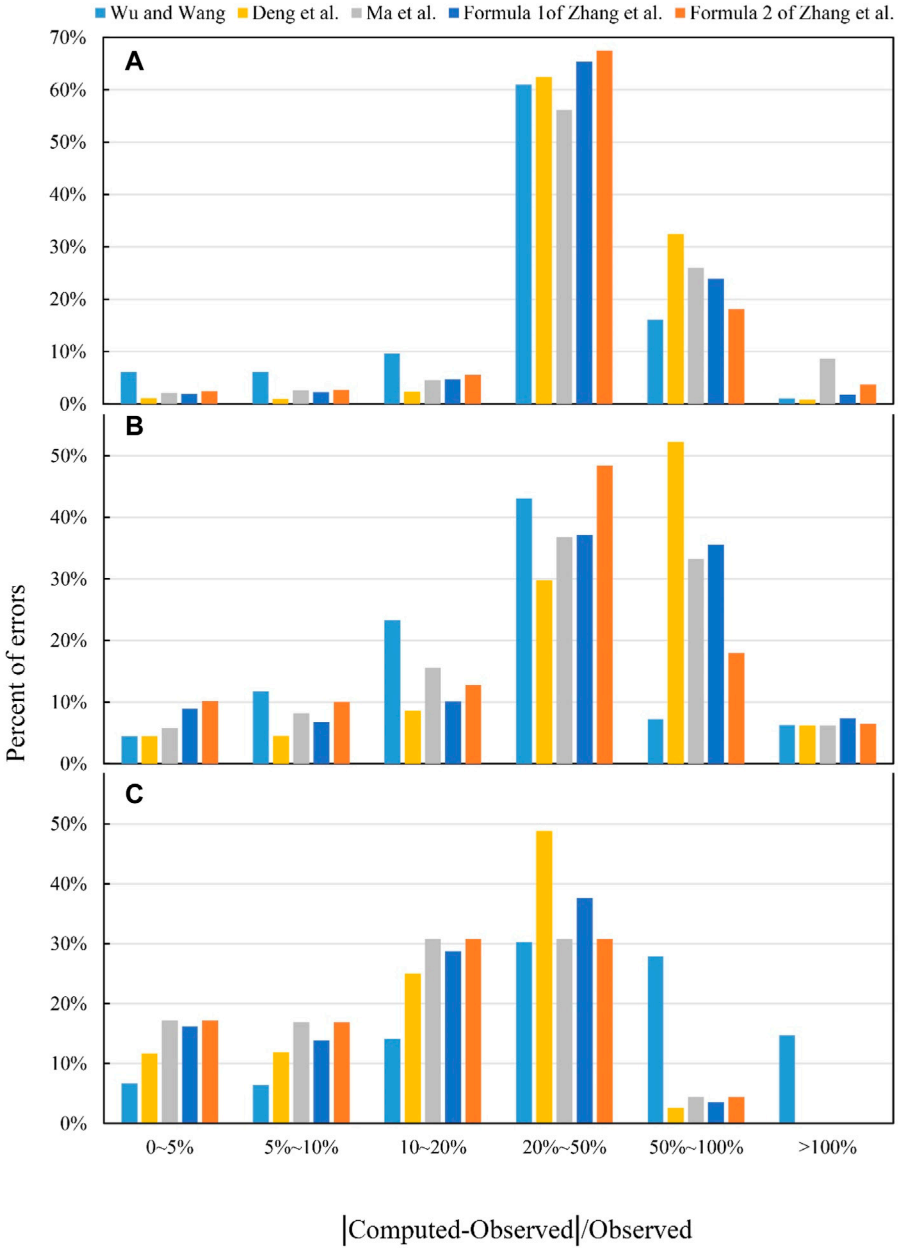

FIGURE 5 | Distribution of the IC_{50} values by the five selected formulae. **(A)** Laboratory data of Brownlie. **(B)** Field data of Brownlie. **(C)** Data from the Yellow and Yangtze Rivers.

field data of Brownlie, respectively. In the data from the Yellow and Yangtze Rivers, nevertheless, the formula allowed ARE to take a relatively small value of 22.3%, and the group of ARE <0.5 occupied a very large percentage of 97.37% of the total. The formula of Ma et al. also yielded considerably large values of 44.37% and 33.1% for ARE in the laboratory data and field data of Brownlie, respectively. In the data from the Yellow and Yangtze Rivers, the formula allowed ARE to take a considerably small value of 18.78%, and the group of ARE <0.5 occupied 97.74% of the total. Hence, the formulae of Deng et al. and Ma et al. performed best in the data from the Yellow and Yangtze Rivers among the three datasets used. Formulae 1 and 2 of Zhang et al. yielded relatively small values of <40% for ARE in the laboratory data and field data of Brownlie, respectively. In the data from the Yellow and Yangtze Rivers, meanwhile, the formulae allowed ARE to take considerably small values of 19.32% and 17.96%, and the group of ARE <0.5 occupied 96.39% and 95.54% of the total. Hence, formulae 1 and 2 of Zhang et al. both performed well in the data from the Yellow and Yangtze Rivers among the three datasets used.

Because different formulae performed at considerably different levels in the different datasets used, ARE appears a

TABLE 10 | Rating standards of data fitting.

Formula	ARE (%)	Ranking
Formula of Wu and Wang		
Laboratory data of Brownlie	29.18	II
Field data of Brownlie	23.50	II
Data from the Yellow and Yangtze Rivers	51.83	V
Formula of Deng et al.		
Laboratory data of Brownlie	41.32	IV
Field data of Brownlie	44.60	IV
Data from the Yellow and Yangtze Rivers	22.30	II
Formula of Ma et al.		
Laboratory data of Brownlie	44.37	IV
Field data of Brownlie	37.10	III
Data from the Yellow and Yangtze Rivers	18.78	I
Formula 1 of Zhang et al.		
Laboratory data of Brownlie	36.74	III
Field data of Brownlie	38.90	III
Data from the Yellow and Yangtze Rivers	19.32	I
Formula 2 of Zhang et al.		
Laboratory data of Brownlie	37.60	III
Field data of Brownlie	31.40	III
Data from the Yellow and Yangtze Rivers	17.96	I

Rank I for 0 < ARE < 20%; rank II for 20% < ARE < 30%; rank III for 30% < ARE < 40%; rank IV for 40% < ARE < 50%; and rank V for ARE > 50%.

suitable index to evaluate the performance of the five selected flow resistance formulae in the three datasets. Assuming that the performance of a formula can be ranked to the highest level "I" when 0 < ARE < 20%, to the relatively high level "II" when 20% < ARE < 30%, to the moderate level "III" when 30% < ARE < 40%, to the relatively low level "IV" when 40% < ARE < 50%, and to the lowest level "V" when ARE > 50%, the detailed ranks of the performance of the five selected flow resistance formulae in the three datasets are provided in **Table 10**.

It can be clearly seen from **Table 10** that the formula of Ma et al. and formulae 1 and 2 of Zhang et al. gained the highest rank I in the data from the Yellow and Yangtze Rivers, while they gained the moderate rank III or the relatively low rank IV in the laboratory and field data of Brownlie. In contrast, the formula of Wu and Wang gained the relatively high rank II in the laboratory and field data of Brownlie, yet the lowest rank V in the data from the Yellow and Yangtze Rivers. Within the two relatively extremal cases, the formula of Deng et al. gained a relatively low rank IV in the laboratory and field data of Brownlie and also a relatively high rank II in the data from the Yellow and Yangtze Rivers.

CONCLUSION

Among the numerous flow resistance formulae for sand-bed channels, this study selected five for evaluation in terms of theoretical advances and the scope and quantity of the data used in the development, including those developed by Wu and Wang (1999), Deng et al. (2007), Ma et al. (2017), and Zhang et al. (2020). In order to cover flow conditions in sand-bed river channels as widely as possible, this study collected 1,636 sets of field measures from the hydrological stations in two large river systems of China (the Yellow and Yangtze Rivers), in addition to the data compiled by Brownlie (1981) that, in complete form, included 3,623 sets of laboratory data and 1,546 sets of field data from different nations and areas. The conclusion of this paper is generally used in alluvial rivers. A detailed statistical analysis of the performance of the five selected flow resistance formulae in yielding the values of the Manning resistance coefficient n using the very large number of datasets, 6,805 sets in total, led to the following important findings:

1) The formula of Wu and Wang yielded n values best fitting the laboratory and field data of Brownie, yet fitting the data from the Yellow and Yangtze Rivers at a relatively low degree. In contrast, the formula of Ma et al. and formulae 1 and 2 of Zhang et al. yielded n values fitting the data from the Yellow and Yangtze Rivers at a very high degree, yet fitting the laboratory and field data of Brownie at a moderate degree. The formula of Deng et al. yielded n values fitting the laboratory and field data of Brownlie and the data from the Yellow and Yangtze Rivers both at a relatively low degree.
2) In all datasets, the Ma et al. formula yielded unreasonable n values of <0 in many cases, while the formula of Deng et al. and formulae 1 and 2 of Zhang et al. yielded n values varying considerably beyond the range of 2:1–1:2. Nevertheless, the Wu and Wang formula yielded n values varying mostly within the scope, typically in cases of $n < 0.04$.
3) By dividing the AREs from the five selected formulae into six groups of 0–0.05, 0.05–1, 0.1–0.2, 0.2–0.5, 0.5–1, and >1, it can be found that, for all five selected formulae, the AREs in the group 0.2–0.5 occupied the largest percentage, while each of the adjacent groups of 0.5–1 and 0.1–0.2 occupied a very large percentage. This means that all five formulae needed to enhance the accuracy of their predicting capability.
4) The formula of Ma et al. and formulae 1 and 2 of Zhang et al. gained the highest rank for fitting the data from the Yellow and Yangtze Rivers, yet gained a moderate rank or a relatively low rank for the laboratory and field data of Brownlie. In contrast, the Wu and Wang formula gained a relatively high rank for the laboratory and field data of Brownlie, yet gained the lowest rank for the data from the Yellow and Yangtze Rivers. Within the two relatively extremal cases, the formula of Deng et al. gained a relatively low rank for the laboratory and field data of Brownlie, yet gained a relatively high rank for the data from the Yellow and Yangtze Rivers.

DATA AVAILABILITY STATEMENT

The original contributions presented in the study are included in the article/**Supplementary Material**. Further inquiries can be directed to the corresponding author.

AUTHOR CONTRIBUTIONS

HP, HH, GY, and HZ contributed to the conception and design of the study. HP organized the database, performed the statistical analysis, and wrote the first draft of themanuscript. HH wrote sections of the manuscript. All authors contributed to manuscript revision, read, and approved the submitted version.

FUNDING

This work was supported financially by the National Natural Science Foundation of China (grant nos. 41971010 and 41561144012) and the National Key Research and Development Program of China (grant no. 2016YFC0402502).

ACKNOWLEDGMENTS

The authors would like to thank the Yellow River Water Conservancy Commission and Yangtze River Water Conservancy Commission of China for permission to access the measured hydrological and river channel data.

SUPPLEMENTARY MATERIAL

The Supplementary Material for this article can be found online at: https://www.frontiersin.org/articles/10.3389/fenvs.2022.840653/full#supplementary-material

REFERENCES

Bjerklie, D. M., Dingman, S. L., and Bolster, C. H. (2005). Comparison of Constitutive Flow Resistance Equations Based on the Manning and Chezy Equations Applied to Natural Rivers. *Water Resour. Res.* 41, W11502. doi:10.1029/2004WR003776

Brownlie, W. R. (1981). *Compilation of Alluvial Channel Data: Laboratory and Field*. Report No. KH-R-43B. Pasadena, California: W. M. Keck Laboratory of Hydraulics and Water Resources, California Institute of Technology.

Carollo, F. G., and Ferro, V. (2021). Experimental Study of Boulder Concentration Effect on Flow Resistance in Gravel Bed Channels. *Catena* 205, 105458. doi:10.1016/j.catena.2021.105458

Chang, Y. L. (1939). Laboratory Investigation of Flume Traction and Transportation. *T. Am. Soc. Civ. Eng.* 104, 1246–1284. doi:10.1061/taceat.0005049

Chien, N., and Wan, Z. H. (1983). *Mechanics of Sediment Movement*. Beijing: Science Publications. (in Chinese).

Deng, A., Guo, Q., and Chen, J. (2007). Study on the Roughness in Sediment-Laden Flows. *J. Sediment Res.* 2007 (05), 24–29. (in Chinese). doi:10.16239/j.cnki.0468-155x.2007.05.005

Di Stefano, C., Nicosia, A., Palmeri, V., Pampalone, V., and Ferro, V. (2020). Flow Resistance Law under Suspended Sediment Laden Conditions. *Flow Meas. Instrumentation* 74, 101771. doi:10.1016/j.flowmeasinst.2020.101771

East Parkistan Water and Power Development Authority (1967). *Flume Studies of Roughness and Sediment Transport of Movable Bed of Sand*. Dahka, Bangladesh: Annu. Rep. of Hydr. Res. Lab.

Einstein, H. A., and Barbarossa, N. L. (1952). River Channel Roughness. *T. Am. Soc. Civ. Eng.* 117, 1121–1132. doi:10.1061/taceat.0006666

Engelund, F., and Hansen, E. A. (1967). *Monograph on Sediment Transport in Alluvial Streams*. Copenhagen K: Technical University of Denmark Østervoldgade 10.

Engelund, F. (1961). Hydraulic Resistance of Alluvial Streams. *J. Hydraulics Division, ASCE* 92 (2), 315–327.

Ferro, V. (2018a). Assessing Flow Resistance in Gravel Bed Channels by Dimensional Analysis and Self-Similarity. *Catena* 169, 119–127. doi:10.1016/j.catena.2018.05.034

Ferro, V. (2018b). Flow Resistance Law under Equilibrium Bed-Load Transport Conditions. *Flow Meas. Instrumentation* 64, 1–8. doi:10.1016/j.flowmeasinst.2018.10.008

Gilbert, G. K. (1914). The Transportation of Débris by Running Water. *U.S. Geol. Surv. Prof. Pap.* 86.

Guy, H. P., Simons, D. B., and Richardson, E. V. (1966). *Summary of Alluvial Channel Data from Flume Experiments, 1956-1961*. Washington: UNITED STATES GOVERNMENT PRINTING OFFICE.

Herschel, C. (1897). On the Origin of the Chezy Formula. *J. Assoc. Eng. Societies* 18, 363–369.

Huang, H. Q. (2010). Reformulation Of The Bed Load Equation Of Meyer-Peter And Müller in Light of The Linearity Theory For Alluvial Channel Flow[J]. *Water Resources Res.* 46 (9), 161–170.

Huang, C., Zhao, X., and Gong, M. (2004). Comparisons Of Flow Resistance Equations In Movable Bed. *J. Sediment Res.* 2004 (5), 1–7. (in Chinese). doi:10.16239/j.cnki.0468-155x.2004.05.001

Jaeger, C. (1961). *Engineering Fluid Mechanics* London: Blackie.

Kamphuis, J. W. (1974). Determination of Sand Roughness for Fixed Beds. *J. Hydraulic Res.* 12 (2), 193–203. doi:10.1080/00221687409499737

Kuhnle, R. A. (1993). Fluvial Transport of Sand and Gravel Mixtures with Bimodal Size Distributions. *Sediment. Geology.* 85, 17–24. doi:10.1016/0037-0738(93)90072-d

Liu, X. L. (1986). Nonuniform Bed Load Transport Rate and Coarsening Stabilization. Master's Thesis. China: Chengdu University of Technology.

López, R., Barragán, J., and Colomer, M. Á. (2007). Flow Resistance Equations without Explicit Estimation of the Resistance Coefficient for Coarse-Grained Rivers. *J. Hydraulic* 338, 113–121. doi:10.1016/j.jhydrol.2007.02.027

Ma, Y., and Huang, H. Q. (2016). Controls of Channel Morphology and Sediment Concentration on Flow Resistance in a Large Sand-Bed River: A Case Study of the Lower Yellow River. *Geomorphology* 264, 132–146. doi:10.1016/j.geomorph.2016.03.035

Ma, Y., Xia, J., and Zhang, X. (2017). Verification and Comparison of Flow Resistance Formulae over Movable Beds. *Eng. J. Wuhan Univ.* 50 (4), 481–486. (in Chinese). doi:10.14188/j.1671-8844.2017-04-001

Manning, R. (1890). On the Flow of Water in Open Channels and Pipes. *Proc. Inst. Civil Eng. Ireland* 20, 161–206.

Mark Powell, D. (2014). Flow Resistance in Gravel-Bed Rivers: Progress in Research. *Earth-Science Rev.* 136, 301–338. doi:10.1016/j.earscirev.2014.06.001

Maynord, S. T. (1991). Flow Resistance of Riprap. *J. Hydraulic Eng.* 117 (6), 687–696. doi:10.1061/(asce)0733-9429(1991)117:6(687)

Meyer-Peter, E., and Müller, R. (1948). "Formulas for Bed Load Transport, Paper Presented at 2nd Meeting," in Int. Assoc. for Hydroaul. Environ.Eng. and Res. (Madrid).

Nash, J. E., and Sutcliffe, J. V. (1970). River Flow Forecasting through Conceptual Models Part I - A Discussion of Principles. *J. Hydrol.* 10, 282–290. doi:10.1016/0022-1694(70)90255-6

Niazkar, M., Talebbeydokhti, N., and Afzali, S. H. (2019). Development of a New Flow-Dependent Scheme for Calculating Grain and Form Roughness Coefficients. *KSCE J. Civil Eng.* 23, 2108–2116. doi:10.1007/s12205-019-0988-z

Nicosia, A., Di Stefano, C., Pampalone, V., Palmeri, V., and Ferro, V. (2021). Assessing an Overland Flow Resistance Approach under Equilibrium Sediment Transport Conditions. *CATENA* 207, 105578. doi:10.1016/j.catena.2021.105578

Peterson, A. W., and Peterson, A. E. (1988). Mobile Boundary Flow: An Assessment of Velocity and Sediment Discharge Relationships. *Can. J. Civ. Eng.* 15 (4), 539–546. doi:10.1139/l88-074

Peterson, A. W., and Howells, R. F. (1973). *A Compendium of Solids Transport Data for Mobile Boundary Channels*. Canada: Department of Civil Engineering, University of Alberta. Report No. HY-1973-ST3.

Qin, R., Liu, S., and Wang, C. (1995). Characteristics Of Channel Resistance And Sediment Transport In The Lower Yellow River. *J. Sediment Res.* (4), 10–18. (in Chinese).

Samaga, B. R., Raju, K. G. R., and Garde, R. J. (1986). Bed Load Transport of Sediment Mixtures. *J. Hydraulic Eng.* 112 (11), 1003–1017. doi:10.1061/(asce)0733-9429(1986)112:11(1003)

Taylor, B. D. (1971). *Temperature Effects In Alluvial Streams[J]*. California Institute of Technology.

van Rijn, L. C. (1982). Equivalent Roughness of Alluvial Bed. *J. Hydraulics Division, ASCE* 108, HY10. doi:10.1061/jyceaj.0005917

van Rijn, L. C. (1984). Sediment Transport, Part III: Bed Forms and Alluvial Roughness. *J. Hydraul. Eng.* 110 (12), 1733–1754. doi:10.1061/(asce)0733-9429(1984)110:12(1733)

Wang, S. (1990). Experimental Study on Hydraulic Resistance of Alluvial Streams. *J. Hydraulic Eng.* 1990 (12), 18–29. (in Chinese).

Wilcock, P. R., and McArdell, B. W. (1993). Surface-based Fractional Transport Rate: Mobilization Thresholds and Partial Transport of a Sand-Gravel Sediment. *Water Resour. Res.* 29 (24), 1297–1312. doi:10.1029/92wr02748

Wu, W., and Wang, S. S. Y. (1999). Movable Bed Roughness in Alluvial Rivers. *J. Hydraulic Eng.* 125 (12), 1309–1312. doi:10.1061/(asce)0733-9429(1999)125:12(1309)

Yadav, A., Sen, S., Mao, L., and Schwanghart, W. (2022). Evaluation of Flow Resistance Equations for High Gradient Rivers Using Geometric Standard Deviation of Bed Material. *J. Hydrol.* 605, 127292. doi:10.1016/j.jhydrol.2021.127292

Yalin, M. S. (1963). An Expression for Bed-Load Transportation[J]. *J. Hydraul. Div. Asce* 89, 221–250.

Yellow River hydrological almanac (2019). *The Yellow River Water Resources Commission*. China: Zhengzhou.

Zhang, H., Zhang, L., Peng, H., Cai, R., and Zhang, L. (2020). Research on Cognition and Calculation Method of Alluvial River Roughness. *J. Hydraulic Eng.* 51 (07), 774–787. (in Chinese). doi:10.13243/j.cnki.slxb.20200130

Zhang, L. (2012a). Analysis of the Present Situation of Open Channels Roughness. *J. Hydraulic Eng.* 43 (10), 1154–1162. (in Chinese). doi:10.13243/j.cnki.slxb.2012.10.007

Zhang, L. (2012b). Reasons for the Abnormal Channel Roughness of the Yellow River and the Solution to its Problems. *J. Hydraulic Eng.* 43 (10), 1154–1162. (in Chinese). doi:10.13243/j.cnki.slxb.2012.11.004

Zhang, R., Xie, J., Wang, M., and Huang, J. (1998). *Dynamics of River Sedimentation.* Beijing: Water Resources and Electric Power Publication. (in Chinese).

Zhao, L., and Zhang, H. (1997). Study of Flow Frictional Characteristics in the Lower Yellow River Channel. *Yellow River* 9, 17–20+62. (in Chinese).

Conflict of Interest: The authors declare that the research was conducted in the absence of any commercial or financial relationships that could be construed as a potential conflict of interest.

frontiers
in Environmental Science

ORIGINAL RESEARCH
published: 02 March 2022
doi: 10.3389/fenvs.2022.859427

The Effect of Extreme Rainfall Events on Riverbank Slope Behaviour

Jeffery Nazrien Ng[1], Aizat Mohd Taib[1]*, Irfan Haziq Razali[1], Norinah Abd Rahman[1], Wan Hanna Melini Wan Mohtar[1], Othman A. Karim[1], Safari Mat Desa[2], Suriyani Awang[2] and Mohd Syazwan Faisal Mohd[2]

[1]Faculty of Engineering and Built Environment, Universiti Kebangsaan Malaysia, Bangi, Malaysia, [2]National Water Research Institute of Malaysia, Ministry of Environment and Water, Seri Kembangan, Malaysia

Many slope failures take place during or after rainfall events. Landslides are one of the tragedies associated with slope failures and often lead to fatal accidents. A study on the effects of extreme rainfall on slope stability considering the historical rainfall data, slope characteristics and properties, and flow boundary conditions was undertaken. This study investigated the behaviour of the Sg Langat slope under the influence of extreme rainfall gathered from historical data. Sg Langat was selected as the research area because of its high riverbank failures. The focus of this study are as follows: 1) to determine the effect of slope angles on slope stability, 2) to assess the development of pore-water pressure based on the changing groundwater levels, and 3) to analyse the influence of extreme rainfall events on the slope behaviour *via* numerical modelling. This study enhances the understanding of certain slope conditions and contributes to the analysis of slope stability through numerical modelling, making it relatively convenient to observe the soil conditions for determining the slope stability of the research area in regards to the effect of extreme rainfall. The results were obtained with respect to the changes in the pore-water pressure and the factor of safety. It was observed that the pressure changes were different for every channel, demonstrating that the generation of negative pore-water pressure was not directly affected by the type of analysis and the rainfall infiltration alone. Moreover, the slopes on all channels presented were considered unstable because of the considerable changes in the negative pore-water pressure at a relatively shallow depth, causing soil strength reduction. The factor of safety recorded for Channel 1 was the lowest at 0.18, whereas Channel 3 had the highest factor of safety of 1.11 but was still considered unsafe as it fell below the standard safety margin of 1.3. Apart from the different rainfall intensities applied, the geometry of the slopes also affected the slope stability.

Keywords: extreme rainfall, slope stability, pore-water pressure, Rainfall, factor of safety

Edited by:
Alfrendo Satyanaga,
Nazarbayev University, Kazakhstan

Reviewed by:
Dayang Zulaika Abang Hasbollah,
University of Technology Malaysia, Malaysia
Aniza Ibrahim,
National Defence University of Malaysia, Malaysia

****Correspondence:***
Aizat Mohd Taib
amohdtaib@ukm.edu.my

Specialty section:
This article was submitted to Freshwater Science, a section of the journal Frontiers in Environmental Science

Received: *21 January 2022*
Accepted: *14 February 2022*
Published: *02 March 2022*

Citation:
Nazrien Ng J, Mohd Taib A, Razali IH, Abd Rahman N, Wan Mohtar WHM, A. Karim O, Mat Desa S, Awang S and Mohd MSF (2022) The Effect of Extreme Rainfall Events on Riverbank Slope Behaviour. Front. Environ. Sci. 10:859427. doi: 10.3389/fenvs.2022.859427

INTRODUCTION

Industrialisation, urbanisation, and population growth have increasingly led to intensive land use. The number of slope failures in Malaysia is increasing year on year. In general, the rise in cases is linked to rapid manmade development (such as highways, roads, dams, and hill residential buildings) that has an impact on the surrounding areas (Che Ghani et al., 2020). Many landslides often occur during the construction stages of infrastructures and have caused significant damage to properties, the environment, and people. The potential of landslide occurrence during slope construction depends on many factors such as topography, soil type, vegetation, and local climate (Jeong et al., 2017). Other factors including non-homogeneous soil layers, tension, cracks, dynamic loading or earthquakes, and seepage flow may also affect landslide occurrence (Rahimi et al., 2011). According to the data of the Korea Meteorological Administration (2002) from 1993 to 2002, the death toll by slope failures including natural hazards and accidents during construction was up to 22.7% of the total death toll by natural hazards in Korea. Thus, slope failure can be considered one of the most serious natural hazards (Duc Long and Dung, 2020). As rainfall can be associated with slope failures, several studies have been conducted to determine the changes in the shear strength of unsaturated slopes (Fredlund et al., 1978; Schreiner, 1987; Rahardjo and Fredlund, 1995; Feuerharmel et al., 2005).

In Malaysia, slope failure is not an uncommon natural disaster that usually takes place during the wet monsoon. The unsaturated conditions in the shallow zone can easily be affected by rainfall infiltrations. Back in 2017, a landslide occurred at Kajang, Selangor. It was reported that the incident happened after heavy rainfall on the same day (Hou et al., 2018). Furthermore, the damage was extensive because of the high rainfall intensity and the insufficient slope protection installed to withstand the moving soil mass. This scenario shows the influence of extreme rainfall that affects the slope strength, thus causing landslides and posing a fatal threat to the residents nearby. Therefore, this study was undertaken to investigate the behaviour of the Sg Langat slope under the influence of extreme rainfall from historical records, considering the different slope angles, changing groundwater level, and various extreme rainfall intensities. As many recent studies have attempted to generate future rainfall models, historical records are often used as a baseline (Coe and Stern 1982). This study attempted to establish the historical rainfall intensities for predicting slope failures. Zhenping Zhang et al. (2021) stated that the use of the orientation and gradient to simulate and predict slope stability over extreme rainfall conditions in soil sloping areas is a novel idea. On top of that, this study explores the properties and conditions of Sg Langat involving extreme rainfall so that the results could be applied to other areas with similar conditions.

RAINFALL

Infiltration is defined as the flow of water to the soil through the surface of the ground. Rainfall is a major cause of slope failures that claim the lives of many and lead to significant economic losses around the world. Rainwater that fails to percolate into the ground turns into runoff and flows down the slope. Both of these scenarios (rainfall infiltration and runoff) contribute to the loss of suction in the soil, resulting in slope failure (Taib et al., 2020). Hence, it is established that rainfall is the main triggering factor for the slope failure; however, the effect of the soil density with the associated soil properties on the stability of the slopes has not received adequate attention (Zhao et al., 2019). One of the most challenging factors that engineers face is adapting to climate change. Since the 1900s, considerable research has been conducted to predict extreme weather events. Global weather patterns, such as temperature and rainfall distributions, can have significant economic and societal consequences (Dijkstra and Dixon 2010). Because of rainfall infiltration, various types of slope stability show failure phenomena, such as erosion, and can cause changes, such as different mass flow movements, depending on the slope morphology, characteristic soil curves, and the shear strength involved. The complicated linkages between rainfall circumstances, pore water pressure, soil strength, safety variables, and movement rates have been revealed (Lee et al., 2021).

Understanding the spatial and temporal characteristics of rainfall variability is important for gaining knowledge of the water balance dynamics on various scales for water resources management and planning (Uhlenbrook, 2009). Laboratory and field tests have proven that a homogeneous slope under rainfall conditions is prone to suffer from surface erosion or shallow landslides, whereas landslide surveys have indicated that deep-seated failures are often induced by rainfall in slopes with pre-existing cracks or weak layers (Zhang et al., 2012). For example, the landslides in the South Auckland region of New Zealand were due to pore pressures within cracks after rainstorms (Chatra et al., 2017). Furthermore, the changes in groundwater hydrology can reduce the effective stress and the shear strength of soil, resulting in rainfall-induced slope failures too (Taylor et al., 2008; Chatra et al., 2017). Regarding deep landslides, their activity is essentially governed by pore water pressure fluctuations, that affect the operational shear strength along the slip surface and are in turn regulated by the seasonal environmental conditions (Rianna et al., 2014). One way to prevent these undesirable rainfall-induced slope failures is to understand the variation in rainfall intensity, which can be used to determine rainfall patterns in the future.

The water infiltration characteristics associated with irrigation activities contribute to slope stability failures (Hou et al., 2018). The infiltration of water significantly reduces the shear strength of soil that is initially in a state of unsaturated condition and contributes to the instability of the slope (Aung et al., 2001). The functional relationship between water content and soil suction, referred to as the soil-water characteristic curve (SWCC), plays a central role in understanding the behaviour of unsaturated soil (Zhou and Jian-lin, 2005). SWCCs have been used to estimate the hydraulic conductivity, shear strength, volume change, and aqueous diffusion functions of unsaturated soils (Thu et al., 2011). For such unsaturated soils, the general practice is to provide the SWCCs or soil-water retention curves (SWRCs), describing the relationship of an unsaturated soil moisture content change and its degree of saturation change with its total suction change, which affects its shear strength behaviour (Egeli and Pulat, 2011; Cavalcante and Mascarenhas, 2021).

Rainfall-induced slope failure is a common geohazard for tropical and sub-tropical areas where residual soils are abundant (Furuya et al., 2006; Cho, 2009; Rahardjo, et al., 2012; Bordoni et al., 2015; Tang et al., 2016). Rainfall decreases the suction of the matrix and increases the weight of soil units, leading to a less stable soil slope (Rahardjo et al., 2005;

TABLE 1 | Category of rainfall distribution.

Category	Intensity
Gentle drizzle (Light rain)	Pouring rate less than 0.5 mm per hour
Heavy moderate rain	Pouring rate from 0.5 to 4.0 mm per hour
Drizzle	Pouring rate more than 0.5 mm per hour
Heavy rain	Pouring rate less than 2.0 mm per hour
Moderately heavy rainfall	Pouring rate from 2.0 to 10.0 mm per hour
Heavy rainfall	Pouring rate from 10.0 to 50.0 mm per hour
Extreme heavy rainfall	Pouring rate more than 50.0 mm per hour

Cho, 2014; Ering and Babu, 2016). According to Zhang et al. (2000), the infiltration rate depends on the initial soil water content, and the presence of stratigraphic instability may influence the infiltration pattern. Fredlund and Xing (1994) described the characteristics of soil curves for soil defined as the relationship between water content and soil suction (Williams, 1982). Water content is defined as the amount of water contained in the pores. It is undeniable that rainfall is the main causing factor for slope failure, hence the effort of research and applying sound techniques and methods to control slope failures shall never rest.

Rainfall in Malaysia

Seasonal wind patterns along with local topographic properties determine the pattern of rainfall distribution in Malaysia. During the northeast season, exposed areas such as the east coast of Peninsular Malaysia, West Sarawak, and the northeastern coast of Sabah experience periods of heavy rainfall. In contrast, the hinterland or areas protected by mountain ranges are relatively free from this influence. To enhance the understanding of the rainfall distribution in Malaysia, the distribution is described with respect to the typical seasons. Hence, **Table 1** shows the categorised rainfall distribution according to the rainfall intensity. Moreover, the minimum and maximum rainfall intensities are presented in **Table 1**, representing the lowest and the highest rainfall intensities calculated for all the areas in Malaysia.

Seasonal Rainfall Changes in Peninsular Malaysia

Seasonal rainfall changes in Peninsular Malaysia as shown in **Figure 1** can be divided into three main types:

For the states on the east coast of Peninsular Malaysia, November to January are the months with the maximum rainfall, while June and July have the minimum rainfall.

Rainfall patterns in the southwest coast of Peninsular Malaysia show two maximum rainfall periods separated by two minimum rainfall periods. The primary maximum usually occurs from October to November, while the secondary maximum occurs from April to May. In the northwest, the primary minimum occurs from January to February, while the secondary minimum occurs from June to July. Elsewhere, primary minimums occur from June to July, while secondary minimums occur in February.

The rainfall pattern on the southwest coast of Peninsular Malaysia is considerably marked by the "Sumatra" incident in the morning from May to August and the maximum and minimum double patterns do not exist. October and November are the months with the maximum rainfall, while February is the month with the minimum rainfall. The maximum from March to May and the minimum from June to July do not exist or are less clear (Suhaila et al., 2010).

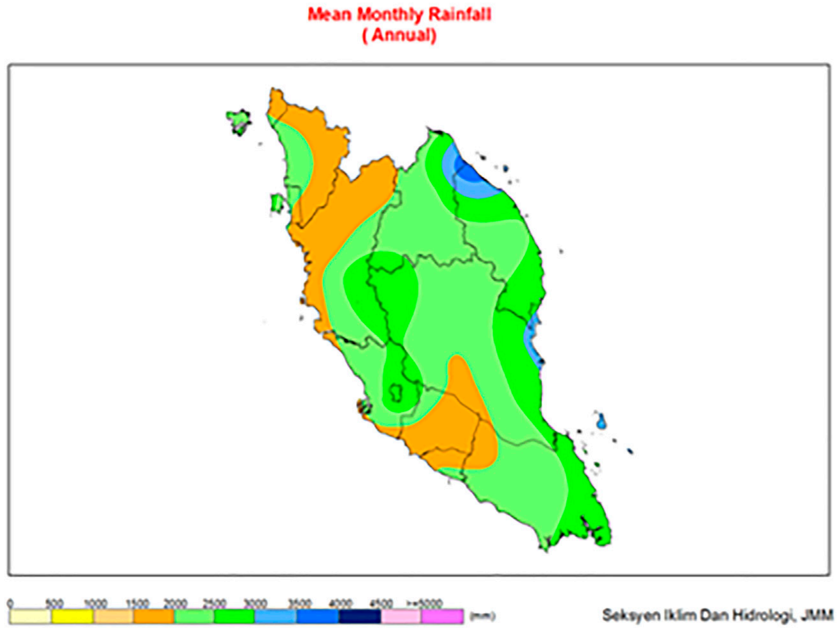

Seksyen Iklim Dan Hidrologi, JMM

FIGURE 1 | Annual mean monthly rainfall in Peninsula Malaysia (Suhaila et al., 2010).

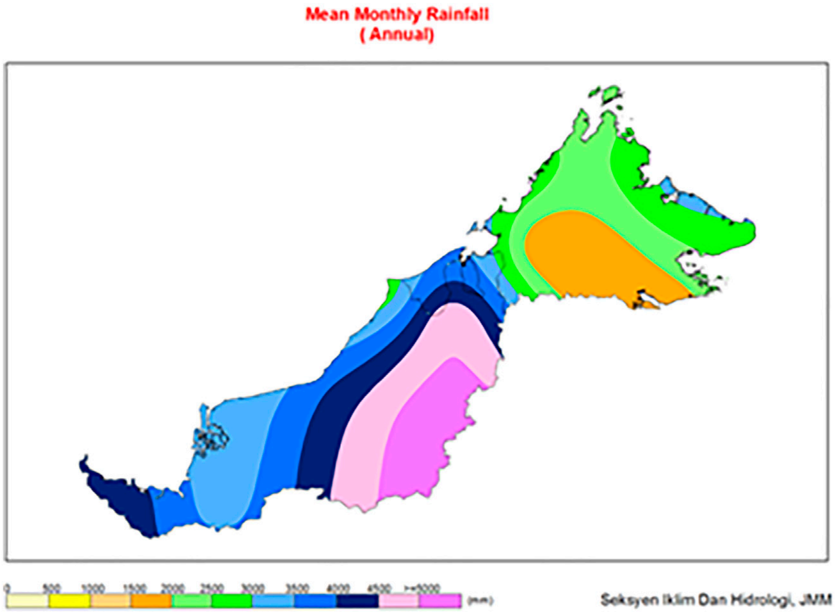

FIGURE 2 | Annual mean monthly rainfall in Sabah and Sarawak (Uhlenbrook 2009; Suhaila et al., 2010).

Seasonal Rainfall Changes in Sabah and Sarawak

Seasonal rainfall changes in Sabah and Sarawak as shown in **Figure 2** can be divided into five main types:

The coastal areas of Sarawak and northeast Sabah experience one maximum and one minimum rainfall pattern. Both areas experience maximum rainfall in the same month, which is January, while the months for minimum rainfall are different. In the coastal areas of Sarawak, minimum rainfall occurs in June or July, while in the northeast area of the Sabah coast, minimum rainfall occurs in April. Under this rule, most of the rainfall is received during the northeast monsoon months, from December to March. Indeed, more than half of the annual rainfall is received in western Sarawak.

The hinterland of Sarawak generally experiences fairly even annual rainfall. However, slightly less rainfall is received during the period June to August, following the prevailing southwest winds. Note that the highest annual rainfall in Malaysia occurs on the hillside of the interior of Sarawak. Long Akah receives an average annual rainfall of more than 5,000 mm.

The northwest coast of Sabah experiences two maximum and two minimum rainfall patterns. The primary maximum occurs in October, and the secondary maximum occurs in June. The primary minimum occurs in February, while the secondary minimum occurs in August. Although the difference in the amount of rainfall received in the two maximum months is small, the difference in the amount of rainfall received at the primary minimum is lower than that at the secondary minimum. In some places, the difference reaches four times as high.

In the central part of Sabah where the conditions are hilly and sheltered by mountain ranges, the rainfall received is lower than that received in other areas, and the distribution is relatively even. However, two maximums and two minimums can be observed. In general, two minimums occur in February and August, while two maximums occur in May and October.

The southern part of Sabah experienced an even distribution of rainfall. The amount of annual rainfall received can be compared to that received in the central part of Sabah. February to April is a relatively dry period as compared to the other months (Uhlenbrook, 2009).

Therefore, this study would be more applicable to West Malaysia because the research area was in Peninsular Malaysia (West Malaysia) and the soil properties and the slope geometry are different from those in East Malaysia.

METHODOLOGY

The numerical modelling of unsaturated soil slopes has progressed quickly, and numerous studies have proposed improved solutions to the slope boundary problems. The general concept in numerical modelling is still important to provide correct calculations, particularly when using finite element methods (Taib et al., 2018). Finite element modelling utilises approximate solutions of ordinary and differential equations to describe the distribution of stresses and strains in soil as well as finite understanding of unsaturated behaviour (Taib et al., 2019). With respect to the research objectives, the geometry models, namely CH1, CH2, and CH3, were set up, and the soil properties (mechanical and hydraulic) and the water level were

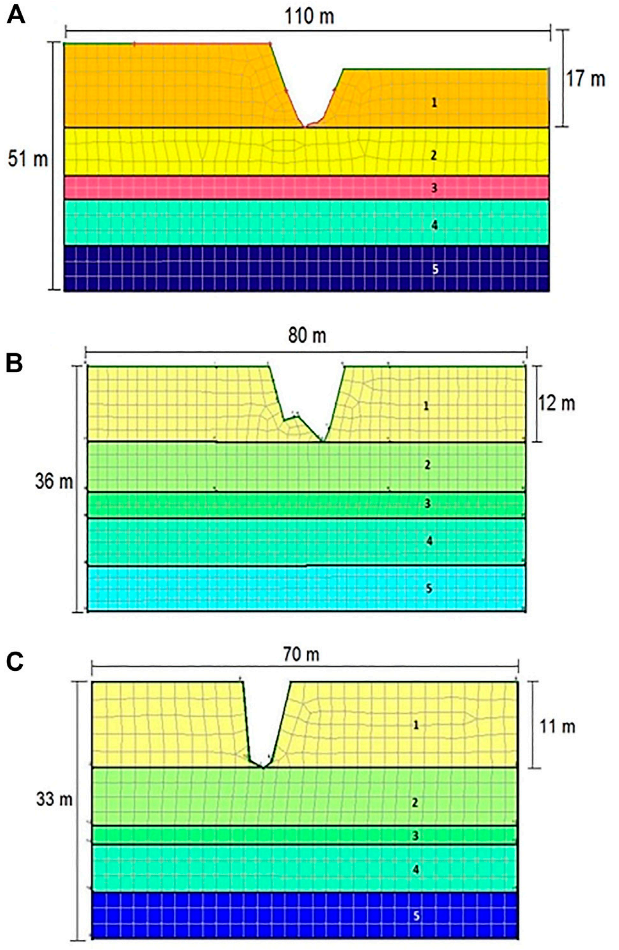

FIGURE 3 | Slope dimension for **(A)** Channel 1, **(B)** Channel 2 and **(C)** Channel 3.

included in the simulation models. The slope geometries are illustrated in **Figure 3**. Each of the geometry models was designed according to the different locations of riverbanks from Sg Langat and with different patterns of slope geometry. Each soil layer was assigned a different colour and indicated by its existing depth.

Furthermore, the rainfall data gathered from the historical records were analysed based on four selected rainfall stations. They were Kg. Jenderam Hilir, Puncak Niaga Putraya, Kolam Takungan Sg Merab, and RTM Kajang. The highest rainfall intensity recorded for a month in the selected years at a location close to the research site was obtained. Next, numerical modelling through a slope model simulation by using Geostudio was undertaken with different groundwater levels (i.e., high, intermediate, and low), various slope angles, and changing rainfall events with different intensities. SLOPE/W and SEEP/W in Geostudio were applied to compute the factor of safety of slopes and analyse both simple and complex problems for a variety of slip surface shapes as well as pore-water pressure conditions. The results obtained from the output of the Geostudio were presented in terms of the pore-water pressure and factor of safety. The generation of the pore-water pressure was measured against the slope depth, and the factor of safety was calculated against the event of extreme rainfall.

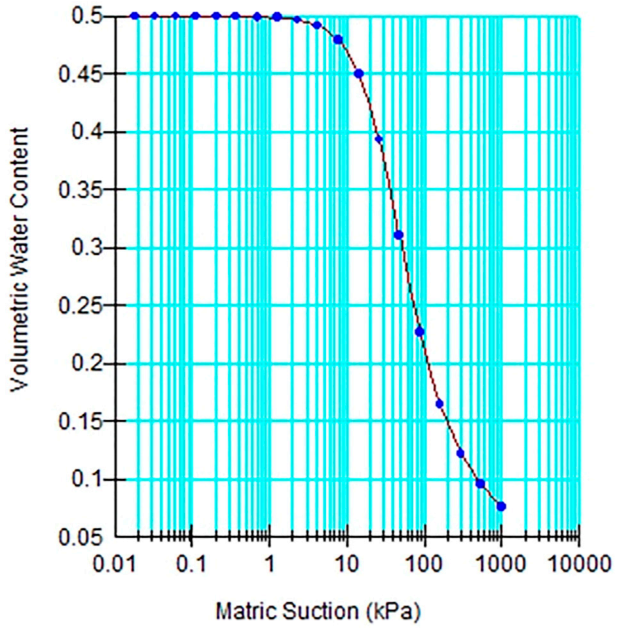

FIGURE 4 | SWCC parameters used in SEEP/W analysis for all channels.

Numerical Modelling

SEEP/W

In SEEP/W, the channels were initially sketched and regions were drawn in the model geometry to differentiate between the upper layer and lower layer soils. Next, materials of models were defined based on the soil hydraulic properties, namely the SWCC parameters (i.e., hydraulic conductivity, hydraulic boundary, and volume water content) and soil types, as shown in **Figure 4**, before these model parameters were assigned to the soil models. The SWCC presented the relationship between the soil-water suction and the water content of the soil. This relationship assisted to define the magnitude of matric suction that occurred in a soil deposit when the water content was less than saturated (Baker and Frydman 2009). The quantity of water retained in the soil at a certain magnitude of suction depended on many factors: particle shape, particle size, distribution of pore spaces, mineralogy, the surface activity of solid grain particles, and chemical composition of interstitial water (Aubertin et al., 2003).

Next, the boundary conditions such as seepage and pressure head were defined and labelled in the model to assign the boundaries of each condition. The element mesh was also applied to the soil models. The mesh sizes were determined automatically, and triangular and rectangular

TABLE 2 | Unsaturated soil parameter.

Channel	Bulk unit weight, γ (kN/m³)	Permeability (m/day)	Stiffness, E (kN/m²)	V(nu)	Strength, c_{ref} (kN/m²)	Φ(phi)
1	18	0.001	10000	0.35	5.00	28.00
2	18	0.001	3000	0.35	5.00	29.00
3	17	0.001	15000	0.35	10.00	28.00

TABLE 3 | SWCC dan permeability function parameter.

θ_s	a	n	m	$k_a, (\frac{m}{s})$	p
0.45	10	1	1	10^{-4}	4

shapes were used. Once the groundwater level was assigned, the groundwater flow analysis can be solved. The rainfall data were applied to the slope *via* the seepage behaviour. Then, the analysis was ready to be conducted. In the output, the pore-water pressure of the slope can be obtained on a different contour level.

SLOPE/W

In SLOPE/W, similar model geometry procedures were conducted as in the SEEP/W models. Initially, materials of models were defined according to the soil mechanical parameters including soil unit weight, cohesion, and angle of friction, thus assigned to the soil models. The phreatic lines were drawn on the soil layer to generate the existing pore-water pressure. Moreover, entry and exit slip surfaces were determined in the model to indicate the critical slip surface. It is important to allow the visualisation of the critical zones before solving the analysis to capture the relevant factor of safety. The entry would be at the highest surface of the slope (crest), and the exits would be at the lowest surface of the slope (toe). The calculation was set, and the analysis can then be solved. The input demonstrated the factor of safety, which can be chosen with respect to the slope stability and the position of the slip surface.

Soil Parameters for Slope Models

The models were analysed as plane strain models with 15-node mesh elements. As the slope geometry was drawn, the soil parameters were assigned to the three channels, as stated in **Table 2**. Among the soil parameters included were the unit weight for both saturated and unsaturated conditions, soil permeability, stiffness, and angle of friction. The constitutive model used to present the slope behaviour was Mohr-Coulomb under the influence of the drained conditions. In addition, general fixities were created in the slope models concerning the flow boundary conditions. General fixities consisted of an open flow along the top surface, lateral flow at both sides, and a close boundary at the bottom layer. These fixities were applied to ensure that a natural water flow took place within the respected boundaries. The rainfall was applied as water infiltration *via* the transient flow analysis. Therefore, **Table 3** presents the SWCC and the permeability function noting the curve parameters.

Computation of Missing Rainfall Data

In the rainfall data obtained, some of the data were found missing and there were errors in the data for a certain date. Some stations had short breaks in the records because of the absence of the observer or may be due to instrumental failures. It is a general practice to estimate missing rainfall records. In this study, the missing data of a station were estimated from the observations of other stations that were as close to and as evenly spaced around the station with the missing record. The stations with missing data were named as the interpolation station, and the gauging stations that are used to calculate the missing station data were called index stations. Hence, in this situation, the simple arithmetic mean method was used to recover and calculate the missing data as follows:

$$\boldsymbol{P_x = \frac{1}{n}\sum_{i=1}^{i=n} P_i \& P_x = \frac{1}{3}\left(P_1 + P_2 + P_3\right)}$$

For example, as shown in **Table 4**, there was a data error that showed −999 on the dates 01/06/2009 and 03/06/2009 at RTM Kajang. From the equation based on the simple arithmetic mean method, P_x, which represents the stations with missing data, was calculated. **Table 5** represents the recovered missing rainfall data.

Rainfall Data at all Stations

Figures 5–8 show the daily rainfall intensity from year 2008–2016. Kampung Jenderam Hilir is located near Sungai Langat, which is close to the Dengkil area. According to the rainfall data for the considered years, on 26 February 2013 in **Figure 5**, Kampung Jenderam Hilir had the highest rainfall intensity, which was 152 mm, as shown in **Figure 9A**. Puncak Niaga Putrajaya is located close to Putrajaya Lake. Based on its rainfall data, on 28 November 2012 in **Figure 6**, Puncak Niaga Putrajaya had the highest rainfall intensity, which was 115.9 mm, as presented in **Figure 9B**. Sungai Merab is located between Dengkil and Bandar Baru Bangi. As pointed out, on 10 October 2013 in **Figure 7**, Kolam Takungan Sg. Merab had the highest rainfall intensity, which was 121 mm, as shown in **Figure 10A**. RTM Kajang is located at Kajang near Jalan Cheras. According to the rainfall data given, 9 April 2012 in **Figure 8** had the highest rainfall intensity, which was 142 mm, in the RTM Kajang area, as

TABLE 4 | Missing data rainfall in the four stations.

	RTM Kajang	kg. Jenderam Hilir	Putrajaya	Kolam Sg.Merab
01/06/2009	−999	26	8.5	6
02/06/2009	1.9	34.5	1	8.5
03/06/2009	−999	7	0	0.5

TABLE 5 | Recovered data rainfall in the four stations.

	RTM Kajang	kg. Jenderam Hilir	Putrajaya	Kolam Sg.Merab
01/06/2009	13.5	26	8.5	6
02/06/2009	1.9	34.5	1	8.5
03/06/2009	2.5	7	0	0.5

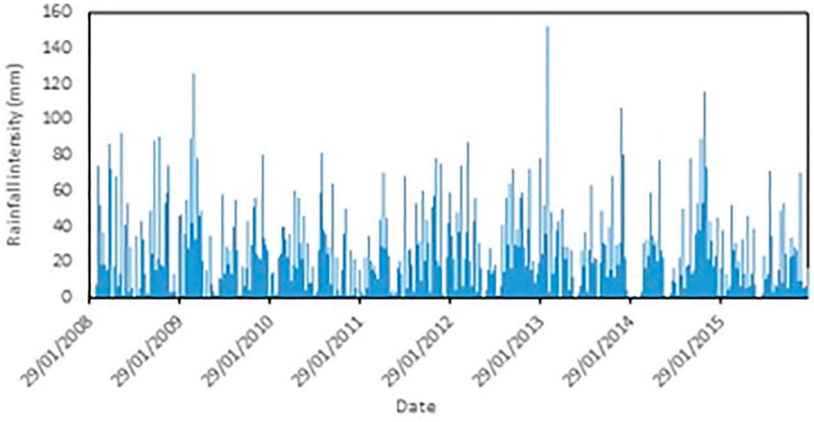

FIGURE 5 | Rainfall intensity at Kg. Jenderam Hilir in 8 years.

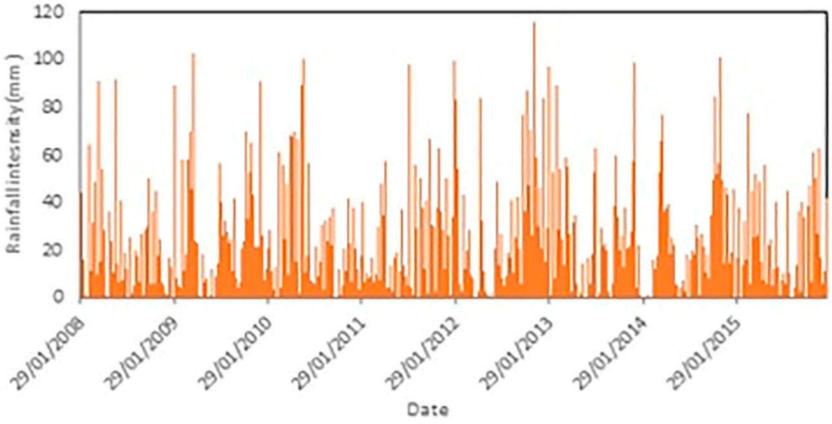

FIGURE 6 | Rainfall intensity at Puncak Niaga Putrajaya in 8 years.

presented in **Figure 10B**. In the end, according to the entire rainfall data obtained from all of the four stations, Kampung Jenderam Hilir had the most extreme rainfall intensity, which was 152 mm, on 26/02/2013. Furthermore, **Figure 11** shows the overall rainfall intensities from all four stations from 2008 until 2016.

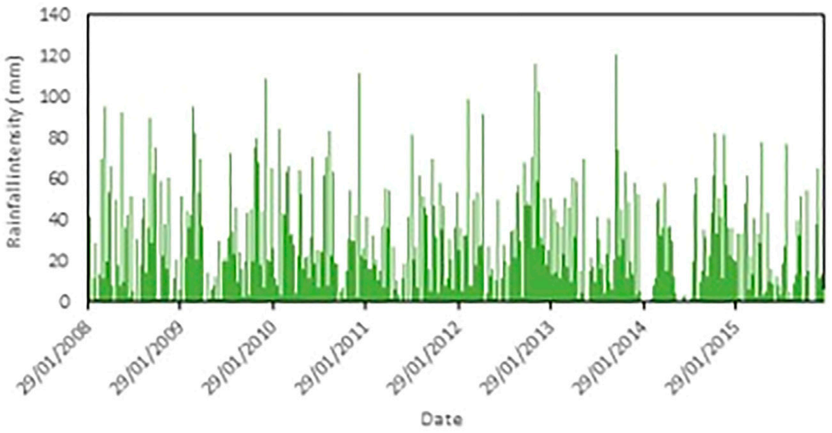

FIGURE 7 | Rainfall intensity at Kolam Takungan Sg. Merab in 8 years.

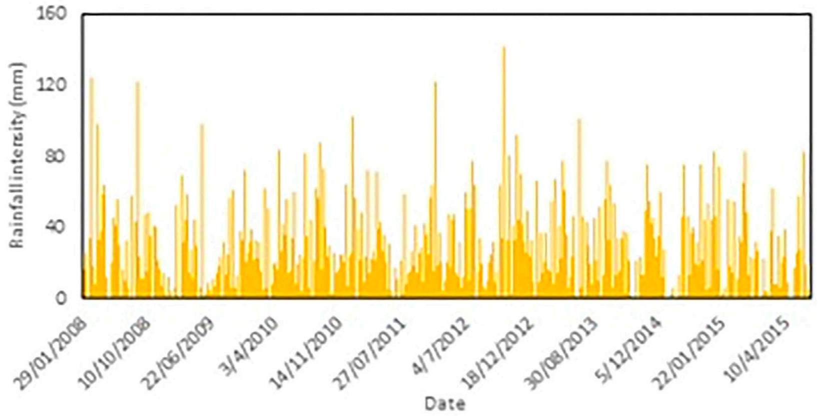

FIGURE 8 | Rainfall intensity at RTM Kajang in 8 years.

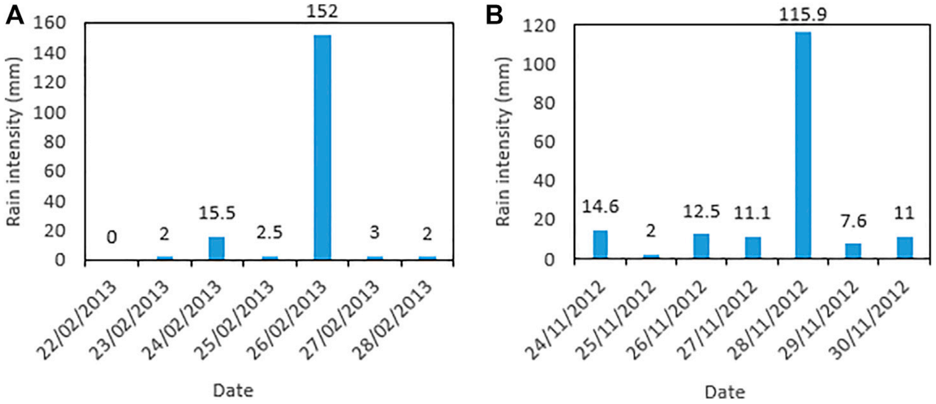

FIGURE 9 | Extreme rainfall in 1-week interval in **(A)** Kg. Jenderam Hilir and **(B)** Puncak Niaga Putrajaya.

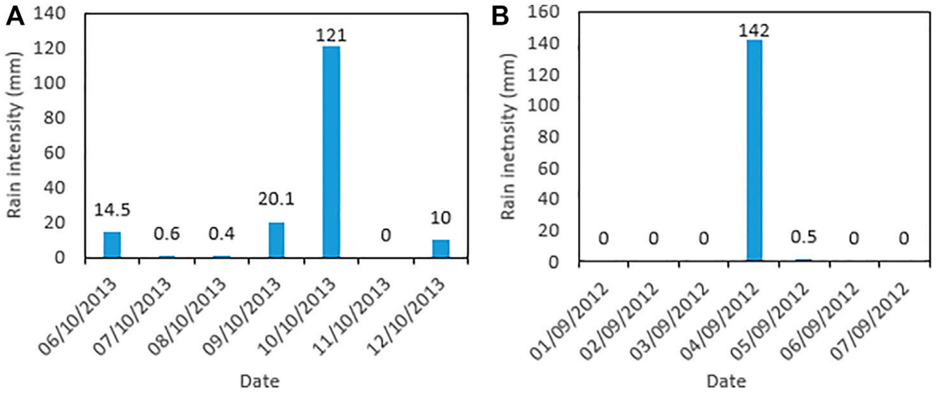

FIGURE 10 | Extreme rainfall in 1-week interval at **(A)** Kolam Takungan Sg. Merab and **(B)** RTM Kajang.

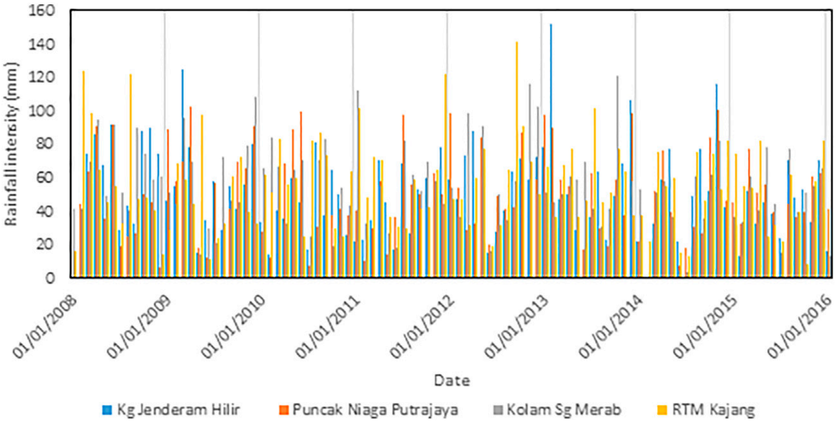

FIGURE 11 | Overall rainfall intensity from 2008—2016 for all four stations.

RESULT AND ANALYSIS

The results from the study are presented in terms of pore-water pressure, factor of safety and the water seepage. The behaviour of Sg Langat slopes is analysed and discussed due to the effect of extreme rainfall within the typical slope behaviour analysis. The seepage analysis is an added behaviour described in the changes of water total head against a period of three weeks of RTM Kajang rainfall station.

Pore-Water Pressure

In this study, the calculation phases were divided into two stages; which were the static (named as phase 1) and consolidation (named as phase 2). The static phase was used to generate the initial conditions which determined the existing pore-water pressure at the site. The following consolidation phase was undertaken with the effect of phreatic level (9.81 kN/m) applied in the slope model. The durations for both calculations were different as the steady-state was conducted immediately under zero-hours, whereas the consolidation phase was simulated as transient for eight years. No water infiltration (i.e. rainfall) was applied at the first stage. The results were localised to represent the initial changes in the existing pore-water pressure underground. The staged construction which involved loading the input under the time interval was incrementally increased. The results for these two phases were presented in the generation of the pore-water pressure.

The results of the pore-water pressure were obtained from SEEP/W for all the analyses with respect to the three channels. Each of the pore-water pressures developed can be seen on different contour levels with values in **Figure 12**. The arrows illustrated between the channel openings show the active pore pressure around the surface of the soil. It can be seen that Channel 1 has slightly higher pore-water pressure followed by Channels 2 and 3. Zero pore-water pressure indicates the location of groundwater level; hence, the zones at the channel openings with high pore-water pressure faced the possibility of soil erosion *via* runoff.

In the RTM Kajang rainfall event, as shown in **Figure 13**, high pore-water pressure changes in the shallower depth can be observed between phase 1 and phase 2 for Channel 1.

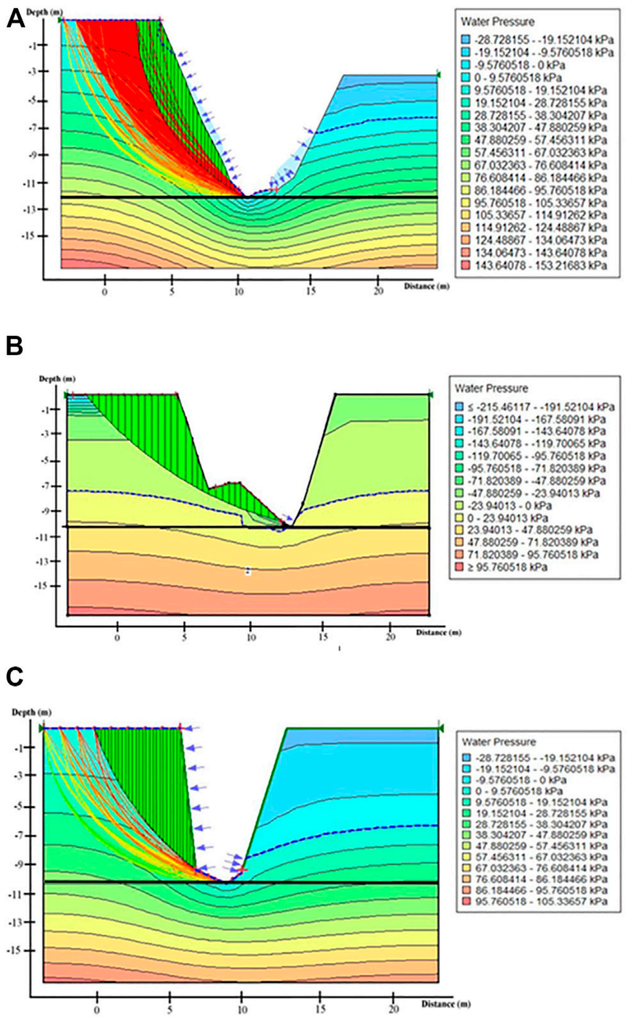

FIGURE 12 | Pore-water pressure based on different contour levels for Channel **(A)** 1, **(B)** 2 and **(C)** 3.

Furthermore, phase 2 of the transient analysis showed smaller changes with lower negative pore-water pressure (i.e. −36 kPa) and at a lower depth than the steady-state analysis (i.e. −40 kPa), indicating the influence of rainfall infiltration. In Channel 2, the generation of pore-water pressure in both phases was observed to be similar to that in the case of Channel 1 but with a smoother negative pore-water pressure profile. The highest pore-water pressure for Phases 1 and 2 in Channel 2 was observed at the same depth (−12 m). In contrast, the pressure changes in Channel 3 were different, demonstrating that the generation of negative pore-water pressure was not directly affected by the type of analysis and the rainfall infiltration alone. The geometry of the slope may induce the changes of phase 2 found at a shallower depth. The changes were observed occurring abruptly with the slight fluctuating reading of negative pore-water pressure profile starting at the depth of −5 m and then developed to the highest value at −29 kPa. Furthermore, all channels were found to shift the pore-water pressure values by the level of groundwater at the depths of −15, −16, and −12 m.

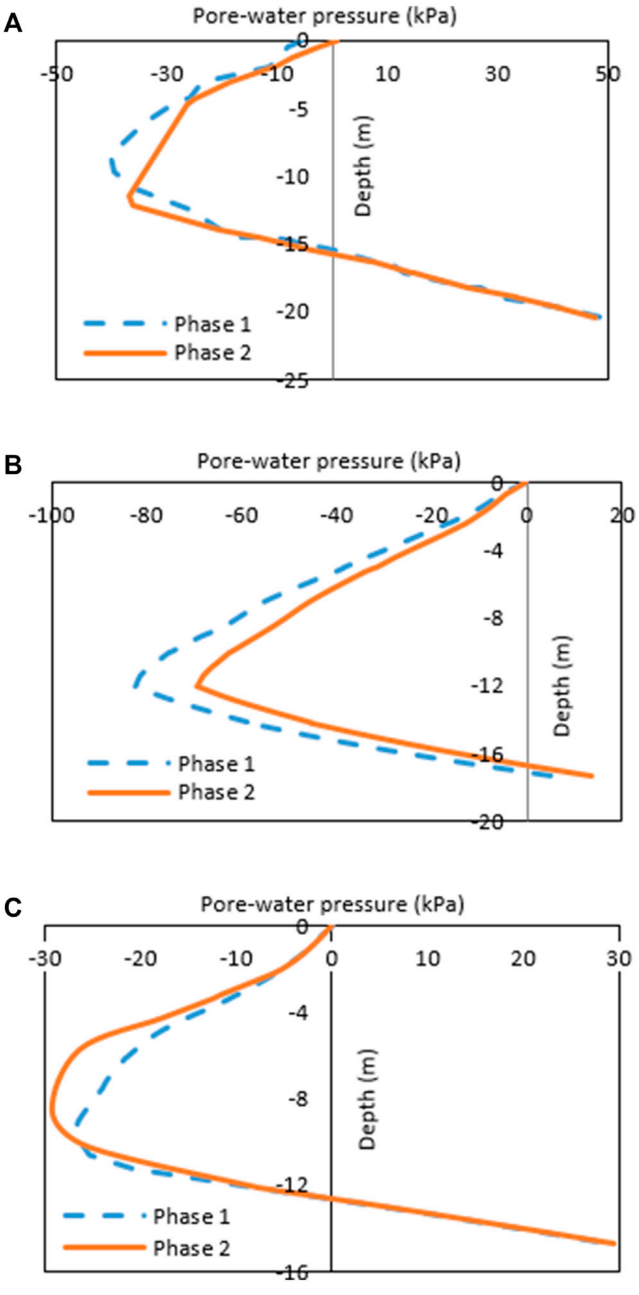

FIGURE 13 | Pore-water pressure measured against depth for Channel **(A)** 1, **(B)** 2 and **(C)** 3.

Throughout the results, the instability of slopes was observed and established by the negative pore-water pressure changes in the soil for the steady-state and consolidation. A comparison with previous studies, such as Cooper et al. (2010), and Pontier et al. (2004) revealed that the slopes on all of the channels presented were still considered unstable because of the considerable changes in the negative pore-water pressure at a shallower depth for both phases due to the rainfall infiltration, causing the soil strength to

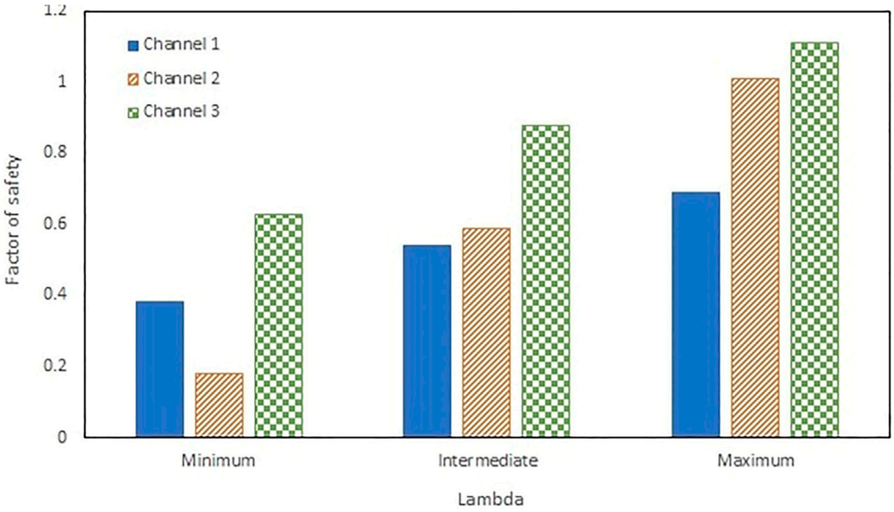

FIGURE 14 | Graph of the factor of safety for all channels.

reduce and leading to slope failure. Hence, the development and the changes in the negative pore-water pressure were analysed using a method similar that has been used in the slope stability analysis by Perrone et al. (2008). Moreover, several studies have stressed that pore-water pressures may also be affected by the different types of soils (; Rahimi et al., 2011 Sagitaningrum, and Bahsan, 2017).

Factor of Safety

The ratio between the available strength and the strength necessary for a state of incipient failure along a probable slip surface is known as the factor of safety of the slope (Khajehzadeh et al., 2012). In engineering, the factor of safety is the ratio of a structure's absolute strength (structural capability) to an actual applied load. It expresses how much stronger a system is than it needs to be for an intended load. The factor of safety of the potential sliding surface inside the slope is the most common index used to assess slope stability. The calculation often relies on the limit equilibrium model, which builds on the assumption that the slope consists of rigid materials and that possible destruction occurs along the potential sliding surface over a large number of the randomly selected sliding surfaces (Lichao Zhang et al., 2021). In terms of the limit equilibrium principle, a factor of safety less than one represents the failure in a slope. Hence, the factor of safety was obtained based on the stresses by using the SLOPE/W package. The SLOPE/W utilised the limit equilibrium method that models heterogeneous soil types, complex stratigraphic and slip surface geometry and variable pore-water pressure conditions under the development of a large selection of soil models. Limit equilibrium methods are used to calculate factors of safety with five input parameters: height of slope, unit weight of slope material, angle of slope, coefficient of cohesion, and internal angle of friction (Mohamed et al., 2012).

The factor of safety from Sg Langat channels was obtained where it described the slip surfaces between an entrance and an exit. The factor of safety of each trial slip surface was drawn with a slip surface colour that helped to visualise both the number of trial slip surfaces with a factor of safety close to the critical value and the most likely shape of the failure zone. The data were divided into three categories, namely the minimum, intermediate, and maximum value of the factor of safety. **Figure 14** presents a bar chart of the factor of safety against the lambda value of the minimum, intermediate, and maximum values for all the channels. Lambda can be defined as the ratio of the interslice shear and interslice normal forces generating the same factor of safety for both moment and force equilibrium (Matsuura et al., 2008).

In other words, lambda is understood as the width of the gap between two slip surfaces. Thus, the factor of safety can be strongly determined by lambda to compare the differences in the factor of safety for each slip surface. **Figure 14** for Channel 1 shows the factor of safety calculated at the convergence of 0.38, 0.54, and 0.69, respectively, for the minimum, intermediate, and maximum values. These values, however, promote slope instability as it fails to reach a factor of safety of more than 1.0 at the least. A comparison with the previous studies which involved a similar situation (Matsuura et al., 2008; Merat et al., 2019) revealed that although Channels 2 and 3 demonstrated a higher factor of safety, even when exceeding the 1.0 values, the factors of safety calculated were still very low to maintain for long-term stability. At these points, lowering the shear strength by means of continuous water infiltration or rigorous runoff on the slope surface may easily initiate a slope failure (Hou et al., 2018). Hence, the value of the factor of safety is controlled by the amount of rainfall infiltration rate into the soil. The higher the rate of infiltration of rain, the less the safety factor value estimated. Continuous rainwater that infiltrates into the unsaturated zone of soil slope decreases the matric suction, increases the shear strength of soil, which corresponds to the minimum factor of safety under the influence of rainfall duration

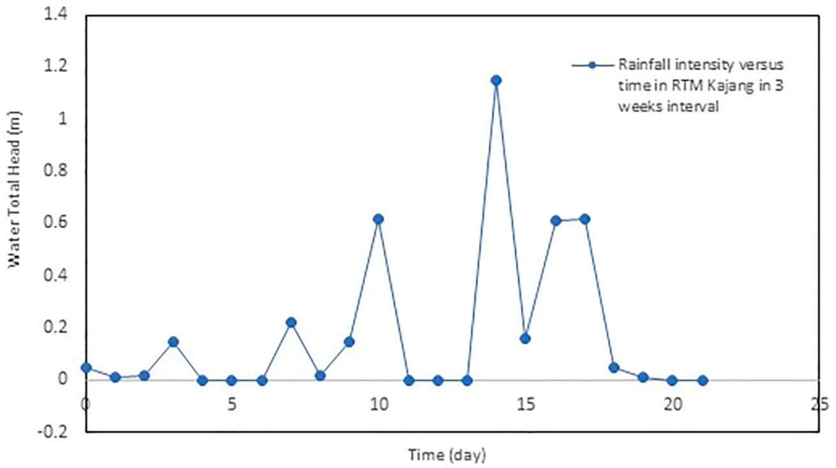

FIGURE 15 | Three sessions of rainfall events applied in SEEP/W.

and consequently, causes slope failure. It is, therefore, highly recommended that the riverbank slope of Sg Langat be protected by both natural and reinforced walls to preserve the slope from further failure due to the influence of rainfall.

Water Seepage

SEEP/W package was used to determine the behaviour of the Sg Langat riverbank under the influence of rainfall; **Figure 15** shows the water seepage of the rainfall in RTM Kajang in 3-weeks intervals. As the rainfall intensity was too low to have affected the slope instability, two recurrent series of rainfall events were applied. The second session of rainfall intensity was multiplied with the original first event of factor 5 and the third session with a factor 7. According to **Figure 15**, in the first session of the rainfall series, the data showed minimal values of water total head and the highest value of the first 7 days was only 0.22 m. The second session showed the highest water total head among all the rainfall series, which was on the 14th day with a value of 1.15 m. Then, the third session of rainfall showed a decreasing pattern of the water total head.

CONCLUSION

The results of the parametric study were presented in the following sections: 1) the influence of rainfall intensity on the strength of soil, 2) the influence of slope angle during heavy rainfall, and 3) the rainfall intensity to cause a shallow slope failure. The relationship between rain infiltration and slope stability was recorded by greater rainfall infiltration, causing the slope to behave unstably and subsequently fail. The results of the analysis revealed that the pressure changes were different for every channel, demonstrating that the generation of negative pore-water pressure was not directly affected by the type of analysis and the rainfall infiltration alone. The geometry of the slope may induce changes in the negative pore-water pressure. Moreover, the slopes on all of the channels presented were still considered unstable as changes in the negative pore-water pressure at a relatively shallower depth were found due to the effect of rainfall infiltration, causing a reduction of the soil strength and thus leading to a slope failure. Furthermore, the extreme rainfall event influenced the factor of safety of the slopes, which corresponded to the minimum factor of safety under the influence of rainfall intensity. The factor of safety recorded for Channel 1 was the lowest at 0.18, whereas Channel 3 had the highest factor of safety of 1.11 but was still considered unsafe as it fell under the minimum factor of safety of 1.3. The slope behaviour of Sg Langat was analysed taking into account the rainfall slope angles, groundwater level, and rainfall intensity (Wang et al., 2001; Mukhlisin and Taha, 2012).

DATA AVAILABILITY STATEMENT

The raw data supporting the conclusion of this article will be made available by the authors, without undue reservation.

AUTHOR CONTRIBUTIONS

All authors listed have made a substantial, direct, and intellectual contribution to the work and approved it for publication.

ACKNOWLEDGMENTS

The author would like to thank the people involved in the research project and acknowledge the University Kebangsaan Malaysia for the financial assistance under grant GUP-2021-022 and National Hydraulic Research Institute of Malaysia for funding this research under the grant KK-2020-009.

REFERENCES

Aubertin, M., Mbonimpa, M., Bussière, B., and Chapuis, R. P. (2003). A Model to Predict the Water Retention Curve from Basic Geotechnical Properties. *Can. Geotech. J.* 40, 1104–1122. doi:10.1139/t03-054

Aung, K. K., Rahardjo, H., Leong, E. C., and Toll, D. G. (2001). Relationship between Porosimetry Measurement and Soil-Water Characteristic Curve for an Unsaturated Residual Soil. *Geotechnical Geol. Eng.* 19, 401–416. doi:10.1007/978-94-015-9775-3_9

Baker, R., and Frydman, S. (2009). Unsaturated Soil Mechanics. Critical Review of Physical Foundations. *Eng. Geology.* 106 (1–2), 26–39. doi:10.1016/j.enggeo.2009.02.010

Bordoni, M., Meisina, C., Valentino, R., Lu, N., Bittelli, M., and Chersich, S. (2015). Hydrological Factors Affecting Rainfall-Induced Shallow Landslides: From the Field Monitoring to a Simplified Slope Stability Analysis. *Eng. Geology.* 193, 19–37. doi:10.1016/j.enggeo.2015.04.006

Cavalcante, A. L. B., and Mascarenhas, P. V. S. (2021). Efficient Approach in Modeling the Shear Strength of Unsaturated Soil Using Soil Water Retention Curve. *Acta Geotech.* 16, 3177–3186. doi:10.1007/s11440-021-01144-6

Chatra, A. S., Dodagoudar, G. R., and Maji, V. B. (2017). Numerical Modelling of Rainfall Effects on the Stability of Soil Slopes. *Int. J. Geotechnical Eng.* 13, 425–437. doi:10.1080/19386362.2017.1359912

Cho, S. (2009). Infiltration Analysis to Evaluate the Surficial Stability of Two-Layered Slopes Considering Rainfall Characteristics. *Eng. Geology.* 105, 32–43. doi:10.1016/j.enggeo.2008.12.007

Cho, S. (2014). Probabilistic Stability Analysis of Rainfall-Induced Landslides Considering Spatial Variability of Permeability. *Eng. Geology.* 171, 11–20. doi:10.1016/j.enggeo.2013.12.015

Coe, R., and Stern, R. D. (1982). Fitting Models to Daily Rainfall Data. *J. Appl. Meteorology* 21, 1024–1031. doi:10.1175/1520-0450(1982)021<1024:fmtdrd>2.0.co;2

Cooper, M., Vidal-Torrado, P., and Grimaldi, M. (2010). Soil Structure Transformations from Ferralic to Nitic Horizons on a Toposequence in Southeastern Brazil. *Rev. Bras. Ciênc. Solo* 34 (5), 1685–1699. doi:10.1590/s0100-06832010000500021

Dijkstra, T. A., and Dixon, N. (2010). Climate Change and Slope Stability in the UK: Challenges and Approaches. *Q. J. Eng. Geology. Hydrogeology* 43 (4), 371–385. doi:10.1144/1470-9236/09-036

Duc Long, P., and Dung, N. T. (2020). Correction to: Geotechnics for Sustainable Infrastructure Development. *Lecture Notes Civil Engineering,Geotechnics Sust. Infrastructure Dev.* 62, C1–C3. doi:10.1007/978-981-15-2184-3_186

Egeli, I., and Pulat, H. F. (2011). Mechanism and Modelling of Shallow Soil Slope Stability during High Intensity and Short Duration Rainfall. *Scientia Iranica* 18 (6), 1179–1187. doi:10.1016/j.scient.2011.09.010

Ering, P., and Babu, G. (2016). Probabilistic Back Analysis of Rainfall Induced Landslide—A Case Study of Malin Landslide, India. *Eng. Geology.* 208, 154–164. doi:10.1016/j.enggeo.2016.05.002

Feuerharmel, C., Bica, A. V. D., Gehling, W., and Flores, J. A. (2005). "A Study of the Shear Strength of Two Unsaturated Colluvium Soils," in Proceedings of the International Symposium on Advanced Experimental Unsaturated Soil Mechanics, Jan 2005, 169–174.

Fredlund, D. G., Morgenstern, N. R., and Widger, R. A. (1978). The Shear Strength of Unsaturated Soils. *Can. Geotech. J.* 15, 313–321. doi:10.1139/t78-029

Fredlund, D. G., and Xing, A. (1994). Equations for the Soil-Water Characteristic Curve. *Can. Geotech. J.* 31 (4), 521–532. doi:10.1139/t94-061

Furuya, G., Suemine, A., Sassa, K., Komatsubara, T., Watanabe, N., and Marui, H. (2006). Relationship between Groundwater Flow Estimated by Soil Temperature and Slope Failures Caused by Heavy Rainfall, Shikoku Island, Southwestern Japan. *Eng. Geology.* 85, 332–346. doi:10.1016/j.enggeo.2006.03.002

Ghani, A. N. C., Taib, A. M., and Hasbollah, D. Z. A. (2020). Effect of Rainfall Pattern on Slope Stability. *Lecture Notes Civil Eng.* 62 (January), 887–892. doi:10.1007/978-981-15-2184-3_115

Gofar, N., Min Lee, L., and Lee, L. M. (2008). Extreme Rainfall Characteristics for Surface Slope Stability in the Malaysian Peninsular. *Georisk: Assess. Manag. Risk Engineered Syst. Geohazards* 2, 65–78. doi:10.1080/17499510802072991

Hou, X., Vanapalli, S. K., and Li, T. (2018). Water Infiltration Characteristics in Loess Associated with Irrigation Activities and its Influence on the Slope Stability in Heifangtai Loess highland, China. *Eng. Geology.* 234, 27–37. doi:10.1016/j.enggeo.2017.12.020

Jeong, S., Lee, K., Kim, J., and Kim, Y. (2017). Analysis of Rainfall-Induced Landslide on Unsaturated Soil Slopes. *Sustainability* 9 (7), 1280–1320. doi:10.3390/su9071280

Khajehzadeh, M., Taha, M. R., El-shafie, A., and Eslami, M. (2012). A Modified Gravitational Search Algorithm for Slope Stability Analysis. *Eng. Appl. Artif. Intelligence* 25 (8), 1589–1597. doi:10.1016/j.engappai.2012.01.011

Lee, W.-L., Martinelli, M., and Shieh, C.-L. (2021). An Investigation of Rainfall-Induced Landslides from the Pre-failure Stage to the Post-Failure Stage Using the Material Point Method. *Front. Earth Sci.* 9 (November), 1–13. doi:10.3389/feart.2021.764393

Lichao Zhang, L., Liu, X., Song, Y., Li, J., Cai, C., Zhao, X., et al. (2021). Characterization of Surface Runoff Pathways and Erosion Using Hydrological Attributes under Simulated Rainfall. *Front. Earth Sci.* 9 (July), 1–13. doi:10.3389/feart.2021.683473

Matsuura, S., Asano, S., and Okamoto, T. (2008). Relationship between Rain And/or Meltwater, Pore-Water Pressure and Displacement of a Reactivated Landslide. *Eng. Geology.* 101, 49–59. doi:10.1016/j.enggeo.2008.03.007

Merat, S., Djerbal, L., and Bahar, R. (2019). "Rainfall Effect on Slope Stability Using Numerical Analysis," in *Recent Advances in Geo-Environmental Engineering, Geomechanics and Geotechnics, and Geohazards. CAJG 2018. Advances in Science, Technology & Innovation (IEREK Interdisciplinary Series for Sustainable Development)*. Editor A. Kallel (Cham: Springer), 419–424.

Mohamed, T., Kasa, A., and Mukhlisin, M. (2012). *Prediction of Slope Stability Using Statistical Method and Fuzzy Logic*, 2.

Mukhlisin, M., and Taha, M. R. (2012). Numerical Model of Antecedent Rainfall Effect on Slope Stability at a Hillslope of Weathered Granitic Soil Formation. *J. Geol. Soc. India* 79 (5), 525–531. doi:10.1007/s12594-012-0077-0

Perrone, A., Vassallo, R., Lapenna, V., and Maio, C. D. (2008). Pore Water Pressures and Slope Stability: a Joint Geophysical and Geotechnical Analysis. *J. Geophys. Eng.* 5, 323–337. doi:10.1088/1742-2132/5/3/008

Pontier, H., Williams, J. B., and May, E. (2004). Progressive Changes in Water and Sediment Quality in a Wetland System for Control of Highway Runoff. *Sci. Total Environ.* 319, 215–224. doi:10.1016/s0048-9697(03)00410-8

Rahardjo, H., and Fredlund, D. (1995). *Procedures for Slope Stability Analyses Involving Unsaturated Soils Asian Institute of Technology, Lecture Series on Slope Failures and Remedial.*

Rahardjo, H., Lee, T. T., Leong, E. C., and Rezaur, R. B. (2005). Response of a Residual Soil Slope to Rainfall. *Can. Geotech. J.* 42, 340–351. doi:10.1139/t04-101

Rahardjo, H., Satyanaga, A., and Leong, E. (2012). Effects of Flux Boundary Conditions on Pore-Water Pressure Distribution in Slope. *Eng. Geology.* 165, 133–142. doi:10.1016/j.enggeo.2012.03.017

Rahimi, A., Rahardjo, H., and Leong, E.-C. (2011). Effect of Antecedent Rainfall Patterns on Rainfall-Induced Slope Failure. *J. Geotech. Geoenviron. Eng.* 137 (5), 483–491. doi:10.1061/(asce)gt.1943-5606.0000451

Rianna, G., Zollo, A., Tommasi, P., Paciucci, M., Comegna, L., and Mercogliano, P. (2014). Evaluation of the Effects of Climate Changes on Landslide Activity of Orvieto Clayey Slope. *Proced. Earth Planet. Sci.* 9, 54–63. doi:10.1016/j.proeps.2014.06.017

Sagitaningrum, F. H., and Bahsan, E. (2017). Parametric Study on the Effect of Rainfall Pattern to Slope Stability. *MATEC Web Conf.* 101, 05005. doi:10.1051/matecconf/201710105005

Schreiner, H. D. (1987). "The Use of Predictive Methods in Expansive Soils Engineering," in Proceedings of the 9th African Regional Conference on Soil Mechanics and Foundation Engineering, Lagos, Nigeria, 135–141. Vol 1.

Suhaila, J., Deni, S. M., Zawiah Zin, W. A. N., and Jemain, A. A. (2010). Trends in Peninsular Malaysia Rainfall Data during the Southwest Monsoon and Northeast Monsoon Seasons: 1975-2004. *Sains Malaysiana* 39 (4), 533–542.

Taib, A. M., Taha, M. R., and Hasbollah, D. Z. A. (2018). Validation of Numerical Modelling Techniques in Unsaturated Slope Behaviour (Pengesahan Teknik Pemodelan Berangka Dalam Tingkah Laku Cerun Tak Tepu). *Jurnal Kejuruteraan SI* 1 (5), 29–35. doi:10.17576/jkukm-2018-si1(1)-05

Taib, A. M., Taha, M. R., and Hasbollah, D. Z. A. (2019). Validation of Numerical Modelling Techniques in Unsaturated Slope. *Behaviour* 1 (5), 29–35.

Taib, A. M., Taha, M. R., Rahman, N. A., Razuhanafi, M., and Yazid, M. (2020). *The Effect of Soil-Root Interaction by Vetiver Grass on Slope (January 2021).*

Tang, J., Niu, X., Wang, S., Gao, H., Wang, X., and Wu, J. (2016). Statistical Downscaling and Dynamical Downscaling of Regional Climate in China: Present Climate Evaluations and Future Climate Projections. *J. Geophys. Res. Atmos.* 121, 2110–2129. doi:10.1002/2015jd023977

Thu, T., Rahardjo, H., and Leong, E. (2011). Elastoplastic Model for Unsaturated Soil with Incorporation of the Soil-Water Characteristic Curve. *Can. Geotechnical J.* 44, 67–77. doi:10.1139/t06-091

Wang, Y.-J., Yin, J.-H., and Lee, C. F. (2001). The Influence of a Non-associated Flow Rule on the Calculation of the Factor of Safety of Soil Slopes. *Int. J. Numer. Anal. Meth. Geomech.* 25 (13), 1351–1359. doi:10.1002/nag.177

Williams, P. J. (1982). *The Surface of the Earth, an Introduction to Geotechnical Science*. New York: Longman.

Wong, C. L., Venneker, R., Uhlenbrook, S., Jamil, A. B. M., and Zhou, Y. (2009). Variability of Rainfall in Peninsular Malaysia. *Hydrol. Earth Syst. Sci. Discuss.* 6 (4), 5471–5503. doi:10.5194/hessd-6-5471-2009

Zhang, G., Wang, R., Qian, J., Zhang, J.-M., and Qian, J. (2012). Effect Study of Cracks on Behavior of Soil Slope under Rainfall Conditions. *Soils and Foundations* 52 (4), 634–643. doi:10.1016/j.sandf.2012.07.005

Zhang, X., Vincent, L. A., Hogg, W. D., and Niitsoo, A. (2000). Temperature and Precipitation Trends in Canada during the 20th Century. *Atmosphere-Ocean* 38, 395–429. doi:10.1080/07055900.2000.9649654

Zhao, B., Zhang, L., Xia, Z., Xu, W., Xia, L., Liang, Y., et al. (2019). Effects of Rainfall Intensity and Vegetation Cover on Erosion Characteristics of a Soil Containing Rock Fragments Slope. *Adv. Civil Eng.* 2019, 1–14. doi:10.1155/2019/7043428

Zhenping Zhang, Z., Fu, X., Sheng, Q., Yin, D., Zhou, Y., and Huang, J. (2021). Effect of Rainfall Pattern and Crack on the Stability of a Red Bed Slope: A Case Study in Yunnan Province. *Adv. Civil Eng.* 2021, 1–21. doi:10.1590/S0100-06832010000500021

Zhou, J., and Jian-lin, Y. (2005). Influences Affecting the Soil-Water Characteristic Curve. *J. Zheijang Univ.-Sci. A.* 6, 797–804. doi:10.1631/jzus.2005.A0797

Conflict of Interest: The authors declare that the research was conducted in the absence of any commercial or financial relationships that could be construed as a potential conflict of interest.

frontiers | Frontiers in Environmental Science

ORIGINAL RESEARCH
published: 24 August 2022
doi: 10.3389/fenvs.2022.957842

New Evacuation Management Criteria for Potential Landslides Based on Experimental Studies

*Sun-Gyu Choi[1], Min-Su Jung[1], Jae-Wook Suk[2], Ho-Jong Kim[1], Hyo-Sub Kang[3], Hyang-Seon Jeong[1] and Hyo-Sung Song[1]**

[1]Disaster Prevention Assessment Center, National Disaster Management Research Institute (NDMI), Ulsan, Korea, [2]Disaster Scientific Investigation Division, National Disaster Management Research Institute (NDMI), Ulsan, Korea, [3]Research Planning Division, National Disaster Management Research Institute (NDMI), Ulsan, Korea

This study developed and verified landslide evacuation management criteria through the analysis of surface behaviors (the surface displacement and slope) to minimize casualties and property damage caused by landslides. First, for the surface-displacement–based evacuation management criteria, short-term–based management criteria were developed through the analysis of experimental results, and long-term–based evacuation management criteria were developed through the analysis of site collapse data. Furthermore, the reliability of the developed criteria was verified through additional experiments and comparison with the results of previous domestic and overseas studies. Next, surface-angle–based evacuation management criteria were developed through the analysis of experimental results, and the reliability of the developed criteria was verified through additional experiments. Finally, the phased management criteria of these two criteria categories were directly compared and their similar results (i.e., warning times) were verified. This analysis confirmed that the investigated surface-angle–based management criteria can serve as an auxiliary form of the surface-displacement–based evacuation management criteria.

Keywords: landslide, evacuation management criteria, surface displacement, surface angle, full-scale experiment

Edited by:
Snehasis Kundu,
National Institute of Technology, India

Reviewed by:
Yongmin Kim,
University of Glasgow,
United Kingdom
Robby Yussac Tallar,
Universitas Kristen Maranatha,
Indonesia

****Correspondence:***
Hyo-Sung Song
song32@korea.kr

Specialty section:
This article was submitted to
Freshwater Science,
a section of the journal
Frontiers in Environmental Science

Received: *31 May 2022*
Accepted: *23 June 2022*
Published: *24 August 2022*

Citation:
Choi S-G, Jung M-S, Suk J-W, Kim H-J, Kang H-S, Jeong H-S and Song H-S (2022) New Evacuation Management Criteria for Potential Landslides Based on Experimental Studies.
Front. Environ. Sci. 10:957842.
doi: 10.3389/fenvs.2022.957842

INTRODUCTION

Natural disasters causing human casualties and property damage occur every year worldwide. Recently, the frequency and scale of natural disasters have been increasing due to rapid climate change and industrialization. Moreover, human casualties and property damage due to natural disasters are on the rise due to the urbanization and broadening of regions with concentrated populations and resources. Landslides, which represent a high proportion of all natural disasters, are closely related to topographical, geological, and rainfall conditions (Popescu, 2002; Kim et al., 2022).

Geographically, approximately 70% of the land of South Korea is composed of mountainous areas; geologically, the proportion of saprolites, which are vulnerable to landslides, is high. In terms of climate, approximately 700 mm of precipitation occurs during the summer, thereby making this country vulnerable to landslides (Kim et al., 2017; Kim and Jeong, 2017; Park et al., 2018). Landslides represent a large percentage of all domestic disasters, and damage from these events has been increasing. According to the Korea Forest Service, the damaged area and cost of restoration due to the landslide are increasing every year, and this increasing trend is clearly observed by calculating the cost of restoration compared to the damaged area (Choi et al., 2019). This is thought to be due to the concentration of human and material resources in the wake of industrialization and urbanization.

Various studies have been conducted to respond to increasing landslide damage including studies related to the cause and characteristics of landslides (Song and Hong, 2007; Choi et al., 2011), the evaluation of vulnerabilities to landslide damage (Kang and Kim, 2015; Kim et al., 2019), landslide prevention and restoration measures (Lee et al., 2018; Jang et al., 2020), and the establishment and operation of evacuation management criteria to reduce human casualties from landslides (Park et al., 2018).

The importance of such topics as the establishment and operation of evacuation management criteria is increasing as it is related to the recent development of smart cities as well as the reduction of human casualties. With respect to evacuation management and operations, the Korea Forest Service manages areas surrounding mountains and has provided a nationwide danger notification service by constructing a landslide forecast and alarm system based on rainfall and geological conditions (Lee et al., 2009). Moreover, the Ministry of the Interior and Safety monitors mountains around residential areas, conducts continuous measurements for areas considered to require special management, and is implementing evacuation management criteria based on measurement information considering the potential collapse of mountains around residential areas (Ministry of the Interior and Safety (MOIS), 2016).

The measurement-based evacuation management criteria being implemented by the Ministry of the Interior and Safety consist of surface-displacement–based evacuation management criteria, which are direct indicators that measure the behaviors of mountains, which incorporate underground slope-, load-, and rainfall-based evacuation management criteria. These criteria are considered to be indirect indicators that consider changes in a measuring instrument rather than the measurement of surface behaviors, which are considered via pore-water-pressure–, volumetric-water-content–, and groundwater-level–based evacuation management criteria. Specifically, the surface-displacement–based evacuation management criteria were determined based on the cumulative displacement and displacement rate obtained by analyzing the measurement data of actual collapse sites. The underground slope–based evacuation management criteria were established by analyzing domestic and overseas management criteria, such as those of Japan's Slope Stability Subcommittee and soil-retaining temporary facilities. The load-based evacuation management criteria were established by referring to load gauge management criteria for temporary soil-retaining facilities and management criteria that were applied to these sites. The rainfall-based evacuation management criteria were established based on rainfall data categorized by region by analyzing the rainfall and geological characteristics of various landslide damage sites. The pore-water-pressure–based evacuation management criteria were established based on excess pore-water-pressure data, while the volumetric-water-content–based evacuation management criteria were established based on the saturations of sandy and clay soils. Finally, the groundwater-level-based evacuation management criteria were established based on changes in the cumulative groundwater level.

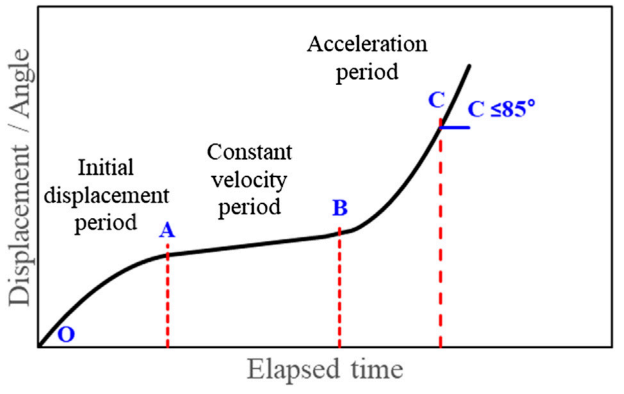

FIGURE 1 | Landslide failure model and phased criteria setting points.

Among the evacuation recommendation criteria, the surface-displacement–based management criteria are the most widely utilized evacuation management criteria worldwide in terms of their intuitiveness and ease of analysis using displacement measurements established through direct surface behavior measurements (Reid et al., 1999; Bazin, 2012). The displacement-based management criteria of the Ministry of the Interior and Safety, as described above, result from data gathered from 10 collapse sites that occurred in South Korea, but they require supplementation because these results were obtained through an analysis involving a small amount of data. Additionally, the underground slope–based evacuation management criteria require supplementation because they were obtained by analyzing relatively simple related criteria and include criteria related to temporary facilities instead of mountains.

Therefore, this study aims to improve the existing surface-displacement–based evacuation management criteria by analyzing data from various experiments (small- and full-scale flume experiments) and the field. We develop and propose surface-angle–based evacuation management criteria that can be utilized as a supplementary indicator of the surface-displacement–based management criteria. Furthermore, the reliability of these two types of evacuation recommendation criteria is analyzed through verification and step-by-step comparison of the two criteria types. This study aims to minimize human casualties by improving the measurement-based evacuation recommendation criteria currently used by the Ministry of the Interior and Safety.

DETERMINING MEASUREMENT MANAGEMENT CRITERIA

Determining Management Criteria

Landslides are caused by geological and topographical factors, physical factors, and human activities. There are many different types of landslide failures, but they can be largely classified into polynomial, growth, and rapid models.

TABLE 1 | Phased criteria setting points for the development of measurement management criteria.

Type	Watch	Caution	Warning	Alert
Polynomial	O	A	B	C (≤85°)

Among these models, the polynomial model is a general slope failure model that can be divided into three periods: the initial displacement, continuous increase of the displacement, and rapid increase of the displacement just before failure. This behavior mainly appears in soils with low adhesion, high confining pressures, and rocks, among other sites. Stages of this process can be determined according to slope failure based on the aforementioned slope failure characteristics, and measurement management criteria can be determined using these stages. **Figure 1** shows the above-mentioned slope failure model, and **Table 1** summarizes the stage divisions and division points determined based on **Figure 1**. For example, the slope failure behaviors of the polynomial model can be divided into the initial displacement, constant velocity, and acceleration periods. If these periods are set as measurement management criteria, they may be divided into the "initial displacement period" from the onset of displacement to the point of a constant-velocity displacement (OA), the "constant velocity period" in which the displacement increases at a constant rate (AB), and the "acceleration period" in which the displacement accelerates (BC). These periods can be designated as three levels of phased management criteria as "watch," "caution," "warning," and "alert." "Watch" begins at initial displacement (O), "caution" begins at the "start point of constant velocity (A)," "caution" occurs at the "end point of constant velocity (start point of acceleration) (B)," and alert occurs at the "end point of acceleration (C)."

The specific analysis method for these criteria is as follows. The "displacement/slope velocity" is calculated based on the velocity/slope displacement unit of the management criteria using the displacement data over time, and the "displacement/slope acceleration" is calculated based on the displacement/slope velocity. However, in the case of the end of the acceleration phase for determining the alert level, the maximum displacement/slope at which the displacement can be measured and the corresponding maximum acceleration values are generally calculated using the measured values. However, the measurement management criteria provide risk levels before considering the damage from failure; therefore, it is difficult to determine the alert level based on the end point of the acceleration phase. To complement this, Xu et al. (2011) analyzed the displacement/slope velocity at which a slope failure occurs using actual failure site data from Wang and Zhang (1999). The article found that the displacement velocity at slope failure may be converted into a slope angle of 89–89.5°. Based on this, the critical failure for pre-warning criteria of was to be 85°.

In this study, the polynomial model was utilized by applying the aforementioned criteria for four graded, initial displacement (O) for "watch," start (A) and end (B) points of constant-velocity period for "caution," "warning," end point of acceleration (C) for "alert" in **Table 1**.

Research Method

Domestic and overseas references, indoor experiments (including small- and full-scale flume experiments), and field data were analyzed to develop measurement-based management criteria for soil slope failure in this study. First, management criteria that can be used to examine the stability of slopes under construction were examined. Additionally, short-term–based management criteria considering short-term–based data, such as heavy rainfall over short time periods, and long-term–based management criteria considering the continuous measurement of the slope and soil were developed. Considering the short-term–based criteria, a slope failure experiment was conducted using small- and full-scale slope failure simulators at the National Disaster Management Research Institute. The surface behaviors were analyzed by installing a surface displacement gauge to verify the behaviors during the failure process. The values of phased management criteria were derived from the displacement measurement data, and the short-term–based management criteria were then developed. The final measurement-based management criteria were developed following the full-scale flume experiment considering the effects of scaling. The long-term–based management criteria were next developed by analyzing domestic and overseas references and field data of previous failures that have either occurred or are predicted to occur in South Korea.

The research on surface-angle–based measurement management criteria globally remains limited. Therefore, the surface-angle–based evacuation management criteria considered in this study were developed by analyzing the surface angle results acquired via the full-scale flume experiment at the National Disaster Management Research Institute.

Finally, the reliability of all management criteria was verified using small- and full-scale flume experiments with different conditions, as well as by considering the results of previous studies. The design and methodology of study is shown in **Figure 2**.

EQUIPMENT AND EXPERIMENTAL CONDITIONS

Introduction of the Slope Failure Simulator

The National Disaster Management Research Institute has a full-scale steep slope failure simulator. This full-scale steep slope failure simulator, which is the largest in Asia, is composed of an artificial rainfall reproduction device for reproducing rainfalls, a model container for constructing slopes, and a control room for the analysis of slope images and verification of the measurement results. The artificial rainfall reproduction device with a size of 4 × 21 m can reproduce a continuous rainfall across the entire slope, and the rainfall intensity can be adjusted from 10 to 160 mm. Furthermore, the injection method can be selected between left, right, and directly downward injections according to the experimental conditions. The model containers are divided into the first, second, and third containers, which have a variable structure in which the angle can be adjusted for

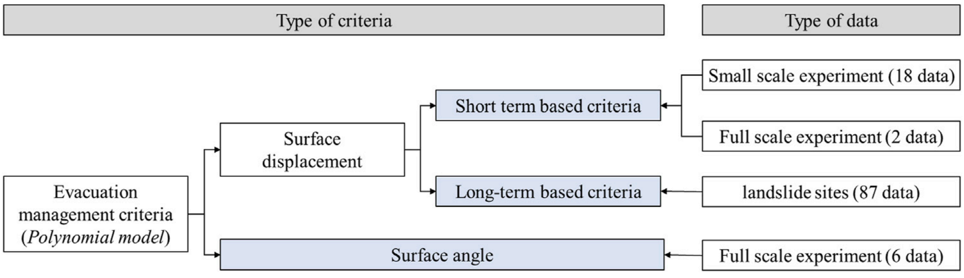

FIGURE 2 | The design and methodology of this study.

different soil types. The first model container can be adjusted to 0–5°, the second model container to 0–15°, and the third model container to 15–40°. The soil layer can be built up to a height of 2.5 m, and soil can be piled up to approximately 250 t. Finally, the control room can adjust the rainfall intensity, method, and slope angle, as well as receive measurement data and acquire images. In addition, the National Disaster Management Research Institute has a small-scale slope failure simulator with a size that is 1/10 the scale of the large simulator.

Experimental Conditions

A soil slope was constructed using the full-scale landslide failure simulator for landslide experiments and data acquisition. The soil used in this experiment was granite weathered soil that consists of 73.8% sand and 22% fine powder. The coefficient of uniformity (Cu) is 6.0, the coefficient of curvature (Cg) is 0.84, the liquid limit (LL) is 29.7%, and the plastic limit is 21.5%, so this soil is classified as SP. The engineering properties (friction angle and cohesion) of soil were measured to 32.1° for friction angle and 22.8 kPa for cohesion intercept. The bottom angle of the slope was 5° for the first model container, 15° for the second model container, and 35° for the third model container, and the surface angle of the slope was 35°. The dimensions of the slope size were 10.6 m in height, 15.2 m in length, 2.5 m in soil depth, and 4 m in width. The weight of the slope was approximately 220 t. When constructing the slope, the soil was built with a dry density of approximately 1.55 t/m3 and a water content of 10%. To measure the process of slope failure due to rainfall, three surface angle gauges were installed at the top (7.5 m), middle (6.3 m), and bottom (5.1 m) from the end of the slope. The surface displacement gauges were installed at the same heights as the surface angle gauges at approximately 1 m from the center of the slope (six gauges total). An imaging device was installed at the top front section of the slope to visually analyze the changes during the failure process.

Lastly, the rainfall was injected using the artificial rainfall reproduction device, and the rainfall intensity was set to 50 mm/h. Because the rainfall intensity (50 mm/h) was determined by average rainfall intensity (until slope failure) over six fields during typhoon “Mitag” in the year 2019. The coefficient of uniformity of the rainfall was 87.2%, which satisfied the reliability of the coefficient of uniformity for domestic and overseas rainfall devices (Jeong et al., 2019).

The slope dimensions, gauge types, and installation positions for the experiment are shown in **Figure 3**. This experiment was performed twice.

Measurement Instruments

Closed-circuit televisions (CCTVs), surface displacement gauges, and surface angle gauges were used to analyze the surface behaviors and develop measurement management criteria. The CCTVs consist of nine cameras in total that can obtained videos at different locations and a recorder for recording videos. The surface displacement gauges are composed of a displacement sensor, a box that contains this sensor, and a fixture for fixing the displacement gauge. For the displacement sensor, a wire sensor (electrical resistance type) was used, which is widely used for surface displacement measurements. A device with a measurement range of up to 2,000 mm was used considering the scale of the empirical experiment. The measurement instrument and data logger for storing the data are interconnected by a wire. The surface angle gauge is composed of an integrated slope measurement instrument (composed of a slope gauge sensor and support) that can transmit data wirelessly, as well as a gateway that can send and receive the data. The slope gauge has an embedded battery, can measure 360° from the reference point, and has a resolution of 0.0001°.

SURFACE BEHAVIOR ANALYSIS RESULTS BASED ON MEASUREMENT INFORMATION

A slope failure was induced by subjecting the above-described slope to a continuous rainfall. The images were acquired during the failure process, and measurements of the slope surface and surface displacement were acquired during failure. The analysis results of the imaging device and measurement instruments (slope surface and surface displacement) were obtained.

The imaging device results demonstrated that the failure behavior obtained via the first experiment occurred via a scour generated at the center approximately 20 min following the onset of rainfall, and the size and number of scours increased with time. Failure occurred at approximately 1000 min from the onset of rain. At the time of failure, a soil depth of approximately 1 m was generated. The failure behavior observed via the second experiment resulted from the generation of scours at

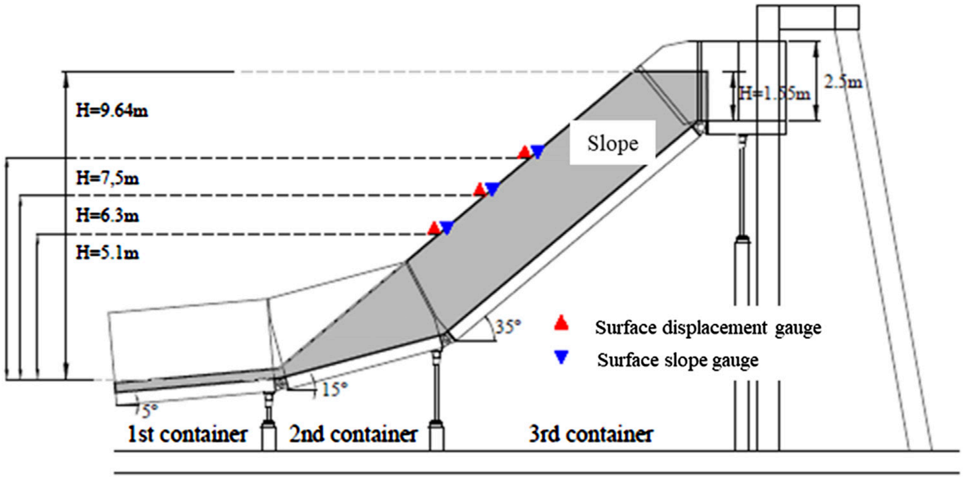

FIGURE 3 | Geometry of the slope and gauge installation positions.

FIGURE 4 | Images of the slope failure after each experiment: **(A)** first and **(B)** second experiments.

approximately 25 min after the start of rainfall. The failure progressed similarly to that of the first experiment, but it progressed slower and occurred approximately 1300 min later the onset of rain. The final images of the slope failures are shown in **Figure 4**.

The results of the surface displacement analysis are shown in **Figure 5A** considering the surface displacement over time for the first experiment. The surface displacement behavior showed a tendency to increase either step-by-step or rapidly at various points during both the first and second experiments. In general, the bottom of the slope showed an abrupt increase, while a more gradual increase was observed toward the top. At the bottom of the slope, a rapid displacement occurred initially. Partial failure is considered to have occurred at the lower portion of the slope as saturation of the bottom portion of the slope occurred due to the continuous rainfall.

Finally, the surface angle analysis was conducted to investigate the variation of the slope angle over time as measured by the slope gauges, and the results are shown in **Figure 5B**. The slope angles in both experiments generally underwent cycles of increasing and decreasing over time. These results were likely obtained due to the creation of scours via the continuous rainfall. Furthermore, a rapid change occurred immediately before the slope failure, as was observed in the image analysis results. The slope angle partially increased or decreased over time depending on the section of the slope, while the slope angle at the actual failure point rapidly increased after slowly increasing.

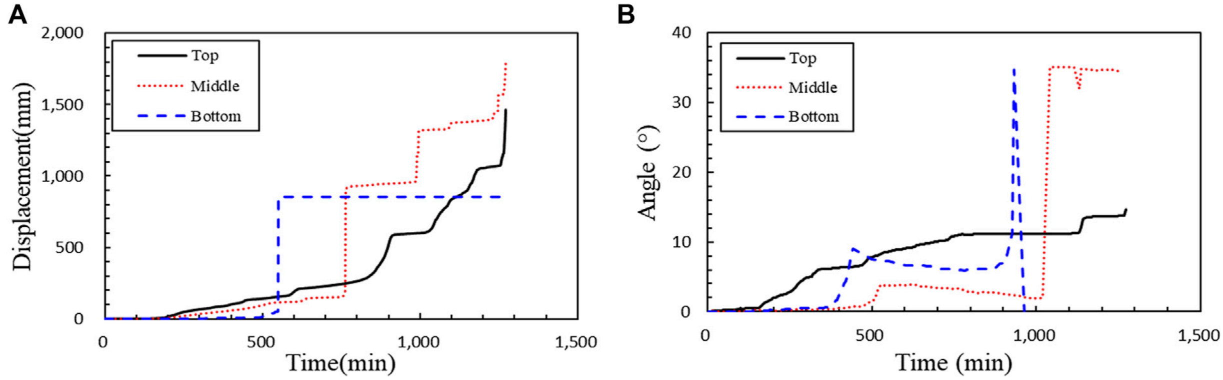

FIGURE 5 | Surface behaviors by position over time: **(A)** surface displacement and **(B)** surface angle.

DEVELOPMENT AND VERIFICATION OF THE SURFACE-DISPLACEMENT–BASED EVACUATION MANAGEMENT CRITERIA

For the surface-displacement–based measurement management criteria, short-term–based measurement management criteria that can be used to examine the stability of a slope under construction or applied when examining heavy rainfall over a short time period were considered. Moreover, long-term–based measurement management criteria that can be applied to soil slope and creep that require continuous management were developed. Furthermore, the reliability of the developed measurement management criteria was verified.

Development of Short-Term–Based Measurement Management Criteria

The short-term–based measurement management criteria were derived through 18 experiments using the small-scale slope failure simulator and two experiments using the full-scale slope failure simulator.

During the 18 small-scale experiments, measurements were performed while changing the rainfall intensity (30, 50, and 100 mm/h), slope gradient (35, 40, and 50°), and dry unit weight (1.30–1.50 g/cm3). Considering the measured data, four levels of management criteria were determined according to the criteria for each level described in **Section 2**. Therefore, "watch" (gray circle), "caution" (yellow triangle), "warning" (orange square), and "alert" (red diamond) were marked at the points corresponding to each level, as shown in **Figure 6A**. Regarding the results of the small-scale experiments, either the minimum or average values may be used to determine these levels. In this study, we utilized the hr. average values according to the method presented in the steep slope management practical handbook. The short-term–based management criteria obtained through the small-scale experiments were denoted as the point at which displacement first occurred for "watch," 1 mm/min for "caution," 5 mm/min for "warning," and 31 mm/min for "alert."

Next, two full-scale flume experiments were conducted using the conditions noted in **Section 3**, and the phased management criteria and averages were analyzed. The analysis method using the full-scale flume experiments was the same as that of the small-scale experiments. However, in the case of the full-scale flume experiments, the experimental time was approximately 18–21 h whereas it was ≤2 h for the small-scale experiments, and scours and partial failures occurred. Therefore, considering the measurement data of the full-scale flume experiments, the measurement management criteria were analyzed only using the data that was directly affected by failure (i.e., the final polynomial graph or total graph) instead of analyzing the entire experiment. Finally, the four aforementioned levels were indicated via this analysis. **Figure 6B** shows a figure of the phased management criteria points obtained using partial data of the full-scale experiment, and their values are shown in **Table 2**. The short-term–based measurement management criteria determined via the full-scale flume experiment were determined as the onset of displacement for "watch," 1 mm/min for "caution," 3 mm/min for "warning," and 17 mm/min for "alert."

To develop the short-term–based measurement management criteria through indoor experiments, the results of the small- and full-scale flume experiments were analyzed. It was found that the criteria determined through the small-scale experiments were higher than those determined through the full-scale flume experiments (except for "watch"). The average values of the small-scale experiments may have been greater due to large differences in the criteria values for each level considering various conditions (rainfall intensity, dry unit weight of soil, and slope angle). Moreover, it appears that the different amounts of time required for failure affected these results. The small-scale experiments were conducted over a relatively short period of approximately 2 h, whereas the full-scale flume experiments required more than 16 h. In the small-scale experiments, failure occurred relatively quickly and displacement occurred rapidly compared to the large-scale experiments due to size differences. Jeong et al. (2011) analyzed the progression of failure over time according to the sizes of the small- and full-scale flume experiments and confirmed that the small-scale experiment generated greater displacements over the same time period compared to the full-scale flume experiment.

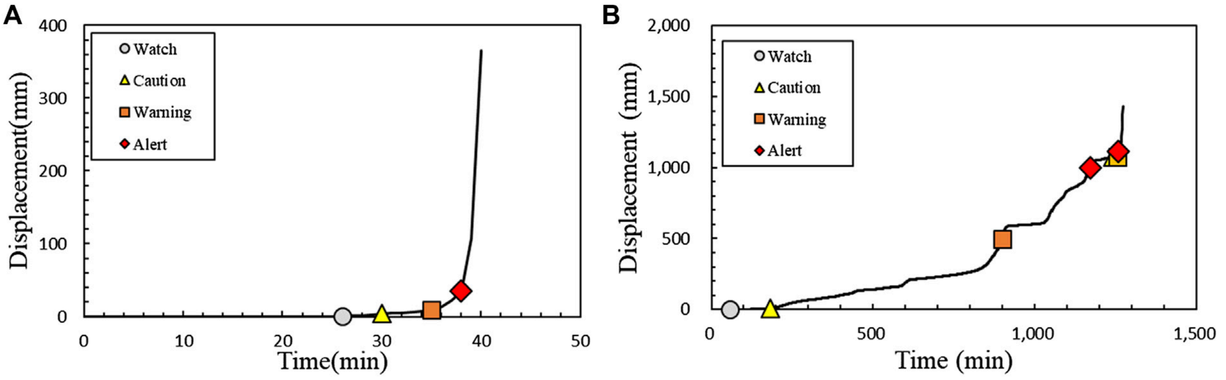

FIGURE 6 | Phased management criteria points (surface displacement) obtained via **(A)** small-scale flume experiments and **(B)** full-scale flume experiments.

TABLE 2 | Results of the long-term–based evacuation management criteria (surface displacement).

Type	Evacuation management criteria (mm/day)			
	Watch	Caution	Warning	Alert
Results	Onset of displacement	2	8	56

Because the small-scale experiment cannot consider the scaling effects, the small- and full-scale flume experiments may not be directly compared. To address this problem, a weight (×2) was given to the results of the full-scale flume experiments, and the short-term–based measurement management criteria applicable to the soil slope were finally developed. Results show the short-term–based measurement management criteria determined through indoor experiments, which were the onset of displacement for "watch," 1 mm/min for "caution," 4 mm/min for "warning," and 21 mm/min for "alert."

Development of Long-Term–Based Evacuation Management Criteria

The long-term–based evacuation management criteria were determined through the data analysis of measurements from eight domestic landslide sites (2012–2014). These data were used to determine the evacuation management criteria for landslides that occurred in 2016 by the Ministry of the Interior and Safety. We aim to improve upon these management criteria by using a different analysis method while considering the same data.

The conventional phased measurement management criteria apply one criterion for one data point, but this study determined multiple criteria for each level to reflect the actual behaviors of slope failure and improve the reliability of these criteria by considering more data. **Figure 7A** shows phased evacuation management criteria that were previously determined, whereas **Figure 7B** shows multiple phased evacuation management criteria points that were determined in this study. The evacuation management criteria shown in **Figure 7B** were determined using 87 data points instead of the eight data points used previously. As a result, "watch" was determined as the onset of displacement, "caution" as 2 mm/day, "warning" as 8 mm/day, and "alert" as 56 mm/day.

Verification of the Evacuation Management Criteria

In this section, the short- and long-term–based evacuation management criteria developed in **Sections 5.1** and **5.2** are verified. The short-term–based evacuation management criteria were verified using 10 small-scale flume experiments and two full-scale flume experiments with different experimental conditions. The soil used in these experiments was granite weathered soil with a specific weight of 2.59, liquid limit of 29.7%, plastic limit of 21.5%, and plasticity index of 6.8%. This soil was classified as SC-SM by the unified taxonomy, and the content of fine particles was analyzed to be approximately 38.0%. Furthermore, the slope conditions and positions of the measuring instruments were to the same as those in **Section 5.2**. The rainfall intensity was 50 mm/h, as in the previous experiments. The phased management criteria were calculated using the measurement management criteria method applied in this study using the displacement data measured during the 10 small-scale flume experiments and two full-scale flume experiments according to the above conditions. **Figure 8** shows the phased criteria points according to the above experiments. The verified management criteria were determined to be the onset of displacement for "watch," 1 mm/min for "caution," 4 mm/min for "warning," and 96 mm/min for "alert." These criteria are greater than the values proposed in this study, which were onset of displacement, 1, 3, and 17 mm/min for "watch," "caution," "warning," and "alert," respectively. The criteria in this study were set more conservative than those for verification. Therefore, they are considered to be reasonable for application under various conditions.

The long-term–based evacuation management criteria were verified through the surface-displacement–based measurement management analysis method that has been used both in Korea and elsewhere. The management criteria (mm/day) determined

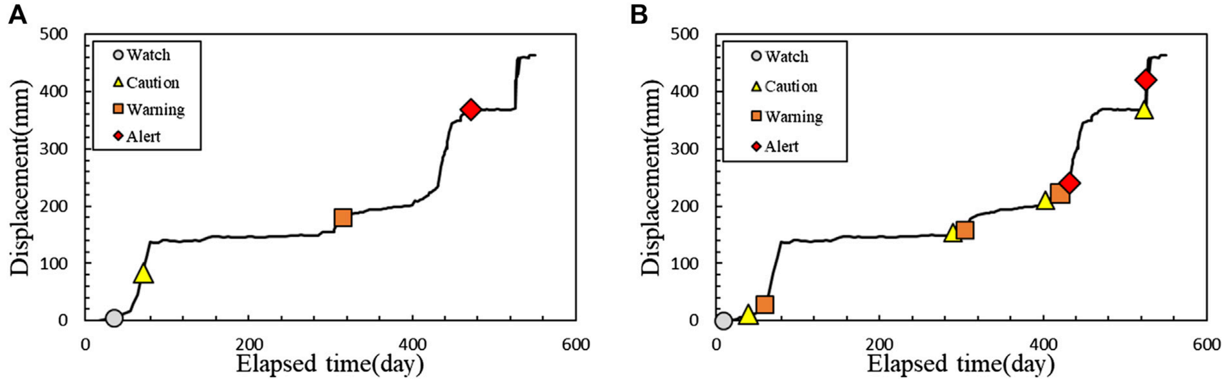

FIGURE 7 | Phased management criteria points determined through an analysis of field measurement data: **(A)** previous analysis data [21] and **(B)** this study.

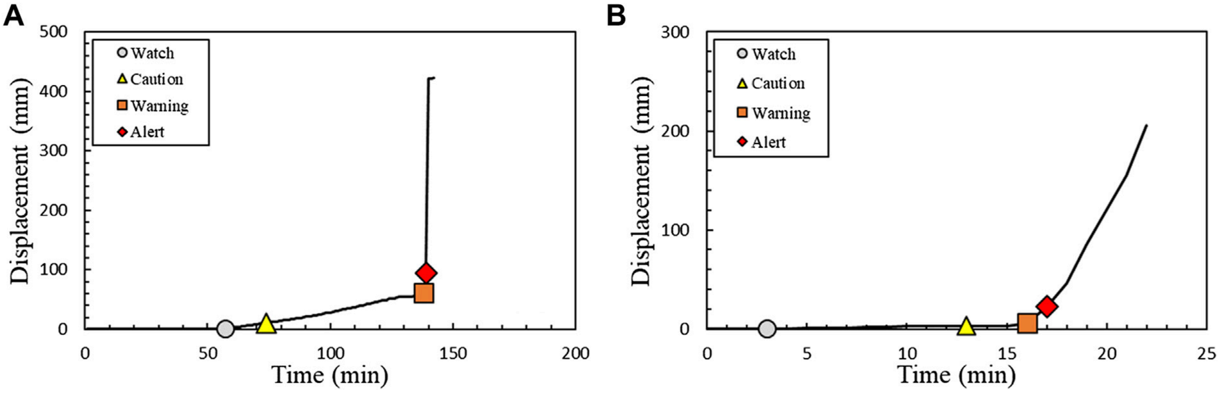

FIGURE 8 | Phased management criteria points for verification (short-term perspective): **(A)** small-scale experiments and **(B)** full-scale flume experiments.

TABLE 3 | Results of the long-term–based evacuation management criteria used for verification (surface displacement).

Type	Evacuation management criteria (mm/day)			
	Watch	Caution	Warning	Alert
Xu et al. (2011)	1	6	26	63
Wang and Zhang, (1999)	13.8	18.6	54.4	94.2
Jeong et al. (2019)	-	-	5	50
Jeong et al. (2011)	-	1	10	100

in previous studies that can be directly compared with the criteria proposed in this study were considered (Task Committee of Japanese Geotechnical Society (TCJGS), 1996; Japan Highways Organization (JHO), 1998; Ministry of the Interior and Safety (MOIS), 2015; Yoo, 2006; Yueping et al., 2010; Cheon et al., 2013). It was found that the average values of the management criteria were 7.4, 8.0, 19.2, and 84.5 mm/day for "watch," "caution," "warning," and "alert," respectively, as shown in **Table 3**.

These criteria were more conservative than the long-term–based measurement management criteria proposed in this study, which were the onset of displacement, 2, 8, and 56 mm/day for "watch," "caution," "warning," and "alert," respectively. Therefore, the measurement management criteria determined in this study may be applied for various ground and geological conditions.

DEVELOPMENT AND VERIFICATION OF THE SURFACE-ANGLE–BASED EVACUATION MANAGEMENT CRITERIA

Development of Evacuation Management Criteria

The surface-angle–based measurement management criteria were developed by analyzing the six surface angle datasets obtained using the experimental conditions described in **Section 3.2**. **Figure 9** shows the results of the full-scale flume experiment over time. The measurement data showed a trend of slowly increasing after the onset of measurements and then rapidly increasing at a certain point. Therefore, according to the criteria defined in **Section 2.1**, the "watch" level was set to the onset of displacement, "caution" level to the beginning start of the

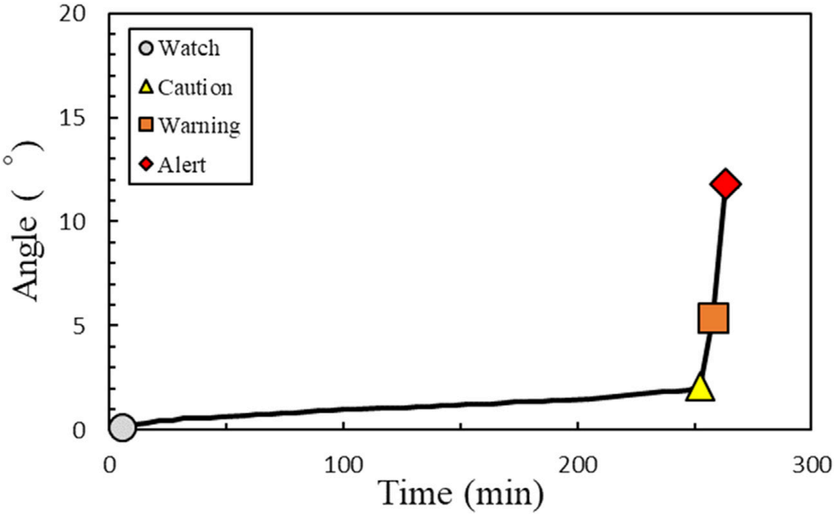

FIGURE 9 | Phased management criteria points determined through the full-scale flume experiments (surface angle).

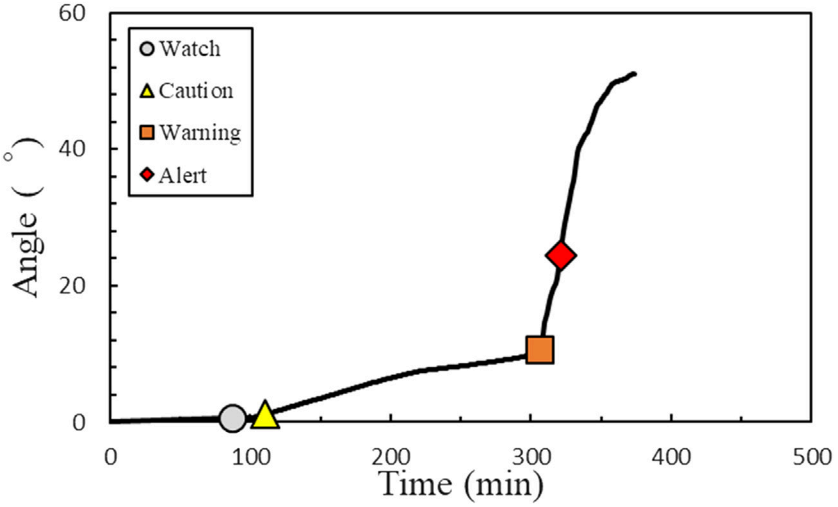

FIGURE 10 | Analysis results for the verification of the measurement management criteria (based on the surface angle).

constant velocity," "warning" level to end point of the constant velocity, and "alert" level to the end point of the acceleration. The final surface-angle–based measurement management criteria were proposed by averaging the results of each dataset for each level. The final measurement management criteria for the full-scale flume experiment were determined as the onset of displacement for "watch," 0.04°/min for "caution," 0.22°/min for "warning," and 1.74°/min for "alert."

The surface-angle–based measurement management criteria developed in this **Section 6.1** were verified. The results of the full-scale flume experiments conducted under the soil and experimental conditions described in **Section 5.3** were used to verify the measurement management criteria, and the criteria determination method described in **Section 6.1** was used as the verification method. Five datasets were analyzed through two full-scale flume experiments. As shown in **Figure 10**, the slope angle slowly increased after the onset of displacement and then rapidly increased. This trend was the same as the trend observed in **Section 6.1**. The final measurement management criteria were derived by averaging the individual data analysis results. As shown in **Table 4**, the "watch" level was determined as the onset of displacement, "caution" level as 0.04°/min, "warning" level as 0.18°/min, and "alert" level as 2.22°/min. These criteria were more conservative than those proposed in this study, which were the onset of displacement, 0.04, 0.22, and 1.74°/min for "watch," "caution," "warning," and "alert," respectively. Therefore, the measurement management criteria proposed in this study may be applied to various soil and geological conditions.

TABLE 4 | Results of surface-angle–based evacuation management criteria for verification.

No.	Evacuation management criteria (°/min)			
	Watch	Caution	Warning	Alert
1	Onset of displacement	0.03	0.20	3.52
2		0.03	0.16	2.78
3		0.05	0.18	2.15
4		0.01	0.13	1.22
5		0.08	0.24	1.40
Results		0.04	0.18	2.22

It should be noted that the surface-angle–based measurement management criteria proposed in this are not sufficiently reliable due to insufficient analysis data and a lack of existing research results. Therefore, it is recommended that the surface-angle–based measurement management criteria proposed in this study be used as supplementary criteria, for application to steep soil slopes where it is difficult to install surface displacement gauges.

The short-term–based evacuation management criteria were verified using 10 small-scale flume experiments and 2 full-scale flume experiments with different experimental conditions. The soil used in these experiments was granite weathered soil with a specific gravity of 2.59, liquid limit of 29.7%, plastic limit of 21.5%, and plasticity index of 6.8%. This soil was classified as SC-SM by the unified classification method, and the content of fine particles was approximately 38.0%. Furthermore, the slope conditions and gauge positions were similar to those in **Section 5.2**, and the rainfall intensity was set to 50 mm/h, as in the previous experiments. The phased management criteria were determined using the measurement management criteria method proposed in this study considering the displacement data measured via the small- and full-scale flume experiments. The final measurement management criteria for verification were determined, as shown in **Table 4**, which were the onset of displacement for "watch," 0.04°/min for "caution," 0.18°/min for "warning," and 2.22°/min for "alert." These criteria are greater than those proposed in this study, which were the onset of displacement, 1, 3, and 17°/min for "watch," "caution," "warning," and "alert," respectively. Therefore, the criteria proposed in this study were more conservative than the verification criteria, and the proposed criteria may be reasonably applied under various conditions.

COMPARISON OF THE SURFACE-DISPLACEMENT– AND SURFACE-ANGLE–BASED PHASED MANAGEMENT CRITERIA

Surface-displacement– and surface-angle–based management criteria were derived in this study by conducting failure experiments using surface displacement and surface angle gauges installed at the same positions. Therefore, the phased measurement times can be directly compared by analyzing the results of these two gauges.

Figure 11 shows the phased measurement management criteria determined based on the surface displacement and surface angle at the same height via empirical experiments. The displacement over time is indicated by the black line, and the phased measurement management criteria are indicated by the open symbols. The surface-displacement–based management criteria were calculated as approximately 170 and 1,238 min for the "caution" level, approximately 901 and 1,257 min for the "warning" level, and 1,172 and 1,260 min for the "alert" level. The slope angle over time is indicated by the blue dotted line, and the phased measurement management criteria are indicated by the closed symbols. The surface-angle–based management criteria were calculated as approximately 168 and 1,226 min for the

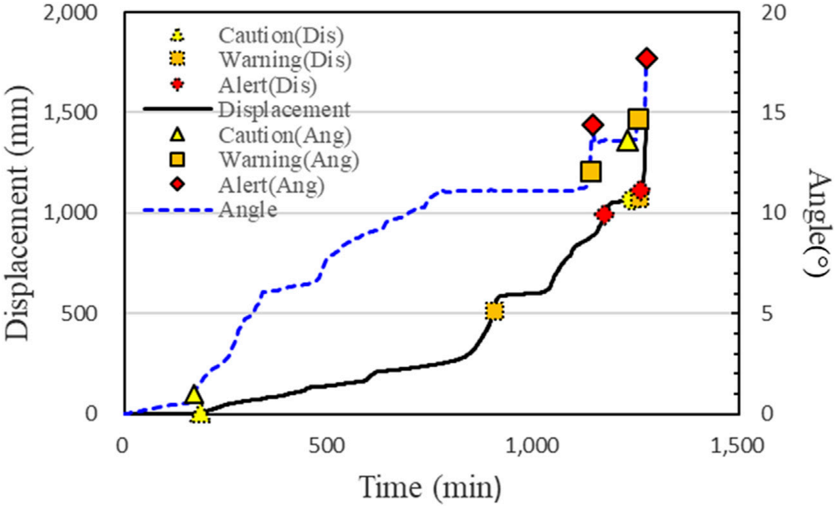

FIGURE 11 | Comparison of the final management criteria for the surface displacement and surface angle at the same positions.

"caution" level, 1,137 and 1,253 min for the "warning" level, and 1,142 and 1,274 min for the "alert" level. The two measurement management levels showed similar values of approximately 170 for the "caution" level, approximately 1,255 min for the "warning" level, and approximately 1,258 min for the "alert" level. By comparing these two measurement criteria systems, it was observed that the same management criteria for both the surface displacement and surface angle occurred at similar times. This confirmed that these two management criteria can be directly compared with and verified using one another, and the surface-angle–based management criteria can be used to supplement the surface-displacement–based evacuation management criteria.

CONCLUSION

This study developed evacuation management criteria based on measurement data to minimize human casualties and property damage due to slope failures considering the criteria used by the Ministry of the Interior and Safety. Surface-displacement–based and surface-angle-based measurement management criteria that can analyze slope surface behaviors were developed. The results of this study may be summarized as follows:

1) Short-term–based measurement management criteria that can be applied to evaluate the stability of a slope under construction or heavy rainfall for a short period of time were developed. The management criteria were determined using small- and full-scale flume experiments, and a weight was given to the results of the full-scale flume experiments to improve the reliability of these experiments. The final short-term-based measurement management criteria proposed in this study were 1 mm/min for the "caution" level, 4 mm/min for the "warning" level, and 21 mm/min for the "alert" level.
2) Long-term–based measurement management criteria for application to soil slope and creep scenarios, which require continuous management, were also developed. These phased management criteria were determined by analyzing the results of domestic and overseas studies, as well as data from sites where failures have occurred or are predicted to occur. The final long-term–based measurement management criteria proposed in this study were 2 mm/day for the "caution" level, 8 mm/day for the "warning" level, and 56 mm/day for the "alert" level.
3) Surface-angle-based measurement management criteria were developed by considering the similarity between the surface angle and displacement behaviors. The measurement management criteria were determined for the four levels of watch-caution-warning-alert based on a polynomial model. The phased measurement management criteria were proposed as the onset of displacement for "watch," 0.04°/min for "caution," 0.22°/min for "warning," and 1.74°/min for "alert." Furthermore, the reliability of these criteria was verified via comparison with the results of empirical experiments conducted using varied experimental conditions. However, the surface-angle-based measurement management criteria proposed in this study exhibited reliability issues due to insufficient analysis data and a lack of existing research results. Therefore, it is recommended that these criteria be used to supplement the surface-displacement–based measurement management criteria or be applied to steep soil slopes where it is difficult to install surface displacement gauges.

DATA AVAILABILITY STATEMENT

The raw data supporting the conclusion of this article will be made available by the authors, without undue reservation.

AUTHOR CONTRIBUTIONS

Conceptualization: CS-G, SJ-W, and JM-S; Methodology: KH-S and JH-S; Formal Analysis: CS-G, KH-J and JH-S; Writing/Original Draft Preparation: CS-G; Writing Review and Editing: SH-S; Supervision: SH-S.

FUNDING

This research was supported by the project "Development of Slope Disaster Vulnerability Assessment based on Empirical Experiments (Ⅱ)" (No. NDMI-PR-2022-07-02) from the National Disaster Management Research Institute (NDMI).

REFERENCES

Bazin, S. (2012). *Guidelines for Landslide Monitoring and Early Warning Systems in Europe – Design and Required Technology*. Vienna, Austria: Safeland, Deliverable D4, 8.

Cheon, D.-J., Park, Y.-J., Lee, S.-H., Kim, J.-S., and Jung, D.-Y. (2013). The Development of Landslide Predictive System Using Measurement Information Based on U-IT. *J. Korea Academia-Industrial Coop. Soc.* 14, 5115–5122. doi:10.5762/KAIS.2013.14.10.5115

Choi, J.-H., Kim, H.-T., Oh, J.-Y., and Kim, Y.-S. (2011). Analysis of the Controlling Factors of an Urban-type Landslide at Hwangryeong Mountain Based on Tree Growth Patterns and Geomorphology. *J. Eng. Geol.* 21 (4), 281–293. The Korean Society of Engineering Geology. doi:10.9720/kseg.2011.21.4.281

Choi, S.-G., Jeong, H., Song, H.-S., Kwon, T.-H., Kim, Y., and Lee, J.-M. (2019). Study of Korea Early Warning System for Slope Failure. *J. Korean Soc. Hazard Mitig.* 19, 73–81. doi:10.9798/KOSHAM.2019.19.5.73

Jang, S.-J., Lee, Y.-T., Lee, K.-Y., Kim, K.-N., Lee, J.-H., and Chun, K.-W. (2020). A Study of Disaster Prevention and Characteristics of Landslides Triggered by the 2019 Typhoon Mitag in Samcheok. *J. Korean Soc. Hazard Mitig.* 20, 221–227. doi:10.9798/KOSHAM.2020.20.2.221

Japan Highways Organization (Jho) (1998). *Design Guideline*, Tokyo, Japan: Japan Highways Organization, 1–37.

Jeong, H. S., Kang, H. S., Suk, J. W., and Kim, H. J. (2019). Rainfall Distribution Characteristics of Artificial Rainfall System for Steep-Slope Collapse Model

Experiment. *J. Korea Acad.-Ind. Coop. Soc.* 20, 828–835. doi:10.5762/KAIS.2019.20.12.828

Jeong, J., Ji, Y., Kim, Y., and Lee, S. A. (2011). Study on the Scale Effect of Landslide Model Test. *Korean Geo-Environmental Soc.* 12, 5–12.

Kang, H.-S., and Kim, Y.-T. (2015). Study on Physical Vulnerability Curves of Buildings by Numerical Simulation of Debris Flow. *J. Korean Soc. Hazard Mitig.* 15, 155–167. doi:10.9798/KOSHAM.2015.15.5.155

Kim, J., Kim, Y., Jeong, S., and Hong, M. (2017). Rainfall-induced Landslides by Deficit Field Matric Suction in Unsaturated Soil Slopes. *Environ. Earth Sci.* 76, 1–17. doi:10.1007/s12665-017-7127-2

Kim, M.-I., Kwak, J., Jun, B., and Kim, N. (2019). Analysis of Landslide Risk Distribution Pattern under Extreme Precipitation. *J. Korean Soc. Hazard Mitig.* 19, 105–112. doi:10.9798/KOSHAM.2019.19.3.105

Kim, Y., and Jeong, S. (2017). Modeling of Shallow Landslides in an Unsaturated Soil Slope Using a Coupled Model. *Geomechanics Eng.* 13 (2), 353–370. doi:10.12989/GAE.2017.13.2.353

Kim, Y., Rahardjo, H., Nistor, M. M., Satyanaga, A., Leong, E.-C., and Sham, A. W. L. (2022). Assessment of Critical Rainfall Scenarios for Slope Stability Analyses Based on Historical Rainfall Records in Singapore. *Environ. Earth Sci.* 81, 39. doi:10.1007/s12665-021-10160-4

Lee, C. H., Eo, G., Lee, S. H., Oh, K. R., and Sim, O. B. (2018). Development of Multilayer Defense System Recovery Techniques for Flood and Landslide: For Residential and Industrial Complex in Chuncheon City. *J. Korean Soc. Hazard Mitig.* 18, 123–131. doi:10.9798/KOSHAM.2018.18.6.123

Lee, C., Youn, H. J., and Woo, C. S. (2009). Development and Verifying of Calculation Method of Standard Rainfall on Warning and Evacuation for Forest Soil Sediment Disaster in Mountainous Area by Using Tank Model. *Jour. Korean For. Soc.* 98, 272–278. (in Korean).

Ministry of the Interior and Safety (Mois) (2015). *The R&D Research on Construction of Monitoring Management System for Evacuating Inhabitant in Steep Slope Site and Development of Monitoring Specification*. Sejong, Korea: Ministry of the Interior and Safety.

Ministry of the Interior and Safety (Mois) (2016). *Guideline of Steep-Slope Management*. (in Korean) Sejong, Korea: Ministry of the Interior and Safety.

Park, S.-J., Lee, C.-W., Lee, S., and Lee, M.-J. (2018). Landslide Susceptibility Mapping and Comparison Using Decision Tree Models: A Case Study of Jumunjin Area, Korea. *Remote Sens.* 10, 1545. doi:10.3390/rs10101545

Popescu, M. E. (2002). "Landslide Causal Factors and Landslide Remediation Options," in 3rd International Conference on Landslides, Slope Stability and Safety of Infra-structures, Singapore, 61–81.

Reid, M. E., LaHusen, R. G., and Ellis, W. L. (1999). *Real-Time Monitoring of Active Landslides*. Reston, Virginia: United States Department of the Interior, United States Geological Survey.

Song, Y. S., and Hong, W. P. (2007). A Case Study on the Analysis of Cause and Characteristics of a Landslide at the Sedimentary Rock Area. *J. Eng. Geol.* 17 (1), 101–113. The Korean Society of Engineering Geology.

Task Committee of Japanese Geotechnical Society (TCJGS) (1996). *Manual for Zonation on Rain-Induced Slope Failure*. Tokyo, Japan: Japanese Geotechnical Society.

Wang, J. D., and Zhang, Z. Y. (1999). *Systematic Project Research on Typical High Speed Loess Landslide (In Chinese)*. Chengdu: Sichuan Science and Technology Publishing House, 140–153.

Xu, Q., Yuan, Y., Zeng, Y., and Hack, R. (2011). Some New Pre-warning Criteria for Creep Slope Failure. *Sci. China Technol. Sci.* 54, 210–220. doi:10.1007/s11431-011-4640-5

Yoo, B. S. (2006). A Study of Failure Analysis Methods Based on Real-Time Monitoring Data for Landslide Warning System. Ph.D. Thesis. Gumi, Korea: Kumoh National Institute of Technology.

Yueping, Y., Wang, H., Gao, Y., and Li, X. (2010). Real-Time Monitoring and Early Warning of Landslides at Relocated Wushan Town, the Three Gorge Reservoir, China. *J. Appl. Geol.* 2, 170–184. doi:10.22146/jag.7260

Conflict of Interest: The authors declare that the research was conducted in the absence of any commercial or financial relationships that could be construed as a potential conflict of interest.

frontiers | Frontiers in Environmental Science

TYPE Original Research
PUBLISHED 30 September 2022
DOI 10.3389/fenvs.2022.972648

OPEN ACCESS

EDITED BY
Songdong Shao,
Dongguan University of Technology,
China

REVIEWED BY
Ehsan Kazemi,
The University of Sheffield,
United Kingdom
Fan Li,
Dongguan University of Technology,
China

*CORRESPONDENCE
Yang Shi,
thushiyang@tsinghua.edu.cn
Jiahua Wei,
weijiahua@tsinghua.edu.cn

SPECIALTY SECTION
This article was submitted to Freshwater Science,
a section of the journal
Frontiers in Environmental Science

RECEIVED 18 June 2022
ACCEPTED 01 September 2022
PUBLISHED 30 September 2022

CITATION
Bai W, Shi Y, Zhao Z and Wei J (2022), Investigation of critical response characteristics of micro-droplets under the action of low-frequency acoustic waves.
Front. Environ. Sci. 10:972648.
doi: 10.3389/fenvs.2022.972648

Investigation of critical response characteristics of micro-droplets under the action of low-frequency acoustic waves

Wenwen Bai[1], Yang Shi[2]*, Zhifeng Zhao[1] and Jiahua Wei[1,2]*

[1]School of Water Resources and Electric Power/Laboratory of Ecological Protection and High-Quality Development in the Upper Yellow River/State Key Laboratory of Plateau Ecology and Agriculture/ Key Laboratory of Water Ecology Remediation and Protection at Headwater Regions of Big Rivers, Ministry of Water Resources, Qinghai University, Xining, China, [2]State Key Laboratory of Hydroscience and Engineering, Tsinghua University, Beijing, China

For the droplets with different size distribution, reasonably selecting the frequency and period of acoustic waves are of great significance to acoustic agglomeration. To investigate critical responses of microdroplets under the action of low-frequency acoustic waves, laboratory experiments and numerical simulations of acoustic interference were conducted, and statistical test and theoretical analysis were carried out. A total of 1,680 sets of experiments were performed, from which about 300,000 particle size samples were collected, with sound frequency of 30–280 Hz and the sound pressure level (*SPL*) of 70–130 dB. Droplet size distribution (DSD), equilibrium response time (*ERT*), the nodal plane in the air chamber and entrainment coefficient were analyzed. The critical *SPL* of acoustic agglomeration was 110 ± 15 dB based on average droplet size increment, and the variation of droplet size indicated that the *ERT* of acoustic intervention on microdroplets under the critical *SPL* was 44 ± 12 s. In addition, lower sound frequencies corresponded to larger widths of droplet size with significant response (*DSSR*), which were jointly affected by sound pressure gradient (*SPG*), the entrainment coefficient and the droplet concentration. For microdroplets with unknown particle size distribution, acoustic intervention with variable frequencies is suggested for fog elimination and precipitation enhancement.

KEYWORDS

acoustic agglomeration, equilibrium response time, critical *SPL*, droplet size with significant response, sound pressure gradient, entrainment coefficient

1 Introduction

In recent years, the issue of atmospheric quality has attracted extensive attention from researchers (Sotty et al., 2019; Liu, 2021). One effective way to improve atmospheric quality is to eliminate the harmful aerosols by technical approaches (Dass et al., 2021; Meng et al., 2021). Acoustic agglomeration technology has great potential in the removal of fine particulate matters and the precipitation enhancement (Zhou et al., 2016; Zhang et al., 2018; Shi et al., 2021b; Wei et al., 2021) due to its safety and convenience. Dynamic reactions of fluid-particle/droplet and particle/droplet was induced and intensified by acoustic waves through inputting external energy (Yang and Fan, 2014). This in turn increased the probability of collision and accelerated the formation of large agglomerates. The main mechanisms of particle/droplet acoustic agglomeration include orthokinetic interactions (Cheng et al., 1983; Dong et al., 2006), hydromechanical interactions such as acoustic radiations and acoustic wake effects (Hoffmann and Koopmann, 1996), and acoustically generated turbulences (Tiwary et al., 1984). Although the orthokinetic mechanism reveals the agglomeration of the polydisperse particles/droplets, it cannot explain the agglomeration process of the monodisperse particles/droplets. The acoustic wake effects and acoustic radiations are complementary to the acoustic agglomeration mechanism. In other words, monodisperse particles/droplets have the opportunity to collide and merge in asymmetric flow fields and scattered sound fields. The mechanism of acoustically generated turbulences involves the existence of velocity differences between particles due to turbulent inhomogeneities, which leads to chaotic particle collisions. The acoustically generated turbulences requires the sound intensity to be large enough to reach a certain critical sound pressure level (*SPL*). Due to the complexity and difficulty of turbulence, acoustically generated turbulence is still controversial. All of those results show that various agglomeration mechanism coexist in acoustic experiments, the effects and corresponding threshold for particles/droplets agglomeration should be further investigated.

Quantitative evaluation of the acoustic agglomeration performance of suspended particles/droplets and determination of the optimal acoustic frequency and *SPL* are of great significance to the optimization of agglomeration efficiency. For example, through intervention of 1,000 Hz and 3,000 Hz acoustics, Shaw and Tu (1979) found that the decrease in dioctyl phthalate (DOP) concentration in the aerosol was more significant at lower sound frequencies (1,000 Hz) when the *SPL* was 145 dB. Cheng et al. (1983) experimentally found that the agglomeration rate of NH_4Cl aerosols increased with the rising acoustic frequency (600–3,000 Hz). Chen et al. (2007) investigated the effects of acoustic agglomeration on removing submicron particles in coal-fired fumes using 1,000 Hz acoustics, and reported that the total particle mass concentrations of $PM_{2.5}$ and PM_{10} were reduced by 58% and 77%, respectively. The agglomeration effect also occurs when acoustic waves interfere with liquid droplets, at lower acoustic frequencies compared to particle agglomeration. For example, Chang et al. (1963) performed acoustic experiments at 500–2,400 Hz, and found that acoustic waves could significantly accelerate the dissipation of water mist. In 2002, Hou et al. (2002) performed an acoustic intervention experiment at relatively lower frequency of 20–50 Hz, and found that the acoustic frequency corresponding to the optimal agglomeration effect is 20 Hz. For 40–100 Hz acoustic intervention on microdroplets, Bai et al. (2020); Bai et al. (2021a); Bai et al. (2021b) found that the particle size increment was significantly affected by the sound frequency, and the droplets isotope values increased after interference of acoustics. He et al. (2021) conducted experiments on droplets by combined sound waves of 200–600 Hz and electric field. The effects of sound wave and electricity on droplet agglomeration have been proved, and the optimal sound frequency was 400 Hz. These studies have reported the optimal acoustic frequency and *SPL*, but the dimension and distribution of droplets are spatiotemporally different. Moreover, previous studies show that the acoustic agglomeration effect was directly influenced by sound field characteristics and particle/droplet size distribution (Qu et al., 2020). The standing wave field had a better agglomeration effect than the traveling wave field (Chang et al., 1963). This may be attributed to the continuous oscillation of fluid medium around the wave node, so the acoustic wave forces the particles/droplets to move towards the node. In addition, it was found that acoustic agglomeration effect enhanced significantly with the increasing particle size difference and particles concentration (Yuen et al., 2017). The previous studies mainly focus on particles agglomeration, so it is necessary to systematically investigate the droplet response to low-frequency acoustic waves.

The droplets agglomeration caused by acoustic waves is manifested in the variation of diameter and concentration. The response of droplets to acoustic intervention, especially the critical *SPL* and the optimal frequency, is worthy of attention. This paper attempts to experimentally investigate the critical *SPL* of low-frequency acoustic intervention. The significance test was adopted to investigate responses of microdroplets subjected to acoustic waves. The control experiments including natural (without acoustic intervention) and acoustic intervention conditions were designed, and the critical *SPL* and its equilibrium response period under the action of sound waves with 30–280 Hz were analyzed. According to the significance test, the droplet size with significant response (*DSSR*) under fixed critical *SPL* and different sound frequencies was obtained, and the influence factors were analyzed. This study has certain reference value for the frequency optimization of acoustic agglomeration.

2 Materials and methods

2.1 Experimental devices

The experiment device consists of an air chamber, sound and aerosol generators, and monitoring devices (Figure 1). The monitoring devices mainly includes temperature and humidity sensors, laser particle analyzer, and microdroplet collection

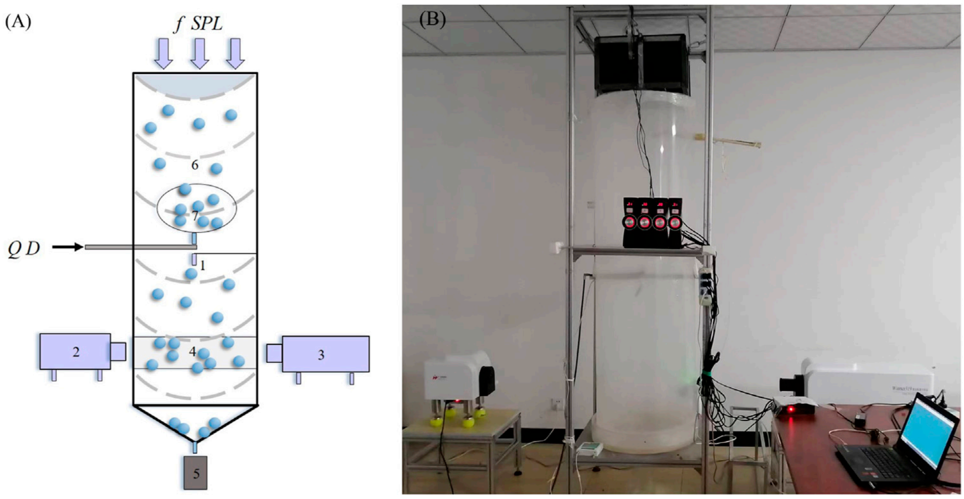

FIGURE 1
Sketch **(A)** and on-site picture **(B)** of the experimental devices (*Q* represents input volume of droplets; *D* represents input diameter of microdroplets; *f* represents frequency of acoustic source; and *SPL* represent intensity of acoustic source. 1-Temperature and humidity sensors; 2-Laser transmitter; 3-Laser receiver; 4-Monitoring region of droplets; 5-Microdroplet collection beaker; 6-Air chamber; 7-Microdroplets).

beaker. The air chamber consists of a cylindrical Plexiglas tube and a conical bottom plate with slope of 1:2, conical bottom plate is used to collection droplets and isolate bottom of the air chamber from environment. The diameter and height of air chamber are 600 mm and 2000 mm, respectively. Sound generator is fixed on the top of air chamber. A plastic film with high sound permeability is adopted to isolate the top of chamber. Microdroplets nozzle, temperature and humidity sensors are all fixed in the middle of air chamber. To pass the laser beam of laser particle analyzer for size observation, a hole with a diameter of 100 mm is placed along the radial direction of the air chamber, with 300 mm away from the bottom of the air chamber. Microdroplet collection beaker is located at the bottom of air chamber. The experimental device could monitor dynamic variations of droplet size before and after acoustic intervention. The sound generator was capable of adjusting the frequency (30–280 Hz constant frequency loading) and *SPL* (70–130 dB) of the sound source. The *SPL*s at different positions of the air chamber could be measured with accuracy of 0.1 dB. The aerosol generator can continuously produce microdroplets from 5 to 100 μm and can control the input volume (*Q*) and its peak shape. The droplets size distribution (DSD) can be continuously observed using particle analyzer (winner 319, Jinan Micro-nano Particle Instrument Co., Ltd.), with the time resolution of 1 s and observable range of 1–500 μm in size dimension, the accuracy was less than or equal to 3%. Environmental parameters such as air temperature and humidity can be real-time monitored with temporal resolution of 1.0 s.

2.2 Experimental process and conditions

The experiments were carried out in the alternation of natural settlement and acoustic intervention. Acoustic frequency was 30–280 Hz with a step of 10 Hz, and the *SPL* was 70–130 dB with a step of 5 dB. To reduce the occasionality and statistical error of the experimental results, three control or replicate experiments were conducted for each scenario, with each group of samples collected for more than 180 s.

To ensure the accuracy of the measurements, the standard solution was used to calibrate the observation instrument before the experiment. Agglomeration tests were carried out at room temperature (20°C). A total of 840 groups of control experiments were performed, with more than 300,000 samples being collected.

2.3 Experimental data processing

(i) Determination of critical *SPL*. For acoustic interventions with fixed acoustic frequency, there is a critical *SPL*, which can effectively influence the droplet size. When the droplet is intervened by acoustic waves with SPL_0 and SPL_1 (SPL_0 + 5 dB), the average droplet size increases by more than 0.1 μm, and the size increment is relatively larger for cases with acoustic intensity of SPL_1. This indicates that stable agglomeration occurs after acoustic intervention, and the corresponding SPL_0 can be determined as the critical *SPL* under a certain sound frequency. Note that increment refers to the droplet size with acoustic action minus that without acoustic operation.

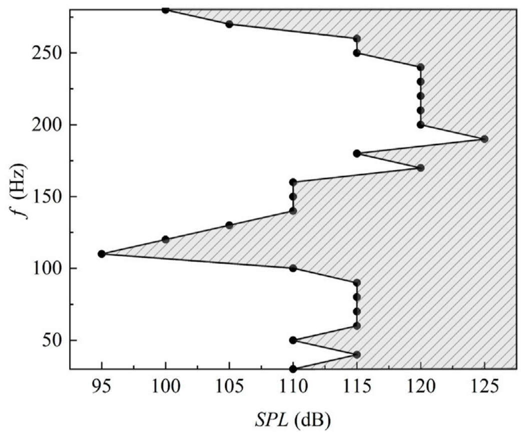

FIGURE 2
The Critical *SPL*s at different acoustic frequencies. (Shaded area represents the effective *SPL* range for acoustic interference).

(ii) Significance test. According to the critical *SPL* determined in section (i), statistical tests are carried out on droplet size. In other words, acoustic wave as the influencing factor, one-way ANOVA is conducted to test the significance level (0.05) of the acoustic waves influence on volume frequency of the each droplet size (different sound frequencies, critical *SPL*s). The corresponding droplet size that passes the significance test can be defined as droplet size with significant response (*DSSR*).

3 Experimental results and analysis

3.1 Critical sound pressure level and variations of droplets size distribution

The critical *SPL* of the acoustic agglomeration for microdroplets in this study was concentrated at 110 dB. The average sizes of the microdroplets in the 840 control groups were counted, and thereby the critical *SPL* and its effective sound pressure distribution for cases of 30–280 Hz as shown in Figure 2. The black dots in the figure represent the critical *SPL* for corresponding certain acoustic frequency, and the shaded area denotes the effective *SPL* range of acoustic operation. The critical *SPL* showed a fluctuating trend with the sound frequency. The maximum critical *SPL* was 125 dB, and the corresponding sound frequency was 190 Hz; the lowest critical *SPL* was 95 dB with sound frequency of 110 Hz. In general, lower sound frequencies corresponded to lower critical *SPL*s.

The peak shape of DSD remained unchanged after acoustic intervention. To obtain a comparison chart of the DSD, the droplet volume frequencies of control groups were averaged. The DSD under the action of acoustic waves with f = 30–90 Hz presented a unimodal trend (Figure 3), with identical peak shape. This indicated that the agglomeration process of microdroplets was greatly restricted by the initial DSD. Further analysis revealed that variation rate of volume frequency for relatively smaller droplets was significantly higher than that for larger ones after acoustic intervention. In addition, the agglomeration effect was related to the volume frequency of droplets, indirectly confirming the effect of particle number on acoustic agglomeration (Shi et al., 2020).

The droplets agglomeration and fragmentation coexisted with acoustic operation, while the aggregation effect dominated. According to the number of intersection points of the volume accumulative frequency curve before and after acoustic intervention (Figure 3 and Supplementary Figure S1 in Supplementary), the agglomeration effects can be subdivided into two types. The first type had two intersection points, the size of microdroplets increased after acoustic intervention, which was mainly caused by the agglomeration of droplets, with the sound frequencies of 30–50 Hz, 90–230 Hz, and 250–280 Hz. The second type had more than two intersection points, the size of microdroplets first increased and then decreased with sound frequencies of 60–80 Hz, and 240 Hz, indicating droplets agglomeration and fragmentation effect (Shi et al., 2020) coexist, thus the volume accumulative frequency of droplet group presented a staggered variation trend.

3.2 Equilibrium response time of microdroplets

The equilibrium response time (*ERT*) of the microdroplets was concentrated at 44 s under the critical *SPL* (Table 1). The *ERT* varied with sound frequencies. The minimum *ERT* was 32 s with sound frequency of 210 Hz; the maximum *ERT* value was 56 s, and the corresponding sound frequency was 140 Hz. The equilibrium response time was impacted by the DSD, the sound field distribution inside the air chamber. The sound field distribution in the air chamber remained unchanged for a constant acoustic frequency. Therefore, the equilibrium response time was mainly influenced by sound frequency.

With the increase of the acoustic intervention period, the particle size generally tended to increase first, and then maintained a dynamic equilibrium. Figure 4 shows the variation of droplet size with acoustic action time under the action of acoustic waves with 90 Hz and 190 Hz. After acoustic operation, the particle size D_{90} (indicating that the volume frequency of droplets smaller than this size accounted for 90% of the total volume) increased because of the droplets agglomeration. In the initial stage, the size of microdroplets generally showed an increasing trend, this can be well demonstrated by D_{90} variation before the three dashed line in Figure 4. The sudden decrease of D_{90} was caused by the fragmentation of microdroplets, but the D_{90} showed an ascending trend at this stage due to stronger agglomeration.

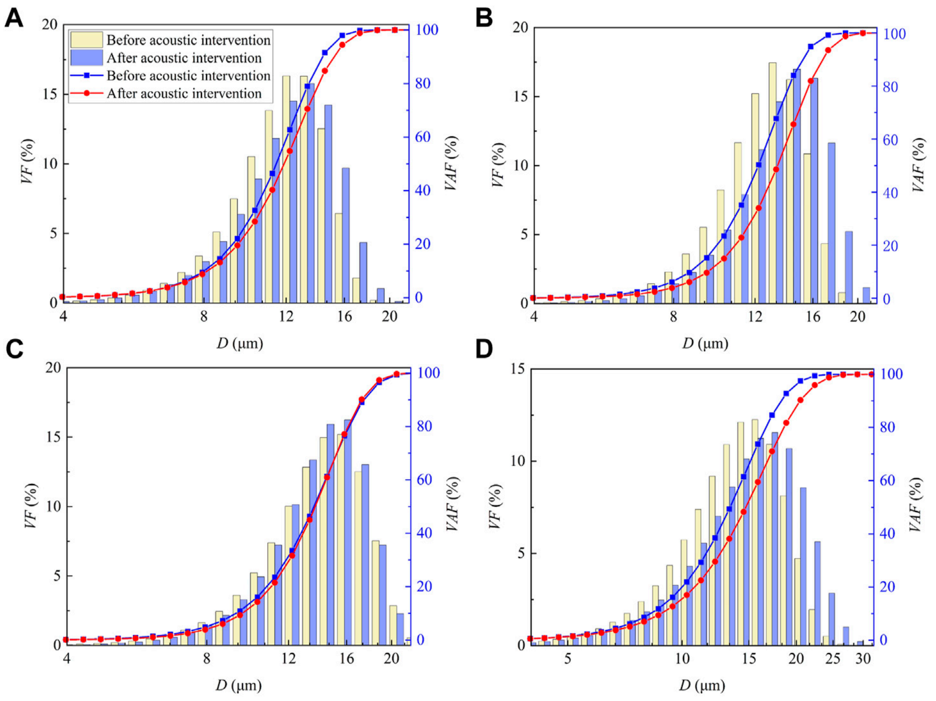

FIGURE 3
Variation of DSD under fixed critical *SPL* and different acoustic frequencies. **(A)** 30 Hz, **(B)** 50 Hz, **(C)** 70 Hz, **(D)** 90 Hz. (*VF*: volume frequency; *VAF*: volume accumulated frequency).

TABLE 1 ***ERT*** **of microdroplets under the action of acoustic waves with fixed critical** ***SPL*** **and different acoustic frequencies.**

f/Hz	30	40	50	60	70	80	90	100	110	120	130	140	150
Mean/s	47	37	34	44	39	43	53	46	43	41	48	56	50
SD	3	3	7	2	2	6	5	7	8	8	2	8	11
f/Hz	160	170	180	190	200	210	220	230	240	250	260	270	280
Mean/s	35	38	35	41	43	32	55	42	40	45	35	54	43
SD	9	5	1	7	3	4	9	4	7	5	5	8	6

From the equilibrium response time on, the agglomeration-fragmentation inside the microdroplets reached a dynamic equilibrium, and average D_{90} remained roughly unchanged.

4 Discussion

4.1 Droplet size with significant response under different sound frequencies

The *DSSR* was varied with acoustic frequency. In general, a lower acoustic frequency corresponded to a larger width of *DSSR*. The significance test was performed to investigate response degree of droplet size for acoustic intervention with fixed critical *SPL* and different frequencies (30–280 Hz). From Figure 5A, widths of *DSSR* for cases with f = 30–110 Hz were obviously larger than those of above 110 Hz. The break points can be clearly seen for D = 4–8 μm after acoustic intervention with f = 110–140 Hz. The critical *SPL*s for acoustic operation with f = 30–110 Hz were generally lower than those with f = 110–280 Hz. This meant that the larger width of *DSSR* may corresponds to the lower critical *SPL*. In addition, effective frequency range of acoustic operation for $D < 4$ μm was significantly larger than that of droplets larger than 4 μm.

The concentration of microdroplets also affected width of *DSSR*. To illustrate the relationship between width of *DSSR* and the droplet concentration, Figure 5B shows DSD before acoustic

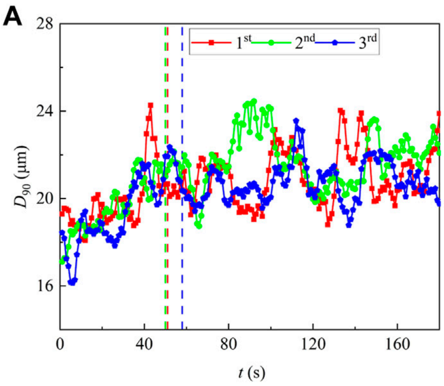

FIGURE 4
Variation of particle size over acoustic operation time under 90 Hz **(A)** and 190 Hz **(B)**. (1st, 2nd, 3rd represent the experimental order; the red, green and blue dashed lines represent equilibrium response time of 1st, 2nd, 3rd experiment respectively).

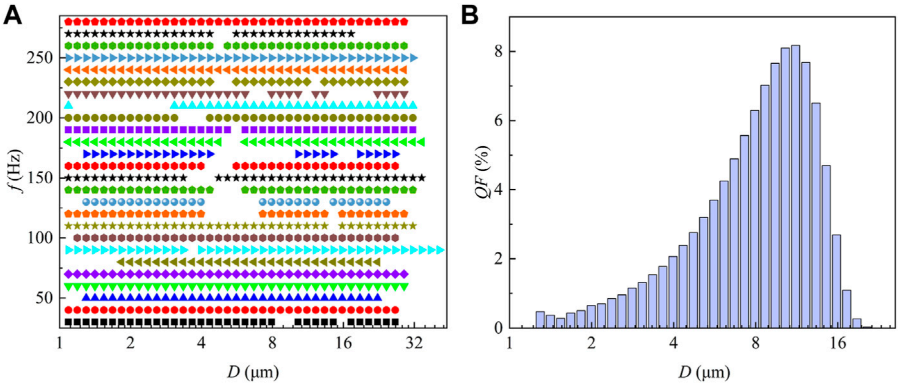

FIGURE 5
Width of *DSSR* with respect to different acoustic frequency **(A)** and DSD **(B)**.

operation. The droplet size corresponding to the largest volume frequency also had the highest concentration (comparing Figure 5B with Figure 3). In addition, the droplet sizes with non-significant response were mainly distributed in range of 4–8 μm with middle concentration (except droplet sizes with non-significant response was 1–3 μm after acoustic intervention with f = 210 Hz). This indicated that the width of *DSSR* was affected by both microdroplets sizes and concentration. Detailed discussion can be found in Section 4.4.

4.2 Numerical simulation of acoustic structures inside air chamber

In this study, a commercial computational fluid dynamics software, COMSOL Multiphysics, was applied to study the distribution of sound field with f = 30 Hz, 120 Hz, 200 Hz and 280 Hz in the air chamber. Detailed simulation information can be found in the work of Shi et al. (2020). As shown in Figure 6, the nodal planes of acoustic waves moved from the top to the bottom in air chamber. The plane number increased with the sound frequency, which was consistent with the experimental results (Bai et al., 2020). Specifically, there were one, two and three acoustic planes in the frequency bands of 30–120 Hz, 130–210 Hz, and 220–290 Hz, respectively. The sound pressure gradient (*SPG*) force near the nodal plane was relatively larger, leading to an increased probability of droplet aggregation. In addition, the width of *DSSR* could be influenced by the number of acoustic planes and their distribution. The pressure distribution in air chamber varied with sound frequency, and could impact the acoustic agglomeration effect of droplet aerosols.

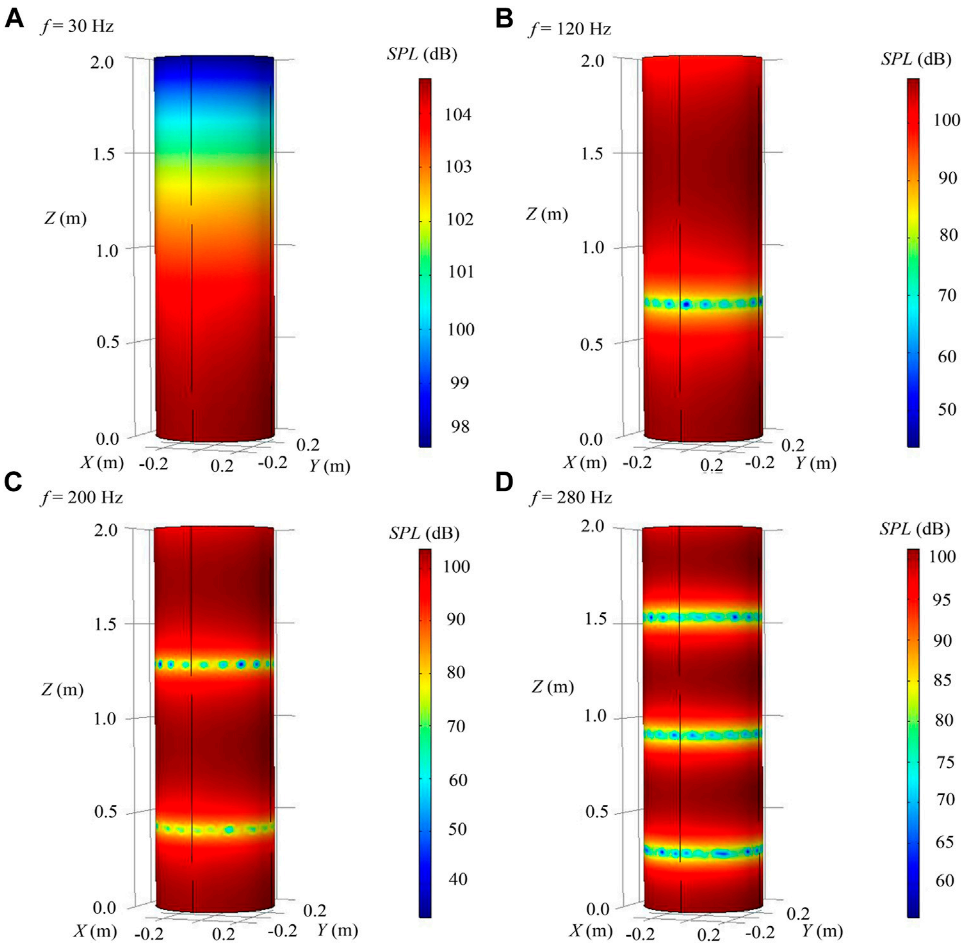

FIGURE 6
Variation characteristics of *SPL* in air chamber. [**(A–D)** represent 30 Hz, 120 Hz, 200 Hz and 280 Hz, respectively; *X-Y-Z* represents the spatial coordinate system, and the *Z* axis is along the axis of the air chamber].

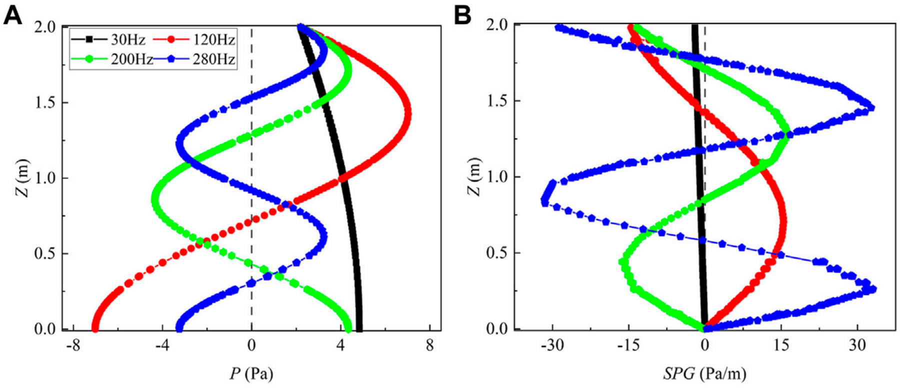

FIGURE 7
Distribution of total sound pressure **(A)** and sound pressure gradient **(B)** along the axis of the air chamber.

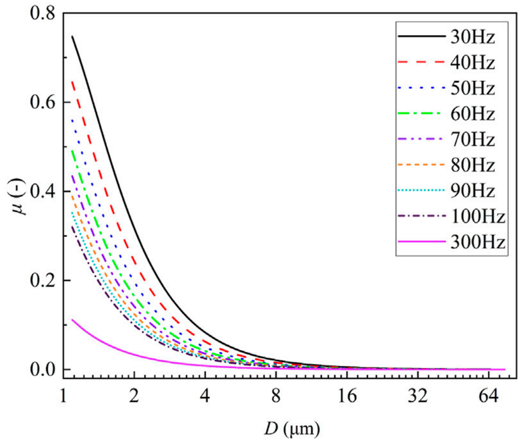

FIGURE 8
Entrainment coefficients of acoustic frequencies for droplets with different sizes.

To investigate the effect of sound pressure gradient on droplets agglomeration, the vertical sound pressure and its gradient along the air chamber axis of 30 Hz, 120 Hz, 200 Hz and 280 Hz was extracted (see Figure 7). The amplitude of sound pressure gradient increased with acoustic frequency. Figure 7A shows that the sound pressure exhibited a sinusoidal variation along the chamber axis. The fluctuation amplitude and the direction were influenced by the chamber size and the sound frequency. The acoustic amplitude and number of alternating directions were positively correlated with the acoustic frequency. Figure 7B confirms that the amplitude of sound pressure gradient along chamber axis also increased with sound frequency.

4.3 Entrainment effect of acoustic frequencies on microdroplets

The acoustic agglomeration was obviously affected by orthokinetic agglomeration, and the entrainment coefficient for droplets with different size varied with the sound frequency. According to the entrainment force of the sound wave exerted on particles (Brandt and Hiedemann, 1936; Cheng et al., 1983; Song et al., 1994; Hoffmann and Koopmann, 1996), and shear forces exerted on droplets in the Stokes flow (Re < 1) (Tiwary and Reethof, 1986), entrainment coefficient can be derived as follows.

$$\mu = \frac{1}{\sqrt{1 + (\omega\tau_p)^2}} \tag{1}$$

where τ_p is the relaxation time of particles, which is proportional to the droplet density and the square of radius, and inversely proportional to flow viscosity; ω is the angular frequency. Regardless of the properties of droplets and environment, the entrainment coefficient of acoustic on droplet is only affected by acoustic frequency.

For cases with sound frequencies of 30–300 Hz, air temperature of 20°C and dynamic viscosity of 0.01809 Pa·s, the entrainment coefficient for droplets with size in range of 1–64 μm were obtained (Figure 8). In general, the lower sound frequency, the larger entrainment effect on the droplets and the larger droplet amplitude caused by acoustic waves. The wider the size spectrum of droplets, the more significant the agglomeration effect. Thus, low-frequency acoustic waves were apt to influences droplets with wider size spectrum.

4.4 Comprehensive analysis of factors affecting droplet size with significant response

The width of *DSSR* was jointly affected by the sound field, especially sound pressure gradient, the entrainment coefficient and the droplet concentration. For cases with low sound frequencies (30–110 Hz), the width of the *DSSR* was mainly subjected to the entrainment effect. With increasing of sound frequency (120–210 Hz), the wavelength declined, and thereby the number of nodal planes in the air chamber rose to 2. For cases with frequency in range of 120–210 Hz, entrainment and agglomeration effects on 1–4 μm droplets were relatively stronger. The volume frequency of droplets above 8 μm varied significantly due to their predominance in concentration. In addition, small droplets were apt to generate larger droplets due to acoustic agglomeration. The width of *DSSR* was jointly affected by the droplet concentration, sound distribution and flow entrainment, resulting in a “breakpoint” in the width of the *DSSR* at D = 4–8 μm for f = 120–210 Hz. As the sound frequency further increased from 220 to 280 Hz, the number of nodal planes in the air chamber increased to 3. Despite the smaller entrainment coefficient of those acoustic operations, the effect of the sound pressure gradient force was stronger. As a result, the width of *DSSR* for acoustic waves with f over 220 Hz was larger.

It has always been a core concern to determine the optimal acoustic parameters to achieve the best agglomeration effect in practice. For a specific DSD, the optimal frequency and effective *SPL* can be determined by laboratory experiments. However, it is inconvenient to conduct experiments due to the inability to simulate DSD and its environmental conditions indoors. Given the width of *DSSR* obtained in this study, acoustic intervention with variable frequency was recommended to obtain better agglomeration performance. Thus, sweep-frequency acoustic intervention was applied to on-site artificial precipitation enhancement (Shi et al., 2021a; Shi et al., 2021b; Wei et al., 2021).

5 Conclusion

In this study, the responses of microdroplets under acoustic intervention of 30–280 Hz are studied through laboratory experiments, numerical simulations and theoretical analysis. Droplet size distribution (DSD), equilibrium response time (*ERT*), the nodal plane in the air chamber and entrainment coefficient were analyzed. The critical *SPL* and its equilibrium response time are presented based on average droplet size increment and the variation of droplet size respectively. The main conclusions are as follows.

(i) For acoustic waves with f = 30–280 Hz, the critical *SPL* is 110 ± 15 dB, and the equilibrium response time was concentrated in 44 ± 12 s, the critical *SPL* and its equilibrium response time varied with acoustic frequency.
(ii) The width of *DSSR* was impacted by the acoustic entrainment, sound distribution, and droplet concentration. The entrainment effect of acoustic waves on the width of *DSSR* decreased with increasing frequency, while the sound pressure gradient effect became significant.
(iii) For the target microdroplets whose optimal frequency is unknown, such as fog or cloud droplets, acoustic intervention with sweep frequency could be used, which can theoretically enhance the intervention effect.

This study did not take into account the trajectory of the droplets under the action of acoustic waves and turbulence flows. In the future, kinematics and dynamic response of droplets under acoustic intervention will be investigated with high-speed cameras.

Data availability statement

The original contributions presented in the study are included in the article/Supplementary Material; further inquiries can be directed to the corresponding authors.

Author contributions

WB: Conceptualisation, Methodology, Writing—Original Draft, Formal Analysis, Investigation; YS: Methodology, Writing—Original draft, Writing—Review and Editing, Supervision, Funding Acquisition; ZZ: Data Curation, Investigation, Formal Analysis; JW: Methodology, Suggestions, Supervision, Project Administration.

Funding

This research was funded by the National Key Research and Development Program [Grant No. 2017YFC0403600]; the Open Research Foundation by State Key Laboratory of Hydroscience and Engineering-Tsinghua University [Grant No. sklhse-2022-B-02]; the National Natural Science Foundation of China [Grant No. 52209092, 52009059]; China Postdoctoral Science Foundation [Grant No. 2021T140385, 2018M641372]; Young Elite Scientist Sponsorship Program by China Association for Science and Technology [Grant No. YESS20200094]; the Shuimu Tsinghua Scholar Program [Grant No. 2021SM010] of Tsinghua University.

Acknowledgments

Zhijie Jiang, Zifei Li, Jing Zhou, Yan Li and Yige Hu participated in the experiment, and their contributions are greatly appreciated.

Conflict of interest

The authors declare that the research was conducted in the absence of any commercial or financial relationships that could be construed as a potential conflict of interest.

Publisher's note

Supplementary material

The Supplementary Material for this article can be found online at: https://www.frontiersin.org/articles/10.3389/fenvs.2022.972648/full#supplementary-material

References

Bai, W., Wei, J., Li, Q., Shi, Y., Ni, S., and Lei, F. (2021a). The hydrogen and oxygen isotope characteristic of droplet collision and deposition under the action of acoustic wave. *J. Appl. Acoust.* 40 (1), 1–11. (in Chinese).

Bai, W., Wei, J., Ni, S., and Shi, Y. (2020). Experimental study on micro-droplet sedimentation under the action of low-frequency acoustic wave. *J. Basic Sci. Eng.* 28 (2), 247–258. (in Chinese).

Bai, W., Wei, J., Shi, Y., Zhao, Z., and Li, Q. (2021b). Microphysical characteristics and environmental isotope effects of the micro-droplet groups under the action of acoustic waves. *Atmos. (Basel).* 12 (11), 1488. doi:10.3390/atmos12111488

Brandt, O., and Hiedemann, E. (1936). The aggregation of suspended particles in gases by sonic and supersonic waves. *Trans. Faraday Soc.* 42 (190), 1101–1110. doi:10.1039/tf9363201101

Chang, H., Kan, C., and Wei, Y. T. (1963). Sonic dissipation of water fog-A preliminary experimental study. *J. Nanjing Univ. Nat. Sci.* 2 (5), 21–28. (in Chinese).

Chen, H., Zhao, B., Xu, J., and Shen, X. (2007). Experimental study on acoustic agglomeration of ultrafine fly ash particles. *Proc. CSEE* 27 (35), 28–32. (in Chinese). doi:10.13334/j.0258-8013.pcsee.2007.35.002

Cheng, M. T., Lee, P. S., Berner, A., and Shaw, D. (1983). Orthokinetic agglomeration in an intense acoustic field. *J. Colloid Interface Sci.* 91 (1), 176–187. doi:10.1016/0021-9797(83)90324-7

Dass, A., Srivastava, S., and Chaudhary, G. (2021). Air pollution: A review and analysis using fuzzy techniques in Indian scenario. *Environ. Technol. Innov.* 22, 101441. doi:10.1016/j.eti.2021.101441

Dong, S., Lipkens, B., and Cameron, T. M. (2006). The effects of orthokinetic collision, acoustic wake, and gravity on acoustic agglomeration of polydisperse aerosols. *J. Aerosol Sci.* 37 (4), 540–553. doi:10.1016/j.jaerosci.2005.05.008

He, F., Li, J., Li, C., Wang, P., Wang, Z., Zhang, M., et al. (2021). Investigation on collision-coalescence of droplets under the synergistic effect of charge and sound waves: Orthogonal design optimization. *J. Phys. D. Appl. Phys.* 55 (7), 075204. doi:10.1088/1361-6463/ac34ac

Hoffmann, T. L., and Koopmann, G. H. (1996). Visualization of acoustic particle interaction and agglomeration: Theory and experiments. *J. Acoust. Soc. Am.* 99 (4), 2130–2141. doi:10.1121/1.415400

Hou, S., Wu, J., and Xi, B. (2002). Experiments on acoustic dissipation of water fog at low frequency. *Exp. Meas. Fluid Mech.* 16 (4), 52–63. (in Chinese).

Liu, D. (2021). Value evaluation system of ecological environment damage compensation caused by air pollution. *Environ. Technol. Innov.* 22, 101473. doi:10.1016/j.eti.2021.101473

Meng, C., Tang, Q., Yang, Z., Cheng, H., Li, Z., and Li, K. (2021). Collaborative control of air pollution in the Beijing–Tianjin–Hebei region. *Environ. Technol. Innov.* 23, 101557. doi:10.1016/j.eti.2021.101557

Qu, G., Fan, F., Zhang, S., and Su, M. (2020). Interaction between monodisperse fine particles in a standing wave acoustic field. *Acta Phys. Sin.* 69 (6), 064704. (in Chinese). doi:10.7498/aps.69.20191681

Shaw, D., and Tu, K. (1979). Acoustic particle agglomeration due to hydrodynamic interaction between monodisperse aerosols. *J. Aerosol Sci.* 10 (3), 317–328. doi:10.1016/0021-8502(79)90047-8

Shi, Y., Wei, J., Bai, W., and Wang, G. (2020). Numerical investigations of acoustic agglomeration of liquid droplet using a coupled CFD-DEM model. *Adv. Powder Technol.* 31 (6), 2394–2411. doi:10.1016/j.apt.2020.04.003

Shi, Y., Wei, J., Li, Q., Yang, H., Qiao, Z., Ren, Y., et al. (2021a). Investigation of vertical microphysical characteristics of precipitation under the action of low-frequency acoustic waves. *Atmos. Res.* 249, 105283. doi:10.1016/j.atmosres.2020.105283

Shi, Y., Wei, J., Ren, Y., Qiao, Z., Li, Q., Zhu, X., et al. (2021b). Investigation of precipitation characteristics under the action of acoustic waves in the source region of the yellow river. *J. Appl. Meteorol. Climatol.* 60 (7), 951–966. doi:10.1175/jamc-d-20-0157.1

Song, L., Koopmann, G. H., and Hoffmann, T. L. (1994). An improved theoretical model of acoustic agglomeration. *J. Vib. Acoust.* 116 (2), 208–214. doi:10.1115/1.2930414

Sotty, J., Garcon, G., Denayer, F. O., Alleman, L. Y., Saleh, Y., Perdrix, E., et al. (2019). Toxicological effects of ambient fine (PM2.5-0.18) and ultrafine (PM0.18) particles in healthy and diseased 3D organo-typic mucocilary-phenotype models. *Environ. Res.* 176, 108538. doi:10.1016/j.envres.2019.108538

Tiwary, R., and Reethof, G. (1986). Hydrodynamic interaction of spherical aerosol particles in a high intensity acoustic field. *J. Sound. Vib.* 108 (1), 33–49. doi:10.1016/s0022-460x(86)80309-1

Tiwary, R., Reethof, G., and McDanie, O. H. (1984). Acoustically generated turbulence and its effect on acoustic agglomeration. *J. Acoust. Soc. Am.* 76 (3), 841–849. doi:10.1121/1.391308

Wei, J., Qiu, J., Li, T., Huang, Y., Qiao, Z., Cao, J., et al. (2021). Cloud and precipitation interference by strong low-frequency sound wave. *Sci. China Technol. Sci.* 64 (2), 261–272. doi:10.1007/s11431-019-1564-9

Yang, X., and Fan, F. (2014). Numerical simulation of the effects of gas temperature and particle density on particle dynamics in acoustic field. *Acta Acust.* 39 (6), 745–751. (in Chinese). doi:10.15949/j.cnki

Yuen, W. T., Fu, S. C., and Chao, C. Y. H. (2017). The effect of aerosol size distribution and concentration on the removal efficiency of an acoustic aerosol removal system. *J. Aerosol Sci.* 104, 79–89. doi:10.1016/j.jaerosci.2016.11.014

Zhang, G., Zhou, T., Zhang, L., Wang, J., Chi, Z., and Hu, E. (2018). Improving acoustic agglomeration efficiency of coal-fired fly-ash particles by addition of liquid binders. *Chem. Eng. J.* 334, 891–899. doi:10.1016/j.cej.2017.10.126

Zhou, D., Luo, Z., Jiang, J., Chen, H., Lu, M., and Fang, M. (2016). Experimental study on improving the efficiency of dust removers by using acoustic agglomeration as pretreatment. *Powder Technol.* 289, 52–59. doi:10.1016/j.powtec.2015.11.009

frontiers | Frontiers in Environmental Science

TYPE Original Research
PUBLISHED 29 August 2022
DOI 10.3389/fenvs.2022.965334

OPEN ACCESS

EDITED BY
Manish Pandey,
National Institute of Technology
Warangal, India

REVIEWED BY
Chongwei Zhang,
Dalian University of Technology, China
Yong Ma,
Sun Yat-sen University, China

*CORRESPONDENCE
Xing Zheng,
zhengxing@hrbeu.edu.cn

SPECIALTY SECTION
This article was submitted to Freshwater Science,
a section of the journal
Frontiers in Environmental Science

RECEIVED 09 June 2022
ACCEPTED 18 July 2022
PUBLISHED 29 August 2022

CITATION
Wang B, Li Y, Gao S, Shen K, Hu Z and Zheng X (2022), Motion characteristics and aero-elastic responses of floating offshore wind turbine under coupling action of waves and winds.
Front. Environ. Sci. 10:965334.
doi: 10.3389/fenvs.2022.965334

Motion characteristics and aero-elastic responses of floating offshore wind turbine under coupling action of waves and winds

Bin Wang[1,2], Ying Li[3], Shan Gao[1,2], Kanmin Shen[1,2], Zhenhong Hu[4] and Xing Zheng[4]*

[1]Key Laboratory of Far-Shore Wind Power Technology of Zhejiang Province, Hangzhou, China, [2]Powerchina Huadong Engineering Corporation Limited, Hangzhou, China, [3]Chinese-German Institute of Engineering, Zhejiang University of Science and Technology, Hangzhou, China, [4]College of Shipbuilding Engineering, Harbin Engineering University, Harbin, China

As a complex multi degree of freedom coupling system, floating offshore wind turbine usually works in complex and changeable marine environment. The research of floating offshore wind turbine often needs to consider the coupling effect of wind, wave and current at the same time. Under the action of wind and wave load, floating offshore wind turbine will produce a large motion response. Generally, the surge motion and pitch motion are the most obvious aspects, and their motion amplitude is also the largest, and large-scale motion of the floating platform will directly affect the relative velocity of the wind loaded flow. Therefore, the surge motion and pitch motion usually have the most obvious impact on the aerodynamic load of wind turbine. In this paper, the motion characteristics and aeroelastic responses of the DTU-10MW semi-floating offshore wind turbine under coupling action of wind and wave are simulated. The motion characteristics and aeroelastic responses of floating offshore wind turbine are calculated under different wind and wave combination conditions, and the influence law of wind and wave action are summarized. The results show that wind load affects the mean value of motion of the floating offshore wind turbine, and wave load affects the amplitude of motion; Finally, the dynamic response of the wind turbine with the included angle of the wind and wave load is discussed and analyzed, and the influence of the incident angle of the wind wave on the motion response of the floating offshore wind turbine is analyzed.

KEYWORDS

floating offshore wind turbine, coupling action, coupling action of waves and winds, motion, aero-elastic responses

Introduction

Under the background of social sustainable development, the development and utilization of offshore wind power reflect the constraint balance among resources and environment and economic development, and has become the mainstream direction of international renewable energy development. Marine wind power does not need to occupy limited land resources, no working noise and environmental pollution. In a large area of sea far from the coastline, the wind power is stable and strong, and the wind energy conversion efficiency is high, which has obvious advantages compared with land wind power (Cao, 2009; Gaumond, et al., 2014; Huijs, et al., 2014; Lo, 2014).

Offshore wind power airports are usually set far away from the coastline and generally in the deep-water area of 100 ~ 200 m. In order to effectively control cost, the installation of wind turbines adopts floating platforms. Compared with fixed wind turbines, floating foundation of floating wind turbines has a certain range of movement under the action of marine environmental loads. The wind turbines are located at an altitude of nearly 100 m from the sea surface, and the slight movement of floating foundation can cause significant changes in the attitude of wind turbines. It affects the system efficiency and puts forward high requirements for the design of fan floating body, transmission and control system.

With the help of the design and analysis technology of large-scale offshore platform, the selection and optimization of floating body in floating offshore wind turbine system, the design of mooring system and the coupling hydrodynamic response analysis of them have a certain foundation (Shi et al., 2018; Zheng et al., 2018). However, due to the difference between hydrodynamic and aerodynamic calculation and analysis technology, some studies ignore the upper turbine load and do not take into account the dynamic response characteristics of wind load; The other part simplifies the load of upper wind turbine as a constant or considers the floating body as fixed when calculating the aerodynamics load. Without considering the real-time spatial position and dynamic characteristics of the structure. (Jonkman and Matha. 2011) used FAST to analyze the hydrodynamic forces of the three types of platforms mentioned. Zhang et al. (2013) designed the floating foundation of a 600 kW fan working in 60 m water depth. The random wave environment suitable for semi-submersible floating body is verified by SESAM. (Latha and Vengatesan. 2013) conducted model test on the hydrodynamic response of a stepped cylindrical (spar) platform wind turbine, and completed numerical prediction by Orcaflex. (Madjid et al., 2011; Madjid, 2013) used two analysis methods to conduct time-domain dynamic simulation and model test for a spar fan moored with single tension bar.

To sum up, each component system of offshore wind turbine integrates the multi domain dynamic coupling analysis technology between water, air and structure. Based on the relevant theories of floating platform, it is a feasible method to calculate and analyze the motion characteristics of floating offshore wind turbine system under wind and wave load by using the existing hydrodynamic analysis method of floating body and the aerodynamic load program of wind turbine. In this paper, FAST code (Wind nrel, 2003) is used to analyze and calculate the motion and aeroelastic response of floating offshore wind turbine, in which BEM (Blade Element Momentum) is used to calculate the aerodynamics load and the potential flow method is used to calculate the motion of floating platform.

Theoretical model

Blade-element momentum theory

The basic idea of the blade element theory is to simplify the wind turbine blade into a number of blade elements with the length of dr along the spreading direction. It is assumed that there is no interaction between each segment of the blade element and that the force acting on the blade element is only directly related to the inflow momentum in the sweep ring of the blade element. Inflow through the adjacent blade element ring does not induce it. In this way, the force on the whole blade can be approximated by the force along the span integral of the two-dimensional airfoil on each blade element. Blade element momentum theory is based on blade element aerodynamic theory and momentum conservation principle. Velocity triangles and force vectors of leaf elements are shown in Figure 1.

In Figure 1, D is the drag force; L is lift force; $v_\infty (1 - a)$ is the axial velocity; $\Omega r (1 + a')$ is the tangential velocity; r is the span location of the blade element; v_∞ is the distant wind speed upstream of the wind wheel; Ω is the angular velocity of the wind wheel; a is axial inducible factor; a' is tangential inducible factor; α is angle of attack; β is torsion angle; φ is inflow angle.

Axial induced factor a and tangential induced factor a' respectively defined by the following formula:

$$\boldsymbol{a} = \frac{\Delta \boldsymbol{v}}{\boldsymbol{v}_\infty} = \frac{\boldsymbol{v}_\infty - \boldsymbol{v}}{\boldsymbol{v}_\infty} \tag{1}$$

$$\boldsymbol{a}' = \frac{\boldsymbol{v}_t}{2\boldsymbol{\Omega r}} \tag{2}$$

where v is the wind speed before the wind wheel, and v_t is the tangential velocity of the airflow at the wind wheel.

The axial induced velocity of the airflow is as follow:

$$\boldsymbol{v}_d = \boldsymbol{v}_\infty (1 - \mathrm{a}) \tag{3}$$

The tangential induced velocity of the airflow is as follows:

$$\boldsymbol{v}_t = \Omega \boldsymbol{r}\left(\mathbf{1} + \mathbf{a}'\right) \tag{4}$$

The relative velocity of airflow synthesis is as follows:

$$\mathbf{w} = \sqrt{\boldsymbol{v}_{\mathrm{d}}^2 + \boldsymbol{v}_t^2} = \sqrt{\boldsymbol{v}_\infty^2 (\boldsymbol{1} - \boldsymbol{a})^2 + \left(\boldsymbol{1} + \boldsymbol{a}'\right)^2 (\boldsymbol{\Omega r})^2} \tag{5}$$

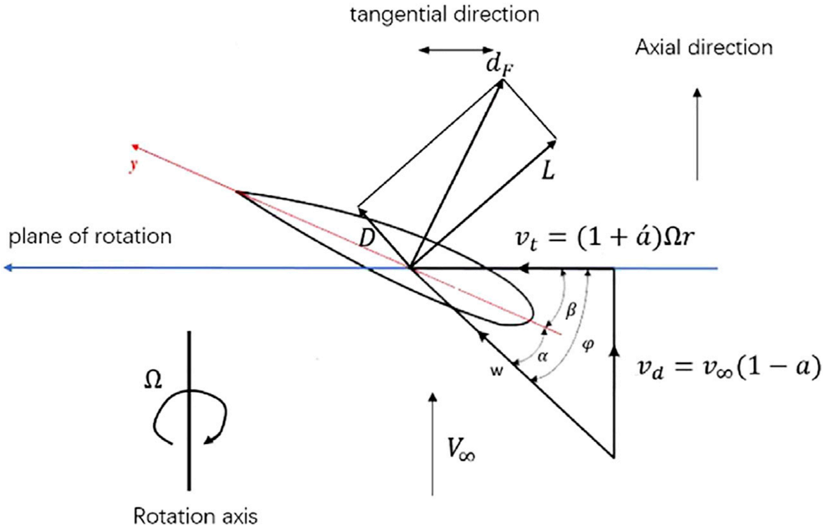

FIGURE 1
Blade element velocity triangles and force vector diagrams.

The inflow angle of airflow is as follows:

$$\boldsymbol{\varphi} = \mathbf{arctan}\left[\frac{\boldsymbol{v_\infty}\,(\mathbf{1}-\mathbf{a})}{(\mathbf{1}+\boldsymbol{a}')\boldsymbol{\Omega r}}\right] \tag{6}$$

According to the conservation of energy and momentum, the thrust and torque received by the wind wheel are shown as follows:

$$dF = 4\pi\rho v_\infty^2 \boldsymbol{a}(\mathbf{1}-\boldsymbol{a})\boldsymbol{r}\boldsymbol{dr} \tag{7}$$

$$dM = 4\pi\rho\Omega v_\infty(1-a)a'\boldsymbol{r}^3\boldsymbol{dr} \tag{8}$$

Based on the blade element theory, the thrust and torque of the wind wheel are respectively shown as follows:

$$dF = N(Lcos\varphi + Dsin\varphi) = \frac{1}{2}\rho W^2 Nc(C_L\cos\varphi + C_D\sin\varphi)dr \tag{9}$$

$$\begin{aligned} dM &= N(Lsin\varphi - Dcos\varphi)r \\ &= \frac{1}{2}\rho W^2 Nc(C_L\sin\varphi - C_D\cos\varphi)rdr \end{aligned} \tag{10}$$

Equations 7, 9 respectively represent the thrust of the wind wheel derived from momentum conservation and blade element theory. Equations 8, 10 respectively represent the torque of the wind wheel derived from momentum conservation and blade element theory. Equations 7, 9 are established simultaneously, and then Equations 8, 10 are established concurrently. In this way, the relationship between axial inducible factor and tangential inducible factor and blade chord length and inflow angle can be obtained:

$$\frac{a}{1-a} = \frac{Nc}{8\pi r}\,\frac{C_L\,\boldsymbol{cos\varphi} + C_D\,\boldsymbol{sin}\,\varphi}{(sin\varphi)^2} \tag{11}$$

$$\frac{a'}{1+a'} = \frac{\boldsymbol{Nc}}{\boldsymbol{8\pi r}}\,\frac{C_L\,\boldsymbol{sin}\,\varphi - C_D\,\boldsymbol{cos}\,\varphi}{sin\varphi cos\varphi} \tag{12}$$

where C_L is the lift coefficient of airfoil, C_D is the drag coefficient of airfoil, which can be generally obtained by referring to the airfoil data table.

When evaluating, first initialize a and a', we assume that $a = a' = 0$; Then, the inflow angle φ is calculated according to the Eq. 6.

After obtaining the inflow angle, the airfoil's angle of attack can be determined by the following formula:

$$\boldsymbol{\alpha} = \boldsymbol{\varphi} - \boldsymbol{\beta} \tag{13}$$

Further, lift coefficient C_L and drag coefficient C_D are obtained by referring to airfoil data table. Then a and a' are obtained by Eqs 11, 12, and repeat the above steps until a and a' are convergent. Finally, the final calculated a and a' can be substituted into Eqs 9, 10 to calculate the aerodynamic loads of the blade.

Potential flow method

Basic assumptions: 1) the floating platform is a rigid body and its elastic deformation is ignored; 2) The waves acting on the floating foundation are micro amplitude waves, and the nonlinear effects such as wave breaking, shallow water effect; 3) The floating foundation makes micro amplitude simple harmonic vibration near its equilibrium position, which simplifies the force and motion of the floating foundation under the action of waves into a linear problem, which is applicable to the superposition principle (Merz, et al., 2009;

Pu et al., 2012; Ning, et al., 2018; Yu et al., 2020; Ma et al., 2022; Yu et al., 2022). Considering only the first-order velocity potential, the frequency domain motion equation of floating platform under the action of inertia force, damping force, hydrostatic restoring force, mooring system restoring force and first-order wave force is established according to the principle of dynamic force balance:

$$\left\{-\boldsymbol{\omega}^2\left[\boldsymbol{M}+\boldsymbol{A}(\boldsymbol{\omega})+\boldsymbol{i\omega}\left[\boldsymbol{B}(\boldsymbol{\omega})_{\boldsymbol{p}}+\boldsymbol{B}_{\boldsymbol{v}}\right]+\boldsymbol{C}+\boldsymbol{C}_{\boldsymbol{e}}\right]\right\}\boldsymbol{X}(\boldsymbol{x},\boldsymbol{\beta})=\boldsymbol{F}(\boldsymbol{\omega},\boldsymbol{\beta}) \tag{14}$$

where ω is the frequency of incident wave; M is the inertia matrix of floating foundation; $A(\omega)$ is the additional mass matrix related to frequency is composed of additional mass A_{ij}; $B(\omega)p$ is the frequency dependent potential flow damping matrix; B_v is the linear damping matrix related to fluid viscosity; C is hydrostatic restoring stiffness matrix; C_e restoring stiffness matrix of mooring system; β is the propagation direction of incident wave; X (x, β) is the motion matrix of floating foundation; F (ω, β) is the wave excitation force matrix, which is composed of wave excitation force acting on large-scale structure and inertial force and drag force acting on small-scale structure; i is an imaginary number unit, which satisfies $i^2 = -1$.

For various marine engineering structures, the wave loads they are subjected to can be classified as drag force, inertia force and diffraction force. For different structures, the proportion of various wave-induced load components is different, so the wave load should be calculated reasonably according to the structure size. When calculating the wave loads acting on the floating platform, since the platform of floating offshore wind turbine is usually a combination of two scales, such as large-scale buoy and small-scale circular pipe, this paper combines Morison equation and potential flow theory to calculate the wave loads on the floating platform. For smaller structures (diameter is generally less than 1/5 of wave wavelength), the existence of structures has no significant influence on wave motion. The main effects of waves on structures are viscous effect and additional mass effect. In this case, the Morison equation can be used to calculate the wave forces. The transverse wave load dF_i^h per unit length is:

$$\boldsymbol{dF_i^h} = \boldsymbol{\rho}\mathrm{A}\dot{\boldsymbol{u}} + \boldsymbol{\rho}\mathrm{AC}_{\boldsymbol{m}}\left(\dot{\boldsymbol{u}} - \ddot{\boldsymbol{\xi}}_{\boldsymbol{j}}\right) + \frac{1}{2}\boldsymbol{\rho}\mathrm{DC}_{\boldsymbol{d}}\left|\boldsymbol{u} - \cdot\,\xi_j\right|\left(\boldsymbol{u} - \cdot\,\boldsymbol{\xi}_{\boldsymbol{j}}\right) \tag{15}$$

where $\rho A\dot{u}$ is Froude-Krylov force; $\frac{1}{2}\rho DC_d|u-\dot{\xi}_j|(u-\dot{\xi}_j)$ is the drag force; and $\rho AC_m(\dot{u}-\ddot{\xi}_j)$ is the added mass force; ρ is the density of seawater; A is the cross-sectional area of slender structure; u and $\dot{u}$ are the velocity and acceleration of wave particles respectively; D is the diameter of slender structure; $\dot{\xi}_j$ and $\ddot{\xi}_j$ are the velocity and acceleration of the floating foundation in the j direction respectively; C_m and C_d are added mass coefficient and drag coefficient respectively.

For the wave load of large-scale structures (the diameter is generally greater than 1/5 of the wavelength), the potential flow theory is usually used to calculate the velocity potential. In the basin where the floating platform is located, the velocity potential consists of three parts consists of three parts: undisturbed incident velocity potential ϕ_ω, diffraction velocity potential of the floating platform ϕ_d and radiation velocity potential ϕ_j which is caused by the movement of the floating platform, that is:

$$f = \mathrm{f}_\omega + \mathrm{f}_\mathrm{d} + \sum_{\mathrm{j}=1}^{6}\mathrm{f}_\mathrm{j} \tag{16}$$

The fluid in the basin near the ocean structure is an ideal fluid, then the problem of solving the velocity potential of wave field can be simplified to solving the Laplace equation with corresponding fluid boundary conditions. The wave field calculation of irregular structures in offshore engineering needs to be realized by numerical method. Usually, the boundary element method is used to calculate the linear wave frequency response of large-scale structures in regular waves. The specific calculation process is as follows (Qu, et al., 2013): 1) the wet surface of the platform is divided into several grids to form several panel elements. Based on the source sink distribution method, it is assumed that the surface sources with equal strength are distributed on each panel element; 2) Combined with Laplace equation and the boundary conditions of radiation potential and diffraction potential, the intensity of surface source is solved; 3) The intensity of the surface source is integrated along the wet surface grid to calculate the radiation potential and diffraction potential respectively, so as to determine the velocity potential in the flow field.

Reference data of OO-Star wind floater semi DTU-10MW

The model used in this paper is OO-Star Wind Floater Semi DTU-10MW (2016). The upper part of this floating wind turbine model is a DTU-10MW wind turbine model, which is a reference wind turbine model designed by the Technical University of Denmark in 2013. On the other hand, the OO-STAR semi-submersible platform is used in the lower part of the floating wind turbine model. The OO-Star Wind Floater Semi DTU-10MW floating offshore wind turbine model is shown in Figure 2 below.

The DTU 10-MW wind turbine is a conventional three-blade upwind variable-speed variable-blade-pitch-to-feather-c*ontrolled turbine. Its rotor diameter is about 178.4 m and the hub height is nearly 119 m. The rated wind speed is 11.4 m/s. Under the rated wind speed, the rotor speed is 9.6 rpm and the power is 10 MW.

The blades are separated into 38 blade elements and the structure of the blades used in BEM can refer to Wandji et al. (2016). Additionally, the radius of the tower top is 5.5 m and the radius of the tower bottom is 8.3 m, which is linearly distributed along the tower.

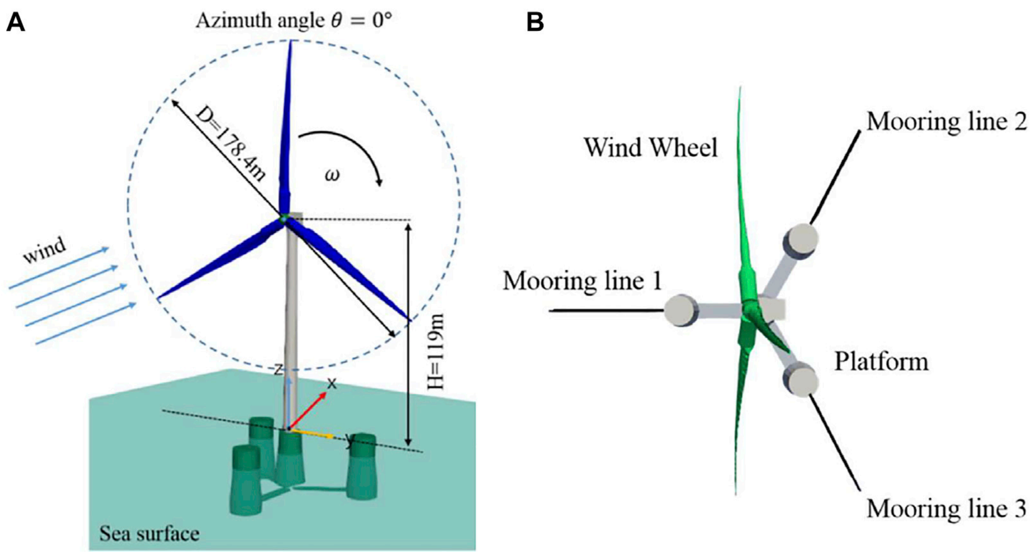

FIGURE 2
Geometry of OO-Star Wind Floater Semi DTU-10MW and mooring system: **(A)** geometry model; **(B)** mooring system.

TABLE 1 Properties of DTU -10 MW wind turbine and OO-Star Semi floating substructure.

Parameters	Value
Number of blades (-)	3
Rated power (MW)	10
Rotor diameter (m)	178.4
Hub height (m)	119
Rated wind speed (m/s)	11.4
Rated speed (rpm)	9.6
Overall substructure mass (kg)	2.1709×10^{7}
Centre of Mass (CM) below MSL (m)	15.225
Substructure roll inertia about CM (kg m^2)	9.43×10^{9}
Substructure pitch inertia about CM (kg m^2)	9.43×10^{9}
Substructure yaw inertia about CM (kg m^2)	1.63×10^{10}
Tower base interface above MSL (m)	11.0
Displaced water volume (m^3)	2.3509×10^{4}
Centre of buoyancy below MSL (m)	14.236
Anchor position below MSL (m)	130
Equivalent weight per length in water (N/m)	3200.6
Extensional stiffness EA (N)	1.506×10^{9}

The OO-Star Semi Floating Substructure is a semi-submersible platform consisting of a star-shaped base buoy that connects a central column and three outer columns. All pillars have a cylindrical upper part and a tapered lower part. The distance between the central column and the outer column is 37 m. The horizontal buoy element connecting the columns is 16 m wide and 7 m high. The total mass of the platform, including ballast, is 21,709 tons.

The mooring system of DTU-10MW semi-submersible floating wind turbine is composed of three mooring lines, each of which is distributed centrally at a horizontal angle of 120°. The properties of the DTU-10MW model, structural attributes of the platform and specific mooring system parameters are shown in Table 1.

Model validation

Thrust and power

To examine the accuracy of different wind speeds, the thrust and power are computed and compared with the value computed by CFD method and HWACStab2 code (Wandji, et al., 2016), which are shown in Figure 3. The results agree with CFD and HWACStab2 code excellently for the wind speeds from 5 m/s to 25 m/s. In this verification part, the degree of freedom of platform movement is turned off to ensure that the influence caused by platform movement is excluded.

Free decays

The free decays of OO-Star semi-submersible platform model are carried out to verify the model. An initial displacement is given for each degree of freedom (DOF) of the floating offshore wind turbine system, and then it is allowed

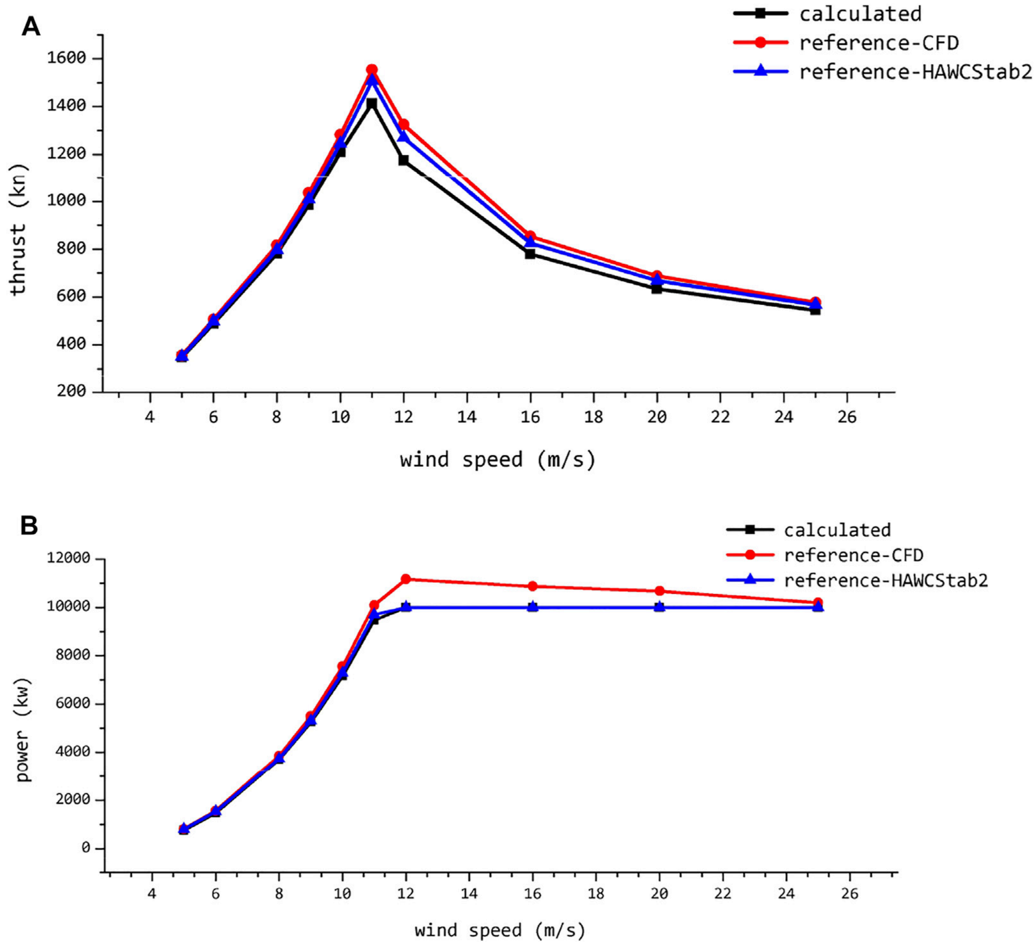

FIGURE 3
The thrust and power under different wind speeds: **(A)** thrust; **(B)** power.

to decay freely to the equilibrium position. An initial displacement of 15 m is given for the surge and heave motions, and an initial deflection angle of 10° is given for pitch and yaw motions. In the free decays simulation process of the floating offshore wind turbine system, the wind turbine is always in the shutdown condition with no incoming wind and wave.

The free decays of the floating offshore wind turbine system are numerically simulated by using FAST code, and the time series responses of the platform movement are obtained, and they are shown in the Figure 4. The natural frequencies of each degree of freedom are obtained by Fourier transform of the time series response.

The natural frequencies obtained are compared with the reference value in the report of DTU (Wandji, et al., 2016) in Table 2. The errors are all smaller than 2% which means the results are in good agreement with the reference data.

Motion characteristics and aero-elastic responses of DTU-10MW FOWT

In this section, the motion characteristics and aeroelastic responses of the DTU-10MW Turbine under the action of wind and wave coupling are studied. By comparing with the output power and thrust of the fix wind turbine, the influence of the floating platform motions on the aeroelastic response of the upper turbine is analysed. The motion characteristics and elastic response of the floating offshore wind turbine are calculated under different wind and wave combination conditions, and the effects of wind and wave are summarized. Finally, the dynamic response of the floating offshore wind turbine with the wind-wave Misalignment is discussed and analysed, and the effect of the incident angle of wave on the motion responses of the floating wind turbine is analysed.

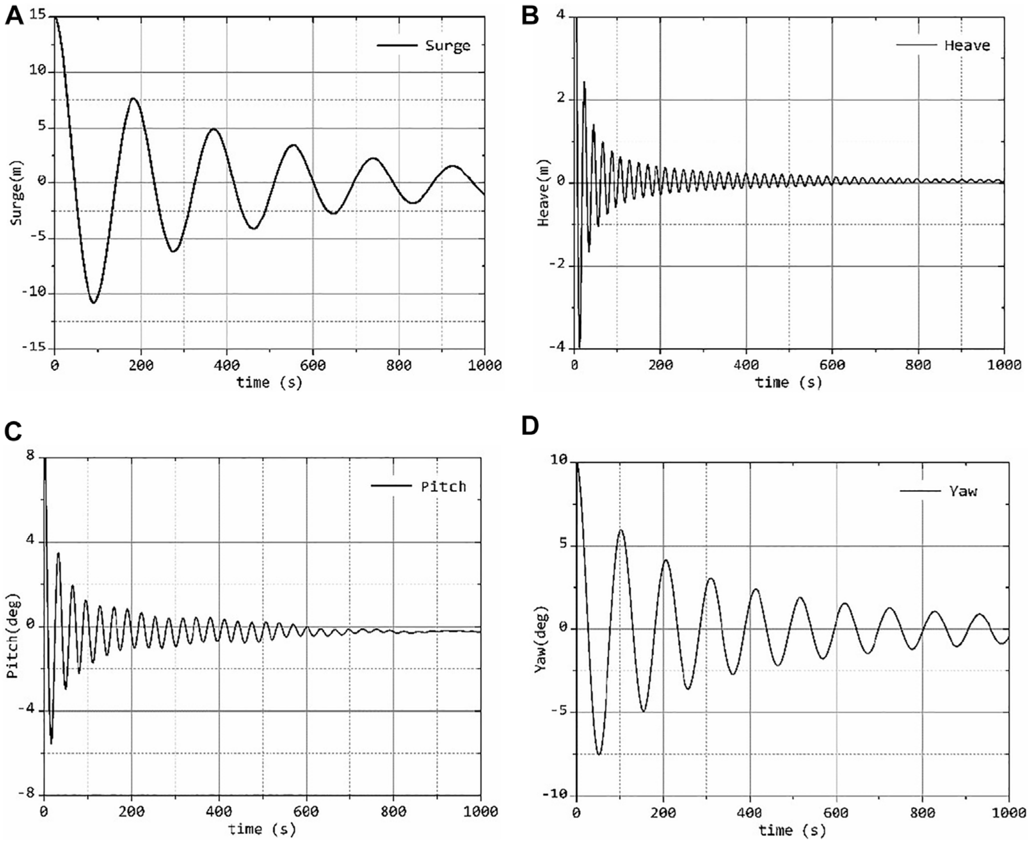

FIGURE 4
The free decay of the OO-Star platform: **(A)** Surge; **(B)** Heave; **(C)** pitch; **(D)** Yaw.

TABLE 2 The natural frequencies of the free decays.

	Surge (m)	Heave (m)	Pitch (deg)	Yaw (deg)
Calculated values	0.0053	0.0476	0.0314	0.0096
Reference values	0.0054	0.0478	0.0316	0.0097
error	1.296%	0.418%	0.633%	0.412%

TABLE 3 The list of the cases.

Case	Wave		Wind	
	Wave form	Period (s)	Wave height (m)	Wind speed (m/s)
DLC 1	Still Water	—	—	5
DLC 2	Still Water	—	—	8
DLC 3	Still Water	—	—	11.4
DLC 4	Regular Wave	10	4	11.4
DLC 5	Regular Wave	10	5	11.4
DLC 6	Regular Wave	12	4	11.4
DLC 7	Irregular Wave	10	4	11.4

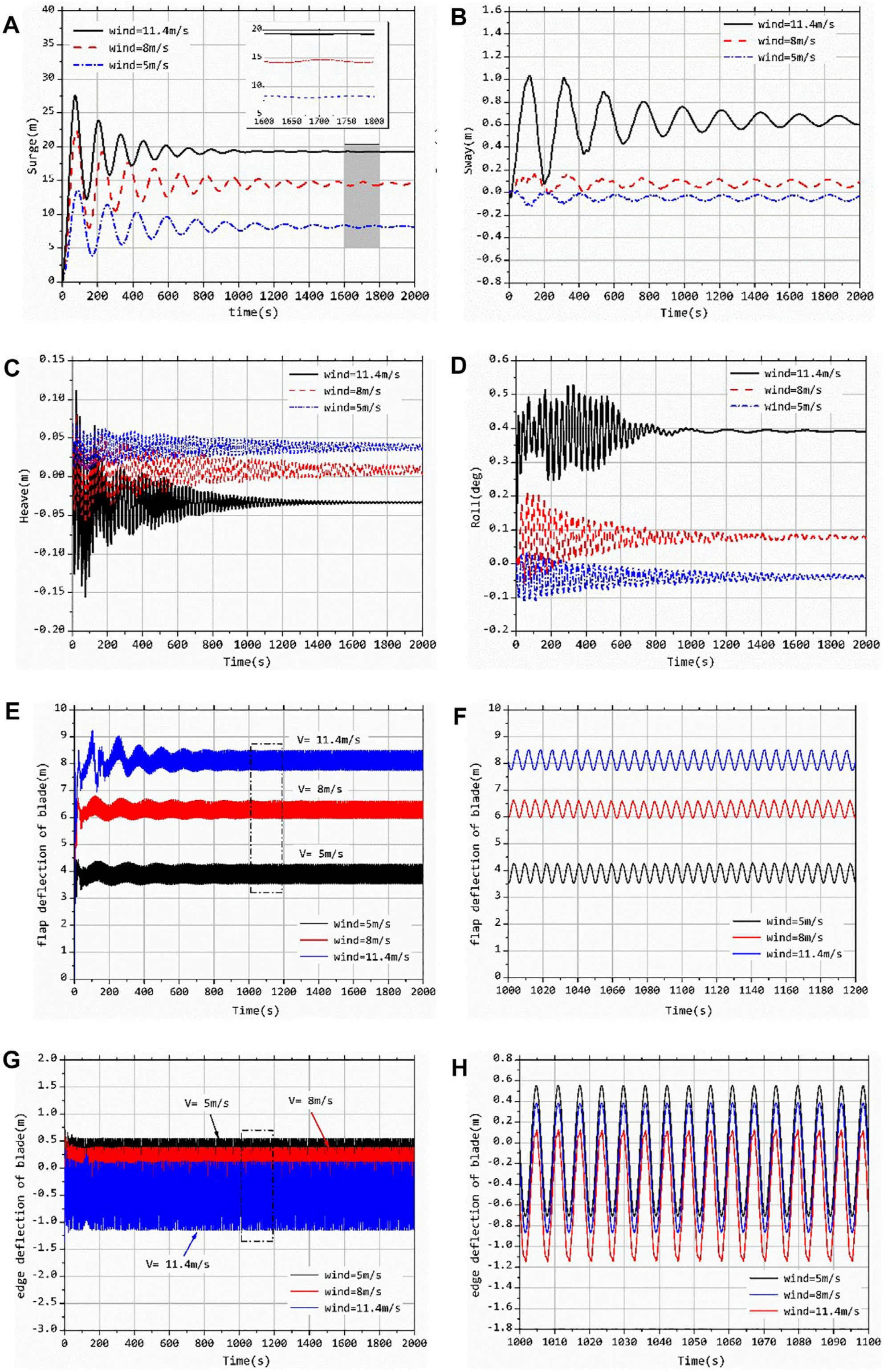

FIGURE 5
Motions of floating platform and deflection under different wind speeds: **(A)** Surge; **(B)** Sway; **(C)** Heave; **(D)** Roll; **(E)** pitch; **(F)** Yaw; **(G)** flap deflection; **(H)** partial enlargement in flap deflection.

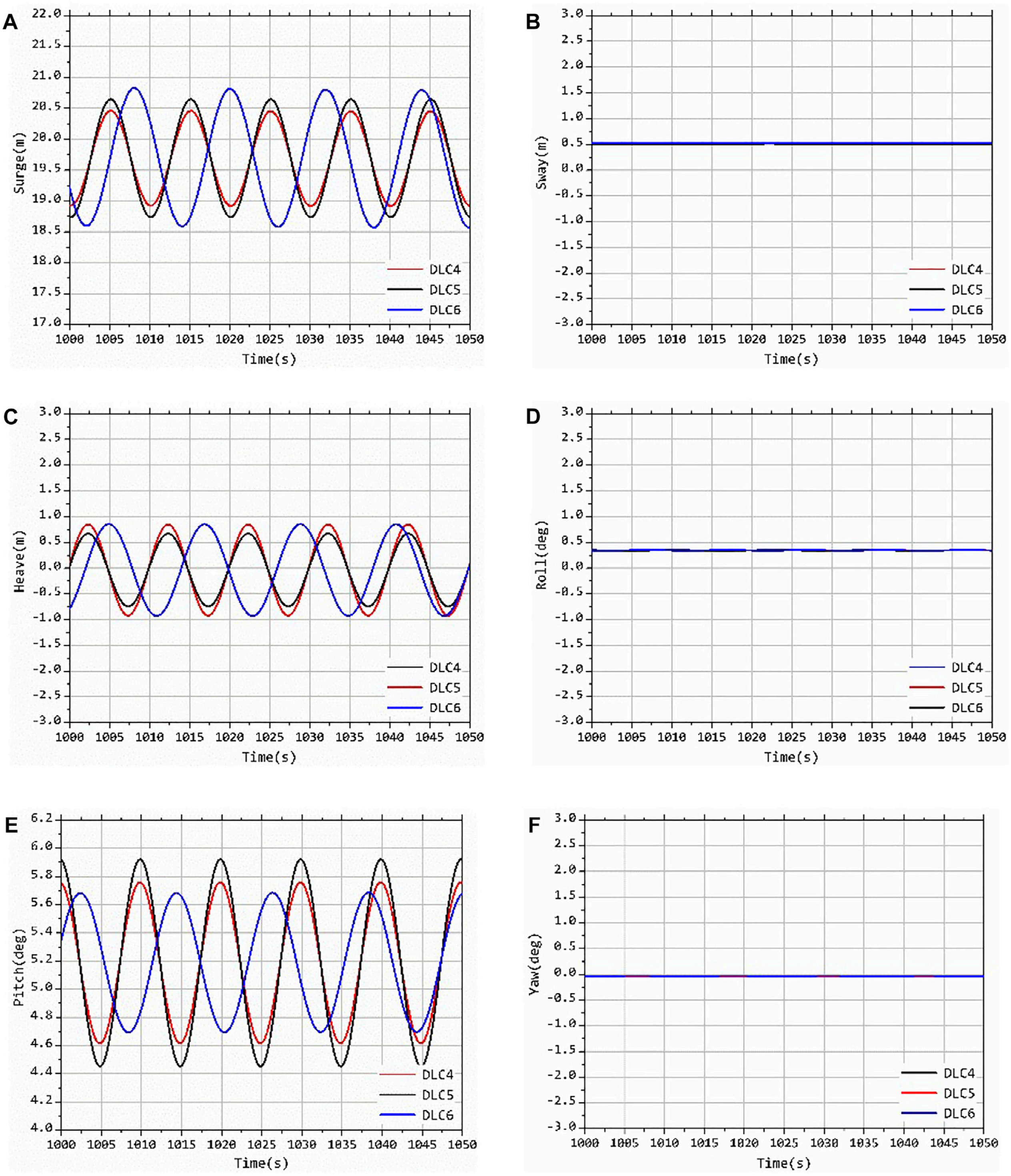

FIGURE 6
Motions of the platform under the regular wave: **(A)** Surge; **(B)** Sway; **(C)** Heave; **(D)** Roll; **(E)** pitch; **(F)** Yaw.

The coupling effect of wind and wave on offshore floating wind turbine in actual operation is mainly considered. The motion characteristics and aeroelastic response of the fan under the coupling action of wind and wave are studied by selecting the combined wind and wave loads with different parameter characteristics. As shown in Table 3, uniform wind

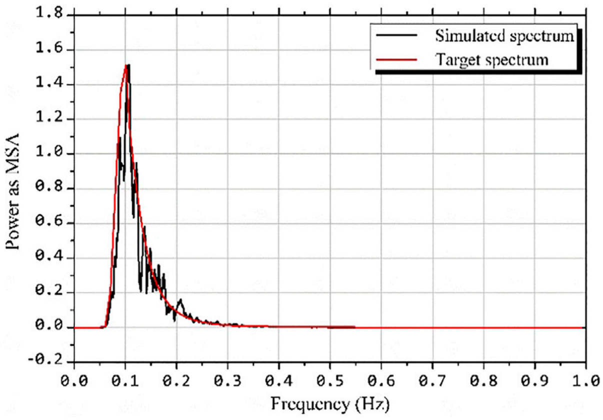

FIGURE 7
Comparison between simulated wave elevation frequency spectrum and target spectrum.

load is selected for wind load; as for hydrostatic load, regular wave load and irregular wave load are selected for wave load, and JONSWAP spectrum is selected for irregular wave. DLC1 ~ DLC3 (Design Load Case) conditions are selected to study the effect of wind speed on the motion characteristics and the aeroelastic response of blades under still water hydrostatic load. DLC4 ~ DLC6 are selected to study the effect of different significant wave heights and wave cycles on the motion characteristics of the turbine under regular waves. DLC7 is selected to study the motion response and aerodynamic load characteristics of floating wind turbine under irregular wave, and the effect of wave load form is analysed by comparing with the motion response of the wind turbine under the regular wave.

Compared with the onshore wind turbine, the floating offshore wind turbine is larger in size which means it needs to bear greater aerodynamic load during operation. What's more is that the complex aerodynamic loads acting on the wind wheel will have a great impact on the motion of the floating platform, which in turn will affect the relative inflow conditions of the upper turbine. Therefore, the motion response calculation of the floating offshore wind turbine is very challenging. All calculation examples in this section adopt the elastic model, that is, the aeroelastic responses of the wind turbine are considered, and the six degrees of freedom of the platform are considered in the simulation of the floating offshore wind turbine.

Effect of the wind load

Motion characteristic

In this section, the corresponding platform motions under different wind speed conditions are calculated, and then the influence of different wind speeds on the motion response of the whole floating wind turbine under hydrostatic load is obtained. The following Figures 5A–F show the time history curve of the six DOFs motion of the floating platform under different wind speeds, in which the wind speeds are set as 5 m/s, 8 m/s and 11.4 m/s respectively.

From the Figure 5, the aerodynamic loads of the turbine make the platform produce a six DOFs motion response, in which surge motion and pitch motion are the main motion forms. Under the action of the aerodynamic thrust generated by the wind wheel, the platform will produce very obvious surge motion and pitch motion (see Figures 5A,E); The aerodynamic load and hydrodynamic load will cause the platform to produce corresponding micro amplitude roll and sway motion (see Figures 5B,D); Heave motion and yaw motion are affected by other motions, resulting in coupling response and fluctuation. Below the rated wind speed, the corresponding displacement response value of each DOF increases with the increase of wind speed, and the surge motion is the most obvious, which indicates that the equilibrium position of each DOF motion of the platform is obviously affected by the wind load under the action of uniform wind. In addition, it is worth noting that with the increase of inflow wind speed, the frequency of platform surge motion increases, beside the time required for platform motion to stabilize under the wind speed of 11.4 m/s is shorter. This is because under the action of wind speed of 11.4 m/s, the equilibrium position of platform surge displacement is largest, the tension degree of mooring lines is larger, and the restoring force provided is larger, which affects the frequency of surge movement. Because of this, when the wind speed increases, the vertical component of the tension provided by the mooring lines increases, resulting in a negative shift in the equilibrium position of the platform heave.

Aero-elastic response

Figures 5G,H have shown the time history curve of blade tip deflection under DLC1 ~ DLC3 working conditions which are consistent with Table 3. As can be seen from the figure that the vibration dominant frequency of blade tip deflection is consistent with the rotation frequency of wind turbine, indicating that the rotation of wind turbine will cause the periodic change of aerodynamic force and then stimulate the periodic change of blade elastic deformation response. Besides, it can be seen that the surge motion of the floating platform will cause corresponding low-frequency fluctuation of blade tip deflection in the range of 0 ~ 1,000 s in Figure 5G, and the surge motion amplitude of the platform is the largest under the wind speed of 11.4 m/s, so the corresponding blade tip deflection fluctuation is also the largest. When the platform motions are relatively stable, the vibration of blades in the direction of the flapwise and the edgewise becomes stable, which is the same as the blades of onshore wind turbine. The inflow wind speed is still the main factor affecting the mean value of blade vibration, but it has little influence on the amplitude of vibration.

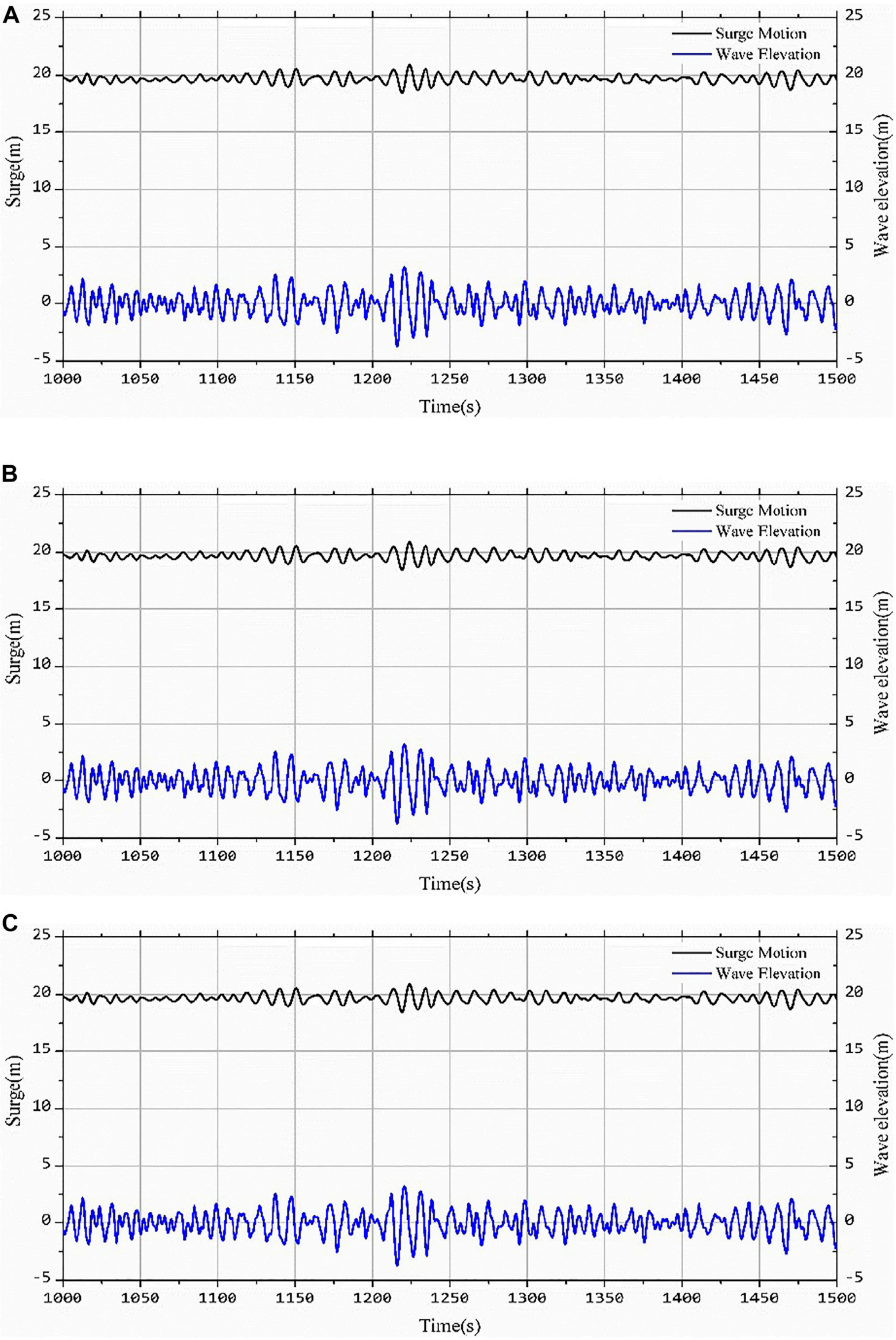

FIGURE 8
Motion response and wave height time history curve of floating fan under the irregular wave: **(A)** Surge; **(B)** Heave; **(C)** Pitch.

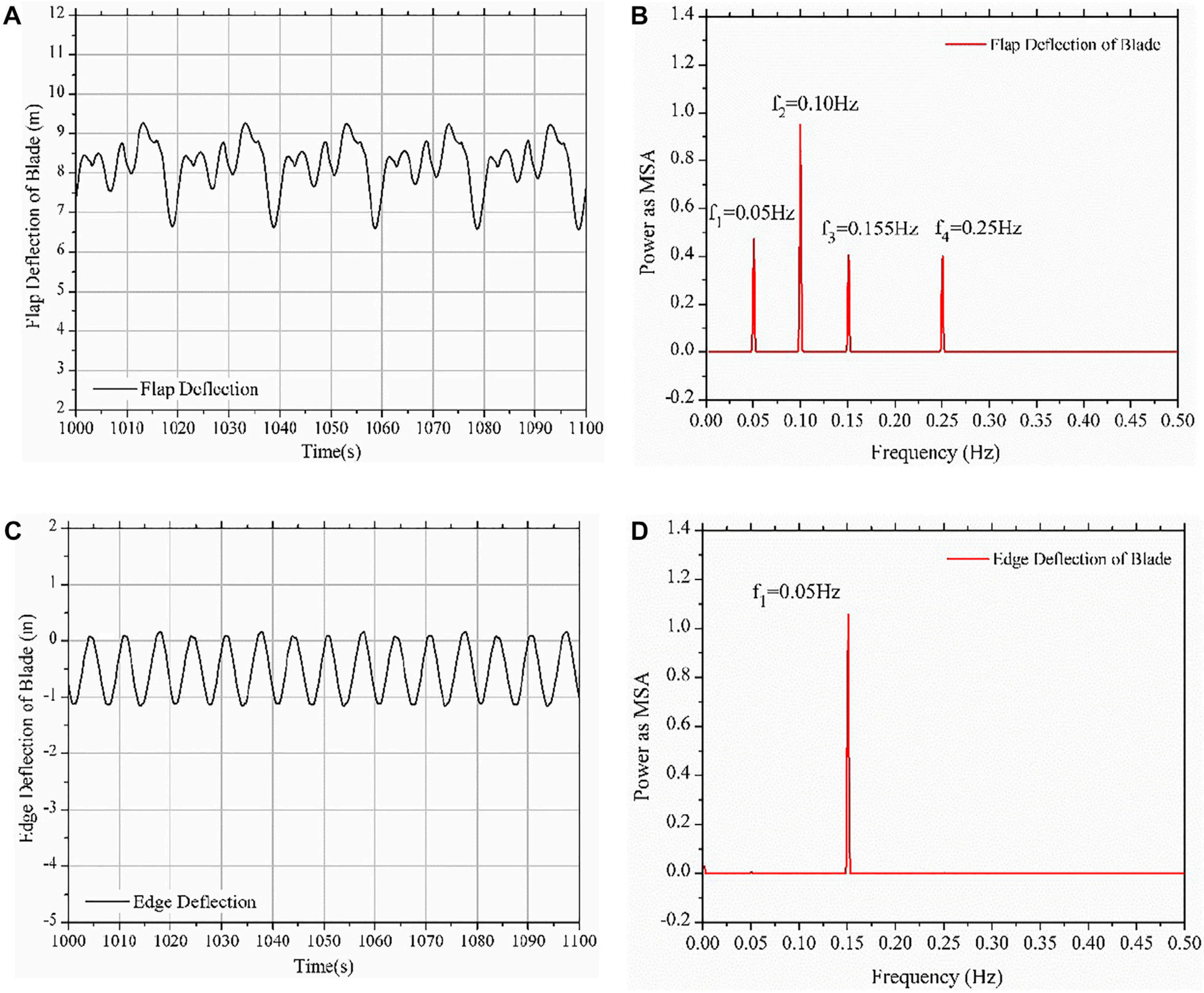

FIGURE 9
Deflections under different regular waves: **(A)** the time history of the flap deflection; **(B)** the power spectrum of the flap deflection; **(C)** the time history of the edge deflection; **(D)** the power spectrum of the edge deflection.

Effect of the wave load

Motion characteristic under regular wave

In this section, the simulation and calculation are carried out for the working conditions of DLC4 ~ DLC6 which have shown in Table 3. The motion responses of the floating wind turbine system under the combined action of regular wave and uniform wind are calculated. The whole simulation time is 2000 s, and 1,000 s ~ 1,050 s of the stable section is taken as the output result. The six DOFs motions of floating offshore wind turbine system under corresponding working conditions of DLC4 ~ DLC6 are given in Figure 6 below.

When the regular wave flows into the front, the motion response of the floating offshore wind turbine produce surge, pitch motion and heave motion caused by the coupling effect. Because the wave and wind load flow directions are perpendicular to the rotation plane of the wind turbine, that is, consistent with the surge direction, the surge motion amplitude response of the floating offshore wind turbine system is the largest in these simulations, and the large-scale surge motion of the platform causes the pitch motion and the heave motion; For the floating platform, the load is very small in the sway, roll and yaw motion directions, so the movement is relatively stable. It can be seen from Figure 6 that after changing the wave conditions, the equilibrium position of each degree of freedom motion is basically the same, but the motion amplitude changes significantly.

It can be seen from Figure 6 that under the action of regular wave and uniform wind, the changes of wave period and

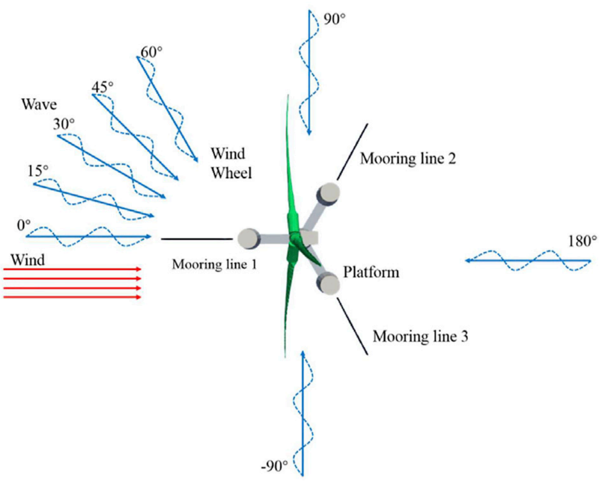

FIGURE 10
Wind-wave load setting.

significant wave height have a great impact on the surge, pitch and heave motion of the floating offshore wind turbine system. The amplitude of surge, pitch and heave will increase with the increase of significant wave height. The increase of wave period will obviously increase the amplitude of surge motion, and the amplitude of heave motion will increase accordingly, but it has little effect on the pitch motion. It can be seen that for the floating offshore wind turbine system, the wind load mainly determines the mean value of each degree of freedom motion, while the wave load mainly affects the amplitude of each degree of the freedom motion.

Motion characteristic under irregular wave

Compared with the regular wave load in the ideal state, the irregular wave load is more accord with the real wave load environment at sea. In this section, the irregular wave incident load is selected based on the typical sea conditions in the South China Sea, and the JONSWAP spectrum is selected as the wave spectrum. The DLC7 working condition is set in Table 3 for specific parameters. Figure 7 shows the comparison results between the frequency spectrum of the wave elevation and the target spectrum used for calculation in the process of wave load simulation. The power spectrum of irregular waves simulated in this paper is in a good agreement with the target spectrum, which shows that the method in this paper can simulate the sea state of irregular waves well, and the simulation setting of irregular wave load is correct.

Figure 8 shows the motion response of the floating offshore wind turbine in the surge, heave and pitch directions under irregular wave load and the time history curve of the wave elevation at the center of the platform. It can be seen from the figure that the surge, heave and pitch motion trends of the floating offshore wind turbine are very consistent, and the change trend is basically the same as that of the wave elevation. There is an obvious sudden change in amplitude of the surge, pitch and heave motion of the floating fan in the period of 1,200 s–1,250 s. It is found that the time history curve of wave elevation corresponds to the maximum change of wave load at this time. This shows that under the action of irregular waves, the motion response of the platform is directly related to the change of waves, that is, the motion response of each degree of freedom increases with the increase of wave height. The equilibrium positions of heave, heave and pitch motion of the platform under this group of working conditions are 19.6926 m, −0.0361 m and 5.187° respectively. Compared with the motion response of the platform under the action of regular wave under DLC4 working condition, it is found that the equilibrium position of each degree of freedom motion is basically the same, and the reason for the slight difference is the slight difference of aerodynamic load caused by the different motion of the platform. It shows again that the main factor is the wind load determining the balance position of the floating offshore wind turbine system under the wind-wave coupling, and the influence of the wave load on the balance position is very small.

Aero-elastic response

The blade elastic deformation is mainly determined by the aerodynamic load acting on the blade. Under the action of regular wave, the blade needs to bear periodic aerodynamic load, so the blade will produce corresponding elastic deformation response. Figure 9 shows the blade flap deflection and edge deflection responses of the blades under DLC4 working condition and the corresponding frequency domain response values.

It can be seen from Figure 9 that under the action of regular wave, the blade has periodic deformation response in the flapwise direction, which is different from the displacement response of onshore fixed wind turbine. Under the action of regular wave, there is a very obvious low-frequency vibration response in the flapwise direction of blade. The frequency of blade vibration can be obtained by Fourier transform of the time history response of blade flap deflection in the stable stage. There are four frequencies: f_1 = 0.05 Hz, f_2 = 0.10 Hz, f_3 = 0.155 Hz and f_4 = 0.25 Hz.

Where f_1 = 0.05 Hz corresponds to one-third rotor rotation frequency, which is caused by the tower shadow effect; f_2 = 0.10 Hz corresponds to wave frequency; f_3 = 0.155 Hz corresponds to rotor rotation frequency; and f_4 = 0.25 Hz corresponds to the first-order vibration frequency of the tower, which shows that wave load, rotor rotation speed and vibration response of the tower will have a great impact on the vibration in the flapwise direction of the blade. On the other hand, the displacement amplitude of the blade in the edge direction is small, and the vibration form is mainly simple

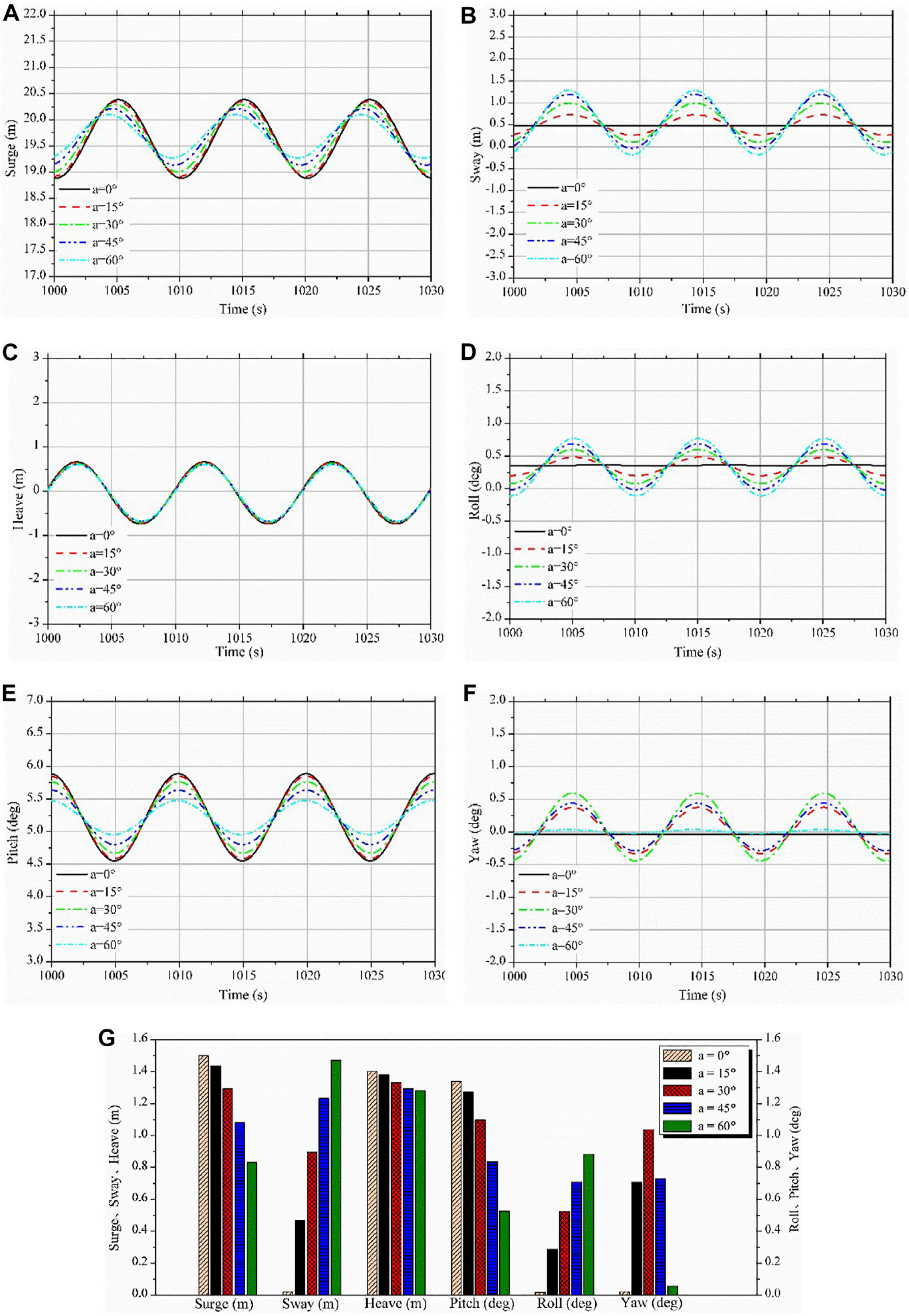

FIGURE 11
Motions of floating platform under different wave incidence angles: **(A)** Surge; **(B)** Sway; **(C)** Heave; **(D)** Roll; **(E)** pitch; **(F)** Yaw; **(G)** Motion amplitude.

TABLE 4 Motion amplitudes of floating offshore wind turbine under different wave direction angles.

Wave direction angles	Surge (m)	Sway (m)	Heave (m)	Roll (deg)	Pitch (deg)	Yaw (deg)
α = 0 deg	1.500	0.021	1.402	1.337	0.017	0.022
α = 15 deg	1.436	0.467	1.379	1.271	0.286	0.708
α = 30 deg	1.292	0.895	1.330	1.099	0.525	1.037
α = 45 deg	1.080	1.234	1.292	0.836	0.707	0.728
α = 60 deg	0.832	1.471	1.280	0.526	0.882	0.056

harmonic vibration. The vibration frequency f in the edge direction also can be obtained by Fourier transform: f_3 = 0.155 Hz, which is consistent with the rotation frequency of the rotor. It shows that the vibration in the edge direction of the blade under the action of regular wave is mainly related to the rotation frequency of the rotor itself, but has little influence on the wave load frequency, tower vibration and other factors. The reason for the inconsistency between the vibration forms in the flapwise and edgewise directions of the blade is the inconsistency between the loading direction of the aerodynamic load and the stiffness of the blade in both directions.

Effect of the wind-wave misalignment

In natural conditions, the environmental load is complex and changeable. When wind wave coupling acts on the floating offshore wind turbine system, there is often the included angle of wind and wave, which is also known as the phenomenon of wind wave misalignment. Relevant research shows that under the high wind speed, there will be a small angle between wind and waves, while under low wind speed, the wind and wave load is prone to a large angle (Fischer, et al., 2011). The statistical results show that the angle between wind and waves is usually within 0 ~ 60° under the wind wave coupling, and the probability of exceeding 60° is less than 5% (Kuhn, 2001). It is clearly pointed out in the design specification manual of floating offshore wind turbine (Veritas, 2013) that the existence of wind wave angle will have a negative impact on the movement of turbine, and the existence of wind wave load angle should be considered in the design condition of floating offshore wind turbine. Therefore, it is necessary to study the effect of the wind - wave misalignment.

In this section, the influence of wave incidence angle on the six DOFs motion responses of floating fan is studied by changing the wave incidence angles. Considering that the wind turbine will control the yaw angle of the wind turbine through the control system to make the wind turbine face the incoming wind load to reduce the yaw moment of the wind turbine, the wind load is set perpendicular to the rotation plane of the wind turbine in the whole simulation process. The uniform inflow wind load is adopted, and the wind speed is set as the rated wind speed of 11.4 m/s. Regular wave loads are adopted for waves, and the incident angles of waves are set to -180 ~ +180°, one group is taken every 15°. The wind-wave load setting is shown in Figure 10.

Figure 11 below shows the six DOFs motion response of the floating offshore wind turbine system at wave incident angle of 0–60°, and the stable section after 1,000 s is taken as the output result.

It can be seen from Figure 11 that the incident angle of waves does not significantly change the equilibrium positions of the respective degrees of freedom motion, but it has a significant influence on the amplitudes of the motion of the platform. For the surge motion, the amplitude decreases slightly with the increase of wave direction angle α and the phase changes slightly. For the sway motion, the amplitude of motion oscillation increases significantly with the increasing of the incident angle α. For heave motion, the change of wave direction angle α has very little effect on it. For roll motion, the amplitude of motion oscillation increases obviously with the increase of wave direction angle α. Similar to the rolling motion, for pitch motion, the amplitude of motion oscillation decreases significantly with the increasing of the wave direction angle α, which is mainly related to the decreasing of the amplitude of the surge motion. The variation of the wave incident angle shadow is slightly different for the yaw motion. The amplitude of the yaw motion increases with the increasing of the wave direction angle in the range of 0 ~ 30° and decreases with the increasing of the wave direction angle in the range of 30 ~ 60°. This is because the mooring lines are arranged symmetrically with respect to the center of 120°. When the angle of incidence of wave is 0 and 60°, the wave load is facing the direction of No.1 and No.3 mooring lines. At this time, the tension of the mooring lines is the greatest, which restrains the swaying motion of the platform to a certain extent. This shows that the yaw motion of the floating offshore wind turbine is not only affected by the form of wave load of wind load, but also related to the layout of the platform and mooring system. Table 4; Figure 11G show the amplitudes of the motions of the floating offshore wind turbine system when wave directions are set between 0 and 60°.

Conclusion and discussions

The purpose of the present research is to study the motion characteristics of floating offshore wind turbine under the wind and wave coupling load. Therefore, FAST code is used to model and calculate the DTU-10MW semi-floating offshore wind turbine under different wind and wave combination conditions. Some results are summarized as follows:

The motion of floating offshore wind turbine system is affected by both wind load and wave load, and the wind load determines the mean value of each motion, while the wave load affects the amplitude of each motion.

When the inflow direction of wind and wave load is directly ahead, the floating offshore wind turbine mainly presents the motion forms of surge, heave and pitch motion.

The increasing of the wave incidence angle will reduce the amplitude of surge, pitch and heave motion response of floating offshore wind turbine, and will increase the amplitude of sway and roll response. The maximum yaw motion response occurs when the included angle of wind and wave is 30°.

The potential flow method is used to calculate the motion of the platform in the model. The results show that it is accurate enough, but there are also some limitations. For example, the treatment of the viscous effect of water is not considered. Further research is needed to improve the model and make it more widely accepted.

Data availability statement

The raw data supporting the conclusion of this article will be made available by the authors, without undue reservation.

Author contributions

BW made the computations, YL conducted the data analysis, SG drew some pictures, KS did the comparison and conducted the data analysis, ZH made the computations and the proofreading, XZ wrote the whole papers.

Funding

This work is supported by the National Natural Science Foundation of China (Nos. 51739001, 52071301, 51909238), Zhejiang Provincial Natural Science Foundation of China (LHY21E090001), Natural Science Foundation of Heilongjiang Province in China (LH2020E071), the Open Fund of the Key Laboratory of Far-shore Wind Power Technology of Zhejiang Province (ZOE20200007).

Acknowledgments

The last authors acknowledge the support of Professor Qingwei Ma at City, University of London for the research topic. We all acknowledge the Frontier Editorial Team and Editor Professor MP for their professional handling of the manuscript, and two dedicated referees who provided very constructive and insightful comments to significantly improve the quality of the work.

Conflict of interest

BW, SG, and KS were employed by the company Powerchina Huadong Engineering Corporation Limited.

The remaining authors declare that the research was conducted in the absence of any commercial or financial relationships that could be construed as a potential conflict of interest.

Publisher's note

References

Cao, H. (2009). *Study on the hydrodynamic performance of semi-submersible floating foundation of offshore wind turbine*. Ph.D. Thesis. Tianji: Tianjin University.

Dong, Y. Q. (1991). *Ship wave external load and hydroelasticity*, 6. Tianjin: Tianjin University Press.

Fischer, T., Rainey, P., Bossanyi, E., and Kuhn, M. (2011). Study on control concepts suitable for mitigation of loads from misaligned wind and waves on offshore wind turbines supported on monopiles. *Wind Eng.* 35 (5), 561–573. doi:10.1260/0309-524X.35.5.561

Gaumond, M., Réthoré, P.-E., Ott, S., Peña, A., Bechmann, A., and Hansen, K. S. (2014). Evaluation of the wind direction uncertainty and its impact on wake modeling at the Horns Rev offshore wind farm. *Wind Energy (Chichester)*. 17, 1169–1178. doi:10.1002/we.1625

Huijs, F., Bruijn, R., and Savenije, F. (2014). Concept design verification of a semi-submersible floating wind turbine using coupled simulations. *Energy Procedia* 53, 2–12. doi:10.1016/j.egypro.2014.07.210

Jonkman, J. M., and Matha, D. (2011). Dynamics of offshore floating wind turbines-analysis of three concepts. *Wind Energy (Chichester)*. 14, 557–569. doi:10.1002/we.442

Kuhn, M. (2001). *Dynamics and design optimisation of offshore wind energy conversion systems*. Ph.D. Thesis. Netherlands: Delft University of Technology.

Latha, S., and Vengatesan, V. (2013). Hydrodynamic response of a stepped-spar floating wind turbine: Numerical modelling and tank testing. *Renew. Energy* 52, 160–174. doi:10.1016/j.renene.2012.09.063

Lo, K. (2014). A critical review of China's rapidly developing renewable energy and energy efficiency policies. *Renew. Sustain. Energy Rev.* 29, 508–516. doi:10.1016/j.rser.2013.09.006

Ma, Y., Hu, C., and Li, L. (2022). Hydrodynamics and wake flow analysis of a Pi-type vertical axis twin-rotor tidal current turbine in surge motion. *Ocean. Eng.* 224, 108625. doi:10.1016/j.oceaneng.2021.108625

Madjid, K., Meissonnier, Q., Gao, Z., and Moan, T. (2011). Hydroelastic code-to-code comparison for a tension leg spar type floating wind turbine. *Mar. Struct.* 24, 412–435. doi:10.1016/j.marstruc.2011.05.006

Madjid, K. (2013). Modeling aspects of a floating wind turbine for coupled wave wind-induced dynamic analyses. *Renew. Energy* 53, 299–305. doi:10.1016/j.renene.2012.12.006

Merz, K. O., Moe, G., and Gudmestad, O. T. (2009). *A Review of hydrodynamic effects on bottom - fixed offshore wind turbines*. Honolulu: ASME 28th International Conference on Ocean.

Ning, D. Z., Zhou, Y., and Zhang, C. W. (2018). Hydrodynamic modeling of a novel dual-chamber OWC wave energy converter. *Appl. Ocean Res.* 78, 180–191. doi:10.1016/j.apor.2018.06.016

Pu, J. H., Cheng, N. S., Tan, S. K., and Shao, S. (2012). Source term treatment of SWEs using surface gradient upwind method. *J. hydraulic Res.* 50, 145–153. doi:10.1080/00221686.2011.649838

Qu, J. S., Guan, Y. F., and Lu, Y. X. (2013). Analysis of dynamic rensponse of jacket platform structure based on SESAM. *J. Jiangsu Ship* 30 (1), 1–5. doi:10.3389/fenrg.2020.0004

Shi, Y., Li, S., Chen, H., He, M., and Shao, S. (2018). Improved SPH simulation of spilled oil contained by flexible floating boom under wave–current coupling condition. *J. Fluids Struct.* 76, 272–300. doi:10.1016/j.jfluidstructs.2017.09.014

Veritas, D. N. (2013). *Design of floating wind turbine structures*. Oslo: Det Norske Veritas As. DNV-OS-J103-2013.

Wandji, W. N., Natarajan, A., and Dimitrov, D. (2016). Development and design of a semi-floater substructure for multimegawatt wind turbines at 50+ m water depths. *Ocean. Eng.* 125 (1), 226–237. doi:10.1016/j.oceaneng.2016.07.021

wind.nrel (2003). NWTC design codes (FAST). Available at: http://wind.nrel.gov/designcodes/simul-ators/OpenFAST (accessed on September 20, 2021).

Yu, Z. L., Zhu, C. C., Tan, J. J., Song, C. S., and Wang, Y. (2022). Fully-coupled and decoupled analysis comparisons of dynamic characteristics of floating offshore wind turbine drivetrain. *Ocean. Eng.* 247, 110639. doi:10.1016/j.oceaneng.2022.110639

Yu, Z. Y., Hu, Z. H., Zheng, X., Ma, Q. W., and Hao, H. B. (2020). Aeroelastic performance analysis of wind turbine in the wake with a new elastic actuator line model. *Water* 12 (5), 1233. doi:10.3390/w12051233

Zhang, R. Y., Tang, Y. G., Hu, J., Ruan, S., and Chen, C. (2013). Dynamic response in frequency and time domains of a floating foundation for offshore wind turbines. *Ocean. Eng.* 60, 115–123. doi:10.1016/j.oceaneng.2012.12.015

Zheng, X., Lv, X., Ma, Q., Duan, W., Khayyer, A., and Shao, S. (2018). An improved solid boundary treatment for wave–float interactions using ISPH method. *Int. J. Nav. Archit. Ocean Eng.* 10, 329–347. doi:10.1016/j.ijnaoe.2017.08.001

frontiers
in Environmental Science

ORIGINAL RESEARCH
published: 10 March 2022
doi: 10.3389/fenvs.2022.855334

In-Situ Test Method for Hydrodynamic Characteristics of Water Flowing Around Piles

Mingwei Liu[1], Liqin Zeng[1]*, Linjian Wu[1], Gang Chen[2], Lilong Shen[3] and Erdi Abi[1]

[1]National Engineering Research Center for Inland Waterway Regulation, School of River and Ocean Engineering, Chongqing Jiaotong University, Chongqing, China, [2]Sichuan Communication Surveying and Design Institute CO.,LTD., Chengdu, China, [3]CCCC Second Harbor Engineering Company Ltd., Wuhan, China

The dynamic characteristics of the flow around the pile directly determine the distribution law of the force of the flow on the pile, which is the basis of the calculation of the flow load of the hydraulic structure. At present, the model test and numerical simulation methods are mainly used to study the flow characteristics around the pile. There are problems of model scale effect and test accuracy in the laboratory model test, and inherent problems in the numerical simulation method, such as the determination of medium parameters, mesh division, and boundary conditions. Therefore, the research results cannot reflect the actual situation of the interaction between water flow and pile. This paper developed a field test system for measuring the hydrodynamic pressures on surface of piles which are the vital foundations of wharves under superhigh Reynolds number. And the analysis methods of *in-situ* data, which can realize the multifunction including calibration and transformation for test data, frequency and time-domain statistical analysis process, were put forward according to the theory of stationary random process and mathematical statistics method. A representative frame wharf located in the upper reaches of the Yangtze River was performed as a case study, and the developed system was utilized to operate the *in-situ* test on this practice. Application showed that the field test system and the analysis methods can be applied to obtain the more accurate distribution of the pile surface hydrodynamic pressure. And the drag coefficient in wharf field ranged from 0.30 to 0.40. These findings in this paper may provide significant technical support for the *in-situ* test in similar structures and some reference for drag force calculation of flow around pile in the engineering design.

Keywords: flow around pile, hydrodynamic pressure, *in-situ* test system, drag coefficient, hydrodynamic characteristics

Edited by:
Jaan H. Pu,
University of Bradford,
United Kingdom

Reviewed by:
Yang Shi,
Tsinghua University, China
Zhen Yan,
Tianjin Research Institute of Water
Transport Engineering, China

****Correspondence:***
Liqin Zeng
zlq_pbl@126.com

Specialty section:
This article was submitted to
Freshwater Science,
a section of the journal
Frontiers in Environmental Science

Received: *15 January 2022*
Accepted: *27 January 2022*
Published: *10 March 2022*

Citation:
Liu M, Zeng L, Wu L, Chen G, Shen L
and Abi E (2022) In-Situ Test Method
for Hydrodynamic Characteristics of
Water Flowing Around Piles.
Front. Environ. Sci. 10:855334.
doi: 10.3389/fenvs.2022.855334

1 INTRODUCTION

The hydrodynamic characteristics of flow around single pile and group of piles directly determine the distribution of fluid force along piles, which presents the significant foundations for the water flow load evaluation on frame-type wharf structures. Currently, the physical model experiments and the numerical simulations are mainly adopted for research on characteristics of the flow around pile. Yang et al. (2020) studied the flow field distribution around square columns with different pile length/pile diameter ratios through experiments. Wang et al. (2019) obtained the hydrodynamic coefficients of each section of the pile under the action of isolated waves through laboratory model tests. Tian et al. (2019) studied the influencing factors of hydrodynamic coefficient of jackup platform in wave flume. Han et al. (2018) studied the hydrodynamic characteristics of an inclined slender flexible cylinder under vortex-induced vibration by using a towing tank experiment. Lin K et al. (2020) obtained the dynamic response and hydrodynamic coefficient of the transverse flow oscillation cylinder with upstream wake interference by using the forced vibration test. Yang et al. (2021) used PIV technology to conduct experiments on the flow field around a multi-cylinder pile group and obtained the isoline map of the time-averaged velocity component, turbulence intensity, and Reynolds shear stress in the clearance area between piles. Ning et al. (2016) studied the hydrodynamic performance of the pile constrained WEC type floating breakwater and found that the parameters such as wave period, wave height, system size, and excitation current had significant influences on the hydrodynamic performance of the system. Wang et al. (2018) proposed a three-dimensional incompressible smooth particle hydrodynamic (ISPH) erosion model to simulate the scouring process around a large vertical cylinder and used high-speed cameras to monitor fluid movement around the pile in real time. In fact, the flow regime of the river is extremely complex. There are some problems about model scale effect and test accuracy in laboratory model tests. Kazemi et al. (2017) established a numerical model based on smooth particle hydrodynamics method to simulate open channel turbulence at limited depth in hydraulic rough bed and obtain hydrodynamic law. Lin J et al. (2020), based on the centralized mass point method and mesh clustering technology, studied the hydrodynamic characteristics of the mesh of pile-post Seine unit under the action of water flow through computer simulation. Liu et al. (2020) used a three-dimensional numerical model to study the distribution of pore water pressure and effective stress on seabed depth under the action of a single pile under wave load. Wu and Yang. (2020), on the basis of the secondary development of ANSYS software, established a numerical calculation model considering fluid-solid interaction under the combined action of earthquake, wave, and water flow, and explored the influence of pile group on the hydrodynamic force of large sea-crossing bridge piles. Wang et al. (2020) studied the vortex-induced vibration response of a cylinder with two degrees of freedom when Re = 150 through numerical simulation, and analyzed the oscillation characteristics and hydrodynamic characteristics. Zhu et al. (2020) used the direct numerical simulation (DNS) method to study the hydrodynamic characteristics and wake structure of cylinder at low and medium Reynolds numbers. Wen et al. (2022) used numerical simulation method to study the hydrodynamic characteristics of coastal bridge deck under the combined action of wave and shore wind. Ramnarayan et al. (2021) compared the hydrodynamic characteristics of two kinds of concave pile breakwaters (GS-PSB and CPS-PSB) through numerical simulation. Deng et al. (2019) studied the influence of wave load on pile caps and found that pile caps are affected by the free surface fluctuation of wave force on pile, and the negative wave force on piles near the leading edge of pile caps is obviously greater than the positive wave force. However, due to the inherent problems of the numerical simulation method, such as medium parameter determination, meshing, and boundary condition determination, the research results cannot reflect the actual situation of the interaction between the water flow and the pile. The existing flow load calculation standard British standard BS (1994) and the Port Engineering Load Code, (2010) assume ideal conditions, which cannot well reflect the flow load of a piled wharf in a mountainous river with large pile diameter and multi-layer transverse and longitudinal supports. To sum up, *in-situ* test is a means of high reliability and accurate measurement results.

In this paper, a new field test system of pile hydrodynamic pressure was designed to detect the hydrodynamic characteristics of flow around the pile based on the *in-situ* test. The new designed test system was installed at the site of the Phase II Project of Guoyuan in Chongqing Port to collect the *in-situ* data. A set of feasible methods for analyzing the hydrodynamic water pressure, including calibration and transformation of test data, outlier adjustment, frequency domain analysis, digital filtering, time-domain statistical analysis, and hydrodynamic pressure calculation, was put forward. Distribution laws of hydrodynamic pressure on piles' surface and drag coefficient of flow around piles under the field condition were obtained.

2 HYDRODYNAMIC PRESSURE FIELD TEST SYSTEM

In-situ tests have complicated and random hydrological conditions. And it takes a long time to carry out field experiments, which easily causes damages to the test system. So, there are high requirements for the test system as follows:

1) The system must accurately test the distribution of hydrodynamic pressure on component's different surfaces,
2) The system must be suitable for the various complex flow conditions,
3) The test system should be reliable,
4) It should be easy for the system to conduct site installation and removal.

2.1 Signal Acquisition Module

The signal acquisition module was designed to measure the dynamic water pressure on the surface of the component and transmit the measured signal to the signal analysis system. It is composed of a miniature dynamic pressure sensor, a miniature dynamic pressure transmitter, a positioning device, and a DH5922 signal acquisition instrument.

Miniature dynamic pressure sensor: The precision of the miniature dynamic pressure sensor is 0.5, the range is 0–200 kPa, and the power supply is ±15/DC. When the sensor probe is placed in a sufficiently small hole, the pressure of the sensor probe is consistent in all directions. Therefore, the hydrodynamic pressure at a certain point on the surface of the

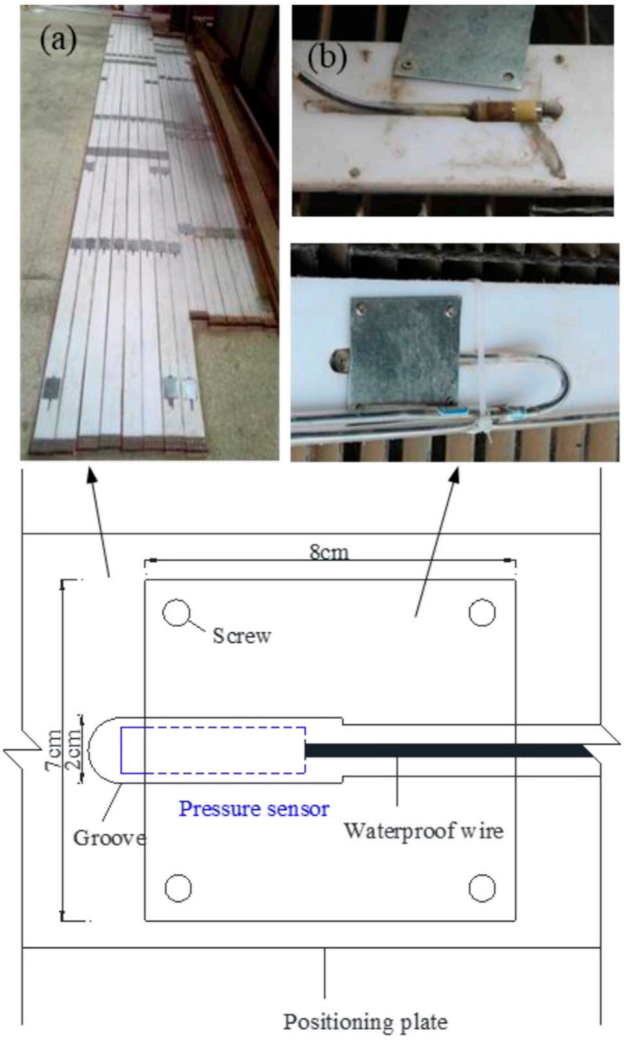

FIGURE 1 | Schematic diagram of positioning piece. **(A)** Positioning plate **(B)** Micro-sensor.

component can be directly measured by micro dynamic pressure sensor and converted into electrical signals.

Miniature dynamic pressure transmitter: The miniature dynamic pressure transmitter converts the corresponding signal measured by the pressure sensor into standard analog signal or digital signal and transmits it to the dynamic signal analysis module through the wire.

Positioning device: In order to install the sensor on the surface of the component easily and quickly on the premise of not damaging the existing structure components, the positioning device is designed, as shown in **Figure 1A**. The micro-sensor is installed in the slot of the positioning part made of PP sheet in advance, and then the positioning part is placed on the surface of the component, as shown in **Figure 1B**. The diameter of the pile was 2 m and the thickness of the positioning part (1 cm) can be ignored. The pore pressure measured by the sensor is the instantaneous hydrodynamic pressure on the pile surface.

According to those requirements, the test system was composed of signal acquisition module, dynamic signal analysis module, and signal output module.

In order to collect more accurate water pressure signal in the test system, the pressure sensor is fixed on the pile post with the positioning device. The positioning part is made of PP material, which has great toughness and is convenient to be made into a circular arc. The pressure sensor is placed in the strip-through hole of the positioning member, the waterproof wire is drawn along the strip-shaped groove, and the sensor is fixed on the positioning part with aluminum skin.

DH5922 signal acquisition instrument: Each acquisition module supports four signal inputs, and Zigbee was used to transmit digital signals from the signal acquisition instrument. It has the characteristics of high integration and high portability, which can meet the demand of multi-channel, high precision, and high-speed dynamic signal measurement, and is convenient for field application.

2.2 Dynamic Signal Transmission Module

Dynamic signal transmission module (**Figure 2**) was mainly used to transmit the signals collected by the acquisition instrument. The acquisition instrument and controller adopt Zigbee wireless transmission, controller, and cloud server support 4G mode connection; each controller can control up to 16 acquisition modules. Digital signal after demodulation of the controller was sent to the cloud storage database for saving, and the cloud database can send the digital signal to the signal output module.

2.3 Signal Output Module

The signal output module (**Figure 2**) displays the changing characteristics of the signal on the screen through the analysis software on the computer. Meanwhile, the analysis software can be used to process the signal and save the data.

The working process of the system involved the pressure sensor sensing dynamic water pressure and electrical signal *via* wire transfer to the transmitter; the signal was amplified and then spread to the dynamic signal transmission system, and dynamic signal transmission module sent signals to computers through cloud servers. Finally, the analysis software displays the changing characteristics of the signals on a computer screen. At the same time, the signal can be preliminarily analyzed and processed by the analysis software, and the data can be saved.

3 APPLICATION

3.1 Field Installation

The field test site was located at the upstream of the Yangtze River. The test system was set on the first four dock shelving. According to the arrangement principle that dense layout of key parts and general sparse arrangement of other parts, to layout test points, the main measuring point fix on the first shelf and the second column pile as well as the rest are the auxiliary. A total of 84 measuring points were arranged.

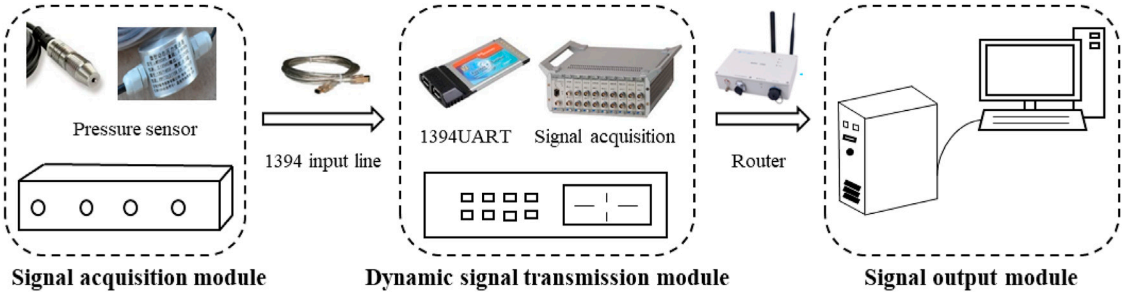

FIGURE 2 | *In-situ* test system of hydrodynamic pressure of pile.

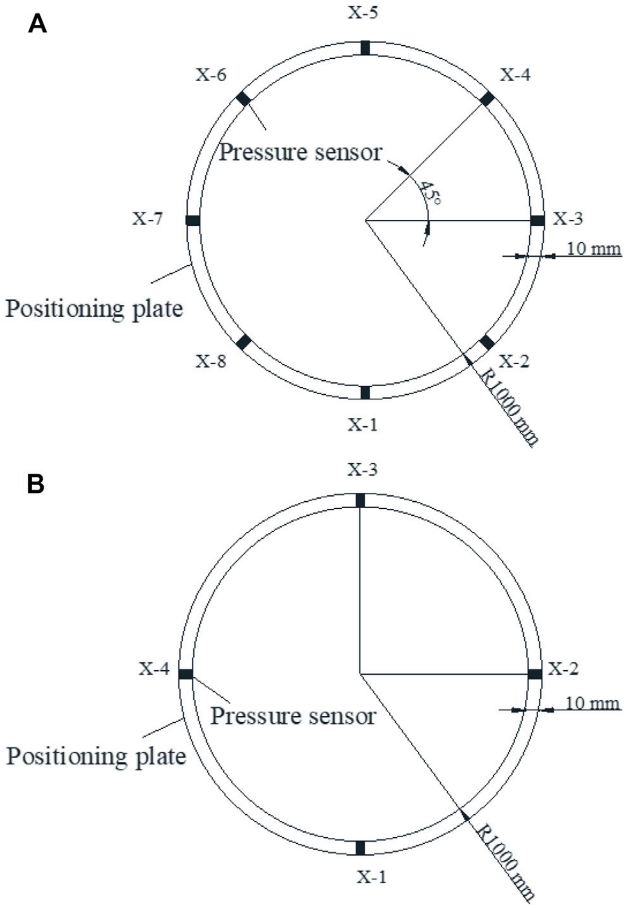

FIGURE 3 | Distribution diagram of pressure sensor on pile (The sensor is named X-Y, where "X" represents the positioning part number and "Y" represents the sensor number in the positioning part). **(A)** The layout of eight sensors **(B)** The layout of four sensors.

Arrangement of measuring points of dynamic water pressure

Install test system in-situ

FIGURE 4 | *In-situ* test installation. **(A)** Arrangement of measuring points of dynamic water pressure **(B)** install test system *in-situ*.

According to the plan, we can install sensors to the corresponding position of locating pieces, promoting the test system to the corresponding elevation and confirming the position of sensors on the pile surface. Then, we can detect the reliability and stability of pressure sensor system after installation and make corresponding records. Consequently, the whole process of installation and testing is completed. The pore pressure sensors are distributed around the circular pile in a symmetrical manner, as shown in **Figure 3**.

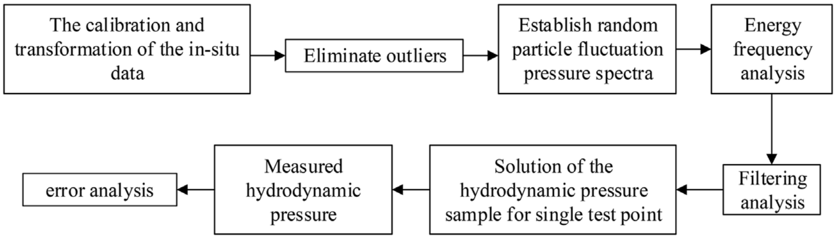

FIGURE 5 | Data acquisition and processing flow of field test system.

The location of measuring points and the *in-situ* installation process are shown in **Figure 4**.

3.2 *In-Situ* Data Collection

1) Acquisition time: The gushing period at the field investigation area is about 15 min. In order to ensure the data integrity, the sensor data collection time period was set as 30 min and the long-time track test was set as 60 min. The testing time was mainly in the daytime, and data collection was carried out for about 8 h continuously. Continuous testing was selected when water flow conditions are relatively ideal, so as to achieve the purpose of long-term observation, large data volume, and integrity.
2) Acquisition environment: The data accuracy can be affected by shipping, construction around the wharf, and wharf platform work conditions, so the collection time is chosen when there is no sail, construction, or operation. When a set of sensor tests is completed, the test system needs to be reset and balanced before testing another group to ensure the stability of every part in the testing system.

To sum up, the ideal hydrological conditions are chosen according to the conditions which were mentioned above. These include conducting the field flow load test on the condition of high velocity and flood peak, and setting the sampling frequency as 100 Hz. Instantaneous voltage signal at different times can be measured at different bents, different piles, different layers, and different flow angles in the wharf area.

3.3 Data Analysis Process

In ocean engineering, the waves are often regarded as superposition of multiple cosine waves. If the value of the wave height is zero, the waves satisfy stability requirement. It is called stationary stochastic theory. For the hydrodynamic pressure studied in this article, the average of the hydrodynamic pressure measured by the pressure sensor can be seen as zero. The fluctuation around zero of hydrodynamic pressure can be regarded as multiple waves' superposition and considered as satisfying the requirement of stability. Therefore, a single sample is representative, and a long enough period of time can be selected from any one sample for statistical analysis, as shown in **Figure 5**.

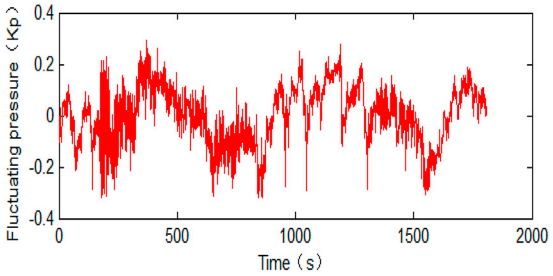

FIGURE 6 | Pulsation pressure signal.

3.3.1 The Calibration and Transformation of the *In-Situ* Data

The data collected on the dock are electrical signals, and the conversion formula between input electrical signals and output pressure signals is established through laboratory tests.

The *in-situ* data collected from wharf field is electrical signals. The calibration and conversion formula acquired by laboratory tests have established a relationship between the input signals and output pressure signals (**Eq. 1**), which will convert the data collected in the field into pressure signals. Three Times Standard Deviation Method is used to adjust outliers. The outlier is adjusted by using the Spline Interpolation Methods or replaced with the interpolation of two adjacent right signals for the value within the range between the two normal signals.

$$Y = 289.0081X - 12067.95 \tag{1}$$

Where, Y is voltage signal, V; X is hydrodynamic pressure, kPa.

3.3.2 Establish Random Particle Fluctuation Pressure Spectra

The mechanism of fluctuating pressure formation in a turbulent region is complicated. At present, the value of fluctuating pressure and the study about hydrodynamic characteristics of structures under fluid-solid coupled interaction mainly depend on the indoor and prototype tests to complete. But their conditions are ideal. And field test results can show the real situation. Based on the theory of stationary random, by taking the average value as zero, the actual fluctuating pressure signal can be obtained from the instantaneous pressure signal, as shown in **Figure 6**.

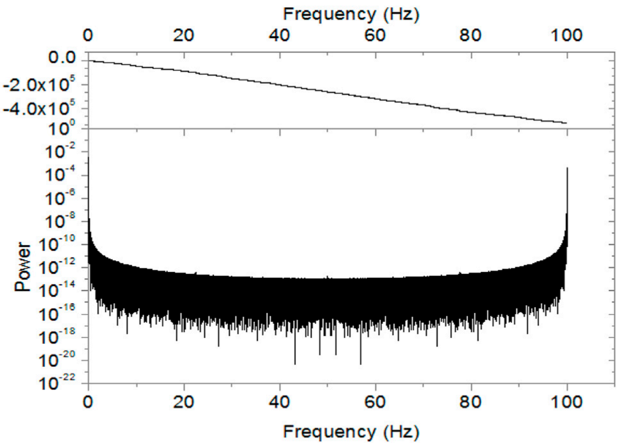

FIGURE 7 | Frequency spectra of a group of collected data after fast Fourier transform.

3.3.3 Energy Frequency Analysis

Turbulent flow is made up of many different sizes of eddy motion, fracture, and stretch of vortex happening during flow motion. Pressure field with characteristics of pulsation was caused by relative movement of vortex form fluctuation pressure. As the energy and frequency of the vortex are different, the pulsation pressure is also different. To determine the energy weight distribution of different pulsating pressures, fast Fourier transform (DFT) was used for energy frequency analysis, as shown in **Figure 7**. DFT operation formula was:

$$X(k) = \sum_{n=0}^{N-1} x(n) W_N^{nk} \tag{2}$$

where, $x(n)$ is N sequences of finite length; $W_N = e^{-j\frac{2\pi}{N}}$ has symmetry, periodicity, and reducibility. Furthermore, $W_N^{n(N-k)} = W_N^{k(N-n)} = W^{-nk}$, $W_N^{k+N/2} = -W_N^k$. The inverse transform (IDFT) is

$$x(n) = \frac{1}{N} \sum_{n=0}^{N-1} X(k) W_N^{-nk} \tag{3}$$

where, $x(n)$, $X(k)$, and W_N^{-nk} are complex numbers and $X(k)$ has N points (k = 0,1..., n-1), so the entire DFT operation requires a total of N^2 complex multiplications and $N(N-1)$ complex additions.

3.3.4 Filtering Analysis

Field data is mingled with certain noise and other useless signals. In order to eliminate or weaken the interference noise and retain the useful signals, the specific frequency band waves need to be filtered out in **Figure 8**. *N-order* low-pass filter Butterworth is chosen, whose characteristic function is as follow:

$$|H_s(\Omega)|^2 = 1/\left[1 + (\Omega/\Omega_c)^{2N}\right] \tag{4}$$

where, N is the order of the filter and Ω_c is passband width or 3dB passband width. When the order increases, the characteristic is closer to $|H_s(\Omega)|^2$, which has an ideal rectangular frequency amplitude characteristic. The above equation can be rewritten as:

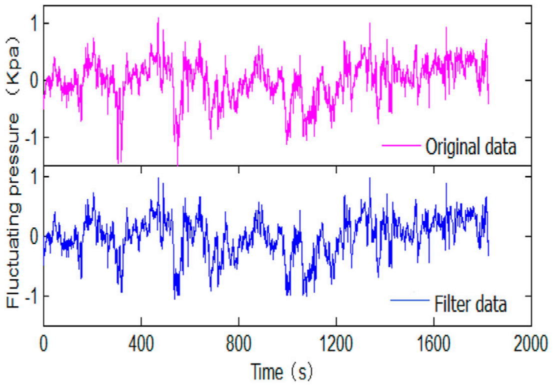

FIGURE 8 | Comparison of fluctuating pressure values before and after filtering.

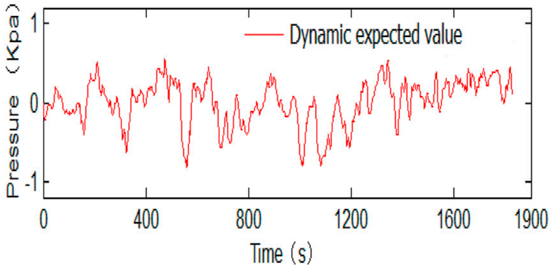

FIGURE 9 | Dynamic expectation curve of fluctuating pressure.

$$H(s) = \frac{(-1)^N}{\prod_{k=1}^{N}\left(\frac{s}{s_{pk}} - 1\right)} = \frac{\Omega_c^2}{\prod_{k=1}^{N}\left(s - s_{pk}\right)} \tag{5}$$

where, $H(s)$ is rectangular frequency side characteristic function; s_{pk} is the pole, and only when the extreme point is located in the left half plane can the system be stable.

Based on DFT, the distribution of different band frequency wave energy weight can be obtained. This paper retains the signal whose energy accounted for 99.9% of total energy of the full frequency band signal by the first filter. And through the further filtering of pressure signal, pressure dynamic expectations value can be obtained, as shown in **Figure 9**.

3.3.5 Solution of the Hydrodynamic Pressure Sample for Single Test Point

The existence of the eddy current will cause strong shore erosion and bed deformation. And it is also the main reason for the change of the single point pressure. Instantaneous pressure fluctuates up and down around the fluctuating pressure dynamic expectation curve in a certain period. The period of fluctuation is just the eddy current cycle, as the "ac" of curve

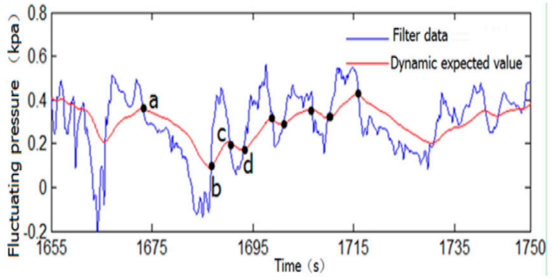

FIGURE 10 | Partial amplification of pulsating pressure signal and eddy current cycle judgment diagram.

shown in **Figure 10**. The absolute value of the difference value between the maximum (or the minimum) in the first half period and the minimum (or the max) in the second half of a period is a hydrodynamic pressure sample value.

3.4 *In situ* Data Analysis

A total of 84 sensors' hydrodynamic pressure values are collected in our study. The distribution of the hydrodynamic pressure on pile surface is influenced by hydrological conditions, such as flow velocity, flow direction, and water depth. And it is also affected by the arrangement of pile foundation and vertical and horizontal contact brace as shown in **Figure 11A**. The combined effect of other piles, braces, and shipping on the main test pile is located in the first single truss of pile at the upstream is minimum, as shown in **Figure 11B**. The NO. 1 locating piece has four sensors, and the NO. 3 locating piece has eight sensors, which are representative. So, take the NO. 1 and NO. 3 **Figure 11C** locating pieces fixed on the main test pile to carry out application analysis.

The measuring time is 30.44 min, and the wharf field hydrology conditions are shown in **Table 1**.

According to the aforementioned data processing method, the characteristic values of hydrodynamic pressure on the surface of the pile are shown in **Table 2**.

The sensor is named X-Y, where "X" refers to the positioning part number, and "Y" refers to the sensor number in the positioning part.

The average value is selected as the characteristic value index of hydrodynamic pressure, because the average value is representative and can better reflect the distribution characteristics of hydrodynamic pressure.

3.5 Data Error Analysis

According to the study (Ong et al., 2009; Ouvrard et al., 2008), the separation angle of the flow around the circular pile is about 108°~114° at superhigh Reynolds number. Combined with the characteristic values of the hydrodynamic pressure on pile surface measured by field test, the profile of the hydrodynamic pressure distribution can be achieved, as shown in **Figure 12**.

Figure 12 shows that the hydrodynamic pressure in the direction of incoming flow is maximum. Then the pressure reduces along the pile perimeter, and negative pressure zone is formed behind the pile. Affected by the flow direction angle, pile hydrodynamic pressure distribution is not symmetrical, which conforms to the general law of hydrodynamic pressure distribution.

Based on the figure of the hydrodynamic pressure distribution around the pile, the drag force F_D of flow around the pile can be obtained by integral calculation around the pile. According to **Eq. 6** in "Port Engineering Load Code", hydrological condition, and other known conditions, we can get the drag coefficient C_D. Dynamic water pressure data of sensor No. 3 was selected, the mean curve of moving water pressure along the pile

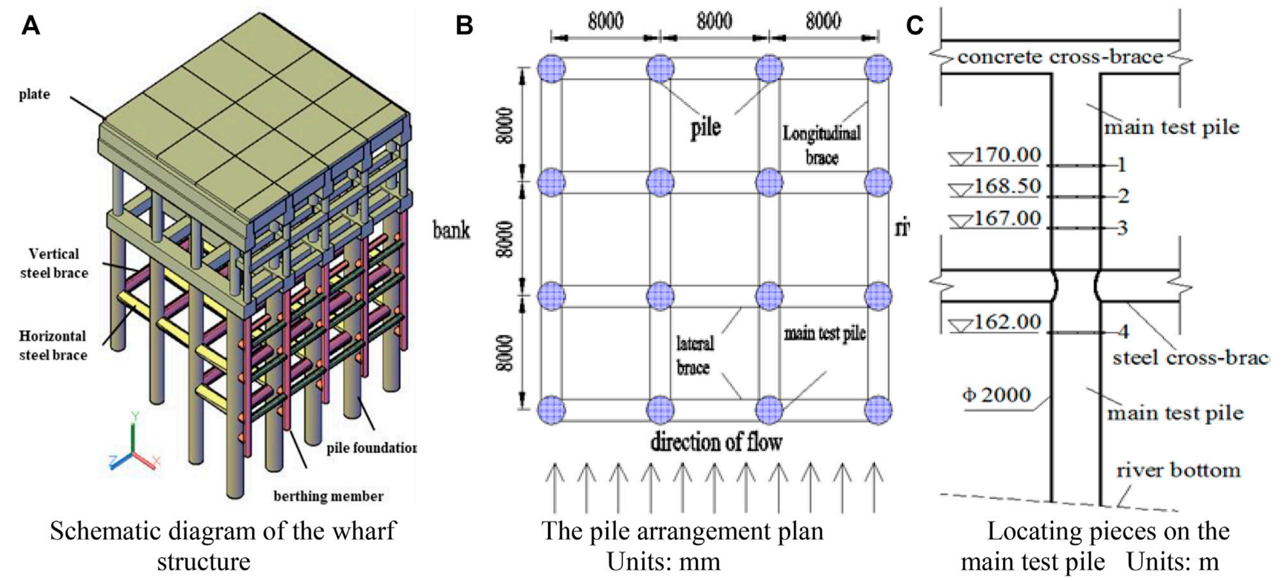

Schematic diagram of the wharf structure

The pile arrangement plan Units: mm

Locating pieces on the main test pile Units: m

FIGURE 11 | Piles layout and locating pieces on the main test pile. **(A)** Schematic diagram of the wharf structure. **(B)** The pile arrangement plan units: mm. **(C)** Locating pieces of the main test pile units: m.

TABLE 1 | The wharf field hydrological conditions.

Number	Water level (m)	Flow direction angle (o)	Average velocity (m/s)	Re (× 10^4)
1	174.25	−10~0	1.19	168~340
3	174.25	−10~0	1.19	168~340

TABLE 2 | The eigenvalues of the hydrodynamic pressure.

Sensors	Submerged depth (m)	Number of samples	The maximum (kPa)	The minimum (kPa)	Average (kPa)	Standard deviation
1-1	4.25	675	1.0610	0.0023	0.2310	0.2022
1-2	4.25	567	1.6760	0.0014	0.2912	0.2837
1-3	4.25	762	0.6655	0.0006	0.1431	0.1119
1-4	4.25	802	1.0542	0.0013	0.2051	0.1630
3-1	7.25	587	1.0343	0.0007	0.1864	0.1411
3-2	7.25	816	0.8826	0.0036	0.1525	0.1226
3-3	7.25	818	1.0782	0.0015	0.2103	0.1780
3-4	7.25	721	1.3133	0.0034	0.2490	0.2241
3-5	7.25	701	1.4270	0.0034	0.2858	0.2645
3-6	7.25	529	1.3725	0.0015	0.2638	0.2501
3-7	7.25	567	1.5064	0.0035	0.2691	0.2505
3-8	7.25	682	0.2188	0.0027	0.0650	0.1458

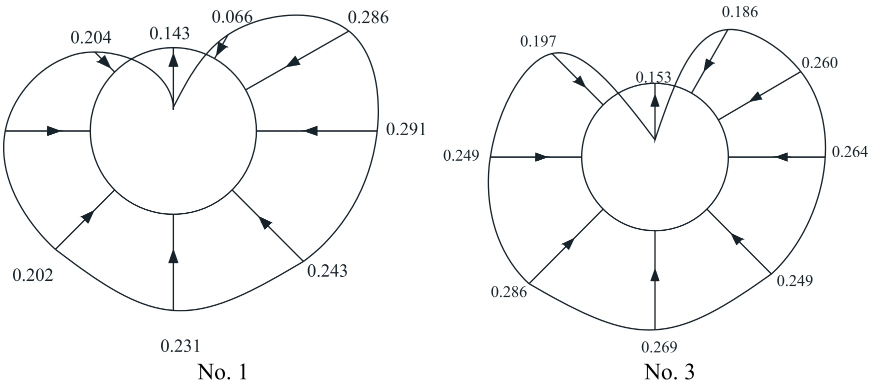

FIGURE 12 | Distribution diagram of hydrodynamic pressure along pile circumference.

TABLE 3 | The calculation of drag coefficient in wharf field.

Number of locating	Water level (m)	Average velocity (m/s)	Re (×10^6)	F_D (kN)	C_D
3-1	174.25	1.205	2.36	0.4852	0.3462
3-2	174.90	1.025	2.40	0.5581	0.3851
3-3	168.25	0.983	1.95	0.3450	0.3599
3-4	171.00	0.721	1.14	0.1674	0.3226

circumference was fitted, and the force analysis was carried out to obtain the resistance around the flow, as shown in **Table 3**.

$$F_D = C_D \frac{\rho}{2} V^2 A \tag{6}$$

Where F_D is flow resistance, kN; C_D is coefficient of resistance around flow; ρ is fluid density, t/m^3; V is flow velocity, m/s; A is the area of the object around the flow in the direction of the incoming flow, m^2.

It is found from the above table that the flow resistance coefficient calculated from the experimental data fluctuates within a certain range, which is about 0.32~0.38. The flow resistance coefficient in BS standard is 0.45~0.47, which is larger than the result of this test due to the ideal conditions in the standard.

In conclusion, the hydrodynamic pressure distribution on the surface of the pile can be successfully obtained by using the field test and analysis method of the dynamic characteristics of the pile flowing around the pile. By analyzing the dynamic water pressure distribution on the surface of the pile under different hydrological conditions, we can further study the dynamic water pressure distribution and flow resistance on the surface of the pile under different flow rates, directions, and water depths.

4 CONCLUSION

In this paper, the field test system of the hydrodynamic pressure around circular pile was developed, which consisted of the fixed pressure sensing system and dynamic signal test and analysis system. And the system was installed in the Phase II Guoyuan Project in Chongqing Port to collect *in-situ* data. Based on the theory of the stationary random process and the mathematical statistics method, a set of methods including the calibration and transformation of test data, the outlier adjustment, frequency domain analysis, digital filter, time-domain statistical analysis, and hydrodynamic pressure calculation were applied. The results indicate that:

1) The results show that the signal of the hydrodynamic pressure in the Yangtze River water flow is mainly low frequency signal. The distribution laws of the hydrodynamic pressure around the pile can be obtained by using the field test system and the method for analyzing the test data, which can lay the foundation of the further research on the distribution laws of the hydrodynamic pressure and drag force for inland hydraulic structure under different flow velocity, different flow direction, and different water depth.
2) By calculating the dynamic water pressure around the pile under different conditions, the resistance coefficient range of the pile flow at large Reynolds number is about 0.30~0.40.

DATA AVAILABILITY STATEMENT

The original contributions presented in the study are included in the article/Supplementary Material, further inquiries can be directed to the corresponding author.

AUTHOR CONTRIBUTIONS

Conceptualization, ML; methodology, ML and LZ; validation, LS; formal analysis, GC and LW; investigation, EA; resources, ML; data curation, LZ and GC; writing—original draft preparation, ML and LZ; supervision, LW. All authors have read and agreed to the published version of the manuscript. All authors have read and agreed to the published version of the manuscript.

FUNDING

This research is funded by the National Natural Science Foundation of China (51479014) and the Talents Plan Project in Chongqing of China, project number: cstc2021ycjh-bgzxm0053.

REFERENCES

British standard BS (1994). *England.*

Deng, L., Yang, W., Li, Q., and Li, A. (2019). CFD Investigation of the Cap Effects on Wave Loads on Piles for the Pile-Cap Foundation. *Ocean Eng.* 183, 249–261. doi:10.1016/j.oceaneng.2019.05

Han, Q., Ma, Y., Xu, W., Fan, D., and Wang, E. (2018). Hydrodynamic Characteristics of an Inclined Slender Flexible cylinder Subjected to Vortex-Induced Vibration. *Int. J. Mech. Sci.* 148, 352–365. doi:10.1016/j.ijmecsci.2018.09.010

Karthik Ramnarayan, S., Sannasiraj, S. A., and Sundar, V. (2021). Hydrodynamic Characteristics of Curved Front Face Pile-Supported Breakwaters in Random Waves. *Appl. Ocean Res.* 117, 102922. doi:10.1016/j.apor.2021.102922

Kazemi, E., Nichols, A., Tait, S., and Shao, S. (2017). SPH Modelling of Depth-Limited Turbulent Open Channel Flows over Rough Boundaries. *Int. J. Numer. Meth. Fluids* 83, 3–27. doi:10.1002/fld.4248

Lin, J, J., Zhang, J.-s., Sun, K., Wei, X.-l., and Guo, Y.-k. (2020). Numerical Analysis of Seabed Dynamic Response in Vicinity of Mono-Pile under Wave-Current Loading. *Water Sci. Eng.* 13, 74–82. doi:10.1016/j.wse.2020.02.001

Lin, K, K., Fan, D., and Wang, J. (2020). Dynamic Response and Hydrodynamic Coefficients of a cylinder Oscillating in Crossflow with an Upstream Wake Interference. *Ocean Eng.* 209, 107520. doi:10.1016/j.oceaneng.2020.107520

Liu, C., Fu, S., Zhang, M., Ren, H., and Xu, Y. (2020). Hydrodynamics of a Flexible cylinder under Modulated Vortex-Induced Vibrations. *J. Fluids Structures* 94, 102913. doi:10.1016/j.jfluidstructs.2020.102913

Ning, D., Zhao, X., Göteman, M., and Kang, H. (2016). Hydrodynamic Performance of a Pile-Restrained WEC-type Floating Breakwater: An Experimental Study. *Renew. Energ.* 95, 531–541. doi:10.1016/j.renene.2016.04.057

Ong, M. C., Utnes, T., Holmedal, L. E., Myrhaug, D., and Pettersen, B. (2009). Numerical Simulation of Flow Around a Smooth Circular cylinder at Very High Reynolds Numbers. *Mar. Structures* 22, 142–153. doi:10.1016/j.marstruc.2008.09.001

Ouvrard, H., Koobus, B., Salvetti, M.-V., Camarri, S., and Dervieux, A. (2008). Variational Multiscale LES and Hybrid RANS/LES Parallel Simulation of Complex Unsteady Flows. *Int. Conf. High Perform. Comput. Comput. Sci.* 5336, 465–478. doi:10.1007/978-3-540-92859

Port engineering load code (2010). *JTS 144-1-2010*. Beijing: Communications Press.

Tian, X., Liu, Y., Liu, G., Xie, Y., and Wang, S. (2019). Experimental Study on Influencing Factors of Hydrodynamic Coefficient for jack-up Platform. *Ocean Eng.* 193, 106588. doi:10.1016/j.oceaneng.2019.106588

Wang, D., Shao, S., Li, S., Shi, Y., Arikawa, T., and Zhang, H. (2018). 3D ISPH Erosion Model for Flow Passing a Vertical cylinder. *J. Fluids Structures* 78, 374–399. doi:10.1016/j.jfluidstructs.2018.01.003

Wang, F., Sun, R., Wang, C. X., Fu, Q., Li, P., and Guo, H. Y. (2019). Experimental Study on Flow Field Induced by Internal Solitary Wave and Load Characteristics on Pile Sections at Different Depth. *Ocean Eng.* 188, 106292,. doi:10.1016/j.oceaneng.2019.106292

Wang, H. B., Ding, L., Zhang, L., Sharma, R. N., and Yang, L. (2020). Numerical Study on Two-Degree-Of-freedom Vortex Induced Vibrations Suppression of a Circular cylinder via Synthetic Jets at Different Excitation Frequencies. *Int. J. Heat Fluid Flow* 84, 108593,. doi:10.1016/j.ijheatfluidflow.2020.108593

Wen, B. H., Qu, K., Lan, G. Y., Sun, W. Y., Yao, Y., Deng, B., et al. (2022). Numerical Study on Hydrodynamic Characteristics of Coastal Bridge Deck under Joint Action of Regular Waves and Wind. *Ocean Eng.* 245, 110450,. doi:10.1016/j.oceaneng.2021.110450

Wu, A. J., and Yang, W. L. (2020). Numerical Study of Pile Group Effect on the Hydrodynamic Force on a Pile of Sea-Crossing Bridges during Earthquakes. *Ocean Eng.* 199, 106999,. doi:10.1016/j.oceaneng.2020.106999

Yang, H., Yang, W., Yang, T., and Li, Q. (2020). Experimental Investigation of Flow Around a Square cylinder with Very Small Aspect Ratios. *Ocean Eng.* 214, 107732. doi:10.1016/j.oceaneng.2020.107732

Yang, Y., Qi, M., Li, J., and Ma, X. (2021). Experimental Study of Flow Field Around Pile Groups Using PIV. *Exp. Therm. Fluid Sci.* 120, 110223. doi:10.1016/j.expthermflusci.2020.110223

Zhu, H., Liu, W., and Zhou, T. (2020). Direct Numerical Simulation of the Wake Adjustment and Hydrodynamic Characteristics of a Circular cylinder Symmetrically Attached with Fin-Shaped Strips. *Ocean Eng.* 195, 106756. doi:10.1016/j.oceaneng.2019.106756

Conflict of Interest: GC was employed by the company Sichuan Communication Surveying and Design Institute CO.,LTD. and LS was employed by the company CCCC Second Harbor Engineering Company Ltd.

The remaining authors declare that the research was conducted in the absence of any commercial or financial relationships that could be construed as a potential conflict of interest.

frontiers | Frontiers in Environmental Science

TYPE Original Research
PUBLISHED 30 August 2022
DOI 10.3389/fenvs.2022.979930

OPEN ACCESS

EDITED BY
Jiaye Li,
Dongguan University of Technology,
China

REVIEWED BY
Leicheng Guo,
East China Normal University, China
Xu-Feng Yan,
Sichuan University, China

*CORRESPONDENCE
Ziru Zhang,
202121180102@mail.bnu.edu.cn
Le Wang,
Lewang@ncepu.edu.cn

SPECIALTY SECTION
This article was submitted
to Freshwater Science,
a section of the journal
Frontiers in Environmental Science

RECEIVED 28 June 2022
ACCEPTED 25 July 2022
PUBLISHED 30 August 2022

CITATION
Shu A, Zhang Z, Wang L, Sun T, Yang W, Zhu J, Qin J and Zhu F (2022), Effects of typical artificial reefs on hydrodynamic characteristics and carbon sequestration potential in the offshore of Juehua Island, Bohai Sea.
Front. Environ. Sci. 10:979930.
doi: 10.3389/fenvs.2022.979930

Effects of typical artificial reefs on hydrodynamic characteristics and carbon sequestration potential in the offshore of Juehua Island, Bohai Sea

Anping Shu[1], Ziru Zhang[1]*, Le Wang[2]*, Tao Sun[1], Wei Yang[1], Jiapin Zhu[1], Jiping Qin[3] and Fuyang Zhu[4]

[1]Key Laboratory of Water and Sediment Sciences of MOE, School of Environment, Beijing Normal University, Beijing, China, [2]School of Water Resources and Hydropower Engineering, North China Electric Power University, Beijing, China, [3]Environmental Planning Research Center, Yunnan Research Academy of Eco-Environmental Sciences, Kunming, China, [4]Power China ZhongNan Engineering Corporation Limited, Chang Sha, China

The ocean system provides abundant food resources and suitable habitats for numerous animal and plant species. However, the ecological health of the ocean system has deteriorated due to intensified human activities over the past decades. To mitigate negative effects, more research efforts are being directed toward marine ecological restoration programs at national and regional scales. As an effective method, artificial reefs are found to have an important role in restoring the ecological system by producing complex flow patterns and attracting more species to settle down. This study aims to select the offshore ground of Juehua Island in the Bohai Sea as an artificial reef–driven ecological restoration site, to tentatively estimate effects of square and M-shaped artificial reefs on localized flow fields, biomass production, and offshore carbon sink capacity. Meanwhile, a relatively complete carbon sink measurement system is accordingly proposed. Our results indicate that both temporal and spatial distribution of nutrients and habitat environments are dependent on flow characteristics modified by artificial reefs of different sizes, shapes, and configurations. Future ecological restoration measures in offshore waters should take carbon sink and relevant influencing factors into consideration.

KEYWORDS

hydrodynamic characteristics, artificial reefs, ecological restoration, carbon sink, offshore of Juehua Island

1 Introduction

Intensive human disturbances to marine ecosystems have caused significant habitat loss, resulting in a decline in biodiversity and ecological services. Meanwhile, as the largest biomes in the biosphere, the ocean is also experiencing aquatic habitat degradation in many places across the globe. It has been documented that marine fisheries released at least 730 million metric tons of carbon dioxide into the atmosphere since 1950, this means an increase in fish populations to reactivate natural carbon pumps could effectively increase the ocean's carbon sink (Mariani et al., 2020). There is an urgent need to improve the impaired ocean ecosystem. For instance, artificial reefs (ARs) appear to be able to attract and breed diverse marine organisms in a similar way as natural reefs (NRs) along coastal regions, so as to protect fishery resources and contribute to diverse marine environments. Also, many factors such as form, structure, size, and configuration of artificial reefs (ARs) have been found to influence hydrodynamic characteristics of local flow fields, especially for water bodies adjacent to deployed artificial reefs, thereby enhancing aggregation and reproduction of living marine organisms (Galdo et al., 2022). Zalmon et al. (2014) evaluated the impact of artificial reefs on an animal community structure and related it to hydrodynamic characteristics of the surrounding environments, finding that the changes in flow fields were conducive to a more rapid accumulation of organic matter. These changes in hydrodynamic characteristics within localized flow fields enable a fast carbon capture from organic matter and incorporation into the global carbon cycle due to tidal as well as oceanic currents.

Climate change is a long-standing challenge that human society must address in the coming decades. One of the well-known reasons for global warming is an increase in the amount of carbon dioxide and other greenhouse gas emissions into the atmosphere following industrial expansion and strong human activities. Therefore, effective measures for controlling and reducing carbon emissions are urgently needed. Also, the fact that total carbon emission reduction within the Earth's original ecosystem is underlined in recent years. The ocean, which operates as the largest carbon pool on the Earth, is an important carbon source and sink, and its role in mitigating climate warming and reducing carbon emissions is increasingly recognized. The marine ecosystem absorbs and stores carbon dioxide in the atmosphere through physical and chemical reactions of non-biological components in the ocean and biological activities of marine organisms, these processes and mechanisms of carbon storage relying on the coastal vegetation ecosystem are called blue carbon, which was first coined in the 2009 UN report. The roles of mangroves, salt marshes, and seagrass beds within coastal ecosystems in carbon storage have been well documented (e.g., Bertram et al., 2021). For example, the mangrove community can be used for breaking waves, protecting coastlines, and assimilating carbon dioxide into biomass through photosynthesis, meanwhile, mangrove roots can capture suspended nutrients, particulate carbon in terrestrial ecosystems, and enhance carbon sequestration as well (Zhu and Yan, 2022). Jennerjahn (2020) estimated that the global carbon storage in mangrove sediments based on carbon accumulation rate could be 32 Tg per year. In addition to plant photosynthesis, wetland sediment is also a main carbon storage sink in the salt marsh ecosystem. Studies have shown that reed straw and biochar can effectively restore degraded salt marshes and enhance blue carbon sinks (Chen et al., 2022). The carbon sequestration in the seagrass bed ecosystem includes a high productivity of seagrass bed plants, clastic carbon capture ability in seawater, and lower decomposition of sediments (Lee et al., 2021). Mangroves, salt marshes, and seagrasses can capture nearly 50 percent of the carbon in marine sediments, but their total coverage is less than 2 percent of the world's ocean surface. It is also shown that large algal beds in habitats associated with high water exchange rates can generate large carbon sinks around them and export large amounts of dissolved organic carbon to offshore areas (Watanabe et al., 2020). Some studies focused on ocean carbon from zooplankton and plant debris particles (i.e., carbon and water and gas exchange of dissolved CO_2). Articulate carbon in water tends to change during different seasons, predictions for southern particulate organic carbon (POC) concentrations in the Baltic Sea suggest a two-to three-fold increase in late spring, as a result, the oxidation of the water below the halocline will decrease and the food supply for organisms with higher nutrient levels will increase (Dzierzbicka-Glowacka et al., 2011). The coastal upwelling currents also affect the transport of particulate carbon. Fischer et al. (2020) found a similar result, despite significant differences observed in different regions, the particulate carbon flux usually increased in springs since 2005. Phytoplankton under seawater was also found to have carbon sequestration potential, and estimates of the subscale rates of ascidians, ctenophores, ascidians, and pteropods show that their carbon sequestration capacity cannot be ignored and should be included in the carbon sink quantification model (Lebrato et al., 2013). Assessment of fluxes in the Northeast Asian Tropical Atlantic (Canary Islands) also suggests that microplankton is a major component of deep-sea carbon exportation (Ariza et al., 2015).

Nowadays, the blue carbon ecosystem has also been gradually concerned. At the same time, human activities have undoubtedly a great impact on the exchange of carbon and other substances between the land and ocean systems at the coastal interface. This is intuitively reflected in a gradual shrinkage of coastal mangroves wetland areas due to high-order expansion of human activities and massive destruction of seaweed beds and phytoplankton (e.g., algae) in water caused by pollution. Studies of coastal lagoons in Portugal have shown that hydrodynamic characteristics of dredged navigable channels affect the stability of coastal ecosystems (e.g., Harris et al., 2021; Martins et al., 2021; Gu et al., 2022). A monitoring program of seagrass ecosystems in

Australia implied that human activities increased the content of CO_2 sequestration but at the expense of damaging the threshold of the ecosystem (Macreadie et al., 2011). Therefore, quantitative assessments of the impact of human activities on blue carbon ecosystems become increasingly important when balancing different concerns from sociology, economics, and other fields. Nevertheless, human activities can be modified and restricted accordingly, which will produce a positive reflection. For instance, Canu et al. (2015) depicted a picture of net CO_2 flux at the air–sea interface by estimating 1) carbon sink ecosystem services in the Mediterranean region by using ecological economic methods and 2) social cost of carbon emissions by combining biogeochemical models. Macroalgae (e.g., algae and kelp) may facilitate an effective use of land and water resources. However, due to the complexity involved in the calculation methods of carbon capture flow of aquatic plants, biological, physical, and social technological factors in the region are all taken into account in the measurement system. Life cycle assessment (LCA) was adopted in relevant studies along with the geographic information system (Muenzel and Martino, 2018). The net global warming potential of greenhouse gas emissions (positive) and absorption (negative), as well as the return on energy investment (EROI), were used as main indicators to assess the environmental impact of carbon capture capacity from aquatic plants at multiple phases during their life cycle. As an offshore ecosystem, salt marshes can also provide carbon sink benefits. However, a range of negative impacts of human activities (such as grazing) are inevitable, In Scotland, carbon sink benefits were evaluated by using the ecosystem service payment scheme (PES) with the necessity of human activities to be considered (Muenzel and Martino, 2018). The carbon sequestration benefit of salt marsh includes carbon reductions due to grazing of salt-marsh vegetation and carbon increases due to methane emission of livestock. By using the social cost of carbon (SCC) approach, British academics have estimated that damages to marine ecosystems, including sediment, come at a cost of \$1.7 billion. A complete comparison of maintaining costs for preventing damages to salt marshes with total recovery benefits (intended to compensate for the loss of salt marshes) suggests that salt-marsh conservation works would be more economical and effective than restoration (Luisetti et al., 2019).

The blue carbon ecosystem along coastal shorelines in China varies between 1,623 and 3,850 km^2 in size, and the total carbon sequestration of mangrove, salt marsh, and seagrass in China is estimated to be 162 TgC, 67 TgC, and 75 TgC, respectively (Gao et al., 2016). Mangrove forest covers an area of 32,834 hm^2 in China, the carbon sequestration density of mangrove vegetation was 8,461 g C m^2, and soil carbon sequestration density (1 m underground) was as high as 27,039 g C m^2 (Liu et al., 2014). The seagrass bed is diverse and covers 8,765.1 km^2 in China, which can be divided into the South China Sea, the Yellow sea, and the Bohai Sea. In addition, 22 species of seagrass have been identified in China, accounting for about 30% of the total number of seagrass species across the world. The total carbon storage capacity of seagrass beds in China is about 0.035 billion tons of CO_2 (Huang et al., 2015). The carbon storage efficiency of seagrass beds in China is estimated to be 32,000 to 57,000 tons of CO_2 based on the carbon storage rate of seagrass beds in the world. A salt marsh is one of the main types of coastal vegetation community in China, distributed in all coastal provinces. The total carbon storage capacity of salt marsh carbon sinks in China ranges between 11,200 and 31,800 tons of CO_2. According to the published estimation of the carbon burial rate of salt marsh in the world, the existing salt marsh in China can capture 9,652–2,748,800 tons of CO_2 per year (Jiao et al., 2018). According to the data of the Food and Agriculture Organization of the United Nations, seaweed farming can effectively capture carbon dioxide as a potential carbon sink. Some studies (Meng and Feagin, 2019) showed the ecological benefits of seaweed farming in China by obtaining the carbon concentration within seaweed tissues and production and implied that different types of seaweed have varying carbon sequestration capacity.

At present, despite numerous studies that have documented the effects of artificial reefs (ARs) in modifying hydrodynamic characteristics in offshore water bodies, there are limited information on the effect of multi-reef combination on hydrodynamics and insufficient data on turbulent flow characteristics. In this regard, the current study mainly concentrates on detailing complex flow characteristics by accounting for different reef configurations. Existing studies on marine carbon sequestration focus on the law of particulate carbon and organic carbon from a geochemical consideration, a systematic description of carbon sink measurement methods are still scarce. In addition, the current mathematical models often ignore the impact of marine fisheries on carbon sequestration, and little work has been done on comprehensive assessments of ecological restoration measures from a carbon-sequestration perspective. Again, there is also a lack of systematic consideration of carbon sink when studying the effect of hydrodynamic characteristics on marine fisheries. In this study, hydrodynamic characteristics around artificial reefs are studied through an ecological restoration project launched near the Juehua Island in the Bohai Sea of China. The response of carbon sink to varying hydrodynamic conditions is also analyzed. Based on the results of carbon sink, we further evaluate flow characteristics and ecological restoration effectiveness following artificial reef deployment and intend to develop a promising ecological restoration scheme by increasing marine carbon sink along with diverse hydrodynamic flow conditions.

2 Materials and methods

2.1 Study site

The Juehua Island National Marine Ranch, as our study site, is located on the southern coast of the Juehua Island, Huludao

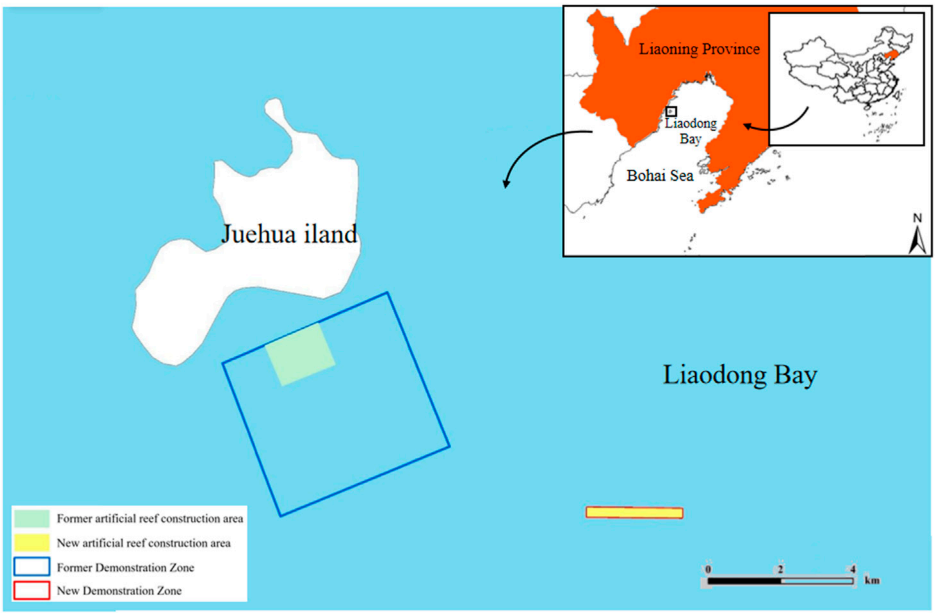

FIGURE 1
Location of the study site.

City, Liaoning Province (120°45′E~ 120°52′41.17″9.63″E and 40°N ~ 40°26′9.82″33′10.46″N, Figure 1). The tide is semidiurnal with a mean tidal range of about 2.06 m (Zhang et al., 2022), and the strength of tidal currents is ~40 cm/s (Huang et al., 1999). Our study site has a typical medium monsoon climate, and the mean annual wind speed is about 7.1 m/s. This ranch is located 12 km from the terrestrial realm with an area of 1,377 ha. The study site is characterized by 10–20 m isobath and suitable for proliferating marine biological resources. Although artificial reefs only cover a total area of 65,987 m^2, the working area of these artificial reefs within this ranch is up to 37, 170, 000 m^3. Two types of artificial reefs were considered, that is, square and M-shaped reefs. A pilot site (about 39 ha) situated in the southeast of this ranch is used to evaluate the performance of artificial reefs in square and M shapes (Zhang et al., 2022). The purposes of this study are twofold: 1) to study *in situ* hydrodynamic changes or characteristics after deploying a series of square and M-shaped reefs; 2) to optimize physical configuration of artificial reefs (e.g., spacings) to enhance biological production.

During spring tides, the flood peak currents move north-eastward between 4° and 69° (the maximum tide of each layer measured at each station spans between 36° and 60°), and the flow direction of the average ebb currents is oppositely south-westward, between 144° and 239° (the maximum ebb tide of each layer stays within the range between 212° and 246°). During neap tides, the rising tides move also toward northeast and vary from 8° to 49° (the maximum flood tide is between 10° and 82°), whereas the average ebb currents propagate toward southwest and stand between 36° and 228° (maximum ebb tide straddles over the range of 206°–236°). The maximum surge tide and the maximum ebb tide transport in directions consistent with their counterparts of the average surge tide and the average ebb tide (i.e., the flow direction of the maximum surge tide is oriented from southwest to northeast, and the flow direction of the maximum ebb tides is reversed from northeast to southwest). In the spring tide period, the residual flow velocity falls within the range of 2.1–8.9 cm/s. During neap tides, the residual flow velocity varied from 4.4 to 21.7 cm/s. The variation of ocean current in the study area has a marginal influence on the placement of artificial reefs, this means the study area is suitable for marine pasture development.

2.2 Artificial reef (AR) arrangement

Figure 2 shows typical square and M-shaped artificial reefs considered in the present study. The square artificial reef (prototype) size is 3.5 m long, 3.5 m wide, and 1.5 m high, and the M-shaped reef (prototype) size is 3.0 m long, 3.0 m wide, and 2.2 m high. An optimization technology for artificial reefs was tested at a smaller scale (i.e., 8.46 ha) in relative to the size of the pilot site (i.e., 39 ha). Field observations suggested that the optimum spacing is 23.57 and 22.43 m for single M-shaped and square reef configuration, respectively, when all these artificial reefs were deployed along wave direction (Shu et al., 2021a).

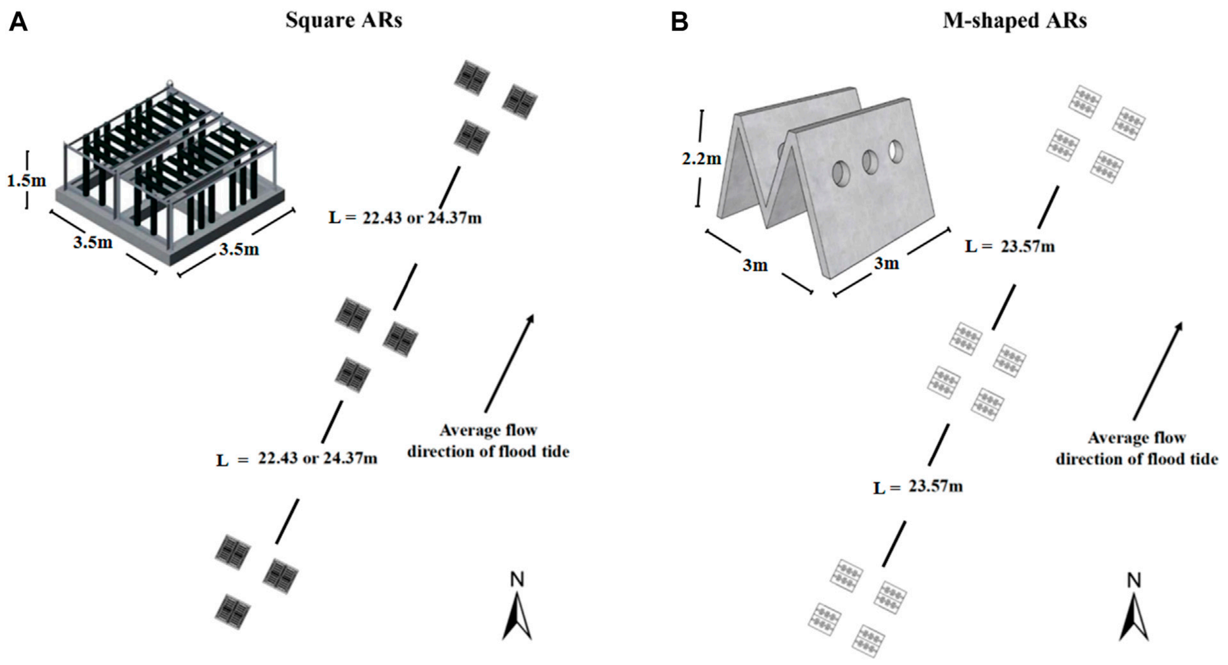

FIGURE 2
Square **(A)** and M-shaped **(B)** artificial reefs placed in the pilot site with three and four reefs making up the respective unit group, black arrow highlights flow direction.

A total of 1,650 M-shaped reefs, 675 square reefs, and 1,232 cubic fish attraction and conservation reefs were placed in the extended pilot site, their configurations are shown in Figure 2. In addition, there are 136 M-shaped breeding reefs and 168 square ecological reefs were installed in the optimized zone according to the optimum spacing as described earlier.

2.3 Experimental setup

The experiment was conducted in a long tilting flume (Length: 25.00 m, width: 0.80 m, height: 0.80 m) at Beijing Normal University. An acoustic Doppler current velocimetry (ADV) was installed 1–2 m in front of the artificial reefs to measure the inflow velocity. The size of the artificial reef model in the experimental flume is scaled to be 1:50 from a prototype. The hydrodynamic characteristics of the artificial reef at four different spacing were investigated. The physical model of different layout spacing of reefs are tested under different flow velocity (i.e., 0.085 m/s, 0.130 m/s, 0.170 m/s, 0.214 m/s, and 0.257 m/s), meanwhile, the particle image velocimetry (PIV) technology was applied to quantify the flow fields generated around artificial reefs. Detailed information about the experimental protocol and physical model of artificial reefs can be found in Shu et al. (2021b; 2021c).

Basic parameters including the length, height, and area were used to describe the variability of flow fields due to the presence of artificial reefs, particularly for upwelling and vortex flow produced around artificial reefs. The maximum upwelling velocity $u_{max\text{-}up}$ and the average upwelling velocity u_{up} were measured to describe the intensity of the upwelling, and the maximum upwelling height $H_{max\text{-}up}$, the maximum upwelling length $L_{max\text{-}up}$, and the total upwelling area A_{up} were used to characterize the spatial scale of the upwelling. The height of the upwelling was calculated with the bottom of the reef as the zero point. At present, there is no unified standard definition for the upwelling phenomenon. Based on previous research results identified in the literature (e.g., Yu et al., 2004), this study defines an upwelling flow field as a region where the ratio between the vertical velocity and the incoming velocity is greater than or equal to 10 percent. Similarly, the parameters including maximum height $H_{max\text{-}bs}$, the maximum length $L_{max\text{-}bs}$ and the total area A_{bs} were used to characterize the scale and magnitude of the back vortex.

2.4 Entropy weight method

Suppose there are n objects in an evaluation index system (n_1, n_2, . . . , n_n) with m indicators (m_1, m_2, . . . , m_m). Let X_{ij} denote the j-th index (j = 1, 2, 3, . . ., m) of the i-th evaluation object (i =

1, 2, 3, . . ., n), the original data related matrix X is then obtained as

$$X = \left(X_{ij}\right)_{n\times m} = \begin{bmatrix} x_{11} & x_{12} & \cdots & x_{1m} \\ x_{21} & x_{22} & \cdots & x_{2m} \\ \vdots & \vdots & \vdots & \vdots \\ x_{n1} & x_{n2} & \cdots & x_{nm} \end{bmatrix}. \tag{1}$$

The original data were made dimensionless to eliminate the dimensional influence, and the relative contribution of the i-th evaluation object under the j-th indicator is thus calculated as follows

$$p_{ij} = \frac{X_{ij}}{\sum_{i=1}^{n} X_{ij}} \left(i = 1, 2 \ldots, n; j = 1, 2 \ldots, m\right). \tag{2}$$

Here, the entropy of the j-th index (e_j) can be determined using the following relation.

$$e_j = -k\sum_{i=1}^{n} p_{ij}\, ln\left(p_{ij}\right), \tag{3}$$

where $k = \frac{1}{\ln n}$, $e_j \geq 0$. The weight of the j-th index (W_j) is thus obtained as

$$W_j = \frac{1 - e_j}{\sum_{j=1}^{m}\left(1 - e_j\right)} \left(j = 1, 2 \ldots\ldots m\right). \tag{4}$$

Finally, a comprehensive score of each index of the i-th evaluation object (Y_i) can be achieved as

$$Y_i = \sum_{i=1}^{m} W_j p_{ij}. \tag{5}$$

2.5 Estimation of net carbon sink

In addition to the carbon sink contribution from offshore wetlands in the original blue carbon system, offshore regions in other kinds of land uses also mean significant carbon sinks. In the existing studies, the main contributor of carbon sink around the offshore region is the phytoplankton. Sometimes, the increase of carbon sink in the coastal waters can also be partially attributed to aquatic animals, particularly in coastal regions of China with rich fishery resources, which can become an effective carbon sink by means of biological fixation (harvesting and forming shells from seawater) and seawater absorption, therefore, diverse aquatic species will have both economic and ecological implications. In this study, artificial reefs were placed in the study site near Juehua Island, offshore of the Bohai Sea, which increased the number of fish and other aquatic animals and demonstrated an impact on carbon sink. The carbon sink was estimated according to its main sources and processes, and the carbon sink effect caused by human disturbance is also evaluated.

TABLE 1 Algal carbon content according to Zhang et al. (2005).

Macroalgae	*Kelp*	*Ulva*	*Wakame*	*Gracilaria*
Content (%)	31.2	30.7	27.9	20.6

After identifying the main sources of ocean carbon emissions and absorption, the following equation for calculating offshore carbon sinks can be obtained.

$$\Delta C = \boldsymbol{C_B} + \boldsymbol{C_P} - \boldsymbol{C_A}, \tag{6}$$

where $\Delta \boldsymbol{C}$ is the ocean net carbon sink (t·km^{-2}·a^{-1}), $\boldsymbol{C_P}$ is the amount of carbon stored in the ocean system (t·km^{-2}·a^{-1}), $\boldsymbol{C_B}$ is the biological carbon sink (t·km^{-2}·a^{-1}),and $\boldsymbol{C_A}$ is the carbon emission from biological activity (t·km^{-2}·a^{-1}).

2.5.1 Biological carbon sinks

Marine biological resources are rich, including macroalgae, shellfish, zooplankton, and macrobenthos. Indeed, existing studies have shown controversial views on the carbon sequestration function of marine animals. Both organic and inorganic carbon in the water can be consumed during the growth process of sea creatures, for example, shellfish can filter organic detritus in the water, and algae can fix and deposit inorganic carbon through photosynthesis. Human activities, such as massive sea fishing, lead to the removal of many creatures into a more complex ecosystem, that is ., carbon circulation through human ingestion, decomposition, and discharge. Thus, the increase in the carbon sink of marine life is represented by the carbon fixed by algae growth ($\boldsymbol{C_a}$) and crustaceans ($\boldsymbol{C_c}, \boldsymbol{C_s}$).

$$\boldsymbol{C_B} = \boldsymbol{C_a} + \boldsymbol{C_s} + \boldsymbol{C_c}. \tag{7}$$

The effect of human intervention on carbon sequestrations by native phytoplankton in the ocean is only considered in terms of the changes in carbon sinks caused by cultured algae. The estimation method of algae carbon sink is given below following related studies on the varieties of marine algae in China (i.e., *kelp, Ulva, wakame*, *and Gracilaria* are major contributors to the amount of carbon sink).

$$\boldsymbol{C_a} = \sum_{i=1}^{n} \boldsymbol{p_i w_{ci}}, \tag{8}$$

in which $\boldsymbol{C_a}$ is the marine carbon sink produced by algae (t·km^{-2}·a^{-1}), $\boldsymbol{p_i}$ is the yield of the i-th algae (t·km^{-2}·a^{-1}), and $\boldsymbol{w_{ci}}$ is the proportion of carbon in the algae (%). According to existing studies, the carbon content of algae is shown in Table 1.

Shellfish, on the one hand, can reduce inorganic carbon in sea water by absorbing HCO_3^- to form calcium carbonate shells, on the other hand, it can absorb organic carbon in water through filter feeding (Fodrie et al., 2017). It is

TABLE 2 Mass and carbon content within mollusk tissue and shellfish following Yue and Wang (2012).

Category		*Mytilus edulis*	Pectinidae	*Ostrea gigas* Thunberg	*Clam*
Mass content	Mollusk tissue (%)	8.47	14.35	6.14	1.98
	Shellfish (%)	91.53	85.65	93.86	98.02
Carbon content	Mollusk tissue (%)	45.98	43.87	44.9	42.84
	Shellfish (%)	12.68	11.44	11.52	11.40

TABLE 3 Oxygen consumption rate of marine organisms invoked from recent studies (e.g., Xu, 2014; Yu et al., 2017; Hu et al., 2021).

Category	*Oratosquilla oratoria*	*Charybdis japonica*	*Hexagrammos otakii*	*Seaurchin*	*Stichopus japonicus*
Oxygen consumption rate ($g \cdot kg^{-1} \cdot h^{-1}$)	1.81	0.34	0.259	0.041	0.011

estimated that the amount of carbon removed from China's offshore waters by harvesting and breeding shellfish is approximately 700,000–990,000 tons per year. Based on previous research, the main shellfish breeding varieties in China's offshore waters are shown in Table 2, the carbon sink of shellfish is estimated as follows:

$$\boldsymbol{C_j} = \boldsymbol{P_j} \times \boldsymbol{R_{st}} \times \boldsymbol{wS_{st}} + \boldsymbol{P_j} \times \boldsymbol{R_s} \times \boldsymbol{wS_t}, \tag{9}$$

$$\boldsymbol{C_s} = \sum_{i=1}^{n} \boldsymbol{C_j}, \tag{10}$$

where $\boldsymbol{C_j}$ is the carbon sequestration amount of the j-th shellfish ($t \cdot km^{-2} \cdot a^{-1}$), $\boldsymbol{P_j}$ is the yield of the j-th shellfish ($t \cdot km^{-2}$), $\boldsymbol{R_{st}}$ is the proportion of soft tissue, $\boldsymbol{R_s}$ is the proportion of shell tissue, and $\boldsymbol{wS_{st}}$ and $\boldsymbol{wS_t}$ represent the carbon content in soft tissue and shell, respectively.

As a benthic creature, crab is considered as a carbon sink because the hard shell is generated during its growth process. The shell contains a large amount of carbon and can exist in nature for a long time. The carbon sink of crab is calculated as follows:

$$\boldsymbol{C_j} = \boldsymbol{P_j} \times \boldsymbol{R_s} \times \boldsymbol{wS_c}, \tag{11}$$

$$\boldsymbol{C_c} = \sum_{i=1}^{n} \boldsymbol{C_j}, \tag{12}$$

where $\boldsymbol{C_j}$ is the carbon sequestration amount of the j-th crab ($t \cdot km^{-2} \cdot a^{-1}$), $\boldsymbol{P_j}$ is the yield of the j-th crab ($t \cdot km^{-2}$), $\boldsymbol{R_s}$ is the ratio of crab shell tissue, and $\boldsymbol{wS_c}$ represents the amount of carbon in the crab's shell. The carbon content of the crab shell is 19.78%, and the mass ratio of the adult crab shell is 53.29%.

2.5.2 Carbon emissions

Since it is difficult to measure the amount of carbon dioxide produced by biological respiration in the ocean, the ratio of carbon dioxide produced by biological respiration to biological oxygen consumption then is used to estimate the amount of carbon dioxide production:

$$\boldsymbol{C_A} = \boldsymbol{\alpha_B} \times \boldsymbol{w_B} \times \boldsymbol{R_c} \times t, \tag{13}$$

where $\boldsymbol{C_A}$ is the carbon dioxide emissions due to biological activities ($t \cdot km^{-2} \cdot a^{-1}$), $\boldsymbol{\alpha_B}$ is the oxygen consumption rate of marine organisms ($g \cdot kg^{-1} \cdot h^{-1}$), $\boldsymbol{w_B}$ is marine biomass ($t \cdot km^{-2}$), R_c is the ratio of carbon dioxide production to oxygen consumption within the same area (i.e., $R_c = \frac{44}{32}$ at the study area), and $\boldsymbol{t}$ is the time for organisms to persist in water (h). In the study site, the main organisms include *Oratosquilla oratoria, Charybdis japonica*, *Hexagrammos otakii,* sea urchin, *and Stichopus japonicus*, their oxygen consumption rates are shown in Table 3.

2.5.3 Carbon storage

Marine carbon storage mainly consists of dissolved carbon dioxide in seawater and carbon deposited in sediment.

$$\boldsymbol{C_P} = \boldsymbol{C_w} + \boldsymbol{C_{sed}}, \tag{14}$$

$$\boldsymbol{C_w} = W \times h \times w, \tag{15}$$

where $\boldsymbol{C_P}$ is the seawater carbon sink ($t \cdot km^{-2} \cdot a^{-1}$), $\boldsymbol{W}$ represents the sea area (km^2), $\boldsymbol{h}$ is the sea depth (m), and $\boldsymbol{w}$ is the solubility (t/m^3).

3 Results

3.1 Ecological evaluation of artificial reefs

In order to estimate the status of marine resources and ecological environment in the Bohai Sea and make a comprehensive evaluation of artificial reef (AR) performance, the entropy weight method (EWM) was used to evaluate the environmental carrying capacity in the study site near Juehua Island. According to previous studies, it

TABLE 4 Relative importance (i.e., weight) of indicators in the pressure-state-response model determined through the entropy weight method (EWM) for the study site.

Criterion	Indicators	Weight	Sign (+ or -)
Pressure	Total amount of pollutants into the sea (TMP)	0.039486	-
	Area of the study area (ASA)	4.01E-15	+
State	Proportion of unclean water surface (PUWS)	0.493,922	-
	Benthic biodiversity (BB)	0.435,354	+
Response	Water quality of rivers into the sea (WQR)	0.031238	-

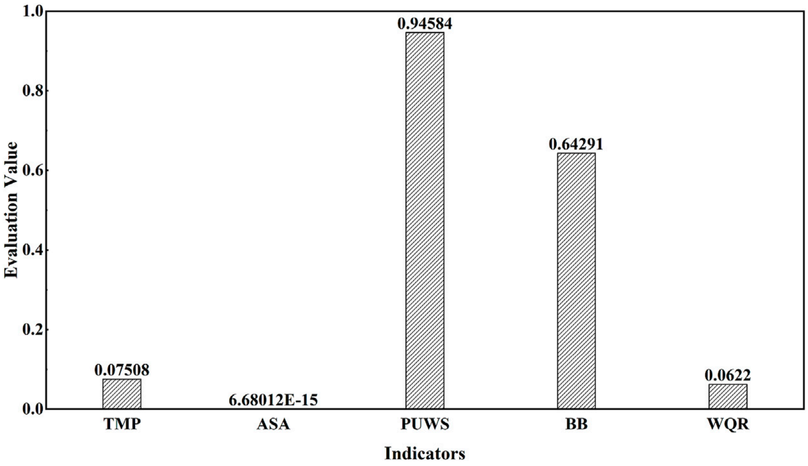

FIGURE 3
Values for indicators considered in the present comprehensive evaluation.

has been found that the pressure on the marine environment mainly comes from the disturbance of human activities, and the diversity of aquatic animals in the ocean and the water quality can be used as indicators to reflect changes in the marine ecological environment. A pressure-state-response model was constructed, where the total amount of pollutants in the sea and the area of the study site were selected as pressure indicators, the proportion of unclean water surface and benthic biodiversity was applied as status indicators, and the water quality of rivers into the sea was response indicator. The original data were compiled from China Marine Ecological Environment Bulletin. According to the procedure of the entropy weight method, the weight for each indicator can be obtained and given in Table 4.

According to the weight analysis of each indicator, Figure 3 shows that the proportions of unclean water surface and benthic biodiversity are the most significant indicators in reflecting pressure on the eco-environmental system within our pilot site (i.e., their weights are 0.49 and 0.43, respectively, Table 4). Indeed, the influence of ocean water quality on the marine ecosystem has been confirmed in previous studies, a pond–wetland complex with constructed root channel technology is used for water quality restoration at the land–water boundary (Wang et al., 2021). Because the control and implementation methods are diverse and relatively simple, the restoration effect is less obvious. As an important indicator, the diversity of aquatic organisms primarily affects the health of the marine ecosystem. By improving aquatic biodiversity, ecosystems impaired due to human-activity disturbances can be well rehabilitated. Also, increased fish sink caused an increased marine sink, which has affected the aquatic biodiversity in the Bohai Sea. To change the biological distribution in the Bohai Sea and restore ecological services, the measures for fish attraction and enhancement through artificial reefs were found to be able to change the biodiversity of the offshore to some extent, thereby changing the status of the offshore carbon sink and affecting the coastal ecosystem.

3.2 Hydrodynamic characteristics of artificial reef–induced flows

Hydrodynamic characteristics of flow fields near artificial reefs at a given spacing and flow rate within a series of flume-based

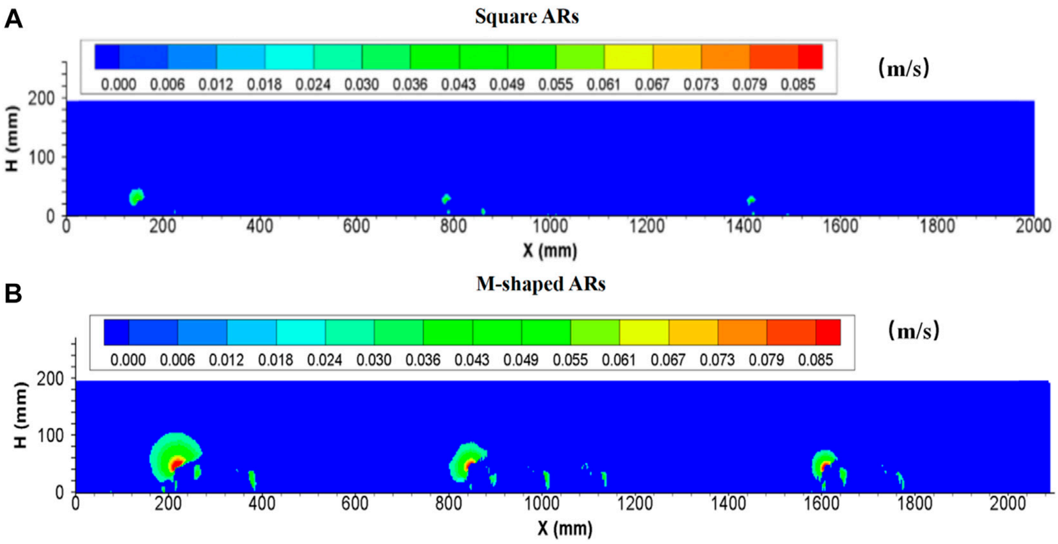

FIGURE 4
Side view of upwelling flows produced by **(A)** square ARs and **(B)** M-shaped ARs (Shu et al., 2021b) under the same experimental condition.

experiments are quantified by analyzing basic parameters associated with upwelling, backswirl, vortex, and turbulent flows (more details for flume experiments can be found in our earlier works, e.g., Shu et al., 2021b; 2021c), the results for hydrodynamic characteristics due to the presence of both M-shaped and square artificial reefs in a laboratory flume were proportionally scaled up to prototype magnitude and detailed in Tables 1, 2. One can observe that the M-shaped reef is superior to the square reef in terms of developing more complex flows. As flow velocity increased, a set of characteristic parameters used to describe upwelling and back vortex, including length and height and total area, are generally shown to increase as well. For a given flow rate, the characteristic parameters for upwelling and back vortex in the square reef case increase first and then followed by a decrease with the reef spacing increasing from 0.75 to 1.50 *L* (note: *L* is the spacing between the artificial reef monocases group in the study site, Figure 2). In contrast, the characteristic parameters of upwelling flow and back vortex in the M-shaped reef case attained their maximum values at the 1.25 *L* spacing. It is interesting to find that characteristic parameters for upwelling and vortex induced by M-shaped artificial reefs were usually larger than those of square-reef counterparts, meaning complex flows produced by M-shaped artificial reefs were of a larger spatial scale. In this regard, M-shaped reefs are more useful in developing marine pasture around coastal regions. More details are given in the following section.

3.2.1 Upwelling flows

In this study, the spatial extent to which the ratio of vertical flow velocity (UV) to incoming flow velocity u_0 being higher than or equal to 0.1 was defined as the upwelling flow region. For square and M-shaped reefs, the distribution of upwelling flows exhibits the similar feature, namely, local upwelling flow usually developed above the surface of the first reef in each group and is followed by a fan distribution of vortex around the reef center, the largest reef upwelling flow region usually was found on the stoss side of the first monomer, the spatial scale of upwelling flows produced by artificial reefs gradually decreased with streamwise distance.

As shown in Figure 4 (also Tables 5, 6), a remarkable difference concerning the upwelling flow area and maximum velocity can be easily identified between M-shaped and square artificial reefs. For example, the maximum upwelling area formed by the M-shaped artificial reef (i.e., 35.2735 m^2) is almost one order-of-magnitude higher than that of the square artificial reef (3.29 m^2). Such a difference can be explained by the artificial reef structure (Gui et al., 2015), that is, the M-shape artificial reefs are designed to have a solid structure with three smaller openings on each side and thus act as barriers for flow entering and exiting (Figure 2); the square artificial reefs are built to have a hollow structure, which permits a quick flow pass with less resistance (Figure 2). Moreover, the M-shaped reef was set as about 1.5 times the height of the square reef, this results in flow blockage across a larger spatial scale Qin (2021).

3.2.2 Back vortex

Similarly, the back vortex region is characterized by slow whirlpools on the lee side and/or inside of a single reef. The maximum height of the back vortex $H_{max\text{-}bs}$, the maximum length of the back vortex $L_{max\text{-}bs}$, and the total area of the back vortex A_{bs} are used to represent the scale of the back

TABLE 5 Summary of hydrodynamic characteristics due to M-shaped reefs according to the flume-based study.

Spacing	Run no.	Q (L/s)	$u_{max\text{-}up}$ (m/s)	u_{up} (m/s)	$H_{max\text{-}up}$ (mm)	$L_{max\text{-}up}$ (mm)	A_{up} (m^2)	$H_{max\text{-}bs}$ (mm)	$L_{max\text{-}bs}$ (mm)	A_{bs} (m^2)	I'_j	I'
0.75	1–1	20	0.3214	0.0923	4.3587	4.3587	22.0391	2.3865	3.2715	42.9194	0.5317	0.3898
1.00	2–1	20	0.2559	0.0848	4.1681	4.1681	17.5764	2.5175	3.2945	43.4347	0.5105	0.3638
1.25	3–1	20	0.3219	0.0912	4.6165	5.0286	25.9330	2.4330	3.6885	46.0026	0.5706	0.3945
1.50	4–1	20	0.3085	0.0912	4.7640	4.3670	24.3240	2.4495	3.5195	45.0785	0.5352	0.3467
0.75	1–2	30	0.4385	0.1417	4.6151	4.4869	22.2199	2.3645	3.6100	42.1495	0.8415	0.5946
1.00	2–2	30	0.2733	0.1297	4.4286	4.0378	17.9835	2.5060	3.4400	44.9943	0.7732	0.5235
1.25	3–2	30	0.4481	0.1489	4.8730	5.0286	27.9557	2.5720	3.7345	46.5187	0.8188	0.5733
1.50	4–2	30	0.3693	0.1335	4.6316	4.3670	24.6742	2.4635	3.6375	45.0900	0.7850	0.5261
0.75	1–3	40	0.6304	0.1844	4.7433	4.3587	22.4664	2.4265	3.5550	41.9707	0.9868	0.7418
1.00	2–3	40	0.3515	0.1724	4.6891	4.2983	19.8667	2.5340	3.5050	44.9997	1.0110	0.6882
1.25	3–3	40	0.6312	0.1907	4.8730	5.1610	28.9753	2.5420	3.6885	47.2552	1.0111	0.7533
1.50	4–3	40	0.5022	0.1828	4.4993	4.4993	26.4254	2.5295	3.6595	45.8974	0.9664	0.6902
0.75	1–4		0.7380	0.2303	4.7433	4.6151	22.8773	2.4610	3.5980	41.7351	1.1726	0.8762
1.00	2–4	50	0.4355	0.2069	4.5588	4.2983	20.6641	2.5530	3.4390	45.3994	1.2506	0.9170
1.25	3–4	50	0.7684	0.2416	5.0012	5.1610	31.3762	2.6360	3.7245	47.5222	1.2463	0.8714
1.50	4–4	50	0.6456	0.2309	5.1610	4.4993	27.2485	2.5495	3.6625	45.5282	1.1676	0.8317
0.75	1–5	60	0.9486	0.2827	5.5125	5.2561	24.5044	2.5680	3.6215	43.5322	1.4792	1.0803
1.00	2–5	60	0.5690	0.2508	4.6891	4.8193	24.2948	2.6630	3.5975	45.2588	1.3982	0.9319
1.25	3–5	60	0.9237	0.2825	5.7836	5.4256	35.2735	2.6850	3.8565	48.0980	1.5408	1.1049
1.50	4–5	60	0.7911	0.2774	5.6903	4.6316	27.7213	2.5465	3.7965	45.7529	1.4121	0.9943

Note: $u_{max\text{-}up}$ = maximum upwelling speed, u_{up} = average upwelling velocity, $H_{max\text{-}up}$ = maximum height of upwelling, $L_{max\text{-}up}$ = maximum length of upwelling, A_{up} = total area of upwelling; $H_{max\text{-}bs}$ = maximum height of backswirl, $L_{max\text{-}bs}$ = maximum length of backswirl, A_{bs} = total area of the back vortex; I'_j= mean longitudinal turbulence strength, and I'= mean vertical turbulence intensity.

vortex. The bottom of the reef was used as a reference datum to calculate the height of the back vortex. For square reefs, under a large range of flow conditions, eddy currents caused by artificial reefs reveal a similar behavior, the back vortex around the first reef monomer in each group is obviously larger than the following eddies. For M-shaped reefs, the back vortex was usually observed between adjacent individual reefs as well as the backside of the last individual reef in each group. Similar to the square-reef case, the characteristic parameters of back eddy currents due to M-shaped reefs at four distances show a positive relationship with velocity.

The values for parameters to describe back eddies induced by M-shaped square and artificial reefs were also compared. It is seen that the size of back eddy current generated by M-shaped reefs is larger than its equivalent caused by square reefs, in particular, a total area of back eddy currents in the former condition is up to about four times higher than that in the latter scenario, which can be attributed to several factors. First, this is because the M-shaped reefs have tilting ramps to force flow to halt and block to a greater degree. Second, the distance between the M-shaped reef group is slightly shorter than that of the square reef group. Third, one more M-shaped artificial reef with very small and limited number of openings is placed in the first row within each reef group, consequently, the flow is severely disturbed under the dual influence of the frontal and tail reefs; thus, a larger scale back vortex is formed in the M-shaped reef configuration.

3.2.3 Longitudinal velocities

Earlier studies suggested that the existence of artificial reefs appears to have an inhibiting effect on flow propagation (e.g., Shu et al., 2021b, 2021c; Harris et al., 2021; Gu et al., 2022). The incoming flow velocity abruptly reduced in the front of artificial reefs, and then the flow separation occurred around the top of the first reef (Figure 5). The flow velocity at the flow separation point increased dramatically, which was significantly different from the flow conditions in the vicinity. The longitudinal velocity of the wake decreases sharply with increasing distance from the separation point, this may assist in forming a distant low flow velocity zone with a moving boundary Qin (2021). This boundary rises gradually from the flow separation point until the maximum level was reached at the second reef group, then declines slightly and finally becomes stable. This is in stark contrast to the longitudinal velocity field without artificial reefs, the vertical length scale with velocities below 0.2 m/s is about ~2 times higher than the height of an individual reef. Beyond this vertical length (i.e., the flow velocity demarcation line), the longitudinal

TABLE 6 Summary of hydrodynamic characteristics due to square reefs according to the flume-based study.

Spacing	Run no.	Q (L/s)	$u_{max\text{-}up}$ (m/s)	u_{up} (m/s)	$H_{max\text{-}up}$ (mm)	$L_{max\text{-}up}$ (mm)	A_{up} (m^2)	$H_{max\text{-}bs}$ (mm)	$L_{max\text{-}bs}$ (mm)	A_{bs} (m^2)	I'_i	I'
0.75	1–1	20	0.1760	0.0954	1.8523	1.0592	1.5601	1.1010	2.8310	10.1067	0.4530	0.2754
1.00	2–1	20	0.1603	0.0982	2.0172	1.2118	1.6471	1.1600	2.8910	10.6145	0.4543	0.2964
1.25	3–1	20	0.2076	0.0961	1.9036	1.2410	1.5414	1.1970	2.8880	9.9695	0.4536	0.3002
1.50	4–1	20	0.1603	0.0876	1.7208	1.0590	1.2784	1.1465	2.8640	10.3669	0.4534	0.2798
0.75	1–2	30	0.2266	0.1184	1.8523	1.1916	1.7354	1.1560	2.8515	10.5726	0.7615	0.5104
1.00	2–2	30	0.2320	0.1305	2.0095	1.2268	1.7698	1.2275	2.9380	10.9557	0.6523	0.3902
1.25	3–2	30	0.2206	0.1206	1.8858	1.3233	1.7650	1.2140	2.9420	11.3030	0.7076	0.4437
1.50	4–2	30	0.2111	0.1241	1.8208	1.0590	1.4360	1.1715	2.9425	10.6972	0.6928	0.4381
0.75	1–3	40	0.3127	0.1645	1.9850	1.2916	1.8406	1.2090	2.9360	10.7082	0.8908	0.6084
1.00	2–3	40	0.2990	0.1515	2.1446	1.3563	2.1903	1.2340	2.9505	11.3659	0.8082	0.4985
1.25	3–3	40	0.3299	0.1638	2.0360	1.3807	2.0066	1.2215	2.8965	10.8344	0.8635	0.5163
1.50	4–3	40	0.2990	0.1638	1.8532	1.2914	1.7512	1.2175	2.8835	10.5204	0.7914	0.5494
0.75	1–4		0.3982	0.2037	2.0023	1.3240	1.9633	1.2050	2.9165	10.7577	0.9771	0.6216
1.00	2–4	50	0.4054	0.1610	2.1446	1.4994	2.6015	1.2655	2.9890	11.5973	0.9552	0.6029
1.25	3–4	50	0.3662	0.2078	2.1173	1.4557	2.6366	1.2440	2.9755	11.1674	0.9846	0.6537
1.50	4–4	50	0.3941	0.2113	1.9532	1.1914	1.8730	1.2530	2.9620	11.5030	0.9951	0.6477
0.75	1–5	60	0.4684	0.2245	2.1173	1.4564	2.2438	1.2315	2.9425	11.1111	1.1470	0.7275
1.00	2–5	60	0.4716	0.1814	2.2446	1.6357	3.1375	1.2915	3.0045	12.1828	1.1483	0.7074
1.25	3–5	60	0.4565	0.2451	2.2360	1.5880	3.2984	1.2465	3.0045	12.2456	1.1506	0.7563
1.50	4–5	60	0.4716	0.2608	1.9532	1.3237	2.5182	1.2695	2.9920	11.4185	1.1448	0.7430

Note: The symbols have the same meanings as detailed in Table 5.

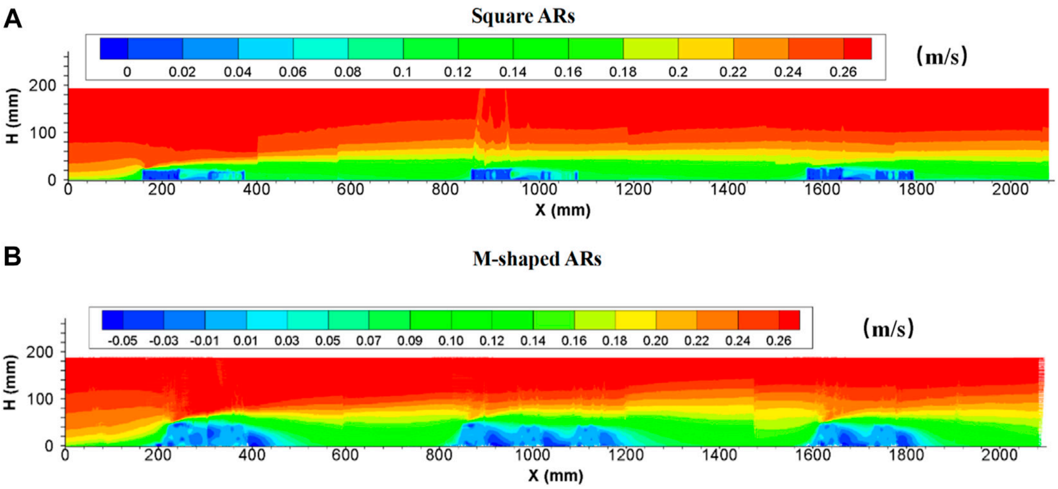

FIGURE 5
Side view of longitudinal velocity field due to the presence of **(A)** square ARs and **(B)** M-shaped ARs under the same experimental condition.

flow velocities are very similar to those observed under flow conditions without artificial reefs. Meanwhile, the average longitudinal velocity near the bed (or artificial reefs) represents a reduction of nearly 75% in relative to measured velocity under no-artificial-reef flows, implying that flow resistance is more obvious due to the presence of artificial reefs.

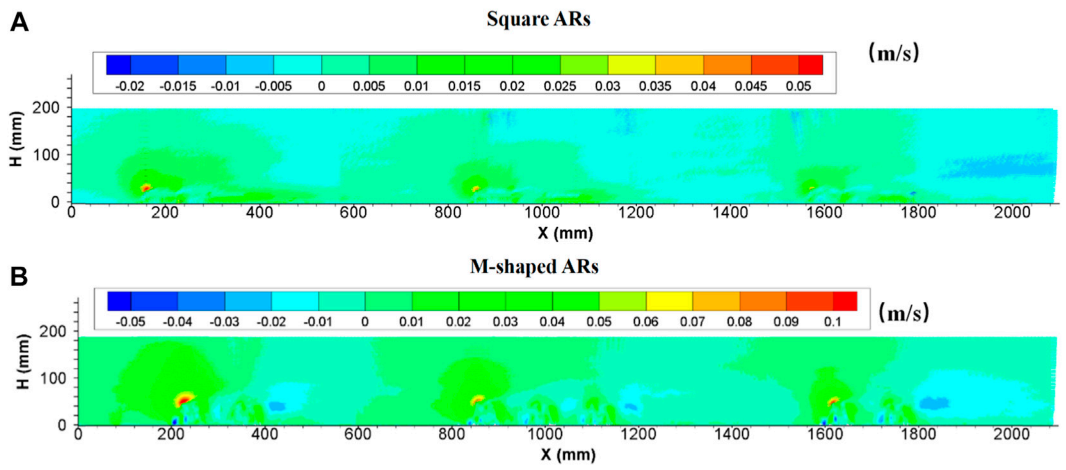

FIGURE 6
Side view of vertical velocity field following the presence of square ARs **(A)** and M-shaped ARs **(B)** under the same experimental condition.

Following the deployment of M-shaped reefs, the spatial distribution pattern of longitudinal velocity was consistent with square-reef situations under the same experimental conditions, both descend and ascend of flow separation point and boundary were well identified, and the vertical length scale with velocities lower than 0.2 m/s is 2.3 times the M-shaped reef height; also, the averaged longitudinal velocity near the bed is decreased to 42% due to the presence of M-shaped artificial reefs, reductions in flow velocity is substantial, especially in the proximity to concrete reefs, due to the appearance of inverse flow velocity originated from eddy currents. Overall, the M-shaped reefs tend to have a relatively strong effect in modifying flow fields as well as flow velocities than the square reefs, which can be primarily attributed to the difference in reef structure highlighted earlier.

3.2.4 Vertical velocities

After a series of square artificial reefs were placed on the bed at a given spacing, the vertical flow velocity often reaches the maximum value in the front or around the top of the first single reef in each group, and the vertical velocity field extends outwardly with the vortex center and turns out to be in an arc distribution. The maximum vertical velocity produced by artificial reefs gradually decreased along the flow direction, this behavior is consistent with the changing behaviors of upwelling flows. Also, it can be found that the presence of artificial reefs can enhance current turbulence and spatial changes associated with the entire vertical velocity domain if compared with the flow fields devoid of artificial reefs. Vertical flow velocities increased around the reef and decreased when the flow was transported far away from the artificial reef. The vertical profile of velocity owing to the presence of M-shaped artificial reefs is largely consistent with square reef–induced counterparts; however, M-shaped reefs seem to be able to change vertical flow velocities to a greater degree than square reefs (details in Figure 6).

3.2.5 Characteristics of turbulence intensity

Since the introduction of the square artificial reef into water bodies, the region subject to artificial reef disturbance was totally filled with strong turbulent flows. The turbulence intensity at the upperstream inlet was practically the same as in flows without artificial reefs, then started to increase suddenly in the front of the first artificial reef and maintained at an incremental rate by following downstream artificial reefs. The turbulent flows are enhanced when arriving to the second reef group, attenuated slightly and then become stabilized, thus forming a distinct turbulence boundary. The longitudinal turbulence intensity is obviously larger than the vertical turbulence intensity in terms of magnitude and extent of influence. The maximum height of this distinct boundary is nearly four times the artificial reef height. In terms of the length of a perturbation along the flow direction, the local flow perturbation length of the longitudinal turbulent strength ($I_l^{'} > 0.14$) is about 13–17 times the reef height, while the local flow perturbation length of the vertical turbulent strength ($I_l^{'} > 0.086$) is about 10–14 times the reef height, and the location of the longitudinal turbulent strength is obviously higher than that of the vertical turbulent strength. The turbulent turbulence occurred on the upper surface of the first reef and extended beyond the rear of the last artificial reef in each group, exhibiting a longitudinal band distribution as shown in Figure 7.

The turbulence currents caused by both square and M-shaped artificial reefs are very similar in many aspects discussed earlier. For each experiment, the magnitude of longitudinal turbulence intensity is higher than the vertical turbulence intensity (Figures 7, 8). The maximum height of

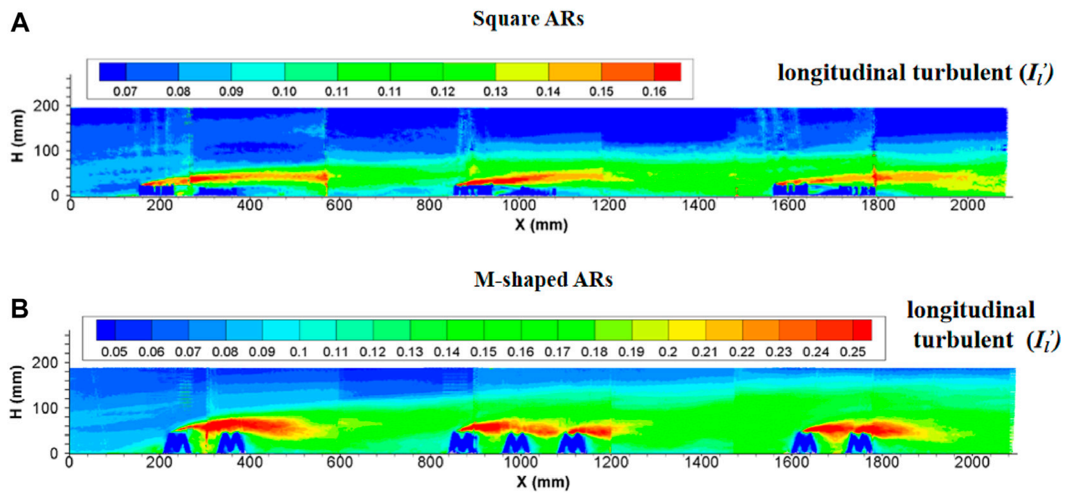

FIGURE 7
Side view of longitudinal turbulence intensity enhanced by **(A)** square ARs and **(B)** M-shaped ARs (Shu et al., 2021c) under the same experimental condition.

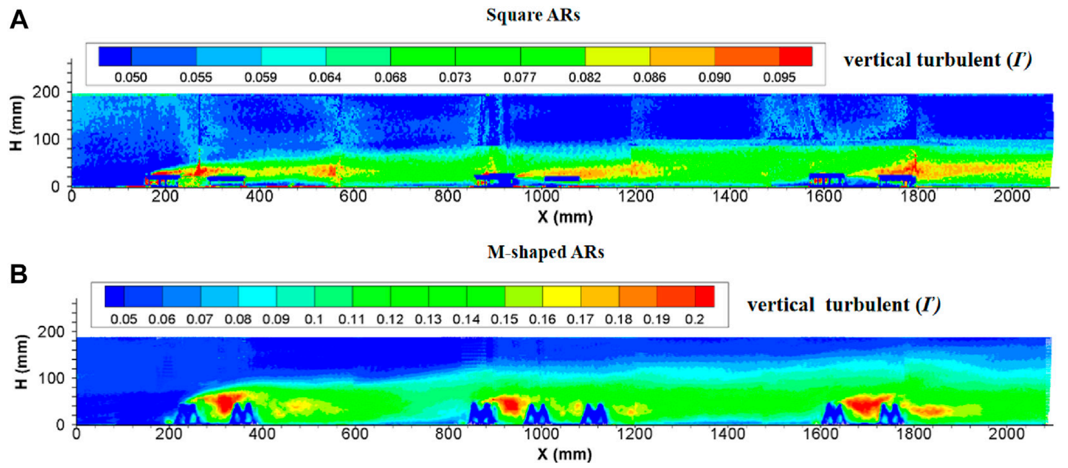

FIGURE 8
Side view of vertical turbulence intensity induced by **(A)** square ARs and **(B)** M-shaped ARs (Shu et al., 2021c) under the same experimental condition.

the vertical turbulence intensity is about four times the M-shaped reef height, the vertical turbulence intensity is roughly three times higher than the reef height. In terms of the perturbation flow length along the streamwise direction, the local flow perturbation length of the longitudinal turbulent intensity (>2.0) is 7–9 times of reef height, whereas the flow perturbation length of the vertical turbulent intensity (>0.16) is 3–5 times of reef height. Comparatively, the M-shaped reefs have a larger effect on the turbulence intensity than the square reefs Qin (2021).

3.3 Net carbon sink

Field investigations of underwater cages indicated that biological resources beneath the coastal water of Juehua Island have been significantly improved. It is shown from Figure 9 that the number of biological resources in the pilot reef area (i.e., 75.25, 142.33, 298.77, and 104.7 g/cage/day) was usually higher than that measured across the control area (i.e., 43.54, 114.36, 168.79, and 55.51 g/cage/day) at the same time from July 2019 to October 2021. The growth rate for biological resources in

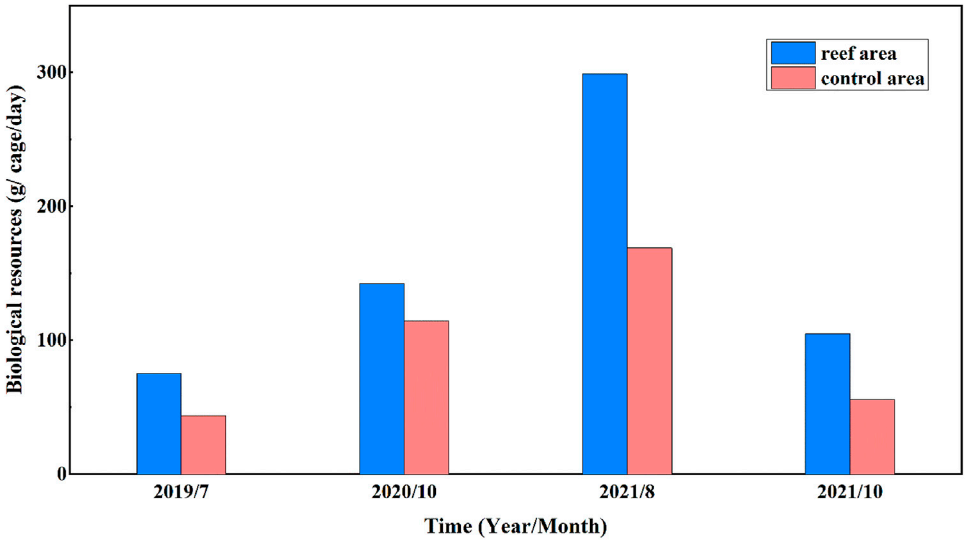

FIGURE 9
Comparison of biological resources in the artificial reef working site and contrasting control area.

TABLE 7 Results of carbon emissions and carbon sinks for Juehua Island offshore.

Classification	Biological net carbon sink ($t\cdot km^{-2}\cdot a^{-1}$)	Carbon emissions from biological activities ($t\cdot km^{-2}\cdot a^{-1}$)	Ocean carbon storage ($t\cdot km^{-2}\cdot a^{-1}$)	Net carbon sink ($t\cdot km^{-2}\cdot a^{-1}$)	Total amount of net carbon sink ($t\cdot a^{-1}$)
M-shaped ARs	0.0637	3.2570	30.1408	26.9466	35.8390
Square ARs	0.0093	0.4730	4.3772	3.9134	5.2048
Total	0.0730	3.7300	34.5180	30.8600	41.0438

the artificial reef working area is up to 72.81%, 24.45%, 77.00%, and 88.62% during the last 4 years if compared with those in the contrasting control area devoid of artificial reefs, indicating artificial reefs with certain configuration appear to have a positive impact on enhancing marine biological resources.

The results of our calculated carbon sinks for the study site are given in Table 7. Flow characteristics near the Juehua Island are unsurprisingly modified by numerous artificial reefs deployed on purpose, which certainly reshapes the temporal and spatial distribution of nutrients, creates a desirable habitat environment for fishes, and finally leads to an increasing fishery carbon sink. In contrast, the biological net carbon sink is very low (i.e., 0.073) and shows a less-evident change, which mainly could be explained by different carbon sink contributions from different species of organisms. There are fewer crustaceans on the Juehua Island, which implies that a lower carbon sink contribution with higher carbon emissions may occur instead. In addition, Flounder was the primary breeding fish released to the Juehua Island study area, therefore, its carbon sequestration could not be stored in the ocean over a long time and the related net carbon sequestration was low. Compared with many different ecological restoration measures taken across coastal islands somewhere else in China, the Juehua marine ranch is not developed by pursuing economic benefits from higher organisms (e.g., including long-term carbon sequestration creatures such as mussels), which in turn makes Juehua Island biological net carbon sequestration on a lower level. In addition, crustaceans also represent as a marine carbon sink. In our calculation method, the difference of ocean carbon storage and influences of meteorological factors are not considered, but instead, our attention is shifted to the changes in carbon sink caused by living organisms and their activities. A parallel comparison of the relative contribution of various carbon sinks within the study site shows that the marine carbon storage is the most dominant marine carbon sink, which is regarded as static in this study, and the changes caused by meteorological factors can be reasonably ignored.

Considering the fact that the spatial scale of upwelling and back vortex induced by M-shaped artificial reefs (ARs) is approximately eight times than that by square artificial reefs (ARs), both carbon emission and carbon sinks for Juehua Island offshore ground are estimated on the basis of the total area of kindred artificial reef and additional area due to artificial reef influence. It is noted here that the offshore ground attached with M-shaped artificial reefs (ARs) is only three times larger than those with square artificial reefs (ARs), but the total amount of carbon sink potential of the Juehua Island offshore from M-shaped artificial reefs (ARs) deployed ground is almost seven times higher than that from the square artificial reefs covered region (Table 7), this clearly demonstrates a dominant role of M-shaped artificial reef in restructuring near-bed flow conditions and its influence on local carbon sink capacity.

4 Discussion

The main objective of ecological restoration in the pilot site of Juehua Island is to improve the aquatic biodiversity. The current ecological restoration measures include an optimization of breeding/releasing technology and artificial reef configuration. The former not only contains the nutrient link with a high ecological transfer efficiency by reconstructing the food network, and but also selects the appropriate breeding varieties and the flow conditions through accounting for local species, economic value, resource shortage degree, seedling breeding basis, and other factors. The latter improves the ecological environment by effectively deploying artificial reefs. Artificial reefs affect the tempo-spatial distribution of nutrients and their corresponding environment by modifying the local hydrodynamic characteristics. These artificial reefs seem to change water movement, and the incoming flow appears to be subject to flow separation, the incoming flow is partially uplifted to form upwelling currents, and the remaining part passes through the reef and generates eddy currents. Upwelling flows can promote seawater exchange vertically, and increase nutrient transport from sea bottoms to surface layers, this process help improve marine primary productivity by enhancing the bait effect and attracting more fish to gather around artificial reefs. On the back side of the reef, a vortex zone with low speed and stable structure will be generated, which is conducive to the nutrients settling and provides a man-made habitat for fish to settle down, and avoid enemies and rope bait. In this sense, a promising ecological and economic marine pasture can be achieved if artificial reefs (with a proper shape, size, and configuration) enable a reproduction of complicated flow conditions and diverse habitats. Nevertheless, the effectiveness of artificial reefs for marine ecological restoration should be assessed over a larger timescale because ecological succession changes and flow condition changes are not comparable.

There are also limitations associated with the present study. First, our understanding of offshore hydrodynamic characteristics produced by artificial reefs still remains incomplete, the primary reason is that our flume-based experiments use unidirectional flows, which is a simplified representation of complex rotating flows in the Juehua offshore, this also makes our interpretation of biological aggregation as a result of artificial reef deployment inadequate, such complex flows should be accounted for in future studies when conducting laboratory experiments. More importantly, the increase in offshore biological resources as well as production due to the presence of artificial reefs is often measured at a multi-decadal scale if compared with instantaneous flow changes due to the artificial reef deployment, this means the effect of artificial reefs on enhancing biological resources appears less convincing within short periods of time (e.g., Figure 9), our ongoing field surveys should last at least for several decades. Third, the present study of carbon sequestration only involves dominant algae and crustaceans in this region, our estimation strongly depends on a simple sampling technique (i.e., hanging basket capture). However, other marine fauna and flora are available in the Juehua offshore as well (e.g., *Charybdis japonica*), these uncertainties underline the importance of a more comprehensive study in the further research efforts.

5 Summary

The ocean plays an important role in carbon capture, and both hydrodynamic and ecological conditions to dictate reproduction and aggregation of organisms in the marine ecosystem largely determine carbon capture potential on offshore grounds. A set of artificial reefs designed in square and M shapes were deployed on a laboratory flume bed to generate complex flows. Because artificial reefs are able to cause flow halt and block, thereby producing well-developed upwelling and back eddy currents. It has been found that the flow turbulence increase with flow velocity and can be enhanced due to the presence of artificial reefs, particularly in the M-shaped artificial reef configurations. Both magnitudes and spatial scales of upwelling flow and back vortex induced by M-shaped reefs are obviously greater than those in square-reef cases, which is more conducive to creating an environment suitable for marine lives.

Diverse flow conditions due to the presence of artificial reefs somehow support the accumulation of marine lives, which could potentially increase the number of organisms and drive the growth of carbon sinks. However, our estimation in the present study site showed that 1) the M-shaped artificial reefs are the primary contributor to the carbon sink potential of the Juehua Island offshore in the carbon sink; 2) the carbon sink in this region brought from biological aggregation was not as high as expected, which was mainly due to limited marine biological species of Juehua offshore that can be accounted for. Therefore, the introduction of appropriate and non-invasive species should be carefully considered during the development of efficient marine pasture rather than only increasing artificial reef–induced disturbances to local flow fields.

Data availability statement

The original contributions presented in the study are included in the article/Supplementary Material; further inquiries can be directed to the corresponding author.

Author contributions

AS: conceptualization and supervision; ZZ: formal analysis and writing–original draft; LW: conceptualization and writing–original draft; TS, WY, JZ, and FZ: analysis and suggestions; JQ: experiments and analysis.

Funding

The research reported in this manuscript is funded by the National key research and development plan (Grant No. 2018YFC1406404), the Natural Science Foundation of China (Grant Nos U1901212 and 52009041), and Fundamental Research Funds for the Central Universities (Grant No. 2020MS024), and the Beijing Advanced Innovation Program for Land Surface Science.

Conflict of interest

FZ is employed by Power China ZhongNan Engineering Corporation Limited.

The remaining authors declare that the research was conducted in the absence of any commercial or financial relationships that could be construed as a potential conflict of interest.

Publisher's note

References

Ariza, A., Garijo, J. C., Landeira, J. M., Bordes, F., and Hernandez-Leon, S. (2015). Migrant biomass and respiratory carbon flux by zooplankton and micronekton in the subtropical northeast Atlantic Ocean (Canary Islands). *Prog. Oceanogr.* 134, 330–342. doi:10.1016/j.pocean.2015.03.003

Bertram, C., Quaas, M., Reusch, T. B. H., Vafeidis, A. T., Wolff, C., and Rickels, W. (2021). The blue carbon wealth of nations. *Nat. Clim. Change.* 11 (8), 704–709. doi:10.1038/s41558-021-01089-4

Canu, D. M., Ghermandi, A., Nunes, P. A., Lazzari, P., Cossarini, G., and Solidoro, C. (2015). Estimating the value of carbon sequestration ecosystem services in the Mediterranean Sea: An ecological economics approach. *Global Environ. Chang.* 32, 87–95. doi:10.1016/j.gloenvcha.2015.02.008

Chen, G., Bai, J., Yu, L., Chen, B., Zhang, Y., Liu, G., et al. (2022). *Effects of ecological restoration on carbon sink and carbon drawdown of degraded salt marshes with carbon-rich additives application.* Land Degradation & Development (Chichester, UK: John Wiley & Sons, Ltd.), 1–12. doi:10.1002/ldr.4306

Dzierzbicka-Glowacka, L., Kulinski, K., Maciejewska, A., Jakacki, J., and Pempkowiak, J. (2011). Numerical modelling of POC dynamics in the southern Baltic under possible future conditions determined by nutrients, light and temperature. *Oceanologia* 53 (4), 971–992. doi:10.5697/oc.53-4.971

Fischer, G., Neuer, S., Ramondenc, S., Muller, T. J., Donner, B., Ruhland, G., et al. (2020). Long-Term changes of particle flux in the canary basin between 1991 and 2009 and comparison to sediment trap records off mauritania. *Front. Earth Sci.* 8, 21. doi:10.3389/feart.2020.00280

Fodrie, F. J., Rodriguez, A. B., Gittman, R. K., Grabowski, J. H., Lindquist, N. L., Peterson, C. H., et al. (2017). Oyster reefs as carbon sources and sinks. *Proc. R. Soc. B* 284, 20170891. doi:10.1098/rspb.2017.0891

Galdo, M. I. L., Guerreiro, M. J. R., Vigo, J. L., Rodriguez, I. A., Lorenzo, R. V., Couce, J. C. C., et al. (2022). Definition of an artificial reef unit through hydrodynamic and structural (CFD and FEM) models—application to the ares-betanzos estuary. *J. Mar. Sci. Eng.* 10 (2), 230. doi:10.3390/jmse10020230

Gao, Y., Yu, G., Yang, T., Jia, Y., He, N., and Zhuang, J. (2016). New insight into global blue carbon estimation under human activity in land-sea interaction area: A case study of China. *Earth-Science Rev.* 159, 36–46. doi:10.1016/j.earscirev.2016.05.003

Gu, S., Zheng, W., Wu, H., Chen, C., and Shao, S. (2022). DualSPHysics simulations of spillway hydraulics: A comparison between single-and two-phase modelling approaches. *J. Hydraulic Res.*, 1–18. doi:10.1080/00221686.2022.2064343

Gui, Q., Dong, P., Shao, S., and Chen, Y. (2015). Incompressible SPH simulation of wave interaction with porous structure. *Ocean. Eng.* 110, 126–139. doi:10.1016/j.oceaneng.2015.10.013

Harris, L., Liang, D., Shao, S., Zhang, T., and Roberts, G. (2021). MPM simulation of solitary wave run-up on permeable boundaries. *Appl. Ocean Res.* 111, 102602. doi:10.1016/j.apor.2021.102602

Hu, F. W., Wang, X. L., Gao, F. X., Li, L., Jian, Y. X., Wang, X., et al. (2021). Influence of temperature, salinity, and anesthetics on the oxygen consumption and ammonia excretion rates in fat greenling(*Hexagrammos otakii*) juveniles. *Mar. Sci.* 45, 54–61. (in Chinese).

Huang, D., Su, J., and Backhaus, J. O. (1999). Modelling the seasonal thermal stratification and baroclinic circulation in the Bohai Sea. *Cont. Shelf Res.* 19 (11), 1485–1505. doi:10.1016/S0278-4343(99)00026-6

Huang, Y. H., Lee, C. L., Chung, C. Y., Hsiao, S. C., and Lin, H. J. (2015). Carbon budgets of multispecies seagrass beds at dongsha island in the south China sea. *Mar. Environ. Res.* 106, 92–102. doi:10.1016/j.marenvres.2015.03.004

Jennerjahn, T. C. (2020). Relevance and magnitude of 'Blue Carbon' storage in mangrove sediments: Carbon accumulation rates vs. stocks, sources vs. sinks. *Estuar. Coast. Shelf Sci.* 247, 107027. doi:10.1016/j.ecss.2020.107027

Jiao, N., Liang, Y., Zhang, Y., Liu, J., Zhang, Y., Zhang, R., et al. (2018). Carbon pools and fluxes in the China Seas and adjacent oceans. *Sci. China Earth Sci.* 61 (11), 1535–1563. doi:10.1007/s11430-018-9190-x

Lebrato, M., Mendes, P. D., Steinberg, D. K., Cartes, J. E., Jones, B. M., Birsa, L. M., et al. (2013). Jelly biomass sinking speed reveals a fast carbon export mechanism. *Limnol. Oceanogr.* 58 (3), 1113–1122. doi:10.4319/lo.2013.58.3.1113

Lee, C. L., Lin, W. J., Liu, P. J., Shao, K. T., and Lin, H. J. (2021). Highly productive tropical seagrass beds support diverse consumers and a large organic carbon pool in the sediments. *Divers. (Basel).* 13 (11), 544. doi:10.3390/d13110544

Liu, H., Ren, H., Hui, D., Wang, W., Liao, B., and Cao, Q. (2014). Carbon stocks and potential carbon storage in the mangrove forests of China. *J. Environ. Manage.* 133, 86–93. doi:10.1016/j.jenvman.2013.11.037

Luisetti, T., Turner, R. K., Andrews, J. E., Jickells, T. D., Kröger, S., Diesing, M., et al. (2019). Quantifying and valuing carbon flows and stores in coastal and shelf ecosystems in the UK. *Ecosyst. Serv.* 35, 67–76. doi:10.1016/j.ecoser.2018.10.013

Macreadie, P. I., Allen, K., Kelaher, B. P., Ralph, P. J., and Skilbeck, C. G. (2011). Paleoreconstruction of estuarine sediments reveal human-induced weakening of coastal carbon sinks. *Glob. Chang. Biol.* 18 (3), 891–901. doi:10.1111/j.1365-2486.2011.02582.x

Mariani, G., Cheung, W. W., Lyet, A., Sala, E., Mayorga, J., Velez, L., et al. (2020). Let more big fish sink: Fisheries prevent blue carbon sequestration—Half in unprofitable areas. *Sci. Adv.* 6 (44), eabb4848. doi:10.1126/sciadv.abb4848

Martins, M., de los Santos, C. B., Masqué, P., Carrasco, A. R., Veiga-Pires, C., and Santos, R. (2021). Carbon and nitrogen stocks and burial rates in intertidal vegetated habitats of a mesotidal coastal lagoon. *Ecosystems* 25 (2), 372–386. doi:10.1007/s10021-021-00660-6

Meng, W., and Feagin, R. A. (2019). Mariculture is a double-edged sword in China. *Estuar. Coast. Shelf Sci.* 222, 147–150. doi:10.1016/j.ecss.2019.04.018

Muenzel, D., and Martino, S. (2018). Assessing the feasibility of carbon payments and Payments for Ecosystem Services to reduce livestock grazing pressure on saltmarshes. *J. Environ. Manage.* 225, 46–61. doi:10.1016/j.jenvman.2018.07.060

Shu, A., Qin, J., Sun, T., Yang, W., Wang, M., and Zhu, J. (2021a). Discussion on water and sediment dynamic characteristics and layout optimization of typical artificial reefs in Liaodong Bay of Bohai Sea. *J. Hydraulic Eng.* 53 (01). (in Chinese). doi:10.13243/j.cnki.slxb.20210246

Shu, A., Rubinato, M., Qin, J., Zhu, J., Sun, T., Yang, W., et al. (2021b). The hydrodynamic characteristics induced by multiple layouts of typical artificial M-type reefs with sea currents typical of liaodong bay, BoHai sea. *J. Mar. Sci. Eng.* 9 (11), 1155. doi:10.3390/jmse9111155

Shu, A., Qin, J., Rubinato, M., Sun, T., Wang, M., Wang, S., et al. (2021c). An experimental investigation of turbulence features induced by typical artificial M-shaped unit reefs. *Appl. Sci.* 11 (4), 1393. doi:10.3390/app11041393

Wang, W., Yang, T., Guan, W., Peng, W., Wu, P., Zhong, B., et al. (2021). Ecological wetland paradigm drives water source improvement in the stream network of Yangtze River Delta. *J. Environ. Sci.* 110, 55–72. doi:10.1016/j.jes.2021.03.015

Watanabe, K., Yoshida, G., Hori, M., Umezawa, Y., Moki, H., and Kuwae, T. (2020). Macroalgal metabolism and lateral carbon flows can create significant carbon sinks. *Biogeosciences* 17 (9), 2425–2440. doi:10.5194/bg-17-2425-2020

Xu, X. H. (2014). *Study on the effects of environmental stress on the immune and digestive physiology of* Charybdis japonica. Xuzhou, China: China Mining University. (in Chinese).

Yu, C. D., Yu, C. G., and Yan, S. Q. (2004). Hydrodynamic simulation to the best layout of artificial ship-reefs. *Oceanol. Limnologia Sinica* 35 (4), 305–312. (in Chinese).

Yu, X. M., Xing, K., and Chen, L. (2017). *Effects of temperature on the oxygen consumption rate, ammonia excretion rate and suffocation point of Oratosquilla oratoria larvae. 2017 Chinese Fisheries Association Annual Conference.* Jiangxi, China: Nanchang. (in Chinese).

Yue, D. D., and Wang, L., M. (2012). Development of Marine mollusk culture in Yangtze River Delta based on direct carbon sink accounting. *J. Shandong Agric. Sci.* 44, 133–136. (in Chinese).

Zhang, J. H., Fang, J. G., and Tang, Qisheng. (2005). Contribution of shallow shellfish culture to the Marine carbon cycle in China. *Adv. Earth Sci.* 20 (3), 359–365. (in Chinese).

Zhang, Z., Wei, Y. A. N. G., Zhang, Z., Tao, S. U. N., and Haifei, L. I. U. (2022). Characteristics of typical biological communities and identification of key environmental factors in the seagrass bed of Xingcheng-Juehua Island, Bohai Sea. *J. Beijing Normal Univ. Nat. Sci.* 58 (1), 90–98. (in Chinese). doi:10.12202/j.0476-0301.2021140

Zhang, Z. Y., and Yang, W. (2022). Energy fluxes and trophic structure of an artificial reef ecosystem in Juehua island based on Ecopath model. *Mar. Environ. Sci.* 2022 (04), 41. (in Chinese). doi:10.13634/j.cnki.mes.2022.04.013

Zhu, J. J., and Yan, B. (2022). Blue carbon sink function and carbon neutrality potential of mangroves. *Sci. Total Environ.* 822, 153438. doi:10.1016/j.scitotenv.2022.153438

Zalmon, I. R., Boina, C. D., and Almeida, T. C. M. (2012). Artificial reef influence on the surrounding infauna-north coast of Rio de Janeiro State, Brazil. *J. Mar. Biol. Assoc. UK.* 92 (06), 1289–1299. doi:10.1017/s0025315411001147

Frontiers in Environmental Science

TYPE Original Research
PUBLISHED 01 September 2022
DOI 10.3389/fenvs.2022.971786

Effect of periodic water-sediment laden flow on damage for steel piles

Mingwei Liu, Liqin Zeng*, Linjian Wu, Chenhao Zhu and Erdi Abi

National Engineering Research Center for Inland Waterway Regulation, School of River and Ocean Engineering, Chongqing Jiaotong University, Chongqing, China

OPEN ACCESS

EDITED BY
Snehasis Kundu,
National Institute of Technology,
Jamshedpur, India

REVIEWED BY
Weilin Chen,
National University of Singapore,
Singapore
Xuanlie Zhao,
Harbin Engineering University, China

*CORRESPONDENCE
Liqin Zeng,
zlq_pbl@126.com

SPECIALTY SECTION
This article was submitted to Freshwater Science,
a section of the journal
Frontiers in Environmental Science

RECEIVED 17 June 2022
ACCEPTED 03 August 2022
PUBLISHED 01 September 2022

CITATION
Liu M, Zeng L, Wu L, Zhu C and Abi E (2022), Effect of periodic water-sediment laden flow on damage for steel piles.
Front. Environ. Sci. 10:971786.
doi: 10.3389/fenvs.2022.971786

Due to the problems of shallow overburden and deep water construction, etc., steel tube piles are mostly used in the substructures of frame-wharves in inland rivers of China, especially in the upper stream of Yangtze River. Affected by the fluctuating backwater area of the Three Gorges, anticorrosion coatings of steel structures generally fell off. The steel piles exposed to the water level fluctuation area are subjected to periodic erosion damage process of water-sediment laden flow, which accelerate the corrosions of the steel pile and greatly affect the durability of the wharf structures. In order to explore the effect of periodic water-sediment laden flow on the damage for steel piles in water level fluctuation area of inland rivers, a series of accelerated periodic erosion tests were carried out in laboratory to acquire the damage laws of steel samples under different working conditions. Results showed that the residual masses of steel samples fluctuated with the increasing number of cycles and that the corrosion depths of steel samples were logarithmically correlated with the experimental time. According to the results of periodic accelerated erosion test based on the water-sediment laden flow and existing corrosion theory, a time-dependent model for the corrosion of steel components under water-sediment laden flow was established, as well as a evaluated method for the resistance degradation of steel pile was proposed. Finally, after 20 years, the actual resistance of the steel structure exposed to the water level fluctuation area was less than 60% compared by the initial structural resistance. The research results can provide important guiding significance for reasonably predicting the durability of hydraulic steel structures.

KEYWORDS

water-sediment laden flow, periodic erosion, steel piles, damage, resistance deterioration

Introduction

Affected by the fluctuating backwater area of the Three Gorges, the multi-layers frame-type wharf structures are mostly used in the upper stream of the Yangtze River. The substructures of these structural types usually adopt the steel structures with high strength, light weight and convenient construction. As the steel structure (Including longitudinal and transverse steel braces, steel berthing component, steel tube) under the wharf is eroded by water-sediment laden flow year round, the anticorrosion coating of the

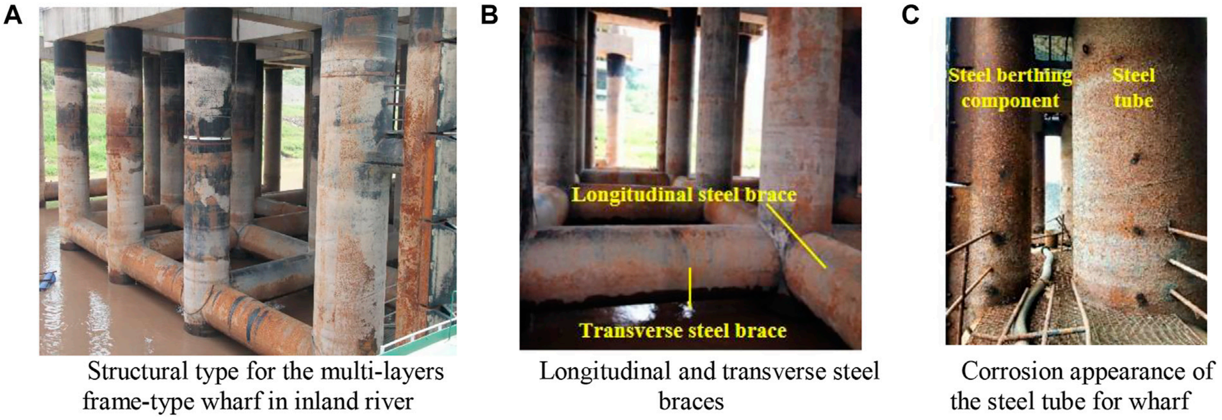

FIGURE 1
Damage morphology of the steel components for the multi-layers frame-type wharf in inland river (Steel component include longitudinal and transverse steel braces, steel berthing component, steel tube).

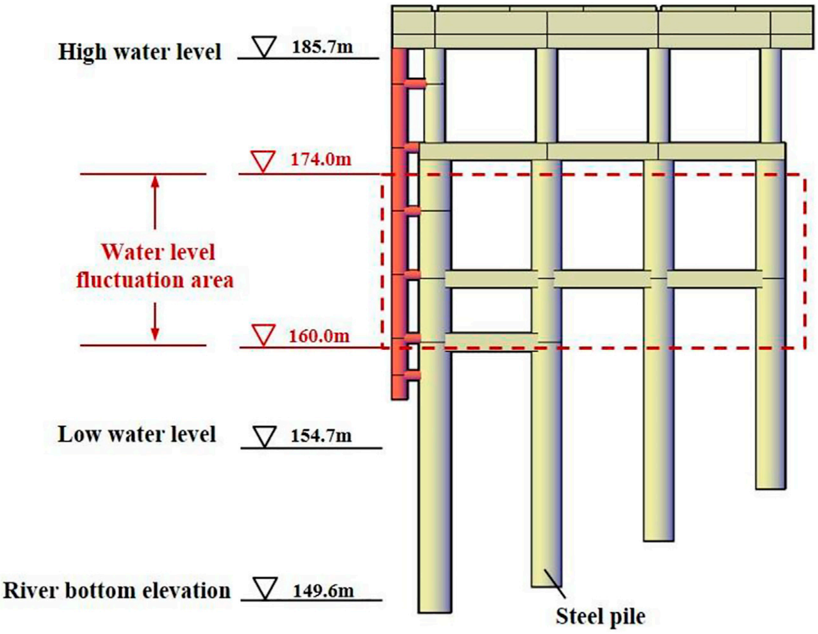

FIGURE 2
The elevation of water level fluctuation area for the multi-layers frame-type wharf in inland river.

steel components have been generally fallen off, as shown in Figure 1. Exposed steel substrates are prone to periodic erosion, which located in the water level fluctuation area (Figure 2).

In the drying stage, the oxygen supply is sufficient under the action of a liquid membrane, and the accumulation of erosive ions is enriched (Thee et al., 2014); under an immersed condition, the corrosion products of steel components dropped off due to the erosion by water-sediment laden flow, and the steel substrate is exposed again. The alternating process of drying and wetting accelerates the corrosion rate of steel components. According to statistic data, the annual total loss of metal due to corrosion processes in the world exceeds 10% account for its annual production (Panteleeva, 2017). The major consulting project of “Research on Chinese corrosion status and control strategy” showed that Chinese annual corrosion cost accounted for about 3.34% of the gross domestic product (GDP) in 2014 (Zhang et al., 2022). The corrosions of steel components have attracted increasing attention.

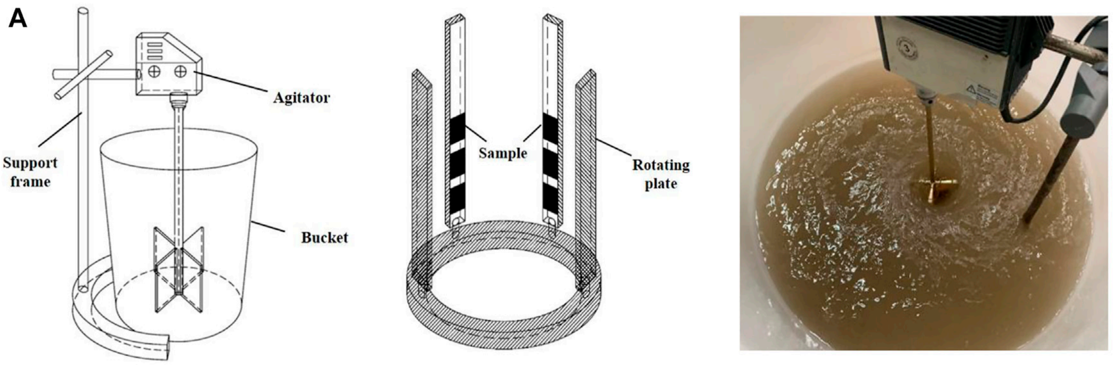

a) Containing sand bucket b) Carrying device c) Steel samples are eroded by water-sediment laden flow

Simple accelerated erosion test device

Potentiostatic accelerated corrosion device

FIGURE 3
Accelerated test devices. Simple accelerated erosion test device include containing sand bucket and carrying device. The sand bucket consists of agitator, support frame, and bucket.

On the basis of field investigations, it was found that the average corrosion rate of steel components of a large wharf exposed to the water level fluctuation area in the upper reaches of the Yangtze River is approximately 0.27 mm/a, the average corrosion rate of steel ones exposed to the atmospheric area is approximately 0.025 mm/a (Wang et al., 2021), and the average corrosion rate of steel structures exposed to the spray/splash area in marine environment is approximately 0.3 mm/a (Jiang et al., 2021). The corrosions of steel structures are very serious in the drying-wetting environment in inland rivers, which can directly affect the durability and safety of steel structures.

The corrosion behaviours of steel structures in marine environments and atmospheric environments have attracted much attention. The splash zone in marine environments has its impact characteristics of high humidity, high salt spray, and frequent wave (Gabreil et al., 2022). Compared with other exposure environments, the corrosion degree of steel components in the splash zone is more serious (Xu et al., 2021). The metal surface is subjected to drying-wetting cycle for a long time under marine environmental conditions, and the chloride ions will accelerate the corrosion rate of the metal (Melchers, 2020). For the atmospheric corrosion of steel, a layer of water film is first adsorbed on the surface of steel (the relative humidity of air is less than 100%); When the thickness of the water film reaches 20–30 molecular layers, electrochemical corrosion under the electrolyte film will occur, subsequently, further form a dense protective rust layer (Zhang, 2019). Many scholars have conducted in-depth explorations on the corrosion behaviours of steel structures under the alternate drying and wetting conditions. Gong et al. (2020a), Gong et al. (2020b) found that the thickness of the rust layer formed in a drying-wetting cycle was larger than that in a soaked environment during the same corrosion time. Results indicated that the drying-wetting cycle was conducive to the rapid formation of the rust layer, and a larger drying-wetting ratio was more likely to result in corrosion and cracking for steel. Hao et al. (2018) studied the electrochemical characterization and stress corrosion cracking (SCC) behaviour for high strength steel in marine environment under drying-wetting cycles and found that the corrosion layer has an impact on the electrochemical and

SCC behaviours. Wang et al. (2021) simulated the atmospheric corrosion evolution process for the low-carbon steel in coastal atmosphere, and the results showed that with the increasing dry-wet cycles, the corrosion rate increased rapidly at first and then slowly until it reached a plateau. However, for the exposure environment in inland rivers, it has strongly differences than those of the aforementioned corrosion environments. According to the water quality analysis for the inland river environment, the chloride content is only 14.5 mg/L, hence, the influence of chloride ions on the corrosion of steel structures can be reasonably ignored. Moreover, the service environment of inland river has its characteristics of a high flow rate and high sediment content during the flood season. After the anticorrosion coating on the surface of steel components fallen off, the corrosion products produced by the steel base material will be continuously eroded by the water-sediment laden flow. The water level of the steel components in wharf rises and falls periodically with the variation of seasons, and the corrosions for steel structures will be accelerated by the alternate drying-wetting conditions.

Periodic erosion on steel structures by water-sediment laden flow will not only weaken the effective bearing area for steel components, but also reduce the strength, plasticity and other major mechanical properties of steel structures, resulting in a decline for the bearing capacity of steel structures (Luo L et al., 2019; Goran et al., 2021). Luo X et al. (2019) showed that the average corrosion rate can effectively reflect the degradation of the bearing capacity for corroded steel bars but do not accurately reflect the degradation of their deformation and capacity. Zhan et al. (2018) used the model of random process to characterize the initial bearing capacity, degradation of geometric parameters and mechanical properties for the corroded steel components and established a degradation model for corroded ones based on the mathematical statistics theory. Zou et al. (2019) established a prediction probability model for the resistance degradation of corroded steel structures exposed to a chlorine-salt environment by using the Monte-Carlo simulation method and found that the initial corrosion time for steel follows a lognormal distribution, and the structural resistance at the same time can be represented by a normal distribution. Sultana et al. (2015) used the finite element method to analysis the influence of random corrosion on the compressive strength of steel structures, and reported that a volume loss of approximately 18% would lead to 45% reduction in the ultimate strength of steel. Zhao et al. (2021) studied the influence of random pitting on the bending capacity of H-shaped steel beams and found that the mass loss and corrosion depth would both affect the bearing capacity of steel components. At present, the resistance degradation model mainly focuses on concrete/reinforced concrete structures, while researches on the resistance degradation model for steel ones under drying-wetting cycles are very limitation and are worthy of further researches and explorations.

TABLE 1 Accelerated corrosion test conditions for steel samples.

Condition name	1	2	3	4	5
Erosion speed (m/s)	1.29	1.71	2.18	2.18	2.18
Sediment concentration (kg/m^3)	4.5	4.5	4.5	20	0.0

In summary, researches regarding the corrosion laws for steel structures mostly resided in the marine and atmospheric environments. To date, there are few reports on the effect of periodic water-sediment laden flow on damage of steel structures under the water level fluctuation area in inland river. Therefore, it is still necessary to carry out relevant researches aimed to the aforementioned problems. According to the characteristics of large flow velocity and high sediment concentration in inland rivers, the indoor accelerated test method was carried out to simulate the periodic erosion water-sediment laden flow acted on steel samples, and the corrosion evolution laws for the steel structures under the water level fluctuation area were revealed, as well as the resistance degradation model for the steel was established to provide a theoretical basis for the anticorrosion design of steel structures.

Cyclic accelerated erosion test under water-sediment laden flow

Experimental devices

Samples preparation

In this test, the Q235 steel block with a size of 3 cm × 3 cm × 0.2 cm (length × width × height) was used to polish the steel surface to class St3 in accordance with "Corrosion Grade and Rust Removal Grade of Steel Surface Before Painting" (State Bureau of Technical Supervision GB8923-88, 2011), and then the steel surface should be wiped clean with alcohol and dried for later use. A total of 150 specimens were prepared for this paper's experiment.

Accelerated test device

Han et al. (2014) studied the initial corrosion behaviors of carbon steel under the field and indoor drying-wetting cycles and found that the corrosion behaviors under both the conditions follow the mathematic equation of $D = At^n$. The indoor corrosion rate by drying-wetting cycles was three times than that of the field test, and these two kinds of conditions had a good correlation. Therefore, we can obtain the corrosion law of steel samples in inland river environments during a short time by the accelerated test. The experimental devices developed by our research group were used during the accelerated test for steel samples, as shown in Figure 3.

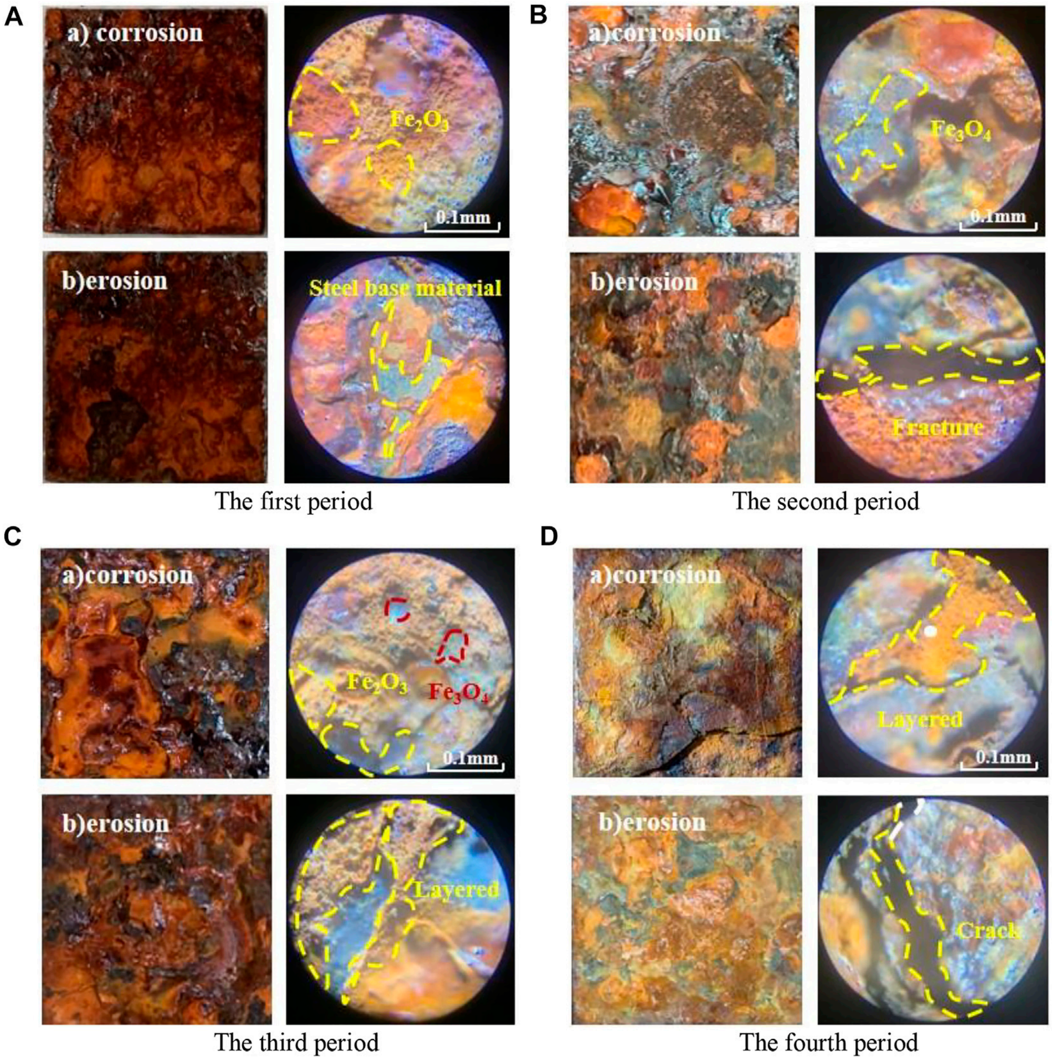

FIGURE 4
Damage morphology of steel samples under periodic water-sediment laden flow. **(A)** The first period. **(B)** The second period. **(C)** The third period. **(D)** The fourth period.

(1) Simple accelerated erosion test device: this device comprises a sand bucket (Including agitator, support frame, bucket) and a carrier, and the carrier is put into the sand bucket to form a complete set of instrument. The device obtains muddy water with different sediment concentrations by manual operation, adjusts the rotating speed of the test machine, simulates different erosion speeds, and obtains sand water flow under different flow velocity conditions. This instrument can be used to explore the erosion change law of steel samples under different erosion conditions, including erosion time, erosion speed, sediment concentration, etc. Moreover, the stirring rods for the experimental device have been improved that the experimental steel samples are placed/installed in the stirring rods, as shown in Figure 3A.

(2) Potentiostatic accelerated corrosion device: the HY3005B direct current (DC) power supply provides an external current for the whole system. The humidifier continuously sprays water mist to create a high humidity environment and form a water film on the steel surface. The steel samples are connected with the DC power supply by wires to form a closed loop, as shown in Figure 3B. At the same time, double-sided adhesive, wood and foam materials are used to fix the position of the steel samples. The corrosion rates of the steel samples are changed by setting the current value, recording the corrosion time, and then weighing and measuring the thickness of the steel samples every 30 h. The current value of this test is set as 25 mA. According to the current distribution law of series and parallel circuits (see in Figure 3B), if we

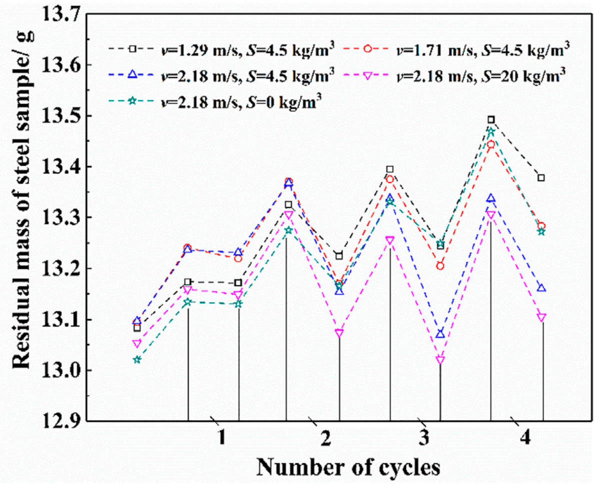

FIGURE 5
Variation of steel sample residual mass with cycle number (each cycle contains corrosion and erosion process).

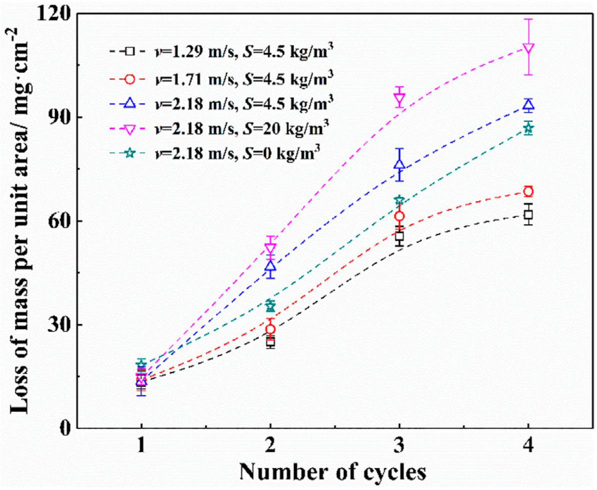

FIGURE 6
Loss of mass per unit area for the steel samples versus the number of cycles.

ignore the heterogeneity between test pieces, the current flowing through each steel sample is consider as 5 mA.

Test plan

Corrosion characteristics of steel structures are mainly related to environmental conditions, dry/wet ratio and exposure time, as well as the flow velocity and sediment concentration of water-sediment laden flow. According to the tested flow velocity of 0.6–3.0 m/s in the middle and upper reaches of the Yangtze River (Shen, 2015), hence, the flow velocities for this paper's experiment are determined from 1 to 2 m/s, as 1.29 m/s, 1.71 m/s and 2.18 m/s, respectively, which represent the minimum, the average, and the maximum flow velocity during the flood season. The erosion velocities by water-sediment laden flow can be adjusted by changing the rotational speed of the rotary head of the simple accelerated erosion test device.

For this paper's experimental investigations, the sediment concentrations are considered as 4.5 kg/m^3 and 20 kg/m^3 on the basis of the tested sediment concentration in the middle and upper reaches of the Yangtze River. According to the pre-test results, the corrosion quality for steel samples hardly increase after the accelerated corrosion time reaches to 150 h, and the loose rust layer on the steel surfaces is almost washed away after erosion for 2 h. Therefore, each accelerated corrosion time and each accelerated erosion time are determined as 150 and 2 h, respectively, with a total of 4 cycles. A total of 6 parallel samples are set for each cycle test, and a total of 150 parallel samples are prepared in this paper's experiment.

Five working conditions are designed according to the field design conditions, as shown in Table 1.

Test results

The corrosion indices for steel samples mainly include mass loss (Zheng et al., 2018), corrosion rate (Song et al., 2021; Wang and Liu, 2021), corrosion depth (Wang and Cheng, 2016), corrosion products (Chen et al., 2021), corrosion morphology (Ming et al., 2022), fractal characteristics (Ren et al., 2022a), roughness (Xu and Wang, 2015), time-dependent model for the rust pit depth to diameter depth ratio (Ren et al., 2022b), etc. This paper focuses on an analysis of corrosion morphology, mass loss, corrosion depth, and other indices. The surface morphology of steel samples is photographed and recorded by a high definition camera (HDV). The masses of steel samples after the process of corrosion and erosion are measured by using a BSM120.4 electronic analytical balance (accurate to 0.1 mg). The masses are weighed as least five times, and the average values are taken as the final mass values. A T112 ultrasonic thickness gauge is used to measure the thickness of steel samples after corrosion and erosion test. The thicknesses are measured at least five times for each sample, and the average values are considered as the final results.

Results

Effect of periodic water-sediment laden flow on damage morphology of steel samples

During the process of periodic water-sediment laden flow, a dense layer of corrosion products is formed on the steel

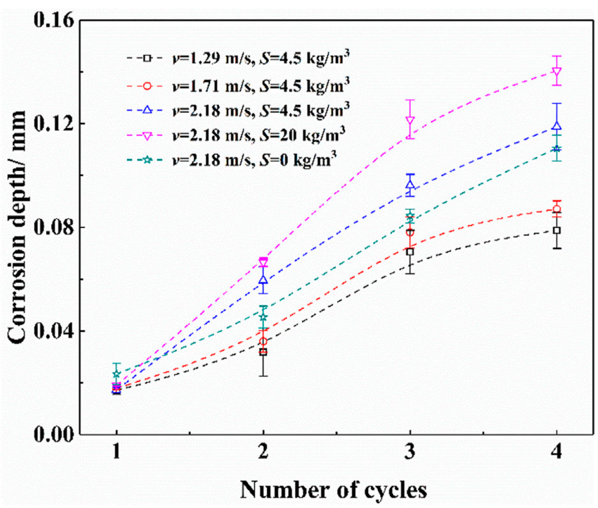

FIGURE 7
Steel corrosion depth versus the number of cycles.

surface by accelerating the current under a high humidity environment, and some of the corrosion products drop off due to the impact and abrasion caused by water-sediment laden flow. After four cycles, a rust layer with a certain apparent strength is generally formed on the steel surface, and the quality of rust product hardly increases. Therefore, four cycles of the alternant washout-corrosion tests are determined.

(1) The first period. The early and unstable rust layer formed on the steel surface is a mixture of ferric oxide (Fe_2O_3; containing crystal water is yellow, losing crystal water is red brown), especially, the rust layer structure and the rust product are loose, and the adhesion strength of corrosion products is low. Early rust products are loose and porous, which demonstrate strong water absorption, low strength, brittleness, easily erosion by water-sediment laden flow and flake off. After the rust layer flakes off, the original steel matrix can expose to a corrosive atmosphere again, as shown in Figure 4A.
(2) The second period. After exposure to the first cycle test, a relatively dense oxide layer is formed on the steel surface, which isolates the rust causing conditions to a certain extent and protects the steel surface. At this stage, the rust products gradually change from the initial iron oxide to ferroferric oxide (Fe_3O_4; black color), and the surface volume expansion of the rust layer is particularly obvious. After the impact of water-sediment laden flow, the damage and shedding of the rust layer mostly occur at the volume expansion, and there are obvious cracks at the falling place. There is a large gap between the cracks, which provides a channel for water and air to enter the steel base material, so that the corrosion reaction on the inner surface of steel can be still occurred slowly, as shown in Figure 4B.
(3) The third period. The surface of the rust layer which almost not fell off is dark black from the macroscopic morphology of the rust layer, which has high strength, good compactness and a certain protective effect on steel corrosion. The surface after the rust layer falling off shows yellow and reddish brown, which is relatively loose and porous. The erosion damage of the samples mainly occurs in this area, and the rust products have obvious stratification after several “drying-wetting cycles”, as shown in Figure 4C.
(4) The fourth period. The residual rust layer on the inner surface overlapped with the newly formed rust products on the outer surface, and the rust layer surface showed obvious stratification and brittle fracture characteristics. From the macroscopic morphology, the rust layer on the steel surface has begun to denude the whole block. From the microscopic morphology of steel samples, the surface rust layer has obvious cracks after repeated wetting and drying cycles. Most of the cracks are caused by the composition, and the growth degree and integrity of the inner and outer rust layers are not consistent. Due to multiple cycles, the rust layer is divided into multiple layers from inside to outside, which has poor cementation ability and prone to relative sliding. The strength of the surface rust layer is weaker than that in early stage, and it is more likely to be damaged and fall off in a large area under a high flow velocity, as shown in Figure 4D.

In summary, a large number of loose corrosion products appear on the steel surface in the early stage of the periodic erosion process under water-sediment laden flow. In the middle stage, loose rust products will fall off and gradually stratify into rust layer. Subsequently, the rust layer on the steel surface will fall off, and a dense rust layer will form inside, which will inhibit the entry of external media. Therefore, the periodic erosion process of water-sediment laden flow can promote the formation and stabilization of a compact and thick inner rust layer of steel samples, thus slowing down the corrosion rate.

Effect of periodic water-sediment laden flow on mass loss of steel samples

The cyclic damage process of steel samples is mainly affected by the damages of atmospheric corrosion and water-sediment laden flow erosion. Under five different working conditions, the variation curve of the residual masses of the steel samples with the number of cycles are exhibited in Figure 5.

Figure 5 shows that the residual masses of the steel sample fluctuate with an increased cycles. In atmospheric environment, steel combined with atmospheric water vapor and oxygen forms hydration oxidation products, so that the quality of steel samples

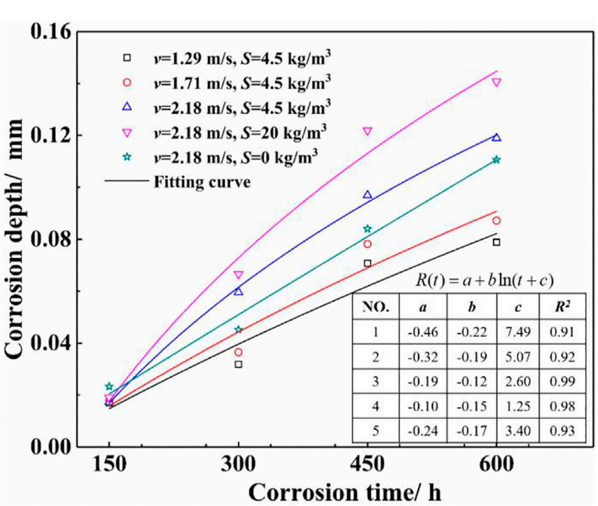

FIGURE 8
Fitted curves of steel corrosion depth with corrosion time.

increases. The quality decline of steel samples is caused by the erosion of corrosion products on the steel surface under the condition of water-sediment laden flow. Therefore, the qualities of the steel samples fluctuate up and down with the experimental cycles.

When the flow velocity is relatively low (1.29 m/s and 1.71 m/s), the residual masses of the steel samples show a slow rising trend with the cycles. This is because that the loose corrosion products on the steel surface are easily washed by the slow flow, while the relatively dense oxidation products are difficult to damage and cannot easily fall off. Therefore, the residual masses of the steel samples show a slow rising trend. At a relatively large flow velocity (2.18 m/s), the rust layer on the steel surface has difficulty remaining intact under the erosion of water-sediment laden flow. The damaged surface and cracks of the rust layer easily provide channels for water vapor to penetrate, and further rust occurred. The rust layer is loose and porous, and the corrosion products interact with each other, which can easily cause damage and spalling in the next erosion. Therefore, the quality of steel components is always dynamically stable with a certain downward trend.

In summary, the residual masses of the steel samples are relatively stable even though they fluctuate exposed to the water level fluctuation zone. On the condition of low sand content or low flow rate, the internal rust layer is not easily washed away, and the exposed steel matrix and interfacial void on the steel surface easily grow the rust layer again. Therefore, the rust layer accumulates slowly, so the residual masses of steel samples rise slowly. On the condition of medium and high sand content or high flow rate, the rust layer of steel members can be easily eroded and damaged, and the corrosion products have difficulty accumulating. Therefore, the quality of steel samples remains dynamic and stable and tends to decrease with the increasing cycle times.

At the end of each cycle, the rusts on the surface of the sample are polished to remove; subsequently, the remaining masses for steel samples are weighed, and the unit weight losses of the samples are recorded. The damage rule of steel samples under different working conditions and the variation process of unit weight loss for samples with the cycles are confirmed, as shown in Figure 6.

Figure 6 exhibits that the unit mass loss of the steel sample with the number of cycles verifies as an initial rapid increase and then slow increase, which is consistent with a logarithmic growth law. Moreover, we can observe that:

(1) On the condition of the same sediment concentration, the unit mass loss of the rust layer increases with the increasing flow velocity.
(2) On the condition of the same flow velocity, the unit mass loss of the rust layer increases with the increasing sand concentration.
(3) As the cycling times increase, the unit mass loss of steel samples gradually slows because that the first three loop component surfaces are mainly composed of a loose rust layer of steel, which is vulnerable to erosion from falling out.
(4) After several cycles, a rust layer with certain apparent strength gradually formed on the steel surface, and the loss of unit mass for steel samples under the fourth cycle is smaller than that of the first three cycles, which is consistent with the steel surface morphology damages.

Effect of periodic water-sediment laden flow on thickness loss of steel samples

The variation of steel corrosion depths with the number of cycles on the conditions of five water flows are elaborated in Figure 7.

Figure 7 states that the corrosion depths of the rust layer on the steel surface with the number of cycles generally change as an initial rapid increase and then a slow increase, which is consistent with the trend of steel loss mass. On the basis of the change law for steel corrosion depths combined with the apparent morphology analysis of steel samples, it can be concluded that:

(1) In the early stage of erosion, the rust layer newly formed on the steel surface is closely attached to the surface of the base-material and it is relatively dense and difficult to wash out. However, the rust layer surface has not formed certain strength, and the loose rust products can be easily washed off, so the steel damage during the early stage of the cycle is less, and the erosion depth is small.

FIGURE 9
Corrosion results for steel components of a certain wharf tested in field.

TABLE 2 Steel corrosion results measured at a certain wharf in the upper reaches of Yangtze River units: mm.

Corrosion depth name of the structure	2013	2019		2021	
	Original thickness	Average remaining thickness	Average corrosion depth	Average remaining thickness	Average corrosion depth
Steel braces	20.00	19.21	0.79	18.92	1.08
Steel berthing components	16.00	15.32	0.68	14.94	1.06
Steel tubes	16.00	15.26	0.74	14.98	1.02
Average values	17.33	16.60	0.73	16.28	1.05

(2) After a certain period of drying and wetting circulation, the rust layer on the steel surface is scoured by water, and part of them would be fallen off. The rust layer has discontinuous growth, stratification, overlapping, gaps and other defects between the layers, as well as the layer is mixed with fine sediment particles. The rust layers would be easily fallen off from blocks under the current erosion. Therefore, in the middle of the cycle, the steel erosion damages are more serious than those of the early stage, and the erosion depths reach to peak values.

(3) At the later stage of the cycle, the rust layer acquired certain strength after repeated washout-corrosion cycles. It is difficult to cause large area damage and fall off for the rust products due to the water flow, but some corrosion products in steel surface can still fall off under the action of washout. Therefore, the increase in erosion thickness of steel samples tends to be slowed down at the late cycle.

Resistance degradation model of steel components

The corrosion damage of steel can not only weaken the effective bearing area of steel structures but also change the steel material properties. Moreover, the strength and safety for the steel components would be reduced, and the resistance degradation process of the steel structure can be accelerated. For this paper's study, a resistance degradation model for the steel components is established to describe the relationship between the steel strength weakening with the service time, which can strongly provide the theoretical supports for life prediction and safety evaluation of the wharf steel structures in inland river.

First, the time-dependent model for the steel corrosion depth is determined. The empirical formula for predicting the corrosion depth of steel components under different working

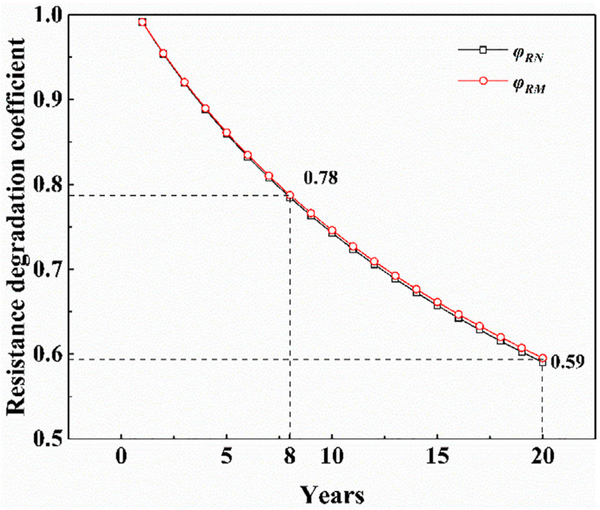

FIGURE 10
Resistance degradation coefficient of the steel components.

conditions is confirmed by fitting the variation trends of the average corrosion depth of steel samples with corrosion time, as shown in Figure 8.

As shown in Figure 8, a logarithmic function is used to fit the scatters, and the fitting correlation is relatively high. Therefore, the function relation of $R(t)$ is finally determined as follows:

$$R(t) = a + b\ln(t + c) \tag{1}$$

In Eq. 1, $R(t)$ is the corrosion depth of the steel component at t years, mm; t is the steel corrosion time, year; a , b and c are normalized parameters and can be determined according to the specific environmental conditions.

We obtain the dimensionless parameters in Eq. 1 according to engineering examples. At the end of 2013, a certain wharf in the upper reaches of the Yangtze River has been operated approximately 8 years. A large number of experimental data in line with the damage of steel components, such as piles, braces, beams, etc., caused by periodic water-sediment laden flow were collected in the field, as shown in Figure 9.

The average corrosion depths for wharf steel components were determined by combining relevant literatures and on-site actual detection measurements, as listed in Table 2.

Assuming that the effective protection life of the anticorrosion coating of steel components is 3 years, the corrosion time of steel components is 4 years. According to the average values for steel components determined in 2013, 2019, and 2021 as exhibited in Table 2, the parameters of a, b, and c are comfirmed by using the Eq. 1, and their calculated results are eqaul to 0.3092, 0.3433, 0.4063, respectively. The prediction model of steel corrosion depth can be obtained as follows:

$$R(t) = 0.3092 + 0.3433\ln(t + 0.4063) \tag{2}$$

In Eq. 2, $R(t)$ is the corrosion depth of the steel component at t years, mm; t is the steel corrosion time, year.

Shi et al. (2012) proposed the time-dependency of steel material strength weakening, and its expression is as follows:

$$f_t = [1 - 0.98w_s]f = \left[1 - 0.98\frac{A_0 - A_t}{A_0}\right]f \tag{3}$$

Where, f_t is steel material strength design value at the certain time t, N/m^2; w_s is the corrosion damage factor; f is the corroded steel strength design value (if the steel material for the significant components is Q235, the $f = 235$ N/m^2); A_0 is the initial section area of steel component, mm^2; and A_t is the actual section area of steel component corroded at time t, mm^2; $A_t = A_0 - \pi DR(t)$, D is outer diameter of steel components, m.

The degradation model for the design bearing capacity of steel components under the tension or compression is as follows (Fan et al., 2009):

$$N_R = A_t \cdot f_t = A_0 f \varphi_{RN} \tag{4}$$

Where, N_R is the axial bearing capacity, N; φ_{RN} is the design bearing capacity degradation coefficient of the steel ring section under the tension and pressure. Inserting the Eq. 3 into Eq. 4, the design bearing capacity degradation coefficient of the steel ring section under the tension and pressure is established.

$$\varphi_{RN} = k \cdot [R(t)]^2 - 0.1 \cdot R(t) + 1 \tag{5}$$

Where, $k = 2.52 \times 10^{-3}$, it can be determined according to the specific environmental conditions.

The flexural bearing capacity degradation model for the main plane of steel components is (Fan et al., 2009):

$$M_R = W_t \cdot f_t = W_0 f \varphi_{RM} \tag{6}$$

Where, M_R is flexural capacity, N·m; W_t is bending section coefficient at time t, m^3; φ_{RM} is the degradation coefficient for the main plane flexural bearing capacity of the ring section. Inserting the Eq. 3 into Eq. 6, the degradation coefficient for the main plane flexural bearing capacity of the ring section is confirmed.

$$\varphi_{RM} = \frac{1500 \cdot \varphi_{RN}}{1500 - 2 \cdot R(t)} \tag{7}$$

According to Eqs 5, 7, the time-dependent formulas for the degradation coefficient φ_{RN} and φ_{RM} are drawn, as shown in Figure 10.

From Figure 10, assuming that no anticorrosive measures are taken on the steel surface exposed to the water level fluctuation area, and the uniform corrosion process of steel components are considered, the bearing capacity of the ring steel components decays to 78% account for its initial resistance after 8 years. After the design corrosion life is reached, the bearing capacity degradation of the steel components is accelerated. After

20 years' service, the actual resistance of the steel structure is less than 60% compared by the initial value.

Conclusion

In this paper, the damage process of wharf steel components is simulated during the service environment of periodic erosion/corrosion by water-sediment laden flow in inland river, as well as the time-varying laws of morphology damage, mass loss and erosion depth of steel samples are obtained and analyzed. The prediction model of steel corrosion under periodic erosion/corrosion by water-sediment laden flow is finally established, and the evaluation method of resistance degradation of wharf steel components is proposed.

(1) At the initial stage of the steel damage test by periodic water-sediment laden flow, the steel surface is mainly composed of a loose rust layer, which can be easily eroded off. In the middle stage of the test, the rust products exhibit obvious stratification phenomena. At the later stage of the test, the rust layer on the steel surface begins to denude over the whole piece, and the steel surface forms a certain apparent strength, which can prevent rust and erosion for the steel structures.

(2)]At the water level fluctuation area, especially, in the upper reaches of the Yangtze River, the corrosion of steel components results in an increase in mass. The mass of the steel components decreases with the rust layer washing out by the water-sediment laden flow. Therefore, the residual mass of the steel components shows a continuous fluctuation, and the fluctuation trend slows down with the increasing flow velocity and sediment concentration. These findings are consistent with the steel surface morphology damage.

(3) On the basis of the research results by this paper, an evaluation method for resistance degradation of steel components under the periodic erosion/corrosion of water-sediment laden flow is proposed. The estimation results show that the actual resistance of the steel structure exposed to the water level fluctuation area in the upper reaches of the Yangtze River is less than 60% compared by the structural initial value after 20 years.

Data availability statement

The original contributions presented in the study are included in the article/supplementary material, further inquiries can be directed to the corresponding author.

Author contributions

Conceptualization, ML; methodology, ML and LZ; validation, LW; formal analysis, CZ and LW; investigation, EA; resources, ML; data curation, LZ and CZ; writing—original draft preparation, ML and LZ; supervision, LW All authors have read and agreed to the published version of the manuscript.

Funding

This research is funded by the National Natural Science Foundation of China, project number: 51479014, and the Talents Plan Project in Chongqing of China, project number: cstc2021ycjh-bgzxm0053.

Conflict of interest

The authors declare that the research was conducted in the absence of any commercial or financial relationships that could be construed as a potential conflict of interest.

Publisher's note

References

Chen, W., Jiao, X., Zhao, Z., Li, H., Liu, R., and Che, Y. (2021). Study on salt spray corrosion behavior and mechanism of hot dip galvanized steel. *J. Shanxi Univ. Sci. Technol.* 39 (04), 130–135. doi:10.3969/j.issn.1000-5811.2021.04.020

Fan, Q., Zhang, Z., and Yin, Y. (2009). *Mechanics of materials*. China: Higher education press.

Gabreil, E., Wu, H., Chen, C., Li, J., Rubinato, M., Zheng, X., et al. (2022). Three-dimensional smoothed particle hydrodynamics modeling of near-shore current flows over rough topographic surface. *Front. Mar. Sci.* 9, 935098. doi:10.3389/fmars.2022.935098

Gong, K., Wu, M., and Liu, G. (2020a). Comparative study on corrosion behaviour of rusted X100 steel in dry/wet cycle and immersion environments. *Constr. Build. Mat.* 235, 117440. doi:10.1016/j.conbuildmat.2019.117440

Gong, K., Wu, M., Xie, F., Liu, G., and Sun, D. (2020b). Effect of dry/wet ratio and pH on the stress corrosion cracking behavior of rusted X100 steel in an alternating dry/wet environment. *Constr. Build. Mat.* 260, 120478. doi:10.1016/j.conbuildmat.2020.120478

Goran, V., Goran, V., Josip, B., Marino, B., and Florian, S. (2021). Long-term marine environment exposure effect on butt-welded shipbuilding steel. *J. Mar. Sci. Eng.* 9 (5), 491. doi:10.3390/jmse9050491

Han, W., Pan, C., Wang, Z., and Yu, G. (2014). A study on the initial corrosion behavior of carbon steel exposed to outdoor wet-dry cyclic condition. *Corros. Sci.* 88, 89–100. doi:10.1016/j.corsci.2014.07.031

Hao, W., Liu, Z., Wu, W., Li, X., Du, C., and Zhang, D. (2018). Electrochemical characterization and stress corrosion cracking of E690 high strength steel in wet-dry cyclic marine environments. *Mater. Sci. Eng. A* 710, 318–328. doi:10.1016/j.msea.2017.10.042

Jiang, J., Xu, T., and Liu, J. (2021). Study on protection characteristics of D32 steel with different metal coatings in ocean low-salinity wet-dry environment. *Equip. Environ. Eng.* 18 (06), 119–124. doi:10.7643/issn.1672-9242.2021.06.018

Luo, L., Chen, Z., Zhao, X., and Zhang, Y. (2019). Deterioration model for resistance of steel member in atmospheric environment. *Struct. Eng.* 35 (02), 52–58. doi:10.3969/j.issn.1005-0159.2019.02.007

Luo, X., Liu, J., and Nie, J. (2019). Cross-section distribution characteristics and tensile behavior of corroded reinforcing steel bars. *J. Build. Mater.* 22 (05), 730–736. doi:10.3969/j.issn.1007-9629.2019.05.009

Melchers, R. (2020). Long-term durability of marine reinforced concrete structures. *J. Mar. Sci. Eng.* 8 (4), 290. doi:10.3390/jmse8040290

Ming, J., Zhou, X., Jiang, L., and Shi, J. (2022). Corrosion resistance of low-alloy steel in concrete subjected to long-term chloride attack: Characterization of surface conditions and rust layers. *Corros. Sci.* 203, 110370. doi:10.1016/j.corsci.2022.110370

Panteleeva, M. (2017). Effective modern methods of protecting metal road structures from corrosion. *IOP Conf. Ser. Earth Environ. Sci.* 90 (1), 012119. doi:10.1088/1755-1315/90/1/012119

Ren, S., Gu, S., Kong, C., Zeng, S., Gu, Y., Li, G., et al. (2022a). Fractal characteristic of corroded steel surface and application to the fracture analyses. *Constr. Build. Mat.* 340, 127759. doi:10.1016/j.conbuildmat.2022.127759

Ren, S., Kong, C., Gu, Y., Gu, S., Zeng, S., Li, G., et al. (2022b). Measurement pitting morphology characteristic of corroded steel surface and fractal reconstruction model. *Measurement* 190, 110678. doi:10.1016/j.measurement.2021.110678

Shen, L. (2015). *Field testing study on pile hydrodynamic characters of inland river suspended vertical wharf*. China: Chongqing Jiaotong University.

Shi, W., Tong, L., Chen, Y., Li, Z., and Shen, K. (2012). Experimental study on influence of corrosion on behavior of steel material and steel beams. *J. Build. Struct.* 33 (7), 53–60. doi:10.14006/j.jzjgxb.2012.07.006

Song, Z., Wang, Z., Wang, J., Peng, B., and Zhang, C. (2021). Atmospheric corrosion behavior of Q235 steel in northern Hebei region. *Mater. Mech. Eng.* 45 (06), 46–51. doi:10.11973/jxgccl202106008

State Bureau of Technical Supervision GB8923-88 (2011). *Corrosion grade and rust removal grade of steel surface before painting*. China: China Standards Press.

Sultana, S., Wang, Y., Sobey, A., Wharton, J., and Shenoi, R. (2015). Influence of corrosion on the ultimate compressive strength of steel plates and stiffened panels. *Thin-Walled Struct.* 96, 95–104. doi:10.1016/j.tws.2015.08.006

Thee, Ch., Hao, L., Dong, J., Xin, M., Xin, W., Li, X., et al. (2014). Atmospheric corrosion monitoring of a weathering steel under an electrolyte film in cyclic wet-dry condition. *Corros. Sci.* 78, 130–137. doi:10.1016/j.corsci.2013.09.008

Wang, Y., and Cheng, G. (2016). Quantitative evaluation of pit sizes for high strength steel: Electrochemical noise, 3-D measurement, and image-recognition-based statistical analysis. *Mat. Des.* 94, 176–185. doi:10.1016/j.matdes.2016.01.016

Wang, Y., Mu, X., Dong, J., Umoh, A., and Ke, W. (2021). Insight into atmospheric corrosion evolution of mild steel in a simulated coastal atmosphere. *J. Mat. Sci. Technol.* 76, 41–50. doi:10.1016/j.jmst.2020.11.021

Wang, Z., and Liu, Y. (2021). Corrosion behavior and mechanism of carbon steel in typical harsh marine atmosphere in *11th national congress on corrosion and protection* Liaoning: Engineering technology Ⅰ, Special topics in Metal science and metal technology. doi:10.26914/c.cnkihy.2021.015821

Xu, S., and Wang, Y. (2015). Estimating the effects of corrosion pits on the fatigue life of steel plate based on the 3D profile. *Int. J. Fatigue* 72, 27–41. doi:10.1016/j.ijfatigue.2014.11.003

Xu, X., Cheng, H., Wu, W., Liu, Z., and Li, X. (2021). Stress corrosion cracking behavior and mechanism of Fe-Mn-Al-C-Ni high specific strength steel in the marine atmospheric environment. *Corros. Sci.* 191, 109760. doi:10.1016/j.corsci.2021.109760

Zhan, J., Luo, L., and Luo, Y. (2018). "Research on modeling of bearing capacity degradation of corroded components," in The 18th National Symposium on Modern Structural Engineering, Hebei: Cangzhou.

Zhang, X., Chen, Z., Luo, H., Zhou, T., Zhao, Y., and Ling, Z. (2022). Corrosion resistances of metallic materials in environments containing chloride ions: A review. *Trans. Nonferrous Metals Soc. China* 32, 377–410. doi:10.1016/S1003-6326(22)65802-3

Zhang, Y. (2019). *A study on corrosion behavior of Q345q bridge steel in typical atmospheric enviroment in northwest China*. Lanzhou: Lanzhou University of Technology.

Zhao, Z., Mo, S., Xiong, Q., Liu, H., and Liang, B. (2021). Moment capacity of H-section steel beam with randomly located pitting corrosion. *Probabilistic Eng. Mech.* 66, 103161. doi:10.1016/j.probengmech.2021.103161

Zheng, S., Zhang, X., Zhao, X., and Liu, Y. (2018). Experimental and restoring force model research on the seismic behavior of corroded steel frame beams in offshore atmospheric environment. *Eng. Mech.* 35 (12), 98–106+115. doi:10.6052/j.issn.1000-4750.2017.09.0684

Zou, X., Long, J., Chen, Y., Ma, Y., and Wang, L. (2019). Prediction method for resistance degradation of corroded pre-stressed concrete bridges. *J. China & Foreign Highw.* 39 (03), 84–89. doi:10.140848/j.issn.1671-2579.2019.03.016

frontiers
in Environmental Science

BRIEF RESEARCH REPORT
published: 25 February 2022
doi: 10.3389/fenvs.2022.846450

A Micro-Scale Study of Flood Risk Assessment in Urban Fluvial Areas Using the Flood Potential Index

Robby Yussac Tallar* and Golan Mauregar Geldoffer

Department of Civil Engineering, Universitas Kristen Maranatha (Maranatha Christian University), Bandung, Indonesia

Worldwide, increasing various methods are being offered to solve the issue of flood disasters in urban fluvial areas, yet there is a relative lack of micro-scale studies concerning the flood potential index (FPI) to forecast future flood events in DKI Jakarta. With recent advances, the information of flood risk assessment can be monitored and communicated by using FPI embedded with a geographical information system (GIS)-based model. Therefore, the main purpose and concerned issue in this paper is how to relate the micro-scale study of flood risk assessment in the urban fluvial area in DKI Jakarta as the study case using FPI. Specific parameters were selected to develop and analyze FPI, involving three considerations: meteorological, physical-environment, and socio-economic aspects. The classification has also been developed by the analysis of data from rainfall, normalized difference vegetation index (NDVI) obtained from Landsat eight interpretation, and population density to produce a flood potential hazard map for each sub-district in DKI Jakarta during 2021–2024. The results of the completed analysis of classification for each sub-district in DKI Jakarta showed 10 sub-districts with high potential, 219 sub-districts with medium potential, and 32 sub-districts with low potential in 2024. Our findings also confirmed that using a GIS approach in identifying and measuring the FPI in DKI Jakarta for micro-scale areas is very helpful in order to develop better adaptive local flood management practices. For future works, the assessment not only produces a visualization of the flood potential index but also estimates possible damage due to the flood hazard itself.

Keywords: flood potential index, GIS, micro scale study, risk assessment, urban fluvial area

Edited by:
Alfrendo Satyanaga,
Nazarbayev University, Kazakhstan

Reviewed by:
Yongmin Kim,
University of Glasgow,
United Kingdom
Abdul Halim Hamdany,
Nanyang Technological University,
Singapore

****Correspondence:***
Robby Yussac Tallar
robbyyussac@yahoo.com
robby.yt@eng.maranatha.edu

Specialty section:
This article was submitted to
Freshwater Science,
a section of the journal
Frontiers in Environmental Science

Received: *31 December 2021*
Accepted: *31 January 2022*
Published: *25 February 2022*

Citation:
Tallar RY and Geldoffer GM (2022) A Micro-Scale Study of Flood Risk Assessment in Urban Fluvial Areas Using the Flood Potential Index.
Front. Environ. Sci. 10:846450.
doi: 10.3389/fenvs.2022.846450

INTRODUCTION

Similar to many metropolitan cities around the world, DKI Jakarta is dealing with flood disasters. According to the previous report from Meteorological, Climatological, and Geophysical Agency of Indonesia (BMKG), DKI Jakarta has been recorded to have extreme floods, which have occurred in 2002, 2007, 2013, 2015, 2016, and the last in 2020. As the occurrence of flood events has become common, the number of flood risk assessments is increasing (Nastiti et al., 2015). Concerning these issues, various methods are being offered by using geographical information system (GIS)-based model applications in order to solve flood risk assessments in large-scale studies (Singh, 2019; Song et al., 2017; Valencia et al., 2020; Zhang H et al., 2019) and the relationships to the position of the groundwater table (Al Adaileh et al., 2019; Freitas 2016; Nistor et al., 2019; Olaniyi Oke, 2018; Suryawan et al., 2019; Syarif et al., 2013; Wu et al., 2011). Another method is by using the water index in order to describe or analyze water-related problems (Tallar and Dhian, 2021; Nayak et al., 2020; Wang et al., 2020;

Williams et al., 2019; Tallar and Suen, 2015; Tallar and Suen, 2016). Therefore, many studies have also combined the water index with a GIS-based model (Kawo and Karuppannan, 2018; Taloor et al., 2020), and further studies developed a flood index by using a GIS based-model (Yang et al., 2017; Zhang Y et al., 2019). Although improved tools and models have been used to analyze data concerning flood events, there is a relative lack of micro-scale studies concerning flood risk assessment combined with the flood potential index (FPI) to forecast future flood events in DKI Jakarta. Therefore, the main purpose and concerned issue in this paper is how to relate the micro-scale study of flood risk assessment in DKI Jakarta as the study case by using FPI. This paper presented the development of FPI as well as a flood potential hazard map for each sub-district in DKI Jakarta during 2021–2024.

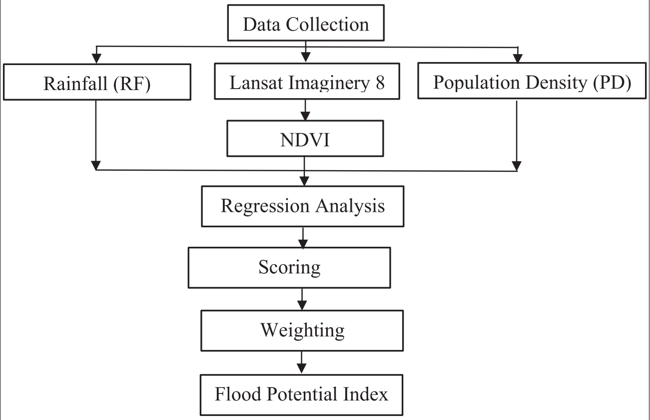

FIGURE 1 | Research flowchart.

MATERIALS AND METHODS

Description of the Study Area

This research was carried out in DKI Jakarta, the capital city of Indonesia, located at 5,019′12″ SL - 60 23′ 54″ SL dan 106,,022′ 42″ EL- 106058′ 18″ EL with an average height of ±7 m above the mean sea level (MSL). The western boundary of DKI Jakarta is Banten Province, and in the south and east, it is bordered by West Java Province. Administratively, DKI Jakarta is divided into five regions consisting of 42 districts and 261 sub-districts in total. The area of DKI Jakarta is 7,660 km^2, with a land area of 662 km^2 and a sea area of 6,998 km^2. The northern boundary of DKI Jakarta includes 32 km of coast, which is the source of 13 rivers, 2 canals, and 2 floodways. DKI Jakarta has a tropical climate with an average annual precipitation of 1.755 mm or about 146 mm per month. This condition causes some areas in DKI Jakarta to be prone to inundation due to high rainfall and high tide. Moreover, the population density is very high. It was recorded that the population in 2021 was more than 10 million residents with a population density of 16,262/km^2 or 42,120/sq mi.

METHODOLOGY

The FPI was developed by using three parameters: rainfall data, normalized difference vegetation index (NDVI), and population density. The parameters used in this study are considered as the representatives of three main aspects: physical, environmental, and socio-economic aspects. **Figure 1** shows that the initial step is to define considered parameters and collect secondary data. The data were collected from rainfall data, NDVI obtained from Landsat eight interpretation, and population density from Central Bureau Statistics of Indonesia (BPS). All the collected data were processed by using ArcGIS software version 10.5 as an application for the digital mapping process with the following steps: scoring, weighting, and overlaying methods. This scoring method gives a score to each parameter in order to determine the level in each classification. These four parameters will be scaled and weighted according to the order of their abilities and conditions of the study area so that the results are obtained in the form of an FPI. In this study, the weighting method of the variables of FPI used is the ranking method. The ranking method is one of the modest methods in assigning weight values of variables by ranking order for each variable (Tallar and Suen, 2016). The class was divided into three classes: high, medium, and low potential. The ranking method was also performed by sorting each parameter used according to the level of importance. The result is an FPI map for DKI Jakarta during 2021–2024.

RESULTS AND DISCUSSION

One of the most crucial water problems in DKI Jakarta comes from flooding. Recently, there has been extensive map coverage of flood hazard zones in DKI Jakarta; however, it is progressively perceived that flood risk related to natural hazards cannot be reduced solely by focussing on the hazard. Therefore, it is necessary to develop an appropriate method of indexing and mapping flood potential in detail. Despite its significance, previous flood risk assessment methodologies often underestimate levels of vulnerability in areas prone to hazards, yet it is the degree of vulnerability within sub-districts that determines the consequences of any given hazard. The result is an FPI map for DKI Jakarta during 2021–2024 (**Figure 2**). The results of the completed analysis of classification for each sub-district in DKI Jakarta showed 10 sub-districts with high potential, 227 sub-districts with medium potential, and 24 sub-districts with low potential in 2021; 12 sub-districts with high potential, 227 sub-districts with medium potential, and 22 sub-districts with low potential in 2022; 10 sub-districts with high potential, 222 sub-districts with medium potential, and 29 sub-districts with low potential in 2023; and 10 sub-districts with high potential, 219 sub-districts with medium potential, and 32 sub-districts with low potential in 2024 (**Table 1**). Based on the results, there are similarities of FPI in the prone areas of flooding in DKI Jakarta during 2021–2024. Flood mitigation and

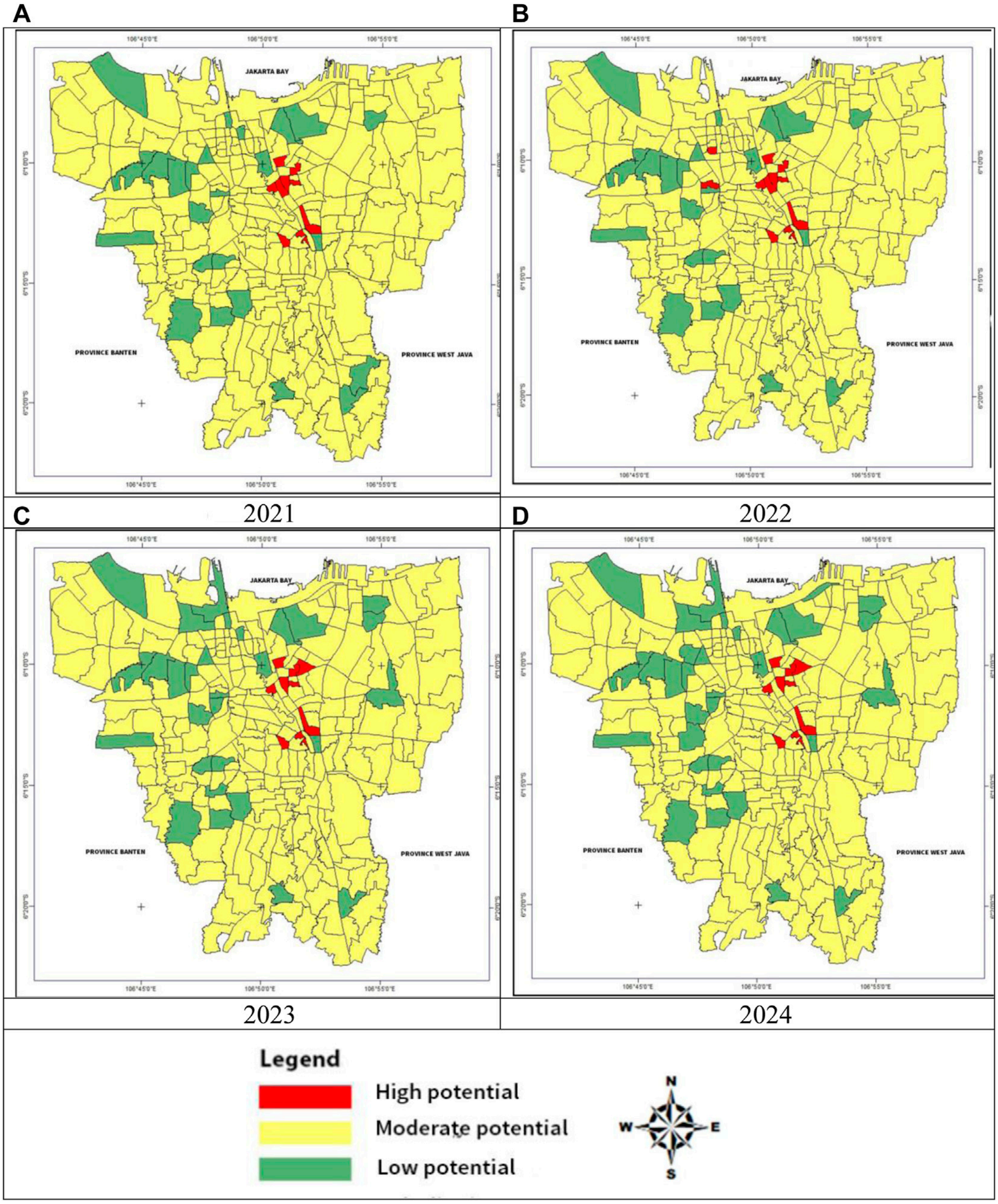

FIGURE 2 | Flood potential index map for DKI Jakarta during 2021–2024.

preparedness programs in the micro-scale should be implemented, such as rainwater harvesting technologies for each sub-district. DKI Jakarta as an urban fluvial area has executed macro-scale flood mitigation and preparedness programs without considering the relationship between flood characteristics for each sub-district. Moreover, climate change-driven global warming is a factor behind repeated instances of severe flooding across the study area; however, this study proved that flood mitigation and preparedness programs can be implemented in local or micro-scale flood risk assessment. The need of appropriate early warning systems to predict flood characteristics, sufficient databases for assessing flood risk analysis, political will and coordination in local levels of

TABLE 1 | FPI classification in DKI Jakarta during 2021–2024.

Year	Number of sub-districts		
	High Potential	Medium Potential	Low Potential
2021	10	227	24
2022	12	228	21
2023	10	222	29
2024	10	219	32

government concerning flood problems, and appropriate mitigation programs are several issues that are aims for reducing vulnerability to flood problems in the micro-scale model.

CONCLUSION

The study presented proposes a general methodology to assess and map FPI at a detailed, micro-scale level. This captures aspects that are considered crucial and representative of reality (physical, environmental, and socio-economic aspects). These results provide as clear a picture as possible of the reality of the FPI map within DKI Jakarta, leading to a better understanding and guidance for future flood risk management activities in DKI Jakarta. Our findings also confirmed that using a GIS approach in identifying and measuring the FPI in DKI Jakarta for micro-scale areas are very helpful in order to develop better adaptive local flood management practices. It is obvious that the GIS-based method has a great role to play in flood risk assessment because flood is one of many natural hazards with multi-dimensional variables. The FPI had several advantages: 1) a low-cost and micro-scale flood monitoring program that could be used in developing countries and 2) a useful tool for water resource agencies, especially for local agencies, to manage waterbodies and to raise public awareness of flood problems for its data as its data could be easily understood and interpreted. At present, there lacks a framework for monitoring and measuring the flood risk assessment in the micro-scale that enables these institutions to operate and develop and link up the three-pillar idea of sustainable development: environmental (the idea of staying within a biophysical carrying capacity), social (providing a society constructed on the values that people wish to live by), and economic (providing an adequate material standard of living). For future works, the assessment not only produces a visualization of FPI but also estimates possible damage due to the flood hazard itself; furthermore, the application of FPI can also be implemented in other countries.

DATA AVAILABILITY STATEMENT

The original contributions presented in the study are included in the article/Supplementary Material, further inquiries can be directed to the corresponding author.

AUTHOR CONTRIBUTIONS

RT devised the project and the main conceptual ideas and wrote the manuscript. GG worked out almost all the technical details and performed the analysis.

ACKNOWLEDGMENTS

The authors gratefully acknowledge the support for this research provided by Maranatha Christian University, Indonesia, and under collaboration research with Hydraulics and Ocean Engineering Department, National Cheng Kung University, Taiwan R.O.C.

REFERENCES

Al Adaileh, H., Al Qinna, M., Barta, K., Al-Karablieh, E., Rakonczai, J., and Alobeiaat, A. (2019). A Drought Adaptation Management System for Groundwater Resources Based on Combined Drought Index and Vulnerability Analysis. *Earth Syst. Environ.* 3 (3), 445–461. doi:10.1007/s41748-019-00118-9

Freitas, C. R. D. (2016). "Drought," in *Natural Hazards in Australasia*. Editors C. R. de Freitas and J. Goff (Cambridge: Cambridge University Press), 32–50.

Kawo, N. S., and Karuppannan, S. (2018). Groundwater Quality Assessment Using Water Quality index and GIS Technique in Modjo River Basin, central Ethiopia. *J. Afr. Earth Sci.* 147, 300–311. doi:10.1016/j.jafrearsci.2018.06.034

Nastiti, K. D., Kim, Y., Jung, K., and An, H. (2015). The Application of Rainfall-Runoff-Inundation (RRI) Model for Inundation Case in Upper Citarum Watershed, West Java-Indonesia. *Proced. Eng.* 125, 166–172. doi:10.1016/j.proeng.2015.11.024

Nayak, J. G., Patil, L. G., and Patki, V. K. (2020). Development of Water Quality index for Godavari River (India) Based on Fuzzy Inference System. *Groundwater Sustain. Develop.* 10, 100350. doi:10.1016/j.gsd.2020.100350

Nistor, M.-M., Rahardjo, H., and Satyanaga, A. (2019). Development Assessment of the Singapore Land: A GIS Spatial-Temporal Approach Based on Land Cover Analysis. *Gt* 14 (2), 60–73. doi:10.21163/gt_2019.142.06

Nistor, M. M., Rahardjo, H., Satyanaga, A., Hao, K. Z., Xiaosheng, Q., and Sham, A. W. L. (2020). Investigation of Groundwater Table Distribution Using Borehole Piezometer Data Interpolation: Case Study of Singapore. *Eng. Geology.* 271, 105590. doi:10.1016/j.enggeo.2020.105590

Olaniyi Oke, M. (2018). Assessment of Meteorological Droughts in Abeokuta, Southwestern, Nigeria. *J. Climatol Weather Forecast.* 06. doi:10.4172/2332-2594.1000235

Singh, A. (2019). Remote Sensing and GIS Applications for Municipal Waste Management. *J. Environ. Manage.* 243, 22–29. doi:10.1016/j.jenvman.2019.05.017

Song, D., Gao, Z., Zhang, H., Xu, F., Zheng, X., Ai, J., et al. (2017). GIS-based Health Assessment of the marine Ecosystem in Laizhou Bay, China. *Mar. Pollut. Bull.* 125 (1), 242–249. doi:10.1016/j.marpolbul.2017.08.027

Suryawan, A., Yuliantoro, I., Subarudiand Prayitno, H. (2019). Resilience Process Due to Drougth of El Nino 2015 at Marampit, the Outermost Island of the Indonesia. *IOP Conf. Ser. Earth Environ. Sci.* 306, 012016. doi:10.1088/1755-1315/306/1/012016

Syarif, M. M., Barus, B., and Effendy, S. (2013). Penentuan Indeks Bahaya Kekeringan Agro-Hidrologi: Studi Kasus Wilayah Sungai Kariango Sulawesi Selatan. *J. Tanah, Lingk,* 15 (1), 12–19. doi:10.29244/jitl.15.1.12-19

Tallar, R. Y., and Dhian, B. A. (2021). A Viable Drought Vulnerability index for Outermost Small Islands in Indonesia. *Groundwater Sustain. Develop.* 15, 100698. doi:10.1016/j.gsd.2021.100698

Tallar, R. Y., and Suen, J.-P. (2016). Aquaculture Water Quality Index: a Low-Cost index to Accelerate Aquaculture Development in Indonesia. *Aquacult Int.* 24 (1), 295–312. doi:10.1007/s10499-015-9926-3

Tallar, R. Y., and Suen, J.-P. (2015). Identification of Waterbody Status in Indonesia by Using Predictive index Assessment Tool. *Int. Soil Water Conservation Res.* 3 (3), 224–238. doi:10.1016/j.iswcr.2015.06.009

Taloor, A. K., Pir, R. A., Adimalla, N., Ali, S., Manhas, D. S., Roy, S., et al. (2020). Spring Water Quality and Discharge Assessment in the Basantar Watershed of Jammu Himalaya Using Geographic Information System (GIS) and Water

Quality Index(WQI). *Groundwater Sustain. Develop.* 10, 100364. doi:10.1016/j.gsd.2020.100364

Valencia, J., Monserrate, F., Casteleyn, S., Bax, V., Francesconi, W., and Quintero, M. (2020). A GIS-Based Methodological Framework to Identify Superficial Water Sources and Their Corresponding Conduction Paths for Gravity-Driven Irrigation Systems in Developing Countries. *Agric. Water Manage.* 232, 106048. doi:10.1016/j.agwat.2020.106048

Wang, P., Qiao, W., Wang, Y., Cao, S., and Zhang, Y. (2020). Urban Drought Vulnerability Assessment - A Framework to Integrate Socio-Economic, Physical, and Policy index in a Vulnerability Contribution Analysis. *Sustain. Cities Soc.* 54, 102004. doi:10.1016/j.scs.2019.102004

Williams, P., Kliskey, A., McCarthy, M., Lammers, R., Alessa, L., and Abatzoglou, J. (2019). Using the Arctic Water Resources Vulnerability index in Assessing and Responding to Environmental Change in Alaskan Communities. *Clim. Risk Manage.* 23, 19–31. doi:10.1016/j.crm.2018.09.001

Wu, J., He, B., Lü, A., Zhou, L., Liu, M., and Zhao, L. (2011). Quantitative Assessment and Spatial Characteristics Analysis of Agricultural Drought Vulnerability in China. *Nat. Hazards* 56, 785–801. doi:10.1007/s11069-010-9591-9

Yang, M., Xiao, W., Zhao, Y., Li, X., Lu, F., Lu, C., et al. (2017). Assessing Agricultural Drought in the Anthropocene: A Modified Palmer Drought Severity Index. *Water* 9 (10), 725. doi:10.3390/w9100725

Zhang, H., Xu, Y., and Kanyerere, T. (2019). Site Assessment for MAR through GIS and Modeling in West Coast, South Africa. *Water* 11 (8), 1646. doi:10.3390/w11081646

Zhang, Y., Huang, S., Huang, Q., Leng, G., Wang, H., and Wang, L. (2019). Assessment of Drought Evolution Characteristics Based on a Nonparametric and Trivariate Integrated Drought index. *J. Hydrol.* 579, 124230. doi:10.1016/j.jhydrol.2019.124230

Conflict of Interest: The authors declare that the research was conducted in the absence of any commercial or financial relationships that could be construed as a potential conflict of interest.

frontiers
in Environmental Science

BRIEF RESEARCH REPORT
published: 08 December 2021
doi: 10.3389/fenvs.2021.806697

Hydrological Performance of Green Roof Systems: A Numerical Investigation

Sang Yeob Kim[1], *Wooyoung Na*[1], *Changhyun Jun*[2]*, *Hyungjoon Seo*[3] *and Yongmin Kim*[4]

[1]School of Civil, Environmental and Architectural Engineering, Korea University, Seoul, South Korea, [2]Department of Civil and Environmental Engineering, Chung-Ang University, Seoul, South Korea, [3]Department of Civil Engineering and Industrial Design, University of Liverpool, Liverpool, United Kingdom, [4]School of Engineering, University of Glasgow Singapore (UGS), Singapore, Singapore

Green roof systems could help reduce peak discharge and retain rainwater in urban areas. The objective of this study was to investigate the hydrological behavior of a green roof system by using the SEEP/W model. The rainfall-runoff relationship within the green roof system was simulated and the results were compared with actual data from a test bed for green roof systems to verify the applicability of SEEP/W. Then, the verified SEEP/W model was used to simulate the green roof system by varying four factors (soil type, rainfall intensity, substrate depth, and green roof slope) to explore the hydrological performance through the peak discharge to rainfall intensity (PD/RI) ratio and the rain water retention rate. The results show that the model presents slightly faster and greater peak time and peak discharge values, respectively, as compared to the observational data. This is attributed to the vegetation conditions in the real green roof system. However, it is also shown that the SEEP/W model can be used to design green roof systems and evaluate their hydrological behavior because of its modeling efficiency. Thus, the SEEP/W model can be used to reliably design and manage green roof systems by further considering the vegetation conditions and water flow dynamics. Furthermore, it would be desirable to consider additional factors, such as vegetation and an insulating pebble layer, in the design and management of green roofs in future work.

Keywords: green roof systems, hydrological performance, rainfall-runoff, SEEP/W model, urban area

Edited by:
Alfrendo Satyanaga,
Nazarbayev University, Kazakhstan

Reviewed by:
Robby Yussac Tallar,
Universitas Kristen Maranatha, Indonesia
Aizat Mohd Taib,
National University of Malaysia, Malaysia

Correspondence:
Changhyun Jun
cjun@cau.ac.kr

Specialty section:
This article was submitted to Freshwater Science, a section of the journal Frontiers in Environmental Science

Received: *01 November 2021*
Accepted: *25 November 2021*
Published: *08 December 2021*

Citation:
Kim SY, Na W, Jun C, Seo H and Kim Y (2021) Hydrological Performance of Green Roof Systems: A Numerical Investigation. Front. Environ. Sci. 9:806697. doi: 10.3389/fenvs.2021.806697

INTRODUCTION

The acceleration of urbanization has induced the stronger impermeability of the subsurface, as farmland, green land, and forest have been replaced by buildings, roads, and pavement (Mentens et al., 2006; Li et al., 2018; Yan et al., 2019). The main environmental problem caused by these impermeable sub-surfaces is that urban hydrological systems should manage a highly fluctuating runoff, which is significantly high during stormwater season (White, 2002). Conventional stormwater systems have only been used for flood reduction and management, while the environmental problems related to urbanization have not been considered (Carter and Fowler, 2008). However, green roof systems can be an effective and eco-friendly rainfall management tool for problems related to uncertain water flows. In addition, green roof systems can also provide environmental benefits such as rainwater retention, peak discharge reduction, and runoff delay (Getter and Rowe, 2006; Feitosa and Wilkinson, 2016; Soulis et al., 2017; Shafique et al., 2018). They can also contribute to reducing the risk of overflow in runoff drainage systems for urban areas (Mentens et al., 2006; Stovin et al., 2017).

Previously, several studies have been conducted to explore how green roofs can absorb rainwater in their planting media, substrate, and drain layer (Scholz, 2004; Teemusk and Mander, 2007; Hilten et al., 2008; Fioretti et al., 2010; Ouldboukhitine et al., 2012; Vijayaraghavan, 2016; Baryła et al., 2018). For instance, Vijayaraghavan (2016) focused on green roof components, such as vegetation, growth substrate, filter layer, and drainage layer, for water absorption and Baryła et al. (2018) investigated the role of substrate in limiting rainwater runoff by assessing its absorption capacity. In addition, Ouldboukhitine et al. (2012) reported that vegetated roof systems, which are a type of green roof system, can reduce the total volume of runoff and peak discharge and can delay the runoff peak time. This helps to mitigate the potential risk of flash flooding, which can be an impact of heavy rain in urban areas (Villarreal et al., 2004). Green roofs have been shown to reduce the total volume of runoff by 60–100%, depending on the type of green roof used (Liesecke, 1998; Moran et al., 2003; Rowe et al., 2003; VanWoert et al., 2005; DeNardo et al., 2005; Hathaway et al., 2008; Speak et al., 2013). Furthermore, the runoff peak time can be delayed by periods ranging from 95 min to 4 h, compared with bare roofs (Liu, 2003; Moran et al., 2003; Simmons et al., 2008; Stovin et al., 2012).

Most of the previous studies on this topic have rarely considered water flow behavior within green roof systems. Several studies have focused on the numerical modeling of green roof systems while considering water flow behavior. She and Pang (2009) established a model that calculates the water content of medium from rainfall using the Storm Water Management Model (SWMM). However, the SWMM is limited in that it does not simulate the detailed physical processes of green roofs. In addition, Kroes et al. (2000) applied the Soil-Water-Atmosphere-Plant (SWAP) model to simulate the influencing factors of green roof systems, but this application was limited to monolithic green roofs, without drainage or storage. Radcliffe and Simunek (2010) developed the HYDRUS model for simulating physical soil changes; however, it was not able to account for green roof water storage structures well. It should be noted that the design of modern green roof systems can permit the storage of rainwater during dry time periods and can allow for rapid drainage during heavy rainfall events.

Thus, the objective of this study was to investigate the hydrological behavior of a green roof system by using the SEEP/W model for design and management purposes. The SEEP/W model was used to simulate water flow behavior within green roofs, considering the physical processes of water flow in a medium and simulating a transient steady state, which presents the difference between inflow and outflow. The simulation results were compared with observational data from a test bed for green roofs established at Nanyang Technological University (NTU) in Singapore. The methodology is presented in the next section, followed by a case study, analyses and discussions of results, and conclusions.

MATERIALS AND METHODS

SEEP/W Model

The SEEP/W model was designed to calculate water flow in both saturated and unsaturated porous materials. It uses the finite element method (FEM) for numerical analysis (Thieu et al., 2001; Krahn, 2004; Chu-Agor et al., 2008). In this numerical analysis, the modeling geometry is primarily created to perform grid generation by defining the element size and shape (e.g., rectangular). Then, the material properties are determined by adopting the soil type (e.g., saturated/unsaturated silt or clay). This step defines the particle size and distribution, which together affect the volumetric water content. Notably, the particle size distribution, which can be represented *via* pore size distribution, determines hydraulic properties such as the soil-water characteristic curve and permeability (Zhai et al., 2019). However, pore size distribution has been rarely used for hydraulic conductivity estimation (Zhai et al., 2018). In this study, the geometric grid generation step is used to represent the pore size distribution, even though it cannot entirely represent the actual pore size distribution. In addition, volumetric water content, which is a function of the material's moisture content, is reflected. Then, the hydraulic conductivity function defines the permeability with respect to the material moisture content of each element, including the residual water content. For the volumetric water content and hydraulic conductivity, the functions are set to estimate water flow. The volumetric water content, which is significantly affected by particle size and distribution, describes the portion of pores that are filled with water. When setting the volumetric water content, is important to specify the hydraulic conductivity of the porous materials that have unsaturated pores. In addition, there are options in the SEEP/W model for material properties and boundary conditions. The model considers two sets of partial differential equilibrium equations and the first governing equation for soil mass is described as follows:

$$\frac{\partial \sigma_{ij}}{\partial x_i} + \rho g_j = 0 \tag{1}$$

where σ_{ij} represents the components of the total stress tensor, ρ is the total mass density, and g_j is *jth* component of the gravitational acceleration vector. The second governing equation for water flow is expressed as follows:

$$\frac{\partial q_x}{\partial x} + \frac{\partial q_y}{\partial v} + \frac{\partial q_z}{\partial z} + \frac{\partial \theta_w}{\partial t} = 0 \tag{2}$$

where q_x, q_y, and q_z are the flow velocities of the solid matrix in the x, y, and z directions, respectively. θ_w is the volumetric water content and t is time. Using Darcy's law, flow velocities, q_i, can be estimated from the following relationship:

$$q_i = -k_i \frac{\partial}{\partial x_i}\left(\frac{u_w}{\rho_w g} + z\right) \tag{3}$$

where k_i is the unsaturated permeability in the i direction, u_w is the pore-water pressure, ρ_w is the water density, g is the gravitational acceleration constant, and z is the vertical

TABLE 1 | Material properties and parameters used in the SEEP/W model.

Property	Value	
Unsaturated (residual) water content [%]	0.05	
Saturated water content [%]	0.3	
Permeability of silty clay [mm/s]	5e-05	
Permeability for clay [mm/s]	1e-06	
Water pressure head at water outlet	0	
a-parameter	$a = \frac{1}{\Psi}\left(2^{\frac{1}{m}} - 1\right)^{(1-m)}$ $(S_p > 1)$	
m-parameter	$m = 1 - \frac{0.5755}{Sp} + \frac{0.1}{Sp^2} + \frac{0.025}{Sp^3}$ $(0 < S_p < 1)$	
Rainfall intensity [mm/min]	2.5	15.0
Substrate depth [mm]	100	300
Slope [degrees]	0	10

coordinate. Then, the initial condition that specifies the pore water pressure distribution is determined. For the green roof test bed simulation, the ground water table is set at the bottom of the drainage layer, and an unsaturated condition, which generates a negative pore pressure, is considered for the substrate. However, as the maximum pore pressure is only 0.25 kPa because of the shallow substrate depth (25 cm), the substrate is set as fully saturated in this study. Finally, the boundary conditions are determined to set the head or total flow rate, which provide a driving force of water flow with the water pressure head at the outlet of the green roof system. More detailed information for the physics in terms of soil water content, hydraulic conductivity, total head, and pore pressure can be found in GEOSLOPE International Ltd. (2017).

Factors in the SEEP/W Model

Numerical simulations using the SEEP/W model are useful for scheme selection, as one factor can be adjusted while the other factors remain constant. This approach can be used to estimate the most influential factor by simulating the water flow behavior within green roof systems. Through the simulation results, the degree of influence of each factor on the hydrological performance of green roofs can be estimated. Different values for each factor can be applied to evaluate the impact of changing each factor on the runoff characteristics in the SEEP/W model.

This study considers four factors: soil type, rainfall intensity, substrate depth, and green roof slope. These factors have been found to be sensitive to the hydrological performance of green roof systems, and can be adjusted by changing their geometry, material properties, volumetric water content, hydraulic conductivity, and boundary conditions. The properties and parameters used in the simulations are summarized in **Table 1**. First, the silt and clay soil types were selected for the evaluation of the material properties effects. Note that the green roof soil type that has been generally used is silty clay because of its significant influence on infiltration, water retention, and plant survival in dry conditions (Eksi et al., 2020; Liu et al., 2020). The hydraulic conductivity of silt and clay was set to 5e-05 and 1e-06 mm/s, respectively. It is worth noting that the hydraulic conductivity of silt is typically larger than 1e-05 mm/s and that of clay is typically less than 1e-05 mm/s (Reynolds and Zebchuk, 1996; Chandel and Kumar, 2016). Secondly, the rainfall intensities were set to 2.5 and 15 mm/min to consider changes in the volumetric water content. Substrate depths of 100 and 300 mm were adopted to determine the impact of water storage on flow rates. Finally, the green roof slopes were set to be 0 and 10 degrees, relevant to the effect of the head and flow rates, which determine the hydraulic conductivity.

CASE STUDY

Green Roof Systems

For conventional roofs, heavy rain induces a large amount of runoff, as the roof instantaneously releases the rainwater during a rainfall event. Green roof systems, however, gradually release rainwater over a period of time, as they can store the rainwater through infiltration into the substrate and drainage layers. In particular, they alleviate potential damage from heavy rainfall by delaying the peak time of runoff, temporarily retaining rainwater through infiltration, reducing peak discharge of runoff, and storing water in the substrate and drainage layer, owing to the absorption capacity of soils.

Green roof systems are basically composed of the substrate and drainage layers, which can mitigate problems from dramatic runoff after heavy rain in urbanized areas. The substrate layer retains water, and the drainage layer discharges the infiltrated water flow. Green roofs can be divided into either extensive or intensive systems with respect to the depth of the substrate layer. Extensive systems have substrate layers with depths of less than 100 mm and can be incorporated on sloped surfaces with angles up to 45degrees (VanWoert et al., 2005; Kosareo and Ries, 2007). In addition, extensive systems can be used on the roofs of buildings that are limited by weight restrictions. Conversely, the intensive system used in this study had a substrate depth of more than 100 mm, and it can only be used on slopes with angles of less than 10 degrees (Kosareo and Ries, 2007).

Test Bed in Singapore

Green roof systems have been promoted as a method to manage rainwater in urbanized countries such as Germany, Japan, Belgium, and Singapore (Osmundson, 1999; Wong et al., 2003; Dunnett and Kingsbury, 2004). In this study, a test bed of a green roof was considered to evaluate the numerical results of the SEEP/W model from observational data located at Nanyang Technological University (NTU) in Singapore. **Figure 1** shows an overall layout of the green roofs at NTU and shows a design concept of its main frame. The dimensions of the green roof system were 2˚m × 2˚m, comprising four plant boxes, each 1˚m × 1˚m. It had an angle of 5 degrees. It is worth noting that previous studies demonstrated that a green roof covering over 70% of the rooftop allows stormwater quantity management (Carter and Fowler, 2008). The dimensions of the green roof in this study are limited owing to the lack of rooftop coverage; however, the test bed is installed for the prototype chamber test.

The test bed of the green roofs was elevated 400 mm from the ground, in order to have a sufficient height to measure the flow rate. **Figure 2** shows that each plant box was filled with soil and

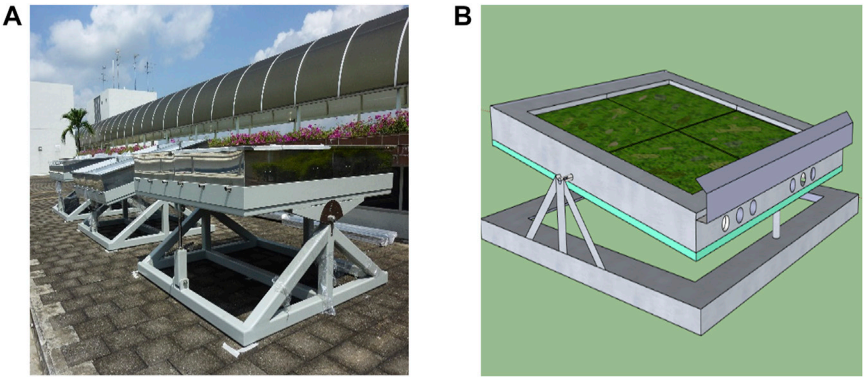

FIGURE 1 | Green roof test bed at NTU in Singapore: **(A)** overall layout; **(B)** design concept of a main frame.

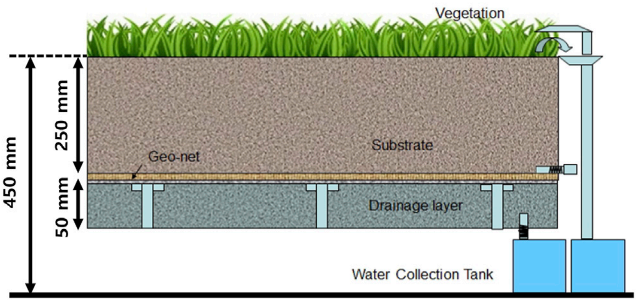

FIGURE 2 | Structural components of the green roofs at NTU (Qin et al., 2012).

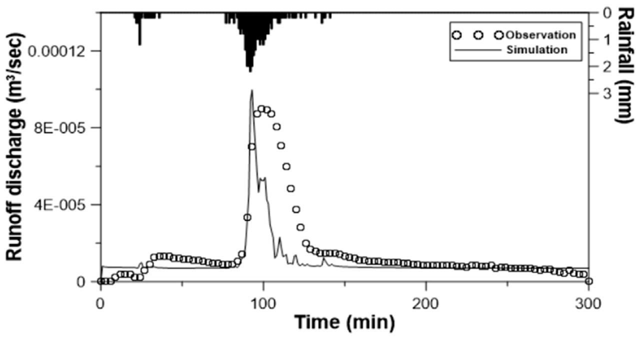

FIGURE 4 | Rainfall-runoff relationship of the simulated results from the SEEP/W model and the observed data of the green roof system at NTU.

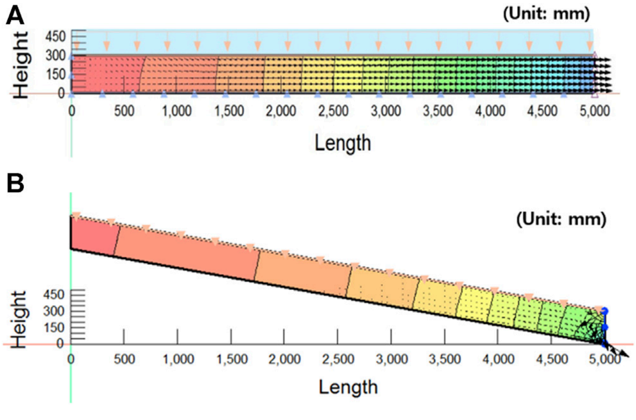

FIGURE 3 | Interface of the SEEP/W model for the simulation of green roof systems: **(A)** without a slope; **(B)** with a slope of 10 degrees.

plants (cuphea with grass) to a depth of 250 mm, and those plants were placed above the substrate layer. The bottom filtration tray, which had a depth of 50 mm filled with pebbles, was located beneath the substrate layer to allow rainwater drainage. In addition, two tanks were prepared to collect the infiltrated water discharge from the surface runoff and the base flow, including the leachate.

RESULTS AND DISCUSSION

Interface of the SEEP/W Model

The SEEP/W model numerically simulated the hydrological behavior of the green roof systems, as shown in **Figure 3**, which presents typical models of green roof systems with 300-mm-thick substrate layers with slopes of 0 and 10 degrees. The upper and right-side boundaries were set to be permeable, whereas the bottom and left-side boundaries were set to be impervious, to simulate the interface conditions of the green roof systems. In addition, the colors of the substrate zones represent the water head within each specific section. The water flows from the left side to the right side because of the head difference during rainfall, and the black arrows indicate the direction of water flow during runoff processes. Here, the size of each black arrow represents the amount of runoff discharge.

Simulation Results of Green Roofs at NTU

The SEEP/W model simulated the actual green roof system at the test bed at NTU, Singapore. The set values of factors for the SEEP/

W model followed the actual data from the green roofs at NTU, which have a slope of 5 degrees. The substrate layer, shown in yellow in **Figure 3**, was filled with soil, and the additional layer in green represents the infiltration tray beneath the soil substrate. Furthermore, the arrows in blue and black represent the rainfall on the green roof and the runoff through the outlet at the right-hand side bottom corner, respectively. **Figure 4** summarizes the comparison between the simulated and experimental rainfall-runoff relationship results.

Due to the rainfall event shown in **Figure 4**, the peak time and peak discharge from the SEEP/W simulation were calculated as 92 min and 99.79 cm^3/s, respectively, while those from the observation data were 102 min and 89.5 cm^3/s, respectively. Specifically, the increase of runoff discharge starts at 85 min in the simulation, while it starts at 86 min in the observational data. The increasing trend continues in both until approximately 91 min. Thereafter, the difference in peak discharge between the simulation and the observational data is 10.29 cm^3/s. Finally, the direct runoff from the test bed ended at ~ 150 min in the simulation case, which was approximately 50 min earlier than in the observational data.

The peak time in the SEEP/W simulation result was faster than the equivalent value in the observational data, while the simulated peak discharge was greater than the observational value. This difference may result from the modeling interface, which simulates only water flow through the substrate layer and does not consider the vegetation in the green roof system. In the actual green roof system, the vegetation can absorb rainwater and hinders the flow of infiltrated water from the surface to the substrate layer. The vegetation may delay the peak time and lower the peak discharge from the observational data, compared with that from the numerical results of the SEEP/W model. However, the simulated and observational runoff discharge trends over time are similar.

The simulation results of the green roofs at NTU show that the SEEP/W model can be used for the design and management of green roofs despite the vegetation consideration limitation. It can therefore contribute to improving the current understanding of flow dynamics within green roof systems. As the SEEP/W model can also describe the hydrological behavior of green roofs under different conditions, and can quantify flow responses at the outlet of the system, the effectiveness of green roofs can be evaluated from the results of its numerical modeling, with respect to storm water mitigation, as a measure for rainwater management in urban areas.

Sensitivity Analysis in Hydrologic Modeling

This study explores the impacts of different factors in the SEEP/W model, regarding the hydrological performance of a green roof system according to four factors, soil type, rainfall intensity, substrate depth, and green roof slope. In the SEEP/W model simulation, the initial conditions depend on material properties and the interface setting. Two soil types, clay and silty clay, were considered in the sensitivity analysis. The hydraulic conductivity of clay and silty clay were 5e-05 and 1e-06 mm/s, respectively. Additionally, rainfall duration in the simulation was set to 10 min. Two indicators were considered to evaluate the effect of each factor in the SEEP/W model, these indicators were the peak discharge to rainfall intensity (PD/RI) ratio and the rainwater retention rate. The PD/RI ratio is calculated as the peak discharge divided by rainfall intensity, and the rainwater retention rate is the ratio of rainfall that does not run off the green roof to potential runoff of total rainfall (Getter et al., 2007). **Figure 5** provides a comparison between the results of various groups, depending on the values of the factors considered.

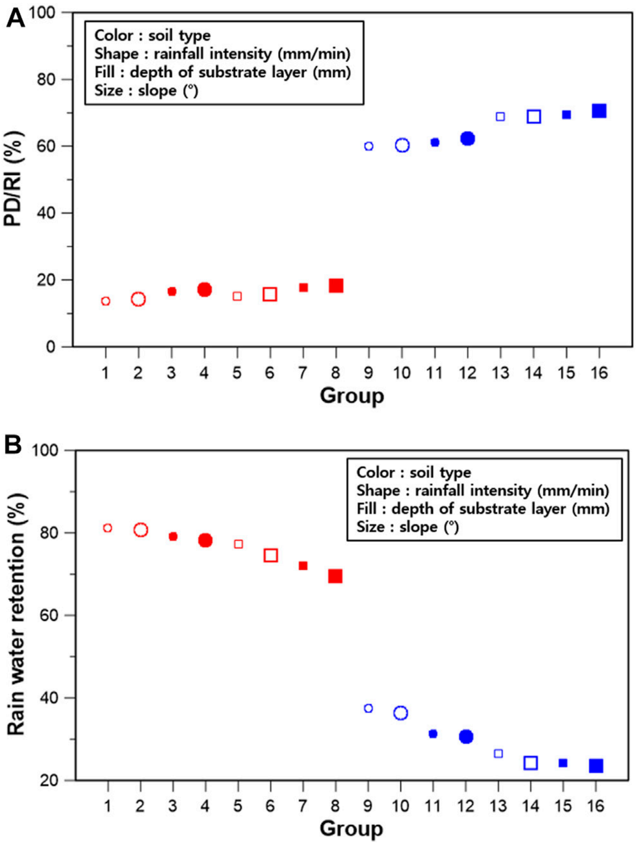

FIGURE 5 | Results of the sensitivity analysis of different factors to assess the hydrological performance of green roof systems: **(A)** PD/RI ratio; **(B)** Rainwater retention rate. Note: red-clay and blue-silty clay; circle-2.5 mm/min and square-15.0 mm/min; open-300 mm and closed-100 mm; small-0 degrees and large-10 degrees.

First, the mean PD/RI ratio value of clay (groups 1–8) was approximately 24.6% of that of silty clay (groups 9–16), and the mean rainwater retention rate value of clay was approximately 261.5% of that of silty clay. The PD/RI and rainwater retention values indicate that the hydrological performance of clay was better than that of silty clay. The hydraulic conductivity determined the drainage characteristics, which is a function of soil properties, such as particle size, particle distribution, and chemical composition. The hydraulic conductivity of clay is typically less than 1e-05 mm/s, and it tends to be impermeable. Silt and silty clay, however, typically have a hydraulic conductivity between 1e-05 and 1e-03 mm/s (Chandel and Kumar, 2016). In addition, the negative ionic characteristics of the clay particle's surfaces may generate hydrogen bonding with water molecules (Barshad, 1952). For this reason, the chemical composition of clay particles mean that they absorb water and form double-layer water, which is one of the reasons for the observed water retention. Thus, the lower hydraulic conductivity and chemical composition of clay may have resulted in the observed lower PD/RI ratio and greater rainwater retention in clay compared with silty clay.

Second, the mean PD/RI value under a rainfall intensity of 2.5 mm/min (groups 1–4 and 9–12) was approximately 88.7% of that under a rainfall intensity of 15 mm/min (groups 5–8 and 13–16). Conversely, the mean rainwater retention value of the groups with relatively lower rainfall intensities were approximately 116.2% of that of the other groups. This is consistent with the results of Teemusk and Mander (2007), who identified the volume and intensity of rainwater as important factors determining the amount of water that is retained in a green roof system. Even though the rainfall intensity, which can be a source of water retention, is high, the water retention rate becomes lower if the rainfall intensity is extremely high, as in the case of storm events (Carter and Rasmussen, 2005; Moran et al., 2005). Thus, the green roof system design should provide practical alternatives, such as selection of clay materials for the substrate, for delaying and attenuating runoff discharge at source.

Third, the mean PD/RI value in substrate layers with depths of 300 mm (groups 1–2, 5–6, 9–10, and 13–14) was approximately 95.0% of that when the depth was 100 mm (groups 3–4, 7–8, 11–12, and 15–16). The mean rainwater retention rate value of the first group was approximately 107.3% of that of the other groups. During a rainfall event, one of the key hydrological mechanisms in a green roof system is storage and infiltration in the substrate layer (Stovin, 2010). This process is directly related to the retention capacity of the soil in a green roof system, and the shape of the hydrograph at the outlet is determined from the relationship between the rainfall characteristics during a storm event and the potential absorption rates in the soil column. Even though there was no significant difference in hydrological performance between the two different substrate layers considered in this study, previous studies have shown that rainfall-runoff relationships in green roof systems can be significantly affected by the substrate layer depth over a long time period (Mentens et al., 2006).

Finally, the mean PD/RI value of green roofs with a slope of 0 degree (groups 1, 3, 5, 7, 9, 11, 13, and 15) was approximately 98.7% of that of green roofs with slopes of 10 degrees (groups 2, 4, 6, 8, 10, 12, 14, and 16). The mean rainwater retention rate value of the first group was approximately 102.7% of that of the other groups. The decrease in slope of a green roof is slightly beneficial in terms of decreasing the PD/RI ratio and increasing the rainwater retention rate. However, the slope of a green roof was found to have less of an impact on its hydrological performance than the other factors (Liesecke, 1998; Mentens et al., 2006).

CONCLUSION

The objective of this study was to investigate the hydrological behavior of a green roof system by using the SEEP/W model, for design and management purposes. The interface of the SEEP/W model was set to simulate a green roof, and its geometry, material property, volumetric water content, hydraulic conductivity, and boundary conditions were explored. A green roof test bed was installed at NTU to measure actual hydrometeorological data, including rainfall and runoff data. The actual data were compared with the simulated results from the SEEP/W model to evaluate the applicability of the model to green roof design and management. For the simulations, different values for four factors (soil type, rainfall intensity, substrate depth, and green roof slope) were considered in order to determine their impact on the hydrological performances of green roofs. The hydrological performance was estimated *via* the PD/RI ratio and the rainwater retention rate. The main findings of this study are as follows:

1) Comparing the simulation results and observational data revealed that the simulated peak time and peak discharge values were slightly faster and greater than those of the observational data, which is attributed to the vegetation conditions in the real green roof system. However, the results show that the SEEP/W model can be used in green roof design because of its effectiveness in terms of modeling the hydrological behavior of a green roof system, while considering water flow dynamics. In future work, additional factors, such as vegetation and an insulating pebble layer, should be considered for the design and management of green roofs. In addition, it should be noted that this study can be further extended to the design, construction, rehabilitation, operation, and maintenance of low-impact development or green infra systems, which are being widely used for critical infrastructure elements in water sensitive urban design.
2) The decrease in the PD/RI ratio and increase in the rainwater retention rate denote a better hydrological performance of the green roofs. The simulation results revealed that the hydrological performance was better for clay than for silty clay because of the lower hydraulic conductivity of the former, and the effects of chemical composition. In addition, a lower rainfall intensity and a thicker substrate layer were shown to result in a better hydrological performance, as they mainly determine the rainfall-runoff relationship. The slope of the green roof, however, was shown to have no significant effect on the hydrological performance, resulting in a negligible difference in the PD/RI ratio and rainwater retention rate. In conclusion, the water flow characteristics are primarily dependent on soil type, which in turn determine the hydrological performance of a green roof system.

DATA AVAILABILITY STATEMENT

The original contributions presented in the study are included in the article/Supplementary Material, further inquiries can be directed to the corresponding author.

AUTHOR CONTRIBUTIONS

Conceptualization, CJ and SK; methodology, CJ, HS, and YK; software, SK and WN; validation, SK and WN; formal analysis, CJ; investigation, CJ, SK, and WN; resources, CJ and SK; data curation, CJ; writing—original draft preparation, CJ and SK; writing—review and editing, CJ, SK, WN, HS, and YK; visualization, SK and WN.

FUNDING

This research was supported by the National Research Foundation of Korea (NRF) grant funded by the Korea Government (MSIT) (2020R1G1A101362412) and in part by the Chung-Ang University Research Grants in 2021.

ACKNOWLEDGMENTS

The corresponding author was formerly affiliated with the School of Civil and Environmental Engineering, Nanyang Technological University. We deeply appreciate the data support from Professor Xiaosheng Qin at Nanyang Technological University.

REFERENCES

Barshad, I. (1952). Adsorptive and Swelling Properties of Clay-Water System. *Clays and Clay Minerals* 1 (1), 70–77. doi:10.1346/CCMN.1952.0010108

Baryła, A., Karczmarczyk, A., and Bus, A. (2018). Role of Substrates Used for green Roofs in Limiting Rainwater Runoff. *J. Ecol. Eng.* 19 (5), 86–92. doi:10.12911/22998993/91268

Carter, T., and Fowler, L. (2008). Establishing green Roof Infrastructure through Environmental Policy Instruments. *Environ. Manage.* 42 (1), 151–164. doi:10.1007/s00267-008-9095-5

Carter, T., and Rasmussen, T. (2005). Use of green Roofs for Ultra-urban Stream Restoration in the Georgia piedmont (USA)," in Proceedings of the 3rd North American Green Roof Conference: Greening Rooftops for Sustainable Communities, Washington, DC, US. May 4-6, 2005.

Castiglia Feitosa, R., and Wilkinson, S. (2016). Modelling green Roof Stormwater Response for Different Soil Depths. *Landscape Urban Plann.* 153, 170–179. doi:10.1016/j.landurbplan.2016.05.007

Chandel, A., and Kumar, U. (2016). "Permeability Characteristics of Clayey Soil Added with Fly Ash. Proceedings of International Conference on Emerging Trends in Civil Engineering (ICETCE-2016)," in Sultanpur, India, October 2016. 207–209.

Chu-Agor, M. L., Wilson, G. V., and Fox, G. A. (2008). Numerical Modeling of Bank Instability by Seepage Erosion Undercutting of Layered Streambanks. *J. Hydrol. Eng.* 13 (12), 1133–1145. doi:10.1061/(asce)1084-0699(2008)13:12(1133)

DeNardo, J. C., Jarrett, A. R., Manbeck, H. B., Beattie, D. J., and Berghage, R. D. (2005). Stormwater Mitigation and Surface Temperature Reduction by green Roofs. *Trans. ASAE.* 48 (4), 1491–1496. doi:10.13031/2013.19181

Dunnett, N., and Kingsbury, N. (2004). *Planting Green Roofs and Living Walls*. Portland, OR: Timber Press.

Eksi, M., Sevgi, O., Akburak, S., Yurtseven, H., and Esin, İ. (2020). Assessment of Recycled or Locally Available Materials as green Roof Substrates. *Ecol. Eng.* 156, 105966. doi:10.1016/j.ecoleng.2020.105966

Fioretti, R., Palla, A., Lanza, L. G., and Principi, P. (2010). Green Roof Energy and Water Related Performance in the Mediterranean Climate. *Building Environ.* 45 (8), 1890–1904. doi:10.1016/j.buildenv.2010.03.001

GEOSLOPE International Ltd (2017). *Heat and Mass Transfer Modeling with GeoStudio 2018*. 2nd Edition. Calgary, Alberta, Canada: GEOSLOPE International Ltd.

Getter, K. L., Rowe, D. B., and Andresen, J. A. (2007). Quantifying the Effect of Slope on Extensive green Roof Stormwater Retention. *Ecol. Eng.* 31 (4), 225–231. doi:10.1016/j.ecoleng.2007.06.004

Getter, K. L., and Rowe, D. B. (2006). The Role of Extensive green Roofs in Sustainable Development. *HortSci* 41 (5), 1276–1285. doi:10.21273/HORTSCI.41.5.1276

Hathaway, A. M., Hunt, W. F., and Jennings, G. D. (2008). A Field Study of green Roof Hydrologic and Water Quality Performance. *Trans. ASABE* 51 (1), 37–44. doi:10.13031/2013.24225

Hilten, R. N., Lawrence, T. M., and Tollner, E. W. (2008). Modeling Stormwater Runoff from green Roofs with HYDRUS-1D. *J. Hydrol.* 358 (3-4), 288–293. doi:10.1016/j.jhydrol.2008.06.010

Kosareo, L., and Ries, R. (2007). Comparative Environmental Life Cycle Assessment of green Roofs. *Building Environ.* 42 (7), 2606–2613. doi:10.1016/j.buildenv.2006.06.019

Krahn, J. (2004). *Seepage Modeling with SEEP/W: An Engineering Methodology*. Calgary, Alberta, Canada: GEOSLOPE International Ltd.

Kroes, J. G., Wesseling, J. G., and Van Dam, J. C. (2000). Integrated Modelling of the Soil–Water–Atmosphere–Plant System Using the Model SWAP 2.0 an Overview of Theory and an Application. *Hydrol. Process.* 14 (11-12), 1993–2002. doi:10.1002/1099-1085(20000815/30)14:11/12<1993:aid-hyp50>3.0.co;2-#

Li, W., Wu, C., and Choi, W. (2018). Predicting Future Urban Impervious Surface Distribution Using Cellular Automata and Regression Analysis. *Earth Sci. Inform.* 11 (1), 19–29. doi:10.1007/s12145-017-0312-8

Liesecke, H. J. (1998). Das retentionsvermogen von dachbegrunungen (Water retention capacity of vegetated roofs). *Stadt und Grun* 47, 46–53.

Liu, K. (2003). Engineering Performance of Rooftop Gardens through Field Evaluation. "Proceedings of the 18th International Convention of the Roof Consultants Institute," in Tampa, Florida, March 13-18, 2003. 93–103.

Liu, L., Sun, L., Niu, J., and Riley, W. J. (2020). Modeling green Roof Potential to Mitigate Urban Flooding in a Chinese City. *Water* 12 (8), 2082. doi:10.3390/w12082082

Mentens, J., Raes, D., and Hermy, M. (2006). Green Roofs as a Tool for Solving the Rainwater Runoff Problem in the Urbanized 21st century? *Landscape Urban Plann.* 77 (3), 217–226. doi:10.1016/j.landurbplan.2005.02.010

Moran, A., Hunt, B., and Jennings, G. (2003). "A North Carolina Field Study to Evaluate Greenroof Runoff Quantity, Runoff Quality, and Plant Growth," in Proceedings of the World Water & Environmental Resources Congress 2003, Philadelphia, Pennsylvania, US, June 23-26, 2003, 1–10. doi:10.1061/40685(2003)335

Moran, A., Hunt, B., and Smith, J. (2005). "Hydrologic and Water Quality Performance from green Roofs in Goldsboro and Raleigh, North Carolina," in Proceedings of the 3rd North American Green Roof Conference: Greening Rooftops for Sustainable Communities, Washington, DC, US, May 4-6, 2005.

Osmundson, T. (1999). *Roof Gardens, History, Design, Construction*. NY, USA: Norton & Co.

Ouldboukhitine, S.-E., Belarbi, R., and Djedjig, R. (2012). Characterization of green Roof Components: Measurements of thermal and Hydrological Properties. *Building Environ.* 56, 78–85. doi:10.1016/j.buildenv.2012.02.024

Qin, X., Wu, X., Chiew, Y. M., and Li, Y. (2012). A green Roof Test Bed for Stormwater Management and Reduction of Urban Heat Island Effect in Singapore. *Bjecc* 2 (4), 410–420. doi:10.9734/BJECC/2012/2704

Radcliffe, D. E., and Simunek, J. (2010). *Soil Physics with HYDRUS—Modelling and Applications*. Boca Raton, FL: CRC Press.

Reynolds, W. D., and Zebchuk, W. D. (1996). Hydraulic Conductivity in a clay Soil: Two Measurement Techniques and Spatial Characterization. *Soil Sci. Soc. America J.* 60 (6), 1679–1685. doi:10.2136/sssaj1996.03615995006000060011x

Rowe, D. B., Rugh, C. L., VanWoert, N., Monterusso, M. A., and Russell, D. K. (2003). Green Roof Slope, Substrate Depth, and Vegetation Influence Runoff," in Proceedings of the 1st North American Green Roof Conference: Greening Rooftops for Sustainable Communities, Chicago, IL, USA, May 29-30, 2003. 354–362.

Scholz, M. (2004). Case Study: Design, Operation, Maintenance and Water Quality Management of Sustainable Storm Water Ponds for Roof Runoff. *Bioresour. Tech.* 95 (3), 269–279. doi:10.1016/j.biortech.2003.07.015

Shafique, M., Kim, R., and Rafiq, M. (2018). Green Roof Benefits, Opportunities and Challenges - A Review. *Renew. Sust. Energ. Rev.* 90, 757–773. doi:10.1016/j.rser.2018.04.006

She, N., and Pang, J. (2009). Physically Based green Roof Model. *J. Hydrol. Eng.* 15 (6), 458–464. doi:10.1061/(ASCE)HE.1943-5584.0000138

Simmons, M. T., Gardiner, B., Windhager, S., and Tinsley, J. (2008). Green Roofs Are Not Created Equal: the Hydrologic and thermal Performance of Six Different Extensive green Roofs and Reflective and Non-reflective Roofs in a Sub-tropical Climate. *Urban Ecosyst.* 11 (4), 339–348. doi:10.1007/s11252-008-0069-4

Soulis, K. X., Ntoulas, N., Nektarios, P. A., and Kargas, G. (2017). Runoff Reduction from Extensive green Roofs Having Different Substrate Depth and Plant Cover. *Ecol. Eng.* 102, 80–89. doi:10.1016/j.ecoleng.2017.01.031

Speak, A. F., Rothwell, J. J., Lindley, S. J., and Smith, C. L. (2013). Rainwater Runoff Retention on an Aged Intensive green Roof. *Sci. Total Environ.* 461-462 (1), 28–38. doi:10.1016/j.scitotenv.2013.04.085

Stovin, V. (2010). The Potential of green Roofs to Manage Urban Stormwater. *Water Environ. J.* 24 (3), 192–199. doi:10.1111/j.1747-6593.2009.00174.x

Stovin, V., Vesuviano, G., and De-Ville, S. (2017). Defining green Roof Detention Performance. *Urban Water J.* 14 (6), 574–588. doi:10.1080/1573062X.2015.1049279

Stovin, V., Vesuviano, G., and Kasmin, H. (2012). The Hydrological Performance of a green Roof Test Bed under UK Climatic Conditions. *J. Hydrol.* 414-415 (11), 148–161. doi:10.1016/j.jhydrol.2011.10.022

Teemusk, A., and Mander, Ü. (2007). Rainwater Runoff Quantity and Quality Performance from a Greenroof: the Effects of Short-Term Events. *Ecol. Eng.* 30 (3), 271–277. doi:10.1016/j.ecoleng.2007.01.009

Thieu, N. T. M., Fredlund, M. D., Fredlund, D. G., and Vu, H. Q. (2001). "Seepage Modeling in a Saturated/unsaturated Soil System," in Proceedings of the International Conference on Management of the Land and Water Resources, Hanoi, Vietnam, October 2001. 20–22.

VanWoert, N. D., Rowe, D. B., Andresen, J. A., Rugh, C. L., Fernandez, R. T., and Xiao, L. (2005). Green Roof Stormwater Retention. *J. Environ. Qual.* 34 (3), 1036–1044. doi:10.2134/jeq2004.0364

Vijayaraghavan, K. (2016). Green Roofs: A Critical Review on the Role of Components, Benefits, Limitations and Trends. *Renew. Sust. Energ. Rev.* 57, 740–752. doi:10.1016/j.rser.2015.12.119

Villarreal, E. L., Semadeni-Davies, A., and Bengtsson, L. (2004). Inner City Stormwater Control Using a Combination of Best Management Practices. *Ecol. Eng.* 22 (4-5), 279–298. doi:10.1016/j.ecoleng.2004.06.007

White, R. (2002). *Building the Ecological City*. Amsterdam, Netherland: Elsevier.

Wong, N. H., Tay, S. F., Wong, R., Ong, C. L., and Sia, A. (2003). Life Cycle Cost Analysis of Rooftop Gardens in Singapore. *Building Environ.* 38 (3), 499–509. doi:10.1016/S0360-1323(02)00131-2

Yan, Z., Teng, M., He, W., Liu, A., Li, Y., and Wang, P. (2019). Impervious Surface Area Is a Key Predictor for Urban Plant Diversity in a City Undergone Rapid Urbanization. *Sci. Total Environ.* 650, 335–342. doi:10.1016/j.scitotenv.2018.09.025

Zhai, Q., Rahardjo, H., and Satyanaga, A. (2018). A Pore-Size Distribution Function Based Method for Estimation of Hydraulic Properties of Sandy Soils. *Eng. Geol.* 246, 288–292. doi:10.1016/j.enggeo.2018.09.031

Zhai, C., Rahardjo, H., Satyanaga, A., and Dai, G. L. (2019). Role of the Pore-Size Distribution Function on Water Flow in Unsaturated Soil. *J. Zhejiang Univ. Sci.* 20 (1), 10–20. doi:10.1631/jzus.A1800347

Conflict of Interest: The authors declare that the research was conducted in the absence of any commercial or financial relationships that could be construed as a potential conflict of interest.

Frontiers in
Environmental Science

Explores the anthropogenic impact on our natural world

An innovative journal that advances knowledge of the natural world and its intersections with human society. It supports the formulation of policies that lead to a more inhabitable and sustainable world.

Discover the latest Research Topics

See more →

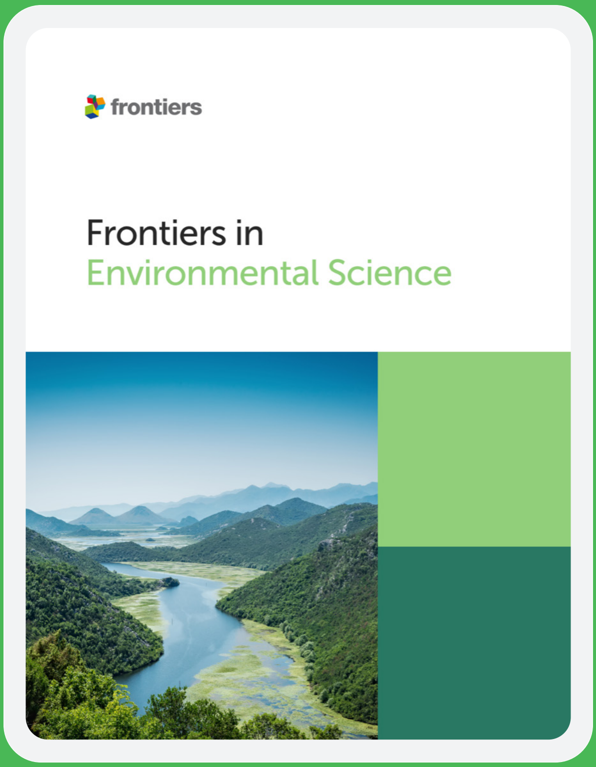

frontiers

Frontiers in
Environmental Science

Frontiers

Avenue du Tribunal-Fédéral 34
1005 Lausanne, Switzerland
frontiersin.org

Contact us

+41 (0)21 510 17 00
frontiersin.org/about/contact